

The Pennsylvania State University  
The Graduate School  
Graduate Program in Astronomy and Astrophysics

THE PHOTOMETRIC AND KINEMATIC STRUCTURE AND  
ASYMMETRY OF DISK GALAXIES

A Thesis in  
Astronomy and Astrophysics  
by  
David R. Andersen

© 2001 David R. Andersen

Submitted in Partial Fulfillment  
of the Requirements  
for the Degree of

Doctor of Philosophy

December 2001

We approve the thesis of David R. Andersen.

Date of Signature

---

Matthew A. Bershady  
Assistant Professor of Astronomy and Astrophysics  
Thesis Adviser  
Co-Chair of Committee

---

Lawrence W. Ramsey  
Professor of Astronomy and Astrophysics  
Co-Chair of Committee

---

Robin B. Ciardullo  
Associate Professor of Astronomy and Astrophysics

---

Steinn Sigurdsson  
Assistant Professor of Astronomy and Astrophysics

---

James J. Beatty  
Associate Professor of Physics and Astronomy and Astrophysics

---

Peter I. Mészáros  
Professor of Astronomy and Astrophysics  
Head of the Department of Astronomy and Astrophysics

## Abstract

We establish a sample of 39 nearby, nearly face-on disk galaxies for a detailed study of their photometric and kinematic structure and asymmetries. For this sample we collected two-dimensional  $H\alpha$  velocity-fields at echelle resolutions with the DensePak integral field unit on the WIYN 3.5m telescope, HI line widths taken with the Nançay radio telescope, and deep  $R$  and  $I$ -band imaging from the WIYN telescope, the 2.1m telescope at KPNO, and the Harlan J. Smith 2.7m telescope at McDonald Observatory. We use these data to put constraints on the shape of disk galaxies and their halos and to study the fundamental disk galaxy scaling relationship between rotation speed and luminosity, i.e., the Tully-Fisher relation. To study the shapes of galaxy disks, we measured both photometric and kinematic asymmetries. From studies of the asymmetry, we were able to show that the now commonly used photometric rotational asymmetry index does not measure disk flocculence as previously suggested; instead it is shown to be equivalent to low order, odd Fourier amplitudes, i.e., lopsidedness. In addition to studying disk lopsidedness, we establish a set of kinematic and photometric indices which we use to present the first measurements of disk ellipticity for galaxies outside the Milky Way. These measurements are decoupled from a phase angle (between the line of nodes and major axis of the un-inclined, elliptical galaxy) which plagues previous estimates of disk ellipticity. Nonetheless, our disk ellipticity measurement of  $0.083 \pm 0.054$  is consistent with these previous estimates. This measurement allows us to put a limit of 0.15 mag on Tully-Fisher scatter due to the intrinsic ellipticity of disk galaxies. Kinematic inclination

angles, one of the primary kinematic indices used to measure disk ellipticity, were derived from model velocity-field fits to our  $H\alpha$  velocity fields. These inclinations are shown to be both accurate and precise and allowed us to create the first Tully-Fisher relation for nearly face-on disk galaxies. We demonstrate that our face-on Tully-Fisher sample is well fit by a published Tully-Fisher relation. In fact, the Tully-Fisher scatter for our data was smaller than that of the parent Tully-Fisher survey. The future of integral field units like SparsePak, newly commissioned on the WIYN telescope, promises more advances in the study of galaxy kinematics. Programs are under way to measure disk masses from stellar absorption line velocity fields; disk masses which will constrain bulge-disk mass decomposition models.



# Table of Contents

List of Tables . . . . .	x
List of Figures . . . . .	xi
Acknowledgments . . . . .	xv
Chapter 1. Introduction . . . . .	1
1.1 Disk Lopsidedness . . . . .	4
1.2 Disk Ellipticity . . . . .	5
1.3 Scaling Relations: A Face-on Tully Fisher Relation . . . . .	9
1.4 Thesis Outline . . . . .	11
Chapter 2. Photometric Properties of Disk Galaxies . . . . .	13
2.1 Introduction . . . . .	14
2.2 Selection Algorithm . . . . .	17
2.3 Photometric Observations . . . . .	28
2.3.1 Preliminary Reductions . . . . .	37
2.4 Analysis . . . . .	38
2.4.1 Photometric Calibrations, Total Magnitudes and Colors . . . .	38
2.4.2 Surface Brightness Profiles and Non-parametric Structural In-	
dices . . . . .	46
2.4.3 Bulge-Disk Decomposition . . . . .	47

	vi
2.4.4 Isophote Fits . . . . .	62
2.4.4.1 Spiral Structure Index . . . . .	62
2.4.4.2 Tests of <i>Ellipse</i> Algorithm . . . . .	63
2.4.4.3 Position Angle and Axis Ratio Measurements . . . . .	67
2.4.5 Asymmetry . . . . .	73
2.4.5.1 Rotational Asymmetry . . . . .	73
2.4.5.2 Fourier Decompositions . . . . .	75
2.5 Discussion . . . . .	82
2.5.1 Sample Characteristics . . . . .	82
2.5.2 Asymmetry . . . . .	87
2.6 Summary . . . . .	91
Chapter 3. H $\alpha$ Velocity-Fields of Face-On Spiral Galaxies . . . . .	97
3.1 Introduction . . . . .	98
3.2 Observations . . . . .	102
3.2.1 DensePak Observations . . . . .	102
3.2.2 21 cm HI line observations . . . . .	110
3.3 Reductions . . . . .	111
3.3.1 DensePak Reductions . . . . .	111
3.3.2 21cm HI line profile reductions . . . . .	123
3.3.2.1 HI line profiles from literature . . . . .	128
3.4 H $\alpha$ Velocity Fields . . . . .	132
3.4.1 Creating Velocity-Field Maps . . . . .	132

3.4.2	Velocity–Field Structure . . . . .	133
3.4.2.1	Projected Rotation Curves . . . . .	136
3.4.2.2	Rotation Curve Asymmetry . . . . .	136
3.4.2.3	Spiral Structure . . . . .	140
3.4.3	Modeling Velocity Fields . . . . .	143
3.4.3.1	$\chi^2$ Minimization of Velocity-Field Models . . . . .	149
3.4.3.2	Model Parameter Velocity-Field Parameter Error Es- timation . . . . .	153
3.4.3.3	DensePak Continuum Measurements: A Check on Telescope Offsets . . . . .	155
3.4.3.4	$\sigma_{\text{mod}}\text{--}V_{\text{rot}}$ relation . . . . .	162
3.5	Comparison of HI and H $\alpha$ Data . . . . .	164
3.5.1	Rotation Speed . . . . .	164
3.5.2	Inclination . . . . .	166
3.6	Summary . . . . .	168
Chapter 4.	Disk Ellipticity . . . . .	174
4.1	Introduction . . . . .	175
4.2	Ellipticity Survey Constraints . . . . .	182
4.2.1	Inclination and Position Angle Differences . . . . .	182
4.2.2	Error Budget on Disk Ellipticity . . . . .	183
4.3	Method for Measuring Disk Ellipticity . . . . .	185
4.3.1	Coordinates . . . . .	185

	viii
4.3.2 Constraints . . . . .	188
4.4 Observations . . . . .	190
4.4.1 Sample Selection . . . . .	190
4.4.2 Observations . . . . .	192
4.4.3 Photometric Measures . . . . .	192
4.4.4 Kinematic Measures . . . . .	193
4.5 Ellipticity Estimates . . . . .	194
4.6 Discussion of Disk Ellipticity . . . . .	201
4.6.1 Ellipticity versus Disk Properties . . . . .	201
4.6.2 Tully-Fisher Scatter and Ellipticity . . . . .	208
4.7 Summary . . . . .	210
Chapter 5. A Face-On Tully-Fisher Relation . . . . .	211
5.1 Introduction . . . . .	212
5.2 Observations . . . . .	214
5.2.1 Total Magnitude . . . . .	215
5.2.2 Rotation Velocity . . . . .	215
5.2.3 Inclination . . . . .	216
5.3 Results . . . . .	217
5.4 Summary . . . . .	225
Chapter 6. Summary . . . . .	228
Appendix. Atlas . . . . .	239

Bibliography . . . . .	398
------------------------	-----

## List of Tables

2.1	Sample Galaxies I. . . . .	22
2.2	Sample Galaxies II. . . . .	25
2.3	Telescope Parameters . . . . .	30
2.4	Photometric Sample Observations . . . . .	31
2.5	Photometric Zero-points . . . . .	43
2.6	Magnitudes . . . . .	44
2.7	Bulge Disk Decompositions . . . . .	54
2.8	Repeatability of Ellipse Measurements . . . . .	66
2.9	Position Angles and Axis Ratios . . . . .	71
2.10	<i>R</i> -Band Disk Asymmetry . . . . .	78
2.11	<i>I</i> -Band Disk Asymmetry . . . . .	80
3.1	DensePak Observations . . . . .	107
3.2	H $\alpha$ Line profile . . . . .	118
3.3	Nançay Observations . . . . .	126
3.4	HI line widths . . . . .	129
3.5	Fits to H $\alpha$ Velocity Fields . . . . .	159
4.1	Ellipticity . . . . .	198
4.2	Ellipticity Properties . . . . .	206
5.1	Face-On Tully-Fisher Relation . . . . .	223

## List of Figures

2.1	Distribution of $D_{25}$ , $B$ , and Recession Velocities in PGC . . . . .	19
2.2	Distribution of $t$ -types and Luminosity in PGC . . . . .	21
2.3	Background Gradient in Mini-Mosaic Image . . . . .	39
2.4	Examples of Galaxy Luminosity Growth Curves . . . . .	41
2.5	Colors and Magnitudes for Sample . . . . .	42
2.6	Examples of $\eta$ Radial Profiles . . . . .	48
2.7	Bulge–Disk Decomposition Residuals . . . . .	53
2.8	Comparison of $R$ and $I$ -band Disk Parameters . . . . .	59
2.9	Comparison of Disk-Bulge Surface Brightnesses and Radii . . . . .	60
2.10	Comparison of Scale Length, $\eta$ radius to Concentration Index . . . . .	61
2.11	Spiral Index Radial Profile . . . . .	64
2.12	Comparison of Measured and PGC Axis Ratios . . . . .	69
2.13	$R$ versus $I$ -band Photometric Position Angles . . . . .	70
2.14	Comparison of Image Structure Indices to $t$ -type . . . . .	83
2.15	Effective Bulge Surface Brightness versus Effective Bulge Radius . . . . .	84
2.16	Photometric Indices for this Study versus the Frei Sample . . . . .	86
2.17	Comparison of Disk Scale Lengths for this Study versus the Courteau Tully–Fisher Sample . . . . .	88
2.18	Comparison of Colors and Surface Brightnesses for this Study versus the Courteau Tully–Fisher Sample . . . . .	89

2.19	Correlation between $A_{180} - \int A_{180}$ versus Photometric Properties . . . .	90
2.20	$A_{180} - A_1$ versus $A_3$ . . . . .	92
2.21	$A_{180}$ versus $A_{1+3}$ . . . . .	93
2.22	$A_{180} - A_{1+3}$ versus Surface Brightness, Concentration Index, and Luminosity . . . . .	94
3.1	DensePak Schematic . . . . .	103
3.2	H $\alpha$ Emission Line Profiles . . . . .	116
3.3	Nançay HI profiles I . . . . .	124
3.4	Nançay HI profiles II . . . . .	125
3.5	Comparison of Velocity Fields . . . . .	134
3.6	Sample Velocity Fields . . . . .	135
3.7	Examples of Rotation Curves . . . . .	137
3.8	Deprojected Rotation Curves . . . . .	138
3.9	Asymmetric Rotation Curve of PGC 71106 . . . . .	141
3.10	Kinematic versus Photometric Asymmetry . . . . .	142
3.11	Signature of Spiral Arms in Velocity Field of PGC 24788 . . . . .	144
3.12	Azimuthal Velocity Field Residuals Linked to Spiral Arms . . . . .	145
3.13	Velocity Field Residuals for Incorrect Inclinations . . . . .	147
3.14	Velocity Field Residuals at Different Inclinations . . . . .	148
3.15	Inclination Errors measured via $\Delta\chi^2$ . . . . .	156
3.16	Predicted and Measured Inclination Errors . . . . .	157
3.17	DensePak Continuum Surface Brightness Profiles . . . . .	158



3.18	$V_{\text{rot}}$ versus $\sigma_{\text{mod}}$ relation . . . . .	165
3.19	HI Width versus $H\alpha$ Rotation Velocity . . . . .	167
3.20	Inverse Tully–Fisher Inclinations . . . . .	169
3.21	Distribution of Inclination and Rotation Velocities . . . . .	172
4.1	Distribution of Axis Ratios in PGC . . . . .	177
4.2	Coordinates of Elliptical Disks . . . . .	179
4.3	Differences in Position Angles and Axis Ratios for Elliptic Disks . . . . .	184
4.4	Error Budget for Ellipticity Measurement . . . . .	186
4.5	Graphical Ellipticity Solution . . . . .	191
4.6	Ellipticity Error Contours . . . . .	196
4.7	Ellipticity Solutions for 28 Galaxies . . . . .	197
4.8	Distribution of Intrinsic Disk Ellipticities . . . . .	202
4.9	Ellipticity versus Lopsidedness . . . . .	204
4.10	The Relation between Disk Ellipticity and Photometric Parameters re- lated to Galaxy Mass . . . . .	205
4.11	Tully-Fisher Scatter versus Ellipticity . . . . .	209
5.1	A Face-On Tully-Fisher Relation . . . . .	221
5.2	Tully-Fisher Scatter . . . . .	222
5.3	Tully-Fisher scatter versus Lopsidedness and Ellipticity . . . . .	226
6.1	$A_{180}$ versus $A_{1+3}$ . . . . .	230
6.2	A Face-On Tully-Fisher Relation . . . . .	233
6.3	Disk Ellipticity Solutions . . . . .	235

6.4	SparsePak . . . . .	237
6.5	SparsePak Spectra . . . . .	238

## Acknowledgments

I would like to first thank my advisor, Matt Bershad, for guiding me through my graduate career. He taught me how to observe, reduce data, and do science. I credit his patience for making me a better writer and astronomer and look forward to future collaborations.

My collaborators on my thesis project, Linda Sparke, Jay Gallagher and Eric Wilcots at the University of Wisconsin–Madison, and Wim van Driel and Delphine Monnier-Ragaine at the Observatoire de Paris all provided their valuable time and energy to my thesis research.

I would also like to thank my thesis committee, Larry Ramsey, Steinn Sigurdsson, Robin Ciardullo and Jim Beatty for their comments and suggestions which served to improve my thesis and spawn new ideas.

This research would not have been done without the consent of McDonald Observatory, WIYN Observatory, Nançay Observatory and the National Optical Astronomy Observatories, and the Time Allocation Committees at each of these institutions. I am grateful for the opportunity to receive data from so many world-class observatories as a graduate student. Many support scientists and personnel were helpful with my observations, but I would especially like to thank Charles Corson, Dave Sawyer and Di Harmer at the WIYN observatory for their expertise and patience in helping us take full advantage of DensePak and the WIYN Bench Spectrograph.

I spent many months of my graduate career in stairwells, hallways and labs, building and testing fiber optic cables. Without the direction from Matt Bershadsky and Larry Ramsey, SparsePak would not have been built. Sam Barden opened his fiber optic lab to us, saving us time and money as we developed our own integral field fabrication techniques. It was my privilege to work with Matt, Don Bucholtz, Scott Buckley, Leland Engel, Justin Harker and LeAnn Andersen as we struggled with technical issues related to constructing 25m and 35m fiber optic cables. In addition to those listed above, Mike Sipior, Rick Williams and Rick Abelman were always there to lend a hand when we were in need.

There are many astronomers at UW-Madison and Penn State who have helped me over the years, either through useful discussions or through observing my sources as part of backup programs. I would especially like to recognize Anna Jangren, John Hoessel, Chris Anderson, Chip Kobulnicky, Bob Benjamin, Chris Conselice, Sarah Gallagher, Andrew Glenn, Nicole Homeier, and John Feldmeier.

The support I received through NASA as a Graduate Student Research Proposal (GSRP) Fellow was critical for supporting me through the last two years of graduate school and freed me to move to UW-Madison so I could work more closely with my advisor.

Sigma Xi's Grant in Aid of Research funded several of the critical observing runs for my thesis. The Pennsylvania NASA Space Grant Consortium and the Zaccheus Daniel Fellowship also provided me with much needed travel money so that I could present my research at meetings.

This research made use of the the Second Palomar Observatory Sky Survey (POSS-II). POSS-II was made by the California Institute of Technology with funds from the National Science Foundation, the National Geographic Society, the Sloan Foundation, the Samuel Oschin Foundation, and the Eastman Kodak Corporation.

This research also has made use of the NASA/IPAC Extragalactic Database (NED) which is operated by the Jet Propulsion Laboratory, California Institute of Technology, under contract with the National Aeronautics and Space Administration.

As a personal note, I would like to thank my family for a lifetime of support. At all times, but especially in the last few weeks of writing, I always could rely on my wife LeAnn for the help and encouragement I needed. Finally, I would like to thank Janet Daniel for doing a great job proofreading the last few chapters as the deadline approached.

## Chapter 1

### Introduction

Two fundamental and intertwined questions of cosmology concern how galaxies form and how galaxies come to have their present structure. The current approach to answering these questions involves comparing numerical and semi-analytical structure-formation models to a suite of critical observations of low and high redshift galaxies (e.g., Navarro, Frenk, & White 1996, 1997; van den Bosch 2000). For nearby disk galaxies the salient observations which test and constrain structure-formation models include measurements of (1) halo shape; (2) disk scaling relations, and (3) mass decompositions. We have collected a unique data set of H $\alpha$  velocity fields and  $R$  and  $I$ -band imaging for a set of 39 nearby nearly face-on disk galaxies to address these measurements. Before describing the survey itself, we present the broader implications of the specific measurements we have undertaken.

The shape of the dark matter halo is most easily apparent through its effects on the disk. Because the disk asymmetries appear to be linked to the shape of the halo, it is important to measure deviations from axisymmetry. For example, the lopsidedness and ellipticity of disks may be used to estimate halo triaxiality (Franx & de Zeeuw 1992; Jog 1997, 1999, 2000). Many galaxies appear to have lopsided light distributions or kinematic features (e.g. Baldwin, *et al.* 1980; Zaritsky & Rix 1997). It has been more of a challenge to measure the disk ellipticity because it is difficult to disentangle the intrinsic shape

of galaxy disks from both projection effects and spiral structure (e.g. Rix & Zaritsky 1995; Schoenmakers *et al.* 1997). If better estimates of ellipticity existed, tighter limits could be placed on halo triaxiality. Numerical simulations have produced disk galaxy halos which are highly triaxial (Dubinski & Carlberg 1991), but other physical processes, such as the dissipative infall of gas during formation, may transform the halo into an oblate spheroid (Dubinski 1994). If measurements could show most disk galaxies were significantly elliptic, the role dissipation plays in the formation process would have to be reexamined.

For spiral galaxies, the fundamental scaling relation is between rotation speed and luminosity (Tully & Fisher 1977; hereafter TF relation). This relation can be interpreted as one between galaxy mass (dominated by the dark matter halo) and the baryons responsible for the luminosity. It is remarkable that the TF relation shows little scatter and seems unrelated to physical scale lengths, surface brightness or other parameters that one might expect to affect the TF relation on simple theoretical arguments concerning virialized systems. Recreating the zero-point, slope and scatter in the TF relation has been a major challenge for structure formation models (Dalcanton, Spergel & Summers 1997; Mo, Mao & White 1998; Steinmetz & Navarro 1999, 2000). While theory struggles with matching the TF zero-point, the next frontier is to understand and interpret the signatures of different physical processes leading to TF scatter. These same processes no doubt play a central role in defining disk galaxies past and present structure. By putting limits on individual sources of TF scatter, such as ellipticity or asymmetry, limits are placed on the contribution of other astrophysical processes which cause TF scatter, which in turn will constrain structure-formation models.

Although the best evidence for the existence of dark matter halos are observations of disk galaxy rotation curves and velocity fields (e.g. Bosma 1981a, 1981b; Begeman 1987; Verheijen & Sancisi 2001), these data are as yet, poorly constrained. While numerous models of both disk and halo mass profiles have been developed (Begeman, Broeils & Sanders 1991; Broeils 1992; van der Kruit 1995), the contributions from halo and disk mass to these decompositions are degenerate. Even more worrisome, some non-standard models, such as modified Newtonian dynamics, in some cases, yield even closer fits to the data (for differing viewpoints see McGaugh & de Blok 1998; de Blok *et al.* 2001 and van den Bosch *et al.* 2001; van den Bosch & Swaters 2001). The current state of ambiguity of rotation-curve mass decompositions could be resolved if more observational constraints — particularly a direct measurement of disk mass — could be placed on halo density profile models.

In our studies, we attempt to constrain the halo shapes of galaxies by measuring disk lopsidedness and ellipticity. We are especially interested in disk ellipticity because it has been suggested to be a source of scatter in the TF scaling relation. By assuming a non-rotating potential with a constant triaxial distortion, Franx & de Zeeuw (1992) calculated the ellipticity required to be responsible for all of the scatter in the TF relation, thereby putting an upper limit of  $\epsilon < 0.1$  on the ellipticity of disk galaxies. It has also been suggested that lopsidedness may be a source of TF scatter because lopsided galaxies may induce increased star formation (Zaritsky & Rix 1997), but a direct measurement of the contribution of lopsidedness to TF scatter has not been made. Therefore, a measurement of ellipticity, and possibly lopsidedness, places limits on other astrophysical sources of TF scatter, including disk mass-to-light ratios. If limits are placed on the variation of



disk mass-to-light ratios, a new constraint will be placed on mass decomposition models. We now turn to describing past measurements and estimates of the specific quantities we will study: (1) lopsidedness, (2) ellipticity, and (3) a face-on TF relation and scatter.

## 1.1 Disk Lopsidedness

Our sample of face-on galaxies lends itself to studies of a variety of asymmetric modes. Many studies have found that between 20–50% of spiral galaxies show significant degrees of asymmetry, both photometric (Rix & Zaritsky 1995; Abraham *et al.* 1996a; Kornreich, Haynes & Lovelace 1998; Rudnick & Rix 1998; Conselice, Bershadsky & Jangren 2000) and kinematic (Baldwin, Lynden-Bell, & Sancisi 1980; Bosma 1981b, Richter & Sancisi 1994; Haynes *et al.* 1998; Swaters *et al.* 1999; Dale *et al.* 2001). While different methods have been developed to measure asymmetry, most studies have focused on measuring lopsidedness. Fourier decompositions, for example, can characterize every mode of both photometric and kinematic asymmetry by an amplitude and a phase angle. In this context, the  $m = 1$  mode corresponds to lopsidedness, and the  $m = 2$  mode of asymmetry corresponds to ellipticity. Higher order modes can be attributed to flocculence. But again in practice, studies using Fourier methods have focused on lopsidedness (Rix & Zaritsky 1995; Zaritsky & Rix 1997; Rudnick & Rix 1998; Kornreich *et al.* 2000).

This focus on measuring lopsidedness arises from the existence of several compelling theories for its cause. Zaritsky & Rix (1997) suggested lopsidedness results from minor mergers. Measuring the frequency and amplitude of lopsidedness therefore may allow the derivation of galaxy accretion rates. Rudnick, Rix & Kennicutt (2000) hypothesized tidal interactions induce both lopsidedness and increased star formation. Another

hypothesis posits lopsided galaxies are really one-armed spirals created either by an instability in the initially concentrated gas disk (Junqueira & Combes 1996) or by disks which had a counter rotating component (Comins *et al.* 1997). Long-lived lopsidedness may result if a disk exists in a triaxial halo (Jog 1999) or is not centered in a halo (Levine & Sparke 1998).

Despite the attention paid to the  $m = 1$  mode, higher order modes could be interesting because such modes may be excited by flocculence due to the stochastic nature of star formation. Rotational photometric asymmetry indices have been used as a structural index helpful in galaxy classification (Abraham 1996b; Bershadsky, Jangren & Conselice 2000). It has been suggested that this parameter’s correlation with color indicates it measures higher order modes of asymmetry, particularly star-formation induced flocculence (Conselice, Bershadsky & Jangren 2000).

In this study, we measure both kinematic and photometric  $m = 1$  asymmetry amplitudes from our sample data to (1) reconcile different measurements methods, (2) test theories of lopsidedness, and (3) determine the importance of higher order modes to Fourier analysis of disk galaxy images. In particular, we address the relation between Fourier amplitudes of photometric data and rotational asymmetry indices. We also focus attention on the  $m = 2$  Fourier mode, which can be interpreted as disk ellipticity, as we discuss next.

## 1.2 Disk Ellipticity

The first estimates of disk ellipticity were made from large galaxy catalogs (Binney & de Vaucouleurs 1981; Grosbøl 1985; Huizinga & van Albada 1992; Lambas, Maddox,

& Loveday 1992; Magrelli, Bettoni, & Galletta 1992; Fasano *et al.* 1993). An analysis of the distribution of spiral galaxy axis ratios revealed a deficit of photometrically face-on objects. This deficit was interpreted as a mean isophotal intrinsic ellipticity  $\epsilon_D \approx 0.1$  where  $\epsilon_D$  denotes the disk ellipticity and is related to the axis ratio of a disk with zero inclination by  $\epsilon_D = b/a(i = 0)$ . However, results of these studies are statistical at best, and are likely suspect because measured photometric axis ratios can be affected by other  $m = 2$  mode asymmetries, such as spiral structure.

A second approach to measuring disk ellipticity was pioneered by Rix & Zaritsky (1995), who chose galaxies for an asymmetry study based on narrow HI line-widths. They assigned inclinations to sample galaxies by inverting the Tully-Fisher relation and solving for the disk inclination. These “inverse Tully-Fisher” inclinations should be quite accurate for nearly face-on systems based on simple geometric arguments of projection. Rix & Zaritsky noticed that several of their galaxies had isophotes which were more elliptical than expected from projection effects alone. However, even if disks were absolutely face-on ( $i = 0$ ), measuring ellipticity would be a complicated analysis because of spiral arm structure. For galaxies with low, but non-zero, inclinations, this analysis becomes yet more complicated. For example, one would expect a random phase angle,  $\phi$ , between the major axis of the elliptical disk and the kinematic major axis. Without knowledge of this parameter, Rix & Zaritsky assumed: (1) A simple relation exists between disk ellipticity and the potential ellipticity. If one assumes an exponential disk sits in a potential with constant ellipticity,  $\epsilon_\Phi$ , the disk ellipticity,  $\epsilon_D$ , is related to the ellipticity of

the potential by

$$\epsilon_D(R) = (1 + h/R)\epsilon_\Phi \quad (1.1)$$

where  $h$  is the scale length. (2) The distribution of  $\phi$  was uniform. If these two assumptions hold, the ellipticity of the potential  $\overline{\epsilon_\Phi} = 0.045^{+0.03}_{-0.02}$ .

Estimates of the ellipticity of the potential have also been made from velocity fields of spiral disks (Schoenmakers *et al.* 1997). A harmonic analysis of HI velocity fields for 7 galaxies revealed  $\epsilon_\Phi \cos 2\phi$  between 0.001 and 0.07 (Schoenmakers 1999). Assuming a simple halo potential and a uniform distribution of phase angles,  $\phi$ , the mean ellipticity of the potential was  $\overline{\epsilon_\Phi} = 0.049 \pm 0.014$ .

The above estimates of disk or potential ellipticities are important first steps yet have been limited by their inability to measure ellipticities for individual galaxies. Each study has been forced to assume a random distribution of phase angles,  $\phi$ , for their sample and then calculate a mean ellipticity on this basis. These limitations subject previous results to uncertainty due to potential or unknown sample biases, small samples, and no knowledge of the distribution of ellipticity.

Unsurprisingly, the first measurement of both  $\epsilon_\Phi$  and  $\phi$  is for the Milky Way. This measurement is based on both local measures such as the Oort constants and global constraints such as kinematics of distant HI regions (Kuijken & Tremaine 1994). The halo ellipticity of the Milky Way appears to be slightly higher than studies of external galaxies would suggest,  $\epsilon_\Phi(\text{MW}) = 0.1$ . However, the analysis of the ellipticity of the Milky Way requires assumptions about the local standard of rest and the distance of the

sun to the center of our Galaxy. These measurements, and therefore the measurement of  $\epsilon_{\Phi}(\text{MW})$ , are uncertain, and have different potential systematics than  $\epsilon_{\Phi}$  studies of external galaxies.

In a pilot study of seven galaxies, we demonstrated a new method for determining disk ellipticity based on differences in kinematic and photometric inclination and position angles (Andersen *et al.* 2001). As we will show more explicitly in Chapter 4, the difference between photometric and kinematic position angles due to ellipticity is greatest at inclinations less than or equal to  $\sim \cos^{-1}(1 - \epsilon)$ . By using the estimates of mean disk ellipticity noted above which ranged from  $\epsilon_{\Phi}$  of 0.05 to 0.1, we can put a limit on the inclinations in which we expect to observe the greatest differences between photometric and kinematic position angles. For example, using Franx & de Zeeuw’s (1992) upper limit on ellipticity,  $\epsilon_{\Phi} < 0.1$  based on the scatter in the Tully-Fisher relation, the effects of ellipticity would be most noticeable at inclinations,  $i < 30^{\circ}$ . We therefore chose nearly face-on galaxies for study. Kinematic parameters were measured from H $\alpha$  velocity fields observed using DensePak (Barden, Sawyer & Honeycutt 1998) on the WIYN 3.5m telescope<sup>1</sup> while photometric axis ratios and position angles were measured from WIYN *I*-band images. The seven galaxies in our pilot study had a mean  $\overline{\epsilon_D} = 0.05 \pm 0.01$ , comparable to other results (if Equation 1.1 holds,  $\overline{\epsilon_{\Phi}} = 0.04 \pm 0.01$ ).

While most previous work on disk ellipticity has focused on constraining halo shape, observations of disk ellipticity are also important for putting limits on other sources of Tully-Fisher scatter. Taking Franx & de Zeeuw’s analysis at face value, the

---

<sup>1</sup>The WIYN Observatory is a joint facility of the University of Wisconsin-Madison, Indiana University, Yale University, and the National Optical Astronomy Observatories.

result from our pilot survey implies almost 50% of TF scatter may be due to ellipticity. The remaining TF scatter presumably is due to some combination of measurement errors and intrinsic variations in galaxy populations. If a substantial fraction of TF scatter could be shown to be directly due to ellipticity, then limits would be placed on other sources of astrophysical scatter, such as galaxy mass-to-light ratios. As previously discussed, such limits in turn constrain the formation histories and content of spiral galaxies.

In this study, we use a sample of 39 spiral galaxies over a range of type and luminosity to measure  $\epsilon_D$  and establish the relation between ellipticity and other photometric and kinematic parameters such as surface brightness, color, luminosity, rotation velocity, photometric and kinematic asymmetry and scatter in the TF relation.

### 1.3 Scaling Relations: A Face-on Tully Fisher Relation

The TF relation describes the empirically established correlation between galaxy luminosity and rotation velocity (Tully & Fisher 1977). As described above, the TF relation is also a relation between galaxy mass (dominated by dark matter), and the baryons responsible for galaxy luminosity (i.e., the stars plus HI gas). The slope, zero-point and scatter of the TF relation all constrain cosmological structure-formation models. To first order, the slope depends on the changes of characteristic mass-to-light ratio and size with mass. The zero-point of the TF relation is related to the mean mass-to-light ratio and mean mass-density. TF scatter, however, as noted above can be due to several astrophysical sources, including variations in the dark matter fraction, mass density, disk mass-to-light ratio, ellipticity, or other forms of asymmetry. Numerous studies have

focused on reducing TF scatter in order to use the relation as a bias-free distance indicator (for a review, see Strauss & Willick 1995). The most important advance has been claimed to be the advent of CCD photometry, which reduced TF scatter from  $> 0.4$  mag to  $0.2\text{--}0.3$  mag (e.g. Pierce & Tully 1988; Willick 1990; Courteau 1992; Bernstein 1994; Giovanelli *et al.* 1997). Another significant advance has been the use of two-dimensional velocity fields in favor of HI line widths for TF studies (e.g. Schommer *et al.* 1993; Raychaudhury *et al.* 1997; Verheijen 2001). Two-dimensional velocity fields can be used to derive kinematic inclinations, which are superior to photometric inclinations, as well as measuring more accurate rotation velocities unaffected by turbulent broadening observed in HI line widths.

One common characteristic of all TF studies is the selection of galaxies with inclinations greater than  $\sim 45^\circ$  with typical inclinations of  $\sim 60^\circ$ . Inclination is the third measurement, in addition to projected rotation speed and luminosity, needed in TF studies, and in some ways it is the most critical. Inclination is used to correct both luminosity and rotation speed for projection effects (which could lead to correlated errors): (1) Observed rotation speeds,  $V_{\text{rot}}$ , are de-projected using the inclination,  $i$  ( $V_{\text{circ}} = V_{\text{rot}} / \sin i$ ); and (2) luminosities are photometrically de-reddened to remove the effect of internal absorption. Despite the difficulties of correcting photometry for internal reddening, TF surveys have favored the use of inclined galaxies for two reasons: (*i*) inclination errors become an increasingly dominant source of measurement error at low inclinations in TF studies, and (*ii*) photometric inclination errors diverge at low inclinations. (Inclination angles derived from modeling two-dimensional velocity fields based on HI data for near face-on galaxies have in the past been viewed as suspect.) Using inclined galaxies in TF

studies, however, present different difficulties: (a) photometric inclinations need to be corrected for the scale height of galaxies, introducing another parameter which can not be directly measured for TF galaxies (Giovanelli *et al.* 1996); and, as noted above, (b) internal galaxy absorption is significant and increases with inclination (Giovanelli *et al.* 1994; Giovanelli *et al.* 1995; Tully *et al.* 1998).

We have discovered, however, that kinematic inclinations, derived from high-quality kinematic data collected with DensePak, are sufficiently accurate and precise to construct a TF relation at unprecedentedly low inclinations. We showed that our 7 pilot study galaxies fell on a TF relation published by Courteau (1997) and exhibited scatter commensurate to relations for more inclined galaxies (Bershady & Andersen 2001). This represents the first attempt to construct a TF relation for face-on systems. We will extend this analysis to the full thesis sample. This is important not only for studying correlations of TF residuals (i.e., the scatter about the mean relation) with asymmetry (as previously discussed), but for mass-modeling as well. By establishing the ability to derive rotation curves for nearly face-on systems, we have opened the door to future surveys which can directly measure total mass (via rotation curves) and disk mass (via the vertical component of disk stellar velocity and estimates of stellar scale-heights).

## 1.4 Thesis Outline

This thesis is organized as follows: In Chapter 2 we describe our disk structure survey, and the measurements of different photometric properties for our sample including the photometric axis ratios and position angles needed for measuring disk ellipticity.



We use these measurements to characterize our sample and reconcile different photometric asymmetry methods. In Chapter 3 we present velocity fields and HI profiles for our sample galaxies, along with descriptions and results of velocity field modeling. Therein, we derive, among other quantities, accurate and precise kinematic inclinations, position angles, and rotation speeds for our sample. We draw upon the foundation of observed disk properties tabulated in Chapter 2 and Chapter 3 to calculate disk ellipticity from differences between kinematic and photometric inclinations and position angles in Chapter 4. In Chapter 5 we present the first “face-on” TF relation — established using our sample. There, we try to determine if TF residuals are correlated with asymmetry, ellipticity, and other disk properties. We summarize our results and discuss the future of kinematic studies with integral field units in Chapter 6. Finally, the appendix contains an atlas of our photometric and kinematic measures for all survey galaxies. These measures include (1) the images and H $\alpha$  velocity fields (discussed in §3.4.1), (2) radial profiles of different asymmetry indices (§2.4.5), (3) radial profiles of surface brightness, encircled energy,  $\eta$  index (§2.4.2), spiral index, position angle and axis ratio (§2.4.4) and (4) rotation curves (§3.4.2) and spectral surface brightness profiles (§3.4.3).

## Chapter 2

# Photometric Properties of Disk Galaxies

## Abstract<sup>1</sup>

We establish a sample of 39 nearby, nearly face-on disk galaxies for a detailed study of their photometric and kinematic properties. In this Chapter, we define the sample and present deep  $R$  and  $I$ -band imaging data, including colors, scale radii, concentration indices, and model bulge-disk parameters. Using these photometric properties, we characterize the photometric properties of our galaxy sample in the context of other surveys. In addition to measuring these disk structure indices and model parameters, we tested different methods for measuring axis ratios and position angles that would be unaffected by spiral structure. These two measurements play a fundamental role in the measurement of disk ellipticity. We find two-dimensional bulge-disk decompositions do not give accurate measures of disk axis ratios and position angles. As an alternative, we have developed a set of criteria that, if followed, do yield accurate axis ratios and position angles measured from isophotal ellipse fits. We also characterize the photometric shape and asymmetry of galaxies via two distinct methods. We find that photometric asymmetries are greater in the outer disk than in the inner disk, and that the

---

<sup>1</sup>Andersen, D.R. & Bershadsky, M.A. 2001, *to be submitted to Ap.J.S.*

$m = 1$  Fourier mode, which can be characterized as lopsidedness, is the dominant, odd Fourier mode. These results dispute the claim that the rotational asymmetry index in normal spiral disks is a measure of disk flocculence, which would be characterized in a Fourier series as high order ( $m > 9$ ) modes. In particular, we explicitly show that the rotational asymmetry index,  $A_{180}$ , is statistically equivalent to the quadrature sum of the two lowest, odd Fourier amplitudes,  $(A_1^2 + A_3^2)$ .

## 2.1 Introduction

As discussed in Chapter 1, the goals of this study are two-fold: We seek to probe the shape of galaxy disks and hence disk galaxy halo potentials by making measurements of kinematic and photometric lopsidedness, and by measuring ellipticity based on a combination of photometric and kinematic indices. In addition to studying the shape of disk galaxies, we are also interested in probing into potential sources of scatter in the Tully-Fisher relation, the fundamental scaling relation for disk galaxies. Kinematic inclinations from high quality  $H\alpha$  velocity fields described in Chapter 3 will allow us to create a “face-on” Tully–Fisher relation (Tully & Fisher 1977; hereafter TF.) We intend to study the residuals of the face-on TF relation as a function of both ellipticity, lopsidedness, and other disk parameters.

To fulfill these two goals requires key imaging observations and photometric analysis which we establish and present here. The essential information includes accurate measures of axis ratios and position angles from images that are unaffected by spiral structure. Such information is required for measurements of disk ellipticity, as described

in Andersen *et al.* (2001) and again in further detail in Chapter 4. Here, we test two different methods for making measurements of axis ratios and position angles: two-dimensional bulge-disk decompositions and ellipse fits. While previous studies would indicate that two-dimensional bulge-disk decompositions would be an ideal method for deriving disk axis ratio and position angle information (de Jong 1996a; Prieto *et al.* 2001), we find this not to be the case for our face-on sample. We were only able to use two-dimensional bulge-disk decompositions to measure disk scale lengths and other model-dependent disk and bulge parameters. Since two-dimensional bulge-disk decompositions did not yield accurate measures of axis ratios and position angles, we determined these indices via fitting ellipses to isophotes, a common practice for the study of nearby and distant galaxies. Unlike other studies, we set several criteria to ensure accurate measures of axis ratios and position angles that are as immune as possible from the unwanted perturbations due to spiral structure. These criteria require making a measure of spiral structure, and also a reliable estimate of disk scale length, following the procedure outlined in Andersen *et al.* (2001).

Our intent, however, is to study other modes of asymmetries as well as ellipticity. While ellipse fitting and bulge-disk decompositions characterized the axisymmetric components and parameters of the sample, the non-axisymmetric components required a separate analysis. Photometric asymmetries have been measured using several different methods (e.g., Rix & Zaritsky 1995; Schade *et al.* 1995; Kornreich *et al.* 1998). Each method has certain advantages; we choose to measure both Fourier asymmetry amplitudes and the rotational asymmetry index from our images. In order to compare our

measurements to those of other studies, we again required information regarding disk scale lengths.

In the process of measuring the key photometric indices and parameters needed to study the shape of galaxy disks, we generated a corpus of photometric information, including radii, concentration indices, and magnitudes. Magnitudes, in particular, are the key photometric index needed for establishing the face-on Tully-Fisher relation. The other indices are critical for characterizing our sample in terms of galaxy type. As we shall see, the initial photometric data contained within the nearby galaxy catalogs from which we selected our sample are suspect. Therefore, the photometric properties which we measure and tabulate for our survey galaxies are of utility for comparing to other well-studied samples of nearby bright spiral galaxies.

In this Chapter, we begin by discussing the selection algorithm and imaging observations and preliminary reductions of the photometric data in §2.2. We describe the various methods for measuring photometric disk parameters in §2.3. In particular, we begin by measuring  $R$  and  $I$ -band total magnitudes from surface brightness profiles in §2.3.1. We discuss the other non-parametric indices which we derived from surface brightness profiles in §2.3.2. Two-dimensional model bulge-disk decompositions are described in §2.3.3. By utilizing the model scale lengths we measure axis ratios and position angles at fixed metric intervals, given in §2.3.4. Finally, in §2.3.5, we describe two different techniques for measuring asymmetry. We make comparisons between the properties of disk galaxies in our sample to the properties measured for other samples containing bright spiral galaxies. and present our findings related to disk asymmetry in §2.4, and finally summarize our results in §2.5

## 2.2 Selection Algorithm

As discussed in Chapter 1, we chose to observe nearly face-on galaxies in order to measure disk ellipticity. Two methods exist for making a selection of nearly face-on disks: (1) one can choose galaxies with photometric axis ratios greater than 0.87 (photometric inclinations less than  $30^\circ$ ) or (2) use HI line widths and absolute magnitudes and invert the Tully-Fisher relationship to solve for inclination (Rix & Zaritsky 1995). These so-called “inverse Tully-Fisher” inclinations yield precise inclinations for nearly face-on spiral galaxies, and also could be used to select galaxies with inclinations less than  $30^\circ$ . We chose to use photometric axis ratios as our “nearly face-on” criterion.

While inverse Tully-Fisher inclinations are more precise than photometric inclinations, choosing galaxies with existing HI line-widths may bias a sample. Many galaxies with HI line-widths are selected on the basis of having photometric inclinations greater than  $45^\circ$  for inclusion in Tully-Fisher studies. Those galaxies with narrow HI line-widths may indeed be nearly face-on, but in this case are necessarily highly elliptic. Hence surveys built upon the availability of HI line-widths as a selection criteria may preferentially include spiral galaxies with asymmetric and elliptical disks. By choosing galaxies with photometric axis ratios greater than 0.87, we introduced a different selection effect: Disks with the greatest ellipticities should also have large phase angles,  $\phi$ , in order to appear nearly face-on.<sup>2</sup> While our sample contains a potential bias, we can account for it when modeling the distribution in ellipticities for the general population of spiral galaxies. In

---

<sup>2</sup> $\phi$  is a second ellipticity parameter describing the angle between the kinematic major axis and the major axis of the elliptical isophote in the plane of the galaxy.

contrast, it is not possible to compensate for the potential bias introduced by selecting galaxies with narrow HI line-widths.

The selection of our sample was also driven by our choice of observing velocity fields with the DensePak integral field unit on the WIYN telescope. DensePak spans  $30 \text{ arcsec} \times 45 \text{ arcsec}$ , so targets were limited to diameters between 45 and 75 arcseconds so they could be well sampled by DensePak in a few pointings. Given the relatively small sizes of target galaxies in our survey, chosen galaxies will typically be some of the faintest and most distant galaxies in the catalogs of nearby galaxies. To maximize the number of galaxies available for study, we chose our sample from the LEDA database<sup>3</sup> which contains all galaxies in common catalogs (e.g. NGC, UGC, IC), plus galaxies only defined in the Principal Galaxy Catalog (PGC) (Paturel, *et al.* 1997). One minor benefit of choosing galaxies from the PGC is that each galaxy has a catalog number regardless of its original source. While the PGC is inclusive of many other galaxy catalogs, galaxies with diameters less than  $\sim 1$  arcminute still fall below the completeness threshold (Figure 2.1).

Besides selecting galaxies based on (1) axis ratio  $b/a + \Delta b/a > 0.87$  ( $i - \delta i < 30^\circ$ ) and (2) apparent disk size  $45'' < D_{25} < 75''$ , we also selected galaxies based on (3) galactic absorption  $A_B < 0.6$  (Schlegel, Finkbeiner & Davis 1998), (4) declinations visible from WIYN,  $\delta_{1950} > -10^\circ$ , (5) observed  $B$ -band magnitudes, (6) observed recession velocities, and (7)  $t$ -types ranging from Sab to Sd ( $t$ -types between 1.5–8.5). We elected not to observe Sa galaxies because these galaxies have less H $\alpha$  emission than later types (Kennicutt, Edgar, Hodge 1989).

---

<sup>3</sup><http://leda.univ-lyon1.fr>

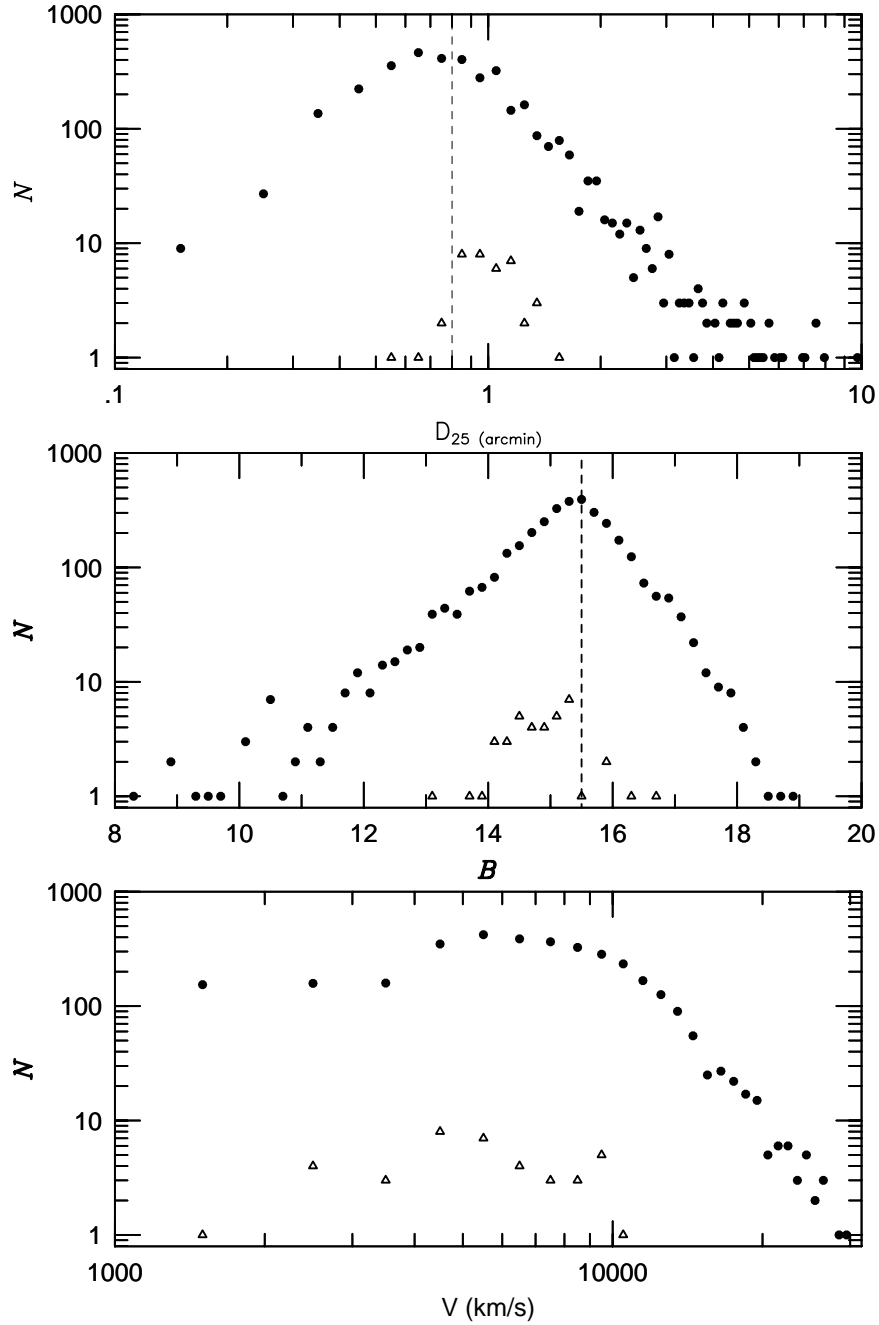


Fig. 2.1. Distribution of diameters ( $D_{25}$ ; top panel), blue magnitudes ( $B$ ; middle panel) and recession velocities ( $V$ ; bottom panel) for galaxies in the PGC meeting the selection criteria in §2.2 (filled circles) and galaxies observed as part of this survey (open triangles). Specifically, these selection criteria include: (1)  $1.5 < t\text{-type} < 8.5$ , (2)  $A_B < 0.6$ , (3)  $\delta_{1950} > -10^\circ$ , (4)  $b/a_{25} + \Delta b/a_{25} > 0.87$ . Completeness criteria for galaxies in the PGC are met for  $D_{25} > 0.8'$  and  $B < 15.5$ . Despite the incompleteness of the parent sample, we endeavored to choose a representative sample of disk galaxies which spanned a wide range in types and luminosities.



Of the 1300 targets met our raw selection criteria, 753 were observable during our longest WIYN DensePak runs (January and December 1999;  $0^h < RA < 13^h$ ). We obtained Second Generation Digitized Sky Survey (DSS2) images of these potential targets. After visual inspection, we eliminated from our sample, galaxies with bars, rings, interacting companions, or foreground stars that contaminated the inner isophotes. This step removed 60% of the sample from consideration. We measured position angles and axis ratios from the DSS2 images using the *IRAF ellipse* routine. Our sample was further refined by requiring (1) the position angle to be relatively constant in the outer portions of the disk and (2) our measurements of  $b/a > 0.87$  on DSS2 images. Between  $0^h < RA < 13^h$  only 70 targets remained. By examining every PGC galaxy in a small slice of right ascension, we ascertained that our selection criteria successfully yielded almost all photometrically face-on galaxies in the PGC. Through the course of our observations, we observed 32 of these 70 targets, plus 7 other galaxies chosen from the same parent sample of 1300 targets, but which lie between  $13^h < RA < 24^h$ . The 39 galaxies which make up our survey were chosen to span a large range of  $t$ -type and luminosity (Figure 2.2). Table 2.1 and 2.2 list the properties of these galaxies as listed in the PGC.

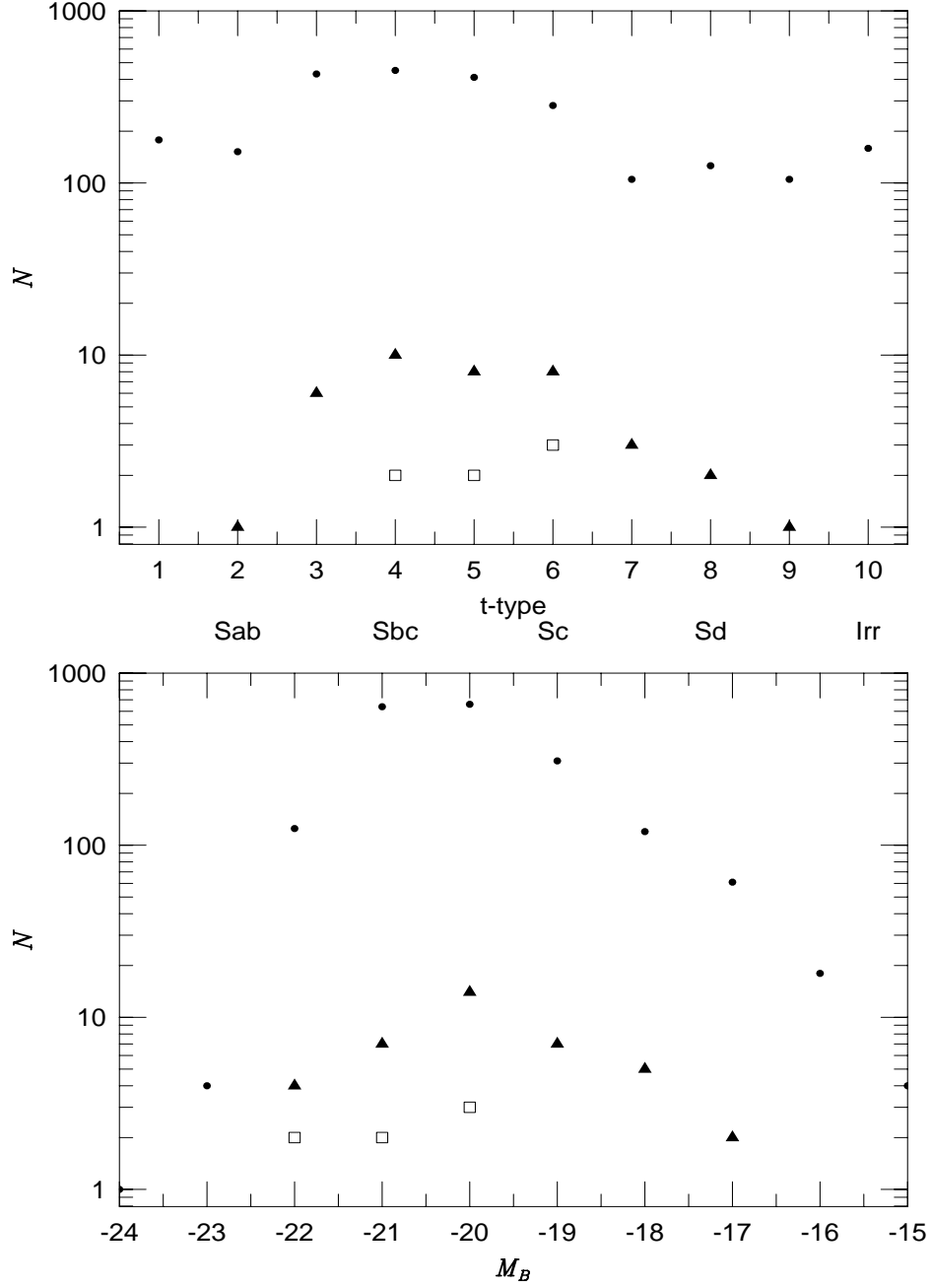


Fig. 2.2. The distribution in type (top panel) and luminosity (bottom panel) for galaxies in the PGC meeting the selection criteria in §2.2 (filled circles) and galaxies observed as part of this study (filled triangles). The selection criteria applied to sample of galaxies in the top panel include, (1) measured  $B$ -magnitudes and (2) recession velocities, (3)  $A_B < 0.6$ , (4)  $\delta_{1950} > -10^\circ$ , (5)  $b/a_{25} + \Delta b/a_{25} > 0.87$ , and (6)  $0.''6 < D_{25} < 2''$ . The bottom panel include all galaxies in the top panel which have  $1.5 < t\text{-type} < 8.5$ . We broadened the sample by both type and luminosity upon completion of our pilot study (open squares).

Table 2.1. Properties of survey galaxies tabulated from the PGC (Paturel *et al.* 1997)

PGC	alternate	RA	DEC	$l_2$	$b_2$	type	t-type
	name	(1950)	(1950)				
2162	UGC 358	00 33 39.0	+01 26 13	115.085	-60.927	Sab	1.8
3512	IC 1607	00 56 15.0	+00 19 04	126.892	-62.228	Sb	3.0
5345	UGC 1014	01 23 47.1	+06 01 04	138.411	-55.54	SBm	9.2
5673	UGC 1087	01 28 46.5	+14 01 13	137.35	-47.471	Sc	5.3
6855	UGC 1322	01 48 49.1	+12 53 04	144.723	-47.183	Sc	5.2
7826	UGC 1546	02 00 35.1	+18 23 22	145.742	-41.036	Sc	5.4
8941	UGC 1808	02 18 16.0	+23 22 20	148.133	-34.845	Sb	3.1
14564	NGC 1517	04 06 29.2	+08 31 04	183.316	-30.236	Sc	6.0
15531	UGC 3091	04 31 21.2	+01 00 36	194.52	-29.574	Scd	6.7
16274	MCG 1-13-8	04 51 19.3	+03 30 46	195.147	-24.022	Sb	2.7
19767	UGC 3569	06 48 12.6	+57 13 23	158.92	22.661	Sd	7.6
20938	UGC 3833	07 21 33.4	+32 54 12	185.776	20.826	Sbc	4.3
23333	IC 2283	08 16 16.2	+24 57 00	198.389	29.557	Sb	3.3
23598	UGC 4380	08 20 40.7	+55 00 58	163.211	35.119	Sc	5.9
23913	UGC 4445	08 27 17.2	+61 09 50	155.616	35.535	Sc	5.3
24788	UGC 4614	08 46 06.2	+36 18 20	186.903	38.488	SBb	2.9
26140	NGC 2794	09 13 14.0	+17 47 54	211.998	39.66	SBbc	4.4
26517	UGC 4978	09 19 29.5	+04 06 39	228.33	35.	Scd	6.6
27792	UGC 5187	09 39 59.1	+41 19 19	180.48	49.151	SBbc	4.3

PGC	alternate	RA	DEC	$l_2$	$b_2$	type	t-type
	name	(1950)	(1950)				
28310	UGC 5274	09 47 27.1	+16 31 12	217.808	46.773	SBc	5.9
28401	UGC 5277	09 47 46.8	+65 43 32	146.371	42.549	SBbc	3.6
31159	IC 616	10 30 06.6	+16 07 06	225.059	55.975	Sc	5.9
32091	MCG -2-28-6	10 42 40.9	-09 48 04	259.165	41.833	Scd	6.9
32638	NGC 3438	10 49 48.6	+10 48 45	237.817	57.468	Sbc	3.8
33465	UGC 6135	11 01 46.7	+45 23 41	165.66	62.14	Sbc	3.7
36925	NGC 3890	11 46 33.4	+74 34 49	128.538	42.143	Sc	4.8
38268	UGC 7072	12 02 39.6	+29 03 37	201.044	79.663	Sd	8.0
38908	UGC 7208	12 09 56.8	+39 23 20	154.619	75.523	Sbc	4.4
39728	NGC 4275	12 17 21.8	+27 53 54	207.098	82.977	Sb	2.8
46767	NGC 5123	13 20 58.7	+43 20 50	103.009	72.793	Sc	5.9
49906	NGC 5405	13 58 40.3	+07 56 35	346.52	64.498	Sc	4.8
55750	IC 1132	15 37 53.7	+20 50 28	32.76	51.093	Sc	5.4
56010	MCG 6-35-5	15 44 37.1	+33 22 38	53.068	51.938	SBc	6.2
57931	UGC 10357	16 20 18.3	+40 33 50	64.166	44.975	Sbc	3.5
58410	UGC 10436	16 29 24.2	+41 15 44	65.158	43.262	SBc	5.3
70962	MRK 318	23 15 05.9	+13 43 38	91.06	-42.989	Sbc	3.8
71106	NGC 7620	23 17 37.3	+23 56 49	97.621	-34.122	Sc	5.9
72144	UGC 12740	23 39 22.1	+23 32 15	103.087	-36.362	Sc	6.0

PGC	alternate	RA	DEC	<i>l</i> 2	<i>b</i> 2	type	t-type
	name	(1950)	(1950)				
72453	UGC 12784	23 45 32.0	+17 11 49	102.139	-42.824	SBbc	3.6

Table 2.2. Sample properties.  $D_{25}$ ,  $b/a_{25}$  are the diameters and axis ratios measured from the isophote at a  $B$ -band surface brightness,  $\mu_B = 25 \text{ mag/''}^2$  tabulated from the PGC (Paturel *et al.* 1997). Galactic absorption in  $B$ -band,  $A_B$  calculated using the Galactic absorption law of Cardelli *et al.* (1989). Apparent and absolute  $B$ -magnitudes tabulated from RC3 catalog (de Vaucouleurs *et al.* 1991).  $M_B$  takes  $H_0 = 75 \text{ km/s}$  and has been calculated from heliocentric recession velocities corrected for peculiar motions associated with the the local group and the Virgo cluster.

PGC	$D_{25}$	$b/a_{25}$	$m_B$	$A_B$	V	$M_B$
mag	arcsec		mag	mag	km/s	mag
2162	0.8	0.90	15.5	0.08	5448	-18.9
3512	0.9	0.87	14.4	0.14	5435	-20.0
5345	1.1	0.80	15.2	0.14	2132	-17.3
5673	1.2	0.93	14.8	0.23	4485	-19.3
6855	1.1	0.81	15.8	0.36	4834	-18.7
7826	0.9	0.92	15.2	0.32	2371	-17.6
8941	0.9	0.92	14.9	0.39	9447	-21.0
14564	1.0	0.85	14.2	1.10	3483	-20.2
15531	1.1	0.85	15.1	0.36	5557	-19.6
16274	0.8	1.00	15.0	0.32	8915	-20.6
19767	0.9	0.83	16.3	0.22	5133	-18.2
20938	0.5	0.88	15.9	0.22	4695	-18.3
23333	0.9	0.86	14.6	0.14	4654	-19.5

PGC	D <sub>25</sub>	$b/a_{25}$	m <sub>B</sub>	A <sub>B</sub>	V	M <sub>B</sub>
mag	arcsec		mag	mag	km/s	mag
23598	0.9	0.95	15.3	0.26	7485	-20.0
23913	1.1	0.97	15.3	0.30	6330	-19.7
24788	0.7	0.83	15.1	0.15	7556	-20.2
26140	1.1	0.83	14.0	0.14	8760	-21.6
26517	1.5	0.84	15.2	0.20	4135	-18.7
27792	0.9	0.81	14.7	0.08	1465	-17.1
28310	1.1	0.99	14.7	0.18	5908	-19.9
28401	1.3	0.90	14.4	0.71	3365	-19.7
31159	1.0	0.85	14.8	0.17	5779	-19.9
32091	1.3	0.92	14.2	0.15	2511	-18.4
32638	0.8	0.93	14.1	0.10	6488	-20.7
33465	0.9	0.95	13.1	0.03	5948	-21.5
36925	0.8	0.92	14.4	0.26	6827	-20.7
38268	1.2	0.85	15.3	0.08	3152	-18.0
38908	1.0	0.91	15.0	0.13	7078	-20.1
39728	0.8	0.90	14.0	0.09	2317	-18.6
46767	1.1	0.89	13.7	0.06	8323	-21.6
49906	0.8	0.94	14.9	0.17	6922	-20.0
55750	1.0	0.92	14.5	0.27	4525	-19.8

PGC	D <sub>25</sub>	$b/a_{25}$	m <sub>B</sub>	A <sub>B</sub>	V	M <sub>B</sub>
mag	arcsec		mag	mag	km/s	mag
56010	0.8	0.96	15.3	0.14	4468	-18.8
57931	0.8	0.88	15.1	0.05	9280	-20.5
58410	1.0	0.97	14.5	0.05	9059	-21.0
70962	0.7	0.80	14.2	0.20	4455	-20.0
71106	1.0	0.96	13.8	0.34	9582	-22.1
72144	0.6	0.95	16.6	0.27	10521	-19.4
72453	1.3	1.00	14.7	0.30	9952	-21.2



### 2.3 Photometric Observations

$R$  and  $I$ -band Harris filters were used for imaging our survey galaxies. Harris filters provide colors which closely match the Kron–Cousins photometric system (Cousins 1978). Images were acquired over 2.5 years from May, 1998 to January, 2001 at the WIYN telescope at KPNO, the 2.1m telescope at KPNO, and the Harlan J. Smith 2.7m telescope at McDonald Observatory. Table 2.3 provides a summary of these telescopes and instruments.

The choice of filters were prompted by several factors: (1)  $R$  and  $I$ -bands have both been used extensively in Tully-Fisher surveys (e.g., Mathewson *et al.* 1992; Giovanelli *et al.* 1994; Courteau 1996<sup>4</sup>) providing us with complimentary samples of inclined galaxies at comparable distances. (2) Images taken in either band were relatively unaffected by Galactic absorption, therefore providing an excellent window for studying normal spiral disks. (3) Another motivation for using the  $R$ -band for this study was to compare  $R$ -band images ( $\lambda_{eff} = 6800\text{\AA}$ ) to DensePak continuum measures ( $\lambda_{eff} = 6800\text{\AA}$ ; Chapter 3). (4)  $I$ -band images were least affected by bursts of star formation, and flocculence due to these bursts and dust lanes – important when trying to study the shape and photometric structure of disk galaxies. (5)  $R$  and  $I$ -band share advantages (2–4) over imaging at shorter wavelengths and are observationally inexpensive when compared to infrared imaging. In addition to our  $R$  and  $I$ -band data, we have  $B$  and  $K$ -band images for a fraction of our sample that will be used to explore a broader color base-line.

---

<sup>4</sup>Courteau uses Lick  $r$ -band.

In the future, these colors will help us understand the stellar populations of our sample and how measures of disk parameters change as a function of wavelength.

As described in §2.2, we desired to measure axis ratios and position angles for our sample. Since spiral structure dominated images out to at least three scale lengths, we chose exposure times which yielded images with sufficient signal to noise to measure axis ratios and position angles out to  $\sim 4.5$  scale lengths in Freeman disks; limiting surface brightnesses for our images were  $\mu_R = 25.5 \text{ mag/arcsec}^2$  and  $\mu_I = 25 \text{ mag/arcsec}^2$ . Typical exposure times were 1000s at the KPNO 2.1m telescope, 600s at the McDonald 2.7m telescope, and 450s at the WIYN 3.5m telescope for both  $R$  and  $I$ -bands.

Observations were taken on 17 nights over 10 imaging runs from 1998 to 2001 with the following distribution at each telescope: WIYN (11 nights; 8 runs)<sup>5</sup>, KPNO 2.1m (3 nights; 1 run) and the Harlan Smith 2.7m (3 nights; 1 run). For each night, we collected a complete set of bias frames taken at the beginning and ending of each night along with dome flats typically taken during twilight hours. Standard stars were observed on four photometric nights. We collected  $R$ -band images for 37 of the 39 galaxies and imaged 38 of the sample galaxies in the  $I$ -band. Repeat observations were used to internally calibrate photometry from runs which were very clear but during which no standard stars were observed. An observation log of objects, telescopes, instruments, filters, exposure times, seeing and quality of the observations can be found in Table 2.4.

---

<sup>5</sup>All WIYN observations for this project were taken as backup targets for observational programs requiring better seeing or dark time. Principal investigators for WIYN runs were Bershadsky & Hoessel.

Table 2.3. Instrument Properties

Observatory	Telescope	Instrument	F/#	Scale "/pix	Field of View arcmin <sup>2</sup>	Read-Noise $e^-$	Gain $e^-/\text{ADU}$	Overscan columns
WIYN	WIYN 3.5m	S2KB	6.3	0.195	$6.7 \times 6.7$	8.0	2.8	32
WIYN	WIYN 3.5m	MiniMo	6.3	0.141	$9.5 \times 9.5$	5.4	1.3	50
KPNO	2.1m	T2KA	7.5	0.305	$10.4 \times 10.4$	4.0	3.6	30
McDonald	2.7m	IGI	8.8	0.57	$7 \times 7$	4.1	2.5	16

Table 2.4. Observing log for photometric data. Q is the photometric zero-point uncertainty. Photometric errors were determined by (1) frame to frame variations in the raw data for selected field stars and (2) comparison of photometry from run to run. Q=1 is photometric, Q=2 when photometric errors were less than 0.05 mag. Q=3 when photometric errors were between 0.05 and 0.10 mag while Q=4 if photometric errors were greater than 0.1 mag.

PGC	Band	Telescope	Instrument	U.T. date	Time	Q	Seeing
					sec		// FWHM
02162	R	WIYN 3.5m	MiniMo	10/16/00	450	1	0.8
	I	WIYN 3.5m	MiniMo	10/16/00	450	1	0.8
03512	R	WIYN 3.5m	MiniMo	10/17/00	450	1	0.7
	I	WIYN 3.5m	MiniMo	10/17/00	450	1	0.7
05345	R	KPNO 2.1m	T2KA	01/21/01	1000	1	0.8
	I	KPNO 2.1m	T2KA	01/20/01	1500	1	0.8
05673	R	KPNO 2.1m	T2KA	01/21/01	600	1	0.8
	I	KPNO 2.1m	T2KA	01/20/01	1500	1	0.8
06855	R	KPNO 2.1m	T2KA	01/20/01	1200	1	0.8
	I	KPNO 2.1m	T2KA	01/20/01	1200	1	0.8
07826	R	KPNO 2.1m	T2KA	01/21/01	500	1	1.2
	R	KPNO 2.1m	T2KA	01/22/01	1200	3	1.0
	R	WIYN 3.5m	MiniMo	11/19/00	450	2	2.2
	I	WIYN 3.5m	MiniMo	11/19/00	450	2	2.2

PGC	Band	Telescope	Instrument	U.T. date	Time	Q	Seeing
					sec		// FWHM
	I	KPNO 2.1m	T2KA	01/22/01	800	3	1.0
08941	R	KPNO 2.1m	T2KA	01/21/01	1000	1	1.2
	R	WIYN 3.5m	S2KB	09/05/99	600	2	0.9
	I	WIYN 3.5m	S2KB	09/05/99	600	2	0.9
14564	R	KPNO 2.1m	T2KA	01/21/01	800	1	0.9
	R	WIYN 3.5m	S2KB	09/06/99	300	2	0.9
	I	WIYN 3.5m	S2KB	09/06/99	450	2	0.9
15531	R	KPNO 2.1m	T2KA	01/21/01	900	1	1.1
	R	WIYN 3.5m	S2KB	09/06/99	300	2	0.9
	I	WIYN 3.5m	S2KB	09/06/99	450	2	0.9
16274	R	KPNO 2.1m	T2KA	01/22/01	400	3	1.2
	I	KPNO 2.1m	T2KA	01/22/01	400	3	1.2
	R	WIYN 3.5m	MiniMo	11/19/00	450	2	1.8
	I	WIYN 3.5m	MiniMo	11/19/00	450	2	1.7
19767	R	KPNO 2.1m	T2KA	01/21/01	400	1	1.0
	I	KPNO 2.1m	T2KA	01/21/01	400	1	1.0
	R	WIYN 3.5m	MiniMo	11/19/00	450	2	1.2
	I	WIYN 3.5m	MiniMo	11/19/00	450	2	0.9
20938	R	KPNO 2.1m	T2KA	01/20/01	1200	2	0.8

PGC	Band	Telescope	Instrument	U.T. date	Time	Q	Seeing
					sec		// FWHM
	R	KPNO 2.1m	T2KA	01/21/01	400	1	1.0
	I	KPNO 2.1m	T2KA	01/20/01	1200	2	0.8
23333	R	KPNO 2.1m	T2KA	01/22/01	1800	4	1.2
	I	WIYN 3.5m	MiniMo	02/08/00	450	4	1.1
23598	R	KPNO 2.1m	T2KA	01/21/01	1200	1	1.0
	R	McD 2.7m	IGI/TK4	05/21/99	600	2	1.6
	R	WIYN 3.5m	MiniMo	12/05/99	300	2	0.7
	I	WIYN 3.5m	S2KB	05/12/99	750	2	0.7
	I	KPNO 2.1m	T2KA	01/21/01	400	1	1.0
23913	I	McD 2.7m	IGI/TK4	05/19/99	800	3	1.6
	R	McD 2.7m	IGI/TK4	05/21/99	600	2	2.0
24788	R	KPNO 2.1m	T2KA	01/20/01	1307	2	0.7
	R	KPNO 2.1m	T2KA	01/21/01	400	1	1.0
	I	KPNO 2.1m	T2KA	01/20/01	1200	2	0.7
26140	R	KPNO 2.1m	T2KA	01/20/01	900	3	0.7
	R	McD 2.7m	IGI/TK4	05/20/99	400	4	1.8
	R	KPNO 2.1m	T2KA	01/21/01	400	1	1.0
	I	WIYN 3.5m	S2KB	05/11/99	300	2	1.4
26517	R	KPNO 2.1m	T2KA	01/21/01	1200	1	1.0

PGC	Band	Telescope	Instrument	U.T. date	Time	Q	Seeing
					sec		// FWHM
	I	KPNO 2.1m	T2KA	01/21/01	400	1	1.0
	I	WIYN 3.5m	MiniMo	03/04/00	450	3	1.2
27792	I	WIYN 3.5m	MiniMo	03/04/00	450	3	1.6
28310	R	KPNO 2.1m	T2KA	01/20/01	1200	3	0.6
	I	WIYN 3.5m	S2KB	05/11/99	1200	2	1.4
28401	R	WIYN 3.5m	MiniMo	11/19/00	450	2	1.5
	I	WIYN 3.5m	MiniMo	11/19/00	450	2	1.5
31159	R	McD 2.7m	IGI/TK4	05/20/99	600	3	1.8
	I	WIYN 3.5m	S2KB	05/11/99	450	2	1.0
32091	I	WIYN 3.5m	MiniMo	03/04/00	450	3	1.6
32638	R	KPNO 2.1m	T2KA	01/21/01	1200	1	1.0
	I	KPNO 2.1m	T2KA	01/21/01	400	1	1.0
	I	McD 2.7m	IGI/TK4	05/21/99	400	1	2.0
	I	WIYN 3.5m	MiniMo	03/04/00	450	4	1.4
33465	R	KPNO 2.1m	T2KA	01/21/01	1000	1	1.0
	I	WIYN 3.5m	MiniMo	03/04/00	450	4	1.3
36925	R	McD 2.7m	IGI/TK4	05/21/99	600	1	2.0
	I	WIYN 3.5m	S2KB	05/11/99	600	2	1.4
38268	R	KPNO 2.1m	T2KA	01/21/01	1200	1	0.9

PGC	Band	Telescope	Instrument	U.T. date	Time	Q	Seeing
					sec		// FWHM
	I	KPNO 2.1m	T2KA	01/20/01	1800	4	0.6
	I	KPNO 2.1m	T2KA	01/21/01	1200	1	0.9
38908	R	McD 2.7m	IGI/TK4	05/19/99	600	3	1.8
	I	WIYN 3.5m	S2KB	05/11/99	450	2	1.1
39728	R	KPNO 2.1m	T2KA	01/21/01	1200	1	0.9
46767	R	McD 2.7m	IGI/TK4	05/19/99	600	3	1.6
	I	WIYN 3.5m	S2KB	05/11/99	300	2	1.1
49906	R	McD 2.7m	IGI/TK4	05/19/99	600	3	1.6
	I	WIYN 3.5m	S2KB	05/11/99	450	2	1.4
55750	R	McD 2.7m	IGI/TK4	05/19/99	462	3	1.8
	I	WIYN 3.5m	S2KB	05/11/99	450	2	1.9
56010	R	McD 2.7m	IGI/TK4	05/19/99	562	3	1.8
	I	WIYN 3.5m	S2KB	05/11/99	750	2	1.8
57931	R	KPNO 2.1m	T2KA	01/21/01	900	1	0.9
	I	McD 2.7m	IGI/TK4	05/20/99	800	2	2.3
58410	R	WIYN 3.5m	S2KB	05/20/98	600	3	1.1
	R	McD 2.7m	IGI/TK4	05/19/99	600	3	1.6
	I	McD 2.7m	IGI/TK4	05/19/99	506	3	1.6
70962	R	WIYN 3.5m	MiniMo	10/16/00	450	1	0.65



PGC	Band	Telescope	Instrument	U.T. date	Time	Q	Seeing
					sec		// FWHM
	I	WIYN 3.5m	MiniMo	10/16/00	450	1	0.45
71106	R	WIYN 3.5m	MiniMo	10/16/00	450	1	0.35
	I	WIYN 3.5m	MiniMo	10/16/00	450	1	0.35
72144	R	WIYN 3.5m	MiniMo	10/16/00	450	1	0.6
	I	WIYN 3.5m	MiniMo	10/16/00	450	1	0.6
72453	R	WIYN 3.5m	MiniMo	10/16/00	450	1	0.8
	I	WIYN 3.5m	MiniMo	10/16/00	450	1	0.7

### 2.3.1 Preliminary Reductions

We used standard IRAF tasks to process images for overscan correction, bias subtraction, and flat-fielding. The standard IRAF cosmic ray cleaning task was augmented using information from neighboring pixels, thus enhancing the cleaning of extended cosmic ray hits (and detector flaws). All *I*-band images were fringe corrected. We created master fringe frames by masking sources and combining all long exposures taken in a night, scaling by the exposure time. The high spatial frequency fringe pattern remained constant from night to night, allowing us to combine fringe frames from different nights. The IRAF *ccdproc* routine scaled this master fringe frame to image frames and subtracted the fringe pattern from data.

Once individual data frames were fully processed, the sky background was calculated using an iteratively clipped mean and subtracted from all frames. Some images taken with the MiniMosaic camera on WIYN contained low-frequency background gradients at 2–5% of sky levels which could not be removed with either flat-fields or overscan corrections. We suspect these features are gain variations because the variation scales with the background. While a 2–5% variation in the sky level only introduces a 2–5% error into the photometry, background gradients will impact measures of axis ratios and position angles made in the outer regions of disks. Since these measurements are critical to this study, we corrected background gradients by fitting a second order polynomial with cross terms to the masked image. After subtracting the resultant fit, large-scale image gradients in the background were well below 0.25%(Figure 2.3). Offsets between

multiple target exposures were applied and frames were combined, yielding fully reduced and combined images in  $R$  and  $I$ -bands for all of our imaging observations.

## 2.4 Analysis

In this section we describe the methodology used for (1) measuring magnitudes, (2) measuring surface brightness profiles, (3) fitting two-dimensional bulge-disk models, (4) measuring axis ratios and position angles, and (5) determining the amplitude of disk asymmetry for our sample galaxies.

### 2.4.1 Photometric Calibrations, Total Magnitudes and Colors

We verified that the curves of growth of the integrated light profile for all but two galaxies reached asymptotic values at large radii, indicating background subtraction was done correctly<sup>6</sup> (see Figure 2.4 and for example, the Atlas for the full sample). Because the signal to noise ratio was so high we have the luxury of using those asymptotic counts from the curves of growth to calculate total  $R$  and  $I$ -band magnitudes after we set photometric zero-points. To calibrate magnitude zero points for our observations, we used Landolt (1983) standards observed during four photometric nights.<sup>7</sup> Air mass corrections have not yet been calculated and applied to these data but they should be small (less than 0.1 magnitudes). In addition to these directly calibrated data, there were several runs which had estimated photometric errors under 0.05 magnitudes, but for which no

---

<sup>6</sup>PGC 26517 and PGC 38268 still showed signs of improper background subtraction. Therefore, all parameters dependent on background measurements were excluded from tables in this Chapter.

<sup>7</sup>1/20/01 and 1/21/01 at the KPNO 2.1m telescope and 10/16/01 and 10/17/01 at the WIYN telescope

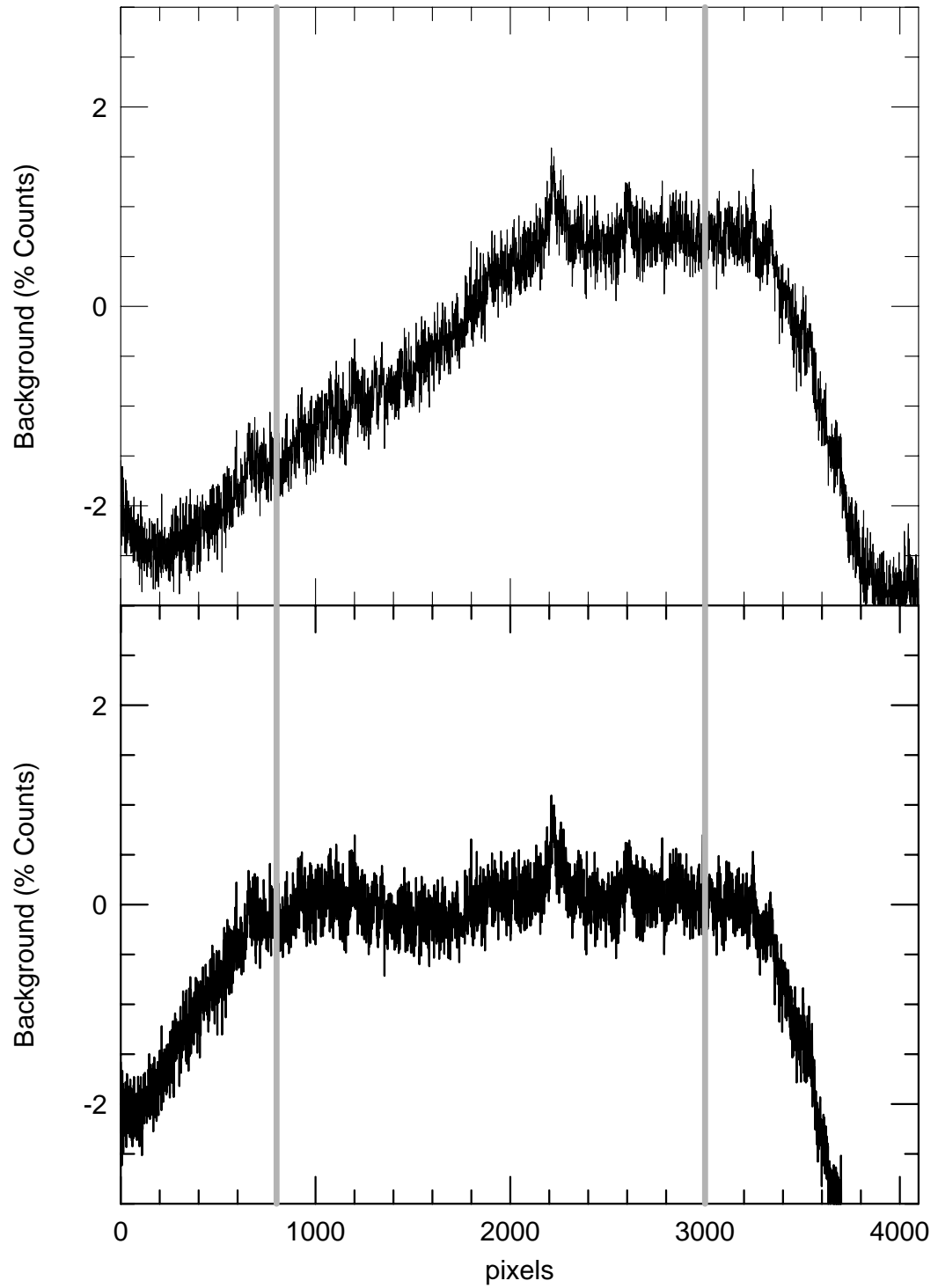


Fig. 2.3. Cross section of Mini-Mosaic image frame (mean of 5 columns), showing gradients as percentage variation in the sky background before (top panel) and after (bottom panel) fitting a polynomial surface between the two vertical solid lines.

standard stars were observed.<sup>8</sup> After correcting asymptotic counts for gain, telescope apertures, and exposure times, we calculated an internal boot-strapped calibration for these runs based on repeat observations of targets taken during directly calibrated runs. The data from the indirectly calibrated runs had magnitude zero-point errors estimated to be less than 0.05 based on both repeat observations taken during directly calibrated runs and exposure to exposure variations. We used our internal calibration to set magnitude zero-points (for fluxes measured in  $e^-/\text{m}^{-2}/\text{s}$ ) for all instrument and telescope combinations (Table 2.5). We also measured magnitudes for some galaxies from the McDonald 05/99 run even though photometric errors were large because we could directly calibrate these data with observed Landolt standard stars during this run. We list all total  $R$  and  $I$ -band magnitudes for galaxies observed during the above runs in Table 2.6. Using  $B$ -band magnitudes tabulated in Table 2.2 from the RC3 (de Vaucouleurs *et al.* 1991), and our measured  $R$  and  $I$ -band magnitudes, we find the mean colors for our sample are  $\overline{B - R} = 0.92 \pm 0.28$  and  $\overline{R - I} = 0.52 \pm 0.08$  (see Figure 2.5). Most of the scatter in  $B - R$  is due to the intrinsic uncertainties in RC3 magnitudes which arise because total  $B$ -magnitudes were calculated from several different original sources. Each source of photographic magnitudes required extensive calibration to be transformed to the RC3 total  $B$ -magnitude system.

---

<sup>8</sup>(1) WIYN 05/98, (2) WIYN 05/99, 3) WIYN 09/99, (4) WIYN 11/00, 5) WIYN 12/00

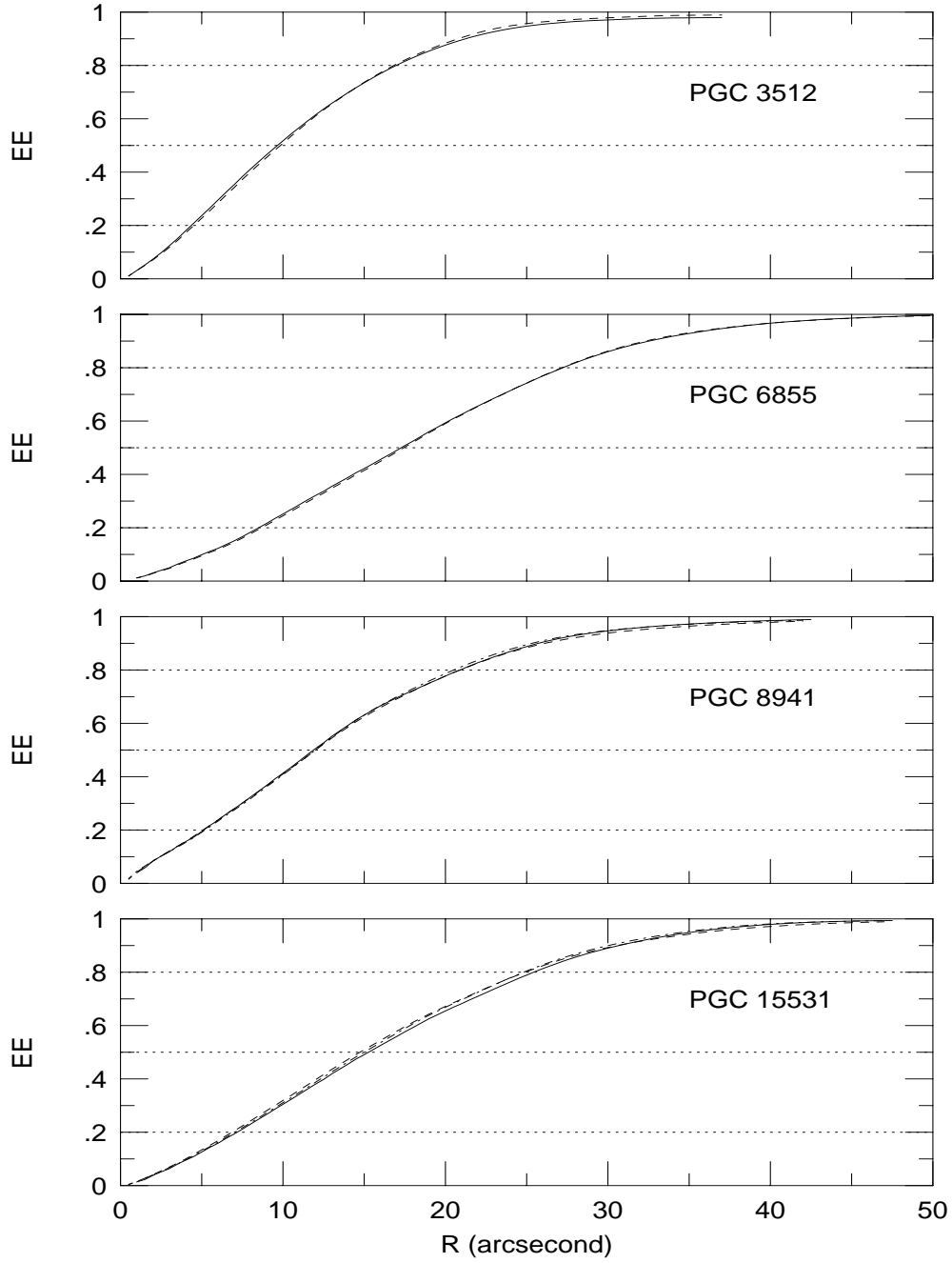


Fig. 2.4. The encircled energy radial profiles for 4 typical sample galaxies. These examples show the asymptotic growth of the light curves for these sky-subtracted images. The dotted lines mark 20%, 50% and 80% of the total flux. The point where the growth curve crosses these lines are used to measure the concentration index,  $C_{80:20} = 5 \log[r(80\%)/r(20\%)]$ , and the half-light radius,  $r_{1/2}$ . The asymptotic flux is used to calculate the total magnitude in  $R$  and  $I$  bands.

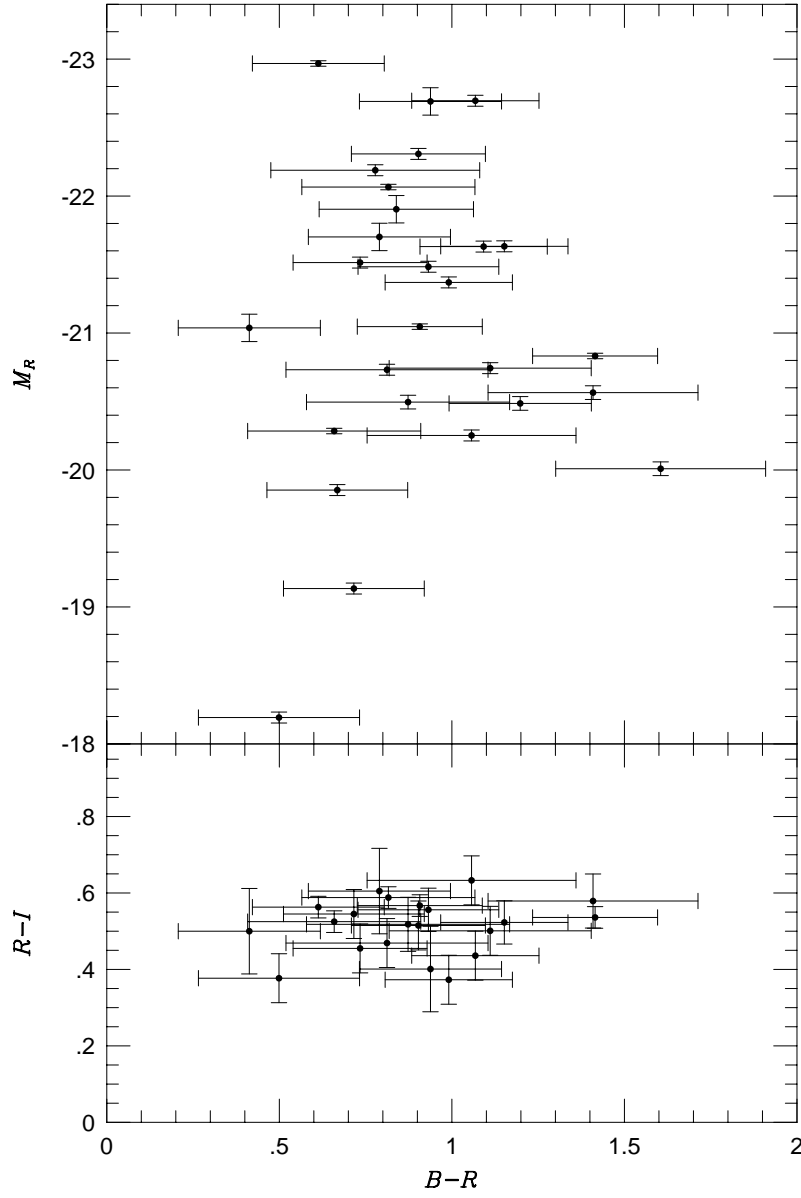


Fig. 2.5. Colors and Absolute magnitudes for our sample. We suspect the large range in  $B - R$  colors is due to larger errors in  $B$ -magnitudes listed in the RC3 catalog (see text).  $\overline{B - R} = 0.92 \pm 0.28$  and  $\overline{R - I} = 0.52 \pm 0.08$ .

Table 2.5. Photometric Zero-points. Magnitude zero-points calculated using fluxes with units  $e^-/\text{m}^2/\text{s}$ .

Band	McDonald	KPNO 2.1m	WIYN	WIYN
	T2K4	T2KB	S2KB	Mini-Mo
<i>R</i>	22.17	23.90	23.65	23.63
<i>I</i>	21.57	23.21	23.11	22.91



Table 2.6.  $R$  and  $I$ -band total magnitudes and structural parameters for survey galaxies

PGC	$m_R$	$m_I$	$r_{\eta=0.2}$	$r_{1/2}$	$C_{80:20}$
2162	$14.08 \pm 0.02$	$13.54 \pm 0.02$	17.5	7.2	3.92
3512	$13.35 \pm 0.02$	$12.76 \pm 0.02$	22.0	10.0	2.78
5345	$14.16 \pm 0.04$	$13.76 \pm 0.05$	37.0	17.2	2.30
5673	$13.30 \pm 0.04$	$12.76 \pm 0.05$	40.5	16.8	2.76
6855	$13.79 \pm 0.05$	$13.21 \pm 0.05$	35.8	17.5	2.42
7826	$13.58 \pm 0.04$	$12.98 \pm 0.05$	32.0	14.5	2.63
8941	$13.44 \pm 0.04$	$12.86 \pm 0.05$	27.5	12.0	2.91
14564	$12.66 \pm 0.04$	$12.10 \pm 0.05$	25.0	10.5	2.84
15531	$13.85 \pm 0.04$	$13.32 \pm 0.05$	35.0	15.0	2.66
16274	$13.67 \pm 0.04$	$12.92 \pm 0.05$	31.0	12.8	2.80
19767	$14.06 \pm 0.04$	$13.39 \pm 0.05$	34.0	14.0	2.63
20938	$14.25 \pm 0.04$		22.0	7.5	3.89
23333	$13.55 \pm 0.05$		25.5	11.5	2.68
23598	$13.67 \pm 0.04$	$13.07 \pm 0.04$	36.0	14.5	2.92
23913			41.0	16.5	2.74
24788	$13.59 \pm 0.04$	$13.11 \pm 0.05$	17.5	9.0	2.94
26140	$12.74 \pm 0.04$	$12.28 \pm 0.05$	28.2	11.5	3.58
27792			39.5	16.0	2.66
28310		$13.86 \pm 0.05$	28.8	13.5	2.78
28401	$13.12 \pm 0.05$	$12.42 \pm 0.05$	38.2	17.5	2.67

PGC	$m_R$	$m_I$	$r_{\eta=0.2}$	$r_{1/2}$	$C_{80:20}$
31159		$13.00 \pm 0.05$	31.0	13.8	2.77
32091			40.0	17.5	2.63
32638	$13.11 \pm 0.04$	$12.57 \pm 0.04$	15.0	6.5	3.30
33465	$12.51 \pm 0.04$		22.5	9.5	3.22
36925	$13.26 \pm 0.10$	$12.61 \pm 0.05$	23.0	9.75	3.04
38908		$13.00 \pm 0.05$	22.2	9.8	3.10
39728	$12.46 \pm 0.04$		22.0	11.0	2.45
46767	$12.56 \pm 0.10$	$12.15 \pm 0.05$	33.0	13.0	3.10
49906	$13.88 \pm 0.10$	$13.36 \pm 0.05$	28.0	11.5	2.72
55750		$12.41 \pm 0.05$	36.5	17.8	2.37
56010		$13.74 \pm 0.05$	29.0	14.5	2.74
57931	$13.86 \pm 0.04$		21.2	7.5	3.49
58410	$13.54 \pm 0.10$		34.0	13.0	3.08
70962	$13.16 \pm 0.02$	$12.59 \pm 0.02$	21.0	7.8	3.16
71106	$12.78 \pm 0.02$	$12.16 \pm 0.02$	22.2	8.8	3.52
72144	$14.80 \pm 0.02$	$14.12 \pm 0.02$	31.0	11.5	3.60
72453	$13.74 \pm 0.02$	$13.10 \pm 0.02$	35.0	13.2	3.14

### 2.4.2 Surface Brightness Profiles and Non-parametric Structural Indices

Disk surface brightness profiles can be used to measure several physically meaningful non-parametric characteristics of galaxy structure. Surface brightness profiles facilitated the measurement of several important structural indices, such as the half light radius,  $\eta$  radii as described below, and the concentration index. These robust measurements of characteristic scale and shape of light distributions can be used to estimate disk sizes and bulge–disk ratios. Since bulge-disk decompositions are model dependent, non-parametric structural indices derived from surface brightness profiles provide a powerful check on the derived model parameters.

We calculated surface brightness profiles for our sample using the IRAF *ellipse* routine (For more on *ellipse* see §2.3.4). *Ellipse* calculated isophotes in rings which had changing position angles and ellipticity. While the rings tend to follow spiral structure, surface brightness profiles derived using circular apertures were virtually indistinguishable because our galaxies are nearly face-on.

We measured two characteristic scales, the half-light radius,  $r_{1/2}$ , and the Petrosian  $\eta$ -radius at  $\eta = 0.2$ , as defined below, from these surface brightness profiles: (1) The half light radius was determined by the intersection between the monotonically increasing curve of growth and half the asymptotic flux. (2) The  $\eta$  index, a dimensionless and isophote-independent index defined as  $\eta \equiv I(r)/\langle I(r) \rangle$ , where  $I(r)$  is the surface brightness in a ring at radius  $r$ , and  $\langle I(r) \rangle$  is the mean surface brightness within the ring of radius  $r$ , is unity at zero radius and decreased to zero at large radii. Profiles of  $\eta$  versus radius, unlike growth curves, are not monotonic (Sandage & Perelmuter 1990;

for examples see Figure 2.6 and Atlas). However, most  $\eta$  profiles were monotonic for  $\eta < 0.5$ . In ranges where the radial profile of  $\eta$  is monotonic, one can define a unique radius which corresponds to a set value of  $\eta$ . The radius measured when  $\eta = 0.2$ ,  $r_{\eta=0.2}$ , contains 99% of the light from a purely exponential profile and was single-valued for all our galaxy profiles. The measured ratio  $r_{\eta=0.2}/r_{1/2} = 2.4 \pm 0.4$  for our sample. The theoretical value of the ratio for exponential profiles should be  $r_{\eta=0.2}/r_{1/2} = 2.16$ , consistent with our measurements. This ratio is inconsistent with Gaussian ( $r_{\eta=0.2}/r_{1/2} = 1.95$ ) and  $r^{1/4}$ -law profiles ( $r_{\eta=0.2}/r_{1/2} = 1.82$ ) (Bershady, Jangren & Conselice 2000).

We also measured the concentration index  $C_{80:20} \equiv 5 \log(r[80\%]/r[20\%])$  measured using radii enclosing 80% and 20% of the light respectively. Theoretically, exponential profiles should have  $C_{80:20} = 2.7$  and  $r^{1/4}$  profiles have  $C_{80:20} = 5.2$ . Concentration indices for our sample varied from  $2.3 < C_{80:20} < 3.9$ . Measurements of  $r_{1/2}$ ,  $r_{\eta=0.2}$  and  $C_{80:20}$  listed in Table 2.6 were made in the *I*-band unless the image quality was superior in the *R*-band. Both *R* and *I*-band images should yield nearly identical measures of concentration index, as Bershady, Jangren & Conselice (2000) showed color systematics were negligible between *B* and *R*-band measures of image concentration.

### 2.4.3 Bulge-Disk Decomposition

The utility of spiral galaxy surface brightness profiles as tools for studying disk structure can be increased by considering the bulge-disk decompositions; bulge-disk decompositions can be used to measure disk scale length, and we hoped two-dimensional bulge-disk decompositions could be used to measure disk axis ratios and position angles. Spiral galaxy surface brightness profiles were first modeled by an exponential disk and

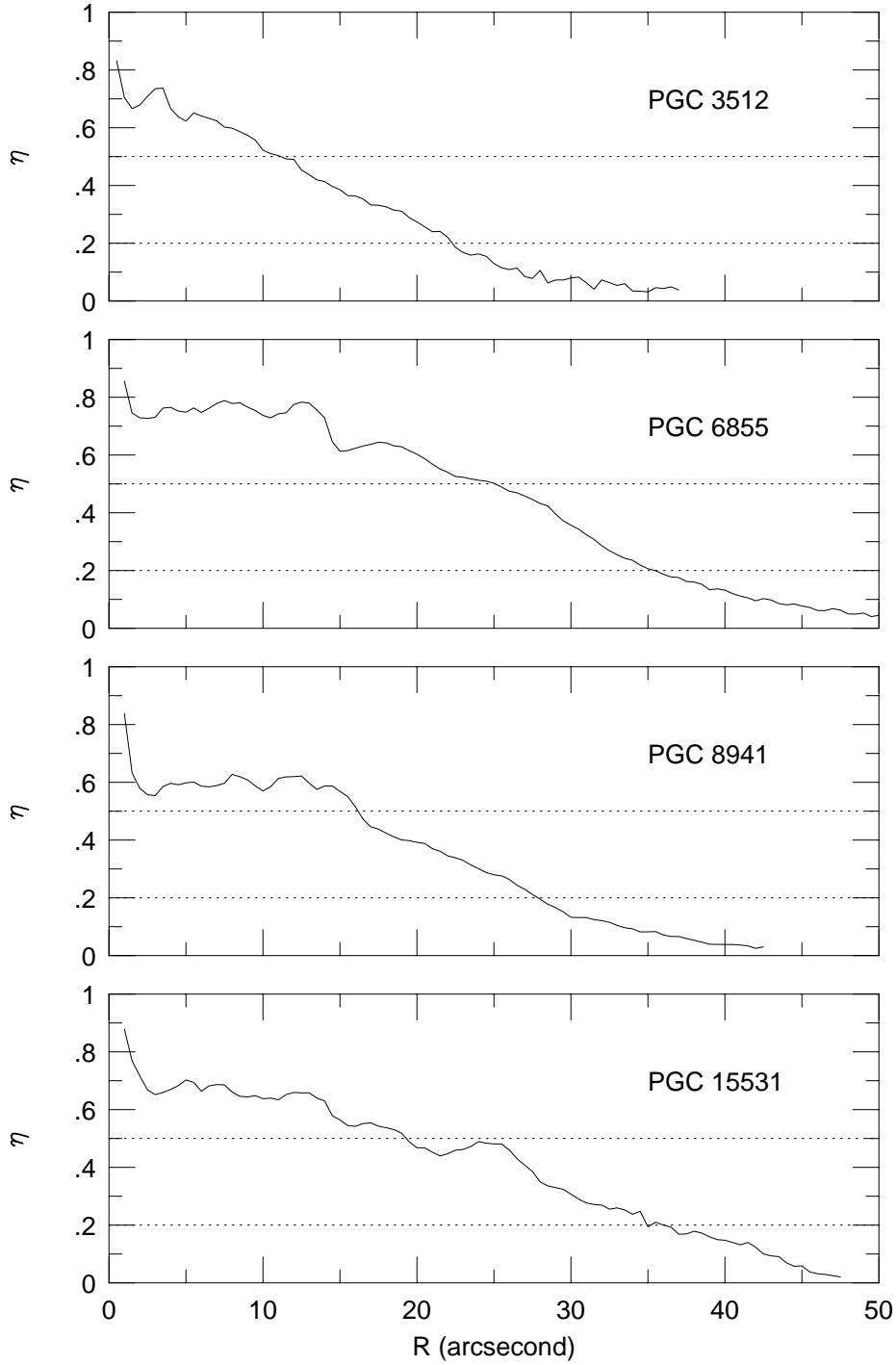


Fig. 2.6. Four examples of  $\eta$  radial profiles.  $\eta \equiv I(r)/\langle I(r) \rangle$ . The function  $\eta$  is non-monotonic, but in most cases is single-valued for  $\eta < 0.5$  (PGC 15531 is an exception).  $r_{\eta=0.2}$ , the radius which corresponds to  $\eta = 0.2$ , contains 99% of the light for a pure exponential disk.

a  $R^{1/4}$  bulges (de Vaucouleurs 1953). However, profiles were found which could not be fit with this simple two component model; these Type II profiles were under-luminous in inner regions (Freeman 1970). To solve this problem, Kormendy (1977) introduced a modified exponential profile,  $I(r) = I_0 \exp[-(\alpha r + \beta^3 r^{-3})]$ , which could model the behaviors of both Type I and Type II surface brightness profiles. Bulge–disk deconvolutions have continued to garner critical attention and improved methodology was the result (Borson 1981; Kent 1986; Schombert & Bothun 1987; Andredakis & Sanders 1994). Two-dimensional bulge–disk decompositions became more common as computational power increased. The primary advantages of this methodology were (1) a better modeling of seeing effects and (2) a decoupling of bulge and disk parameters; bulges and disks with different ellipticities and position angles were modeled independently (de Jong 1996a; Moriondo *et al.* 1998; Möllenhoff & Heidt 2001). Two-dimensional galaxy models even included bars (de Jong 1996a), lenses and rings (Prieto *et al.* 2001). The link between bulge-disk decompositions and Hubble type was one of the main themes of these studies. Results of bulge-disk decompositions showed the bulge to disk ratio and bulge surface brightness were both correlated with Hubble type (Borson 1981; Simien & de Vaucouleurs 1986; Andredakis & Sanders 1994; de Jong 1996b).

Our aim in using bulge-disk decompositions was to measure scale lengths for our sample galaxies so that they could be used as a criterion for measuring other disk parameters including axis ratios, position angle and asymmetry. Bulge-disk decompositions are typically model-dependent fits to galaxy light profiles. They can be performed on surface brightness profiles or on the full two-dimensional images. We adopted two-dimensional bulge-disk decompositions because of their anticipated ability to measure photometric

axis ratios and position angles. Our expectation was that by fitting the entire disk with a single model, the effect of spiral structure on model parameters would be mitigated; we expected that the large azimuthal variations of spiral arms would cancel out when fitting a single model. Although our anticipations and expectations turned out to be illusory, our bulge–disk decompositions provided useful information.

For our two-dimensional bulge-disk decompositions, we adopted the model components used by de Jong (1996a) which included an exponential disk,

$$\mu_{\text{disk}}(r) = \mu_0 + 1.086r/h, \quad (2.1)$$

where  $\mu_0$  is the central disk surface brightness and  $h$  is the disk scale length, and exponential bulge,

$$\mu_{\text{bulge}}(r) = \mu_e + 1.823(r/r_e - 1) \quad (2.2)$$

where  $\mu_e$  is the effective bulge surface brightness and  $r_e$  is the effective bulge radius. De Jong also used a model component for bars, but since barred galaxies were excluded from our sample, we avoided adding additional complexity to our bulge-disk fits. Unlike de Jong, we did not smooth our bulge–disk models by a Gaussian with a FWHM equal to the seeing. Ignoring the effect of seeing will tend to lengthen the bulge scale length and decrease the bulge central surface brightness. Given the comparable sizes of the seeing disk and the bulge scale length, our data set was not ideal for studying bulge characteristics.

We fit the bulge–disk models by minimizing  $\chi^2$ , the square of the difference between model and observed counts divided by the noise calculated from the image, over four square arcminutes (with point sources masked). We found a multidimensional downhill simplex method (Press *et al.* 1992) was the most efficient means for minimizing  $\chi^2$ . Operating from an initial guess, the algorithm stepped through multidimensional space towards the direction which corresponds to the greatest decrease of the function  $\chi^2$ . The way in which the parameters changed as they moved through multidimensional space has been compared to the movement of amoebas; this metaphor gives the algorithm its commonly used name. Amoeba was susceptible to being caught in local minima and yielding solutions which were sensitive to both the initial conditions and initial step sizes. To prevent amoeba from falling into a local minimum we restarted the algorithm three times from the previous solution using initial step sizes that should have been large enough to move amoeba out of a local minima. After  $\chi^2$  minimization, we found the strongest residuals resulted from spiral structure (Figure 2.7).

Before proceeding with bulge–disk fits for all galaxies, we examined images to find galaxies with bulges offset from disk centers. While some galaxies showed significant lopsidedness, we did not notice large offsets of bulge and disk centers. Therefore, we decided to symmetrize all images before proceeding. The most important effect of symmetrization is it forces the bulge and disk to have a common center; this is a concern but as we address it later, it appears not to significantly affect results. Symmetrization was performed by rotating images  $180^\circ$  around their centers and creating a difference image. Positive residuals were subtracted from the original image, yielding symmetrized



images relatively free of flocculence and all odd asymmetry terms (The method for creating symmetrized images is closely related to measurements of rotational asymmetry described in §2.3.5.1).

The advantages of performing bulge-disk decompositions on symmetrized galaxy images were (1) a significant reduction in residuals, (2) improved bulge fits, and (3) symmetrizing images removed most stars and made masking our potentially contaminating stars easier. However, our concern was that disk scale length measurements would be affected by the symmetrization process, so we compared scale lengths from two-dimensional bulge-disk fits of symmetrized images to scale lengths measured (1) by fitting a straight line to the flat region of the exponential surface brightness, (2) by employing the IRAF one-dimensional bulge-disk decomposition routine, *nfit1d* and (3) by fitting two-dimensional bulge-disk decompositions to a subset of both symmetrized and (4) unsymmetrized images. All four measurements of disk asymmetry were in good agreement, with a mean difference of scale lengths of less than 0.3 arcseconds and standard deviations less than 2.0 arcseconds. The closest matching set of scale lengths were those from two-dimensional bulge-disk decompositions of symmetrized and unsymmetrized images. The standard deviation of the difference between the two measures was only 1.4 arcseconds. Because decompositions of symmetrized images yielded better bulge fits, we chose to measure all bulge-disk parameters from symmetrized images (Table 2.7). Fitting symmetrized images comes at the expense of forcing bulges and disks to have a common center.

Table 2.7. Two-Dimensional bulge-disk decomposition parameters using symmetric images. Tables lists the central disk surface brightnesses ( $\mu_0$ ), scale length ( $h$ ), effective bulge surface brightness ( $\mu_e$ ), effective bulge radius ( $r_e$ ) and disk-to-bulge ratio (D/B).

PGC	$R$					$I$				
	$\mu_0$	$h$	$\mu_e$	$r_e$	D/B	$\mu_0$	$h$	$\mu_e$	$r_e$	D/B
	mag/ $''^2$	$''$	mag/ $''^2$	$''$		mag/ $''^2$	$''$	mag/ $''^2$	$''$	
2162	19.66	4.6	19.16	1.	7.07	19.07	4.4	18.57	1.1	5.31
3512	19.34	6.3	20.24	1.4	23.9	18.53	5.1			
5345	21.33	12.2	22.	0.1		21.07	13.1	24.26	4.7	
5673	20.52	11.5	21.31	2.5	22.9	19.94	11.4	20.63	2.8	16.4
6855	21.06	12.8	21.68	1.7	52.3	20.47	12.9	21.03	2.	36.5
7826	20.39	9.8	22.4	3.5	26.4	19.77	9.8	21.76	3.6	24.3
8941	19.92	8.1	19.02	1.	14.8	19.58	8.7	18.79	1.4	9.81
14564	19.07	7.1	20.04	2.	16.3	18.5	7.2	19.59	2.	18.4
15531	20.82	10.7	21.37	1.8	30.4	20.24	10.3	20.92	2.	26.0
16274	20.21	8.8	20.78	1.4	35.0	19.47	8.6	19.97	1.6	24.0
19767	20.85	9.5	22.17	2.	40.2	20.15	9.3	21.36	1.9	38.2
20938	19.03	5.	19.04	1.8	4.02		4.9		1.7	
23333	20.95	8.4	22.72	3.5	15.9		7.5		2.4	
23598	20.63	9.	21.42	1.9	24.6	19.94	9.1	20.83	2.4	17.3
23913		12.1				20.58	11.7	21.54	3.6	13.4
24788	19.54	5.4	19.72	0.8	28.5	19.03	5.3	19.37	1.2	14.0

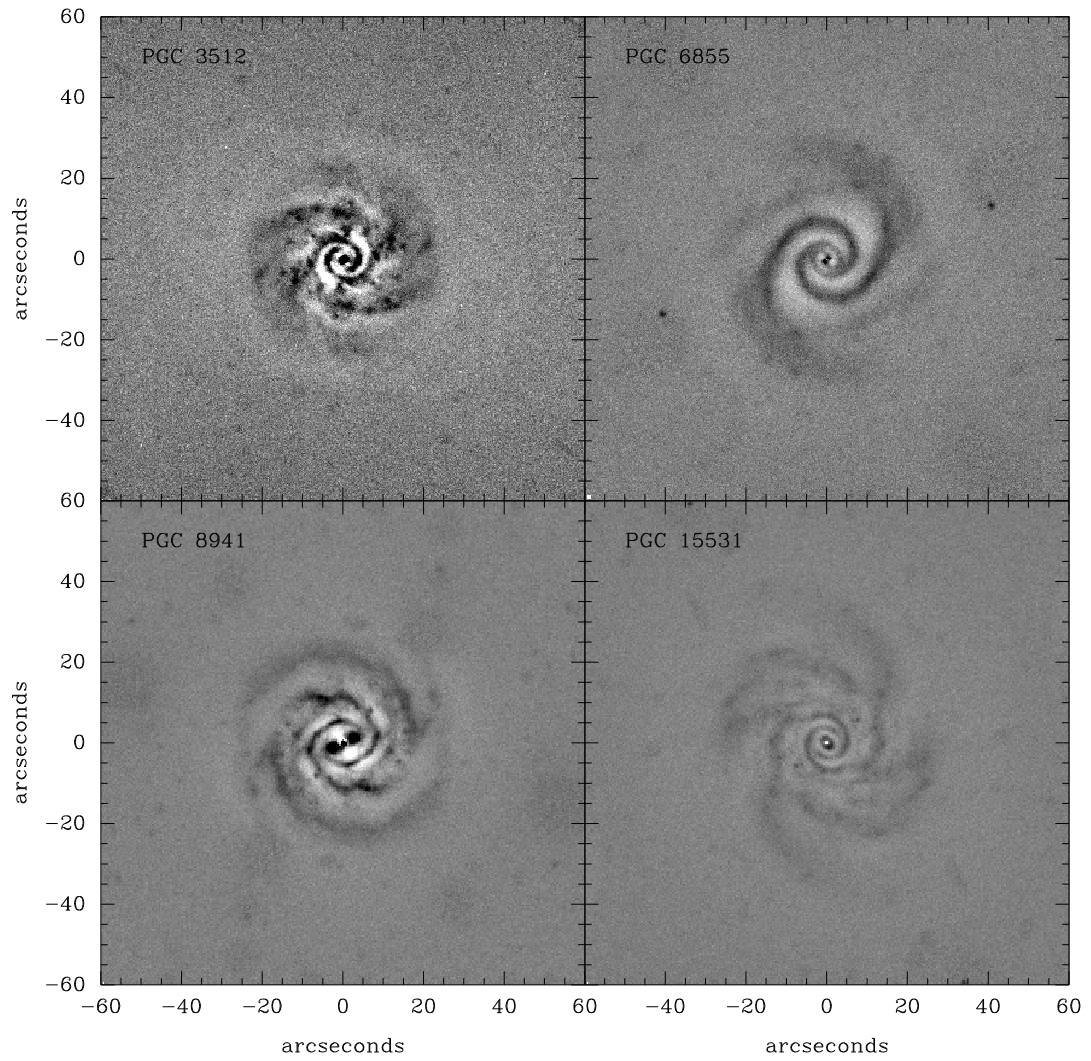


Fig. 2.7. Residuals of two-dimensional bulge-disk fits to four symmetrized sample galaxies show a variety of different spiral structure. Spiral structure dominates the residuals for galaxies in our sample.

PGC	$R$					$I$				
	$\mu_0$	$h$	$\mu_e$	$r_e$	D/B	$\mu_0$	$h$	$\mu_e$	$r_e$	D/B
	mag/ $\mu^2$	$\mu$	mag/ $\mu^2$	$\mu$		mag/ $\mu^2$	$\mu$	mag/ $\mu^2$	$\mu$	
26140	19.55	8.2	18.66	1.5	6.86	18.95	8.3	18.3	1.6	7.77
27792							9.5			
28310	21.48	9.4	21.88	2.4	11.6	20.67	9.4	21.29	2.7	11.2
28401	20.66	16.	20.51	2.3	21.7	19.84	14.6	19.68	2.3	18.2
31159		9.4				19.85	10.	20.49	2.6	13.9
32091							13.6		3.4	
32638	19.77	6.6	19.63	3.8	1.44	19.02	6.1	19.	3.6	1.49
33465	20.36	10.2	18.35	1.5	3.81					
36925		6.8				18.98	7.	19.79	3.	6.02
38908						18.86	5.6	19.14	1.3	12.6
46767		7.8				18.74	7.7	18.64	1.8	8.75
49906		7.1				19.66	7.1	20.93	2.2	17.6
55750		12.7				19.69	12.5	20.81	2.2	47.6
56010		9.				20.63	9.9	22.22	3.8	15.4
57931	21.03	8.5	20.41	3.7	1.55					
58410	19.88	8.7	18.87	1.	15.8		9.			
70962	18.58	5.	18.84	1.9	4.66	18.09	5.2	18.47	2.4	3.48
71106	18.89	5.6	18.45	1.4	5.57	18.33	5.8	18.2	1.7	5.44

PGC		<i>R</i>					<i>I</i>				
	$\mu_0$	$h$	$\mu_e$	$r_e$	D/B		$\mu_0$	$h$	$\mu_e$	$r_e$	D/B
	mag/ $\mu^2$	"	mag/ $\mu^2$	"			mag/ $\mu^2$	"	mag/ $\mu^2$	"	
72144	21.1	6.8	21.23	1.9	7.68		20.2	6.6	20.44	1.5	9.81
72453	20.6	9.4	19.86	1.4	11.8		19.81	8.9	19.17	1.4	11.7

We performed an inter-comparison of disk parameters derived from our two-dimensional bulge-disk decomposition in order to provide a consistency check on the model fits. A comparison of  $R$  and  $I$ -band images yielded  $\overline{\mu_0(R) - \mu_0(I)} = 0.63 \pm 0.15$ , consistent with the color of an average Sbc galaxy ( $R - I = 0.62$ , Fukugita *et al.* 1995). A least square fit to surfaces brightnesses yielded  $\mu_0(I) = 0.96\mu_0(R) + 0.06$  with a residual standard deviation of 0.15 magnitudes and a correlation coefficient of 0.99 (Figure 2.8).<sup>9</sup>  $R$  and  $I$ -band scale lengths were statistically equivalent. As de Jong (1996b) showed, scale lengths for galaxies measured in the  $B$  versus  $K$ -band do not differ by a large amount, so it is not surprising that  $R$  and  $I$ -band scale lengths are so similar.  $R$  and  $I$ -band images of galaxies are affected by almost same amount of reddening, and the light is coming from roughly the same stellar populations. Galaxies in our sample displayed a range in central disk and bulge surface brightnesses which are related:  $\mu_e = 1.6\mu_0 - 10.3$  for the  $I$ -band with a residual standard deviation of 0.73 magnitudes and a correlation coefficient of 0.85 (Figure 2.9). In general, disk central surface-brightnesses are brighter than the bulge effective surface brightness,  $\overline{\mu_0 - \mu_e} = -0.68$ . An even weaker relation existed for bulge and disk scale lengths:  $r_e = 0.129h + 0.37$  with a correlation coefficient of 0.66. On average,  $\overline{h/r_e} = 4.1$  which is smaller than the value of  $\sim 10$  found by de Jong (1996b) for  $K$ -band disk-bulge scale lengths. This discrepancy may be explained

---

<sup>9</sup>The correlation coefficient,  $\rho$ , is defined as  $\rho \equiv \frac{\sigma_x}{\sigma_y} \frac{\Delta y}{\Delta x}$  where  $\sigma_x$  and  $\sigma_y$  are the standard deviations of the fit residuals and  $\frac{\Delta y}{\Delta x}$  is the slope of the best fit linear regression. If  $0.8 < \rho < 1.0$ , the quantities,  $x$  and  $y$ , are highly correlated, and can be thought of as two different measures of the same quantity. Another useful statistical measure related to the correlation coefficient is simply  $\rho^2$ , which is the fractional contribution of  $x$  to  $y$ . Hence, if  $\rho = 0.8$  for quantities  $x$  and  $y$ , then  $x$  can account for 64% of the variations in  $y$ .

because the seeing disk was roughly the same radius as the bulge and we did not smooth our model bulge-disk decompositions with the seeing kernel.

Although we hoped we could extract disk axis ratios and position angles from two dimensional bulge-disk decompositions, both model disk axis ratios and position angles were affected by spiral structure. Both the axis ratio and position angle were more highly correlated with the strongest spiral than to axis ratios and position angles found from other methods described in §2.4.4.

While our two-dimensional bulge-disk decompositions failed to yield accurate axis ratios and position angles, or bulge parameters consistent with de Jong’s analysis, they did provide us with useful measures of disk properties including disk scale lengths and disk central surface brightnesses. Scale lengths derived from our two-dimensional bulge-disk decompositions were related to the characteristic radii we calculated from the surface brightness distributions.  $r_{1/2}/h = 1.49 \pm 0.17$  and  $r_{\eta=0.2}/h = 3.53 \pm 0.55$  for *I*-band scale lengths. These ratios were concentration-like indices, and are correlated with  $C_{80:20}$  and surface brightness (Figure 2.10)<sup>10</sup> The standard deviation of  $r_{1/2}/h$  was smaller because the ratio was closer to unity and therefore less affected by the shape of the light profile of galaxies.

---

<sup>10</sup>The ratio of  $r_{1/2}/h$  and  $r_{\eta=0.2}/h$  differ from pure concentration indices because although  $r_{1/2}$  and  $r_{\eta=0.2}$  are measured by taking the full light profile into account, the scale length,  $h$ , is measured only for the disk.

#### 2.4.4 Isophote Fits

In order to measure disk ellipticity, we needed to make measurements of axis ratios and position angles from surface photometry to combine with kinematic parameters. We measure photometric axis ratios and position angles by using the STSDAS ISOPHOTE package *ellipse* (Jedrzejewski 1987). *Ellipse* fits rings to image isophotes. Before isophotes were fit, foreground stars were identified, and data around all stars was excluded from the fit. We also required fitted rings to remain centered on the bulge centroid at all radii. If centers were allowed to wander from isophote to isophote, *ellipse* was unduly influenced by small background gradients and centers moved further from the center in each successive ring. Results of *ellipse* fits are presented in the atlas. Beyond the final points displayed in the figures therein, *ellipse* diverged. Determining axis ratios and position angles from elliptical fits to isophotes of near face-on galaxies was difficult because: (1) spiral structure affected the fits out to 2.5–3 scale lengths, and (2) there is limited flux beyond 3 scale lengths and fits begin to fail. In this section, we discuss how we dealt with these difficulties; we describe measurements of the spiral structure, tests of *ellipse* at low surface brightnesses, and finally measurements of axis ratios and position angles for survey galaxies.

##### 2.4.4.1 Spiral Structure Index

Spiral structure is clearly responsible for the highly variable measures of position angle and ellipticity as a function of radius out to radii,  $r < 2-4h$ . This is clearly seen by the strong correlation of *ellipse* position angle with spiral arms at these radii (Figure 2.11). We have defined the spiral structure index,  $\Sigma$ , at any radius  $R$ , as the ratio of the



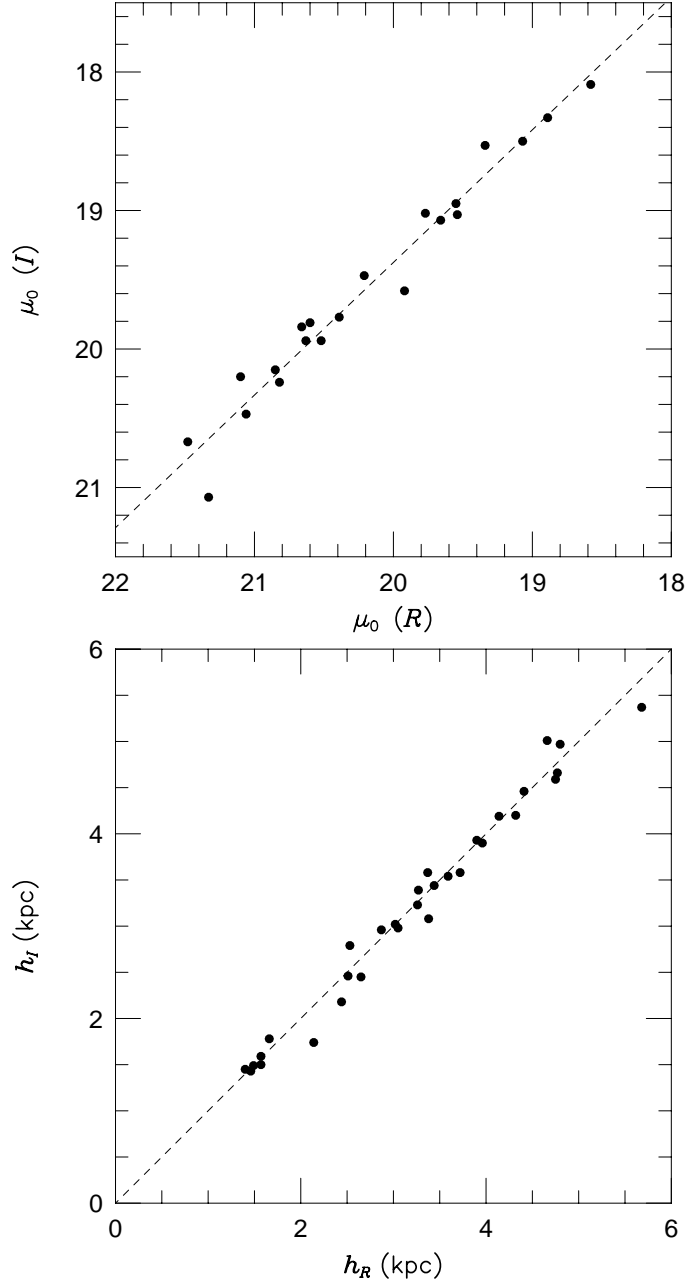


Fig. 2.8. Top Panel: central disk surface brightness in  $R$  and  $I$ -band.  $\overline{\mu_0(R) - \mu_0(I)} = 0.63$ . Bottom Panel: scale length measured in  $R$  and  $I$  bands were statistically identical. Conversion from arcseconds to kpc assumed  $H_0 = 75$  km/s/Mpc.

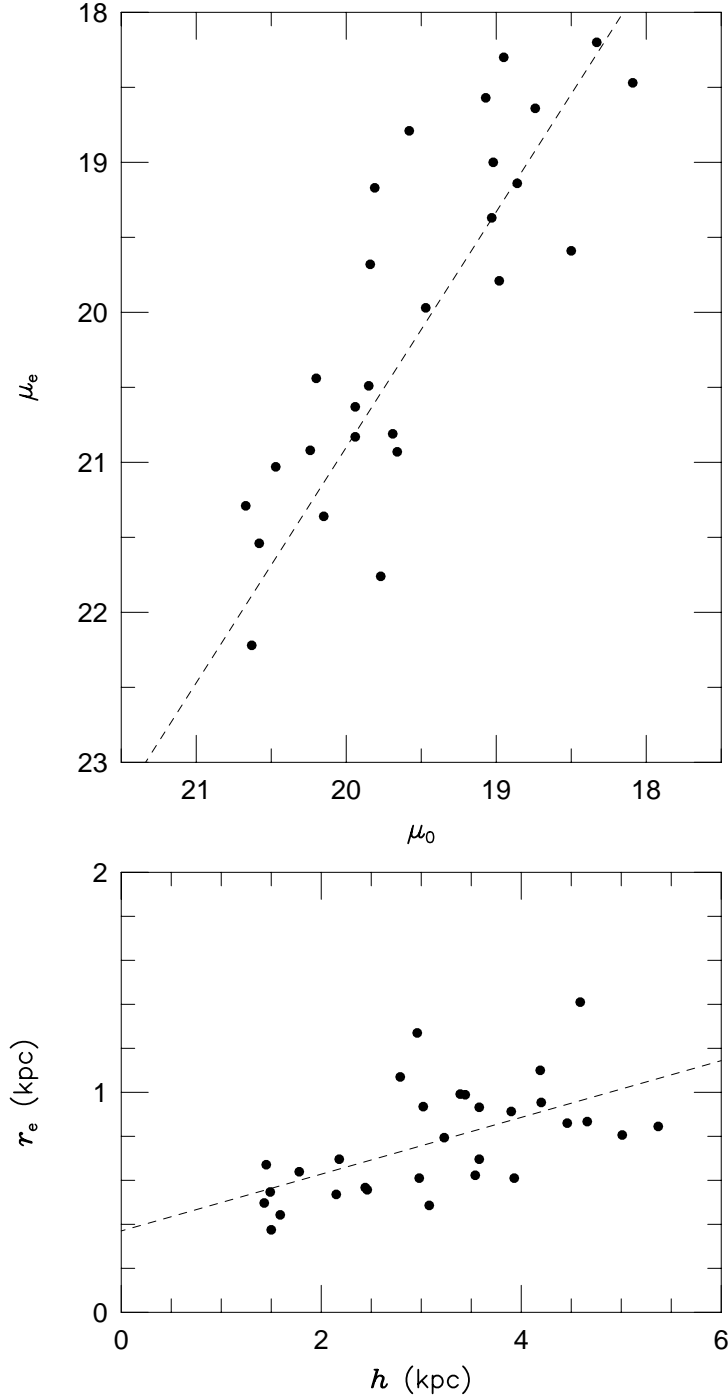


Fig. 2.9. Top Panel: Disk central surface brightnesses were brighter than effective bulge surface brightness in the  $I$ -band, although the bulge surface brightnesses have a greater dynamic range. Bottom Panel: There is a weak relation between disk and bulge scale length in the  $I$ -band for  $H_0 = 75$  km/s/Mpc. The ratio of  $h/r_e$  is half the expected value which was probably a result of seeing disks which were comparable in size to bulge radii for our sample.

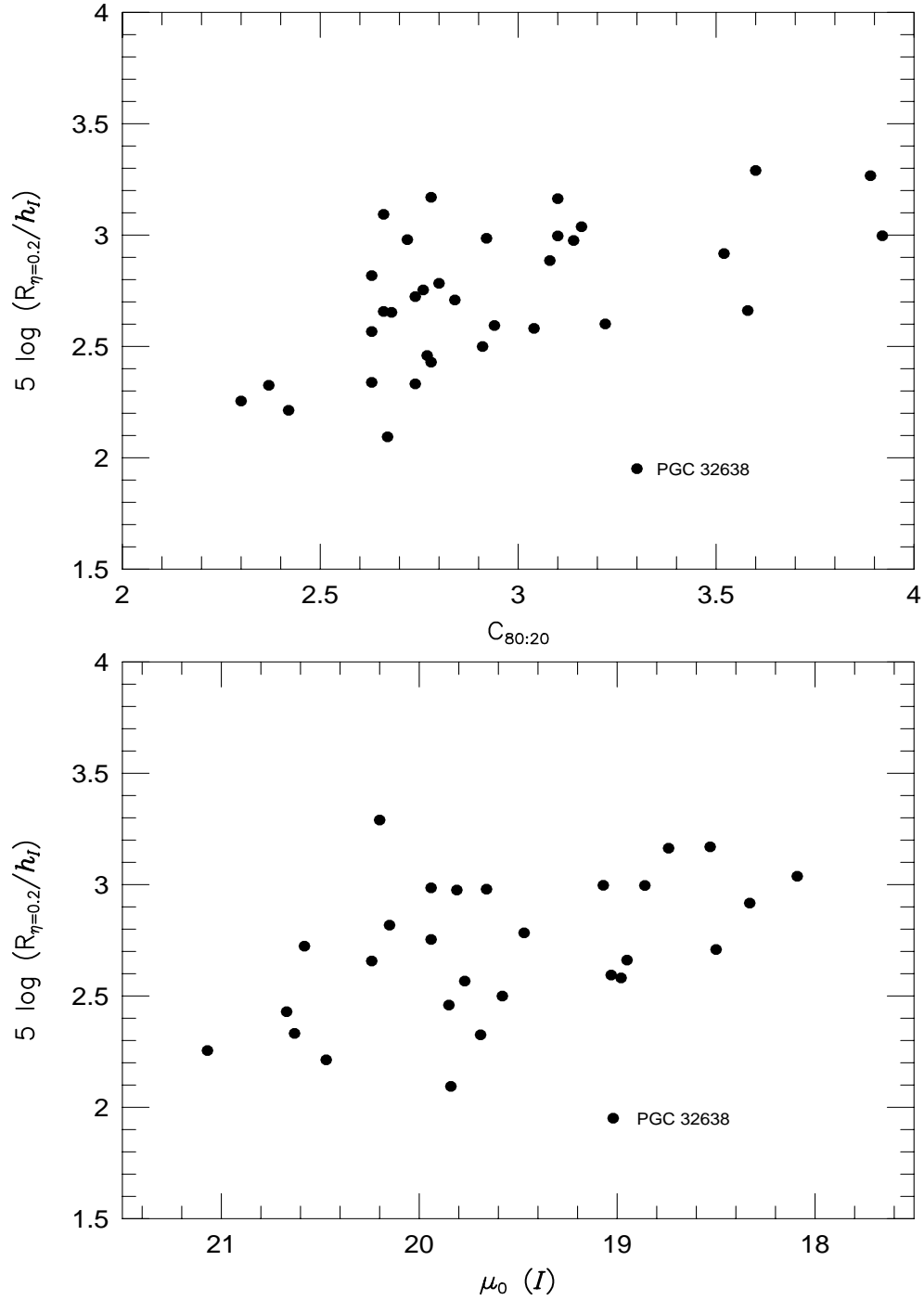


Fig. 2.10. A concentration index created with  $I$ -band scale lengths,  $h$ , and  $r_{\eta=0.2}$  versus  $C_{80:20}$  (top panel) and  $I$ -band surface brightness,  $\mu_0$  (bottom panel). The trend of  $r_{\eta=0.2}/h$  versus  $C_{80:20}$  and  $\mu_0$  are very weak. PGC 32638 was an outlier, indicating a possible problem in measurements of  $r_{\eta=0.2}$  or  $h_I$ .

measured pixel variance within an elliptical aperture tracing an isophote to the expected variance due to source ( $\sigma_S$ ) and background ( $\sigma_B$ ) counting statistics:

$$\Sigma(R) \equiv \frac{\sigma(R)}{(\sigma_S^2(R) + \sigma_B^2)^{1/2}}. \quad (2.3)$$

We measured the standard deviation of the background,  $\sigma_B$ , from beyond four galaxy scale lengths, and we assume source counts measured in electrons have a Poisson error distribution. As such,  $\Sigma$  provides a useful quantitative measure of spiral arm “contamination” for some galaxies, but failed for others (Figure 2.11). A value of  $\Sigma$  consistent with unity indicates spiral structure should not affect measurements of position angle and axis ratio. We found only two galaxies which had measures of  $\Sigma \approx 1$  while position angles still clearly were following spiral arms. These included PGC 2162 and PGC 72453.

#### 2.4.4.2 Tests of *Ellipse* Algorithm

Since spiral structure remains strong to three scale lengths for most galaxies, measurements of axis ratios and position angles needed to be made at radii beyond three scale lengths (Andersen *et al.* 2001; §2.3.4.3). Once an annuli free of the effects of spiral structure has been identified, we needed to show the ability to make accurate, reproducible measurements of the axis ratios and position angles beyond three scale lengths. Since the signal to noise ratio per pixel is low at these large radii ( $S/N \approx 2$ ), we tested whether measurements from *ellipse* were reproduced reliably using different seed conditions for the ellipse. Table 2.8 presents the results of our “repeatability test” for PGC 46767

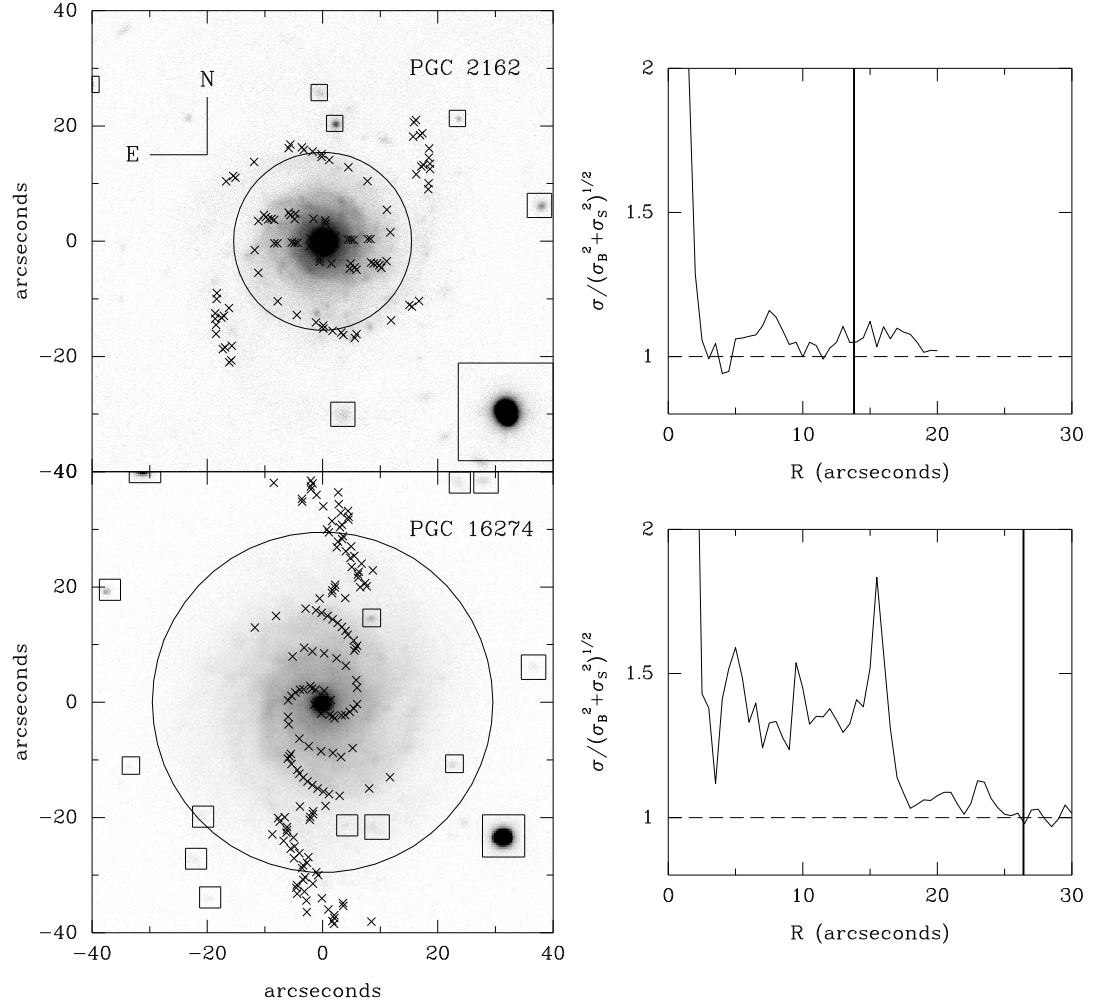


Fig. 2.11. Images in the left panel are PGC 2162 and PGC 16274 with measures of position angles marked with x's. The two panels on the right are measures of the spiral structure index,  $\Sigma \equiv \frac{\sigma(R)}{(\sigma_S^2(R) + \sigma_B^2)^{1/2}}$ , versus radius. Three disk scale lengths are marked as circles on the image and a vertical line in the plots. While  $\Sigma$  was a useful parameter for measuring spiral arm “contamination” in most galaxies, it failed for the case of PGC 2162 and PGC 72453. As illustrated in the image, PGC 2162 has several weak arms which are traced out by the *ellipse* fits to isophotes, but the spiral index is consistent with unity never-the-less. For most galaxies, like PGC 16274,  $\Sigma$  is unity only at radii beyond which spiral structure no longer influences measures of position angle.

measurements of axis ratios and position angles for different initial conditions. Measurements were made at 35 arcseconds which corresponds to roughly 3.5 scale lengths. The signal to noise per pixel was roughly 2. Under these conditions, *stdas.ellipse* reproduced a  $1-\frac{b}{a} = 0.089 \pm 0.009$  and  $\text{PA} = -19 \pm 3^\circ$ . This repeatability test showed position angle and axis ratio did not depend strongly on initial conditions.

Another concern of using *ellipse* beyond three galaxy scale lengths was whether uncertainty in the sky background would have an effect on axis ratios and position angles. Indeed small changes in adopted values for the background could lead to large changes in measured scale lengths measured at large radii. However, we found that axis ratios and position angle measurements were reproduceable regardless of the background level as long as spatial gradients did not exist in the images. Spatial gradients could affect measurements of axis ratios and position angles, but we took care to remove any low frequency gradients from our images (see §2.2.3).

Table 2.8. Repeatability of ellipse measurements. Axis ratios and position angles of PGC 46767 were measured for different initial conditions.

INITIAL	PA=-45°		0°		+45°	
$1-b/a$	$1-b/a$	PA	$1-b/a$	PA	$1-b/a$	PA
0.05	0.077	-19°	0.096	-19°	0.097	-18°
0.15	0.086	-20°	0.099	-17°	0.099	-15°
0.25	0.086	-19°	0.072	-26°	0.082	-20°
0.35	0.097	-18°	0.095	-23°	0.081	-16°

#### 2.4.4.3 Position Angle and Axis Ratio Measurements

For each galaxy, we examined radial trends of *ellipse* fit parameters axis ratio,  $b/a$  and position angle, P.A., to determine if a single P.A. and  $b/a$  could be assigned to the disk portion of the light profile. In practice, at best we could define an outer annulus in the light profile in which we could estimate characteristic values. We required three conditions to be met within this annulus: (1) the spiral structure index should be unity or have just shown a large break towards smaller values, (2) the annulus must be roughly between three and four scale lengths, and (3) P.A. and  $b/a$  should be constant in the annulus. Changing P.A.'s or  $b/a$  indicated either warping or spiral arms were affecting the *ellipse* fits.

Not all galaxies in our sample met these criteria. **PGC 2162**, **PGC 23913**, **PGC 24788** and **PGC 72453** had strong spiral arms which persisted to the faintest isophotal levels fit by *ellipse*. **PGC 70962** had a very large spiral structure index out to five scale lengths. **PGC 5345** and **PGC 7826** do not show strong spiral structure, but outer isophotes have non-constant, twisting position angles consistent with warping. **PGC 14564**, **PGC 20938**, **PGC 26517** and **PGC 56010** show trends in either increasing or decreasing axis ratios. Therefore we were unable to measure axis ratios and position angles, and hence unable to measure ellipticity, for these 11 galaxies (28% of sample).

For the remaining galaxies, we chose an annulus roughly between three and four scale lengths in which to make measurements of P.A. and  $b/a$  (Table 2.9). We compared our measurements of  $b/a$  to  $b/a_{25}$  from the PGC and found poor agreement (Figure



2.12); *ellipse* measurements of  $b/a$  were made beyond 3 scale lengths, while the  $B$ -band surface brightness,  $\mu_B = 25$ , corresponds to a radius of 3 scale lengths for Freeman disks. This radius is smaller than the mean radius used for this study and is likely influenced by spiral structure. However, P.A. and  $b/a$  measurements made in  $R$  and  $I$ -bands were statistically equivalent for our sample (Figure 2.13).

Table 2.9.  $R$  and  $I$ -band measurements of position angles and axis ratios. We included the inner and outer radii defining the annuli in which these quantities were measured.  $r_1$  and  $r_2$  are the inner and outer radii of the annuli in which we made measurements of  $b/a$  and P.A. Quoted errors are the standard deviations on P.A. and  $b/a$  in the annuli.

PGC	$r_1$	$r_2$	$R$		$I$	
	"	"	P.A.	$1 - b/a$	P.A.	$1 - b/a$
03512	25	29.5	$150 \pm 7$	$0.075 \pm 0.040$	$156 \pm 9$	$0.073 \pm 0.030$
05673	43	49.5	$83 \pm 2$	$0.116 \pm 0.009$	$83 \pm 7$	$0.095 \pm 0.014$
06855	40.5	47.5	$131 \pm 3$	$0.108 \pm 0.023$	$137 \pm 5$	$0.114 \pm 0.029$
08941	26.5	34	$39 \pm 11$	$0.069 \pm 0.015$	$30 \pm 16$	$0.035 \pm 0.017$
15531	33	43.5	$19 \pm 4$	$0.132 \pm 0.024$	$22 \pm 6$	$0.160 \pm 0.027$
16274	26	33.5	$174 \pm 5$	$0.123 \pm 0.019$	$178 \pm 9$	$0.107 \pm 0.016$
19767	30	38	$179 \pm 6$	$0.191 \pm 0.036$	$184 \pm 10$	$0.136 \pm 0.034$
23333	22.5	26.5	$59 \pm 8$	$0.119 \pm 0.005$	$56 \pm 14$	$0.072 \pm 0.018$
23598	32.5	37.5	$50 \pm 9$	$0.109 \pm 0.026$	$44 \pm 12$	$0.092 \pm 0.028$
26140	33.5	41.5	$48 \pm 2$	$0.223 \pm 0.014$	$52 \pm 2$	$0.202 \pm 0.014$
27792	30.5	40			$135 \pm 4$	$0.212 \pm 0.023$
28310	31	37.5	$61 \pm 7$	$0.131 \pm 0.022$	$74 \pm 11$	$0.093 \pm 0.036$
28401	43.5	50	$98 \pm 9$	$0.131 \pm 0.034$	$91 \pm 2$	$0.183 \pm 0.022$
31159	37.5	43	$12 \pm 3$	$0.225 \pm 0.022$	$3 \pm 3$	$0.170 \pm 0.047$
32091	38.5	50			$66 \pm 7$	$0.100 \pm 0.030$
32638	13.5	23	$179 \pm 3$	$0.086 \pm 0.028$	$178 \pm 9$	$0.078 \pm 0.025$

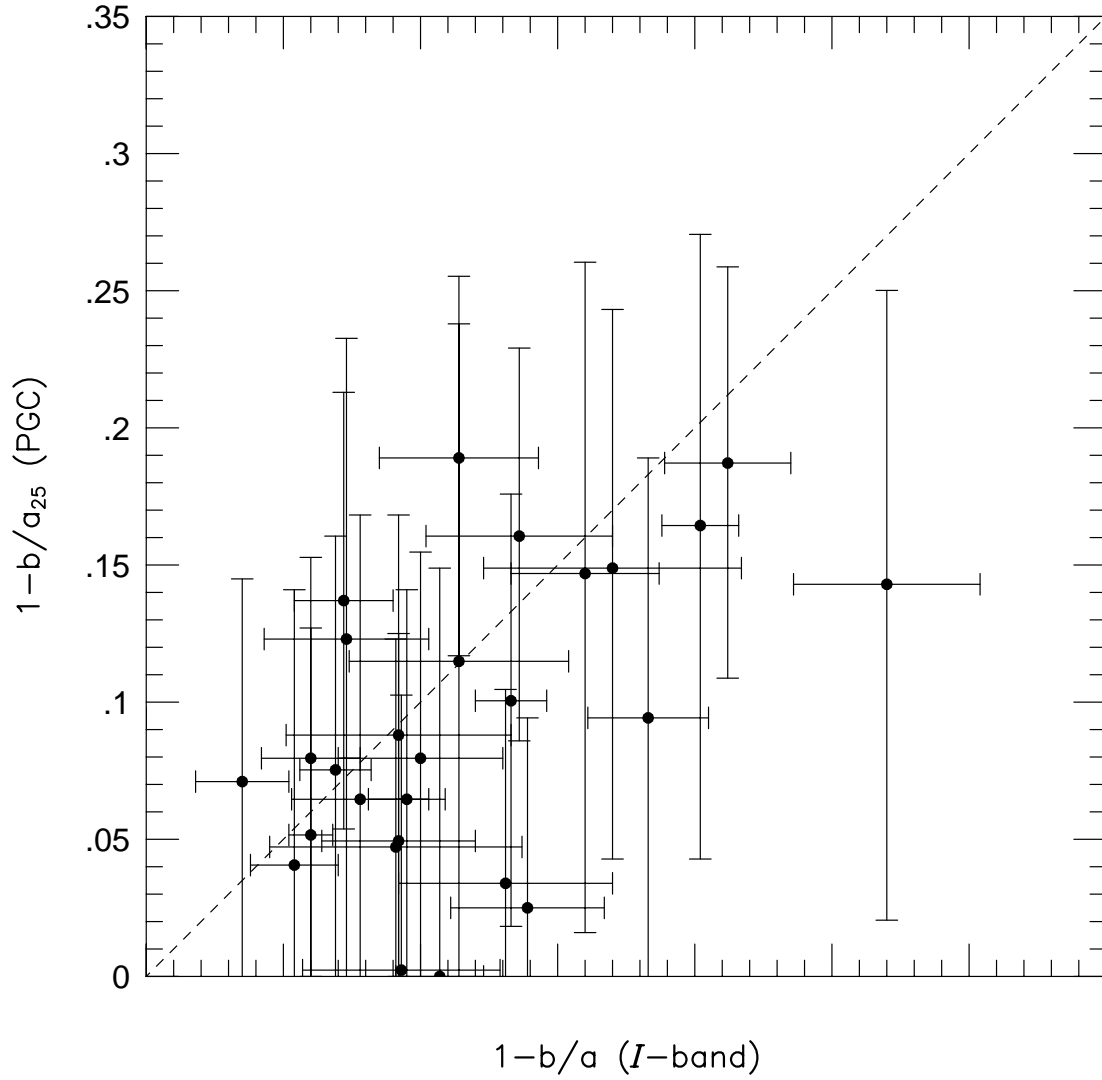


Fig. 2.12. Axis ratios measured at  $\mu_B = 25$  mag/arc<sup>2</sup> tabulated in the PGC (Paturel *et al.* 1995) versus axis ratios measured via the *ellipse* algorithm. We found only a very weak correlation between the two measures. The measurements of  $b/a_{25}$  were made without regard to spiral structure at  $\sim 3$  scale lengths, while we selected regions in which spiral structure should not influence our measures.

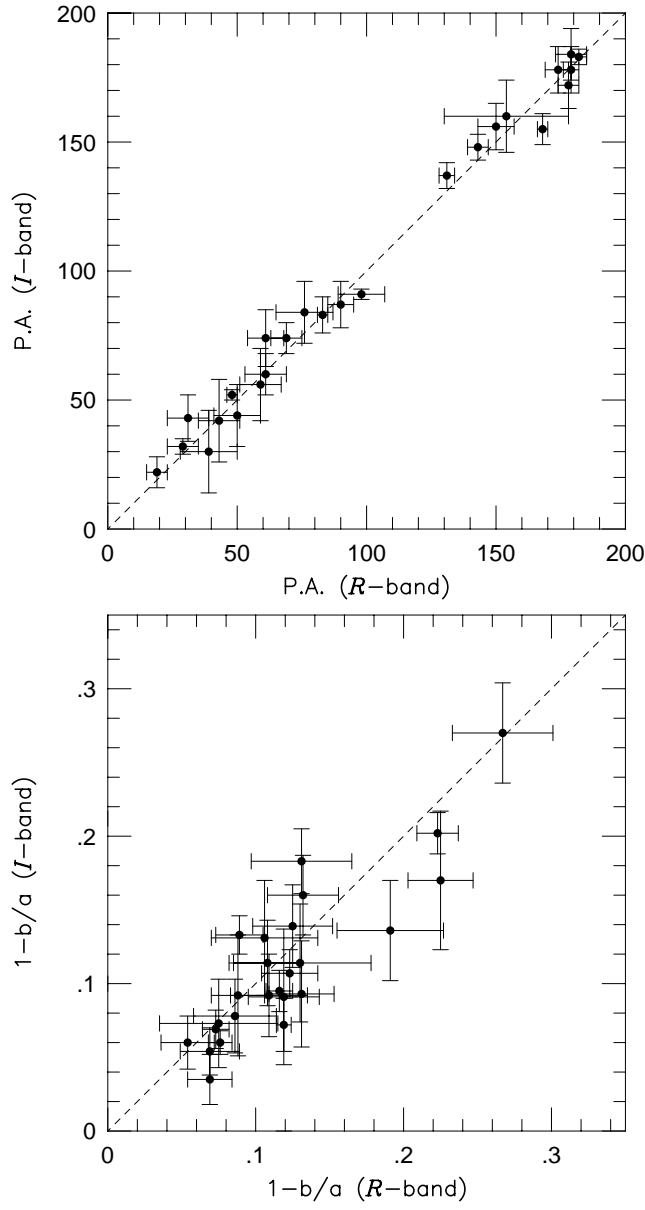


Fig. 2.13.  $R$  versus  $I$ -band position angles (top panel) and axis ratios (bottom panel). Both quantities are highly correlated. We would not expect a difference between measurements in different bands if axis ratios and position angles were measuring the projected shape and orientation of disks.

PGC	$r_1$	$r_2$	$R$		$I$	
	$//$	$//$	P.A.	$1 - b/a$	P.A.	$1 - b/a$
33465	20.5	26.5	$61 \pm 8$	$0.069 \pm 0.020$	$60 \pm 8$	$0.054 \pm 0.016$
36925	19	24.5	$76 \pm 11$	$0.073 \pm 0.009$	$84 \pm 12$	$0.069 \pm 0.013$
38268	35	45.5	$29 \pm 6$	$0.267 \pm 0.034$	$32 \pm 3$	$0.270 \pm 0.034$
38908	27	40	$154 \pm 24$	$0.088 \pm 0.018$	$160 \pm 14$	$0.092 \pm 0.041$
39728	30.5	39.5	$89 \pm 5$	$0.119 \pm 0.011$		
46767	43.5	51	$143 \pm 4$	$0.089 \pm 0.016$	$148 \pm 5$	$0.133 \pm 0.013$
49906	30	32.5	$168 \pm 2$	$0.076 \pm 0.008$	$155 \pm 6$	$0.060 \pm 0.008$
55750	37.5	47	$178 \pm 4$	$0.054 \pm 0.018$	$172 \pm 9$	$0.060 \pm 0.018$
57931	23.5	31.2	$69 \pm 6$	$0.130 \pm 0.048$	$74 \pm 6$	$0.114 \pm 0.040$
58410	40	50	$90 \pm 5$	$0.125 \pm 0.027$	$87 \pm 9$	$0.139 \pm 0.028$
71106	30	36	$31 \pm 8$	$0.106 \pm 0.036$	$43 \pm 9$	$0.131 \pm 0.039$
72144	20	27	$43 \pm 8$	$0.119 \pm 0.024$	$42 \pm 16$	$0.091 \pm 0.046$

## 2.4.5 Asymmetry

### 2.4.5.1 Rotational Asymmetry

The rotational asymmetry parameter,  $A_{rot}$ , is a quantitative parameter based on comparing a source image with its rotated counterpart. (Schade *et al.* 1995; Abraham *et al.* 1996; Conselice 1997). As in previous definitions, we adopt:

$$A_{rot} = \frac{\sum |I_0 - I_{180}|}{2 \sum |I_0|} \quad (2.4)$$

where  $I_0$  is the flux per pixel in the unrotated frame and  $I_{180}$  is the flux in the pixel  $180^\circ$  from the original pixel.

Operationally, rotational asymmetry measurements consisted of (1) defining an image center (2) rotating the image about the center by  $180^\circ$ , (3) performing a comparison of the resultant rotated image with the original image within an annulus or disk and (4) correcting this raw asymmetry by a measure of random contributions from the background.

In contrast to previous algorithms (e.g., Conselice *et al.* 2000), we found the image center which minimized rotational asymmetry by using the amoeba algorithm. In our implementation, amoeba tests for the minimum value of rotational asymmetry within a half light radius at different centers until the absolute minimum is reached. This center found using amoeba was close to the centroid calculated from the first moment of the light profile.

We corrected the rotational asymmetry by taking background noise into account. Because rotational asymmetry is a pixel-to-pixel comparison between two images, a significant fraction of  $A_{rot}$  can be due to noise. To make the noise correction, we calculated the pixel to pixel differences in a blank patch of the image using the same method described above, including finding a center which minimizes the difference. Our final measurement of rotational asymmetry was then

$$A_{180} = \frac{\sum |I_0 - I_{180}|}{\sum |I_0|} - \frac{\sum |B_0 - B_{180}|}{\sum |I_0|}, \quad (2.5)$$

which follows Conselice *et al.* (2000).

Another departure from previous studies is that here we explore annular regions in order to exclude the bulge and better sample the disk alone. We measured rotational asymmetries for both the  $R$  and  $I$ -band images for our sample (See Atlas and Table 2.10 and 2.11). Values of  $A_{180}$  quoted in the tables were means calculated between 1.5 and 2.5 scale lengths. Values of  $\int A_{180}$  were calculated within a disk with radius  $r_{\eta=0.2}$  and should be directly comparable to values in Conselice *et al.* (2000). We find  $\int A_{180} = 0.69A_{180}$  with a correlation coefficient of 0.93 in both the  $R$  and  $I$ -band. That  $A_{180}$  is greater  $\int A_{180}$  is hardly surprising; the disks are more likely to be asymmetric than bulges, so the contribution of bulge luminosity acts to diminish the amplitude of asymmetry. However, this result is surprising because the measurements are so highly correlated; even though the bulge and disk would presumably have different asymmetries, this is not reflected in the relation. Since the annular measure of  $A_{180}$  has a greater dynamic range, we use it as our standard measure of rotational asymmetry. A comparison of  $A_{180}$  measured in

the  $R$  versus  $I$ -band showed  $A_{180}(I) = 0.84A_{180}(R) - 0.03$  with a correlation coefficient of 0.96. Even though there was a scaling relation between these quantities, rotational asymmetries measured in the these two bands were fundamentally the same.

#### 2.4.5.2 Fourier Decompositions

A Fourier analysis of disk asymmetry yields information not only about the magnitude of asymmetry, but also the phase and spatial frequency, including even modes. Each mode of asymmetry can be measured independently. All these measures are not possible to obtain from rotation asymmetries. Each mode of asymmetry can be measured independently. We take the same approach to Fourier asymmetry analysis as Rix & Zaritsky 1995. The Cartesian coordinates of the original image were transformed to polar coordinates sampled at much lower resolution. We used 12 azimuthal bins and 45 radial bins to sample galaxies from five to fifty arcseconds in radius. Azimuthal bins at the smallest radii average  $\sim 3$  raw pixels of data. Once the coordinates were transformed, a Fourier series was fit to each bin in radius:

$$\Sigma(R, \phi) / \langle \Sigma(R, \phi) \rangle = \sum_{m=1}^{\infty} A_m(R) e^{im[\phi - \phi_m(R)]} \quad (2.6)$$

where  $\Sigma$  here refers to surface brightness fluxes measured at a point  $R, \phi$  in the disk. In practice, we measure the amplitudes and phases of the first five components; since each mode is orthogonal it does not matter in which order, or how many modes are fit. Tables 2.10 and 2.11 quote  $A_1$ ,  $A_3$ , and  $A_{1+3}$  where  $A_{1+3}(R) = [A_1^2(R) + A_3^2(R)]^{1/2}$  calculated between 1.5 and 2.5 scale lengths.



We find Fourier amplitudes in the  $R$  and  $I$ -bands were highly correlated;  $A_1(I) = 0.85A_1(R)$  with a correlation coefficient of 0.97. Note the ratio of  $R$  to  $I$ -band asymmetries is the same for both rotational asymmetries and the  $m = 1$  Fourier amplitude. Furthermore, the dominant odd mode in the Fourier series was  $m = 1$ ; the quadrature sum of  $A_1$  and  $A_3$ ,  $A_{1+3}$ , is much more highly correlated with  $A_1$  than  $A_3$ , the next largest odd Fourier amplitude. The correlation coefficient between  $A_1$  and  $A_{1+3}$  was 0.95, and only 0.58 between  $A_3$  and  $A_{1+3}$ .

Galaxies in our sample had a lower than expected degree of lopsidedness. Only 7 of 37 (19%) galaxies showed significant lopsidedness ( $A_1 > 0.2$ ), lower than expected based on earlier work by Zaritsky & Rix (1997) who found 30% of late type field galaxies had  $A_1 > 0.2$ . We may have found fewer highly asymmetric galaxies because: (1) Almost half of our disks had  $t\text{-types} < 4.5$  indicating a large fraction of our galaxies were early-type disks. Rudnick & Rix (1998) found only 20% of early-type galaxies were asymmetric, a result consistent with our measurement. (2) By selecting galaxies based on narrow HI line widths, Zaritsky & Rix (1997) may have preferentially observed asymmetric galaxies (See §2.2) (3) We preferentially selected symmetric galaxies from DSS2 images. Since neither sample is likely to be representative of the spiral galaxy population, the difference in the fraction of lopsided disks may not be significant.

Our Fourier decomposition of disk images also yielded some clues into the nature of lopsidedness. As Rudnick, Rix & Kennicutt (2000) point out, if  $m = 1$  modes were due to one-armed spirals, the phase angle of the  $m = 1$  mode of asymmetry would change according to the pitch angle of the arm. Rudnick, Rix & Kennicutt (2000) did not find any evidence for this effect; rather lopsided galaxies tended to have fixed phase angles.

Our measures of  $m = 1$  amplitudes and phases confirmed this result. Lopsidedness is most likely not an amplified  $m = 1$  spiral mode in most galaxies.

Table 2.10.  $R$ -band disk asymmetry parameters.  $A_{180}$  through  $A_{1+3}$  were measured in an annulus between 1.5 and 2.5 scale lengths.  $\int A_{180}$  was measured in a disk out to

$r_{\eta=0.2}$

PGC	$A_{180}$	$A_1$	$A_3$	$A_{1+3}$	$\int A_{180}$
02162	$0.08 \pm 0.03$	$0.07 \pm 0.04$	$0.03 \pm 0.01$	$0.08 \pm 0.04$	$0.06 \pm 0.02$
03512	$0.16 \pm 0.05$	$0.16 \pm 0.08$	$0.06 \pm 0.02$	$0.18 \pm 0.07$	$0.12 \pm 0.02$
05345	$0.50 \pm 0.17$	$0.52 \pm 0.08$	$0.19 \pm 0.06$	$0.55 \pm 0.09$	$0.28 \pm 0.03$
05673	$0.10 \pm 0.04$	$0.09 \pm 0.05$	$0.05 \pm 0.03$	$0.11 \pm 0.06$	$0.08 \pm 0.03$
06855	$0.24 \pm 0.08$	$0.28 \pm 0.11$	$0.04 \pm 0.02$	$0.28 \pm 0.11$	$0.17 \pm 0.02$
07826	$0.11 \pm 0.03$	$0.12 \pm 0.07$	$0.10 \pm 0.03$	$0.17 \pm 0.05$	$0.07 \pm 0.02$
08941	$0.25 \pm 0.14$	$0.11 \pm 0.08$	$0.18 \pm 0.08$	$0.22 \pm 0.10$	$0.18 \pm 0.02$
14564	$0.30 \pm 0.09$	$0.18 \pm 0.11$	$0.11 \pm 0.02$	$0.22 \pm 0.09$	$0.20 \pm 0.02$
15531	$0.09 \pm 0.02$	$0.08 \pm 0.02$	$0.07 \pm 0.02$	$0.11 \pm 0.02$	$0.08 \pm 0.02$
16274	$0.06 \pm 0.02$	$0.04 \pm 0.03$	$0.07 \pm 0.05$	$0.09 \pm 0.05$	$0.05 \pm 0.02$
19767	$0.08 \pm 0.02$	$0.11 \pm 0.09$	$0.04 \pm 0.02$	$0.12 \pm 0.08$	$0.06 \pm 0.02$
20938	$0.14 \pm 0.03$	$0.09 \pm 0.02$	$0.07 \pm 0.02$	$0.12 \pm 0.02$	$0.12 \pm 0.04$
23333	$0.11 \pm 0.06$	$0.12 \pm 0.06$	$0.08 \pm 0.04$	$0.14 \pm 0.07$	$0.06 \pm 0.02$
23598	$0.23 \pm 0.06$	$0.05 \pm 0.04$	$0.19 \pm 0.04$	$0.20 \pm 0.04$	$0.12 \pm 0.05$
23913	$0.22 \pm 0.06$	$0.20 \pm 0.11$	$0.10 \pm 0.04$	$0.24 \pm 0.08$	$0.16 \pm 0.06$
24788	$0.16 \pm 0.03$	$0.09 \pm 0.04$	$0.08 \pm 0.02$	$0.12 \pm 0.03$	$0.12 \pm 0.04$
26140	$0.09 \pm 0.02$	$0.07 \pm 0.02$	$0.06 \pm 0.03$	$0.10 \pm 0.02$	$0.06 \pm 0.04$
26517	$0.12 \pm 0.04$	$0.18 \pm 0.02$	$0.11 \pm 0.06$	$0.22 \pm 0.04$	$0.09 \pm 0.04$

PGC	$A_{180}$	$A_1$	$A_3$	$A_{1+3}$	$\int A_{180}$
28310	$0.15 \pm 0.04$	$0.10 \pm 0.03$	$0.10 \pm 0.01$	$0.15 \pm 0.02$	$0.12 \pm 0.04$
28401	$0.22 \pm 0.04$	$0.29 \pm 0.11$	$0.12 \pm 0.06$	$0.33 \pm 0.08$	$0.13 \pm 0.02$
31159	$0.22 \pm 0.04$	$0.19 \pm 0.04$	$0.10 \pm 0.06$	$0.22 \pm 0.04$	$0.13 \pm 0.08$
32638	$0.14 \pm 0.03$	$0.09 \pm 0.02$	$0.05 \pm 0.03$	$0.11 \pm 0.02$	$0.14 \pm 0.04$
33465	$0.08 \pm 0.03$	$0.03 \pm 0.02$	$0.04 \pm 0.02$	$0.05 \pm 0.02$	$0.09 \pm 0.03$
36925	$0.19 \pm 0.05$	$0.15 \pm 0.06$	$0.04 \pm 0.01$	$0.16 \pm 0.06$	$0.13 \pm 0.08$
38268	$0.21 \pm 0.03$	$0.16 \pm 0.05$	$0.15 \pm 0.08$	$0.23 \pm 0.04$	$0.14 \pm 0.02$
38908	$0.25 \pm 0.04$	$0.15 \pm 0.02$	$0.14 \pm 0.04$	$0.20 \pm 0.03$	$0.18 \pm 0.06$
39728	$0.32 \pm 0.07$	$0.14 \pm 0.03$	$0.15 \pm 0.06$	$0.21 \pm 0.04$	$0.20 \pm 0.03$
46767	$0.33 \pm 0.09$	$0.14 \pm 0.02$	$0.16 \pm 0.11$	$0.22 \pm 0.09$	$0.27 \pm 0.08$
49906	$0.27 \pm 0.12$	$0.12 \pm 0.11$	$0.13 \pm 0.06$	$0.19 \pm 0.11$	$0.21 \pm 0.06$
55750	$0.21 \pm 0.06$	$0.17 \pm 0.06$	$0.09 \pm 0.05$	$0.20 \pm 0.06$	$0.14 \pm 0.08$
56010	$0.29 \pm 0.16$	$0.34 \pm 0.18$	$0.07 \pm 0.02$	$0.35 \pm 0.18$	$0.17 \pm 0.06$
57931	$0.25 \pm 0.10$	$0.17 \pm 0.09$	$0.15 \pm 0.07$	$0.24 \pm 0.10$	$0.10 \pm 0.03$
58410	$0.23 \pm 0.03$	$0.12 \pm 0.06$	$0.13 \pm 0.03$	$0.18 \pm 0.04$	$0.17 \pm 0.02$
70962	$0.57 \pm 0.03$	$0.48 \pm 0.06$	$0.20 \pm 0.08$	$0.52 \pm 0.03$	$0.51 \pm 0.02$
71106	$0.38 \pm 0.07$	$0.25 \pm 0.08$	$0.20 \pm 0.05$	$0.32 \pm 0.09$	$0.25 \pm 0.02$
72144	$0.07 \pm 0.01$	$0.10 \pm 0.04$	$0.10 \pm 0.03$	$0.14 \pm 0.04$	$0.07 \pm 0.02$
72453	$0.13 \pm 0.04$	$0.08 \pm 0.03$	$0.11 \pm 0.04$	$0.14 \pm 0.03$	$0.12 \pm 0.02$

Table 2.11.  $I$ -band disk asymmetry parameters.  $A_{180}$  through  $A_{1+3}$  were measured in an annulus between 1.5 and 2.5 scale lengths.  $\int A_{180}$  was measured in a disk out to

$r_{\eta=0.2}$

PGC	$A_{180}$	$A_1$	$A_3$	$A_{1+3}$	$\int A_{180}$
02162	$0.04 \pm 0.02$	$0.05 \pm 0.04$	$0.02 \pm 0.01$	$0.06 \pm 0.03$	$0.04 \pm 0.02$
03512	$0.11 \pm 0.03$	$0.15 \pm 0.06$	$0.06 \pm 0.02$	$0.16 \pm 0.06$	$0.08 \pm 0.02$
05345	$0.36 \pm 0.14$	$0.41 \pm 0.08$	$0.13 \pm 0.07$	$0.43 \pm 0.09$	$0.23 \pm 0.03$
05673	$0.08 \pm 0.03$	$0.10 \pm 0.03$	$0.04 \pm 0.02$	$0.10 \pm 0.03$	$0.07 \pm 0.03$
06855	$0.16 \pm 0.04$	$0.24 \pm 0.08$	$0.03 \pm 0.02$	$0.25 \pm 0.08$	$0.13 \pm 0.02$
07826	$0.06 \pm 0.01$	$0.11 \pm 0.06$	$0.08 \pm 0.02$	$0.14 \pm 0.05$	$0.04 \pm 0.02$
08941	$0.23 \pm 0.12$	$0.12 \pm 0.06$	$0.16 \pm 0.06$	$0.20 \pm 0.08$	$0.15 \pm 0.03$
14564	$0.22 \pm 0.07$	$0.14 \pm 0.08$	$0.09 \pm 0.02$	$0.18 \pm 0.07$	$0.16 \pm 0.02$
15531	$0.06 \pm 0.02$	$0.07 \pm 0.02$	$0.05 \pm 0.02$	$0.09 \pm 0.02$	$0.05 \pm 0.02$
16274	$0.04 \pm 0.01$	$0.05 \pm 0.03$	$0.07 \pm 0.05$	$0.09 \pm 0.05$	$0.03 \pm 0.02$
19767	$0.04 \pm 0.01$	$0.09 \pm 0.07$	$0.03 \pm 0.02$	$0.10 \pm 0.06$	$0.03 \pm 0.02$
20938	$0.11 \pm 0.03$	$0.10 \pm 0.02$	$0.07 \pm 0.02$	$0.12 \pm 0.03$	$0.06 \pm 0.04$
23333	$0.08 \pm 0.04$	$0.12 \pm 0.06$	$0.07 \pm 0.03$	$0.14 \pm 0.06$	$0.04 \pm 0.02$
23598	$0.14 \pm 0.05$	$0.05 \pm 0.04$	$0.17 \pm 0.04$	$0.18 \pm 0.04$	$0.07 \pm 0.04$
23913	$0.18 \pm 0.05$	$0.18 \pm 0.10$	$0.09 \pm 0.04$	$0.21 \pm 0.08$	$0.23 \pm 0.03$
24788	$0.15 \pm 0.03$	$0.09 \pm 0.04$	$0.06 \pm 0.02$	$0.11 \pm 0.04$	$0.10 \pm 0.04$
26140	$0.05 \pm 0.02$	$0.05 \pm 0.02$	$0.04 \pm 0.02$	$0.06 \pm 0.02$	$0.04 \pm 0.02$
26517	$0.02 \pm 0.03$	$0.15 \pm 0.04$	$0.10 \pm 0.06$	$0.19 \pm 0.05$	$0.02 \pm 0.02$

PGC	$A_{180}$	$A_1$	$A_3$	$A_{1+3}$	$\int A_{180}$
28310	$0.11 \pm 0.04$	$0.11 \pm 0.04$	$0.11 \pm 0.02$	$0.16 \pm 0.03$	$0.08 \pm 0.02$
28401	$0.20 \pm 0.02$	$0.31 \pm 0.09$	$0.10 \pm 0.05$	$0.33 \pm 0.07$	$0.10 \pm 0.02$
31159	$0.12 \pm 0.05$	$0.14 \pm 0.05$	$0.08 \pm 0.04$	$0.17 \pm 0.05$	$0.09 \pm 0.02$
32091	$0.06 \pm 0.01$	$0.18 \pm 0.09$	$0.06 \pm 0.02$	$0.19 \pm 0.09$	$0.04 \pm 0.02$
32638	$0.09 \pm 0.02$	$0.08 \pm 0.02$	$0.04 \pm 0.02$	$0.10 \pm 0.02$	$0.11 \pm 0.04$
33465	$0.03 \pm 0.02$	$0.03 \pm 0.01$	$0.04 \pm 0.01$	$0.05 \pm 0.01$	$0.06 \pm 0.02$
36925	$0.13 \pm 0.04$	$0.13 \pm 0.05$	$0.06 \pm 0.01$	$0.15 \pm 0.04$	$0.09 \pm 0.02$
38268	$0.17 \pm 0.02$	$0.17 \pm 0.04$	$0.14 \pm 0.07$	$0.23 \pm 0.03$	$0.10 \pm 0.02$
38908	$0.17 \pm 0.04$	$0.10 \pm 0.04$	$0.14 \pm 0.04$	$0.18 \pm 0.04$	$0.12 \pm 0.02$
46767	$0.26 \pm 0.06$	$0.13 \pm 0.03$	$0.15 \pm 0.10$	$0.21 \pm 0.09$	$0.18 \pm 0.02$
49906	$0.18 \pm 0.09$	$0.12 \pm 0.10$	$0.12 \pm 0.06$	$0.18 \pm 0.10$	$0.15 \pm 0.02$
55750	$0.14 \pm 0.03$	$0.16 \pm 0.05$	$0.08 \pm 0.04$	$0.18 \pm 0.06$	$0.12 \pm 0.02$
56010	$0.24 \pm 0.10$	$0.30 \pm 0.13$	$0.05 \pm 0.02$	$0.30 \pm 0.13$	$0.14 \pm 0.02$
57931	$0.13 \pm 0.03$	$0.09 \pm 0.03$	$0.09 \pm 0.04$	$0.14 \pm 0.04$	$0.08 \pm 0.06$
58410	$0.10 \pm 0.04$	$0.07 \pm 0.02$	$0.10 \pm 0.03$	$0.13 \pm 0.02$	$0.09 \pm 0.06$
70962	$0.51 \pm 0.02$	$0.44 \pm 0.06$	$0.17 \pm 0.06$	$0.47 \pm 0.04$	$0.40 \pm 0.02$
71106	$0.28 \pm 0.05$	$0.23 \pm 0.05$	$0.14 \pm 0.04$	$0.27 \pm 0.06$	$0.18 \pm 0.02$
72144	$0.04 \pm 0.02$	$0.20 \pm 0.09$	$0.08 \pm 0.04$	$0.22 \pm 0.08$	$0.04 \pm 0.02$
72453	$0.10 \pm 0.02$	$0.07 \pm 0.03$	$0.09 \pm 0.03$	$0.12 \pm 0.02$	$0.09 \pm 0.02$

## 2.5 Discussion

### 2.5.1 Sample Characteristics

Because of our selection of galaxies with small diameters (so we could observe their velocity fields with DensePak), we chose galaxies out of the PGC which had not been studied in detail previously. Throughout the course of this Chapter, we discussed several instances of data culled from the PGC not agreeing with our observations: axis ratios from the PGC were not in good agreement with axis ratios measured using *ellipse* (Figure 2.12) and the scatter in  $B - R$  was much larger than expected for a population of disk galaxies (Figure 2.5).  $T$ -types, too, appeared to be uncorrelated with other structural parameters (Figure 2.14). Of the parameters,  $C_{80:20}$ ,  $\mu_0$ ,  $B - R$  and  $A_{180}$  which should be correlated with  $t$ -type, only  $\mu_0$  showed any trend with  $t$ -type. Only the segregation of early from late-type disks pointed out by de Jong (1996b) in the plot of effective bulge surface brightness,  $\mu_e$ , to bulge effective radius,  $r_e$ , indicated that tabulated  $t$ -types were partially accurate (Figure 2.15). The Hubble typing of sample galaxies showed other weaknesses: Several galaxies which were classified as barred spirals clearly were not barred when imaged with improved spatial resolution. This leads us to believe that the tabulated types for these galaxies may be unreliable overall except in distinguishing crudely between systems on the basis of parameters related to bulge size and surface brightness. The accuracy of  $t$ -types for our sample are in question probably because typing was performed on low spatial resolution images.

Because tabulated Hubble and  $t$ -types for our sample were unreliable, we used structural parameters to show the large range of galaxy types observed in our sample. For

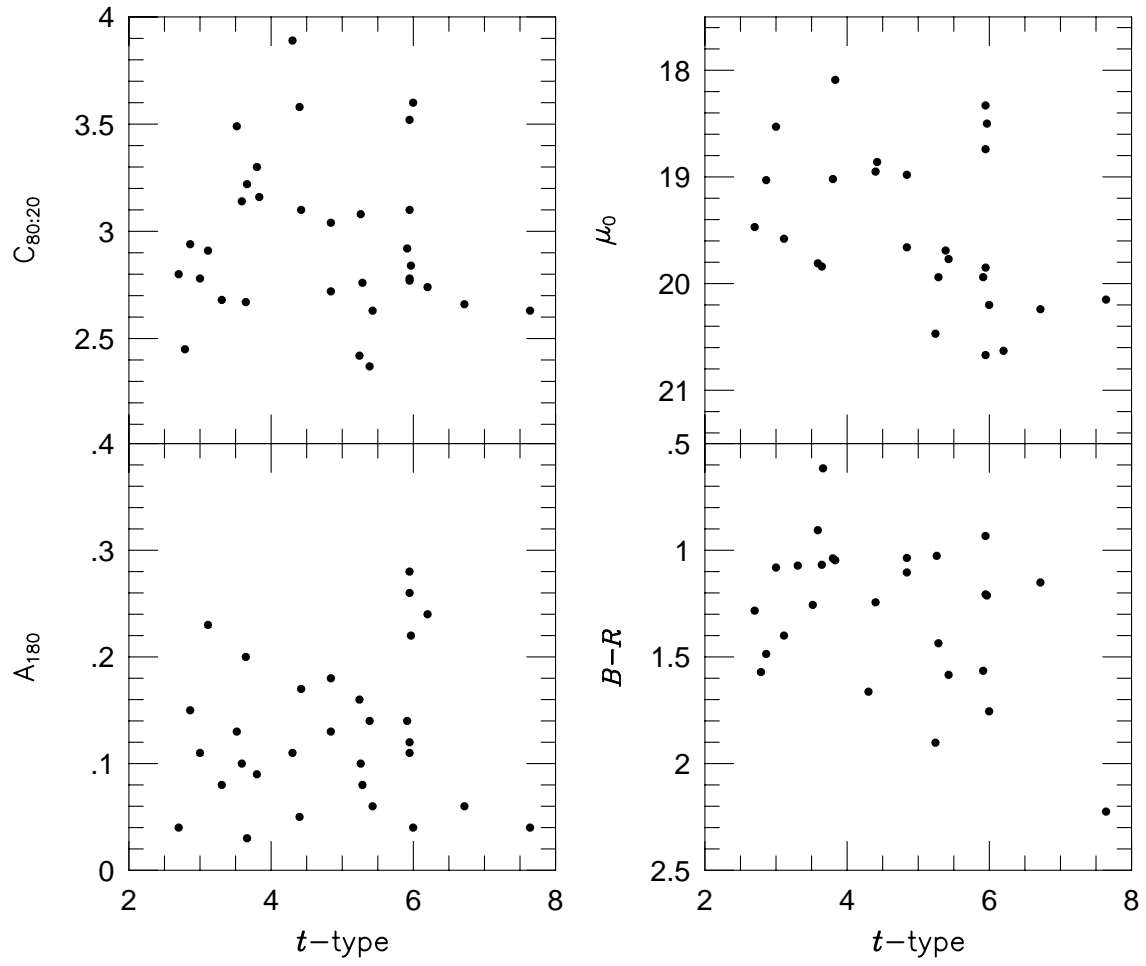


Fig. 2.14. Our image structure indices and mode parameters versus PGC tabulated  $t$ -types for our sample. Only a weak correlation exists between disk surface brightness,  $\mu_0$ , and  $t$ -type.



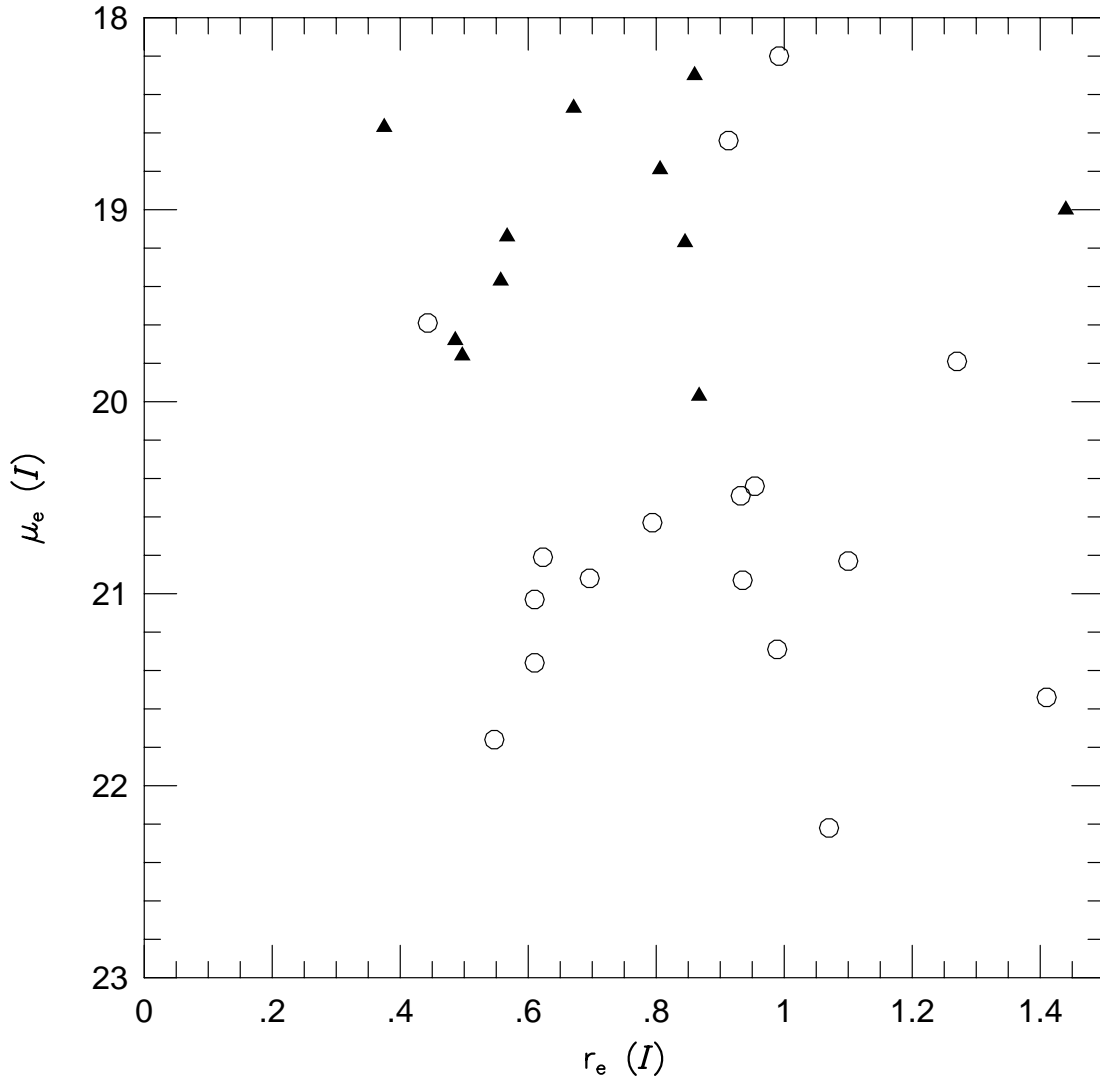


Fig. 2.15. Effective bulge surface brightness versus effective bulge radius. While  $t$ -types did not correlate well with other parameters, PGC tabulated  $t$ -types were well segregated when comparing bulge effective surface brightnesses and bulge effective radii. Solid triangles are early type ( $t\text{-type} < 4.5$ ) and open circles are later type disks.

example, we compared the structural parameters measured for our galaxies to structural parameters measured for the Frei *et al.* (1996) catalog of local Hubble-type galaxies by Bershad, Jangren & Conselice (2000) in Figure 2.16. Our measurements of asymmetry and concentration are consistent with those of disk galaxies in the Frei *et al.* (1996) sample. Some early disk galaxies in the Frei *et al.* (1996) sample have slightly higher concentration indices than any galaxy in our sample. This is reasonable since we tried to avoid selecting Sa or S0 galaxies. The effective surface brightnesses measured for our sample were also in good agreement, although this is a mystery. *B*-band surface brightnesses were measured for Bershad, Jangren & Conselice (2000), while we used *R*-band surface brightnesses in Figure 2.16. If one assumes a reasonable color correction, the two data sets should not overlap; we will continue studying this problem until we resolve this discrepancy.

The motivation behind many of our selection criteria was to choose galaxies similar to galaxies used in Tully-Fisher studies, but at low inclinations. We can now demonstrate this, *a posteriori*, in a quantitative fashion. For example, Courteau’s (1996; 1997) Tully-Fisher sample share a similar dynamic range in redshifts and disk scale lengths (Figure 2.17). While both surveys suffer from a Malmquist-related bias (more distant disks tend to be larger), our selection of galaxies with  $D_{25} < 1.5$  arcminutes forced us to observe smaller galaxies at a given redshift than Courteau (1996). This difference should not influence comparisons of Tully-Fisher relations since there is considerable overlap in the size distribution (Figure 2.17). More relevant is the comparison of the range in surface brightnesses, colors, and absolute magnitudes for the two samples. Courteau (1996) measured only Lick *r*-band magnitudes (similar to Gunn *r*-band). By using the color

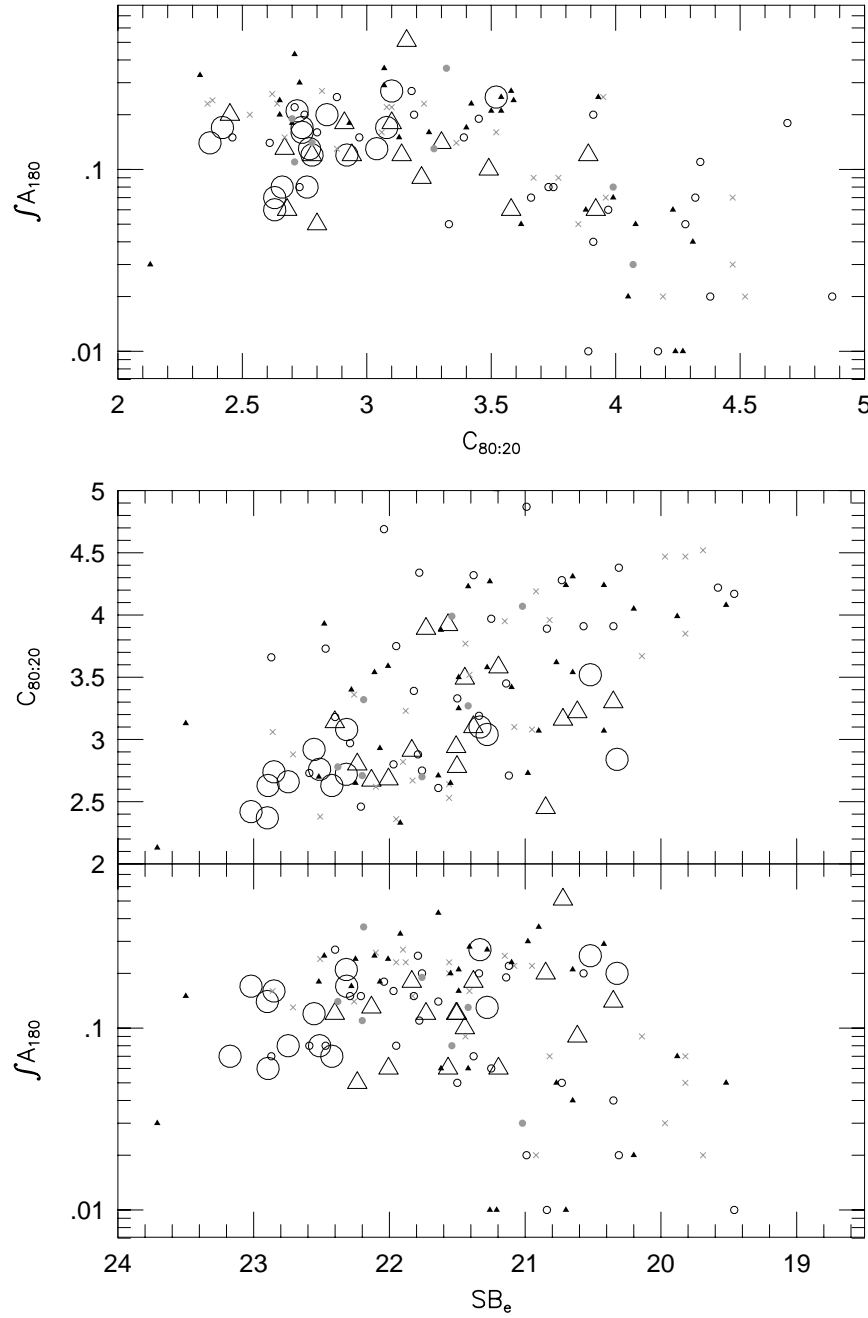


Fig. 2.16. Comparison of key photometric indices for this study versus the Frei *et al.* (1996) sample (Bershady, Jangren, & Conselice 2000).  $\int A_{180}$  is the integrated rotation asymmetry measured in a disk of radius  $r_{\eta=0.2}$  as described in §2.4.5.  $C_{80:20} \equiv 5 \log[r(80\%)/r(20\%)]$  described in §2.4.2.  $SB_e$  is the surface brightness at the half-light radius. Disks in the Frei *et al.* (1996) sample (small symbols; ellipticals marked by “x”, early-type disks marked by filled triangles, late-type disks marked by open circles, and irregulars marked by grey filled circles) shared the virtually the same range of disk properties as our sample galaxies (large triangles are early-type disks with  $t\text{-type} \leq 4.5$ , and large open circles are late-type disks).

correction  $R - r = -0.36$  (Fukugita *et al.* 1995), we find our sample share the same range in color (Courteau’s  $B$ -band magnitudes also came from the RC3 catalog), central surface brightness and absolute  $r$ -magnitudes (Figure 2.18).

Comparisons of our sample to Bershad, Jangren & Conselice (2000) and Courteau (1996; 1997) suggested our survey did contain a representative sample of luminous disk galaxies. In particular, our sample is (1) comparable to Courteau in type, distance and scale and (2) similar in form to the Frei *et al.* (1996) sample of bright nearby galaxies, but more distant.

### 2.5.2 Asymmetry

Rotational asymmetries have been linked to flocculence, so we expected the difference between a rotational asymmetry index measured between 1.5-2.5 scale lengths,  $A_{180}$ , and the rotational asymmetry index measured in a disk with radius  $r_{\eta=0.2}$ ,  $\int A_{180}$ , to show large variations that would correlate strongly with concentration index or surface brightness, but instead found no trends with either quantity (Figure 2.19). In fact,  $\int A_{180}$  was very highly correlated with  $A_{180}$ .

In order to further test whether rotational asymmetries measured disk flocculence, we decided to compare our measurements of rotational asymmetry to Fourier asymmetry amplitudes. Operationally, the process of determining rotational asymmetries yields a combination of all odd components of a Fourier series expansion. For our comparisons of rotational asymmetry and Fourier amplitudes, we chose to make measurements in a common annulus between 1.5 and 2.5 scale lengths for  $I$ -band images because (1) Jog (1999) suggested that lopsidedness is stable beyond 1.4 scale lengths, (2) Zaritsky & Rix

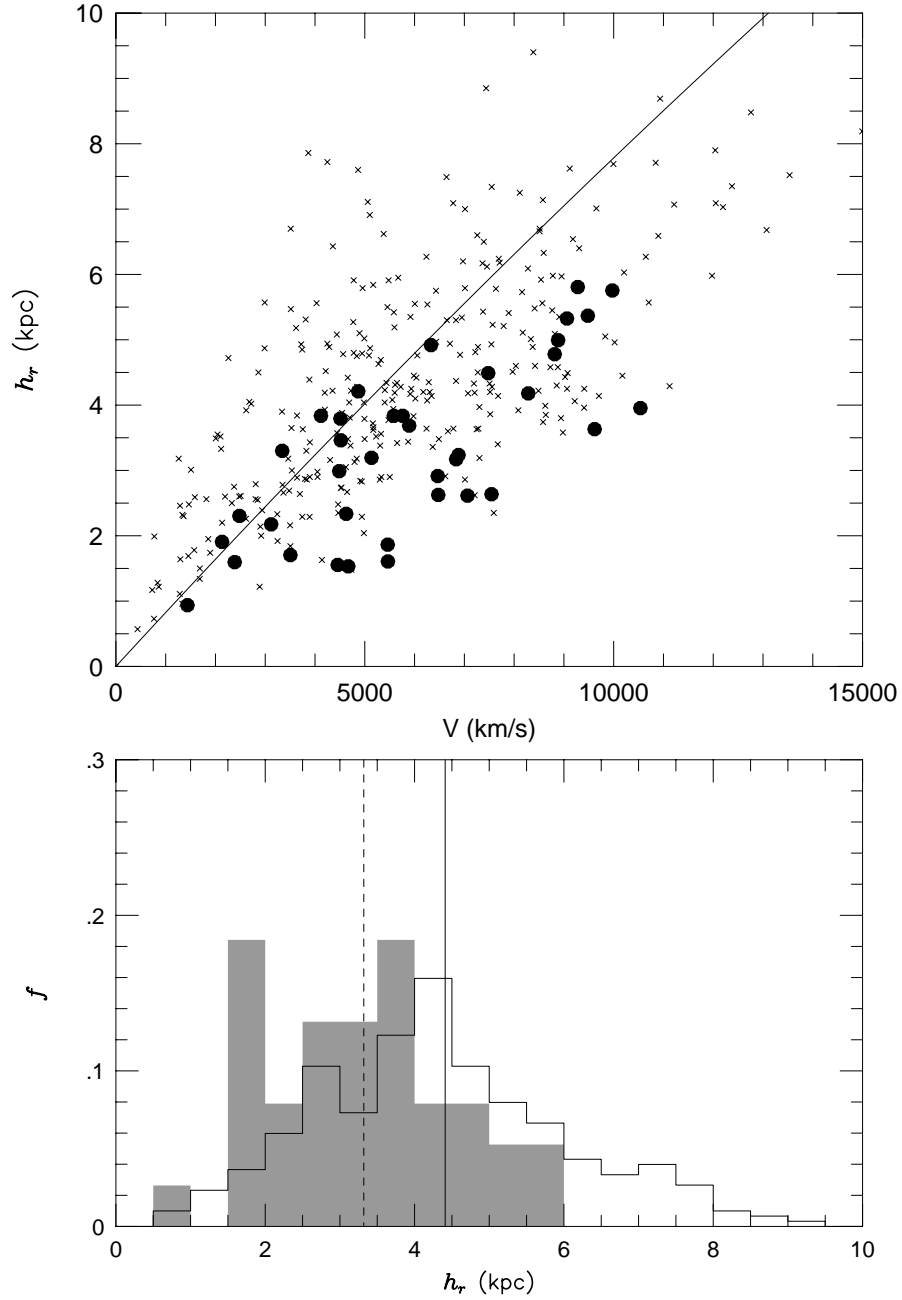


Fig. 2.17. Top panel: Our sample (filled circles) and the Tully–Fisher sample of Courteau (1996; “x”) share comparable ranges in recession velocities and physical sizes ( $H_0 = 70 \text{ km/s/Mpc}$ ). While both studies suffer from a Malmquist-like bias where the mean physical size increases with recession velocity, the selection criterion of choosing galaxies with scale lengths less than 12 arcsec (solid line) limits us to slightly smaller targets. Bottom Panel: The normalized distribution of physical scale lengths illustrates the mean size difference for the two samples. The open histogram is the normalized distribution of 301 Courteau sample galaxies. The shaded histogram shows 38 of our 39 galaxies (We do not have a measured scale length for PGC 39728). The mean scale lengths for Courteau’s sample (solid line) and our sample (dashed line) differ by 1.1 kpc.

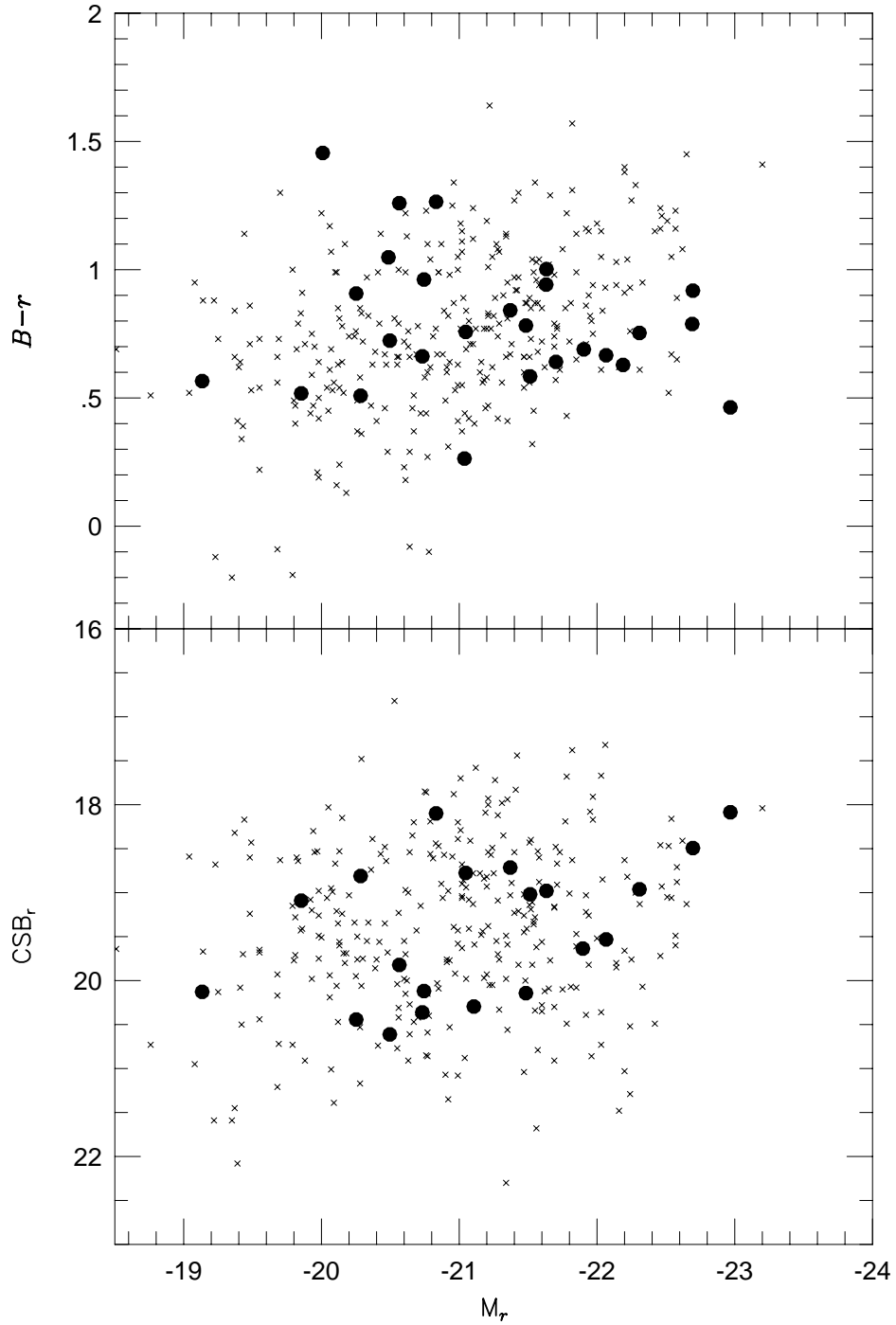


Fig. 2.18. Absolute magnitude,  $M_r$  ( $H_0 = 70$  km/s/Mpc), versus Color,  $B - r$  (top panel), and central surface brightness (bottom panel) for Courteau's (1996) sample ("x") and our survey (filled circles). We applied the color correction,  $R - r = -0.36$ , to compare our Kron-Cousins  $R$  magnitudes to Courteau's Lick  $r$  magnitudes. Contributions from both the disk and bulge contribute to the central surface brightness. Our survey has similar properties to the primarily Sb and Sc galaxies that make up the Courteau sample.

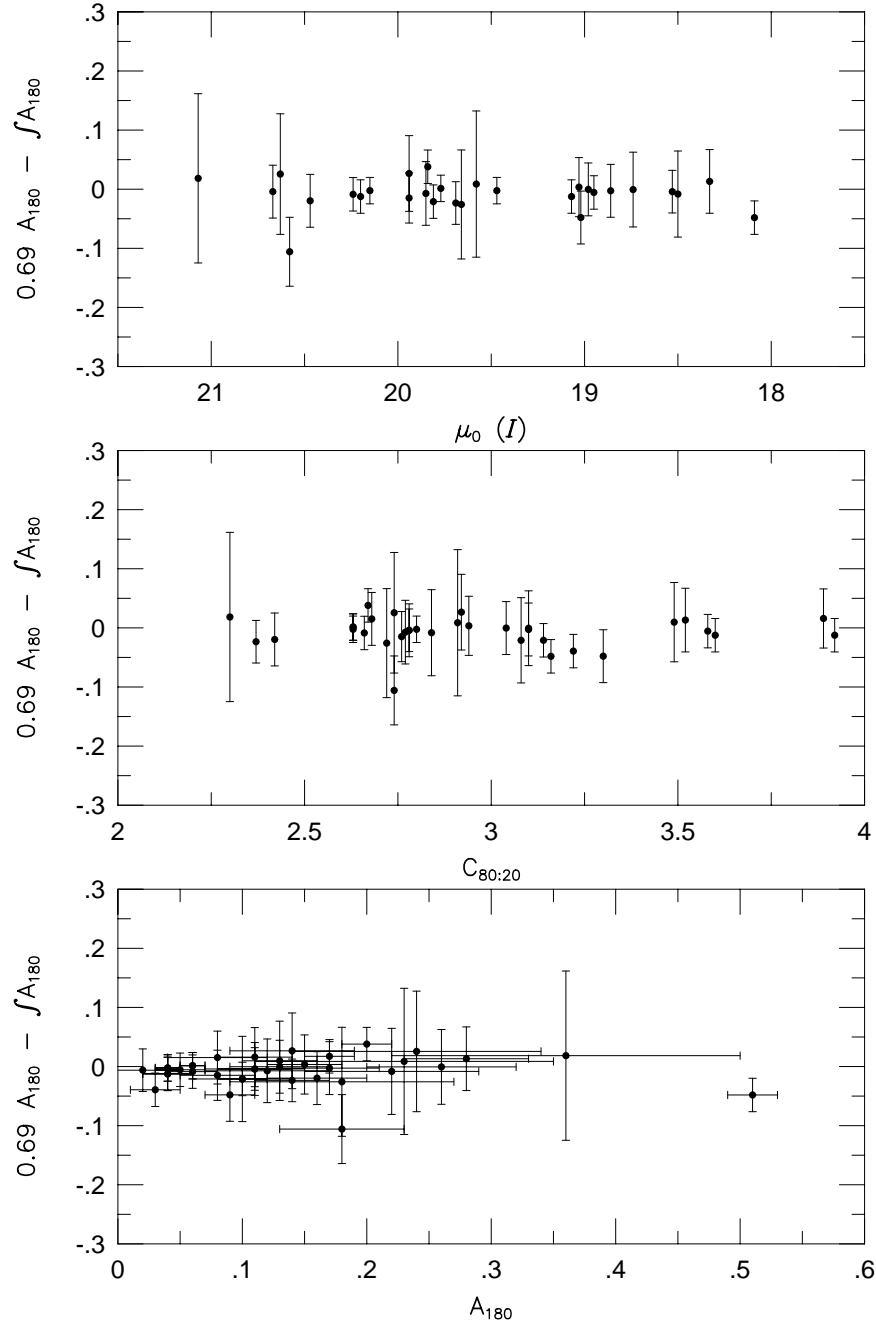


Fig. 2.19. Central disk surface brightness,  $\mu_0$  (top panel), concentration index,  $C_{80:20}$  (middle panel), and rotational asymmetry,  $A_{180}$  (bottom panel) versus the difference between rotational asymmetries measured in an annulus at 1.5 to 2.5 scale lengths,  $A_{180}$ , and within a disk with radius  $r_{\eta=0.2}$ ,  $\int A_{180}$ . After scaling the rotational asymmetry,  $A_{180}$ , by 0.69 there appears to be no statistically significant trends between  $I$ -band rotational asymmetries. The correlation coefficient between  $A_{180}$  and  $\int A_{180}$  is 0.93, signifying that these quantities were statistically identical.

(1997) and Rudnick & Rix (1998) studied Fourier decompositions in the same region, and (3) in §2.3.5 we showed measurements of  $A_{180}$  and  $\int A_{180}$  were essentially equivalent. Although we found that the Fourier amplitude  $A_1$  did not correlate strongly with  $A_{180}$  (the correlation coefficient was 0.82), the difference was related to  $A_3$  (Figure 2.20). This result motivated us to measure  $A_{1+3} \equiv A_1^2 + A_3^2$ . A comparison of  $A_{180}$  and  $A_{1+3}$  yielded  $A_{1+3} = 0.86A_{180} + 0.05$  with a correlation coefficient of 0.91 (Figure 6.1). This finding suggests  $A_{180}$  is not a measure of disk flocculence (i.e., high-order, high-frequency modes); instead rotational asymmetry is a measure of low order, odd asymmetric modes dominated by lopsidedness. While flocculence must contribute to  $A_{180}$ , the magnitude of the contribution is small; the difference  $A_{180} - A_{1+3}$  does not exhibit strong trends with luminosity, concentration index or type (Figure 2.22), an unexpected result if  $A_{180}$  measured flocculence, where the strength of the latter is expected to be related to the intensity of star-formation.

## 2.6 Summary

In this Chapter, we presented photometric data and measurements of structural parameters for 39 nearly face-on spiral disks. We showed the intrinsic characteristics of this sample: luminosity, concentration index, radii, bulge-disk scale lengths and surface brightnesses and asymmetry, spanned a broad range. Galaxy properties for our face-on sample were comparable to the more inclined disks studies of at least one major Tully-Fisher survey. Indeed, by employing fits to the velocity fields described in Chapter 3, we will study the Tully-Fisher relation for face-on disks in Chapter 4.



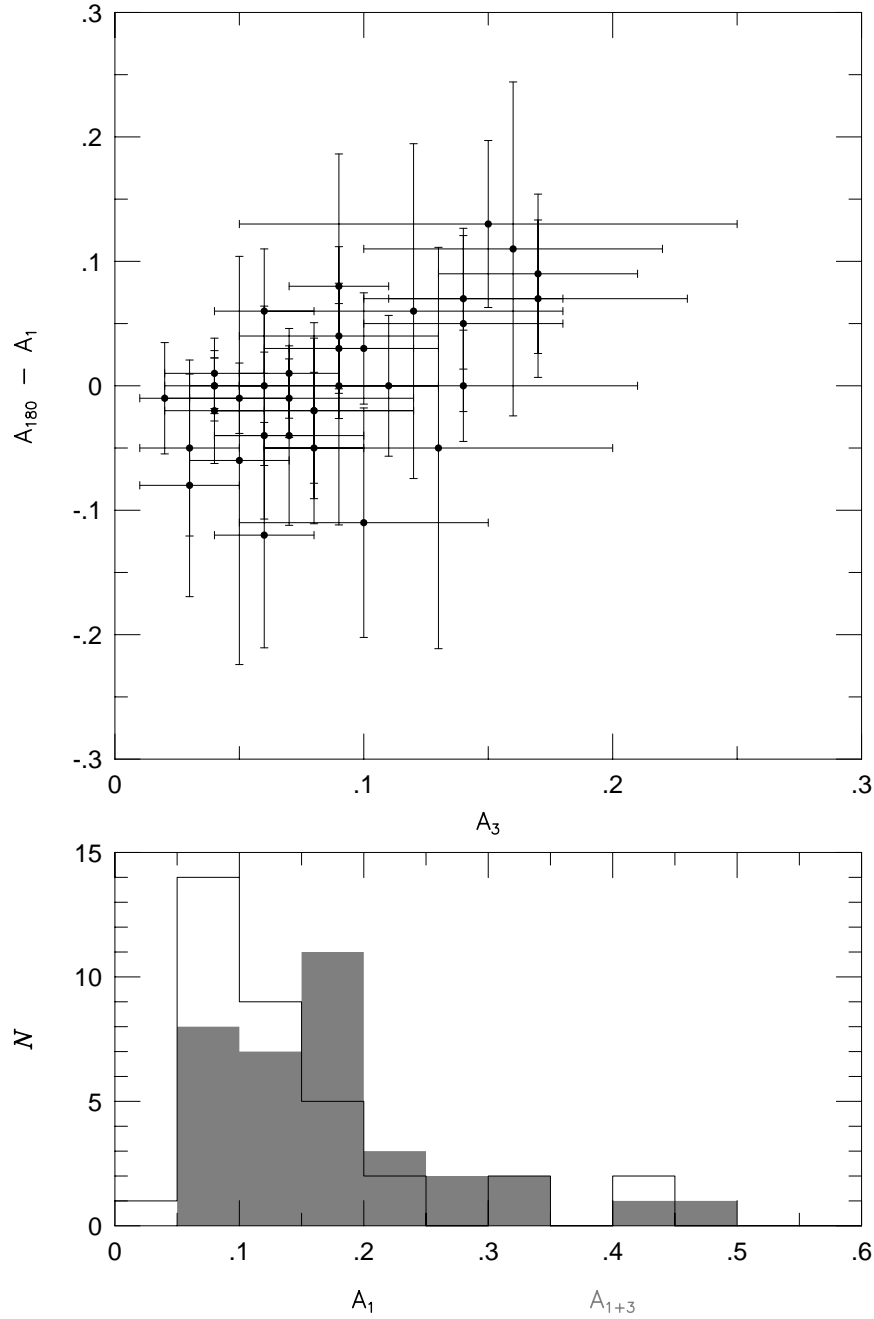


Fig. 2.20. Top Panel: The difference between  $I$ -band measurements of rotational asymmetry and the first Fourier asymmetry amplitude ( $A_1$ ) were related to  $A_3$ . This relation motivated us to measure  $A_{1+3}$ , the quadrature sum of the amplitudes  $A_1$  and  $A_3$ . Bottom Panel:  $\sim 20\%$  of galaxies were significantly lopsided ( $A_1 > 0.2$ ; open histogram). The shaded histogram shows the distribution of our  $A_{1+3}$  asymmetry measurement. All measures in this plot were calculated in annuli between 1.5 and 2.5 scale lengths.

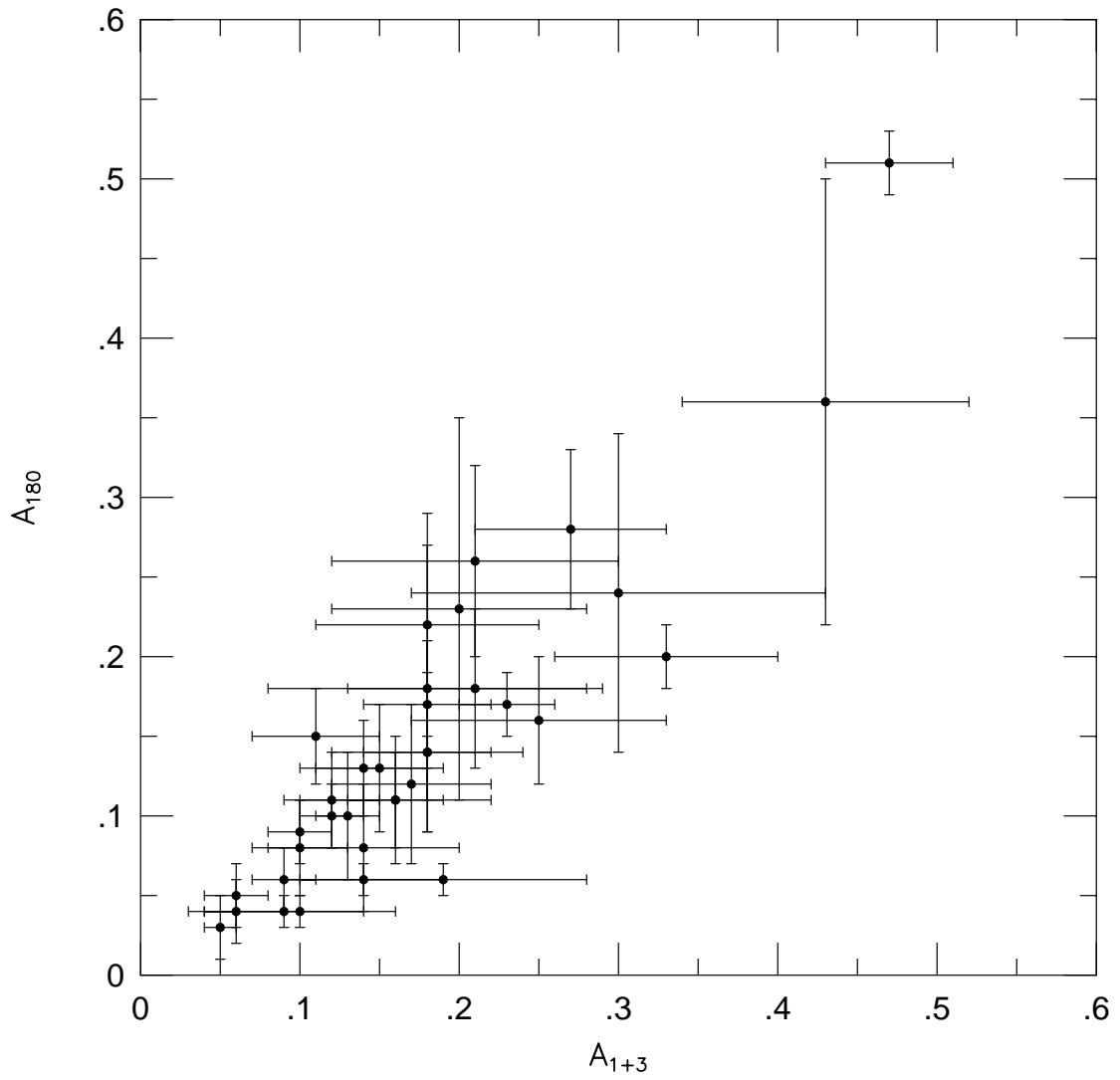


Fig. 2.21. Rotational asymmetry,  $A_{180}$  versus the sum of the  $m = 1$  and  $m = 3$  Fourier amplitudes,  $A_{1+3}$ . The correlation coefficient for the relationship between  $A_{180}$  and  $A_{1+3}$  was 0.91, implying  $A_{180}$  is very closely related to the first two Fourier amplitudes (lopsidedness and three-armedness).  $A_{180}$  does not appear to be a measure of flocculence.

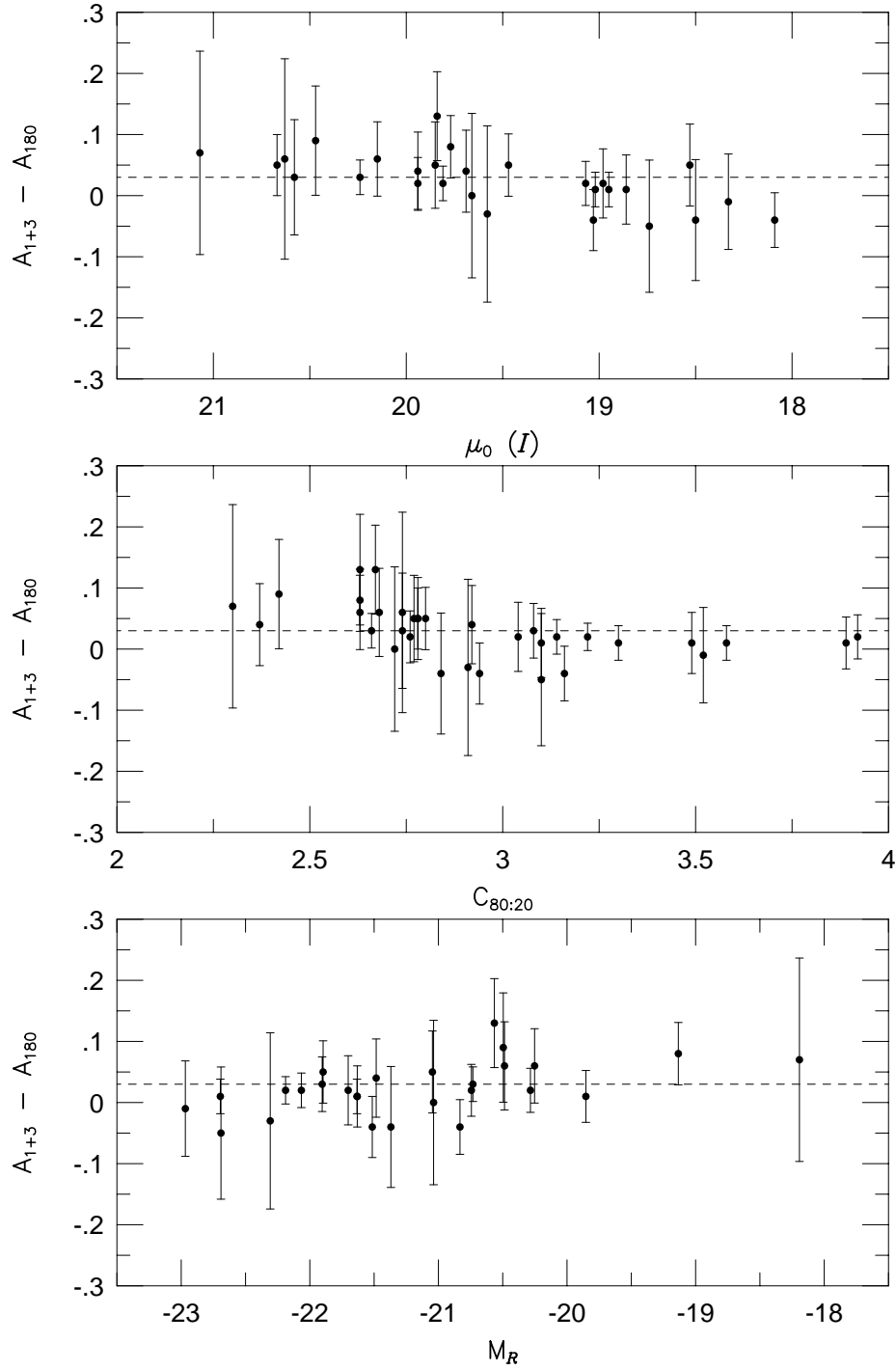


Fig. 2.22. The differences between rotational asymmetry and  $A_{1+3} \equiv (A_1^2 + A_3^2)^{1/2}$  exhibit strong trends with disk surface brightness (top panel), concentration index (middle panel) or absolute magnitude (bottom panel). If rotational asymmetry were a measure of flocculence, we expected to find systematic trends in these plots as flocculence is greater in galaxies which have lower surface brightnesses, are more diffuse, and less luminous.

Measuring axis ratios and position angles for face-on disk galaxies was difficult: Spiral structure, warping, and limited signal made such measurements complicated. Attempts at using two-dimensional bulge-disk decompositions failed to provide consistent axis ratios. We therefore developed a measure of spiral structure and used it, along with other criteria, to develop a set of guidelines for making axis ratio and position angle measurements. By applying these guidelines, we were able to measure axis ratios and position angles for 28 galaxies in our sample. We will use these photometric indices, in combination with kinematic indices derived in Chapter 3, to estimate the intrinsic ellipticity of disk galaxies in Chapter 4. Intrinsic disk ellipticity is an important quantity because it can account for a significant fraction of scatter in the Tully-Fisher relation (Franx & de Zeeuw 1992), and provide clues into the structure of the gravitational potentials for spiral galaxies (Jog 2000).

The intrinsic ellipticity of disks is an  $m = 2$  asymmetry mode which is difficult to measure because viewing angles and spiral structure strongly affect  $m = 2$  amplitudes and phase angles. Odd Fourier modes, however, are much easier to measure. In this Chapter, we used two different methods to measure the odd asymmetry modes: Fourier decompositions and rotational asymmetry. We established the distribution of different Fourier amplitudes for our sample. We found that the fraction of galaxies with an  $m = 1$  amplitude,  $A_1 > 0.2$  was lower than the fraction found in other asymmetry surveys (20% of our galaxies were lopsided compared to 30% of Zaritsky & Rix's (1997) sample). We also showed that  $A_1$  was the dominant Fourier amplitude, indicating lopsidedness is the dominant source of odd Fourier mode asymmetries. We further confirmed the observations of Rudnick & Rix that galaxies with large lopsidedness amplitudes,  $A_1$ ,

did not show signs of being one-armed spirals, i.e., the phase angle corresponding to the  $m = 1$  mode was constant with radius, thus ruling out the asymmetry theories of Junqueira & Combes (1996) and Comins *et al.* (1997) described in Chapter 1.

Rotational asymmetry have been described as a measure of flocculence (Conselice, Bershadsky & Jangren 2000). In the terminology of Fourier decompositions, flocculence is the contribution to asymmetry from high order modes;  $m > 9$  modes would describe flocculence (Kranz *et al.* 2001). The interpretation of  $A_{180}$  as a measure of flocculence was based on increasing amplitudes for the rotational asymmetry,  $A_{180}$ , at bluer colors. To test whether  $A_{180}$  measured flocculence, we compared both rotational and Fourier decomposition asymmetries for our sample. We found that  $A_{180}$  was highly correlated with the quadrature sum of the  $A_1$  and  $A_3$  Fourier amplitudes implying rotational asymmetry is dominated by low order (non-flocculent) asymmetric modes. Because Fourier decompositions require higher signal to noise ratios and greater spatial resolution, rotational asymmetry becomes a powerful tool for measuring lopsidedness in distant galaxies.

## Chapter 3

# H $\alpha$ Velocity-Fields of Face-On Spiral Galaxies

## Abstract<sup>1</sup>

Using the integral field unit DensePak on the WIYN 3.5m telescope we have obtained velocity fields of 39 nearly face-on disks at echelle resolutions. By virtue of the high quality of these kinematic data, we were able to derive accurate and precise kinematic inclinations at unprecedentedly low inclinations for 36 of these galaxies. Inclinations are derived via modeling the kinematic data as single, inclined disks in circular rotation. We find that DensePak H $\alpha$  kinematic data are of sufficient precision to derive accurate inclinations down to  $15^\circ$ . HI line profiles observed with the Nançay radio telescope for 25 of these sample galaxies, plus line widths for an additional 12 galaxies available from the literature, allow us to test our DensePak data and determine the validity of our modeling and derived inclinations. This paper presents the kinematic data, modeling techniques, and inter-comparisons of HI and optical data. These results, combined with the photometric analysis in Chapter 2 complete the foundation for the present study of disk asymmetry and the TF relation of face-on spiral galaxies.

---

<sup>1</sup>Andersen, D.R., Bershady, M.A., Sparke, L.S., Gallagher, J.S., Wilcots, E.M., van Driel, W, & Ragaigue, D. 2001, *to be submitted to Ap.J.S.*

### 3.1 Introduction

The rotation curves of spiral galaxies are perhaps the most compelling proof for the existence of dark matter. As such, the most important element of a velocity field for spiral disks is the major axis position–velocity relationship, i.e. the rotation curve. If galaxy mass followed their light distributions most of the mass would be concentrated toward the center, and one would expect a nearly Keplerian rotation curve which would fall rapidly with radius. Instead, these rotation curves remain constant or even rise at large radii (Freeman 1970; Rubin, Ford & Thonnard 1980; Bosma 1981a; 1981b; Begeman 1987; Verheijen & Sancisi 2001). Assuming a reasonable mass to light ratio which remains roughly constant in disks, disk mass alone can not reproduce both the sharply rising inner slope and flat outer regions of a typical spiral galaxy rotation curve; massive, dark halos were required to reproduce the flat outer regions of rotation curves (Begeman, Broeils & Sanders 1991; Courteau & Rix 1999; Palunas & Williams 2000). Therefore, the rotation speed of a spiral galaxy is related to its total mass.

Keeping in mind that galaxy mass is linked to rotation speed, the Tully-Fisher relation (Tully & Fisher 1977; hereafter TF) between luminosity and rotation speed of spiral galaxies can be re-couched as a physical relationship between the baryons responsible for luminosity and the total galaxy mass which is dominated by the contribution due to dark matter. The observed scatter in the TF relation is quite small,  $\sim 0.2$ – $0.3$  magnitudes (e.g. Courteau 1992; Bernstein *et al.* 1994; Giovanelli *et al.* 1997) and is induced by a variety of astrophysical processes, presumably including asymmetries

(Zaritsky & Rix 1997), ellipticity (Franx & de Zeeuw 1992), and variations in disk-to-halo mass ratio and disk mass-to-light ratio. Each of these properties is linked to the structure and formation of galaxies. Therefore, understanding the TF error budget is an exercise in putting limits on the nature and formation scenarios for disk galaxies.

However, linking TF scatter to measures of the above disk properties is very difficult. Ellipticity and photometric asymmetry have been measured in face-on disks (Rix & Zaritsky 1995; Zaritsky & Rix 1997; Andersen *et al.* 2001), but have not been measured for disks that are part of a TF study. Although it is theorized that variations in disk mass-to-halo ratios will not induce TF scatter (e.g. Steinmetz & Navarro 1999; van den Bosch 2000), measurements of disk mass would never-the-less constrain rotation curve mass models. Direct disk mass measurements would also provide a check on the typically assumed disk mass-to-light ratio and hence halo density profiles. Disk mass, however, is a difficult measurement to obtain directly. Direct measurements of disk mass need to be made for relatively face-on disks so the  $z$ -component of the velocity ellipsoid can be measured. The total mass budget, therefore, requires an accurate inclination to correct for projected rotation curves. Accurate and precise measurements of inclinations less than  $30^\circ$  would make possible these studies of disk mass, and studies of the relation between asymmetry, ellipticity and TF scatter.

The study of galaxy velocity fields have yielded important clues into the structure and dynamics of galaxies. Traditionally, studies have required accurate and precise inclinations and have therefore modeled the velocity fields of inclined galaxies. While a few studies have investigated disk kinematics at low inclinations (Kornreich *et al.* 2000; Kranz *et al.* 2001), most kinematic studies of disk galaxies have been done at



$i > 45^\circ$  where projected rotation velocities are large. For example, HI velocity fields have been used to study warps and elliptical orbits (Briggs 1990; Christodoulou, *et al.* 1993; Schoenmakers, Franx & De Zeeuw 1997; Schoenmakers 1999). Recently, H $\alpha$  velocity fields have been used to study spiral galaxy kinematics: Fabry-Perot and multiple long-slit observations have been used to study the streaming motions of ionized gas in spiral arms (Rozas *et al.* 2000; Kranz *et al.* 2001).

Inclined galaxies have been chosen for kinematic studies primarily because the most popular method for determining kinematic inclinations fails for face-on systems; tilted-ring fits do not consider data at azimuthal angles where differences between velocity field models with different inclinations are maximized (Begeman 1989). HI kinematic studies have employed tilted-ring fits anyway, because the relatively low spatial sampling of the inner regions of disk and warping at large radii complicate global model fits of galaxies. One question which arises is whether the past and current limitations of HI synthesis maps have overly restricted previous kinematic surveys in inclined systems.

To date, most kinematic studies of spiral disks have been done in HI. HI observations are advantageous because they allow for studies of gas out to large radii, although HI is sometimes depleted in central regions because gas is either ionized or in the molecular phase. However, radio synthesis observations require long exposures. For example, NGC 2403 was observed with the Westerbork Synthesis Radio Telescope (Sicking 1997) for 48 hours with a circular beam of 13 arcseconds (Schoenmakers *et al.* 1997). In contrast, it takes only a fraction of the time to recover relatively high spatial resolution H $\alpha$  velocity fields from Fabry-Perot or integral field units. Recently, Fabry-Perot observations have been made for a number of normal spiral galaxies (Schommer *et al.* 1993;

Jiménez-Vicente *et al.* 1999; Jiménez-Vicente & Battaner 2000). We have mapped H $\alpha$  velocity fields for most sample galaxies in 2 hours using an integral field unit with 3 arcsecond fibers. Indeed, integral field units are now just starting to be used for a wide range of kinematic studies as well (Krabbe *et al.* 1997; Andersen *et al.* 2001; Davies *et al.* 2001). In contrast to HI studies, optical velocity fields typically sample the inner regions of disks at higher spatial resolution while they do not extend to large radii. In this sense they are complimentary. However, for the study of the dynamics of the optically luminous disk, it is the inner regions ( $r < 3$ -4 scale lengths) that are particularly important. In addition, the new wave of infrared instruments on 10m class adaptive optics telescopes offers the promise of exploring the evolution of disk kinematics out to redshifts that cannot be matched presently by radio telescopes. As such, optical integral field spectroscopy proffers a new and powerful window on the kinematics of spiral disks.

In this chapter, we use H $\alpha$  echelle observations with the integral field unit (IFU) DensePak (Barden, Sawyer & Honeycutt 1998) on the WIYN 3.5m telescope to construct two-dimensional velocity fields of 39 nearly face-on galaxies. DensePak and Nançay observations are described in §3.2, and in §3.3 we describe the reductions. We demonstrate the ability to fit single, inclined, circular velocity-field models to these kinematic maps in §3.4. We show that the inclinations derived from these models are shown to be accurate and precise in §3.5. Finally, we summarize our results in §3.6. The ability to measure accurate and precise inclinations, coupled with photometric data described in Chapter 2, is crucial to our ability to measure disk ellipticity (Chapter 4) and study the face-on Tully-Fisher relation (Chapter 5).

## 3.2 Observations

In Chapter 2, we describe the collection and analysis of  $R$  and  $I$ -band images for survey targets. Here, we report observations of both  $H\alpha$  velocity fields using the integral field unit (IFU), DensePak on the WIYN 3.5m telescope, and HI line profiles with the Nançay radio telescope. The motivation and selection criteria for our survey of disk structure and kinematics also are described in Chapter 2.

### 3.2.1 DensePak Observations

We observed 39 sample galaxies with DensePak during 11 nights on 6 separate observing runs. The DensePak IFU is a fiber optic-array mounted at the Nasmyth f/6.3 focus imaging port on the WIYN 3.5m telescope. The WIYN Observatory, located on Kitt Peak south of Tucson, Arizona, stands 6875 feet above sea level and is home to the second largest telescope on the mountain. Dedicated in October, 1994, the WIYN telescope employs an altitude–azimuth mount design. DensePak is an array of 91 fibers arranged in a seven by thirteen fiber rectangle sub-tending an area of  $30'' \times 45''$ . Fibers have an active core diameter of three arcseconds ( $300\ \mu\text{m}$ ). Cladding and buffer increase the total fiber diameter to four arcseconds ( $400\ \mu\text{m}$ ). In addition to the 91 fibers arranged in a rectangle, another 4 fibers are spaced around the rectangle roughly an arcminute from the center and are used to measure the “sky” flux. Of the original 91 DensePak fibers, 86 fibers remain — 5 fibers are broken (Figure 3.1).

DensePak feeds the WIYN Bench Spectrograph, a fiber-fed spectrograph designed to provide low to medium resolution spectra. We used the Bench Spectrograph camera (BSC) and 316 lines/mm echelle grating in order 8 to cover  $6500\text{\AA} < \lambda < 6900\text{\AA}$ , with a dispersion of  $0.195\text{ \AA/pix}$  ( $8.6\text{ km/s/pix}$ ) and an instrumental FWHM of  $0.51\text{ \AA}$  ( $22.5\text{ km/s}$ ). We required the highest resolution available with this instrument; fitting velocity field models to galaxies with observed rotation velocities of less than  $100\text{ km/s}$  required centroids with accuracies of roughly  $5\text{ km/s}$ . The system throughput for this setup is roughly 4% estimated from comparing our mean spectral continuum fluxes to calibrated *R*-band images.

Since galaxy rotation curves typically peak at roughly two scale-lengths (Courteau & Rix 1999; Willick 1999) and  $\text{H}\alpha$  emission is only detected out to 3–4 scale-lengths (Rubin, Waterman & Kenney 1999; Dale *et al.* 2001), we desired spatial coverage of galaxies out to at least 2.5 lengths. Initial scale-lengths were measured from the Second Generation Digitized Sky Survey. Galaxies with scale-lengths less than six arcseconds only required one DensePak position to cover several scale-lengths. However, higher spatial resolutions were required to yield successful velocity field fits; disk scale-lengths needed to be sampled by more than a single fiber. In these cases, two overlapping DensePak positions offset by a half-fiber diameter were used. For scale-lengths between  $6''$  and  $9''$ , we used two DensePak positions offset to cover a  $45'' \times 45''$  area, and for scale-lengths between  $9''$  and  $12''$ , we used three DensePak positions. The first two positions were offset  $27''$  from each other. For the third position, DensePak was rotated, centered, and offset south of the first two positions. These three DensePak positions covered almost one square arcminute. In order to observe the  $\text{H}\alpha$  line emission at three scale-lengths

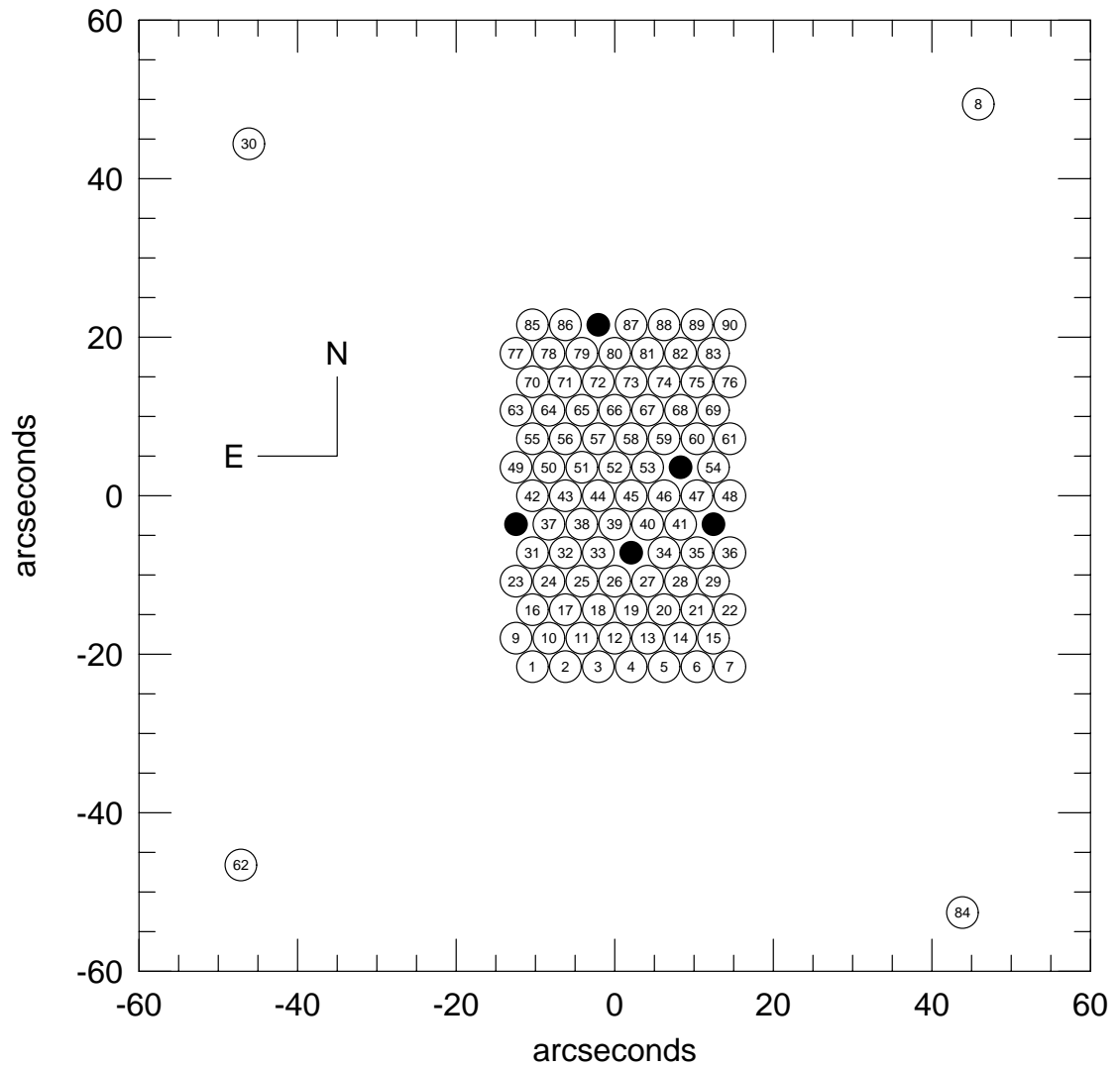


Fig. 3.1. Schematic of DensePak in the telescope focal plane. Fibers are identified according to their position in the output slit. There are empty spaces in the slit between fibers 22–23, 26–27, 33–34, 36–37, 41–42, 53–54 and 86–87. Solid black disks mark broken fibers in the fiber bundle. Spatial orientation is for a zero rotation offset.

and improve cosmic-ray rejection, we typically took 2 ~30 minute exposures at each position.

To center DensePak on our target we used a slit-viewing camera built into the fiber-mounting module known as WIFOE. Use of this camera involves inserting a pellicle for simultaneous viewing of the source and the rear-illuminated IFU. In this way, we aligned fiber 45 on a nearby guide star, and then zeroed the telescope offsets. After moving to our target, we could see the target galaxy in the slit-viewing camera only if the galaxy had a high central surface brightness and the sky was dark and clear. If we saw the galaxy, we confirmed it was centered on fiber 45 and performed the first offset. If the galaxy was not visible, we performed a blind offset. After guiding was established, we began our observations. Typically, after two thirty minute exposures, guiding was turned off and the second set of telescope offsets were applied. After guiding was re-established, we took our next two exposures. If a third position was required, we re-acquired the nearby guide star and rotated DensePak. Since DensePak was not on the rotator axis, the star shifted a few arcseconds as DensePak was rotated  $90^\circ$ . After re-centering the guide star on fiber 45, we moved DensePak back to the source, applied the final telescope offset and took our final two exposures after re-establishing guiding. We found that rotating DensePak added up to ten minutes of overhead to our observations; we therefore preferentially chose galaxies which required only two DensePak footprints to sample the disk out to 2.5 scale-lengths.

We encountered problems with both the alignment with the pellicle and the non-guided offsets. For some of our observations, the pellicle did not properly align images in the slit-viewing camera, so our spectra were not centered as expected. However,

when fitting velocity field models (see §3.4.3 for details) to multiple pointings, model centers were easily determined from the data. Hence, the unaligned pellicle did not diminish the quality of the data. However, inaccurate telescope offsets did complicate data handling. We performed tests at the telescope on the accuracy of our offsets by removing each offset in turn and re-centering on the guide star. We discovered that the guide star moved as much as a fiber diameter (3 arcseconds) after removing the telescope offsets. Therefore, as discussed in §3.4.3, we were forced to let telescope offsets be a free parameter in our model fits; thereby introducing extra fit parameters which should have been unnecessary. More tests need to be done to determine an accurate method for applying telescope offsets using DensePak on WIYN.

At the beginning and end of each night, dome flats and bias frames were taken. We also observed Thorium Argon (ThAr) line lamps at the beginning of the night, before and after the dewar was filled, and again at the end of the night. The BSC dewar has a hold time of 12 hours and was typically refilled during the course of the night. We observed sub-pixel shifts of  $\sim 0.1$  pixels in the centroids of the ThAr emission-lines, so when reducing spectra we calibrated wavelengths using the ThAr frame taken closest to a given observation as long as refilling the dewar did not place in the intervening time. Table 3.1 lists the dates, exposure times and number of pointings of our DensePak observations for the 39 targets.

Table 3.1. Observation log for our six DensePak runs on the WIYN telescope.

PGC	Run ID	U.T. date	exp. time	pointings
02162	e	12/22/99	3600, 3600	2
03512	e	12/21/99	3600, 2400	2
05345	e	12/20/99	3600, 3600	2
05673	f	12/29/00	3600, 3600, 3000	3
06855	f	12/30/00	3000, 3000, 3000	3
07826	e	12/22/99	3600, 3600	2
08941	b	01/23/99	3600, 3600	2
14564	b	01/22/99	3600, 1800	2
15531	b	01/23/99	3600, 3600, 3600	3
16274	e	12/19/99	3600, 3600	2
19767	f	12/29/00	3000, 3000	2
20938	e	12/19/99	3600, 3600, 2400, 2400	4
23333	e	12/22/99	3600, 3600	2
23598	b	01/22/99	3600, 3600	2
23913	b	01/22/99	3600, 3600	2
24788	f	12/30/00	2400, 2400	2
26140	b	01/21/99	3600	1
26140	f	12/29/00	2400, 2400	2
26517	f	12/30/00	3000, 3000	2
27792	e	12/21/99	3600, 3600	2



PGC	Run ID	U.T. date	exp. time	pointings
28310	b	01/22/99	3600, 3600	2
28401	e	12/19/99	2400, 1800	2
31159	c	03/28/99	3600	1
31159	f	12/29/00	3000, 2400	2
32091	e	12/21/99	3600, 3600	2
32638	f	12/30/00	2400, 2400	2
33465	e	12/22/99	2400, 2400	2
36925	c	03/28/99	3600	1
38268	e	12/21/99	3600, 3600	2
38908	b	01/22/99	3600	1
38908	f	12/30/00	3000, 3000	2
39728	e	12/22/99	2400	1
46767	b	01/22/99	3600, 3600	2
46767	b	01/23/99	3600	1
49906	c	03/28/99	3600	1
49906	f	12/29/00	3000, 3000	2
55750	c	03/28/99	3600, 3000	2
56010	c	03/28/99	3600, 1200	2
56010	c	03/29/99	2400	1
57931	d	09/03/99	3600, 3600	2

PGC	Run ID	U.T. date	exp. time	pointings
58410	a	05/22/98	3600, 3600	2
70962	e	12/22/99	2400	1
71106	e	12/20/99	2400, 2400	2
72144	e	12/19/99	3600, 3600	2
72453	e	12/21/99	3600, 3600	2

Table Notes: Run Identification

- a. UW allocation: Principal Investigator (PI): Bershady, Observers: Bershady & Andersen
- b. UW allocation, PI: Bershady, Gallagher, Sparke, Wilcots, Observer: Andersen
- c. UW allocation, PI: Bershady, Gallagher, Sparke, Wilcots, Observers: Andersen & Madsen
- d. UW allocation, PI: Bershady, Observer: Anderson
- e. NOAO allocation, PI: Andersen, Observer: Andersen
- f. UW allocation, PI: Bershady & Andersen, Observer: Andersen

### 3.2.2 21 cm HI line observations

The Nançay telescope is a meridian transit-type instrument of the Kraus/Ohio State design, consisting of a fixed spherical mirror, 300 m long and 35 m high, a tiltable flat mirror (200×40 m), and a focal carriage moving along a 90 m long curved rail track, which allows the tracking of a source on the celestial equator for about 1 hour. Located in the centre of France, it can reach declinations as low as  $-39^\circ$ . It has an effective collecting area of roughly 7000 m<sup>2</sup> (equivalent to a 94-m diameter parabolic dish). Due to the elongated geometry of the mirrors, at 21-cm wavelength it has a half-power beam width of  $3'.6$  E-W  $\times$   $22'$  N-S for declinations below  $30^\circ$ ; at higher declinations the N-S HPBW increases (see plot in Matthews, van Driel & Monnier-Ragaigne 2000). Typical system temperatures were  $\sim 40$  K for our project. For a technical description of the Nançay decimetric radio telescope and the general methods for data handling and reduction see, e.g., Theureau et al. (1998) and references therein.

Observations at Nançay of 25 sample galaxies were made in the periods March to August 1999 and January to June 2001 using a total of about 110 hours of telescope time. We obtained our observations in total power (position-switching) mode using consecutive pairs of two-minute on- and two-minute off-source integrations. Off-source integrations were taken at approximately  $20'$  E of the target position. The autocorrelator was divided into two pairs of cross-polarized receiver banks, each with 512 channels and a 6.4 MHz bandpass. This yielded a channel spacing of  $2.64 \text{ km s}^{-1}$ , for an effective velocity resolution of  $\sim 3.3 \text{ km s}^{-1}$  at 21-cm, which was smoothed to a channel separation of 7.91 and a velocity resolution of 9.50 km/s during the data reduction, in order to search

for faint features. The center frequencies of the two banks were tuned to the known redshifted H I frequency of the target.

### 3.3 Reductions

#### 3.3.1 DensePak Reductions

Spectra obtained from DensePak closely resembled WIYN HYDRA spectra (i.e., multi-fiber spectral data), thus basic spectral extraction, flattening, wavelength calibration and sky subtraction were done using the NOAO *IRAF* package *dohydra*. Prior to running *dohydra*, data were overscan and bias-corrected and trimmed using *IRAF ccdproc*. After bias subtraction, we used our own method for removing cosmic rays: Since two or more frames were taken at each position, we calculated pair-wise differences and statistical thresholds, pixel-by-pixel, of the expected variance due to read-noise and shot-noise. To cosmic-ray clean and combine the 2 or more exposures for each pointing, pixels which were more than 5 times the standard deviation greater than corresponding pixels on different frames, were flagged as cosmic rays and masked from the final, mean-combined, two-dimensional spectral image. Removing cosmic rays from the two-dimensional images is preferable to removing cosmic rays after spectral extraction (as is the procedure used by *dohydra*). The latter technique averages cosmic rays falling in pixels that are part of extracted apertures with good data from other pixels in that part of the aperture. This (1) corrupts data which would otherwise be useful; and (2) reduces the difference between cosmic rays and spectra. After cosmic-ray cleaning, *dohydra* was used to extract 90 individual spectra. These one dimensional spectra were

field flattened with dome flats and wavelength calibrated using ThAr emission spectra. Finally, the four sky spectra were averaged and the mean sky spectrum was subtracted from all other spectra.

The quality of data from DensePak varied across the slit formed by the 90 fibers. In particular, comparisons of dome flat fluxes showed the first eight fibers in the top of the slit had less than half the flux of most fibers. After field flattening, this low throughput was translated into greater values for the continuum noise in these fibers. We believe this poor performance may be due to the fact that (1) fibers 1-8 underwent the tightest bend near the slit end of DensePak of all the fibers;<sup>2</sup> and (2) fibers 1-8 were at the top end of the DensePak slit. If the slit is not centered within the baffles at the spectrograph entrance, these fibers could suffer from further vignetting. (3) Alternatively, these fibers may be otherwise over-stressed, e.g. because these fibers are on an outer face of the array (see Bershady *et al.* 2001).

Once spectra were processed with IRAF *dohydra*, we identified extracted H $\alpha$  emission-line characteristics. We used a line-fitting algorithm which yielded accurate measures of emission-line velocity centroids. Beauvais & Bothun (1999) compared different model line profiles and found the best fits to a variety of different simulated line profiles were obtained with Vogt profiles (a combination of Gaussian and Lorentzian profiles). Another method for measuring line centroids avoided using models altogether, instead measuring intensity-weighted centroids (Courteau 1997). Both these studies, however, note that Gaussian fits yielded comparable results for signal to noises greater

---

<sup>2</sup>Bershady *et al.* (2001) present evidence that this tight bend radius increases the focal ratio degradation of fibers for a similar integral field unit, SparsePak, thereby leading to greater losses in the spectrograph

than 20. Since our typical  $H\alpha$  lines had high signal to noise ratios and we were primarily interested in creating velocity fields using line centroids, we fit the  $H\alpha$  emission-lines with single Gaussians. Most emission-lines in our data were symmetric and were well-fit by a single Gaussian. Some  $H\alpha$  profiles sampled by fibers within a fiber radius of the galaxy center were skewed or even bimodal as would be expected when the fiber diameter is larger than the local dynamical scale. Since the fraction of such lines was small, we flagged these lines during visual inspection after running our automated line fitting algorithm and did not include them in the data fit by our velocity field models.

Our algorithm measured Gaussian fluxes, widths, centers and centroid errors for any number of emission-lines at any given wavelength, as follows: Because the signal to noise ratio of each channel in the spectra is important for accurate profile fitting, our algorithm first established measurement errors for each channel. We defined a window of  $\sim 200\text{\AA}$  ( $\sim 1000$  pixels) including the  $H\alpha$  emission-line, usually using  $6600\text{\AA} < \lambda < 6800\text{\AA}$ . In this window, we calculated an iterative clipped mean and standard deviation. We used a very tight clipping criterion: All channels with counts greater than the standard deviation were rejected, repeating until the number of channels did not decrease further. This procedure removed almost all effects of emission-lines, imperfectly subtracted sky lines, and residual cosmic rays from the continuum mean and standard deviation. We normalized the standard deviation of the iteratively clipped data by the standard deviation of a Gaussian distribution which also had been truncated at  $1\sigma$ . With the continuum standard deviation,  $\sigma_{\text{cont.}}$ , established, we assumed remaining errors on channel counts were based on Poisson counting errors. Therefore the final

error,  $\sigma_i$ , on each channel  $i$  was calculated as follows:

$$\sigma_i = \{\sigma_{\text{cont.}}^2 + (\text{Counts}_i - \text{Counts}_{\text{cont.}})\}^{1/2} \quad (3.1)$$

where all counts were calculated in  $e^-/\text{pixel}$ ,  $\text{Counts}_i$  was the counts for channel  $i$ , and  $\text{Counts}_{\text{cont.}}$  was the iterative mean calculated in the  $200\text{\AA}$  window.

Once electron counts and standard deviations had been calculated for every channel, we used the Marquardt–Levinson algorithm to fit a Gaussian to lines roughly centered in selected regions. Once the amplitude, center ( $\lambda_C$ ) and width ( $\sigma_G$ ) of the Gaussian were determined from the fit, we calculated the area beneath the curve, yielding the flux ( $f_G$ ).

In order to estimate the error on the Gaussian centroid, we performed a Monte Carlo simulation of Gaussian emission-lines using different signal to noise ratios and widths. A fit to the results of the Monte Carlo was used to calculate the centroid error ( $\Delta\lambda_C$ ) for the observed data:

$$\Delta\lambda_C = 9.208(\sigma_G + 0.26)\sigma_{\text{cont.}}/f_G. \quad (3.2)$$

For typical  $\text{H}\alpha$  emission-lines in our survey this yielded an error of  $0.04\text{ \AA}$  ( $\sim 2\text{ km/s}$ ) on the central velocity of the Gaussian.

We found that features which had Gaussian fits that did not reach the signal to noise threshold  $\zeta \equiv f_G/\sigma_{\text{cont.}}/(2\sigma_G)^{1/2} > 5$  were also not identified as emission-lines by visual inspection. We also required the width of the line must be equal to or greater than the resolution element. On visual inspection, we discarded lines that were skewed

or required multiple Gaussian profiles and lines that met the signal to noise and width requirements but none-the-less did not look plausible. Figure 3.2 shows a sample of the output with Gaussian fits chosen for their range of properties: an example of sky continuum, a line which did not meet the signal to noise threshold, a weak line which did have sufficient signal to noise, typical, strong and skewed lines.

Table 3.2 contains an example of DensePak  $H\alpha$  line-fits which we present. This table contains DensePak line-fits for the first pointing of PGC 14564. Offsets listed in the table refer to offsets West and North of the kinematic center (as determined by model fitting described in §3.4.3).



Table 3.2. Gaussian fits to H $\alpha$  emission-line profiles from for the first pointing of PGC 14564

Fiber	West	North	$\lambda_C$	$\Delta\lambda_C$	$f_G$	$\sigma_G$	Counts <sub>cont.</sub>	$\sigma_{\text{cont.}}$
Number	arcsec	arcsec	Å	Å	$e^{-1}/\text{hr}$	Å	$e^{-1}/\text{hr/res.}$	
1	-21.4	-23.5					1775.	58.
2	-17.2	-23.5					257.	14.
3	-13.1	-23.5					159.	10.
4	-8.9	-23.5	6637.69	0.04	860.1	0.37	92.	7.
5	-4.8	-23.5	6637.67	0.03	1218.2	0.46	101.	7.
6	-0.6	-23.5	6637.72	0.02	1905.9	0.49	106.	7.
7	3.5	-23.5	6637.75	0.04	1191.3	0.49	91.	6.
8	34.8	47.5					12.	4.
9	-23.4	-19.9					65.	7.
10	-19.3	-19.9	6638.13	0.14	303.3	0.54	26.	5.
11	-15.2	-19.9	6638.07	0.12	392.5	0.59	38.	5.
12	-11.	-19.9	6637.60	0.05	608.3	0.47	34.	4.
13	-6.8	-19.9	6637.54	0.02	1371.3	0.47	53.	4.
14	-2.7	-19.9	6637.64	0.01	2593.4	0.52	69.	5.
15	1.4	-19.9	6637.73	0.02	2056.6	0.51	69.	5.
16	-21.4	-16.3					3.	4.
17	-17.2	-16.3	6638.25	0.11	372.9	0.62	30.	4.
18	-13.1	-16.3	6637.79	0.03	1094.4	0.47	57.	5.

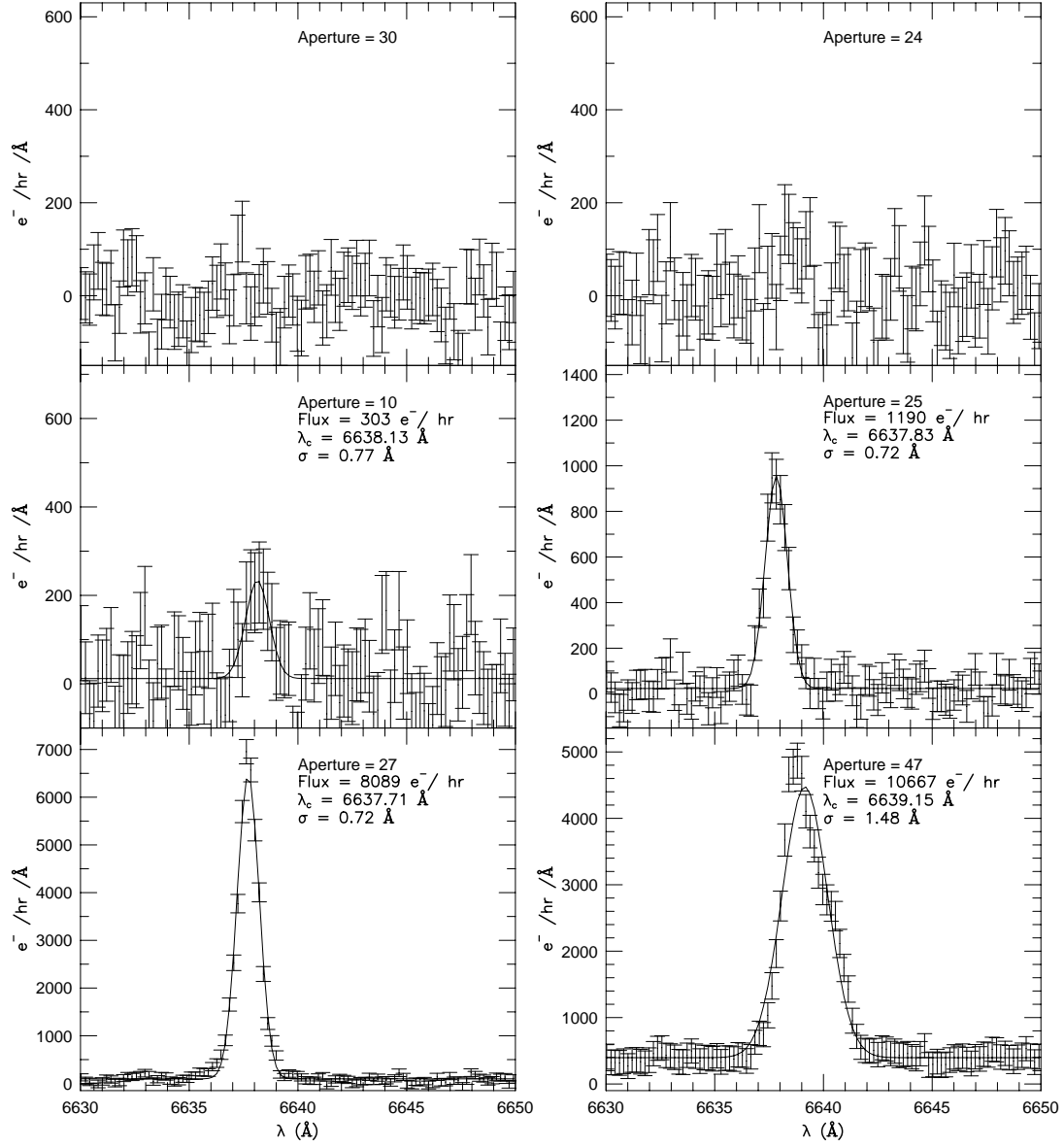


Fig. 3.2. H $\alpha$  emission-line profiles for 6 fibers selected from the first pointing of PGC 14564. Fiber 30 was a sky fiber and illustrates the typical background fluctuations. The solution for a Gaussian H $\alpha$  emission-line in Fiber 24 did not meet the signal to noise criterion:  $\zeta \equiv f_G/\sigma_{\text{cont.}}/(2\sigma_G)^{1/2} > 5$ .  $\zeta = 8$  for the emission-line in aperture 10. The H $\alpha$  emission-line for aperture 25 was typical for most observed galaxies. Aperture 27 showed very strong H $\alpha$  emission. The H $\alpha$  profile in aperture 47 was highly skewed, showing signs of bimodality.

Fiber	West	North	$\lambda_C$	$\Delta\lambda_C$	$f_G$	$\sigma_G$	Counts <sub>cont.</sub>	$\sigma_{\text{cont.}}$
Number	arcsec	arcsec	Å	Å	$e^{-1}/\text{hr}$	Å	$e^{-1}/\text{hr}/\text{res.}$	
19	-8.9	-16.3	6637.62	0.01	2639.5	0.48	100.	5.
20	-4.8	-16.3	6637.50	0.01	4008.3	0.52	116.	5.
21	-0.6	-16.3	6637.59	0.01	3304.5	0.55	117.	5.
22	3.5	-16.3	6637.83	0.02	1925.1	0.50	87.	4.
23	-23.4	-12.7					5.	4.
24	-19.3	-12.6					22.	4.
25	-15.2	-12.7	6637.83	0.02	1190.8	0.50	53.	4.
26	-11.	-12.7	6637.75	0.01	4844.4	0.50	119.	4.
27	-6.8	-12.7	6637.71	0.01	8089.8	0.50	200.	5.
28	-2.7	-12.7	6637.63	0.01	6047.5	0.52	211.	5.
29	1.4	-12.7	6637.85	0.01	4726.9	0.50	221.	6.
30	-57.2	42.5					-8.	3.
31	-21.4	-9.1					13.	4.
32	-17.2	-9.1	6638.54	0.06	446.5	0.48	43.	3.
33	-13.1	-9.1	6637.97	0.02	2031.2	0.58	98.	4.
34	-4.8	-9.1	6637.87	0.01	9078.2	0.51	343.	7.
35	-0.6	-9.1	6637.88	0.01	6439.9	0.52	373.	8.
36	3.5	-9.1	6638.20	0.01	6156.6	0.62	303.	6.
37	-19.3	-5.5	6638.84	0.03	629.3	0.37	20.	4.

Fiber	West	North	$\lambda_C$	$\Delta\lambda_C$	$f_G$	$\sigma_G$	Counts <sub>cont.</sub>	$\sigma_{\text{cont.}}$
Number	arcsec	arcsec	Å	Å	$e^{-1}/\text{hr}$	Å	$e^{-1}/\text{hr}/\text{res.}$	
38	-15.2	-5.5	6638.79	0.02	1796.0	0.50	83.	4.
39	-11.	-5.5	6638.46	0.01	4348.0	0.62	179.	4.
40	-6.8	-5.5	6638.22	0.01	8579.8	0.61	377.	7.
41	-2.7	-5.5	6638.20	0.01	8836.9	0.64	599.	10.
42	-21.4	-1.9	6638.88	0.08	307.78	0.41	2.	4.
43	-17.2	-1.9	6638.86	0.01	2053.5	0.45	52.	4.
44	-13.1	-1.9	6638.89	0.01	4208.0	0.53	127.	4.
45	-8.9	-1.9	6638.79	0.01	6668.8	0.68	272.	5.
46	-4.8	-1.9	6638.75	0.01	8813.1	0.77	640.	10.
47	-0.6	-1.9	6639.15	0.01	10667.	1.04	1093.	17.
48	3.5	-1.9	6639.51	0.01	9863.4	0.95	847.	13.
49	-23.4	1.7					-19.	3.
50	-19.3	1.7	6639.04	0.05	330.4	0.36	12.	3.
51	-15.2	1.7	6639.19	0.02	2564.6	0.63	70.	4.
52	-11.	1.7	6639.36	0.01	5410.9	0.76	176.	5.
53	-6.8	1.7	6639.78	0.01	8719.6	0.93	386.	7.
54	1.4	1.7	6640.28	0.02	8942.2	0.92	997.	15.
55	-21.4	5.3					-4.	4.
56	-17.2	5.3	6639.71	0.03	1117.0	0.59	34.	4.

Fiber	West	North	$\lambda_C$	$\Delta\lambda_C$	$f_G$	$\sigma_G$	Counts <sub>cont.</sub>	$\sigma_{\text{cont.}}$
Number	arcsec	arcsec	Å	Å	$e^{-1}/\text{hr}$	Å	$e^{-1}/\text{hr}/\text{res.}$	
57	-13.1	5.3	6639.93	0.01	6034.	0.61	107.	4.
58	-8.9	5.3	6640.26	0.01	9775.3	0.73	246.	6.
59	-4.8	5.3	6640.66	0.01	12156.	0.68	454.	8.
60	-0.6	5.3	6640.92	0.01	8534.5	0.67	572.	9.
61	3.5	5.3	6641.04	0.01	4080.1	0.58	445.	7.
62	-58.2	-48.4					6.	3.
63	-23.4	8.9					6.	4.
64	-19.3	8.9					12.	4.
65	-15.2	8.9	6640.03	0.01	3646.0	0.56	52.	4.
a6	-11.	8.9	6640.19	0.01	7131.5	0.60	147.	4.
67	-6.8	8.9	6640.76	0.01	10398.	0.69	250.	6.
68	-2.7	8.9	6641.15	0.01	10148.	0.63	393.	8.
69	1.4	8.9	6641.42	0.01	5291.6	0.55	372.	8.
70	-21.4	12.5					12.	5.
71	-17.2	12.5					15.	4.
72	-13.1	12.5	6640.41	0.02	1763.7	0.59	59.	4.
73	-8.9	12.5	6640.74	0.02	3932.2	0.61	128.	5.
74	-4.8	12.5	6641.17	0.01	5587.5	0.61	183.	5.
75	-0.63	12.5	6641.55	0.01	4297.8	0.55	235.	7.

Fiber	West	North	$\lambda_C$	$\Delta\lambda_C$	$f_G$	$\sigma_G$	Counts <sub>cont.</sub>	$\sigma_{\text{cont.}}$
Number	arcsec	arcsec	Å	Å	$e^{-1}/\text{hr}$	Å	$e^{-1}/\text{hr/res.}$	
76	3.5	12.5	6641.65	0.01	4702.6	0.53	218.	6.
77	-23.4	16.1					7.	4.
78	-19.3	16.1					13.	5.
79	-15.2	16.1					30.	5.
80	-11.	16.1	6640.89	0.03	1028.6	0.48	59.	4.
81	-6.8	16.1	6641.09	0.01	2689.3	0.53	105.	5.
82	-2.7	16.1	6641.40	0.02	2602.5	0.55	146.	7.
83	1.4	16.1	6641.68	0.01	3912.5	0.54	133.	5.
84	32.8	-54.5					19.	4.
85	-21.4	19.7					77.	6.
86	-17.2	19.7					43.	5.
87	-8.9	19.7	6641.18	0.02	1243.1	0.48	74.	5.
88	-4.8	19.7	6641.26	0.02	2599.9	0.49	105.	6.
89	-0.6	19.7	6641.39	0.02	1727.4	0.48	102.	5.
90	3.5	19.7	6641.64	0.03	1321.0	0.51	89.	5.

### 3.3.2 21cm HI line profile reductions

We reduced our HI spectra using the standard Nançay spectral line reduction packages available at the Nançay site. With this software we subtracted baselines (generally third order polynomials), averaged the two receiver polarizations, and applied a declination-dependent conversion factor to convert from units of  $T_{sys}$  to flux density in mJy. The  $T_{sys}$ -to-mJy conversion factor is determined via a standard calibration relation established by the Nançay staff through regular monitoring of strong continuum sources. This procedure yields a calibration accuracy of  $\sim 15\%$ . In addition, we applied a flux scaling factor of 1.26 to our spectra based on statistical comparisons (see Matthews et al. 1998, Matthews *et al.* 2000) of Nançay survey data of samples of late-type spirals with past observations of these galaxies made at Nançay and elsewhere.

From the 25 galaxies observed with Nançay from the two campaigns (March–August, 1999 and January–June 2001), 18 had sufficient signal to measure line widths and integrated HI flux (Figures 3.3 and 3.4; Table 3.3). Several of the 21-cm observations had poor base-lines. These included: PGC 3512, PGC 16274, PGC 26140, PGC 32091, PGC 32638, PGC 33465, PGC 36925, PGC 57931. Hopefully, base-line determinations can be improved. PGC 23913 exhibited an unresolved HI profile, and three galaxies displayed significantly lopsided profiles: PGC 14564, PGC 23598, and PGC 72453.

Table 3.3. Nançay Observations

PGC	rms	S/N	$I_{HI}$	$W_{50}$	$W_{20}$	$V_{HI}$	$\sigma_{V_{HI}}$	$\log M_{HI}$
	mJy		Jy km/s	km/s	km/s	km/s	km/s	$\log M_{\odot}$
03512	5.82					5436		
08941	5.31	6.69	4.72	152		9447	5.3	10.16
14564	2.96	26.33	10.06	172	197	3483	2.1	9.71
15531	5.60	5.63	4.23	151	190	5552	12.4	9.74
16274	3.74					8883		
19767	4.21	10.34	5.35	136	159	5136	5.2	9.77
23598	2.80	10.41	2.57	113	132	7478	4.7	9.78
23913	3.52	34.82	4.39	32	55	6330	1.5	9.87
24788	2.86	11.56	4.63	153	185	7545	5.5	10.04
26140	1.79					8760		
28310	2.7	7.55	2.65	136	147	5905	4.9	9.59
31159	4.9	3.26	2.32	183	192	5781	10.3	9.51
32091	3.03					2511		
32638	2.80	5.45	1.83	165	219	6527	15.1	9.51
33465	4.41					5935		
36925	7.67					6826		
38908	3.87	13.84	7.61	186	211	7084	4.0	10.20
39728	1.97	8.81	2.08	143	193	2316	9.0	8.67
46767	2.89	8.47	4.06	262	318	8065	9.9	10.07



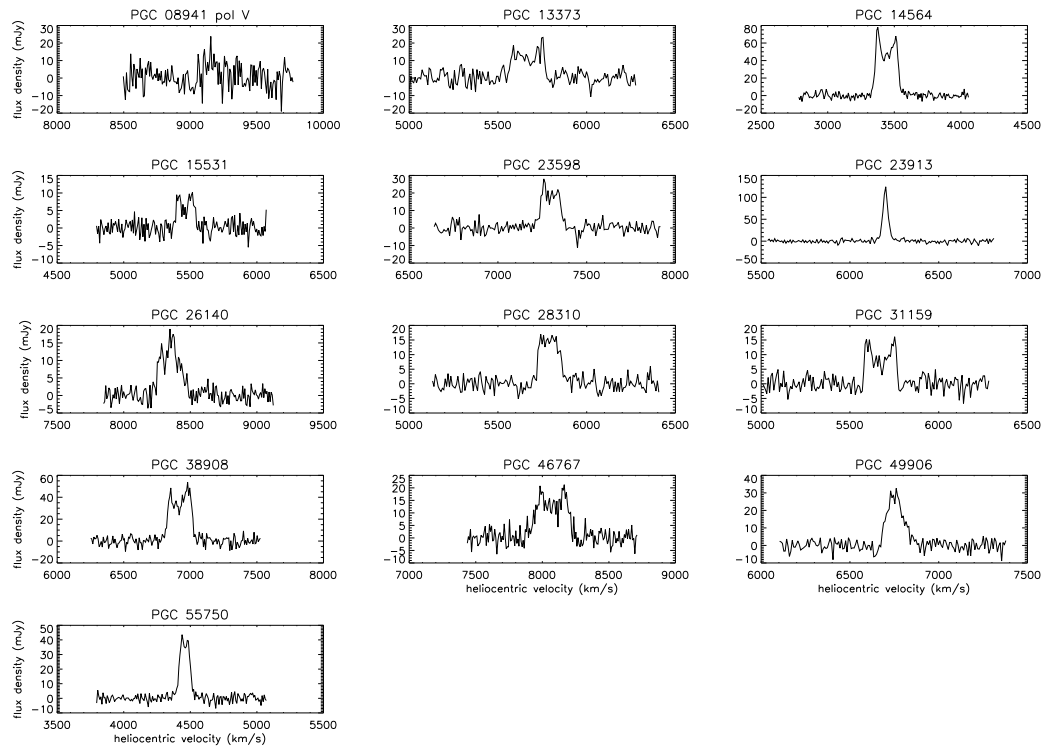


Fig. 3.3. Nançay HI profiles observed between March and August 1999.

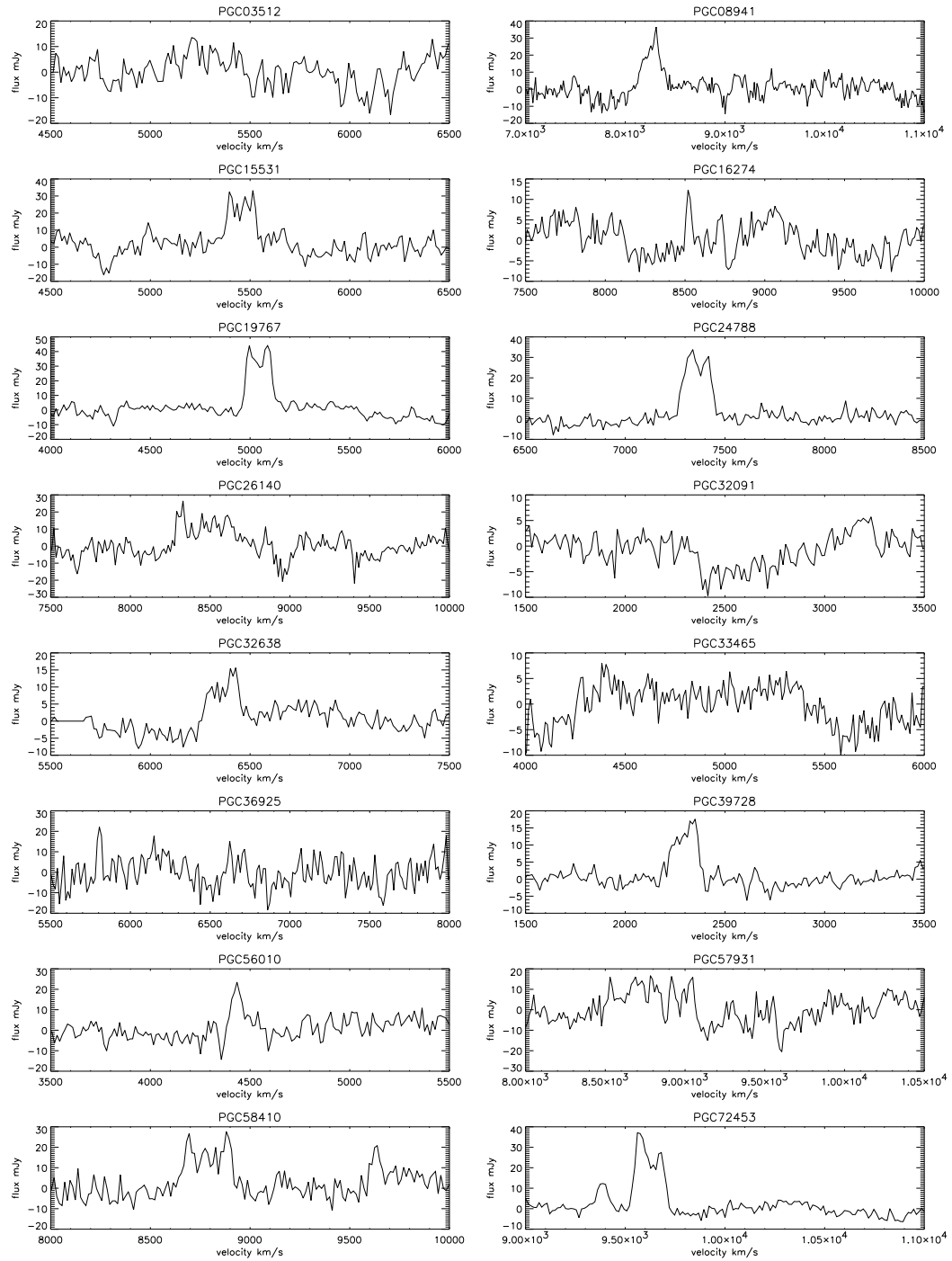


Fig. 3.4. Nançay HI profiles observed between January and June 2001.

PGC	rms	S/N	$I_{HI}$	$W_{50}$	$W_{20}$	$V_{HI}$	$\sigma_{V_{HI}}$	$\log M_{HI}$
	mJy		Jy km/s	km/s	km/s	km/s	km/s	$\log M_{\odot}$
49906	2.89	11.07	3.12	100	154	6751	7.4	9.79
55750	2.35	19.57	3.58	87	109	4458	2.7	9.48
56010	4.80	4.78	4.80	61	155	4469	22.6	9.60
57931	6.09					9280		
58410	5.21	5.09	4.44	241	307	9055	17.8	10.18
72453	3.24	11.26	4.38	150	182	9932	5.6	10.26

Table Notes:

Column 2: rms is the root mean squared noise level of the spectrum

Column 3: S/N is the ratio of peak line flux to the rms noise level

Column 4:  $I_{HI}$  is the integrate line flux

Column 5:  $W_{50}$  velocity width at 50% the peak line flux. According to Fouqu  et al. (1990), the uncertainty in  $W_{50}$  is  $2\sigma_{V_{HI}}$ .

Column 6:  $W_{20}$  velocity width at 20% the peak line flux. According to Fouqu  et al. (1990), the uncertainty in  $W_{20}$  is  $3\sigma_{V_{HI}}$ .

Column 7:  $V_{HI}$  is the heliocentric central radial velocity of a line profile in the optical convention

Column 8:  $\sigma_{V_{HI}}$ , the uncertainty in  $V_{HI}$ , is  $\sigma_{V_{HI}} = 4R^{1/2}P_W^{1/2}(S/N)^{-1}$  where  $R$  is the instrumental resolution (15.6 km/s),  $P_W = (W_{20} - W_{50})/2$  (Fouqu  et al. 1990).

Column 9:  $\log M_{HI}$  is the total HI mass,  $M_{HI} = 2.356 \times 10^4 D^2 I_{HI}$  where  $D$  is the distance calculated assuming  $H_0 = 75$  km/s/Mpc.

### 3.3.2.1 HI line profiles from literature

A search of the literature revealed more HI line width measurements from a variety of sources (Table 3.4). When HI line profiles existed from multiple sources, we adopted the measurement with the highest accuracy. Together with the Nançay observations, HI line widths were measured for 30 of our 39 sample galaxies.

The HI line widths from Nançay were consistent with measurements gathered from the literature. For the 11 galaxies with both Nançay and literature measurements of  $W_{50}$ , the standard deviation of the difference is 8.5 km/s, significantly less than the mean propagated error on the difference, 17.6 km/s. Therefore, we draw no distinction between data from the literature and Nançay observations in further analysis.

Table 3.4. HI Line Widths from Literature

PGC	$W_{20}$	$\sigma_{W_{20}}$	$W_{50}$	$\sigma_{W_{50}}$	Sources
	km/s	km/s	km/s	km/s	
05345	52.485	13.317	27.05	9.7	1,2
05673	147.75	12.85	134.05	9.7	2
06855	136.5	10.7	115.7	8.1	3
07826	96.078	8.325	87.4	11.3	4,5
08941	157.22	12.85	147.315	6.864	1,6
14564	198.929	7.385	179.638	4.617	7,8
19767	147.9	15.86	137.14	11.94	9
20938			169.608	8.496	10
23333	139.12	13.28	134.42	7.103	11,12
23598			121.366	10.49	13
23913			47.366	12.506	13
24788			147.764	17.613	10
26517	126.5	10.7	125.7	8.1	14
27792			129.866	8.474	13
28401	59.5	10.7	37.7	8.1	3
33465	285.9	15.86	239.14	11.94	15
36925	149.9	15.86	138.14	11.94	15
38268	189.992	9.84			16
39728	163.28	7.082	148.96	7.46	17

PGC	$W_{20}$	$\sigma_{W_{20}}$	$W_{50}$	$\sigma_{W_{50}}$	Sources
	km/s	km/s	km/s	km/s	
46767	292.9	15.86	253.14	11.94	15
55750	108.046	6.413	92.606	16.261	18,19,20
57931	176.411	12.543	170.187	11.784	12,15,19
58410	248.9	15.86	231.317	8.677	12,15
70962	242.348	6.029	209.086	9.729	19,21,22
71106	266.78	8.465	236.862	7.34	6,17
72144			125.315	6.975	6
72453	179.2	13.28	157.296	10.02	4

## Table References:

- 1: Haynes & Giovanelli 1984, AJ, 89, 758
- 2: Lu *et al.* 1993, ApJS, 88, 383
- 3: Theureau *et al.* 1998, A&AS, 130, 333
- 4: Rubin *et al.* 1976, AJ, 81, 687
- 5: Giovanelli & Haynes 1993, AJ, 105, 1271
- 6: Giovanelli *et al.* 1986, AJ, 92, 250
- 7: Garwood *et al.* 1987, AJ, 322, 88
- 8: van Driel *et al.* 1995, ApJ, 444, 80
- 9: Schneider *et al.* 1992, ApJS, 81, 5
- 10: Bicay & Giovanelli 1986, AJ, 91, 705
- 11: Bothun *et al.* 1985, ApJS, 57, 423
- 12: Haynes *et al.* 1997, AJ, 113, 1197
- 13: Haynes *et al.* 1988, AJ, 95, 607
- 14: Theureau *et al.* 1998, A&AS, 125, 409
- 16: Haynes & Giovanelli 1991, ApJS, 77, 331
- 17: Gavazzi 1987, AJ, 320, 96
- 18: Lewis 1987, ApJS, 63, 515
- 19: Lewis *et al.* 1985 ApJS, 59, 161
- 20: Richter & Huchtmeier 1991, A&AS, 87, 425
- 21: Freudling, Haynes, Giovanelli 1992, ApJS, 79, 157
- 22: Bieging & Biermann, 1983, AJ, 88, 161
- 23: Biermann *et al.* 1979, A&A, 75, 19

### 3.4 H $\alpha$ Velocity Fields

#### 3.4.1 Creating Velocity-Field Maps

Since the geometry of the DensePak array was regular (with the exception of five broken fibers), producing rudimentary velocity fields using the Gaussian centroids was straightforward. To produce a smooth velocity field, however, required the use of either two-dimensional polynomial fits or interpolation schemes. In Andersen *et al.* (2001), we used high (5–7) order polynomials to fit the velocity fields. A feature of polynomial fits was that they often diverged sharply outside the range of data so careful masking was required.

Interpolation is a more recent technique we have used for producing smooth velocity field maps. The *patch* routine within the GIPSY analysis package (van der Hulst *et al.* 1992; Vogelaar & Terlouw 2001) was used to produce these interpolated velocity fields maps as follows: A second-order two-dimensional spline was fit over a box extending  $13'' \times 13''$  in area which contained at least four fiber centers. The value of the polynomial at the center of the box defined the coordinate's velocity. The process was repeated as the box was moved over a grid with a scale of 4 pixels/arcsec.

We tested the above methods by sampling the smoothed velocity fields with the DensePak footprints at observed positions. By comparing each DensePak fiber's observed velocity centroid and the mean velocities calculated from the smoothed velocity-field maps, we ascertained that the smoothed velocity-field maps created via the GIPSY interpolation yielded better representations of the velocity fields compared to the single high order polynomial fit to the entire velocity field. Figure 3.5 offers a comparison



of the two techniques for PGC 23598. We performed this test on five galaxies which were part of our pilot study: PGC 23598, PGC 28310, PGC 36925, PGC 46767 and PGC 58410. In each case, the standard deviation on the difference between smoothed and observed velocities was smaller for the interpolated velocity field by a factor of 1.6. Therefore, interpolated velocity field were a superior representation of the data and we use this method to represent velocity fields throughout the rest of this work. Examples of velocity fields are presented in Figure 3.6. The atlas contains velocity fields for all 39 sample galaxies.

### 3.4.2 Velocity–Field Structure

HI observations of spiral galaxy velocity fields reveal a large variety of non-circular motions. These include large scale asymmetries, motions associated with individual spiral arms, solid body rotation, and kinematic warping (Bosma 1981b). After examining our sample of velocity fields for the kinematic signatures of these non-circular motions, we found evidence for kinematic asymmetry and streaming motions associated with spiral arms. However, we do not find evidence for solid body rotation or kinematic warping in our sample. Solid body rotation is a signature of barred galaxies, so our selection of unbarred galaxies mitigates the impact this effect had on our velocity fields. Kinematic warping, manifested by a twisting of the kinematic position angle with radius, is exhibited in a large fraction of disks at large radii. Few galaxies in other surveys show signs of warping within three scale-lengths (Briggs 1990), which is where we measure H $\alpha$  emission for our sample.

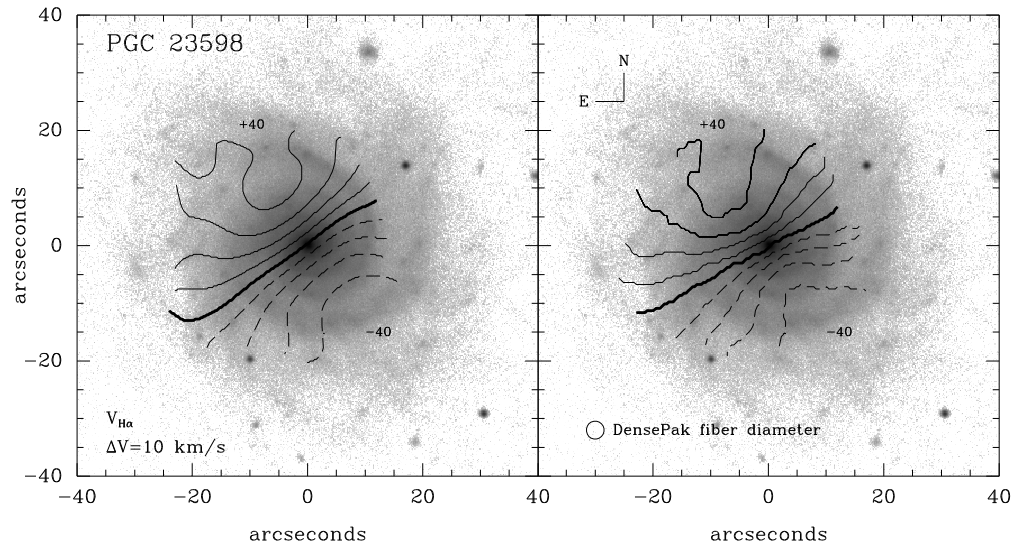


Fig. 3.5. Two representations for the H $\alpha$  velocity field of PGC 23598. The left panel contains the result of a 7<sup>th</sup> order polynomial fit with cross terms to the observed velocities and the right panel displays an interpolated surface generated using the GIPSY *patch* routine.

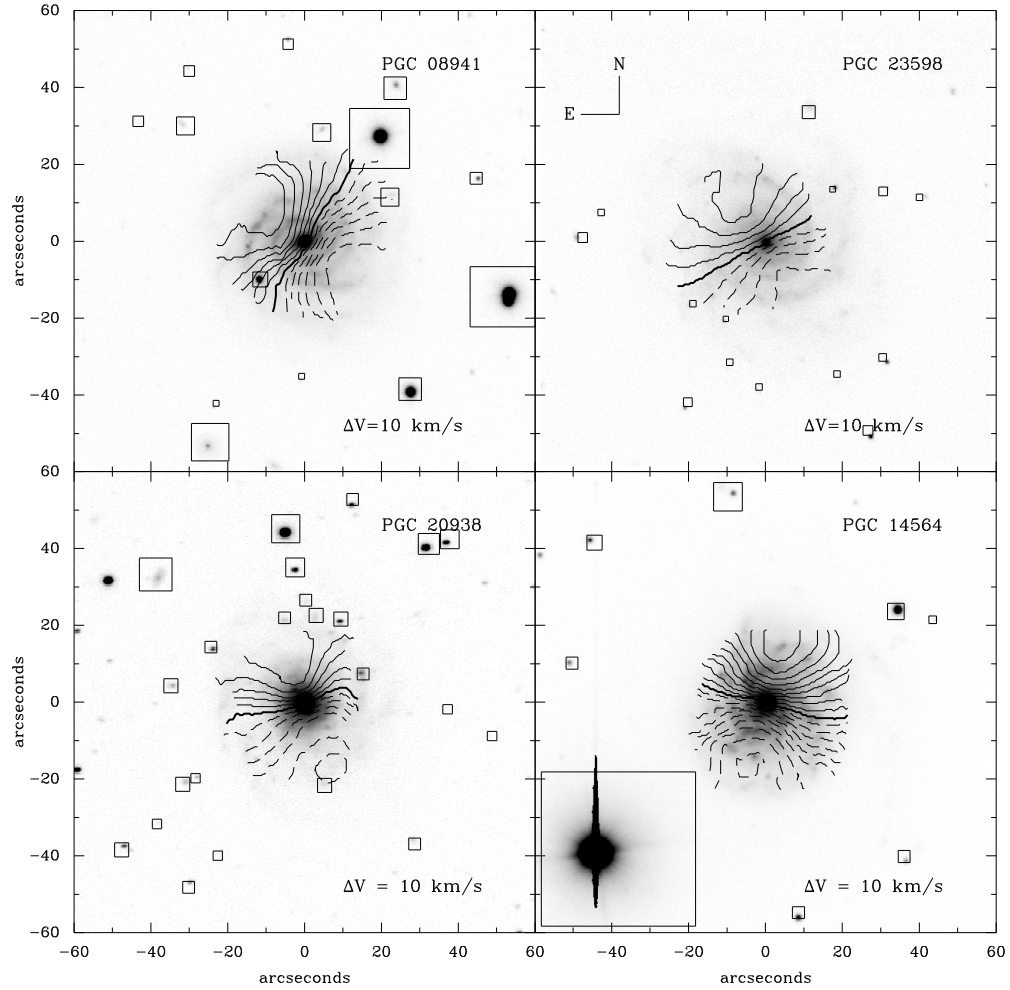


Fig. 3.6. Velocity fields for four representative galaxies from our survey. Solid lines are iso-velocity contours which are receding with respect to the systematic velocity, marked with a thick solid line. Dashed lines mark approaching iso-velocity contours. Even galaxies such as PGC 23598 with observed rotation velocities less than 50 km/s have well-defined major and minor axes. Both PGC 14564 and PGC 20938 have twisting iso-velocity contours which could indicate bulk flows along spiral arms.

### 3.4.2.1 Projected Rotation Curves

As a complement to the full velocity field, we also produced H $\alpha$  position-velocity diagrams for our sample to better study characteristics of disk structure. To correct velocities off the major axis, we needed to employ the results of our velocity-field fits described in §3.4.3. Using the kinematic inclinations, DensePak fiber data taken from positions specified by  $R$  and  $\theta$  in the galaxy plane can be inclination corrected to yield rotation curves with small residuals from a rotation curve such as the one described by Equation 3.7. The rotation curves illustrated in Figure 3.7 can be further corrected to deprojected, physical units so samples of rotation curves can be directly compared. The observed rotation velocity can be deprojected by dividing by  $\sin i$ , and we converted arcseconds to kpc for the examples in Figure 3.8. In the future, we could use these rotation curves to model disk and halo masses in the inner regions of disks.

### 3.4.2.2 Rotation Curve Asymmetry

Kinematic asymmetry has been studied using both HI velocity fields and line profiles indicating that  $\sim 50\%$  of galaxies have  $m = 1$  mode asymmetries (lopsidedness) in either their neutral gas distribution or their velocity fields (Baldwin, *et al.* 1980; Haynes, *et al.* 1998; Kornreich *et al.* 2000). These results imply asymmetries are maintained for several rotation time scales or that galaxy harassment is very common in the field (Richter & Sancisi 1994; Jog 1999). Most kinematic asymmetry studies have been done at  $i > 45^\circ$  where projected rotation velocities are large. It is important to study kinematic asymmetries at lower inclinations because (1) the link between kinematic and photometric asymmetries can be explored (most photometric studies of disk asymmetry

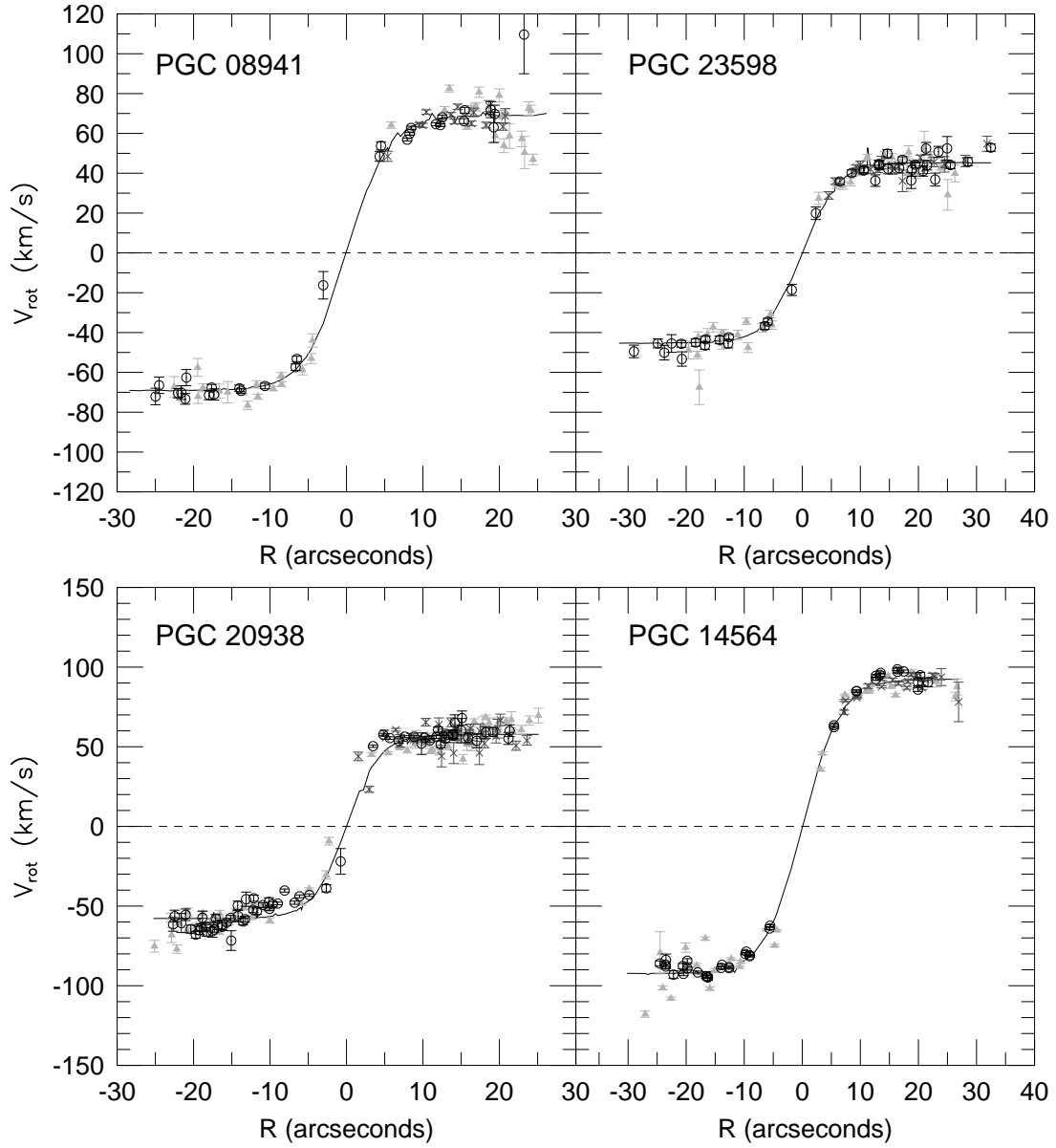


Fig. 3.7. Rotation curves for four representative galaxies. After fitting velocity-field models to the data, as described in §3.4.3, each DensePak velocity centroid can be projected to the major axis radius,  $R$ , where  $R$  is measured in the galaxy plane. Positions  $|\theta| < 20^\circ$ , where  $\theta$  is the angle from the major axis in the galaxy plane, are marked with dark, open circles. Slightly lighter x's mark data  $20^\circ < |\theta| < 40^\circ$ . Finally, light filled triangles mark data  $40^\circ < |\theta| < 60^\circ$ . It is difficult to distinguish between data from different regimes in  $\theta$ , an indication of a good velocity-field fit. The solid lines mark the model hyperbolic tangent rotation curve (Equation 3.7). The rotation curve of PGC 20938 is asymmetric, in contrast to the others.

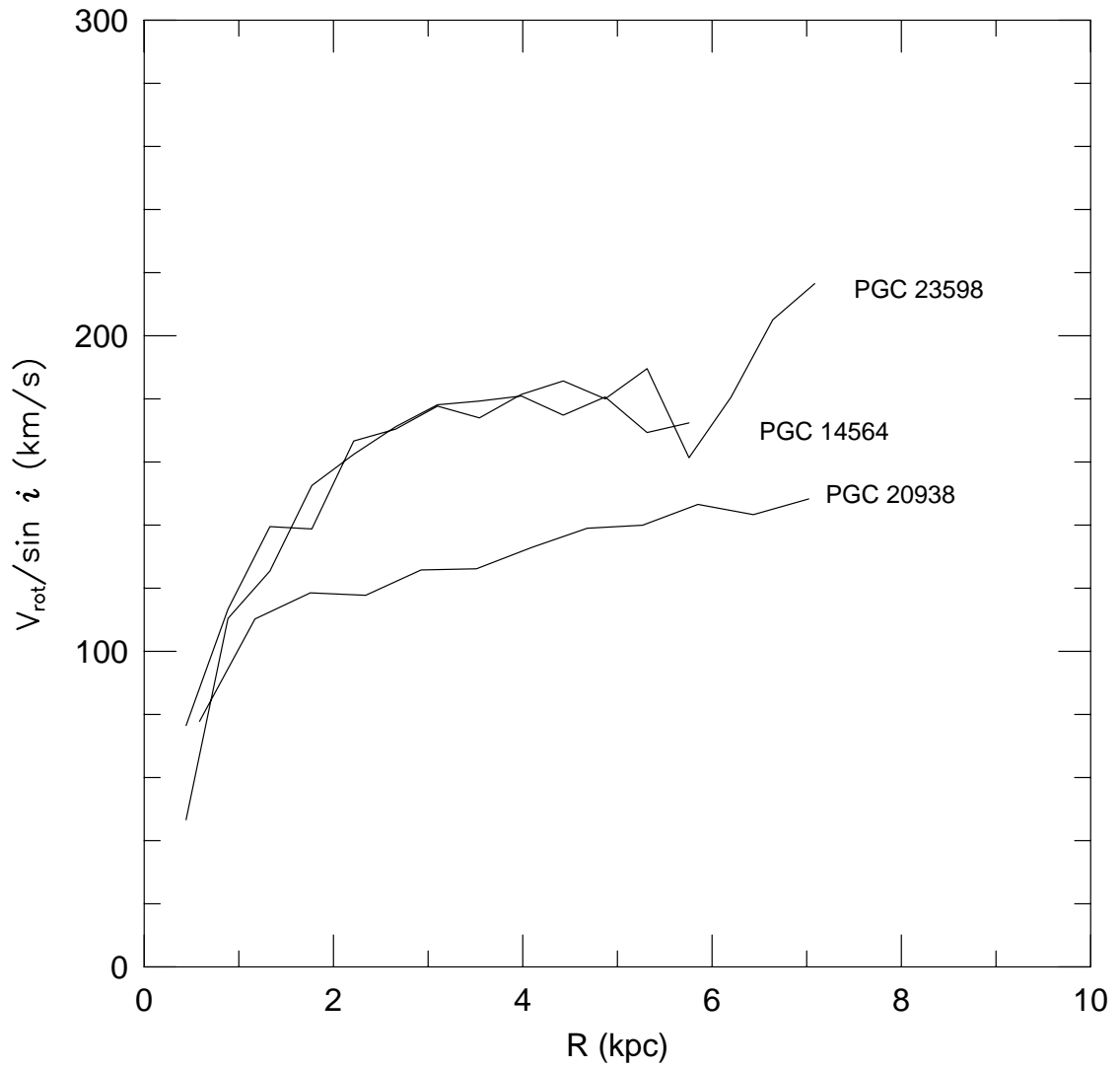


Fig. 3.8. Examples of deprojected galaxy rotation speed versus radius for three representative galaxies. Data from Figure 3.7 was reflected around  $R = 0$  and averaged in one arcsecond radial bins. These mean rotation speeds were then deprojected using the kinematic inclination angle,  $i$ , and the coordinates for the radius were transformed from arcseconds to kiloparsecs assuming  $H_0 = 75 \text{ km/s/Mpc}$ .

are performed on nearly face-on galaxies); (2) projection effects and extinction are minimized in face-on disks; and (3) kinematic asymmetry studies at low inclinations probe non-planar asymmetries as opposed to non-circular asymmetries that can be studied for more inclined spiral galaxies (Kornreich *et al.* 2000).

For our sample, we explore general kinematic asymmetries in the specific context of the projected rotation curves. We examined the rotation curves extracted from within twenty degrees of the major axis and discovered that 7 or 35 galaxies in our sample exhibited significant asymmetries. Galaxies with asymmetric rotation curves included PGC 5673, PGC 6855, PGC 20938, PGC 24788, PGC 27792, PGC 46767 and PGC 71106 (e.g., Figure 3.9). To measure rotation curve asymmetries, we adopted the formulation of Dale *et al.* (2001):

$$A_{kin} = \sum \frac{||V(R)| - |V(-R)||}{[\sigma^2(R) + \sigma^2(-R)]^{1/2}} / \frac{1}{2} \sum \frac{|V(R)| + |V(-R)|}{[\sigma^2(R) + \sigma^2(-R)]^{1/2}} \quad (3.3)$$

where  $V(R)$  was the velocity at each point in the rotation curve and  $\sigma(R)$  was the error on that velocity.  $A_{kin}$  is summed over all radii,  $R$ , for which data exists on both sides. For PGC 71106, we found  $A_{kin} = 0.20$  for  $R < 20''$ , a value significantly above the mean  $A_{kin} = 0.14$  associated with the sample of cluster spiral galaxies studied by Dale *et al.* (2001). A comparison of the distribution of kinematic and photometric asymmetries of galaxies in our sample showed that there was not a strong correlation between kinematically and photometrically asymmetric galaxies (Figure 3.10). In general, it does not appear that photometric and kinematic asymmetries are highly correlated; only 18 galaxies have published measures of kinematic and photometric asymmetries, but there

is no indication that photometric and kinematic asymmetries are related (Kornreich *et al.* 2000; Kornreich *et al.* 2001). This result implies different mechanisms trigger the different asymmetry modes.

### 3.4.2.3 Spiral Structure

Analytic calculations of gas shocks in spiral arms suggest that a perturbation in the velocity field on the order of 10 to 30 km/s should be associated with massive spiral arms (Roberts 1969). This kinematic signature of spiral arms can be obfuscated by 10 to 15 km/s velocity fluctuations in the gas caused by turbulence and expanding supernovae shells (Beauvais & Bothun 1999). Only a few unbarred galaxies show a strong kinematic signature associated with spiral arms (Visser 1980; Adler & Westpfahl 1996; Aalto *et al.* 1999; Alfaro *et al.* 2000; Kranz & Rix 2001). Indeed, our pilot study of 7 galaxies showed little evidence for radial or azimuthal variations in the residuals of the velocity field model. There was evidence that PGC 46767 showed a small sinusoidal variation in the fit residuals, but the phase of the sinusoid was unmatched to the spiral arms. This non-detection of spiral arms was unsurprising; we chose galaxies with very weak spiral arms for the pilot study in order to facilitate measurements of photometric axis ratios and position angles. For the selection of galaxies in our larger sample, we relaxed the requirement on spiral arm strength, which was qualitative anyway. As a result, we found six galaxies showed sinusoidal variations in azimuthal residuals from velocity-field models (see §3.4.3 below). These variations are likely evidence for streaming motions along their spiral arms. Galaxies which exhibited this signature were: PGC 14564, PGC 20938, PGC 24788, PGC 46767, PGC 71106 and PGC 72453. PGC 24788 best



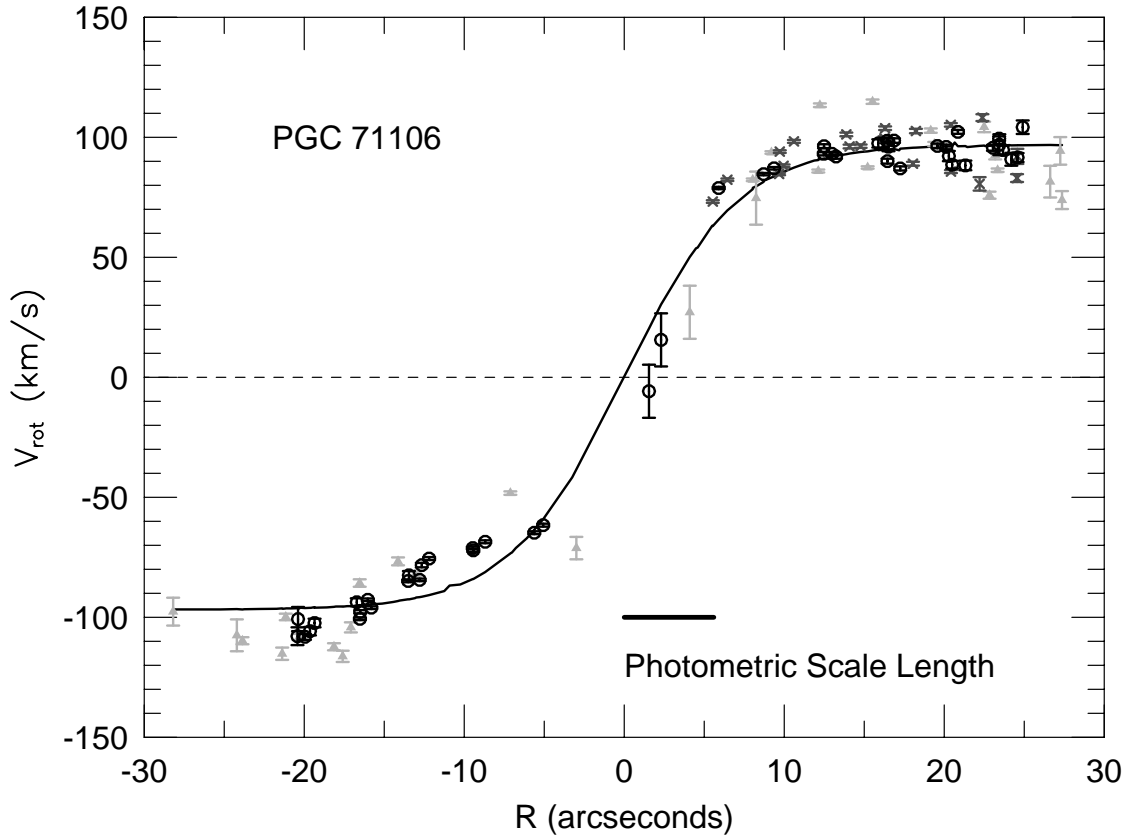


Fig. 3.9. The observed rotation curve of PGC 71106 showed a strong asymmetry 10 arcseconds from the center of the approaching side. Velocity centroids from DensePak fibers which had  $|\theta| < 20^\circ$  ( $\theta$  is the angle from the major axis in the galaxy plane) are open circles. Data with  $20^\circ < |\theta| < 40^\circ$  are marked with an “x” and data with  $40^\circ < |\theta| < 60^\circ$  are marked with filled triangles. The line represents the best fit hyperbolic tangent fit to the velocity field (Equation 3.7). The kinematic asymmetry measured from the rotation curve was 0.20 (Equation 3.3; Dale *et al.* 2001), which is significant.

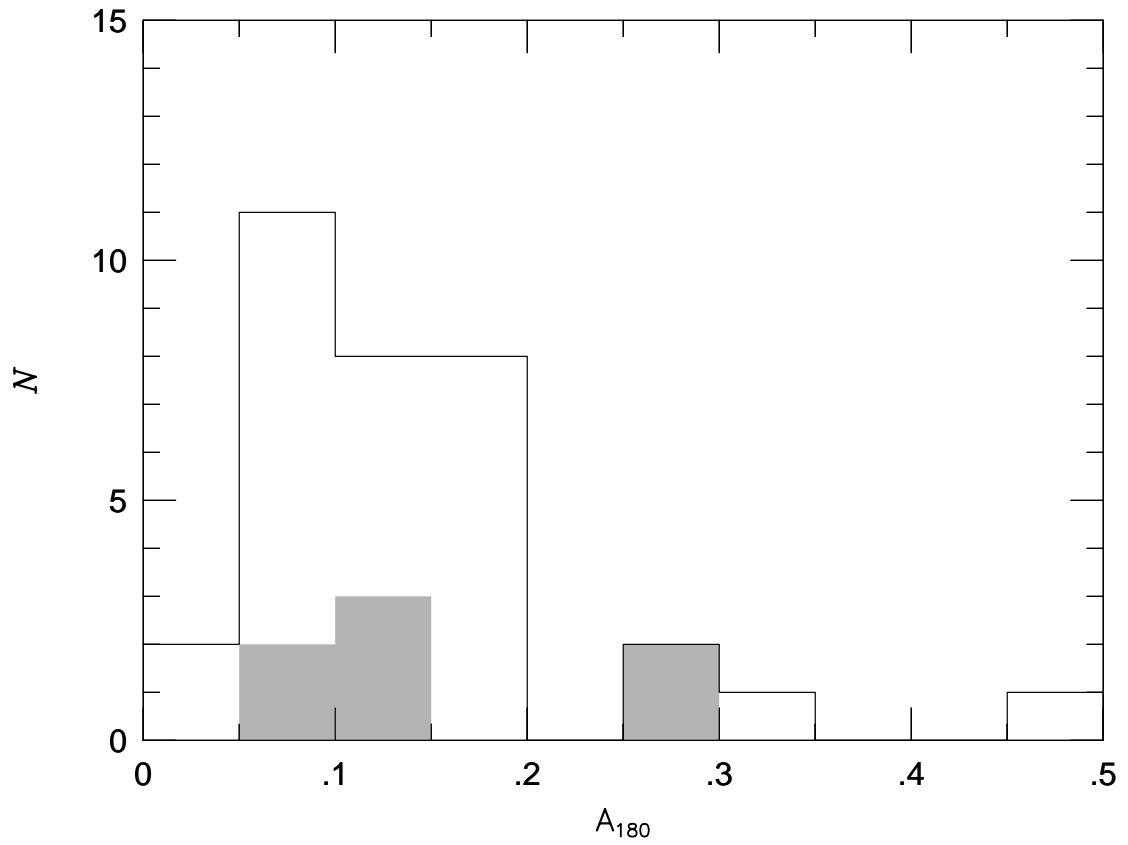


Fig. 3.10. The distribution of rotational asymmetry parameters (Chapter (2)) for our sample. Galaxies with significant rotation curve asymmetries were shaded. While half of the photometrically asymmetric galaxies were also kinematically asymmetric, 5 of 7 kinematically asymmetric galaxies show no significant photometric asymmetry.

illustrates the kinematic signature of spiral arms in our sample, as shown in Figure 3.11. The deprojected amplitude of the sinusoidal character of the velocity field residuals for this galaxy is  $\sim 20$  km/s and appears to be correlated with the light distribution (Figure 3.12).

### 3.4.3 Modeling Velocity Fields

Most galaxies in our sample do not show signs of rotation curve asymmetries, warps, solid body rotation, or spiral structure. Therefore, we have explored the ability of a single, inclined, differentially rotating, circular disk model to fit the DensePak H $\alpha$  velocity fields instead of tilted ring disks (eg. Begeman 1987).

There were two major advantages of using a single velocity field model over using tilted rings: (1) a single velocity field model used the entire data set to constrain the fit. Since we typically have  $\sim 150$  fibers with H $\alpha$  emission for a survey galaxy, we prefer to use all data to constrain inclination, position angle and other fit parameters, rather than breaking the galaxy into three or more rings with fewer than 50 measured velocity centroids per ring. (2) A single model is better able to model low-inclination disks because tilted ring fits tend to diverge unless the fit is weighted by  $|\cos \theta|$  ( $\theta$  is an angle measured from a galaxy's major axis in the galaxy plane) and data with  $|\theta| < \theta_{max} = 45^\circ$  is cut from the fit to minimize the effects of warping on fitting tilted rings (Begeman 1989). However, the greatest differences between two velocity field models with slightly different inclinations occur at  $\theta > 45^\circ$ , precisely where tilted-ring fits do not consider the data (Figure 3.13). Nearly face-on galaxies show the smallest differences between velocity

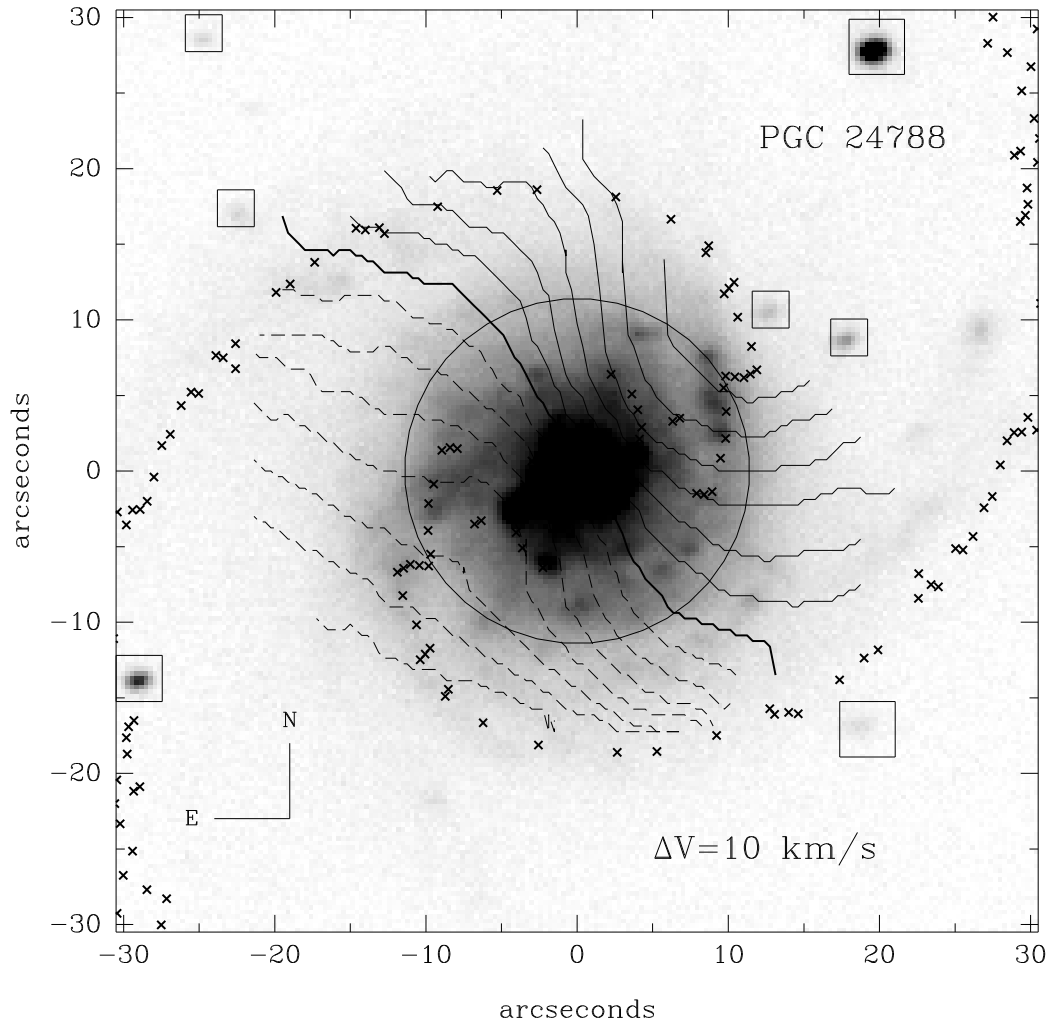


Fig. 3.11. The velocity field of PGC 24788, which shows twisting associated with spiral arms. Spiral arms are emphasized by x's marking the position angle of the best fit ellipse at each radius (Chapter 2). The circle has a radius of 12 arcseconds.

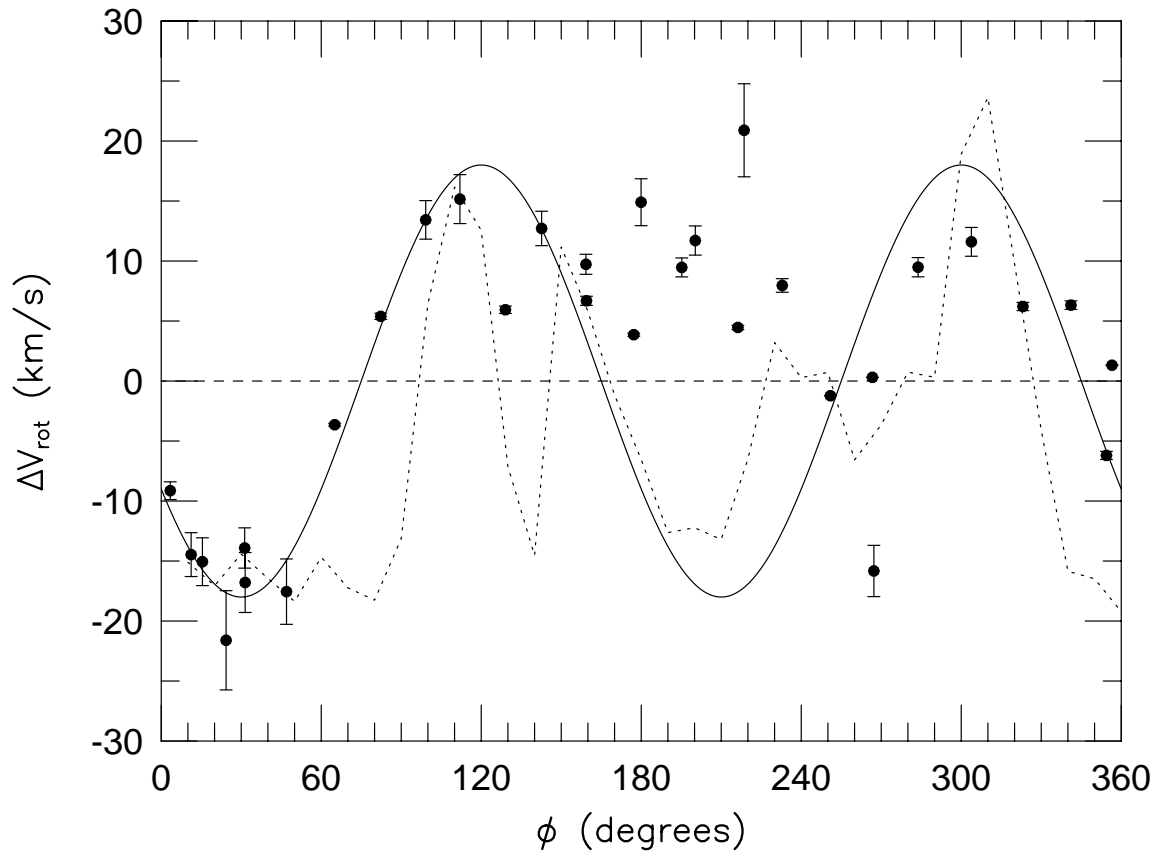


Fig. 3.12. The deprojected velocity residuals from the best fitting model (Equations 3.4 – 3.7) for data  $10''$ – $15''$  from the center show a sinusoidal variation with position angle (measured from North) that corresponds to the light distribution (dotted line) measured between  $12''$ – $13''$  from the center. The 20 km/s amplitude is consistent with the expected velocity variation across massive spiral arms (Roberts 1969; Kranz & Rix 2001). From a Fourier analysis of the images described in Chapter 2, strong spiral structure can be described by a Fourier amplitude and phase. The sine curve has the same phase as the  $m = 2$  Fourier component, while the amplitude was chosen to match the kinematic data.

fields with slightly different inclinations, so it imperative to use data at all azimuthal angles to accurately fit velocity field models at inclinations less than  $30^\circ$  (Figure 3.14).

The simplest velocity-field model involves the assumption that the rotation curve of a galaxy is radially symmetric and the velocity field is axisymmetric. An expression for the velocity at any point in the galaxy plane,  $V_{\text{mod}}(R, \theta)$  where  $R$  and  $\theta$  are the radius and azimuthal angle, is then given by the expression

$$V_{\text{mod}}(R, \theta) = V_{\text{sys}} + V_{\theta}(R) \cos \theta \quad (3.4)$$

where  $V_{\text{sys}}$  is the systematic recession velocity, and  $V_{\theta}(R)$  is the *observed* (i.e., uncorrected for inclination) rotation speed. Relations between these quantities and an observed radius and azimuthal angle,  $r$  and  $\phi$ , are given by

$$R = r \cos(\phi - \text{P.A.}) / \cos \theta \quad (3.5)$$

and

$$\tan \theta = \tan(\phi - \text{P.A.}) / \cos i \quad (3.6)$$

where  $r$  and  $\phi$  are the radii and azimuthal angle in the observer's plane, and the *P.A.* is the position angle and  $i$  the inclination. We made another simplifying assumption after examining the rotation curves of the sample galaxies in the atlas. The rotation curves typically showed a steady rise to a peak velocity. Thus, the rotation curve required only two free parameters – the peak velocity and a characteristic scale-length,  $h_{\text{rot}}$ . A single

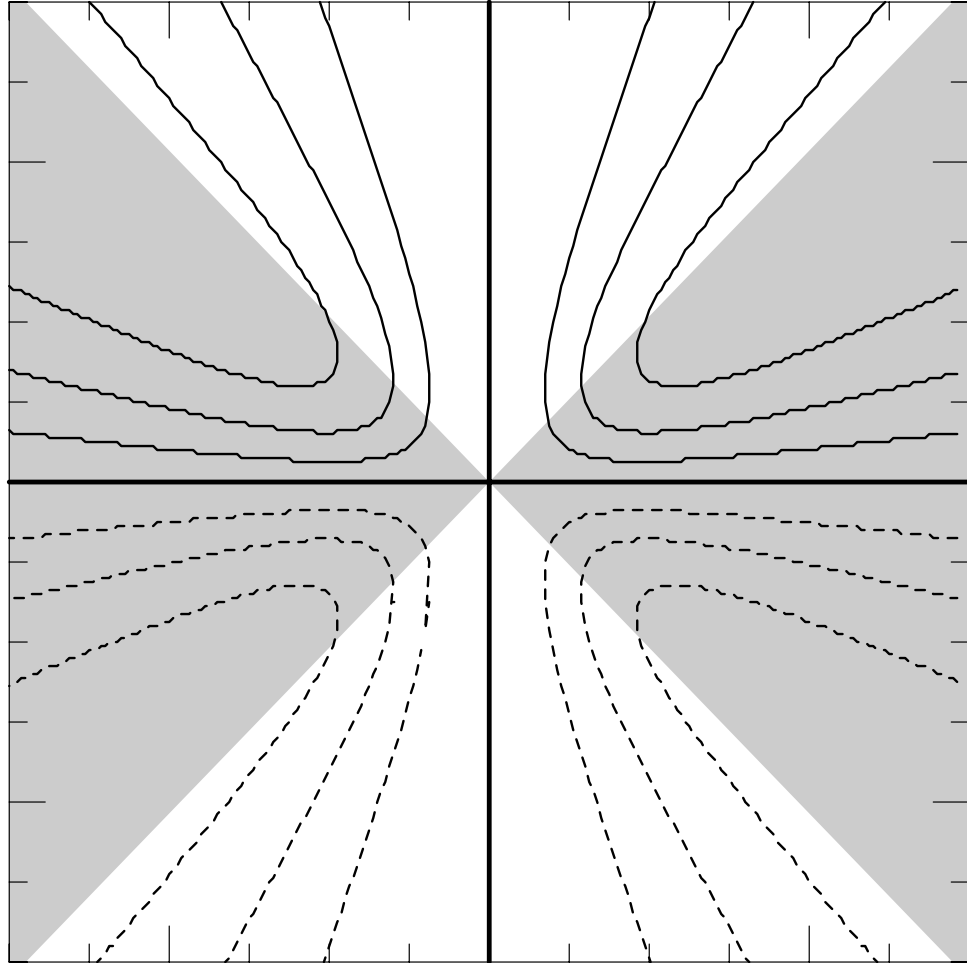


Fig. 3.13. The difference between velocity fields (calculated from Equations 3.4–3.7) with inclinations of 10 and 20 degrees are shown here. The vertical dark line is the major axis and the horizontal dark line is the minor axis. The difference between models is zero on both the major and minor axes. The greatest differences between nearly face-on models at different inclinations occur 45 degrees from the major axis. Tilted-ring fits typically consider only data with  $|\theta| < 45^\circ$  (unshaded regions;  $\theta$  is the angle from the major axis in the *galaxy* plane). Given the relatively small differences in velocity fields in nearly face-on systems, it is important to include all data in the fit.

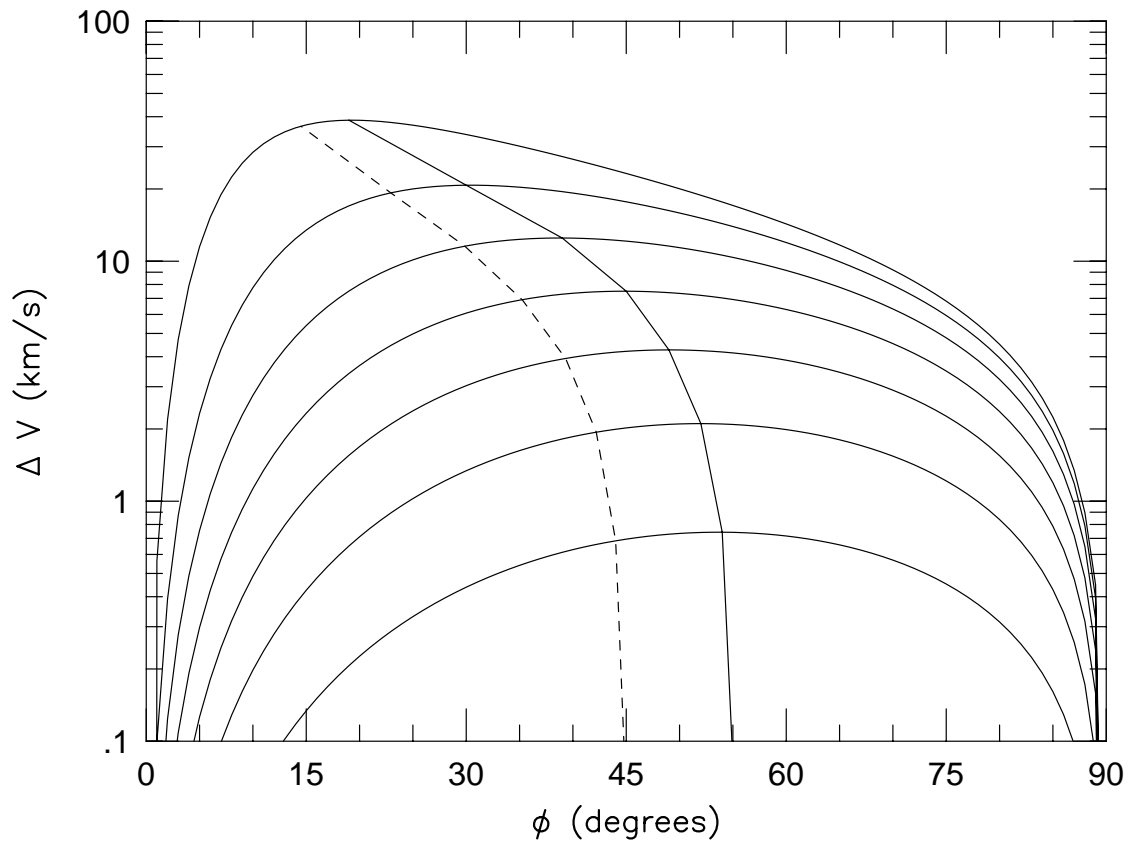


Fig. 3.14. The differences in velocity as a function of  $\phi$  where  $\phi$  is measured from the major axis in the *observer's* frame. These differences assume (1) measurements are made on the flat part of the rotation curve, (2)  $V_{\text{rot}} = 160 \sin i$  km/s for the mean inclination and (3) velocity fields obey Equations 3.4—3.6. Starting from the bottom, the solid curves represent mean inclinations of  $15^\circ, 25^\circ, 35^\circ, 45^\circ, 55^\circ, 65^\circ$  and  $75^\circ$  with inclination differences of  $\pm 5^\circ$ . The dashed line represents  $\theta = 45^\circ$  for each of these different inclinations, where  $\theta$  is the angle from the major axis in the *galaxy* plane. The solid line represents the maximum velocity difference as a function of  $\phi$  for different inclinations. Classical tilted-ring fits do not utilize data to right of dashed line, thereby missing over half the signal used to estimate inclination.



inclined hyperbolic tangent rotation curve, i.e.

$$V_{\theta}(R) = V_{\text{rot}} \tanh(R/h_{\text{rot}}), \quad (3.7)$$

was sufficient to fit the shape of these rotation curves with a minimum of free parameters. Though hyperbolic tangent models for rotation curves are not directly motivated by a physical model, the standard parameterization of dark halo density profiles yields an arctangent model for the rotation curve (Gilmore *et al.* 1990) which has a virtually identical shape. In our model, the free variables were inclination, position angle, center, central velocity, observed rotation velocity, and hyperbolic tangent scale-length.

#### 3.4.3.1 $\chi^2$ Minimization of Velocity-Field Models

We found a best fit velocity-field model to each galaxy’s observed kinematic data from DensePak using non-linear  $\chi^2$  minimization. We generated a smooth model using equations 3.3–3.6 with the seven free parameters listed above plus two free parameters corresponding to telescope offsets for each additional DensePak pointing. We accounted for the effect of beam smearing by mapping the model over the region spanned by the observations on a grid with a scale of four “pixels” per arcsecond. One can compare an IFU fiber and a radio beam; both smooth or “smear” signal velocities within a given radius. By determining the mean velocity within a DensePak fiber as part of our fitting procedure, we are, in effect, applying a beam-smearing correction. This correction was important:  $\chi^2$  calculated for a given set of free parameters changed on the order of 10% if sampled with fewer than four pixels per arcsecond ( $\sim 12$  pixels per fiber diameter) and

remained relatively constant at higher spatial resolutions. Since the fitting algorithm was computationally intensive, a spatial resolution of four pixels per arcsecond was used for all model fits. The pixelated velocity field was then sampled with the DensePak footprint. After assuming the  $H\alpha$  flux was constant over a DensePak fiber, we calculated the mean velocity over the  $\pi R^2 \approx 113$  pixels.

Since  $\chi^2$  was not directly computable, we needed to find the minimum of the  $\chi^2$  space by searching over all the multidimensional space of the free parameters. Searching over a grid of at least seven free parameters was impractical so we adopted a multidimensional downhill simplex method (Press *et al.* 1992) for finding the minimum of  $\chi^2$ . While this algorithm is not computationally efficient, it only requires function evaluations and does not require one to function compute derivatives. Operating from an initial guess, the algorithm steps through multidimensional space towards the direction which corresponds to the greatest decrease of the function  $\chi^2$ . The way in which the parameters change as they move through multidimensional space has been compared to the movement of amoebas; this metaphor gives the algorithm its commonly used name. Amoeba is susceptible to being caught in local minima and yielding solutions which are sensitive to both the initial conditions and initial step sizes. Fitting galaxy velocity fields therefore requires many iterations of the amoeba algorithm seeded with different initial guesses and step sizes so that a stable solution is found.

When first fitting galaxy velocity fields, we kept several parameters fixed in order to simplify the steps amoeba needed to take. Since we expected all sample galaxies to have inclinations less than  $30^\circ$ , we examined the shape of velocity fields over a range of inclinations. The difference between velocity fields was most apparent at  $45^\circ$  from

the major axis. In the same way, velocity fields with different  $h_{\text{rot}}$  varied the most at small radii along the major axis. Since these effects were symmetric, we began fitting velocity fields keeping inclination and  $h_{\text{rot}}$  fixed to reasonable values. We also assumed the telescope offsets were correct (but assumed the kinematic center was unknown). After we held these parameters fixed, amoeba minimized  $\chi^2$  by varying the remaining parameters. After the initial fit was determined, we allowed all free parameters to vary and re-fit. To ensure we had found the true  $\chi^2$  minimum and not just a local minimum, we perturbed our solution by varying both the initial conditions and step-sizes. We continued perturbing our amoeba solutions until differences in inclination and position angles were less than  $< 0.01^\circ$ . Similarly, all velocity solutions and position solutions were required to be stable to  $< 0.01$  km/s or arcseconds respectively.

Although the velocity-field residuals were small, typically less than 6 km/s, our velocity centroiding errors were even smaller, resulting in minimum reduced- $\chi^2$ ,  $\chi_\nu^2$ , for these fits which were typically much greater than unity ( $2 < \chi_\nu^2 < 15$ ). For any  $\chi^2$  fit where  $\chi_\nu^2$  is much greater than unity there are several possible explanations: (1) the residuals of our velocity field model fit were not Gaussian, (2) error-bars on the line centroids were underestimated, or (3) our model was not a good representation of the data. In reality, velocity fields of real galaxies are very complicated in detail. Indeed, one would not expect our simple model to approximate the true velocity field. Since our DensePak observations are of high precision, it is reasonable to suppose we are seeing the true complexities of disk kinematics. Presumably a class of models exists which would better match the data. Such models would need to possess high spatial frequency composed to match all the fluctuations in the observed velocity fields. Some

of these components may be random in nature, so such a complex model would need be statistical. Further, since we are not interested here in modeling the random motions of HII regions and the non-random, high spatial frequency streaming associated with spiral arms, and we assumed these variations would be randomly spaced in the galaxy, we simply compensated for these contributions by adding a “fuzziness” term to our model. Specifically, we follow the probability theory arguments of Rix *et al.* (1997) by adding an extra error term,  $\sigma_{\text{mod}}$ , into the  $\chi^2$  sum (Rix *et al.* 1997):

$$\chi^2_{\delta} = \sum_i \frac{(V_{\text{mod}_i} - V_{\text{obs}_i})^2}{\sigma_{\text{mod}}^2 + \sigma_{\text{obs}_i}^2}. \quad (3.8)$$

For each galaxy, we chose a value for  $\sigma_{\text{mod}}$  which normalized the reduced- $\chi^2_{\delta}$  to unity based on an initial fit using the standard  $\chi^2$  definition. We then re-fit the galaxy velocity field with amoeba to find a new minimum-valued solution using Equation 3.8. We adjusted  $\sigma_{\text{mod}}$  to lower values as needed to keep  $\chi^2$  within 1% of the difference between the number of observed velocities and the degrees of freedom. Table 3.5 contains solutions for all the sample galaxies along with the added noise term  $\sigma_{\text{mod}}$ . Using this fitting algorithm, we were able to fit 36 of 39 galaxies (a 90% success rate). Of the three galaxies for which we could not fit velocity-field models, two were at very low inclinations, while the third had insufficient data. These three are described as follows:

**PGC 05345** is a Magellanic Irregular that has limited H $\alpha$  scattered in separated regions. The small amount of H $\alpha$  in the galaxy is all at the same velocity ( $\sigma_{rms} = 2.5$  km/s). These two factors added together to prevent the fitting algorithm from converging.

**PGC 23913** also have a very small velocity gradient ( $\sim 20$  km/s), which implied a very low inclination. The velocity gradient is so small, the fitting algorithm did not settle on a model center.

**PGC 70962** only had H $\alpha$  flux in 39 fibers. The velocity field model only converged when more data was available for a galaxy.

### 3.4.3.2 Model Parameter Velocity-Field Parameter Error Estimation

Once galaxies were fit with our simple velocity field and the reduced- $\chi^2_\delta$  was unity (Equation 3.8), we assumed the error distribution was Gaussian and used the standard differences in  $\chi^2$  to map out confidence intervals in parameter space. Figure 3.15 presents an example of this  $\chi^2$  mapping for inclination, and further demonstrates that error distributions indeed are close to being Gaussian in nature. After mapping out  $\chi^2$  space for multiple pairs of variables, and then running Monte Carlo simulations of velocity-field fits, we found no evidence for detectable cross-correlations between parameters. Therefore, we were able to calculate a changing  $\chi^2$  while varying a single parameter to determine errors. Confidence intervals at 68% are quoted on several model parameters in Table 3.5.

Because differences in model velocities at low inclination are relatively small (3.14), we created a simulation to test whether we could measure accurate inclinations for  $i < 30^\circ$ . We created Monte Carlo simulations of typical DensePak data using Equations 3.4–3.7. After fitting this simulations data as described in §3.4.3.1, we were able to determine the standard deviation of model parameter residuals. The resultant estimates of expected inclination errors as a function of inclination were surprisingly small: At

$i = 10^\circ$  we expected  $\Delta i \approx 6^\circ$  for typical DensePak data. Errors estimated for individual galaxies via the method described in §3.5.3.2 matched our Monte Carlo simulations (Figure 3.16). Based on our simulations, several galaxies had unexpectedly high inclination errors: PGC 6855, which has an asymmetric rotation curve, PGC 24788, which has a strong spiral distortion, PGC 28401, which has  $V_{\text{rot}} = 8$  km/s and has an inclination errors consistent with  $i = 0$ , and PGC 56010, which has only 70 velocity measurements, uncentered on the galaxy.

### 3.4.3.3 DensePak Continuum Measurements: A Check on Telescope Offsets

Figure 3.17 presents sample radial profiles of measured continuum flux (i.e., surface-brightness) from DensePak. These plots can be generated directly from the data tables, e.g. Table 3.2, and are all included in the atlas. In addition to demonstrating our ability to measure such profiles spectroscopically, these surface brightness profiles are important because they indicate (1) our velocity field model centers agree with the photometric centers of the galaxies, and (2) by letting telescope offsets vary during the model velocity-field fitting process we were able to improve the combination of DensePak pointings. In other words, after  $\chi^2_{\delta}$  minimization of the velocity-field models, where telescope offsets were free parameters, the surface-brightness profile became tighter. Keep in mind that the velocity-field model fits rely on the emission-line (kinematic) data only; the tightness of the surface-brightness profile is not coupled to the fit. Based on variations in model telescope offsets coupled with our observing experience, we find errors in telescope offsets could be as great as 2 arcseconds.

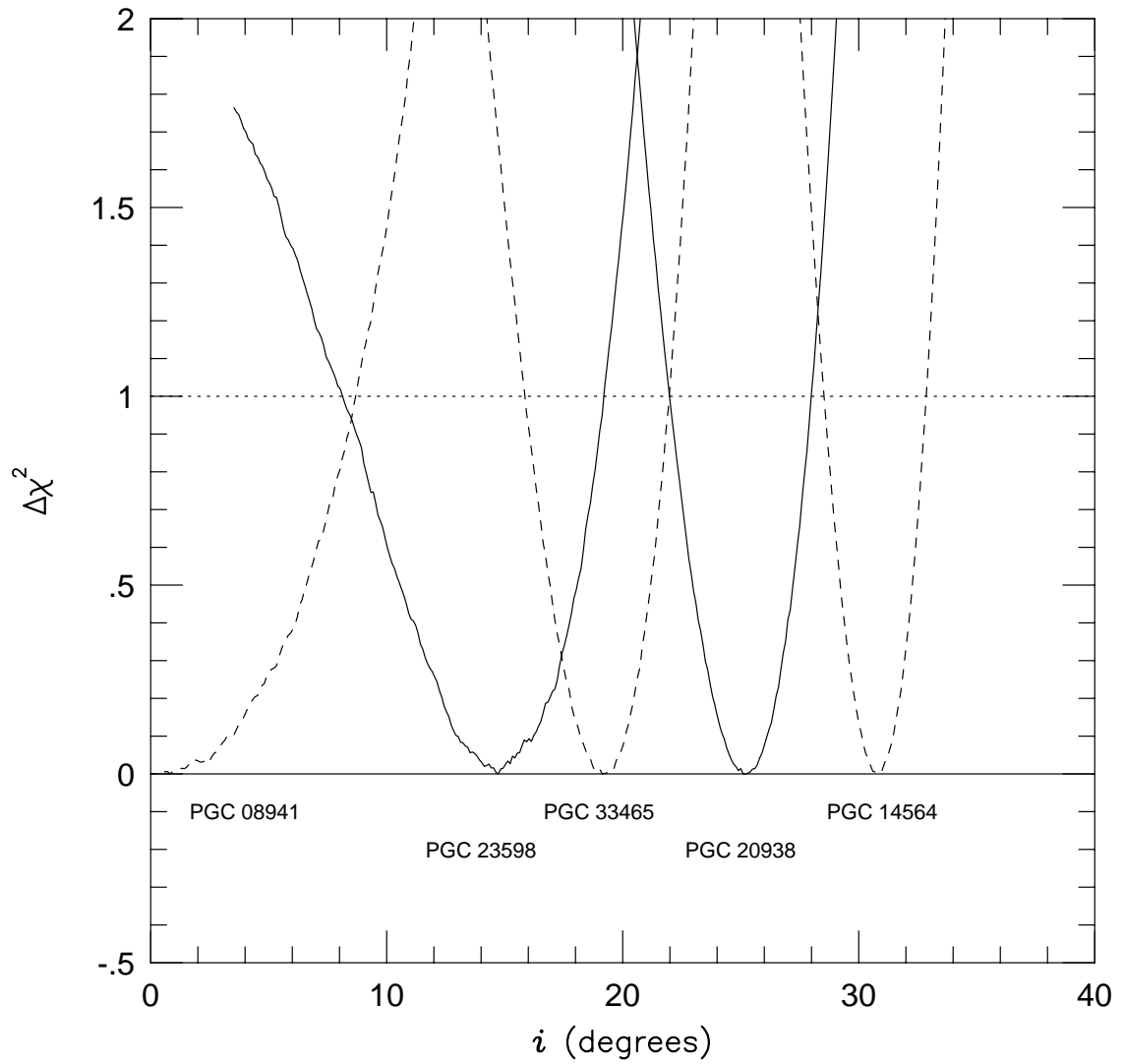


Fig. 3.15. One dimensional map of  $\Delta\chi^2$  as a function of inclination with all other parameters held fixed for five representative galaxies from our sample. For a model fit which has Gaussian distributed residuals,  $\Delta\chi^2 = 1$  yields the 68% confidence limit on 1 free parameter. Given the shape of the  $\chi^2$  as a function of inclination, it appears the errors are close to Gaussian in nature.



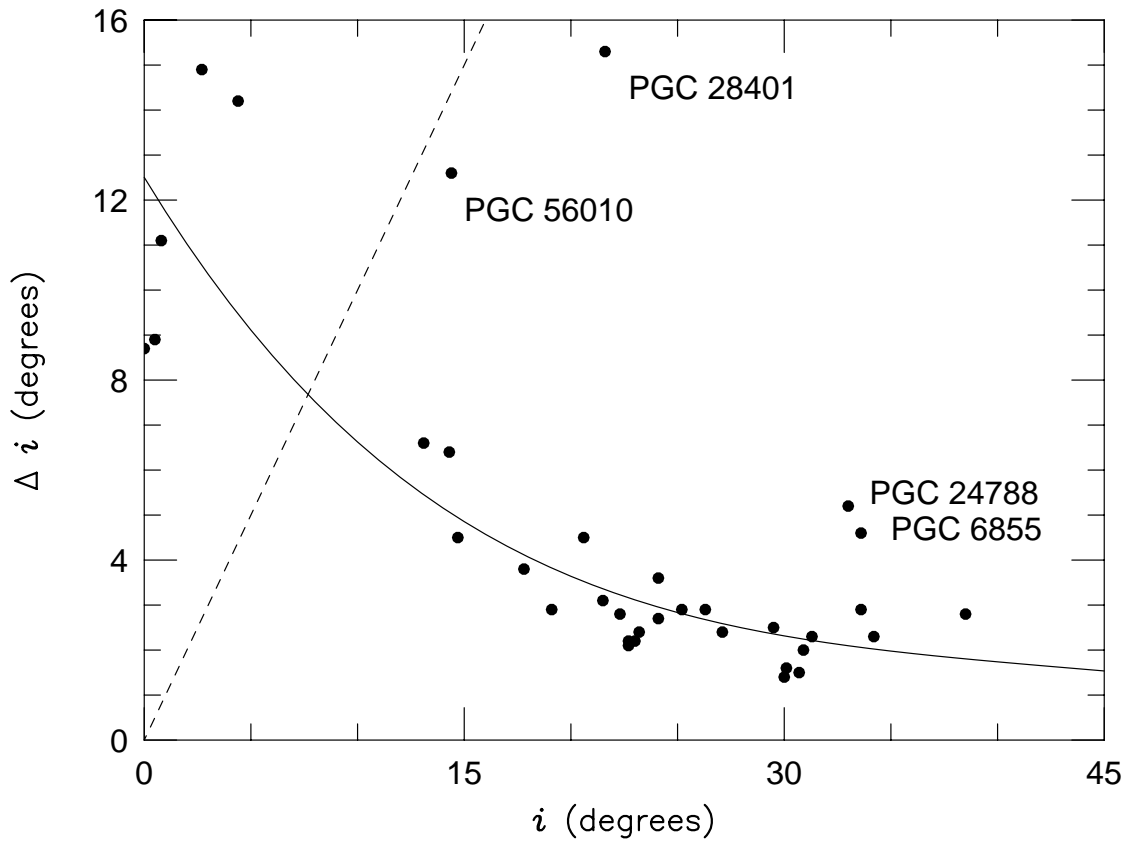


Fig. 3.16. A measurement of our ability to derive accurate kinematic inclinations from DensePak H $\alpha$  velocity fields for face-on disks. The solid curve is our Monte Carlo prediction of inclination errors for velocity fields “observed” with two DensePak pointings and fit with a single inclined-disk velocity-field model. Our Monte Carlo simulation used the following assumptions: (1) Equations 3.4-3.7 apply, (2)  $(\sigma_{mod}^2 + \sigma_{obs_i}^2)^{1/2} = 5$  km/s as defined by Equation 3.8, (4)  $h_{rot} = 5''$  and (3) 150 data points were available sampling an area equivalent to  $40'' \times 40''$ . The dotted lines represents  $\Delta i/i = 1$ . For our data,  $\Delta i/i = 1$  at  $i \approx 7.5^\circ$ , and the ratio drops rapidly for higher inclinations.

Table 3.5. H $\alpha$  Velocity Field Parameters

PGC	$\sigma_{\text{mod}}$	$N$	$i$	PA	$V_{\text{rot}}$	$h_{\text{rot}}$	$V_{\text{sys}}$
	km/s		deg	deg	km/s	arcsec	km/s
02162	2.9	149	$20.6^{+4.5}_{-6.4}$	$284.8 \pm 0.6$	$35.0 \pm 0.4$	$1.7 \pm 0.4$	$5464.6 \pm 0.3$
03512	2.8	125	$30.1^{+1.6}_{-1.9}$	$301.1 \pm 0.3$	$82.4 \pm 0.5$	$6.7 \pm 0.1$	$5460.2 \pm 0.2$
05673	2.7	227	$23.0^{+2.2}_{-3.1}$	$77.9 \pm 0.4$	$58.0 \pm 0.2$	$8.4 \pm 0.2$	$4518.3 \pm 0.2$
06855	3.6	160	$33.6^{+2.9}_{-3.8}$	$321.8 \pm 0.6$	$52.0 \pm 0.5$	$10.4 \pm 0.4$	$4868.5 \pm 0.3$
07826	1.7	128	$33.6^{+4.6}_{-5.7}$	$204.4 \pm 0.8$	$31.2 \pm 0.4$	$10.9 \pm 0.3$	$2386.4 \pm 0.2$
08941	3.2	143	$0.0^{+8.7}_{-0.0}$	$58.5 \pm 0.3$	$69.1 \pm 0.5$	$5.2 \pm 0.2$	$9480.3 \pm 0.3$
14564	4.7	148	$30.9^{+2.0}_{-2.4}$	$346.7 \pm 0.4$	$92.3 \pm 0.5$	$6.3 \pm 0.2$	$3505.6 \pm 0.4$
15531	3.3	186	$0.5^{+8.9}_{-0.5}$	$206.6 \pm 0.4$	$65.9 \pm 0.4$	$6.9 \pm 0.2$	$5582.8 \pm 0.3$
16274	4.6	140	$30.7^{+1.5}_{-2.0}$	$169.0 \pm 0.4$	$113.1 \pm 0.6$	$5.7 \pm 0.2$	$8883.8 \pm 0.4$
19767	1.8	128	$0.8^{+11.1}_{-0.8}$	$43.6 \pm 0.4$	$53.0 \pm 0.4$	$8.4 \pm 0.2$	$5134.4 \pm 0.2$
20938	4.7	258	$25.2^{+2.9}_{-3.3}$	$20.1 \pm 0.5$	$58.3 \pm 0.5$	$4.1 \pm 0.3$	$4668.0 \pm 0.3$
23333	2.4	125	$26.3^{+2.9}_{-3.3}$	$228.1 \pm 0.5$	$60.2 \pm 0.4$	$9.0 \pm 0.2$	$4626.6 \pm 0.2$
23598	1.2	143	$14.7^{+4.5}_{-6.6}$	$31.1 \pm 0.4$	$45.3 \pm 0.2$	$5.8 \pm 0.2$	$7479.0 \pm 0.2$
24788	7.3	115	$33.0^{+5.2}_{-6.2}$	$313.3 \pm 1.0$	$73.6 \pm 1.4$	$10.4 \pm 0.5$	$7546.2 \pm 0.7$
26140	8.2	134	$27.1^{+2.4}_{-2.5}$	$56.7 \pm 0.4$	$150.0 \pm 1.2$	$4.4 \pm 0.3$	$8815.3 \pm 0.8$
26517	3.6	97	$0.0^{+16.5}_{-16.5}$	$21.3 \pm 0.9$	$48.4 \pm 0.6$	$6.2 \pm 0.3$	$4118.7 \pm 0.4$
27792	3.4	133	$38.5^{+2.8}_{-3.4}$	$325.4 \pm 0.8$	$46.1 \pm 0.5$	$9.4 \pm 0.4$	$1437.8 \pm 0.3$
28310	2.7	131	$34.2^{+2.3}_{-2.3}$	$8.4 \pm 0.5$	$63.8 \pm 0.4$	$8.9 \pm 0.2$	$5891.3 \pm 0.3$
28401	2.2	149	$21.6^{+15.3}_{-21.6}$	$62.6 \pm 2.6$	$8.5 \pm 0.4$	$7.9 \pm 1.4$	$3340.7 \pm 0.2$

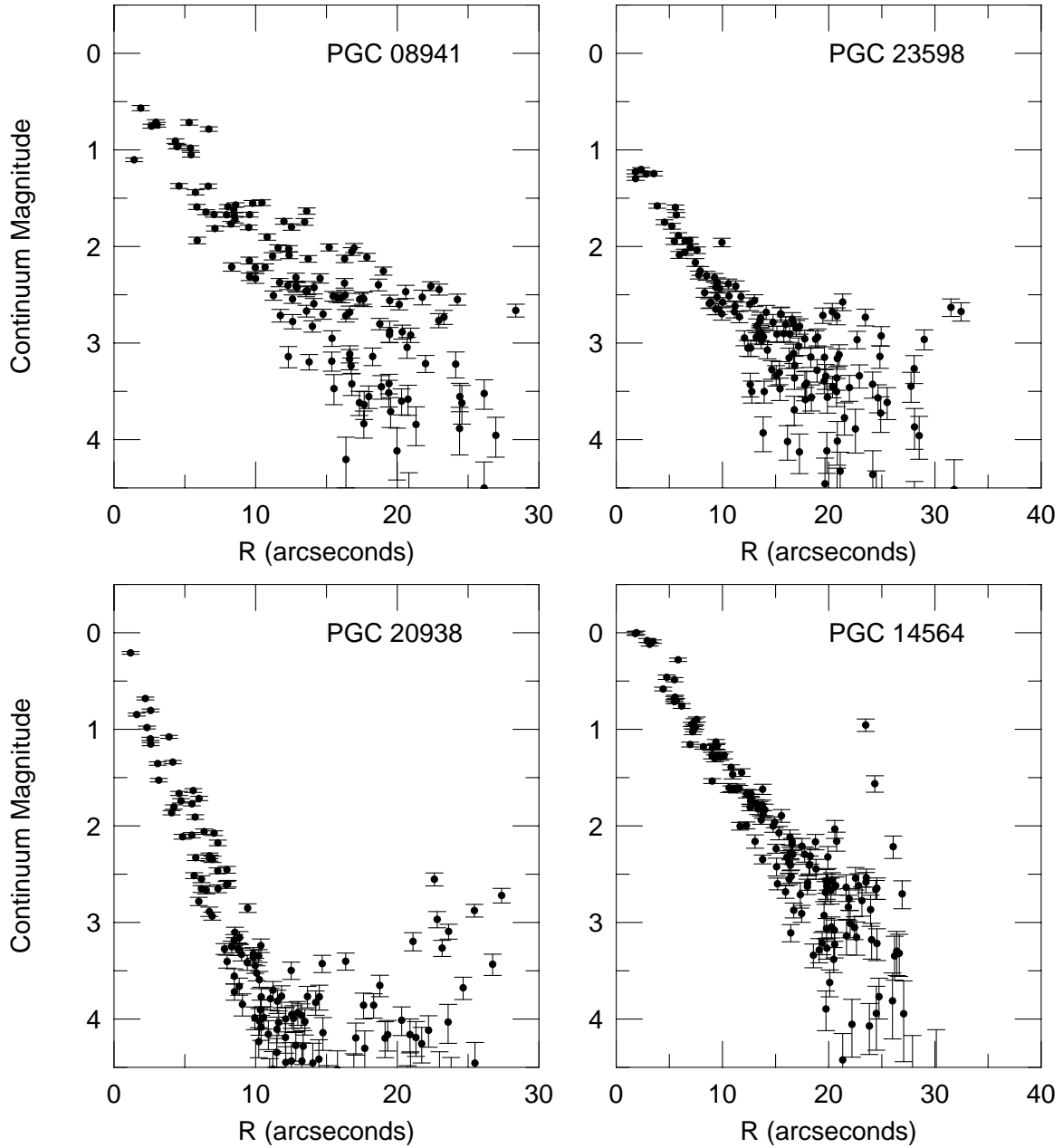


Fig. 3.17. Continuum magnitudes, calculated from  $-2.5 \log \text{Counts}_{\text{cont.}}$  (see §3.3.1), with arbitrary zero-point, as measured between  $6600\text{\AA} < \lambda\lambda < 6800\text{\AA}$ , for four representative galaxies. Radial surface brightness profiles combine measurements from two or more DensePak pointings, with the centers and telescope offsets determined from velocity-field modeling described in §3.4.3. Since both the offsets and the centers are model parameters determined independently from these continuum measures, the tight correlation exhibited by these surface brightness profiles indicates: (1) Galaxies in our sample share the same kinematic and photometric centers. (2) Telescope offsets determined through fits to the velocity fields are accurate.

PGC	$\sigma_{\text{mod}}$	$N$	$i$	PA	$V_{\text{rot}}$	$h_{\text{rot}}$	$V_{\text{sys}}$
	km/s		deg	deg	km/s	arcsec	km/s
31159	3.0	150	$22.7^{+2.2}_{-2.7}$	$352.6 \pm 0.4$	$84.8 \pm 0.4$	$7.2 \pm 0.2$	$5760.2 \pm 0.3$
32091	3.7	143	$2.7^{+14.9}_{-2.7}$	$117.6 \pm 0.8$	$41.4 \pm 0.6$	$8.9 \pm 0.4$	$2481.4 \pm 0.4$
32638	4.1	129	$22.3^{+2.8}_{-3.1}$	$193.1 \pm 0.4$	$88.0 \pm 0.6$	$2.5 \pm 0.2$	$6475.7 \pm 0.4$
33465	4.2	124	$19.1^{+2.9}_{-3.3}$	$91.5 \pm 0.3$	$99.2 \pm 0.6$	$2.9 \pm 0.2$	$6465.0 \pm 0.4$
36925	2.8	76	$23.2^{+2.4}_{-3.1}$	$225.5 \pm 0.4$	$75.2 \pm 0.5$	$1.6 \pm 0.2$	$6835.6 \pm 0.4$
38268	2.9	130	$29.5^{+2.5}_{-3.1}$	$206.8 \pm 0.5$	$64.7 \pm 0.5$	$8.3 \pm 0.2$	$3118.9 \pm 0.3$
38908	3.9	80	$23.6^{+2.9}_{-3.0}$	$330.6 \pm 0.4$	$92.4 \pm 0.7$	$2.4 \pm 0.2$	$7055.2 \pm 0.4$
38908	5.2	139	$24.1^{+2.7}_{-2.8}$	$331.0 \pm 0.4$	$91.8 \pm 0.7$	$2.9 \pm 0.2$	$7063.0 \pm 0.5$
39728	2.8	70	$31.3^{+2.3}_{-2.5}$	$96.9 \pm 0.4$	$75.8 \pm 0.5$	$7.6 \pm 0.2$	$2278.7 \pm 0.3$
46767	5.1	226	$22.7^{+2.1}_{-1.8}$	$153.6 \pm 0.3$	$111.2 \pm 0.6$	$5.3 \pm 0.2$	$8284.2 \pm 0.4$
49906	2.7	142	$4.4^{+14.2}_{-4.4}$	$182.8 \pm 0.9$	$30.5 \pm 0.4$	$7.8 \pm 0.4$	$6882.9 \pm 0.2$
55750	2.6	137	$13.1^{+6.6}_{-13.1}$	$205.9 \pm 0.6$	$37.8 \pm 0.4$	$9.0 \pm 0.4$	$4510.5 \pm 0.2$
56010	3.1	69	$14.4^{+12.6}_{-14.4}$	$143.6 \pm 1.3$	$28.0 \pm 0.8$	$6.1 \pm 0.7$	$4486.4 \pm 0.4$
57931	3.1	117	$21.5^{+3.1}_{-3.6}$	$252.0 \pm 0.4$	$70.3 \pm 0.5$	$4.1 \pm 0.2$	$9279.1 \pm 0.4$
58410	4.2	151	$30.0^{+1.4}_{-1.5}$	$267.0 \pm 0.3$	$112.5 \pm 0.5$	$5.2 \pm 0.2$	$9062.0 \pm 0.4$
71106	8.1	148	$14.3^{+6.4}_{-14.3}$	$1.2 \pm 0.7$	$96.8 \pm 0.9$	$7.0 \pm 0.3$	$9617.4 \pm 0.6$
72144	2.6	115	$24.1^{+3.6}_{-5.3}$	$207.2 \pm 0.6$	$51.3 \pm 0.5$	$4.1 \pm 0.2$	$10537.1 \pm 0.3$
72453	4.0	132	$17.8^{+3.8}_{-4.9}$	$72.5 \pm 0.4$	$67.0 \pm 0.6$	$4.5 \pm 0.3$	$9973.2 \pm 0.3$

#### 3.4.3.4 $\sigma_{\text{mod}}\text{---}V_{\text{rot}}$ relation

Upon reviewing the results of our velocity-field model fits, we found (1) three galaxies had very large  $\sigma_{\text{mod}}$  values and (2) a correlation between the model velocity ( $V_{\text{rot}}$ ) and  $\sigma_{\text{mod}}$  existed for the rest of the galaxies (Figure 3.18).

The three galaxies with the largest values of  $\sigma_{\text{mod}}$ , PGC 24788, PGC 26140 and PGC 71106 were each peculiar. PGC 24788 showed the strongest evidence for streaming motions due to spiral arms. PGC 71106 showed the greatest kinematic asymmetry of our sample galaxies. PGC 26140 was an AGN with the largest value of  $V_{\text{rot}}$ . The ratio of  $\sigma_{\text{mod}}$  and  $V_{\text{rot}}$  for PGC 26140 was consistent with the rest of the sample.

One possible explanation for the  $\sigma_{\text{mod}}\text{---}V_{\text{rot}}$  relation is beam-smearing. This instrumental effect would increase with larger model velocities leading to greater values of  $\sigma_{\text{mod}}$ . However, after examining the dispersion of model pixels in a fiber footprint, we determined this effect was insignificant through most of the disk, and only marginally significant in the inner parts of the galaxy where the velocity field is changing rapidly. Since most of the fibers in our test were not affected by beam smearing, and by sampling a smooth, model velocity field with the DensePak footprint we largely account for beam smearing, we believe beam smearing does not introduce the relation between  $\sigma_{\text{mod}}$  and  $V_{\text{rot}}$ .

Another possible explanation is that  $\sigma_{\text{mod}}$  is a physical quantity related to the velocity dispersion of HI regions in the disk or with streaming motions associated with the spiral arms. If true, however, one expected  $\sigma_{\text{mod}}$  to be correlated with either inclination or  $V_{\text{rot}}/\sin i$ . However,  $\sigma_{\text{mod}}$  was most strongly correlated to  $V_{\text{rot}}$ . The relation is weaker

for  $\sigma_{\text{mod}}$  versus inclination or  $V_{\text{rot}}/\sin i$ . Hence the cause of this unexpected relationship remains unresolved.

### 3.5 Comparison of HI and H $\alpha$ Data

Since accurate measures of disk inclinations are critical to estimating disk ellipticity (Andersen *et al.* 2001) and studying the Tully-Fisher relation for nearly face-on systems (Bershady & Andersen 2001), we needed to confirm that results of our model fits were accurate. A check on several of these quantities came from HI lines profiles. By combining HI widths from new observations taken from Nançay (Table 3.3) and with values from the literature (Table 3.4) we have line-widths for 33 of the 36 galaxies with velocity field solutions. These observations allowed us to make several consistency checks.

#### 3.5.1 Rotation Speed

One critical experiment was determining whether our measurements of disk rotation speed were accurate. We examined the ratio of HI line widths ( $W_{20}$ ) to twice the rotation velocity ( $2 V_{\text{rot}}$ ), and found that at small rotation velocities this ratio was far from unity and at large  $2V_{\text{rot}}$  ( $> 125$  km/s) this ratio was typically 1.25. (Top panel of figure 3.19). When  $W_{20}$  was corrected for turbulent broadening via the formula:

$$W_R^2 = W_{20}^2 + W_t^2 - 2W_{20}W_t[1 - \exp -(W_{20}/W_c)^2] - 2W_t^2 \exp -(W_{20}/W_c)^2 \quad (3.9)$$

where  $W_t$  is the turbulent broadening of 38 km/s and  $W_c = 120$  km/s is the transition velocity from quadrature to linear summation (Tully & Fouqué 1985), we find all but the three measurements with  $2V_{\text{rot}} < 60$  km/s appeared highly correlated. For all galaxies

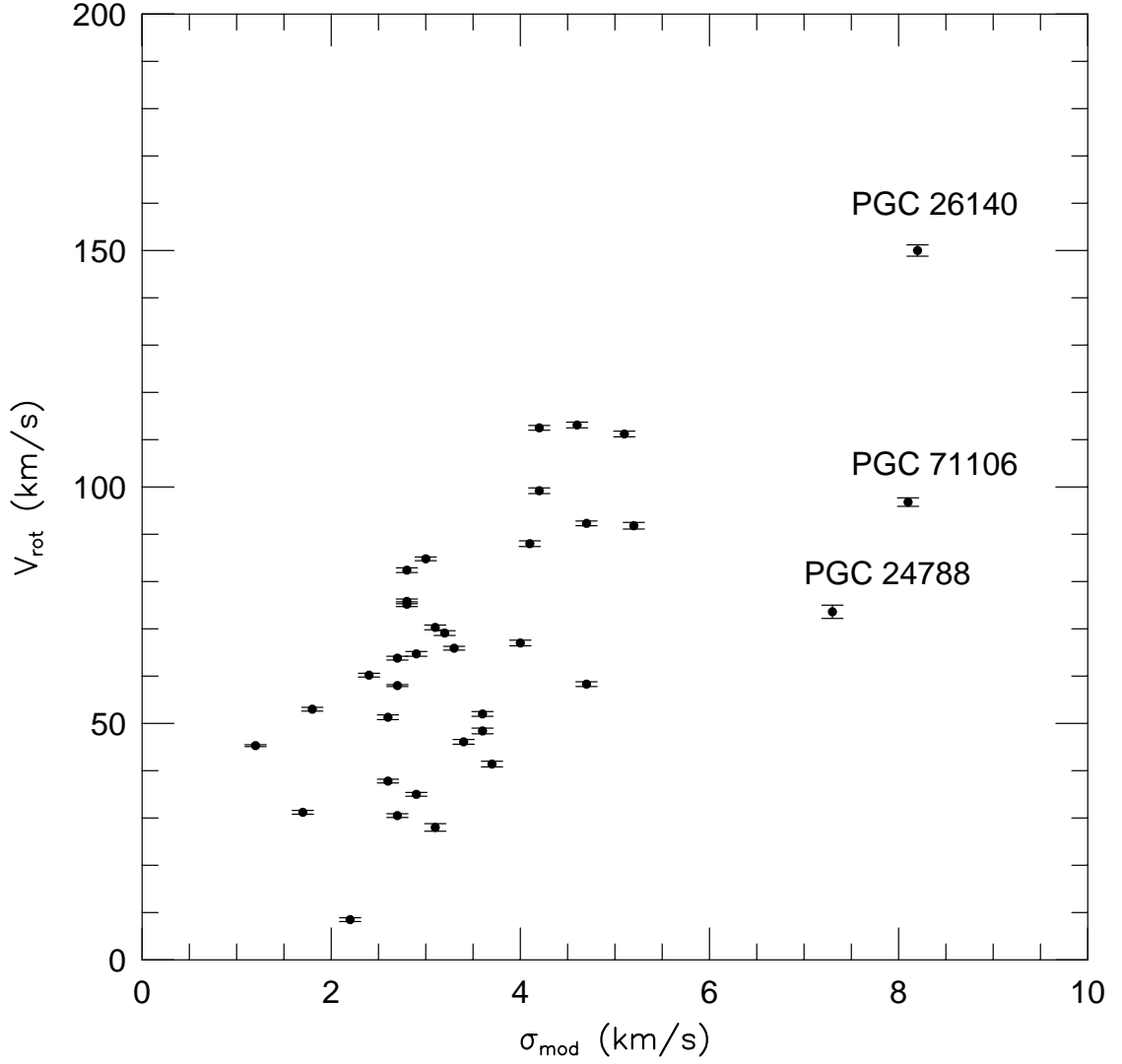


Fig. 3.18. The correlation between the model projected velocity,  $V_{\text{rot}}$  and the additional error term added to  $\chi^2_{\delta}$ ,  $\sigma_{\text{mod}}$  (Equation 3.8). This correlation was unexpected and is not understood.  $\sigma_{\text{mod}}$  only shows weaker correlations with inclination and  $V_{\text{rot}}/\sin i$ . The outliers include: PGC 24788, which shows the strongest spiral arm structure and PGC 71106, which shows the strongest rotation curve asymmetry. PGC 26140 is an AGN and also has the largest  $V_{\text{rot}}$  in our sample; however, the ratio of  $V_{\text{rot}}/\sigma_{\text{mod}}$  for this galaxy is consistent with the rest of the sample.



with  $2V_{\text{rot}} < 60$  km/s:  $W_R = 2.01V_{\text{rot}} + 4$  km/s with a correlation parameter of 0.91 and a standard deviation in the residuals of 20 km/s.

### 3.5.2 Inclination

Deriving accurate and precise inclinations of nearly face-on disk galaxies is difficult. Measurements of photometric disk axis ratios have constant errors as a function of axis ratio. Therefore, random errors on photometric inclinations diverge at small inclinations, and derived inclinations become increasingly subject to systematic errors due to intrinsic ellipticity. For these reasons, estimates of disk inclination from two-dimensional kinematic maps provide a critical, independent alternative. Historically, HI data has been of insufficient resolution and signal to noise to tackle inclinations under  $40^\circ$  (Begeman 1989). The importance of DensePak data is its ability to open up accurate and precise kinematic inclinations estimates down to  $i = 15^\circ$ . Using Monte Carlo simulations of velocity fields “observed” with DensePak, we estimated  $\Delta i = 5^\circ$  at  $i = 15^\circ$  (Figure 3.16). The magnitude of these errors are consistent with measured errors based on  $\Delta\chi^2$  (Figure 3.15). However, it is important to have another independent check on our results. To do so, we estimate inclinations by inverting the Tully-Fisher relation (Rix & Zaritsky 1995). We stress that this method is independent of both kinematic model fits and photometric disk axis ratios. We derived inverse Tully-Fisher inclinations from

$$\sin i = W_R 10^{(M_r + 7.44)/-5.29} \quad (3.10)$$

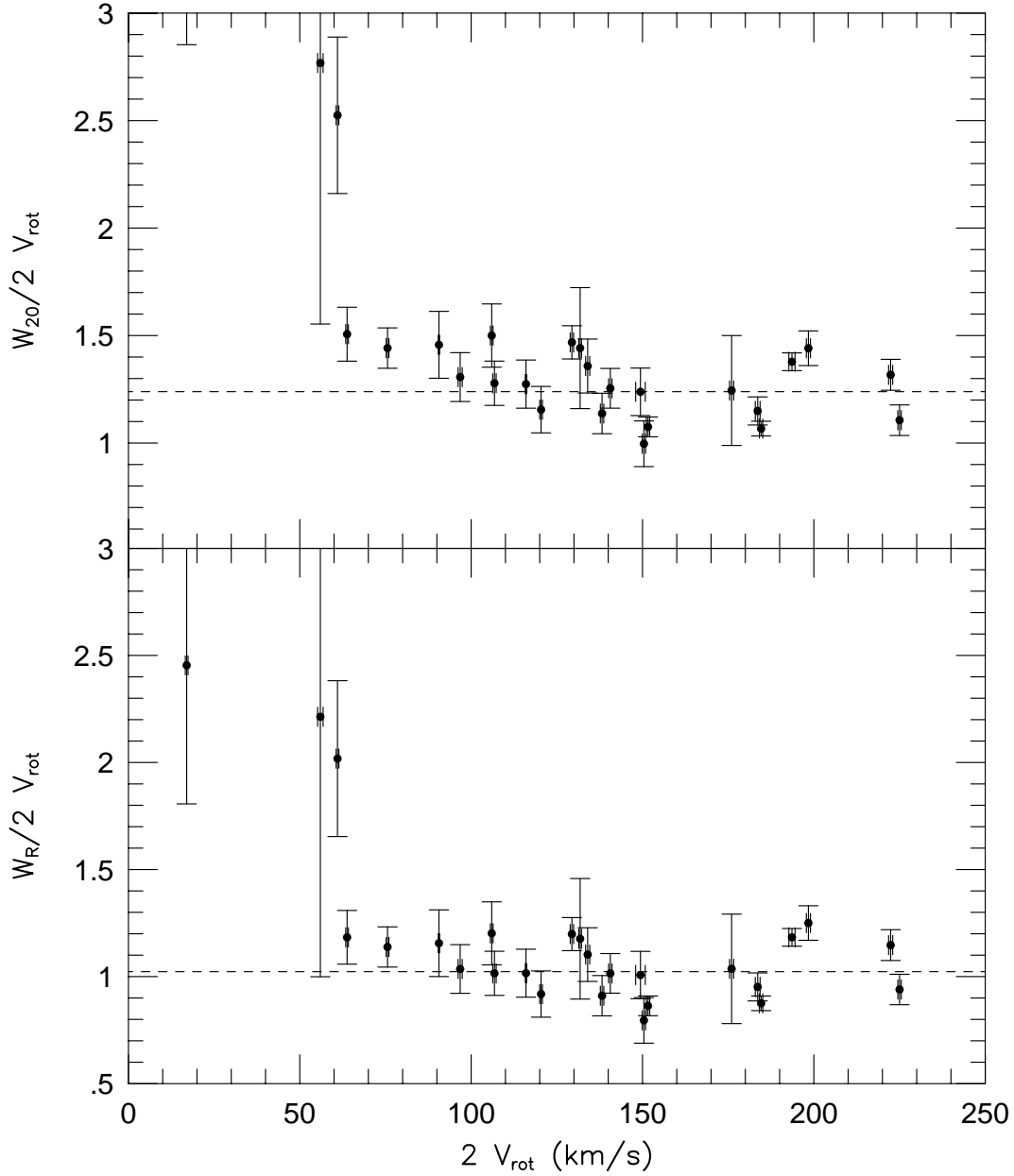


Fig. 3.19. The ratio of uncorrected HI line widths,  $W_{20}$ , (top panel) and corrected HI line widths,  $W_R$ , (bottom panel) to twice the rotation-speed derived from velocity-field modeling of DensePak two-dimensional  $\text{H}\alpha$  kinematic maps versus this rotation speed. Note none of these quantities are corrected for inclinations. The ratio of  $W_{20}$  to  $\text{H}\alpha$  rotation speed shows an increasing trend at low rotation speeds ( $V_{\text{rot}} < 30 \text{ km/s}$ ). After applying the turbulent velocity correction of Tully & Foqué (1985) to derive  $W_R$  in Equation 3.9, results improve. For all but the lowest rotation speeds, the ratio approaches unity for  $V_{\text{rot}} > 30 \text{ km/s}$ . Dotted lines indicate the mean of the ratio for rotation velocities greater than 60 km/s to better highlight the differences between corrected and uncorrected velocity widths.

where coefficients were taken from Courteau (1997).  $W_R$  is calculated from Equation 3.9 and  $M_r$  is the absolute Lick  $r$ -band magnitude, estimated for our sample by using the color term  $R - r = -0.45$  (Fukugita *et al.* 1995) to correct our Johnson  $R$ -magnitudes tabulated in Chapter 2. Once the color correction had been applied, we calculated the absolute magnitude assuming  $H_0 = 70$  km/s/Mpc. An advantage of what we call “inverse Tully-Fisher inclinations” ( $i_{ITF}$ ) at low inclinations is that one calculates  $\sin i$  instead of  $\cos i$ . In this inclination regime,  $\sin i \approx i$  while  $\cos i \approx 1$ . We find that our kinematic model inclinations are in agreement with inverse Tully-Fisher inclinations. The standard deviation of the difference between these two inclinations is  $5.9^\circ$ ; the two inclinations have a correlation coefficient of 0.73 (Figure 3.20). We also calculated inverse Tully-Fisher inclinations using the  $H\alpha$  model values for  $V_{\text{rot}}$  and found a very similar relationship: the standard deviation between the inclination differences was  $4.5^\circ$  with a correlation coefficient of 0.78.

The difference between inverse Tully-Fisher inclinations and our kinematic inclinations was comparable to mean kinematic inclination error of  $3.3^\circ$ . Coupled with the good agreement between the HI line-widths and  $H\alpha$  rotation-speeds, we were confident that our kinematic model fitting and derived inclinations are reasonable, free of significant systematics, and with reliably estimated errors. As such, we use them to construct a face-on Tully-Fisher relation and measure disk ellipticity for our sample in Chapter 5.

### 3.6 Summary

We gathered  $H\alpha$  emission-line data for 39 nearly face-on spiral galaxies with the DensePak IFU on WIYN. From the spectrally resolved emission-line data we derived

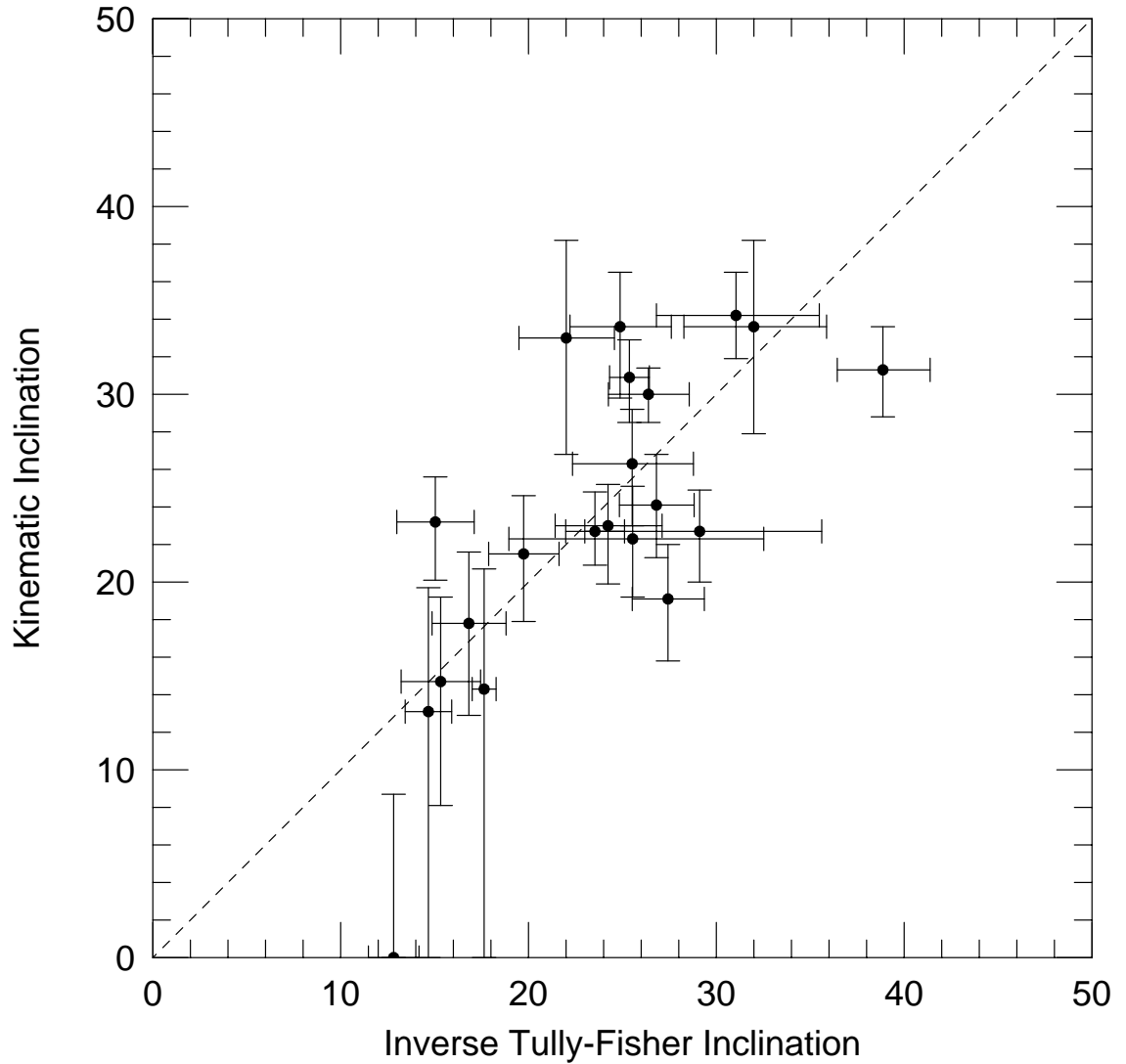


Fig. 3.20. Kinematic versus inverse Tully-Fisher inclinations, as defined in text, for our sample. This shows our kinematic inclination angles are consistent with inverse Tully-Fisher inclinations. Inverse Tully-Fisher inclinations were calculated using  $R$ -band magnitudes and the Tully-Fisher coefficients determined by Courteau (1997) for quiescent Hubble flow galaxies. The standard deviation of the difference is only  $5.9^\circ$ , just slightly larger than the mean kinematic inclination error of  $3.3^\circ$ .

fluxes, widths, centroids and mean continuum levels. Using the line centroids, we created  $H\alpha$  velocity-field maps and rotation curve diagrams. The high quality DensePak velocity fields clearly showed rotation and the position angle of the kinematic major axis for galaxies with observed rotation velocities as low as 50 km/s. We also presented surface brightness profiles produced from maps of the continuum levels. These surface brightness profiles indicate DensePak observations could be used to measure equivalent widths and absorption line features. We also augmented the available HI line profiles gathered from the literature with new 21-cm observations from the Nançay radio telescope. We measured line widths and HI fluxes from these HI line profiles.

We detected kinematic asymmetries in several galaxies through different means. Three galaxies had substantially lopsided HI profiles. Seven galaxies exhibited significant rotation curve asymmetries, and six galaxies showed kinematic twists that are a signature of spiral arm distortions. Kinematic asymmetries did not correlate with either photometric asymmetry or other modes of kinematic asymmetry. The lack of a relation between different asymmetry parameters is perhaps surprising; many of the theories which describe physical mechanisms behind disk asymmetry would excite both kinematic and photometric modes. More work is needed before the physical basis for photometric and disk asymmetry can be achieved.

We successfully fit the observed two-dimensional velocity fields with a simple hyperbolic-tangent velocity-field model. From these fits kinematic inclinations, position angles, rotation speeds and disk rotation scale-lengths were derived for 36 of the 39 sample galaxies. The resulting sample distribution in inclination and rotation speeds is shown in Figure 3.21. Our sample have inclinations less than  $40^\circ$ , and rotation velocities

less than 120 km/s. The range of kinematic inclinations for our sample is consistent with selecting galaxies with photometric inclinations less than  $30^\circ$  (as per our criteria in Chapter 2) if disk ellipticity is  $\sim 5\text{--}10\%$ .

The key to measuring disk ellipticity and creating a face-on Tully-Fisher relation is accurate and precise measures of kinematic inclination angles. We tested the accuracy of our kinematic model fits by comparing model parameters to with indices measured from HI line profiles. Measured rotation speeds were consistent with HI line widths for observed rotation speeds greater than 30 km/s. Kinematic inclination angles were also consistent with inverse Tully-Fisher inclinations derived from HI line widths and absolute  $R$ -magnitudes (tabulated in Chapter 2).

We believe that the precision of our kinematic inclinations has been increased by abandoning tilted-ring fits for these  $H\alpha$  velocity fields. The prime motivation for using tilted ring fits does not apply to our sample; we are not detecting  $H\alpha$  at radii where warping is of concern. Specifically, we do not observe large position angle twists for our sample. Hence, a single model can be employed which greatly increases our precision. We also weigh all data equally, in contrast to tilted ring fits which ignore data in regions which are most sensitive to difference between different inclinations. This gives us further gains in precision over the traditional methods used with HI velocity fields. Inclinations errors measured using  $\chi^2$  statistics are consistent with inclination errors derived from Monte Carlo simulations and are of higher precision than other face-on inclination measures.

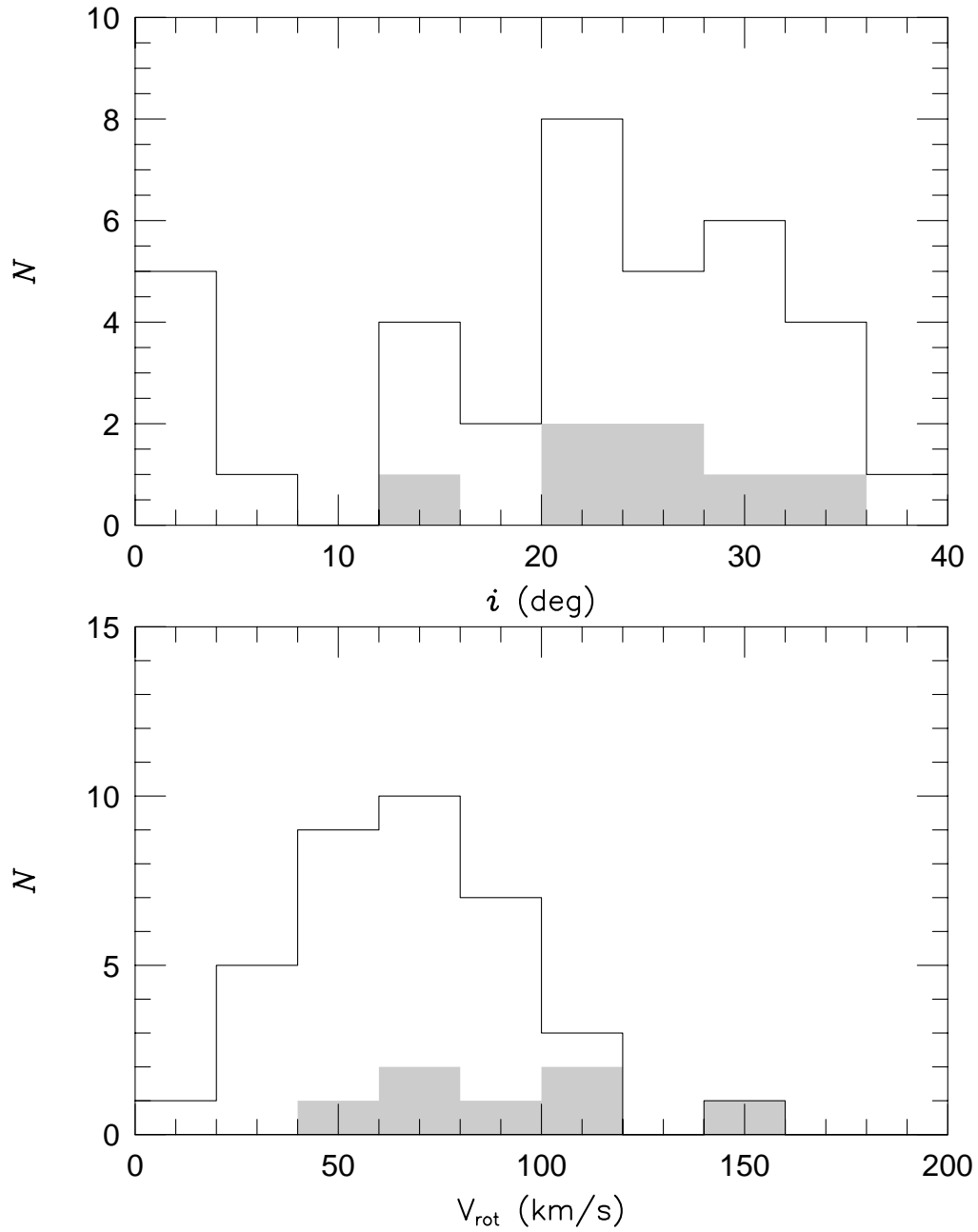


Fig. 3.21. Distribution of derived inclination angles and rotation velocities for 36 sample galaxies. Galaxies in our pilot study (Andersen *et al.* 2001) are shaded in grey. Our complete sample tends to have galaxies with lower rotation velocities and inclinations, although there appears to be a deficit of galaxies with inclinations less than  $20^\circ$ . (The excess of galaxies with inclinations of zero is not real. These galaxies all have very large errors on their inclinations, and help to fill in the gap between 4 and 12 degrees.)

In summary, kinematic inclination estimates using  $H\alpha$  kinematic data from DensePak in this survey are accurate with a typical precision of less than  $5^\circ$  for inclinations greater than  $15^\circ$ .



## Chapter 4

### Disk Ellipticity

#### Abstract<sup>1</sup>

We present measurements of disk ellipticity calculated from photometric and kinematic disk indices for 28 spiral galaxies. Measurements of disk ellipticity help constrain the shape of dark matter halos, and can be used to put limits on the fraction of Tully-Fisher scatter due to other astrophysical processes. We describe a method for measuring galaxy disk elongation,  $\epsilon_D$ , from differences between photometric and kinematic inclination and position angles. The mean disk ellipticity for our sample is  $\overline{\epsilon_D} = 0.084 \pm 0.053$ . If we assume the halo potential is non-rotating and has a constant elliptical distortion, we can estimate a halo ellipticity of  $\overline{\epsilon_\Phi} = 0.065 \pm 0.041$  which is slightly high, but consistent with previous estimates of halo ellipticity. Our measurements of disk ellipticity correlate with other disk properties, including luminosity, surface brightness, and image concentration. Based on these relations, we suggest that disk ellipticities are correlated with masses of dark matter halos. Finally, we show that if most spiral galaxies in TF studies have comparable ellipticities, approximately 0.15 magnitudes of TF scatter would be due to disk ellipticity.

---

<sup>1</sup>Andersen, D.R., Bershady, M.A. & Sparke, L.S., 2001, *to be submitted to Ap.J.*

## 4.1 Introduction

As outlined in Chapter 1, disk ellipticity appears to be linked to the shape of the dark matter halo. Here, we repeat arguments linking disk ellipticity to halo shape in greater detail with an emphasis on the importance of measuring disk ellipticity, the difficulties of the measurement, and the attempts made at estimating disk ellipticity to date.

Binney (1978) was the first to show triaxial halos could affect disks by inducing warping and twists seen in many disks. Triaxial halos have also been shown to induce global asymmetries in disks (e.g., Weinberg 1995; Jog 1997). In particular, the axis ratio of halos lead to disks which are intrinsically elliptical (Franx & de Zeeuw 1992; Jog 2000). Hence the ellipticity of disks may plausibly be used to estimate the axis ratios of dark matter halos. However, it has been a challenge to measure disk ellipticity because it is difficult to disentangle the intrinsic shape of galaxy disks from both projection effects and spiral structure (e.g. Zaritsky & Rix 1995; Schoenmakers *et al.* 1997). If better estimates of ellipticity existed, tighter limits could be placed on halo triaxiality.

Halo triaxiality could either arise through tidal interactions or may be a result of the formation process. Numerical simulations have produced disk galaxy halos which are highly triaxial (Dubinski & Carlberg 1991), but other physical processes, such as the dissipative infall of gas during formation, may transform the halo into an oblate spheroid with  $a = b$  in the plane of the galaxy with the scale height of the halo  $c < a$  (Dubinski 1994). Even after dark matter halos have formed, tidal interactions may lead to triaxial halos (Weinberg 1995). Once measurements of disk ellipticity become

available, questions about the degree of halo triaxiality and the causes of halo triaxiality can begin to be addressed.

Binney & de Vaucouleurs (1981) were the first to notice that there was a deficit of galaxies which appeared to be photometrically face-on when they examined the axis ratio distribution of spiral and lenticular galaxies in the Second Reference Catalog (RC2). The distribution of axis ratios shows a deficit of objects with both  $b/a \approx 0$  and  $b/a \approx 1$ . These two ends of the distribution are virtually independent of each other and depend on the intrinsic distribution of  $c/a$  and  $b/a$  respectively. We have recreated this analysis using the PGC here (Figure 4.1). Several studies have concluded the intrinsic axis ratio of galaxy disks is  $b/a \sim 0.9$  (Grosbol 1985; Huizinga & van Albada 1992; Lambas, Maddox, & Loveday 1992; Magreli, Bettoni, & Galletta 1992; Fasano *et al.* 1993). Results of these studies are statistical at best and are suspect because measured photometric axis ratios can be affected by other asymmetries such as spiral structure.

If one describes galaxies in terms of a Fourier analysis, disk ellipticity contributes to the overall  $m = 2$  Fourier amplitude. Greater contributions to the  $m = 2$  component can come, however, from spiral arms or projection effects. Rix & Zaritsky (1995) pioneered a study of the  $m = 2$  Fourier components of disk galaxies, including disk ellipticity, by selecting spiral galaxies with HI narrow line widths. They assigned inclinations to sample galaxies by inverting the Tully-Fisher relation (Tully & Fisher 1977; hereafter TF) and solving for the disk inclination. These “inverse Tully-Fisher” inclinations should be quite accurate for nearly face-on systems based on simple geometric arguments of projection. Rix & Zaritsky then measured the  $m = 2$  Fourier amplitude,  $A_2$ , from  $K$ -band images to minimize the effect of spiral structure. They found values of

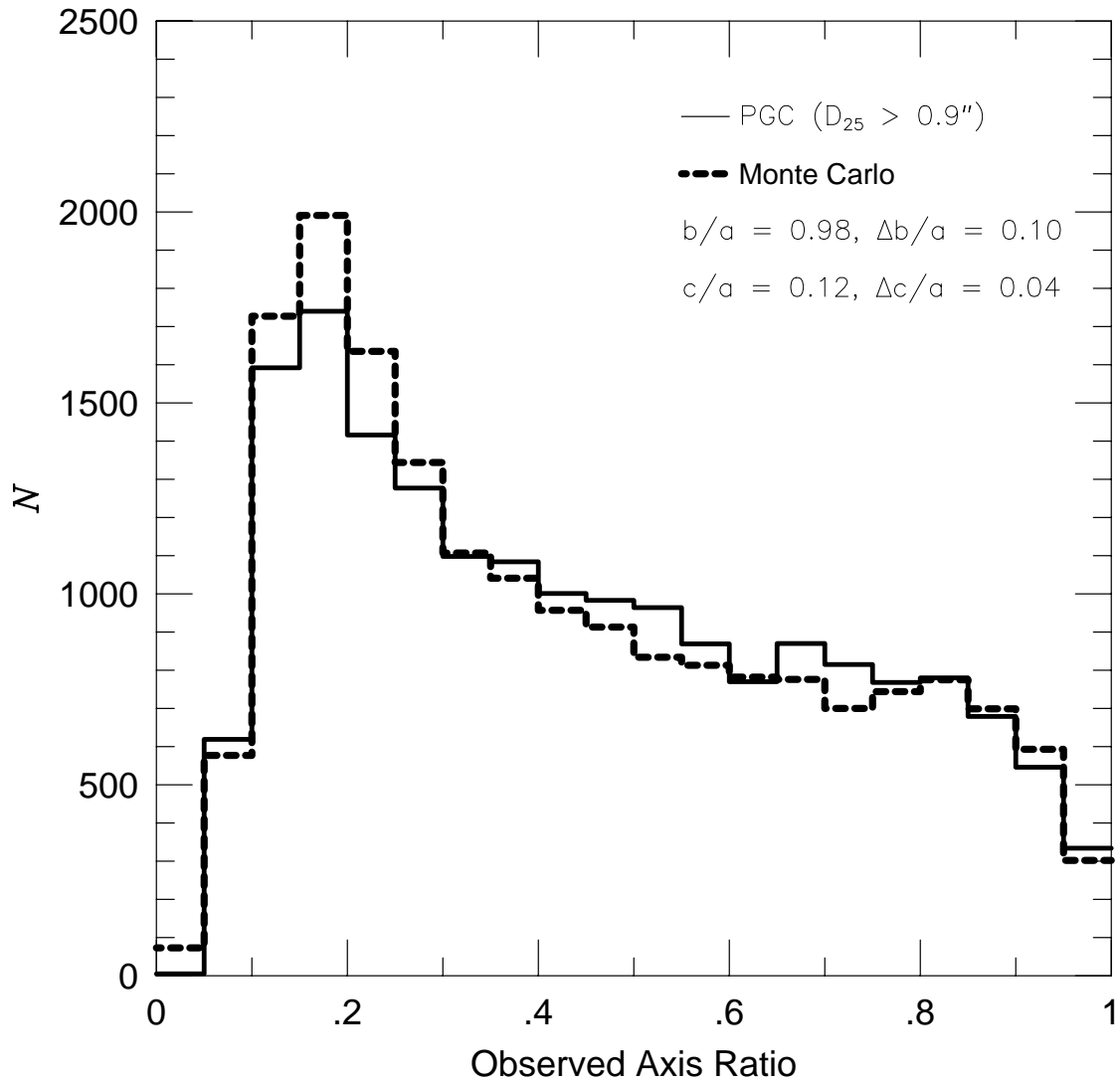


Fig. 4.1. Axis ratios for all galaxies in the PGC with diameters  $D_{25} > 0.9'$ . The sample shows a clear deficit of galaxies with axis ratios close to 1 or 0. We fit a model to these data that allowed for a mean axis ratio and scatter about the mean. The best fit mean intrinsic axis ratio for the sample was 0.98. However, axis ratios can not be greater than unity by definition, thus the scatter tends to lead to many more galaxies with intrinsic axis ratios less than 0.98 than greater than 0.98. Thus, the mean observed intrinsic axis ratio is 0.9.

$A_2$  which were significantly greater than expected from disks at these low inclinations. While they conjectured that this effect was due to disk ellipticity, even if disks were absolutely face-on ( $i = 0$ ), measuring ellipticity is a complicated analysis because of spiral arm structure.

For galaxies with low, but non-zero, inclinations, the above analysis becomes yet more complicated. For example, one would expect a random phase angle,  $\phi$ , between the major axis of the elliptical disk and the kinematic major axis (Figure 4.2). Without knowledge of this parameter, Rix & Zaritsky assumed the distribution of phase angles,  $\phi$ , was uniform. They used a simple relation between disk ellipticity and the potential ellipticity based on a model of an exponential disk sitting in a potential with constant ellipticity,  $\epsilon_\Phi$ , to relate the disk ellipticity,  $\epsilon_D$ , to the ellipticity of the potential by

$$\epsilon_D(R) = (1 + h/R)\epsilon_\Phi \quad (4.1)$$

where  $h$  is the scale length. Based on these assumptions, the mean ellipticity of the potential for Rix & Zaritsky's sample of 19 spiral galaxies is  $\overline{\epsilon_\Phi} = 0.045^{+0.03}_{-0.02}$ .

A similar analysis can be done for velocity fields. Schoenmakers *et al.* (1997) described a harmonic analysis of HI velocity fields which were used to measure  $\epsilon_\Phi \sin(2\phi)$ . The amplitude of  $\epsilon_\Phi \sin(2\phi)$  varied from 0.001 to 0.07 for a sample of seven galaxies; assuming a random distribution of  $\phi$ ,  $\overline{\epsilon_\Phi} = 0.049 \pm 0.014$  for these disk galaxies (Schoenmakers 1999).

Each of the above estimates of disk or potential ellipticity have been statistical in nature. Without knowledge of the phase angle,  $\phi$ , one can not make an independent

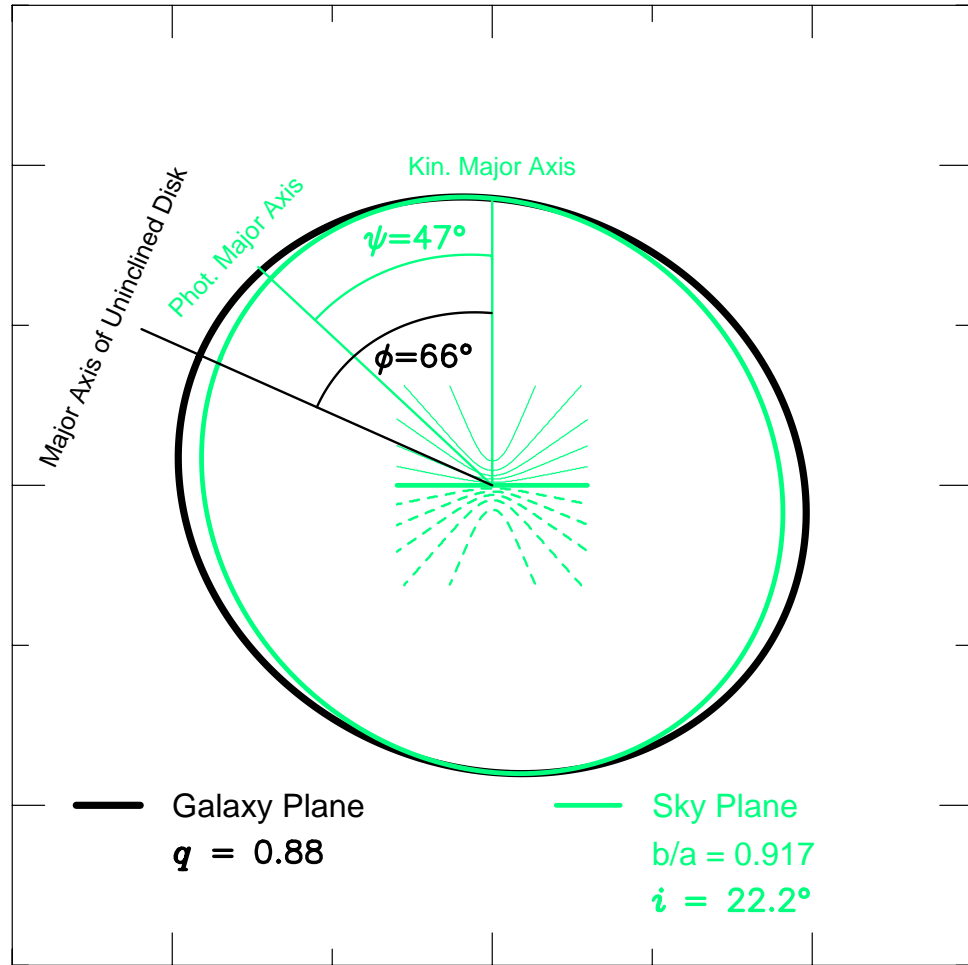


Fig. 4.2. The dark ellipse represents a galaxy isophote in the galaxy plane ( $i = 0^\circ$ ) for a galaxy with an intrinsic axis ratio of  $q = 0.88$ . This galaxy has already been rotated by a phase angle  $\phi = 66^\circ$  (dark dashed line). The ellipse can be represented by the vector  $\vec{r}'$  described above. The same ellipse viewed in the sky plane after inclining it  $22.2^\circ$  is light. The resultant ellipse ( $\vec{r}''$ ) has an observed axis ratio of  $\frac{b}{a} = 0.917$  and a difference of position angles of  $\psi = 47^\circ$  (light solid line). The difference between  $\phi$  and  $\psi$  (according to the approximation in the text) is  $\theta_{\max}$  and for this example equals  $19^\circ$ .

measure of  $\epsilon_D$  or  $\epsilon_\Phi$ . Due to small statistics or suspect measurements of disk axis ratios, the results of these estimates of ellipticity are uncertain. Without larger samples and a method to make an independent measure of ellipticity, the variations in disk ellipticity will not be known.

The first independent measurement of both  $\epsilon_\Phi$  and  $\phi$  was made for the Milky Way. Using a specific model for the rotation curve and assuming constant ellipticity with radius, Kuijken & Tremaine (1991) used a variety of properties measured from both the local neighborhood and from global Galactic properties to constrain  $\epsilon_\Phi(\text{MW}) \cos(2\phi)$ . Galactic measures needed to constrain  $\epsilon_\Phi(\text{MW}) \cos(2\phi)$  include Oort constants, the axis ratio of the velocity ellipsoid, the radial velocity of the local standard of rest relative to the Galactic center, HI tangent point velocities, velocity fields of tracer objects such as Carbon stars and Cepheids, and kinematics of distant HI gas. They found  $\epsilon_\Phi(\text{MW}) = 0.1$ . However, the analysis of the ellipticity of the Milky Way requires assumptions about the local standard of rest and the distance of the sun to the center of our Galaxy. These measurements, and therefore the measurement of  $\epsilon_\Phi(\text{MW})$ , are uncertain, and have different potential systematics than  $\epsilon_\Phi$  studies of external galaxies.

As part of a pilot study we demonstrated a new method for determining disk ellipticity, based on differences in kinematic and photometric inclination and position angles (Andersen *et al.* 2001). Kinematic parameters were measured from H $\alpha$  velocity fields observed using DensePak (Barden, Sawyer & Honeycutt 1998) on the WIYN 3.5m telescope while photometric axis ratios and position angles were measured from WIYN *I*-band images. Using our method to measure disk ellipticity, we found that seven galaxies had  $0.01 < \epsilon_D < 0.20$ . The mean disk ellipticity for our pilot study galaxies was

$\bar{\epsilon}_D = 0.05 \pm 0.01$ . This measurement of disk ellipticity is consistent with other estimates of disk ellipticity which assume a random distribution of phase angles,  $\phi$ , for small numbers of galaxies. Our method allows us to measure both  $\phi$  and  $\epsilon_D$ . With a larger sample of spiral galaxies with a broader range of properties, we hope to better understand the distribution of ellipticities, not just measure a mean and standard deviation, and determine if ellipticity is correlated with other physical parameters.

Measurements of ellipticity are important for putting limits on sources of TF scatter. By assuming a non-rotating potential with a constant triaxial potential, Franx & de Zeeuw (1992) showed that if  $\epsilon_\Phi = 0.1$  then all of the scatter in the TF relation would be induced by ellipticity. The result from our pilot survey implies almost 50% of TF scatter may be due to ellipticity. The total TF “error budget” is relatively small,  $\sim 0.4$  magnitudes of scatter. Contributions to this scatter are numerous and includes combinations of both measurement errors and intrinsic variations in galaxy populations. Since the total amount of TF scatter has been measured, if any one source of TF scatter could be identified and measured, limits would be placed on other sources of astrophysical scatter, such as galaxy mass-to-light ratios. Limits on the variation in galaxy mass-to-light ratios constrain models of the formation histories and content of spiral galaxies.

In this study, we use a sample of 28 spiral galaxies over a range of type and luminosity to measure  $\epsilon_D$  and establish relations between ellipticity and photometric disk properties such as surface brightness, luminosity, concentration index, and disk lopsidedness. We revisit the selection algorithm used for this survey, quantifying the effect ellipticity has at different inclinations, and estimating the error budget on ellipticity in



§4.2. We describe our geometric model of ellipticity in §4.3 and describe the set of equations that can be solved to yield disk ellipticity. We briefly review the photometric and kinematic measurements needed to measure ellipticity in §4.4. If the reader is familiar with our measurements of photometric axis ratios and position angles described in Chapter 2 and our model kinematic inclinations and position angles described in Chapter 3, this section may be skipped without loss of continuity. We use these measurements to calculate disk ellipticity, tabulate the results and describe our error analysis in §4.5. In §4.6, relationships between ellipticity and other disk parameters are described, as well as assessing the impact ellipticity has upon TF scatter. The results are summarized in §4.7.

## 4.2 Ellipticity Survey Constraints

We claimed in Chapter 1 that intrinsic elongation ( $\epsilon_D$ ) for spiral disks is ideally measured at low kinematic inclinations. The magnitude of differences between kinematic and photometric quantities for a given ellipticity as a function of inclination give qualitative reasons for making measurements at low inclination. After examining these differences in greater detail, we bound the range of kinematic inclination in which statistically significant measurements of  $\epsilon_D$  can be made, given realistic error estimates on photometric and kinematic indices.

### 4.2.1 Inclination and Position Angle Differences

The misalignment of photometric and kinematic position angles is an indication of disk elongation. Disks with large differences between photometric and kinematic position

angles,  $\psi$ , can only exist at inclinations where  $i < \cos^{-1}(1 - \epsilon_D)$ . As an example, for  $\epsilon_D = 0.1$ ,  $\psi = 90^\circ$  is possible for  $i < 26^\circ$ . The difference between kinematic and photometric inclinations is greatest at low inclinations. If  $\epsilon_D$  is not 0.1, but closer (and not equal) to one, both  $\psi$  and  $(\frac{b}{a} - \cos i)$  change as a function of inclination. The range of inclinations in which  $\psi = 90^\circ$  exists shrinks, and the magnitude of difference between kinematic and photometric quantities decreases as well. As another example, if  $\epsilon_D = 0.05$ ,  $\psi = 90^\circ$  only for  $i < 18^\circ$ . Figure 4.3 shows both  $\psi$  and  $\frac{b}{a} - \cos i$  as a function of inclination for this example. Notice that measurements from galaxies in our sample fall along the difference curves generated for  $\epsilon_D = 0.05$  in most cases.

#### 4.2.2 Error Budget on Disk Ellipticity

The greatest differences between kinematic and photometric inclination and position angles exist for face-on disks. However, both photometric and kinematic inclination angles become increasingly difficult to measure in face-on systems. As described in §3.4.3.2, the kinematic inclination error increases to  $7^\circ$  at inclinations of  $10^\circ$ , and increases further at lower inclinations. While the errors on axis ratio remain relatively constant with inclination, the error on photometric inclination also increases rapidly at low inclination. Even though effects of disk ellipticity are maximized at low inclinations, it was unclear whether correspondingly higher errors in measurements negate this advantage.

Given that the estimate of mean ellipticity from other studies is  $\sim 0.05$ , we test whether our data is of sufficient quality to make a meaningful measurement of  $\epsilon_D = 0.05$  which requires  $\epsilon_D - \Delta\epsilon_D > 0$ . Assuming a phase angle,  $\phi = 0$ , and a set of measurement

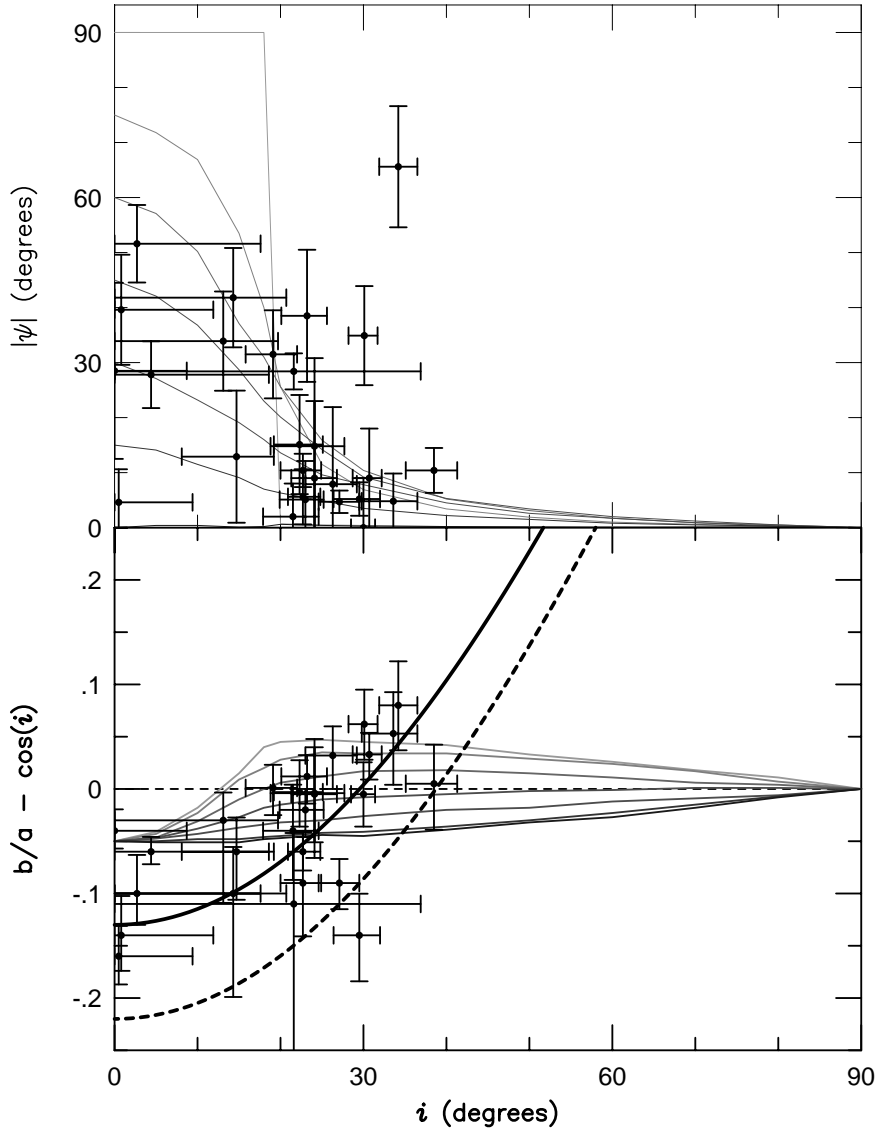


Fig. 4.3. Differences in photometric and kinematic position angles ( $\psi$ ) (top panel) and differences of photometric axis ratios ( $b/a$ ) and  $\cos i$  (bottom panel) versus inclination. Curves illustrate trends for an intrinsic ellipticity ( $\epsilon$ ) of 0.05, for different intrinsic phase angles:  $\phi = 90^\circ, 75^\circ, 60^\circ, 45^\circ, 30^\circ, 15^\circ$  and  $0^\circ$  (line darkness increase for decreasing  $\phi$ ). Measurements of  $b/a$ ,  $i$  and  $\psi$  (discussed in Chapters 2 and 3) are needed to measure disk ellipticity (method and measurements discussed in Chapter 4). In the top panel, the density of points in the region of overlapping  $\phi$  suggest the intrinsic ellipticity for much of our sample is roughly 5%. As ellipticity increases,  $\phi$  curves stretch out to larger radii; the cutoff in  $\psi$  occurs at roughly  $\cos^{-1}(1 - \epsilon)$ . In the bottom panel, the heavy solid line indicates the selection effect of choosing galaxies with  $b/a > 0.87$ . The heavy dotted line corresponds to  $b/a + \delta b/a > 0.87$ . Notice data does not fall above the  $\epsilon = 0.05$  curves. As  $\epsilon$  increases, the model curves describing the difference in  $b/a - \cos i$  for different  $\phi$  broaden, encompassing both more negative and more positive differences.

errors:  $\Delta \frac{b}{a} = 0.02$ ,  $\Delta \psi = 5^\circ$ , and a smoothly varying error in inclination (Figure 3.16),  $\Delta \epsilon_D < 0.05$  for all  $i < 48^\circ$  (Figure 4.4). There is sharp upturn in  $\Delta \epsilon_D$  at  $i \approx 35^\circ$ . For a second set of measurement errors more typical of our measurements ( $\Delta \frac{b}{a} = 0.04$  and  $\Delta \psi = 10^\circ$ )  $\Delta \epsilon_D < 0.05$  for  $i < 25^\circ$ . This simple error analysis justifies our selection of nearly face-on galaxies for the purpose of measuring disk ellipticity.

### 4.3 Method for Measuring Disk Ellipticity

In this section, we describe a geometric model of disk ellipticity. We begin by describing the transformation of coordinates for an elliptic disk from the galaxy plane to the observer's plane. With this description of disk ellipticity in the observer's plane, we describe the constraints on the model which allow us to solve for disk ellipticity.

#### 4.3.1 Coordinates

The coordinate system was chosen so the major axis of the unrotated ellipse would fall on the y-axis and positive rotation angles would be measured counter clock-wise (same as position angle measures; Figure 4.2). For convenience, we define the intrinsic disk axis ratio,  $q \equiv (1 - \epsilon_D)$ .

The model is based on the ability of describing a galaxy isophote in the galaxy plane (inclination,  $i = 0$ ) as an ellipse:

$$\vec{r} = \begin{pmatrix} -q \sin \theta \\ \cos \theta \end{pmatrix} \quad (4.2)$$

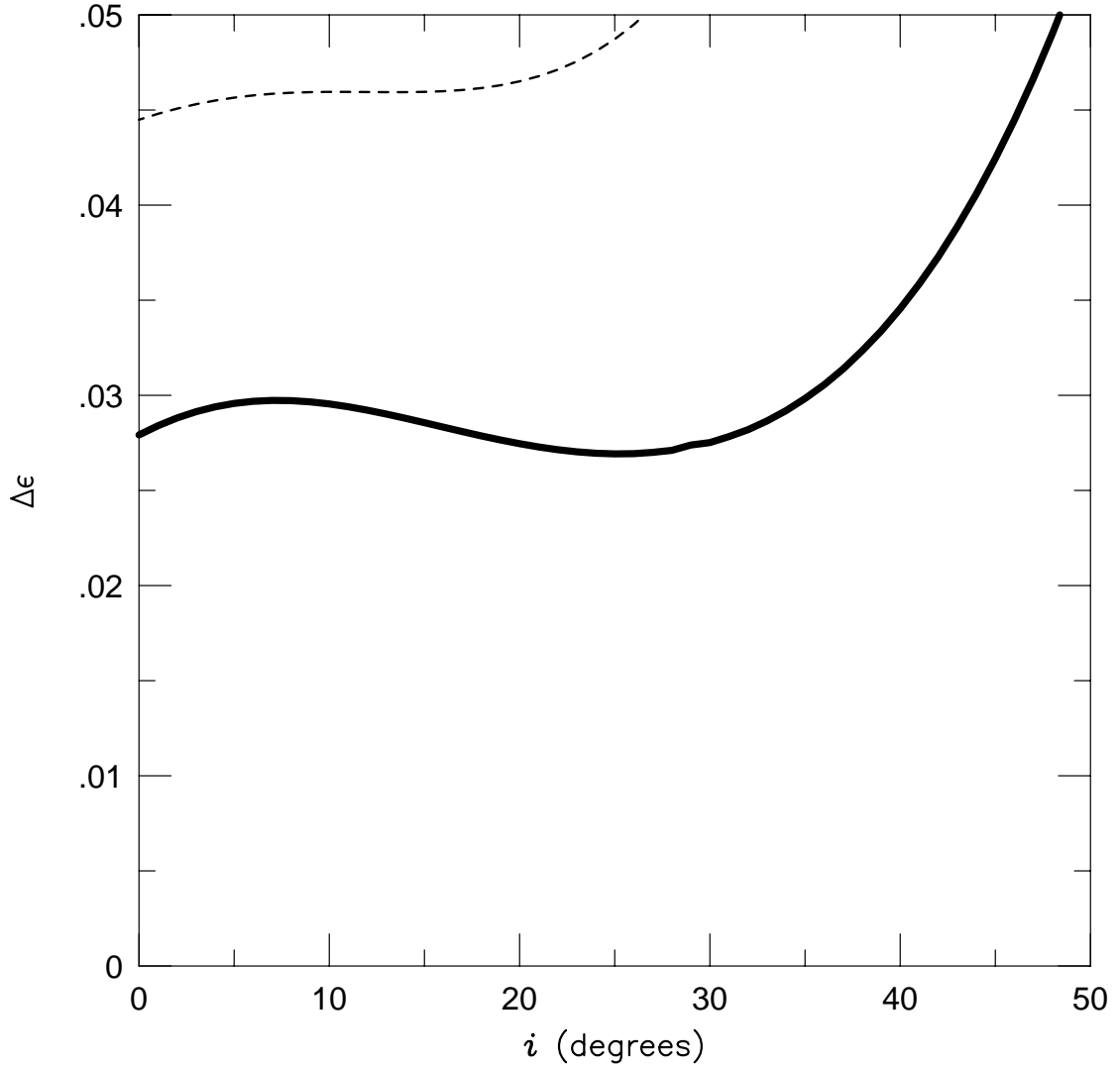


Fig. 4.4. Errors in intrinsic ellipticity  $\Delta\epsilon$  versus inclination calculated from expected errors on kinematic inclination, photometric axis ratio ( $b/a$ ) and the difference in kinematic and photometric position angles ( $\psi$ ). Both solid and dashed curves assume the same kinematic errors as a function of inclination. Errors were estimated from Monte Carlo simulations (for  $i = 5^\circ, 10^\circ$  and  $20^\circ$ ,  $\Delta i = 9^\circ, 5^\circ$  and  $2.5^\circ$  respectively). The solid curve used  $\Delta b/a = 0.2$  and  $\Delta\psi = 4^\circ$ . The dashed curve used  $\Delta b/a = 0.4$  and  $\Delta\psi = 10^\circ$ . To reliably measure  $\epsilon < 0.05$  we need to choose galaxies with inclinations less than 30 degrees.

where  $\theta$  is a free angle such that as it varies from 0 to  $2\pi$ ;  $\vec{r}$  traces out an ellipse. In order to account for all viewing angles, this ellipse is rotatable by a phase angle  $\phi$  *before* being inclined about the original (un-rotated) minor axis:

$$\vec{r}' = \begin{pmatrix} \cos \phi & -\sin \phi \\ \sin \phi & \cos \phi \end{pmatrix} \begin{pmatrix} -q \sin \theta \\ \cos \theta \end{pmatrix} = \begin{pmatrix} -\cos \theta \sin \phi - q \cos \phi \sin \theta \\ \cos \phi \cos \theta - q \sin \phi \sin \theta \end{pmatrix} \quad (4.3)$$

where  $\phi$  is defined as a counter clock-wise rotation from the original major axis, i.e. perpendicular to what will become the line of nodes after the ellipse is inclined.

The vector  $\vec{r}''$  describes the inclined ellipse in the observer's plane (of which we only see 2 dimensions – the z component of the vector is left out here. Again refer to Figure 4.2):

$$\vec{r}'' = \begin{pmatrix} \cos i & 0 \\ 0 & 1 \end{pmatrix} \begin{pmatrix} -\cos \theta \sin \phi - q \cos \phi \sin \theta \\ \cos \phi \cos \theta - q \sin \phi \sin \theta \end{pmatrix} = \begin{pmatrix} -\cos i (\cos \theta \sin \phi + q \cos \phi \sin \theta) \\ \cos \phi \cos \theta - q \sin \phi \sin \theta \end{pmatrix} \quad (4.4)$$

where  $i$  is the inclination angle. To make notation clearer later,  $x(q, \theta, \phi, i)$  and  $y(q, \theta, \phi, i)$  are defined such that:

$$\vec{r}'' = \begin{pmatrix} x(q, \theta, \phi, i) \\ y(q, \theta, \phi, i) \end{pmatrix}. \quad (4.5)$$

With this basic equation for the ellipse in the observer's plane, the final step is to rotate by a position angle in the sky plane. Since this angle is equated to the kinematic

position angle,  $\text{PA}_{\text{kin}}$ , and since  $\text{PA}_{\text{kin}}$  is well-determined from velocity field models, this step is unnecessary.

#### 4.3.2 Constraints

Note that the vector  $\vec{r}''$  describes an ellipse using three quantities which we can not measure directly from either photometric or kinematic data: the intrinsic elongation,  $q$ , phase angle,  $\phi$ , and parametric angle,  $\theta$ . In order to determine these three unknowns, we construct three equations constraining these quantities using the following disk measurements: kinematic inclination,  $i$ , difference in kinematic and photometric position angles,  $\psi \equiv \text{PA}_{\text{phot}} - \text{PA}_{\text{kin}}$ , and photometric axis ratio,  $\frac{b}{a}$ .

Since  $\theta$  is a variable, it needs to be constrained to a single value. This can be done arbitrarily, so we choose to define  $\theta_{\text{max}}$  so that  $\vec{r}''$  lies on the major axis of the inclined ellipse. To determine the maximum of  $\vec{r}''$  and impose the first constraint on the three unknowns, we find the root of  $\frac{\partial \vec{r}''}{\partial \theta}$  (where the second derivative is negative) and define  $\theta$  at this point to be  $\theta_{\text{max}}$ . For convenience, we rename:

$$R^2 = |\vec{r}''|^2 = \cos^2 i (\cos \theta \sin \phi + q \sin \theta \cos \phi)^2 + (\cos \theta \cos \phi - q \sin \theta \sin \phi)^2. \quad (4.6)$$

The first constraint on  $q$ ,  $\phi$ , and  $\theta$  is:

$$\begin{aligned} \left. \frac{\partial R^2}{\partial \theta} \right|_{\theta_{\text{max}}} = 0 &= 2 \cos^2 i (\cos \theta_{\text{max}} \sin \phi + q \sin \theta_{\text{max}} \cos \phi) (q \cos \theta_{\text{max}} \cos \phi - \sin \theta_{\text{max}} \sin \phi) \\ &- 2 (\cos \theta_{\text{max}} \cos \phi - q \sin \theta_{\text{max}} \sin \phi) (\sin \theta_{\text{max}} \cos \phi + q \cos \theta_{\text{max}} \sin \phi). \end{aligned} \quad (4.7)$$

The second constraint is an expression for the difference between photometric and kinematic position angles ( $\psi$ ):

$$\tan \psi = \frac{-x}{y} = \frac{\cos i (\cos \theta_{max} \sin \phi + q \sin \theta_{max} \cos \phi)}{\cos \theta_{max} \cos \phi - q \sin \theta_{max} \sin \phi}. \quad (4.8)$$

Since we have measured the photometric axis ratio for galaxies, we can use this as a third and final constraint on the observed ellipse. Maxima and minima of the ellipse are separated by  $90^\circ$  in  $\theta$ . This allows us to write:

$$\left(\frac{b}{a}\right)^2 = \left(\frac{R|_{\theta_{min}}}{R|_{\theta_{max}}}\right)^2 = \left(\frac{R|_{\theta_{max}+90^\circ}}{R|_{\theta_{max}}}\right)^2 = \frac{\cos^2 i (q \cos \theta_{max} \cos \phi - \sin \theta_{max} \sin \phi)^2 + (\sin \theta_{max} \cos \phi + q \cos \theta_{max} \sin \phi)^2}{\cos^2 i (q \sin \theta_{max} \cos \phi + \cos \theta_{max} \sin \phi)^2 + (\cos \theta_{max} \cos \phi - q \sin \theta_{max} \sin \phi)^2}. \quad (4.9)$$

Equations 4.6–4.8 are a set of three non-linear equations with three unknowns,  $q$ ,  $\theta_{max}$  and  $\phi$  for which we can solve using the Newton–Raphson method (Press *et al.* 1992).

To check our solutions, we use an approximation for equation 4.8, obtained if  $q \approx 1$  and  $i \approx 0$ :

$$\tan \psi \approx \tan(\theta_{max} + \phi). \quad (4.10)$$

This approximation seems to hold for all sample galaxies. Graphical solutions can be obtained by using the approximation for  $\psi$  (Equation 4.10) to replace  $\theta_{max}$  in equations 4.7 and 4.9, and then rewriting these equations in terms of quadratic equations of  $q$ . The intersection of  $q$  and  $\phi$  for graphs of these quadratic equations are solutions to equations



4.7–4.9. We have found that these solutions are consistent with the Newton-Raphson method solutions (e.g., see Figure 4.5).

## 4.4 Observations

Before we use the above set of equations to solve for the disk ellipticity,  $\epsilon_D \equiv 1 - q$ , of our sample, we review the observations described in detail in Chapters 2 and 3. We draw upon critical measurements from this observational foundation including photometric axis ratios ( $b/a$ ), photometric position angles ( $\text{P.A.}_{\text{phot}}$ ), kinematic inclinations ( $i$ ), and kinematic position angles ( $\text{P.A.}_{\text{kin}}$ ).

### 4.4.1 Sample Selection

We selected galaxies for the survey from the Principal Galaxy Catalog (PGC; Paturel *et al.* 1997) based on (1) axis ratio,  $b/a + \Delta b/a > 0.87$  ( $i - \delta i < 30^\circ$ ), (2) apparent disk size,  $45'' < D_{25} < 75''$ , (3) galactic absorption,  $A_B < 0.6$  (Schlegel, Finkbeiner & Davis 1998), (4) declinations visible from WIYN,  $\delta_{1950} > -10^\circ$ , (5) observed  $B$ -band magnitudes, (6) observed recession velocities, and (7)  $t$ -types ranging from Sab to Sd ( $t$ -types between 1.5–8.5).

We obtained Second Generation Digitized Sky Survey (DSS2) images of these potential targets. After visual inspection, we eliminated from our sample, galaxies with bars, rings, interacting companions, or foreground stars that contaminated the inner isophotes. We measured photometric position angles and axis ratios from the DSS2 images using the *IRAF ellipse* routine. Our sample was further refined by requiring (1)

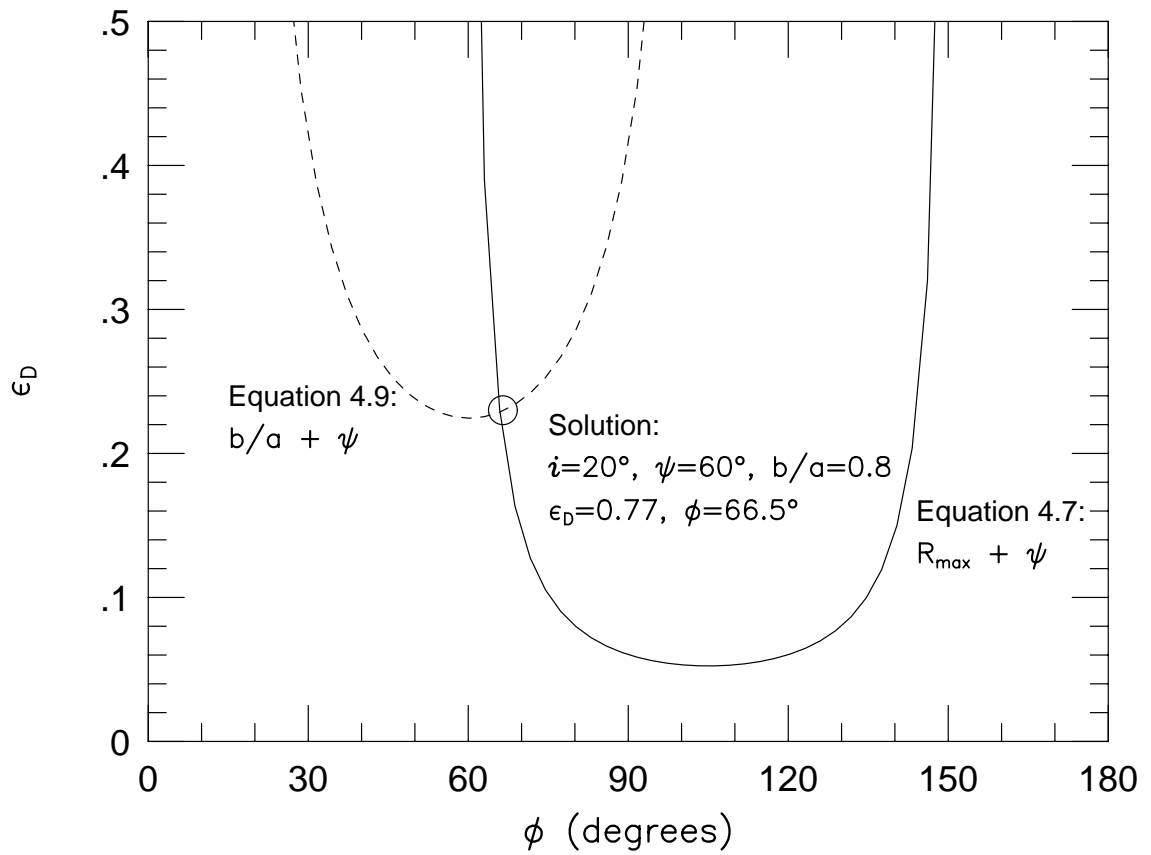


Fig. 4.5. Newton-Raphson and graphical solution for galaxy with inclination of  $20^\circ$ , difference in position angle of  $\psi = 60^\circ$  and observed photometric axis ratio  $b/a = 0.8$ . The dashed curve is the quadratic equation that results if the assumption used to make Equation 4.10 hold, and is used to simplify Equation 4.9. The solid curve again assumes Equation 4.10 holds, and simplifies Equation 4.7.

the photometric position angle to be relatively constant in the outer portions of the disk and (2) our measurements of  $b/a > 0.87$ .

#### 4.4.2 Observations

We obtained  $R$  and  $I$ -band imaging and  $H\alpha$  velocity fields for 39 galaxies which met the above selection criteria. Imaging observations were acquired over 2.5 years from May, 1998 to January, 2001 at the WIYN 3.5m telescope at KPNO, the 2.1m telescope at KPNO, and the Harlan J. Smith 2.7m telescope at McDonald Observatory.

$H\alpha$  velocity fields were obtained using the DensePak integral field unit on the WIYN telescope during 11 nights on 6 separate observing runs. DensePak is an array of 91 fibers arranged in a seven by thirteen fiber rectangle sub-tending an area of  $30'' \times 45''$ .

DensePak feeds the WIYN Bench Spectrograph, a fiber-fed spectrograph designed to provide low to medium resolution spectra. We used the Bench Spectrograph camera (BSC) and 316 lines/mm echelle grating in order 8 to cover  $6500\text{\AA} < \lambda < 6900\text{\AA}$ , with a dispersion of  $0.195\text{ \AA/pix}$  ( $8.6\text{ km/s/pix}$ ) and an instrumental FWHM of  $0.51\text{ \AA}$  ( $22.5\text{ km/s}$ ). We required the highest resolution available with this instrument; fitting velocity field models to galaxies with observed rotation velocities of less than  $100\text{ km/s}$  required centroids with accuracies of roughly  $5\text{ km/s}$ .

#### 4.4.3 Photometric Measures

We required three conditions to be met within an annulus for a measurement of photometric axis ratio and position angle to be made: (1) the spiral structure index,

$\Sigma(R) \equiv \frac{\sigma(R)}{(\sigma_S^2(R) + \sigma_B^2)^{1/2}}$ , should be unity or have just shown a large break towards smaller values, (2) the annulus must be roughly between three and four scale lengths, and (3) P.A.<sub>phot.</sub> and  $b/a$ , determined by the IRAF *ellipse* routine should be constant in the annulus. Changing measures of P.A.<sub>phot.</sub>'s or  $b/a$  indicated either warping or spiral arms were affecting *ellipse* fits.

Not all galaxies in our sample met these criteria. **PGC 2162**, **PGC 23913**, **PGC 24788** and **PGC 72453** had strong spiral arms which persisted to the faintest isophotal levels fit by *ellipse*. **PGC 70962** had a very large spiral structure index out to five scale lengths. **PGC 5345** and **PGC 7826** do not show strong spiral structure, but outer isophotes have non-constant, twisting position angles consistent with warping. **PGC 14564**, **PGC 20938**, **PGC 26517** and **PGC 56010** show trends in either increasing or decreasing axis ratios. Therefore we were unable to measure axis ratios and position angles, and hence unable to measure ellipticity, for these 11 galaxies (28% of sample). For the remaining galaxies, we chose an annulus roughly between three and four scale lengths in which to make measurements of P.A. and  $b/a$  (Table 2.9).

#### 4.4.4 Kinematic Measures

We fit velocity-field models to each galaxy's observed kinematic data from DensePak using non-linear  $\chi^2$  minimization. Although the velocity-field residuals were small, typically less than 6 km/s, our velocity centroiding errors were even smaller, resulting in minimum reduced- $\chi^2$ ,  $\chi_\nu^2$ , for these fits which were typically much greater than unity ( $2 < \chi_\nu^2 < 15$ ). In order to measure errors on our velocity-field model parameters, we

adopted a modified  $\chi^2$  sum. Specifically, we added into the  $\chi^2$  sum (Rix *et al.* 1997):

$$\chi_\delta^2 = \sum_i \frac{(V_{\text{mod}_i} - V_{\text{obs}_i})^2}{\sigma_{\text{mod}}^2 + \sigma_{\text{obs}_i}^2}. \quad (4.11)$$

For each galaxy, we chose a value for  $\sigma_{\text{mod}}$  which normalized the reduced- $\chi_\delta^2$  to unity based on an initial fit using the standard  $\chi^2$  definition. We were able to generate velocity-field fits for 36 of the 39 sample galaxies (a 90% success rate). Only PGC 5345, PGC 23913 and PGC 70962 do not have measured kinematic inclination and position angles.

Once galaxies were fit with our velocity field and the reduced- $\chi_\delta^2$  was unity, we assumed the error distribution was Gaussian and used the standard differences in  $\chi^2$  to map out confidence intervals in parameter space. Table 3.5 contains kinematic inclinations, position angles and error estimates for 36 sample galaxies.

## 4.5 Ellipticity Estimates

Using Equations 4.6–4.8 and the measurements of photometric axis ratios,  $b/a$ , photometric position angles,  $\text{P.A.}_{\text{phot.}}$ , kinematic inclination angles,  $i$ , and kinematic position angles,  $\text{P.A.}_{\text{kin.}}$ , we were able to determine solutions for disk ellipticity for 28 sample galaxies. We calculated a mean disk ellipticity,  $\epsilon_D = 0.084 \pm 0.053$ , and a median disk ellipticity,  $\epsilon_{D,\text{med.}} = 0.64$ .

Before attaching significance to the above measurements of disk ellipticity, we must establish whether our sample of galaxies are indeed elliptical by asking how many disks have ellipticity solutions consistent with  $\epsilon_D = 0$ . One method for determining errors on  $\epsilon_D$  and  $\phi$  is to perform a Monte Carlo based on the measurements and errors

associated with  $b/a$ ,  $i$ , and  $\psi$ . One can then map the set of solutions from this Monte Carlo simulation onto the solution plane of  $\epsilon_D$  and  $\phi$ , and identify confidence intervals based on these solutions. These confidence intervals will most likely not include  $\epsilon_D = 0$  as a likely solution, because the mapping from  $b/a$ - $i$ - $\psi$ -space to  $\epsilon_D$ - $\phi$ -space is highly non-linear. Ellipticity is a positive-definite quantity; it takes finely tuned values of  $b/a$ ,  $i$ , and  $\psi$  to have  $\epsilon_D = 0$ . Gaussian errors, therefore, will not include zero as a likely solution.

In order to solve this problem, we developed a method to determine if a given disk ellipticity solution is consistent with  $\epsilon_D = 0$ . We posed the question of whether, given the measurements and an errors ellipsoid on the parameters  $b/a$ ,  $i$ , and  $\psi$ , there would be a solution for  $\epsilon_D = 0$  within a given confidence interval on the error ellipsoid. Figure 4.6 is a cartoon which illustrates the process of mapping an error ellipsoid to the  $\epsilon_D$ - $\phi$  plane. Thus, we are able to test whether the disk ellipticity for sample galaxies is consistent with zero for an error ellipsoid containing 68%, 90%, 95% or 99% of  $b/a$ ,  $i$ , and  $\psi$  measures with Gaussian distributed errors. Using this error ellipsoid mapping instead of the Monte Carlo approach outlined above yields error estimates that are quite conservative. Solutions and contours containing 68% of expected measurements on  $b/a$ ,  $i$ , and  $\psi$  are presented in Figure 6.3 and solutions with these conservative “errors” are tabulated in Table 4.1.

Table 4.1. Disk Ellipticity Parameters

PGC	$b/a$	$i$	$\psi$	$\phi$	$\epsilon$
		deg	deg	deg	
3512	$0.927 \pm 0.030$	$30.1^{+1.6}_{-1.9}$	$34.9 \pm 9.0$	$74.6^{+12.4}_{-14.8}$	$0.129^{+0.052}_{-0.049}$
5673	$0.905 \pm 0.014$	$23.0^{+2.2}_{-3.1}$	$5.1 \pm 7.0$	$24.5^{+90}_{-90}$	$0.023^{+0.043}_{-0.023}$
6855	$0.886 \pm 0.029$	$33.6^{+2.9}_{-3.8}$	$-4.8 \pm 5.0$	$-81.2^{+90}_{-90}$	$0.064^{+0.079}_{-0.064}$
8941	$0.965 \pm 0.017$	$0.0^{+8.7}_{-0.0}$	$-28.5 \pm 16.0$	$-28.5^{+30}_{-43.0}$	$0.035^{+0.032}_{-0.032}$
15531	$0.840 \pm 0.027$	$0.5^{+8.9}_{-0.5}$	$-4.6 \pm 6.0$	$-4.6^{+11.6}_{-11.4}$	$0.160^{+0.051}_{-0.057}$
16274	$0.893 \pm 0.016$	$30.7^{+1.5}_{-2.0}$	$9.0 \pm 9.0$	$70.6^{+90}_{-90}$	$0.054^{+0.063}_{-0.054}$
19767	$0.864 \pm 0.034$	$0.8^{+11.1}_{-0.8}$	$-39.6 \pm 10.0$	$-12.6^{+24.3}_{-14.6}$	$0.136^{+0.064}_{-0.081}$
23333	$0.928 \pm 0.018$	$26.3^{+2.9}_{-3.3}$	$7.9 \pm 14.0$	$75.7^{+90}_{-90}$	$0.042^{+0.071}_{-0.042}$
23598	$0.908 \pm 0.028$	$14.7^{+4.5}_{-6.6}$	$12.9 \pm 12.0$	$19.0^{+43.2}_{-36.6}$	$0.066^{+0.064}_{-0.063}$
26140	$0.798 \pm 0.014$	$27.1^{+2.4}_{-2.5}$	$-4.7 \pm 2.0$	$-9.6^{+7.9}_{-10.9}$	$0.106^{+0.044}_{-0.048}$
27792	$0.788 \pm 0.023$	$38.5^{+2.8}_{-3.4}$	$-10.4 \pm 4.1$	$-52.5^{+34.0}_{-24.7}$	$0.084^{+0.064}_{-0.062}$
28310	$0.907 \pm 0.036$	$34.2^{+2.3}_{-2.3}$	$65.6 \pm 11.0$	$82.0^{+7.2}_{-9.5}$	$0.232^{+0.070}_{-0.064}$
28401	$0.817 \pm 0.022$	$21.6^{+15.3}_{-21.6}$	$28.4 \pm 3.3$	$38.8^{+38.9}_{-15.8}$	$0.159^{+0.158}_{-0.044}$
31159	$0.830 \pm 0.047$	$22.7^{+2.2}_{-2.7}$	$10.4 \pm 3.0$	$17.7^{+32.8}_{-10.2}$	$0.108^{+0.098}_{-0.082}$
32091	$0.900 \pm 0.030$	$2.7^{+14.9}_{-2.7}$	$-51.6 \pm 7.0$	$-51.8^{+13.4}_{-24.4}$	$0.100^{+0.090}_{-0.056}$
32638	$0.922 \pm 0.025$	$22.3^{+2.8}_{-3.1}$	$-15.1 \pm 9.0$	$-50.2^{+90}_{-90}$	$0.041^{+0.052}_{-0.041}$
33465	$0.946 \pm 0.016$	$19.1^{+2.9}_{-3.3}$	$-31.5 \pm 8.0$	$-61.2^{+25.0}_{-17.8}$	$0.057^{+0.037}_{-0.029}$
36925	$0.931 \pm 0.013$	$23.2^{+2.4}_{-3.1}$	$38.5 \pm 12.0$	$67.2^{+10.8}_{-21.0}$	$0.093^{+0.050}_{-0.053}$
38268	$0.730 \pm 0.034$	$29.5^{+2.5}_{-3.1}$	$5.2 \pm 3.0$	$9.3^{+12.2}_{-10.3}$	$0.165^{+0.083}_{-0.083}$

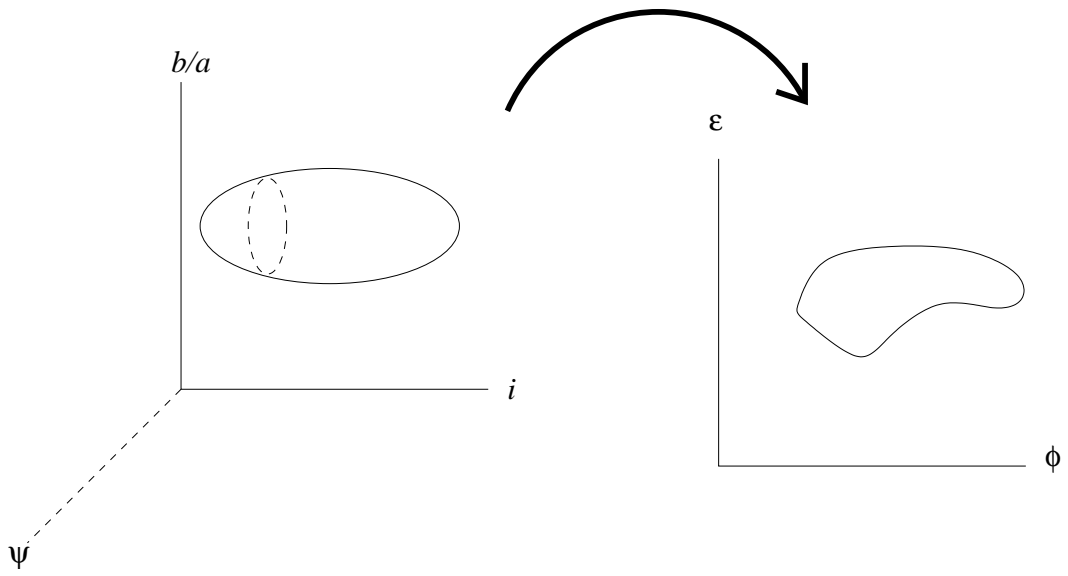


Fig. 4.6. Cartoon of the mapping the error ellipsoid for the observed quantities  $b/a$ ,  $i$ ,  $\psi$  to the two-dimensional  $\epsilon_D$ - $\phi$ -space. We used these maps of error ellipsoids to determine if our measurements were consistent with a disk ellipticity of zero.



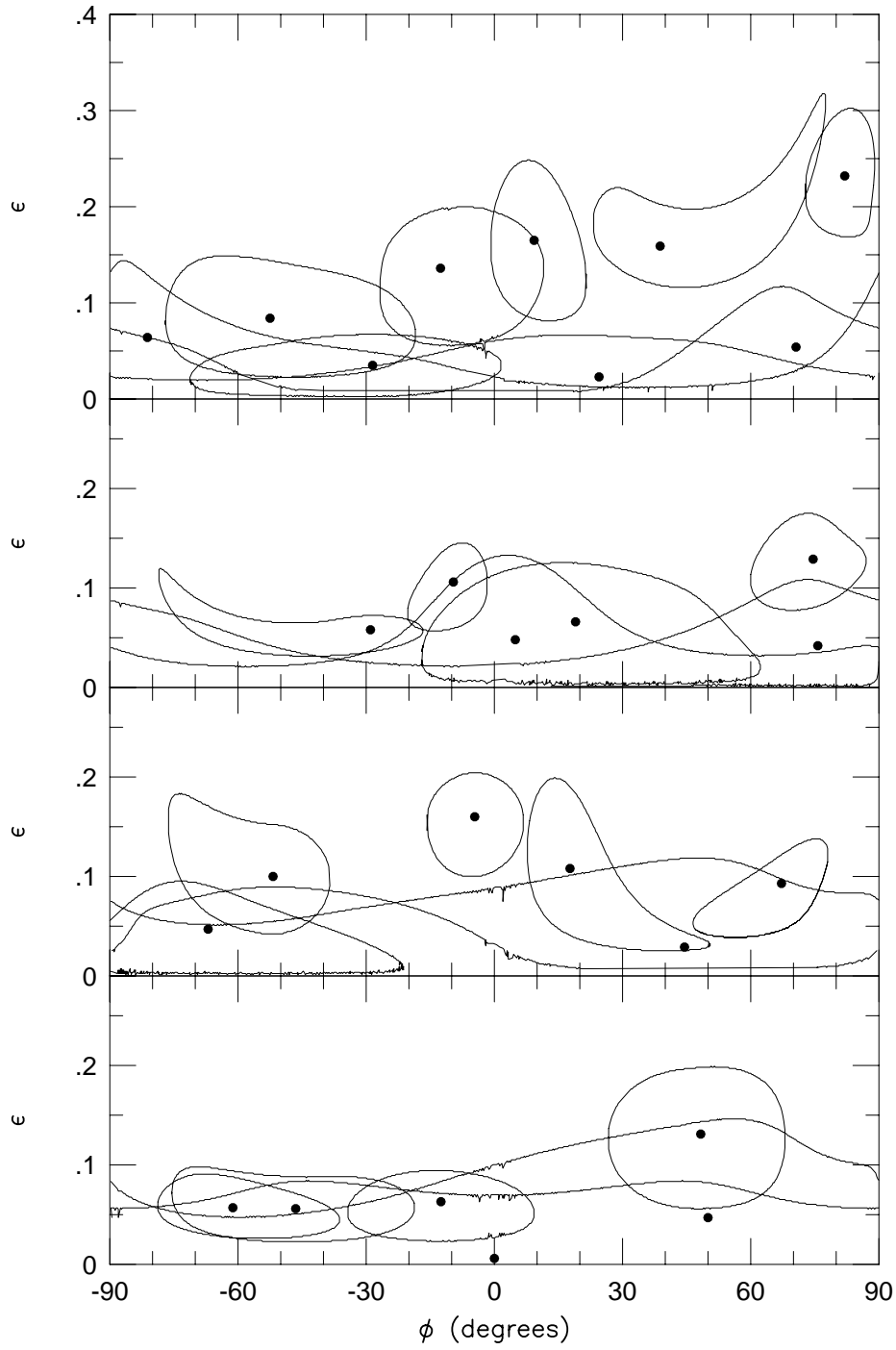


Fig. 4.7. Contours containing all solutions for disk ellipticity within an error ellipse containing 68% of the likely measurements of  $b/a$ ,  $i$ , and  $\psi$ . If solutions were consistent with zero,  $\phi$  becomes undefined. Hence, for the 9 galaxies with solution for  $\epsilon_D$  consistent with zero at the 68% confidence interval, there are solutions consistent with all phase angles.

PGC	$b/a$	$i$	$\psi$	$\phi$	$\epsilon$
		deg	deg	deg	
38908	$0.908 \pm 0.041$	$24.1^{+2.7}_{-2.8}$	$9.0 \pm 14.0$	$44.5^{+90}_{-90}$	$0.029^{+0.093}_{-0.029}$
39728	$0.881 \pm 0.011$	$31.1^{+2.3}_{-2.5}$	$-7.9 \pm 5.0$	$-67.0^{+46.2}_{-33.3}$	$0.047^{+0.052}_{-0.046}$
46767	$0.867 \pm 0.013$	$22.7^{+2.1}_{-1.8}$	$-5.6 \pm 5.0$	$-12.5^{+21.8}_{-22.0}$	$0.063^{+0.034}_{-0.040}$
49906	$0.940 \pm 0.008$	$4.4^{+14.2}_{-4.4}$	$-27.8 \pm 6.1$	$-29.0^{+12.2}_{-50.0}$	$0.058^{+0.065}_{-0.026}$
55750	$0.940 \pm 0.018$	$13.1^{+6.6}_{-13.1}$	$-33.9 \pm 9.0$	$-46.5^{+28.0}_{-29.2}$	$0.056^{+0.045}_{-0.033}$
57931	$0.886 \pm 0.040$	$21.5^{+3.1}_{-3.6}$	$2.0 \pm 6.0$	$4.9^{+90}_{-90}$	$0.048^{+0.089}_{-0.048}$
58410	$0.861 \pm 0.028$	$30.0^{+1.4}_{-1.5}$	$0.0 \pm 9.0$	$0.0^{+90}_{-90}$	$0.006^{+0.082}_{-0.006}$
71106	$0.869 \pm 0.039$	$14.3^{+6.4}_{-14.3}$	$41.8 \pm 9.0$	$48.3^{+19.7}_{-21.8}$	$0.131^{+0.073}_{-0.074}$
72144	$0.909 \pm 0.046$	$24.1^{+3.6}_{-5.3}$	$14.8 \pm 16.0$	$50.0^{+90}_{-90}$	$0.047^{+0.104}_{-0.047}$

Using the  $b/a$ ,  $i$ ,  $\psi$  error ellipsoid maps to  $\epsilon_D$ - $\phi$ -space, we were able to determine that 9 of 28 (25%) of our sample galaxies had solutions consistent with circular disks within the 68% confidence limit defined by the error ellipsoid. These galaxies included: PGC 5673, PGC 6855, PGC 16274, PGC 23333, PGC 32638, PGC 36925, PGC 38908, PGC 57931, PGC 58410, and PGC 72144. At the other extreme, 10 of the 28 galaxies (36%) were inconsistent with  $\epsilon_D$  solutions at all tested confidence limits. These galaxies included: PGC 3512, PGC 15531, PGC 26140, PGC 28310, PGC 28401, PGC 31159, PGC 33465, PGC 49906, PGC 55750 and PGC 71106. For the intermediate cases, PGC 8941, PGC 23598, and PGC 39728 first showed solutions consistent with  $\epsilon_D = 0$  at the 90% confidence limit. PGC 27792 and PGC 19767 first showed solutions consistent with  $\epsilon_D = 0$  at the 95% confidence limit, and finally PGC 32091, PGC 36925, and PGC 46767 first showed solutions consistent with  $\epsilon_D = 0$  at the 99% confidence limit. That 54% of the sample have ellipticities inconsistent with circular disks at above a 90% confidence limit lends credence to past studies that concluded disks were intrinsically non-circular.

Now that we have established that we are making significant measurements measurements of disk ellipticity, we turn to comparing our results with those of previous surveys. At first our mean disk ellipticity seems high in comparison to past estimates (Compare our measured disk ellipticity,  $\epsilon_D = 0.084 \pm 0.053$ , to Rix & Zaritsky's estimate of the halo ellipticity  $\epsilon_\Phi = 0.045 \pm 0.03$ .) Even after making the same assumptions that led to equation 4.1, our estimate of  $\epsilon_\Phi = 0.065 \pm 0.041$  is slightly greater. The difference may be related to the treatment of the positive-definite quantity,  $\epsilon_D$ . Rix & Zaritsky and Schoenmakers correct their measurements of disk ellipticity by using the equation

in Franx, Illingworth, & Heckman 1989:

$$\tilde{\epsilon}_D = (\epsilon_D^2 - \sigma_{\epsilon_D}^2)^{1/2} \quad (4.12)$$

where  $\tilde{\epsilon}_D$  has now the corrected disk ellipticity and  $\sigma_{\epsilon_D}$  is the standard deviation on  $\epsilon_D$ . Until we measure true standard deviations on  $\epsilon_D$ , we are left with using the error generated from the error-ellipsoid mapping of the 68% confidence limit. Since this is an overestimate of the disk ellipticity standard deviation, we expect our mean corrected disk ellipticity to be a lower limit. We find  $\langle \tilde{\epsilon}_D \rangle = 0.059 \pm 0.059$  which corresponds a mean halo ellipticity of  $\langle \tilde{\epsilon}_\Phi \rangle = 0.046 \pm 0.046$ , in very close agreement with other studies.

By applying the “positive-definite quantity” correction, the distribution of disk ellipticities changes substantially. Figure 4.8 shows that the peak in the distribution of ellipticities moves from  $\sim 0.5$  to  $< 0.2$  after applying the correction. Until we measure true standard deviations for our ellipticity measurements, we can not quantify the distribution of disk ellipticities, but Figure 4.8 suggests the best fitting distribution of ellipticities may have a mean of 0 with a large scatter (which, by definition, lead to all positive disk ellipticities).

## 4.6 Discussion of Disk Ellipticity

### 4.6.1 Ellipticity versus Disk Properties

As noted in the introduction, ellipticity contributes to the  $m = 2$  Fourier mode. We expected a correlation between the  $m = 1$  mode, characterized as lopsidedness, and ellipticity because theoretical predictions suggest both lopsidedness and ellipticity will be

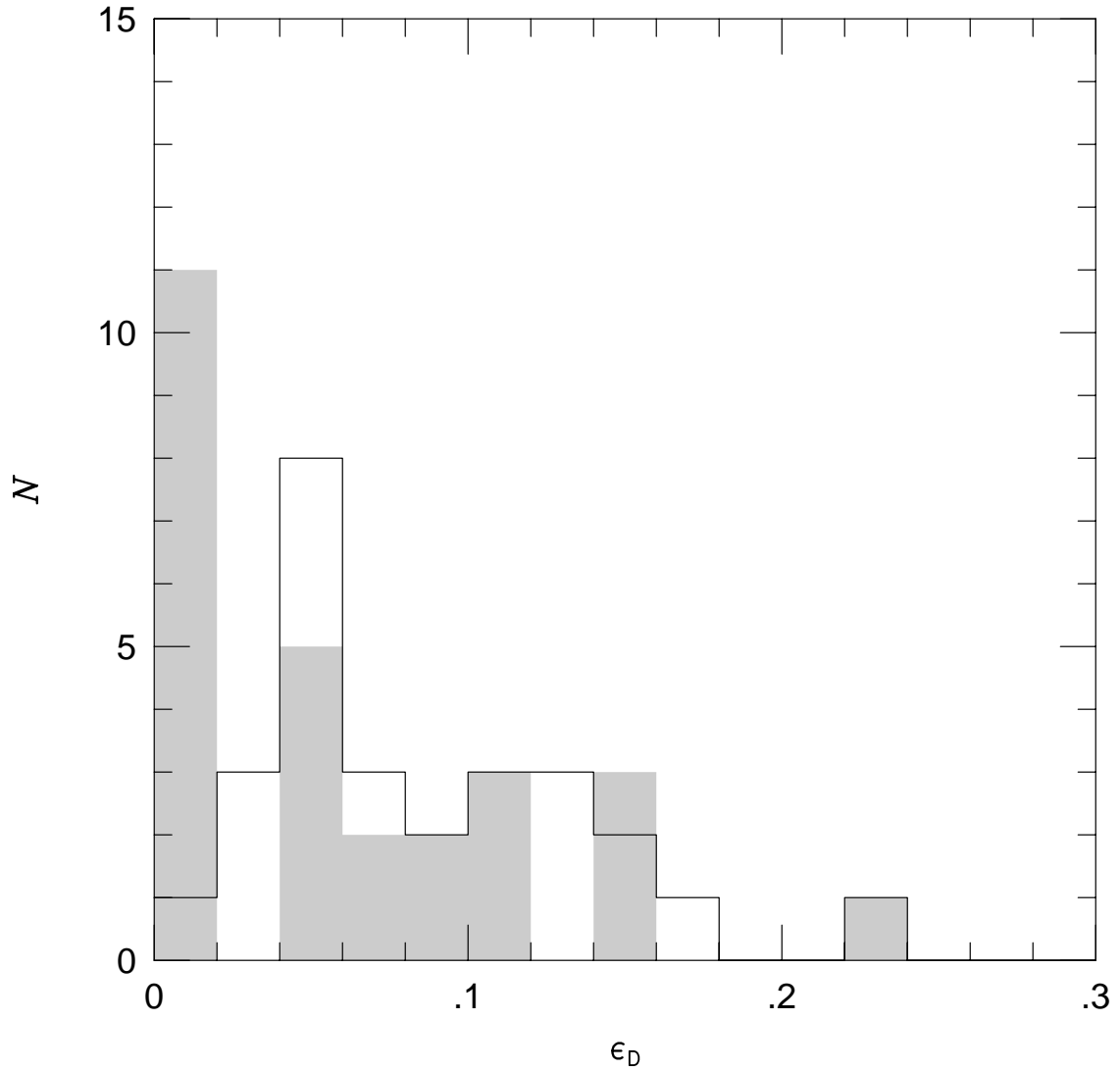


Fig. 4.8. Distribution of disk ellipticities before (solid line) and after (shaded regions) making the “positive-definite quantity” correction. After applying this correction, the peak in the distribution moves from  $\epsilon_D = 0.05$  to  $\epsilon_D < 0.02$ . The peak of the distribution will be close to zero, but since ellipticity is a positive definite quantity, any variations in the measure of ellipticity will lead to disk ellipticities, on average, greater than the peak ellipticity.

excited by tidal interactions (Weinberg 1995; Rudnick, Rix & Kennicutt 2000). There does appear to be a weak relationship between the two parameters, but the residual between the two relationships is 0.06 in  $A_1$  and the correlation coefficient is only 0.33 (Figure 4.9). It is interesting to note, however, that there are galaxies which are not lopsided, but which have relatively large ellipticities. On the other hand, there does not appear to be any galaxies which are significantly lopsided but have small ellipticities.

While no statistical trends were evident between lopsidedness and disk ellipticity, we found an envelope of disk ellipticities defined through several other photometric disk properties including the concentration index, disk central surface brightness, and absolute  $R$ -band magnitude. But for two notable exceptions, the galaxies with the greatest disk ellipticities are also diffuse, low surface brightness, and low luminosity galaxies (Figure 4.10). The two exceptions, PGC 26140 and PGC 71106 are clearly interacting: The position angle of PGC 26140 is aligned with an early type galaxy about 2 arcminutes from its center. PGC 71106 has a diffuse blue extended object within three scale lengths of the center. If we exclude these objects, we find that galaxies which are more diffuse, have lower surface brightnesses, and are less luminous, are statistically more likely to have intrinsically elliptic disks (Table 4.2).

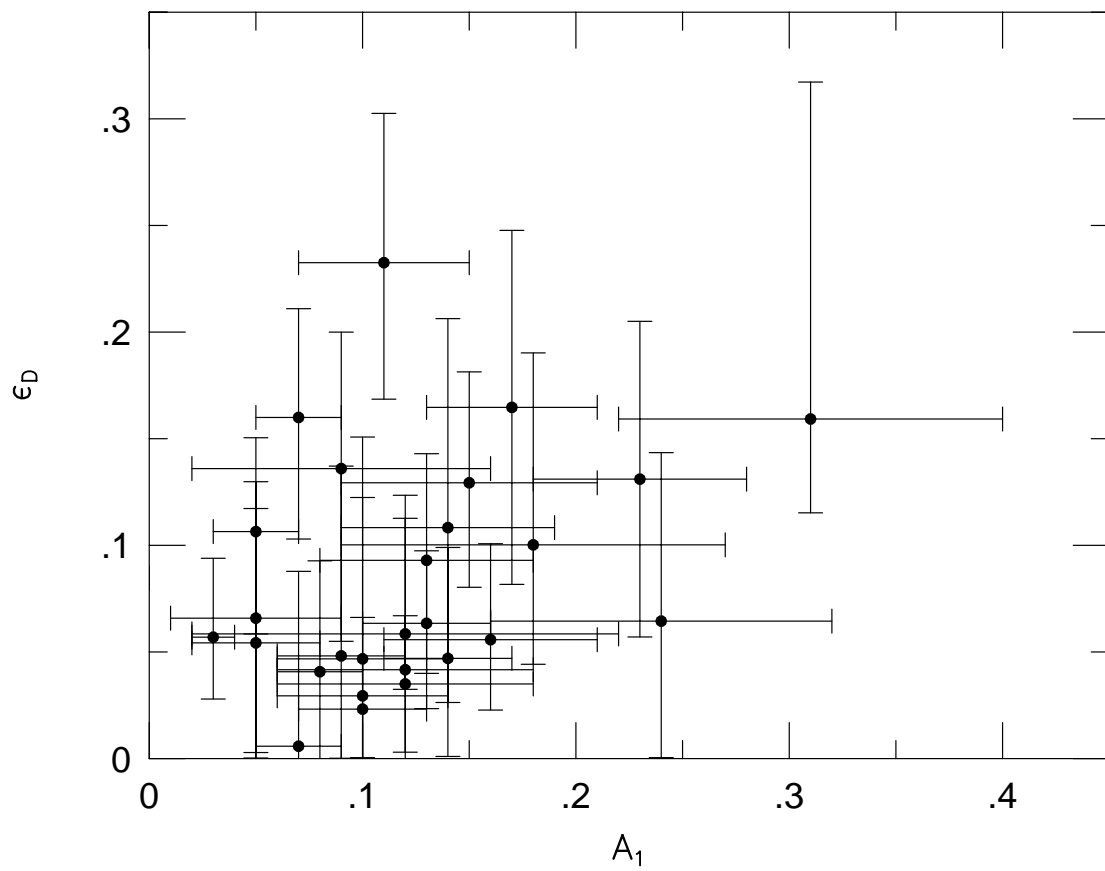


Fig. 4.9. Relationship between lopsidedness as measured by the Fourier  $m = 1$  amplitude versus disk ellipticity. While it was expected that perhaps these two modes of disk asymmetry would be correlated, only a very weak relationship existed for these data.

Table 4.2. Ellipticity versus Disk Properties. We divided our sample in half by lopsidedness,  $A_1$ , concentration index,  $C_{80:20}$ ,  $I$ -band central disk surface brightness,  $\mu_0$  and absolute  $R$ -band magnitude and measured ellipticity in each half of the sample. The “Mean Value” was used to divide the sample in half. In each case, high and low divide the sample by intrinsic property (e.g., for  $A_1$  the high value is measured for the most lopsided galaxies. Note that for  $M_R$ , high refers to the highest luminosity galaxies).

Disk	Mean	High	Low
Property	Value	$\overline{\epsilon_D}$	$\overline{\epsilon_D}$
$A_1$	0.115	$0.089 \pm 0.044$	$0.077 \pm 0.064$
$C_{80:20}$	2.8	$0.059 \pm 0.042$	$0.097 \pm 0.057$
$\mu_0(I)$	19.8	$0.062 \pm 0.031$	$0.116 \pm 0.065$
$M_R$	-21.1	$0.049 \pm 0.022$	$0.101 \pm 0.063$



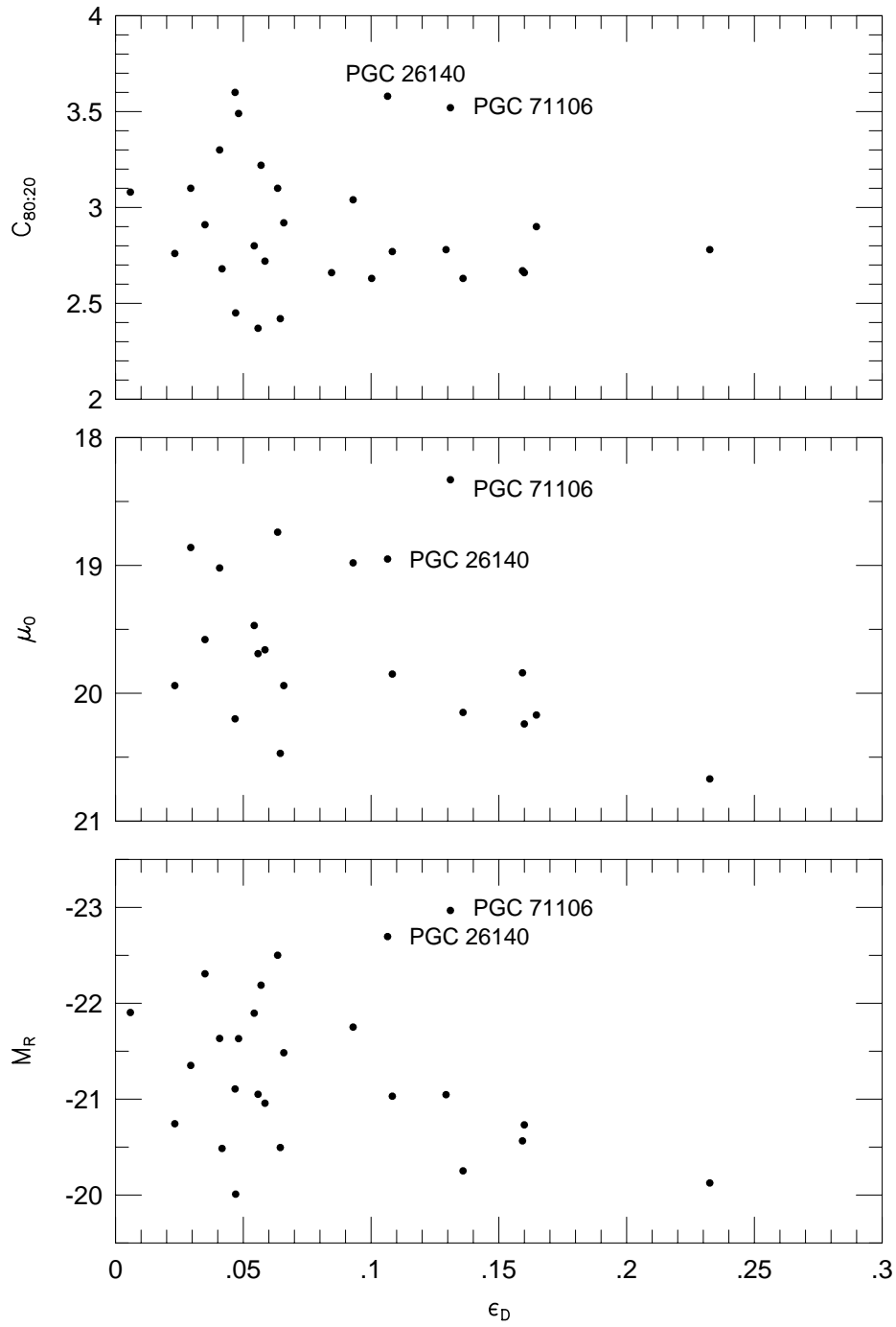


Fig. 4.10. The relationship between concentration index, central disk surface brightness and absolute magnitude versus disk ellipticity. If one excludes PGC 26140 and PGC 71106, two interacting galaxies, it appears that galaxies which are either less luminous, more diffuse, or lower surface brightness are more likely to have higher ellipticities. Based on these trends, less massive galaxies are more likely to have triaxial halos.

If one accepts the notion that disk ellipticity is related to the triaxiality of the halo, there are two different theories which could account for the distribution of elliptic disks in Figure 4.10. The first suggestion is that one accepts the simulations of Dubinski & Carlberg (1991) that galaxies are formed with a distribution of triaxial halos. For a range of galaxy types, there is going to be a range in the dark matter-to-baryon mass fraction. Fainter, lower surface-brightness galaxies have been shown to be more dark matter dominated. Hence, we suggest that the dissipation of energy due to the infalling gas (baryons) as disks are forming will not be as important in low luminosity systems. As energy is dissipated by the infalling gas, halos lose their triaxiality ( $\epsilon_{\Phi} \rightarrow 0$ ) and become oblate spheroids (Dubinski 1994). Therefore, massive disks will be oblate and display no disk ellipticity, while low luminosity, dark matter dominated galaxies may remain triaxial. Qualitatively, galaxies in Figure 4.10 with initially large ellipticities and luminosities became more circular while the ellipticity of low luminosity galaxy disks have remain unchanged.

A second theory which has been used to explain how halos can become triaxial has been forward by Weinberg 1995. He suggests halo triaxiality is induced through tidal interactions. We see clear evidence of this for the interacting galaxies PGC 26140 and PGC 71106 by virtue of their high disk ellipticities. Tidal interactions could explain the rest of the trends of luminosity and ellipticity as well. If when galaxies form, the dissipation of energy due to the infalling gas efficiently produces oblate halos, we propose that all disks were initially circular and only through minor mergers and tidal interactions have halo triaxialities and disk ellipticities been induced. Since these interactions are stochastic in nature, each galaxy in our sample has had a history of harassment. However,

low mass galaxies are more sensitive to mergers which would therefore create larger ellipticities. In this theory, all galaxies in Figure 4.10 have initial ellipticities of zero. Lower mass galaxies are more likely to have encounters with objects of similar mass, which increases the ellipticity of these objects. However, if tidal interactions were the dominant cause of disk ellipticity, one would expect a statistical correlation between disk ellipticity and lopsidedness, which also is thought to be due to tidal interactions.

#### 4.6.2 Tully-Fisher Scatter and Ellipticity

Our disk ellipticity measurements have other important cosmological implications related to the TF scatter due to disk ellipticity. We simulated samples of elliptic galaxies with inclinations between  $45^\circ$  and  $75^\circ$  and asked how much TF scatter would be due to incorrect photometric redshifts derived from axis ratios. As Figure 4.3 demonstrates, even an intrinsic disk ellipticity of  $\epsilon_D = 0.05$  can create inclination errors as great as  $3^\circ$  at inclinations of  $50^\circ$ . Our simulation took a random distribution of disk ellipticities with a standard deviation of 0.05, based on our measurements, and calculated the photometric inclination error for a given mean disk ellipticity and random phase angle,  $\phi$ . We then propagated that inclination error into the TF relation calculated for two extreme slopes of  $L \propto v^4$  and  $L \propto v^{2.8}$ . Figure 4.11 shows the results of repeating the simulation for different mean ellipticities. For our mean value of  $\epsilon_D = 0.084$ , between 0.13 and 0.17 magnitudes of TF scatter would be due to errors in photometric inclinations directly related to disk ellipticity.

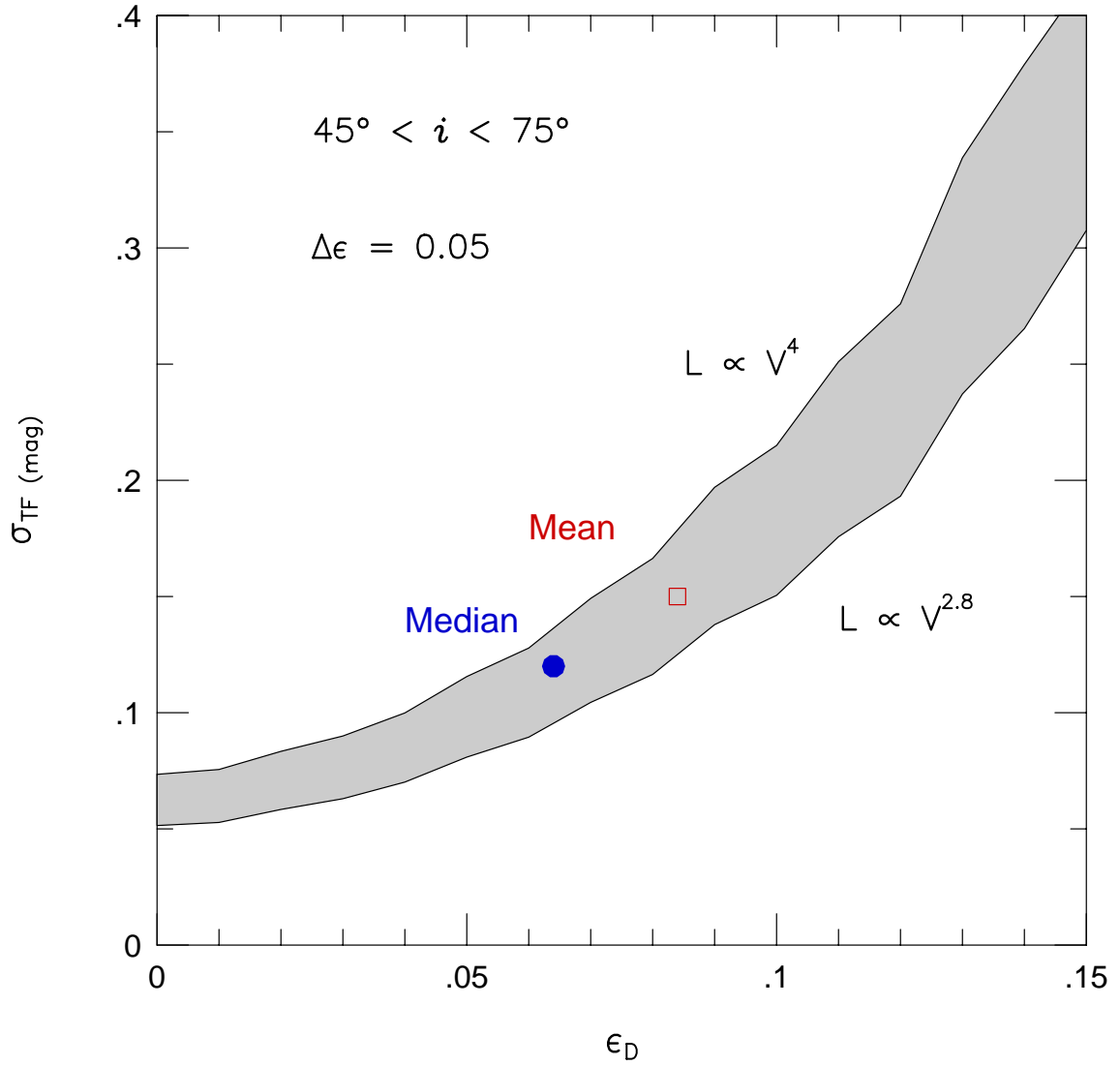


Fig. 4.11. A simulation of the effect disk ellipticity would have on photometric inclination errors which lead to TF scatter. All simulated galaxies have inclinations between  $45^\circ$  and  $75^\circ$ . We bounded the expected result by using two TF slopes,  $L \propto V^4$  and  $L \propto V^{2.8}$ . Based on our measurements of disk ellipticity, between 0.125 and 0.175 magnitudes of TF scatter is due to inclination errors which are a result of disk ellipticity.

## 4.7 Summary

We have presented measurements of disk ellipticity for 28 galaxies in our galaxy survey of photometric and kinematic disk properties. The range of disk ellipticities fell between 0.01 and 0.23 with a mean of  $\overline{\epsilon_D} = 0.084 \pm 0.053$ . The median disk ellipticity was 0.064. Our measurements of  $\epsilon_D$  are slightly greater than but consistent with other measurements of ellipticity for spiral galaxies.

We find that 25% of our galaxies have ellipticities consistent with  $\epsilon_D = 0$  at 68% confidence limit, while 30% of disks in our sample are completely inconsistent with  $\epsilon_D = 0$ . If we correct disk ellipticities for the effect of measuring positive definite quantities, we find that the peak shifts from 0.04 to 0. We will revisit this analysis after we determine Gaussian errors on our quantities.

We found evidence that tidal interactions induce disk ellipticity; two of our sample were clearly interacting and had large disk ellipticities. Disk ellipticity,  $\epsilon_D$ , also is correlated with concentration index, surface brightness and luminosity. Galaxies with the lowest luminosity, surface-brightness, and concentration index exhibited the greatest mean disk ellipticities. These data suggest a trend exists between the shape and mass of dark matter halos, i.e., massive halos may be more spheroidal while less massive halos are triaxial.

Finally, we show that photometric inclinations for TF samples will be in error, leading to scatter in the TF relation. The effect of ellipticity on TF scatter based only on this inclination effect is between 0.1 and 0.15 magnitudes for our measured ellipticity if the scatter in ellipticity is 0.05.

## Chapter 5

### A Face-On Tully-Fisher Relation

#### Abstract<sup>1</sup>

We demonstrate the ability to study the Tully-Fisher relation for galaxies with inclinations less than  $35^\circ$ . The 24 galaxies in our sample have a mean inclination of  $26^\circ$  and span a range in inclinations from  $15^\circ$  to  $35^\circ$ . This “face-on” Tully-Fisher sample is well-fit by a published Tully-Fisher relation for more inclined systems, yet exhibits less scatter. The tight correlation between luminosity and deprojected rotation velocity for our face-on sample lends further credence to the accuracy and precision of our derived kinematic inclinations and rotation speeds. Face-on Tully-Fisher samples are advantageous because galaxy magnitudes and photometric structural parameters do not need to be corrected for differential effects with inclination due to internal absorption and the vertical component of the disk stellar velocity ellipsoid is available for improved mass-decomposition studies. Not all of our sample galaxies were well-fit by a Tully-Fisher relation. Four galaxies had residuals greater than 0.8 magnitudes. We suggest their large Tully-Fisher residuals are related to kinematic asymmetry. We found no other disk property which correlated with TF scatter.

---

<sup>1</sup>Andersen, D.R. & Bershad, M.A. 2001, *to be submitted to Ap.J.*, L.

## 5.1 Introduction

The fundamental scaling relation for spiral galaxies is the empirical relationship between rotation speed and luminosity (Tully & Fisher 1977; hereafter TF relation). The tight correlation between these quantities has been critical to attempts to measure galaxy distances and map the dynamics of the local universe (see Strauss & Willick 1995 for a review). As such, substantial effort has been put into understanding the TF relation in the local universe (e.g., Pierce & Tully 1988; Aaronson *et al.* 1989; Willick 1990; Courteau 1992; Bernstein *et al.* 1994; Giovanelli *et al.* 1997). These studies have found the slope of the TF relation steepens systematically from blue to red passbands and is surprisingly tight, with a measured rms scatter of 0.4 magnitudes.

Often overlooked in discussions of the TF relation is the importance of inclination. Of the three measurements needed in TF studies (projected rotation speed, luminosity and inclination), inclination in some ways is the most critical. Because one common characteristic of all TF studies to date is that galaxies were selected with inclinations greater than  $\sim 45^\circ$  with typical inclinations of  $\sim 60^\circ$ , inclinations are needed both to correct luminosities for internal absorption — a correction that becomes larger and more uncertain at higher inclinations (Giovanelli *et al.* 1994; Giovanelli *et al.* 1995; Tully *et al.* 1998) — and to de-project observed rotation velocities ( $V_{\text{circ}} = V_{\text{rot}}/\sin i$ ). Inclination errors, therefore, could lead to correlated systematic errors in the the TF relation. Unfortunately, inclination determinations are subject to substantial uncertainty. For most TF studies, inclinations,  $i$ , are calculated from photometric axis ratios,  $b/a$  through the

relation  $\cos^2 i = \frac{(b/a)^2 - q_0^2}{1 - q_0^2}$  where  $q_0 \approx 0.2$  and is the intrinsic flattening, assumed to be the same for all galaxies (Tully & Fouqué 1985; Courteau 1996; Giovanelli *et al.* 1996).

Some of the pitfalls related to using photometric inclinations can be avoided if instead of using HI line widths and photometric inclinations for TF studies, two-dimensional velocity fields are obtained (e.g., Schommer *et al.* 1993; Raychaudhury *et al.* 1997; Verheijen 2001). Two-dimensional velocity fields can be used to derive kinematic inclinations, which are superior to photometric inclinations because disk scale heights are irrelevant, as well as measuring more accurate rotation velocities which do not need to be corrected for turbulent broadening (Tully & Fouqué 1985; Courteau 1997; Giovanelli *et al.* 1997; Verheijen & Sancisi 2001). However, previous HI mapping limitations have been used to propagate the belief that kinematic inclinations can not be determined below inclinations of  $40^\circ$  (Begeman 1989).

We have discovered that kinematic inclinations, derived from high-quality kinematic data collected with DensePak, are sufficiently accurate and precise to determine kinematic inclinations and therefore construct a TF relation at unprecedentedly low inclinations. Specifically, we showed that 7 pilot study galaxies fell on a TF relation published by Courteau (1997) and exhibited scatter commensurate with the observed scatter of more highly inclined samples (Bershady & Andersen 2001). This represents the first attempt to construct a TF relation for face-on systems. We extend this analysis to the full thesis sample here. This is important not only for studying correlations of TF residuals (i.e., the scatter about the mean relation) with asymmetry (as discussed in Chapter 1), but for mass-modeling as well. By establishing the ability to derive rotation curves for nearly face-on systems, we have opened the door to future surveys which



can directly measure total mass (via rotation curves) and disk mass (via the vertical component of disk stellar velocity).

In §5.2, we review our survey selection criteria and the relevant photometric and kinematic measures needed for this work. Readers familiar with §2.2–2.4 and §3.2 and 3.4 may move to §5.3 without loss of continuity. In §5.3, we describe color and internal absorption corrections we make which allow us to directly compare our data with the published TF relation of Courteau (1997), along with a discussion of outliers, and relations between TF scatter and kinematic and photometric disk properties. We summarize our results in §5.4.

## 5.2 Observations

A more complete description of the selection criteria and descriptions of observations can be found in §2.2, §2.3 and §3.2. In review, we obtained  $R$  and  $I$ -band imaging and  $H\alpha$  velocity fields for 39 galaxies which met following selection criteria: (1) axis ratio,  $b/a + \Delta b/a > 0.87$  ( $i - \delta i < 30^\circ$ ), (2) apparent disk size,  $45'' < D_{25} < 75''$ , (3) galactic absorption,  $A_B < 0.6$  (Schlegel, Finkbeiner & Davis 1998), (4) declinations visible from WIYN,  $\delta_{1950} > -10^\circ$ , (5) observed  $B$ -band magnitudes, (6) observed recession velocities, (7)  $t$ -types ranging from Sab to Sd ( $t$ -types between 1.5–8.5), and (8) no bars, rings, or interacting companions.

Imaging observations were acquired during 17 nights over 10 imaging runs between May, 1998 and January, 2001 at the WIYN 3.5m telescope at KPNO, the 2.1m telescope at KPNO, and the Harlan J. Smith 2.7m telescope at McDonald Observatory.

H $\alpha$  velocity fields observed at resolutions of  $\frac{\lambda}{\Delta\lambda} \approx 13,000$  were obtained using the DensePak integral field unit on the WIYN telescope during 11 nights on 6 separate observing runs. DensePak is an array of 91 fibers arranged in a seven by thirteen fiber rectangle sub-tending an area of  $30'' \times 45''$ .

### 5.2.1 Total Magnitude

The key photometric observation required for the study of the face-on TF relation are magnitudes. As discussed in §2.4.1, we calculated total magnitudes from the asymptotic flux measured from galaxy surface brightness growth curves. To calibrate magnitude zero points for our observations, we used Landolt (1983) standards observed during four photometric nights. In addition to these directly calibrated data, there were several runs where no standard stars were observed but which were sufficiently clear (estimated photometric errors were less than 0.05 magnitudes) to warrant measuring magnitudes through an internal boot-strapped calibration. Air mass corrections have not yet been calculated and applied to these data but they should be small (less than 0.1 magnitudes). We found the mean  $R - I$  color for our sample was  $\overline{R - I} = 0.52 \pm 0.08$ . All available total  $R$  and  $I$ -band magnitudes for our sample galaxies are tabulated in Table 2.6.

### 5.2.2 Rotation Velocity

As discussed in §3.4.3, we successfully fit the observed two-dimensional velocity fields with a simple hyperbolic-tangent velocity-field model. From these fits, we were able to derive accurate and precise measurements of kinematic inclinations, position

angles, rotation speeds and disk rotation scale-lengths for 36 of the 39 sample galaxies. All galaxies in our sample have projected rotation velocities less than 120 km/s. We tested the accuracy of our derived rotation velocities by comparing them to HI line widths corrected for turbulent broadening. After applying this correction, we found that HI line widths were highly correlated with our H $\alpha$  velocity-field model rotation speeds. The precision of our model with regard to rotation speeds was also very high. Rotation velocity errors calculated from the  $\chi^2$  statistic were less than 1.5 km/s.

### 5.2.3 Inclination

The most critical measurement required to construct a face-on TF relation, the derivation of accurate and precise inclinations of nearly face-on disk galaxies, is difficult. Measurements of photometric disk axis ratios have constant errors as a function of axis ratio. Therefore, random errors on photometric inclinations diverge at small inclinations, and derived inclinations become increasingly subject to systematic errors due to intrinsic disk ellipticity. For these reasons, estimates of disk inclination from two-dimensional kinematic maps provide a critical, independent alternative. Historically, HI data for galaxies with inclinations under  $40^\circ$  has been of insufficient resolution and signal to noise to fit with velocity-field models (Begeman 1989). The importance of DensePak data is its ability to open up accurate and precise kinematic inclination estimates down to  $i = 15^\circ$ . Using Monte Carlo simulations of velocity fields “observed” with DensePak, we estimated the inclination error,  $\Delta i = 5^\circ$  at  $i = 15^\circ$  as described in §3.4.3. The magnitude of these errors are consistent with inclination errors measured from the  $\chi^2$  statistic. We checked the accuracy of our kinematic inclinations against inclinations derived using HI

line widths and inverting the TF relation, and found a good correlation between these inverse TF inclinations and our kinematic inclinations, with residuals between the two measures consistent with measurement errors.

### 5.3 Results

Of the 39 galaxies in our sample, we were able to measure absolute magnitudes and the deprojected rotation velocity,  $V_{\text{circ}} \equiv \frac{2V_{\text{rot}}}{\sin i}$ , for 24 galaxies. We were unable to fit our velocity-field model to three galaxies: PGC 5345, PGC 23913, and PGC 70962. Ten galaxies in our sample had kinematic inclinations which were consistent with zero. These galaxies include: PGC 8941, PGC 15531, PGC 19767, PGC 26517, PGC 28401, PGC 32091, PGC 49906, PGC 55750, PGC 56010 and PGC 71106. Finally, we did not have calibrated  $R$  or  $I$ -band magnitudes for two galaxies: PGC 27792 and PGC 38268. The 24 remaining galaxies have a mean inclination of  $\bar{i} = 26^\circ$ , with inclinations spanning a range from  $15^\circ$  to  $35^\circ$ .

Using these data, we can make a comparison of the relation between luminosity and rotation speed in our data and TF relations measured for data at higher inclinations. As we showed in Chapter 2, the TF sample of Courteau (1996, 1997) shares comparable scale lengths, colors, and surface brightnesses and distances with our survey galaxies. Galaxies in his sample all had inclinations greater than  $40^\circ$ , with a mean inclination of  $64^\circ$ . Courteau extracted observed rotation velocities from  $\text{H}\alpha$  rotation curves, which allows us to make a direct comparison to our observed rotation velocities.

Before comparing our data to TF relations published by Courteau, we needed to make a color correction to our data. Courteau used Lick  $r$ -band magnitudes (Willick

1991) which are comparable to Gunn  $r$ -band magnitudes (Thuan & Gunn 1976), while our data has been calibrated on the standard Kron-Cousins photometric system (Cousins 1978). To transform from our observed, total  $R$ -band magnitudes to total, corrected  $r$ -band magnitudes, we made corrections for Galactic absorption (Cardelli *et al.* 1989) and used  $R - r = -0.36$  (Fukugita *et al.* 1995). In addition, there were several galaxies which either had no calibrated  $R$ -band magnitudes or had suspect  $R$ -band data. For these galaxies, we applied a color correction of  $R - I = 0.52$ , based on the mean color calculated from our data. We also applied the same internal absorption correction used for Courteau’s sample, but note that this amounts to a constant offset: Courteau fit a relation to the observed axis ratios so that TF scatter was minimized. The best fit to the  $r$ -band internal absorption,  $A_{i,r}$  was:

$$A_{i,r} = 0.95[\log(a/b) - 0.418] \quad (5.1)$$

for all axis ratios greater than  $b/a < 0.80$  such that  $A_{i,r} = 0$  and inclinations of  $i = 70^\circ$  (which corresponds to the rough mean inclination of Courteau’s sample). For axis ratios greater than 0.8 (which would include all of our sample),  $A_{i,r} = -0.30$ .

After applying the color and extinction corrections, we can directly compare our survey data to TF relations found in Courteau (1997). He made several measurements of rotation velocities using different methods, and calculated best-fit TF relations for different subsamples of data. Comparing Courteau’s different methods for extracting velocities to our data, we estimated that our asymptotic rotation velocities from a hyperbolic-tangent rotation-curve model would match most closely with his measurement of the

maximum model velocity,  $V_{max}$ , fit to  $H\alpha$  rotation curves. We compared our sample to the subsample of Courteau’s designated as being in the “quiet” Hubble flow, since for our sample the differences were small between the observed recession velocities and the heliocentric velocities corrected for Local Group motion and Virgo infall. Moreover, recession velocities of our galaxies were greater than 2000 km/s with a mean recession velocity of  $V_{cen} = 6500$  km/s. Non-flow corrections to this mean recession velocity are less than 1%.

According to Courteau (1997), the relation between absolute  $M_r$  magnitudes and the maximum rotation speed,  $V_{max}$  is:

$$M_r = -5.29 \log(V_{max}) - 7.44. \quad (5.2)$$

Our data match this relation quite well, as illustrated in Figure 6.2. The difference in TF zero-point between our data and Equation 5.2 is only 0.12 magnitudes. However, given the uncertainty in the internal absorption correction applied to the data, this zero-point correction is quite small. For the rest of the analysis, we use a new TF zero-point of  $-7.32$  instead of  $-7.44$ . Table 5.1 lists the relevant TF data for the 24 galaxies and includes differences between our measurements and Courteau’s TF relation.

Most surprisingly, the TF scatter for our sample is only 0.44 mag. This scatter is remarkably small because it is not the result of a fit to our data, rather it is the residual about an externally established TF relation established with a sample that exhibited a TF scatter of 0.46 mag. The distribution of residuals to the TF relation are not Gaussian for our galaxies. There are four galaxies which appear to be outliers: PGC 20938, PGC

24788, PGC 31159 and PGC 39728 (Figure 5.2). We suspect there is a correlation between these outliers and kinematic asymmetry: Of the 5 galaxies in this sample which exhibit strong kinematic asymmetries in their rotation curves, two are outliers (and a third, PGC 6855 is in the tail of the distribution). If we exclude these four outliers from our analysis, the observed TF scatter is just 0.28 mag.

Table 5.1. Tully-Fisher Parameters. A color transformation and an internal absorption correction have been applied to our  $R$ -band magnitudes to yield corrected Lick  $r$ -band magnitudes,  $m_r^c$ .  $M_r$  is the absolute  $r$ -band magnitude for  $H_0 = 70$  km/s/Mpc.  $\Delta$  TF $_r$  is calculated from Equation 5.2.

PGC	$m_r^c$	$V_{\text{rot}}$	$i$	$V_{\text{cen}}$	$M_r$	$\frac{2V_{\text{rot}}}{\sin i}$	$\Delta$ TF $_r$
	mag	km/s	deg	km/s	mag	km/s	mag
2162	14.69 $\pm$ 0.04	35. $\pm$ 0.4	20.6 $^{+4.5}_{-6.4}$	5464.6	-19.77	198.9 $^{+86.4}_{-33.9}$	-0.47
3512	13.92 $\pm$ 0.04	82.4 $\pm$ 0.5	30.1 $^{+1.6}_{-1.9}$	5460.2	-20.54	328.6 $^{+20.1}_{-14.9}$	-0.09
5673	13.82 $\pm$ 0.06	58. $\pm$ 0.2	23. $^{+2.2}_{-3.1}$	4518.3	-20.22	296.8 $^{+43.9}_{-24.4}$	-0.01
6855	14.23 $\pm$ 0.06	52. $\pm$ 0.5	33.6 $^{+2.9}_{-3.8}$	4868.5	-19.98	187.9 $^{+21.3}_{-13.0}$	-0.81
7826	14.04 $\pm$ 0.07	31.2 $\pm$ 0.4	33.6 $^{+4.6}_{-5.7}$	2386.4	-18.62	112.7 $^{+20.5}_{-11.8}$	-0.63
14564	12.64 $\pm$ 0.06	92.3 $\pm$ 0.5	30.9 $^{+2.}_{-2.4}$	3505.6	-20.85	359.4 $^{+27.4}_{-19.6}$	-0.20
16274	14.13 $\pm$ 0.06	113.1 $\pm$ 0.6	30.7 $^{+1.5}_{-2.}$	8883.8	-21.38	443.0 $^{+27.9}_{-18.5}$	-0.25
20938	14.78 $\pm$ 0.06	58.3 $\pm$ 0.5	25.2 $^{+2.9}_{-3.3}$	4668.0	-19.34	273.8 $^{+38.7}_{-26.2}$	0.69
23333	14.13 $\pm$ 0.07	60.2 $\pm$ 0.4	26.3 $^{+2.9}_{-3.3}$	4626.6	-19.27	271.7 $^{+36.4}_{-24.9}$	0.04
23598	14.17 $\pm$ 0.06	45.3 $\pm$ 0.2	14.7 $^{+4.5}_{-6.6}$	7479.0	-20.97	357.0 $^{+285.9}_{-81.5}$	-0.33
24788	14.16 $\pm$ 0.06	73.6 $\pm$ 1.4	33. $^{+5.2}_{-6.2}$	7546.2	-21.00	270.2 $^{+56.2}_{-32.2}$	-1.00
26140	13.32 $\pm$ 0.06	150. $\pm$ 1.2	27.1 $^{+2.4}_{-2.5}$	8815.3	-22.18	658.5 $^{+62.1}_{-49.3}$	-0.13
28310	14.93 $\pm$ 0.08	63.8 $\pm$ 0.4	34.2 $^{+2.3}_{-2.3}$	5891.3	-19.69	227.0 $^{+14.4}_{-12.4}$	-0.09
31159	14.08 $\pm$ 0.08	84.8 $\pm$ 0.4	22.7 $^{+2.2}_{-2.7}$	5760.2	-20.49	439.4 $^{+56.3}_{-36.6}$	0.62
32638	13.71 $\pm$ 0.06	88. $\pm$ 0.6	22.3 $^{+2.8}_{-3.1}$	6475.7	-21.12	463.8 $^{+71.3}_{-48.9}$	0.12
33465	13.15 $\pm$ 0.06	99.2 $\pm$ 0.6	19.1 $^{+2.9}_{-3.3}$	6465.0	-21.67	606.3 $^{+122.3}_{-76.7}$	0.18



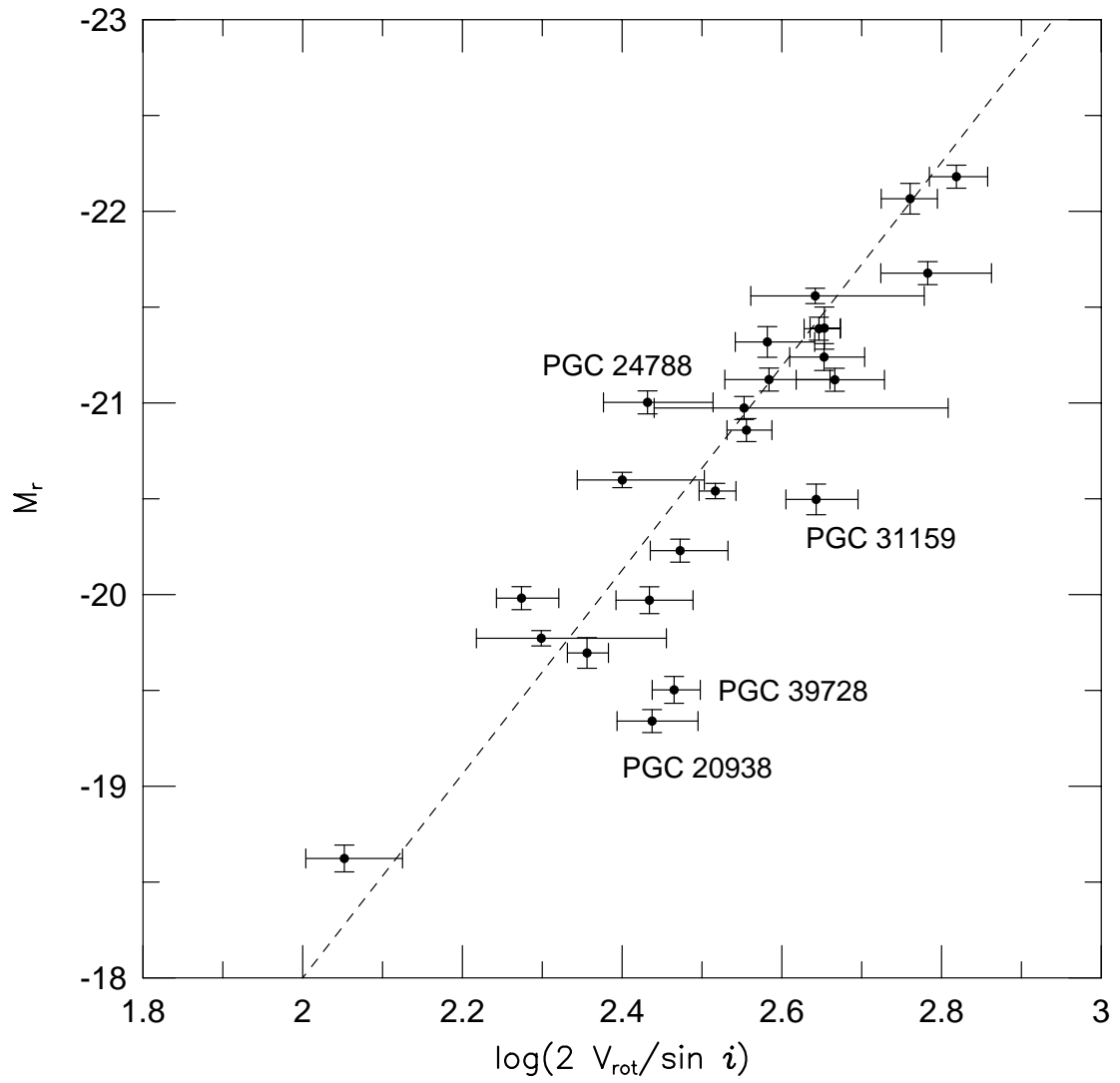


Fig. 5.1. A Tully-Fisher relation for a sample of galaxies with a mean inclination of  $26^\circ$ . The dashed line represents the best fit TF relation to a subsample of galaxies in the quiet Hubble flow taken from Courteau (1997; Equation 5.2, including the zero-point of -7.44). Only 0.44 magnitudes of scatter was exhibited about this relation.

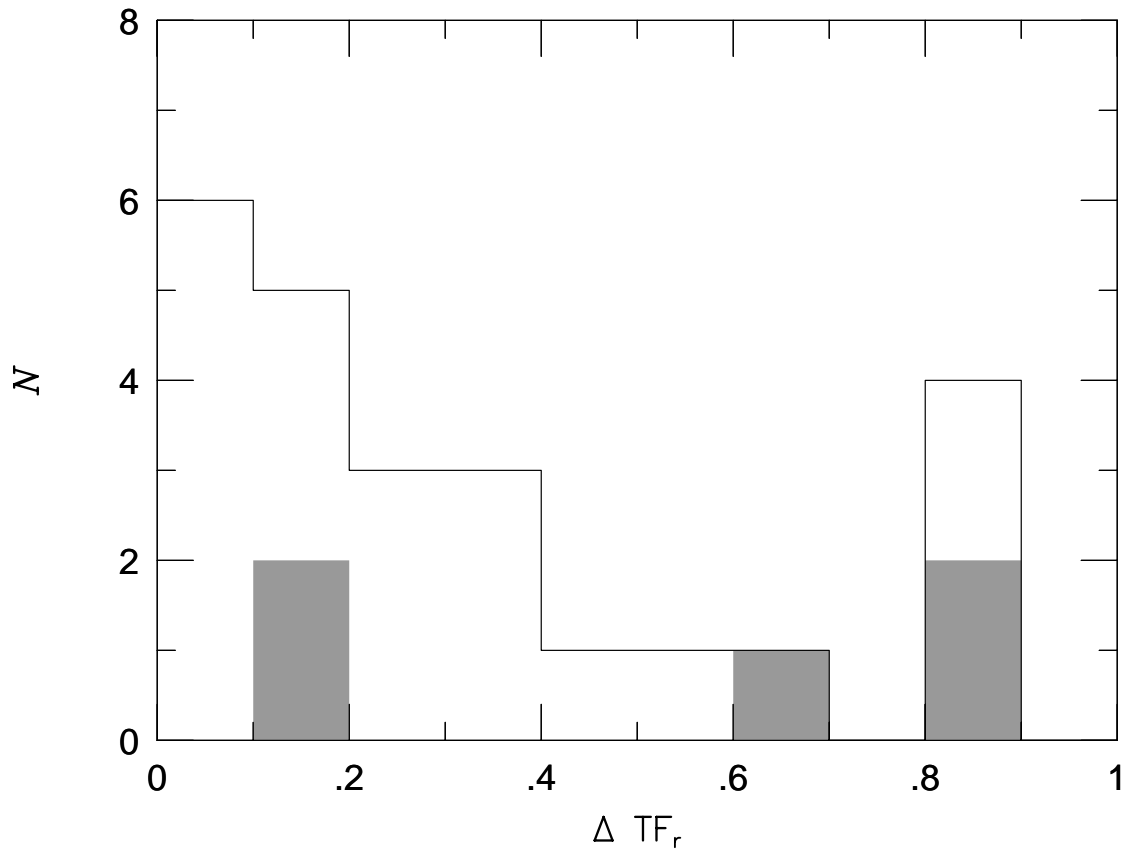


Fig. 5.2. The distribution of the absolute values of TF scatter for our sample of nearly face-on galaxies. The galaxies marked by grey represent galaxies identified as being kinematically asymmetric. It appears kinematic asymmetries may account for large TF residuals for some of the four galaxies identified as outliers.

PGC	$m_r^c$	$V_{\text{rot}}$	$i$	$V_{\text{cen}}$	$M_r$	$\frac{2V_{\text{rot}}}{\sin i}$	$\Delta \text{TF}_r$
	mag	km/s	deg	km/s	mag	km/s	mag
36925	13.63±0.08	75.2±0.5	23.2 <sup>+2.4</sup> <sub>-3.1</sub>	6835.6	-21.31	381.7 <sup>+55.8</sup> <sub>-33.7</sub>	-0.52
38908	13.78±0.07	91.8±0.7	24.1 <sup>+2.7</sup> <sub>-2.8</sub>	7063.0	-21.23	449.6 <sup>+55.8</sup> <sub>-42.4</sub>	-0.07
39728	13.06±0.07	75.8±0.5	31.3 <sup>+2.3</sup> <sub>-2.5</sub>	2278.7	-19.50	291.8 <sup>+22.8</sup> <sub>-17.8</sub>	0.68
46767	13.30±0.08	111.2±0.6	22.7 <sup>+2.1</sup> <sub>-1.8</sub>	8284.2	-22.06	576.3 <sup>+47.1</sup> <sub>-46.0</sub>	-0.32
57931	14.49±0.06	70.3±0.5	21.5 <sup>+3.1</sup> <sub>-3.6</sub>	9279.1	-21.12	383.6 <sup>+73.8</sup> <sub>-45.8</sub>	-0.31
58410	14.17±0.11	112.5±0.5	30. <sup>+1.4</sup> <sub>-1.5</sub>	9062.0	-21.39	450.0 <sup>+21.5</sup> <sub>-18.1</sub>	-0.22
72144	15.29±0.04	51.3±0.5	24.1 <sup>+3.6</sup> <sub>-5.3</sub>	10537.1	-20.59	251.2 <sup>+67.1</sup> <sub>-30.5</sub>	-0.76
72453	14.21±0.04	67.±0.6	17.8 <sup>+3.8</sup> <sub>-4.9</sub>	9973.2	-21.55	438.3 <sup>+161.8</sup> <sub>-74.3</sub>	-0.44

Figure 6.2 not only shows the first face-on TF relation, but also contains the first TF sample for which measurements of lopsidedness and ellipticity have been made. It has been suggested that both these asymmetries will induce TF scatter (Franx & de Zeeuw 1992; Zaritsky & Rix 1997). In Chapter 4, we simulated the expected TF scatter caused by photometric inclination errors due to ellipticity, but Franx & de Zeeuw suggested that ellipticity would also affect rotation speeds thereby inducing further TF scatter due to ellipticity. While we should have observed a relation between TF scatter and either ellipticity or disk lopsidedness for our sample galaxies, no correlation was apparent (Figure 5.3). The phase angle,  $\phi$ , of the intrinsic disk ellipticity also should be linked to TF scatter, but has not yet been studied.

## 5.4 Summary

We present a TF relationship established for 24 galaxies with a mean inclination of  $26^\circ$ . This is the first time the TF relation has been measured for a sample of galaxies with inclinations less than  $35^\circ$ . With the exception of a small zero-point correction, our sample is in complete agreement with the TF relation of Courteau (1997), measured for a sample of galaxies in the quiet Hubble flow. While we applied a constant internal reddening correction of -0.3 mag to our data, we did so only to make a direct comparison to Courteau’s data. Reddening corrections for galaxies with inclinations under  $35^\circ$  are negligible.

We have examined the TF residuals discovering that four of the galaxies were outliers to the main distribution. We suspect these outliers have kinematic asymmetries in their velocity fields which affect our derived kinematic inclinations or rotation speeds.

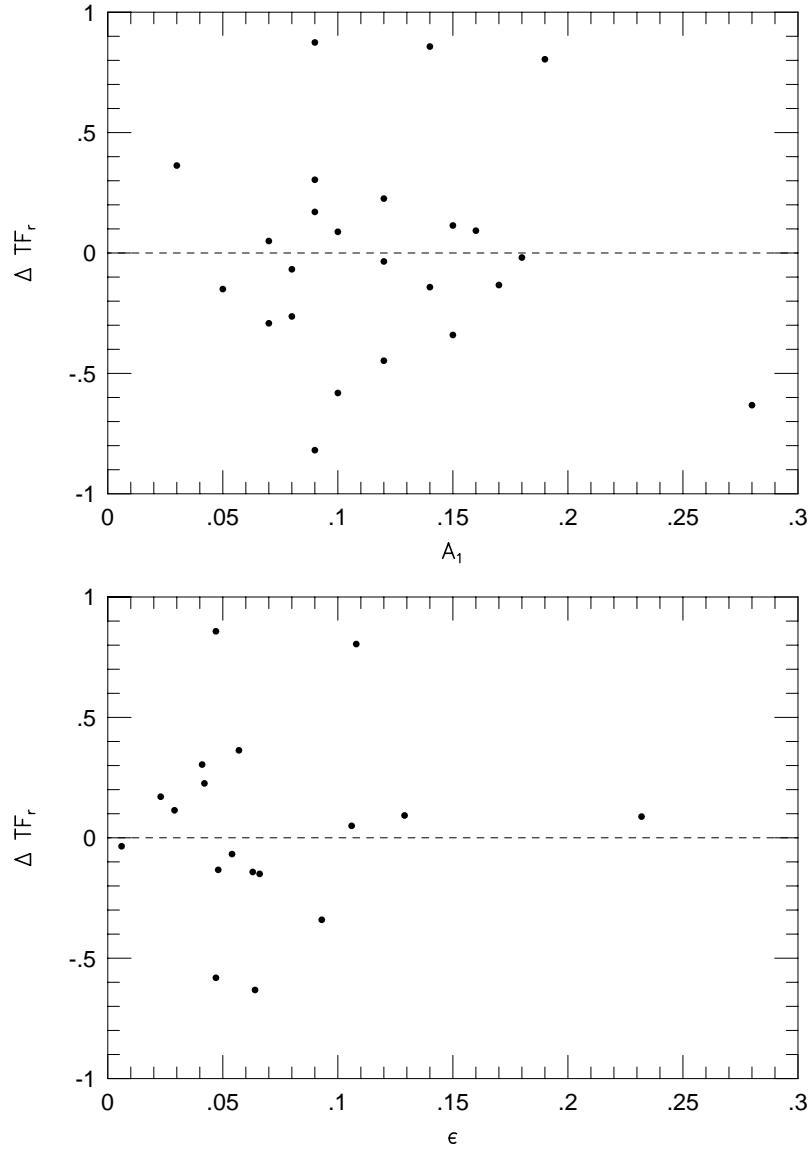


Fig. 5.3. Tully-Fisher scatter,  $\Delta TF_r$ , versus lopsidedness,  $A_1$  and intrinsic disk ellipticity,  $\epsilon$ . Although predictions were made that relations would be seen between these parameters, we detected no correlation between either lopsidedness or disk ellipticity versus TF scatter.

If these were excluded from the fit, the scatter fell to just 0.28 magnitudes, significantly smaller than the 0.46 mag of scatter observed for Courteau’s TF sample.

This data also provides the first test of whether TF scatter is related to an intrinsic disk ellipticity or photometric lopsidedness. Others have suggested that these two asymmetries could account for a significant fraction of TF scatter (Franx & de Zeeuw 1992; Zaritsky & Rix 1997; Bershady & Andersen 2001; Andersen *et al.* 2001). Franx & de Zeeuw’s analysis indicates roughly 0.2 mag of TF scatter should be due to ellipticity if the halo ellipticity,  $\epsilon_{\Phi} = 0.05$ , as estimated in Chapter 4. We will need to examine the link between TF scatter, phase angle, and ellipticity to determine if a link exists between ellipticity and TF scatter, but no such correlation is seen between  $\epsilon_D$  and TF scatter alone. However, our sample of 24 galaxies do not exhibit a large range in either Fourier amplitudes corresponding to lopsidedness or intrinsic disk ellipticities. Only 1 of our galaxies has a  $A_1$  lopsidedness amplitude greater than 0.2 for our TF sample — Zaritsky & Rix were basing their claim on a sample where 30% of the galaxies were lopsided. We have also identified individual galaxies which exhibit large TF scatter and lopsidedness from other samples (Bershady & Andersen 2001). Samples with larger ranges in lopsidedness amplitudes and ellipticities may be needed to study this potential source of TF scatter in greater detail.

## Chapter 6

### Summary

We collected deep  $R$  and  $I$ -band images,  $H\alpha$  velocity fields, and HI line widths for a sample of 39 normal, nearly face-on galaxies. Through a variety of non-parametric indices and modeling techniques we attempted to describe the photometric and kinematic structure and asymmetries of these disk galaxies. Our collection of data for disk galaxies is unique; there are no other set of galaxies to our knowledge for which two-dimensional photometric bulge-disk decomposition parameters, non-parametric photometric structure indices, photometric rotational and Fourier asymmetry measures, and velocity-field model parameters have been assembled. This data has allowed us to make significant contributions to the study of disk asymmetry and disk ellipticity. Furthermore, we have been able to establish the first Tully-Fisher relation for nearly face-on galaxies.

The study of disk asymmetry is still in its infancy. Although it had been recognized early on that galaxy photometric axisymmetry was an important component of galaxy morphology (e.g., Curtis 1918; Hubble 1926), only in the past decade have quantitative approaches emerged to measure such asymmetry (e.g. Rix & Zaritsky 1995; Schade *et al.* 1995; Kornreich *et al.* 1998). These various methods that were developed to measure photometric asymmetry all found that a significant fraction of galaxies show significant asymmetry. There has been, however, a difference of opinion about the characterization of these asymmetries: Are these different asymmetry methods measuring

lopsidedness, flocculence, or both? Fourier analyses of images yielded amplitudes corresponding to different modes; most often, however, only the first Fourier amplitude was measured, and interpreted as lopsidedness in the disk. The sector analysis of Kornreich *et al.* (1998) and the rotational asymmetries developed by Schade *et al.* (1995) and used by Conselice *et al.* (2000) have been reported to be measures of galaxy flocculence, which would be characterized as high order Fourier modes. For the first time, we measured both rotational asymmetries and Fourier amplitudes for a sample of disk galaxies. We showed in Chapter 2 that rotational asymmetry indices were not measures of flocculence, but rather were clearly measures of low order odd asymmetry modes (See Figure 6.1, first presented in Chapter 2). Rotational asymmetries really are measures of lopsidedness with an extra component that is added if galaxies are three-armed. While this could be interpreted as a failure of rotational asymmetries to measure flocculence, the relation between rotational asymmetries and lopsidedness makes rotational asymmetries a powerful tool for detecting lopsidedness in distant galaxy populations where Fourier analysis is impossible.

The data that separates our survey of disk galaxies from others, however, is the kinematic data obtained with the DensePak integral field unit on the WIYN 3.5m telescope. This instrument allowed us to map H $\alpha$  velocity fields out to 3 scale lengths at resolutions of  $\frac{\lambda}{\Delta\lambda} \approx 13,000$  with three arcsecond fibers. These high quality H $\alpha$  velocity fields have great utility. They had sufficient spectral and spatial resolution to measure kinematic asymmetries in the rotation curves and detect spiral structure for galaxies with inclinations less than 30°. To date, virtually every galaxy asymmetry study focused on either kinematic or photometric asymmetries, not both. The link between kinematic and



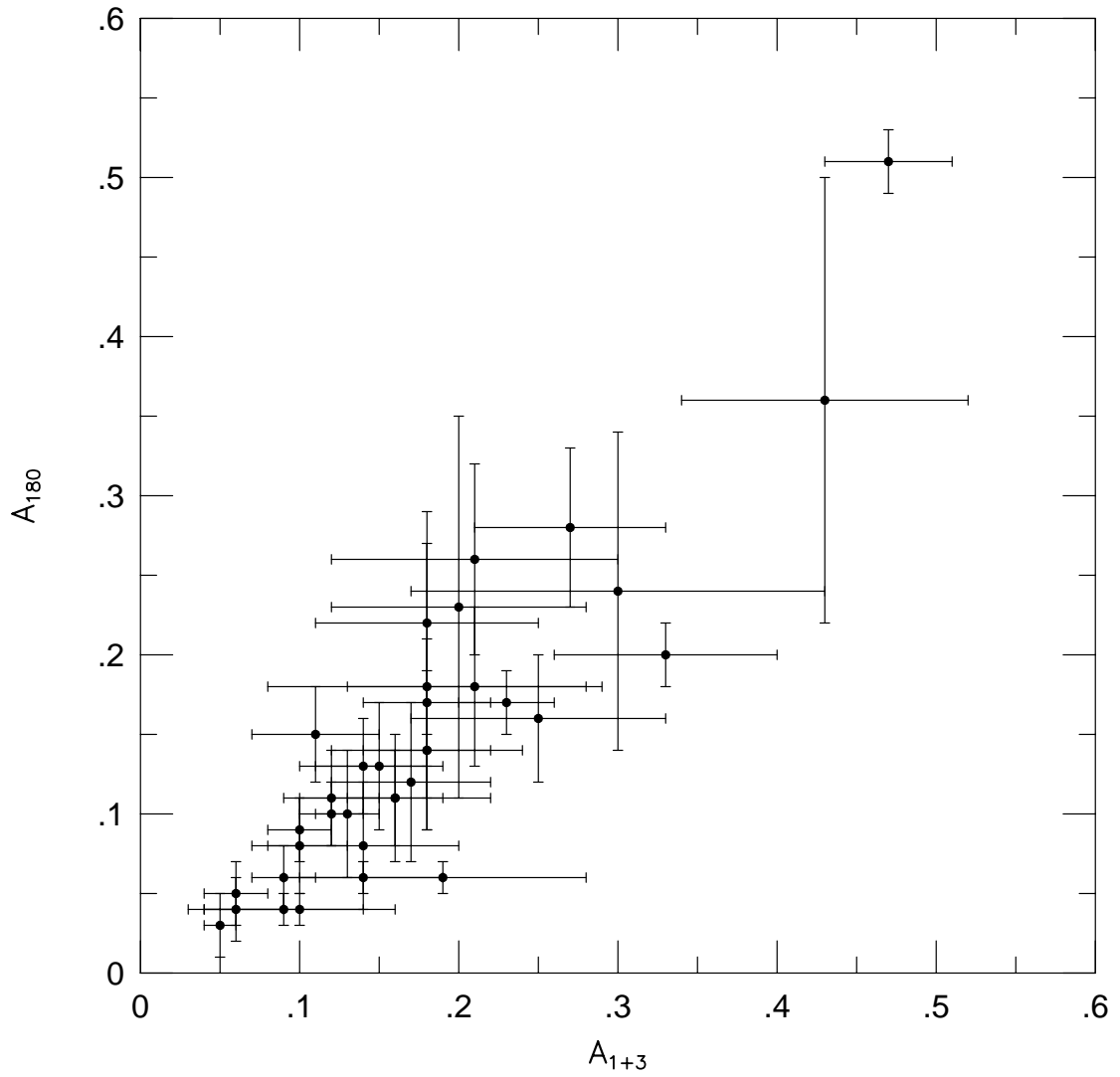


Fig. 6.1. The rotational asymmetry,  $A_{180}$  versus the quadrature sum of the first two odd Fourier amplitudes,  $A_{1+3} \equiv (A_1^2 + A_3^2)^{1/2}$ . The rotational asymmetry index  $A_{180}$  is very closely related to the first two Fourier amplitudes (lopsidedness and three-armedness).  $A_{180}$  and does not appear to be a measure of flocculence, as reported elsewhere (Conselice, Bershady & Jangren 2000).

photometric asymmetry is tenuous; only 18 galaxies have published kinematic and photometric asymmetry measures (Kornreich *et al.* 2000; Kornreich *et al.* 2001). Our data offers a sample of 39 galaxies which can be studied for their kinematic and photometric asymmetries. Determining the mechanisms which activate kinematic or photometric asymmetries will provide important clues into the structure and content of galaxy disks.

In addition to allowing us to map kinematic asymmetries, our H $\alpha$  velocity fields were of sufficient quality that we could determine inclinations for nearly face-on systems. The most commonly used method for determining kinematic inclinations is described by Begeman (1989) and consists of fitting a series of tilted rings at each radius. Developed for use with HI velocity fields that are often warped or twisted, tilted ring models employ weighting functions and cutoff azimuthal angles to produce best fits for rings at a given radius that are unaffected by warping or twisting velocity isocontours. In the process, however, a great deal of the velocity field is not used to constrain the fit. Since velocity fields are rarely affected by warping within three disk scale lengths where our data exist, we instead used a single, inclined velocity field with circular orbits to fit all data in our H $\alpha$  velocity fields. By using all the data in the H $\alpha$  velocity fields, we were able to obtain accurate inclinations for galaxies with inclinations as low as  $15^\circ$ . Since deriving kinematic inclinations for nearly face-on galaxies is without precedent, we used HI line widths measured with the Nançay radio telescope and taken from the literature to check the accuracy and precision of these inclinations. We showed in Chapter 3 that HI line widths and inverse Tully-Fisher inclinations derived from them were consistent with both our model rotation speeds and our model inclinations.

Perhaps even a better indication of the accuracy and precision of our kinematic inclinations is the construction of a face-on Tully-Fisher relation (hereafter TF) for 24 of our sample galaxies which had inclinations consistent with being greater than zero. In Chapter 5, we fit a Tully-Fisher relation taken from the literature (Courteau 1997), and showed that the TF scatter of our face-on sample galaxies around the published TF relation was *less* than the scatter measured for the original sample (Figure 6.2, first presented in Chapter 5). This would not be possible, unless our kinematic inclinations were quite accurate. The advantages of working with face-on TF samples are many: Corrections for internal absorption are unimportant, as are assumptions about the scale height of the galaxy. Scatter in the face-on TF samples can be correlated with several quantities which are ideally measured in face-on systems such as photometric asymmetry, disk ellipticity, and even measurements of disk mass.

While measurements of disk mass will have to wait for the future, we were able to measure disk ellipticity for 28 of our sample galaxies. As we showed in Chapter 4, we again utilized our kinematic inclinations to help describe the intrinsic ellipticity of disk galaxies. We employ a novel method which uses the differences between kinematic and photometric inclination and position angles to constrain a geometric model of an elliptic disk and solve for the intrinsic disk ellipticity,  $\epsilon_D$ , and phase angle between the line of nodes and the position angle of the major axis in the galaxy plane,  $\phi$ . Other studies of disk ellipticity did not have sufficient constraints to separate the two model parameters, which forced those studies to assume a random distribution of the phase angle in order to make a measurement of ellipticity (e.g., Rix & Zaritsky 1995; Schoenmakers *et al.* 1997). While ellipticity and the phase angle were measured separately for the Milky

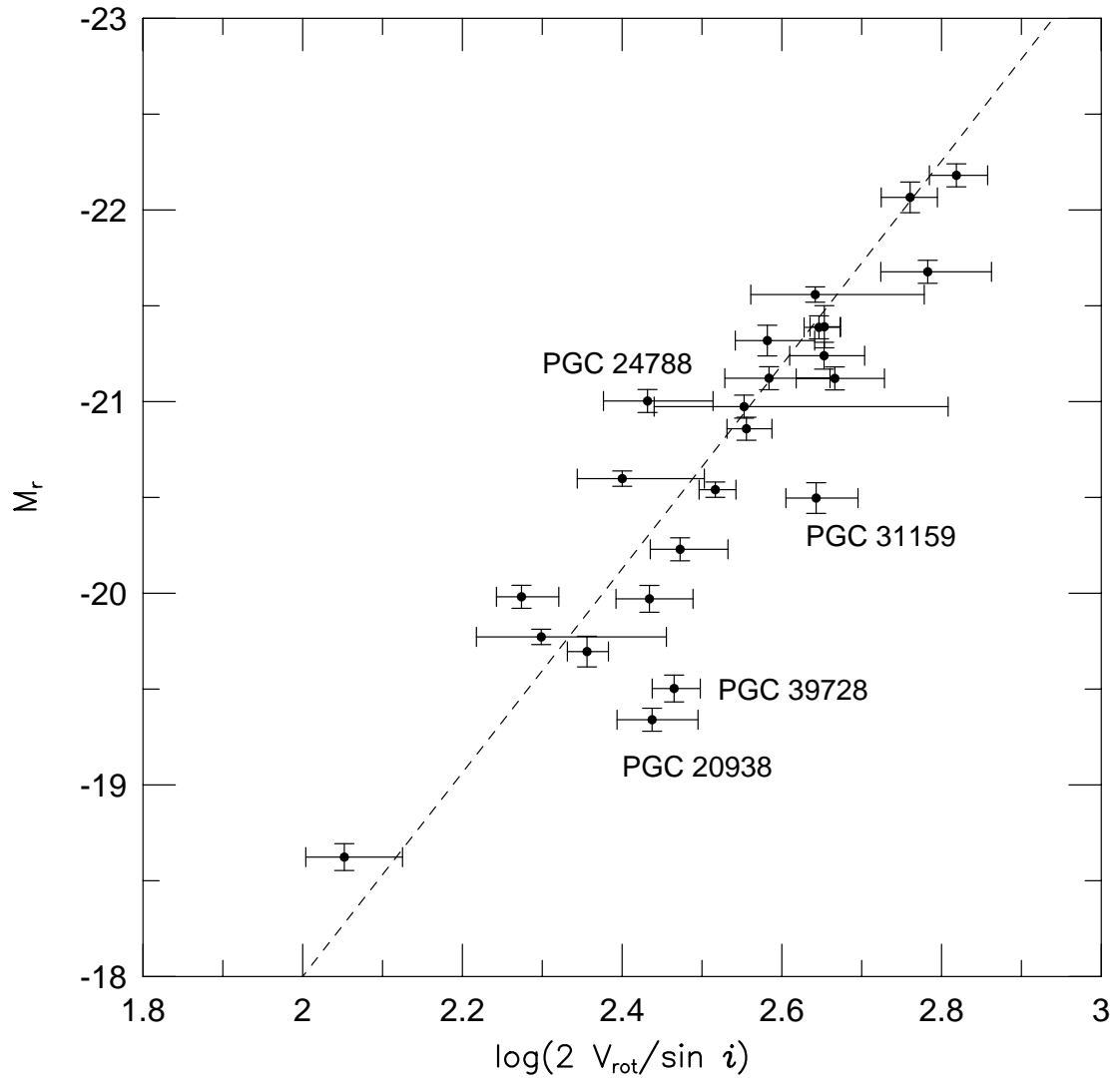


Fig. 6.2. A Tully-Fisher relation for a sample of galaxies with a mean inclination of  $26^\circ$ . The dashed line represents the best fit TF relation to a subsample of galaxies in the quiet Hubble flow taken from Courteau (1997; Equation 5.2). Only 0.44 magnitudes of scatter was exhibited by our sample.

Way (Kuijken & Tremaine 1991), our separate measurements of  $\epsilon_D$  and  $\phi$  are the first for external galaxies (Figure 6.3, first presented in Chapter 4).

Having established the ability to measure accurate galaxy inclinations down to  $15^\circ$ , we look to the future and plan measurements of disk mass which will be used to constrain mass decomposition models. Disk masses can be estimated from observations of the stellar velocity dispersion ellipsoid for galaxies with inclinations less than  $40^\circ$  (Gerssen *et al.* 1995). With accurate inclinations, we can also produce de-projected rotation curves, and for the first time, disk mass decompositions could be made for galaxies where disk mass would not be a free variable. By measuring disk mass from the velocity dispersion ellipsoid and measuring the total mass from the rotation curve, observations will have significant impact on different cosmological numerical and semi-analytic structure-formation models.

Unfortunately, the combined throughput of the DensePak integral field unit and the Bench spectrograph is not great enough to map our stellar velocity fields at several disk scale lengths. Hence, we have designed and built a new integral field unit for the WIYN telescope which will be capable of mapping absorption line velocity fields.

SparsePak is a new fiber-optic bundle built for the WIYN telescope's Bench Spectrograph, successfully installed and tested on WIYN in May 2001 (Figure 6.4). Each of SparsePak's 82 fibers have a physical size of 500 microns. The sparsely packed grid has dimensions of order  $70 \times 70$  arcsec. There are 7 sky fibers (part of the 82 total fibers) placed another 20-40 arcsec away from the grid (see Bershadsky *et al.* 2001 for a complete description and characterization of SparsePak). The greater diameter of SparsePak fibers increases the collecting area by a factor of 2.8 over DensePak, allowing us to reach

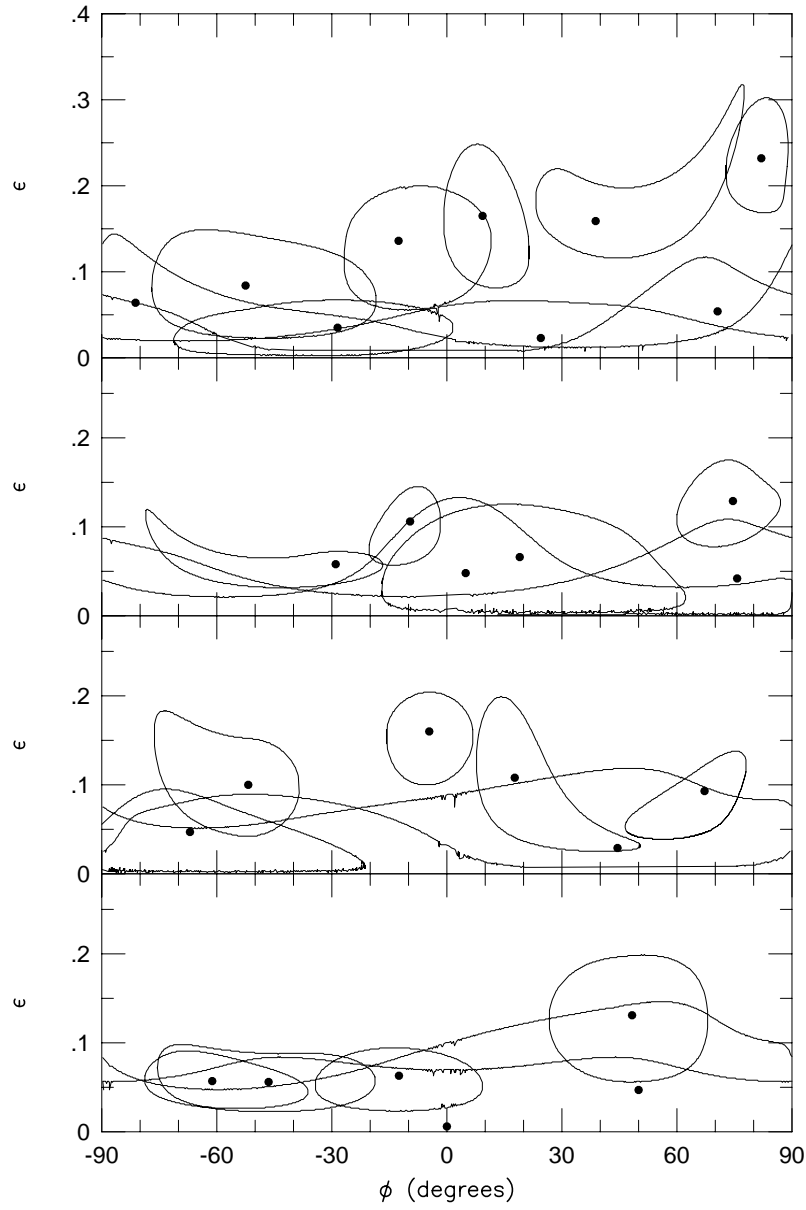


Fig. 6.3. Contours containing all solutions for disk ellipticity within an error ellipse containing 68% of the likely measurements of  $b/a$ ,  $i$ , and  $\psi$ . If solutions were consistent with zero,  $\phi$  becomes undefined. Hence, for the 9 galaxies with solution for  $\epsilon_D$  consistent with zero at the 68% confidence interval, there are solutions consistent with all phase angles.

correspondingly lower surface brightnesses with the Bench spectrograph in its current state. In a related effort to push absorption line spectroscopy to fainter surface brightnesses, upgrades are planned for the Bench spectrograph which should further add to these gains.

SparsePak has had first light.<sup>1</sup> We have mapped  $H\alpha$  velocity fields for several galaxies and successfully observed the Ca II near-infrared triplet (Figure 6.5) in a handful of targets. We were even able to measure the width of absorption lines at three scale lengths. Our initial commissioning data indicates that measuring disk masses for at least normal surface brightness galaxies, i.e., “Freeman” disks, is within our reach.

---

<sup>1</sup>See <http://www.astro.wisc.edu/~mab/research/sparsepak/> for more.

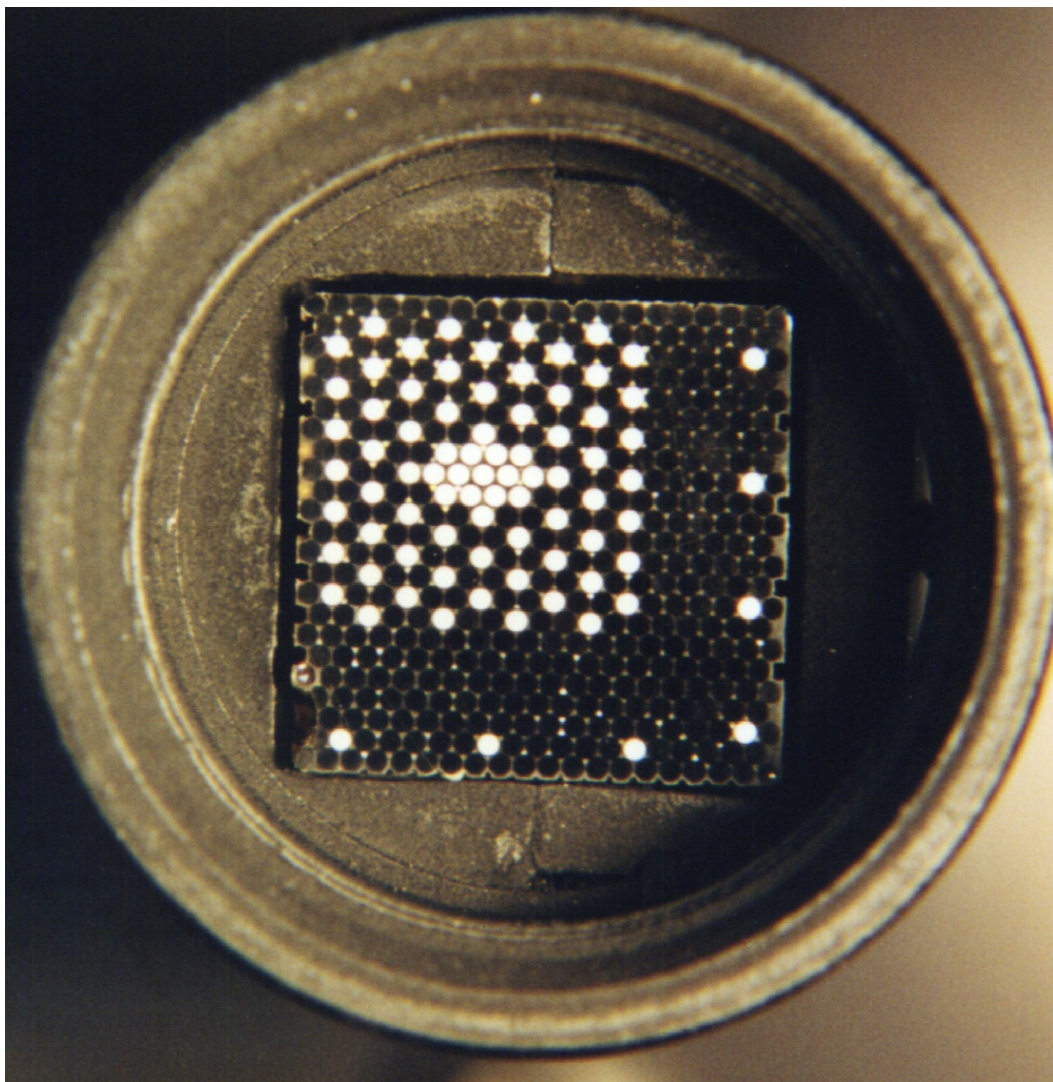


Fig. 6.4. Photograph of SparsePak in head mount. Light fibers are “active,” i.e., they are 25m in length and feed the Bench Spectrograph. Individual fibers are  $500\mu\text{m}$  in diameter which translates into  $5''$  at the WIYN Nasmyth imaging port. The grid of fibers in the upper right corner covers an area of  $70\times 70 \text{ arcsec}^2$ . The 7 fibers around the edge are to be used to subtract the mean sky spectra. The fiber array is about  $1/2$  inch on a side and is mounted in a 1 inch diameter mounting clamp.



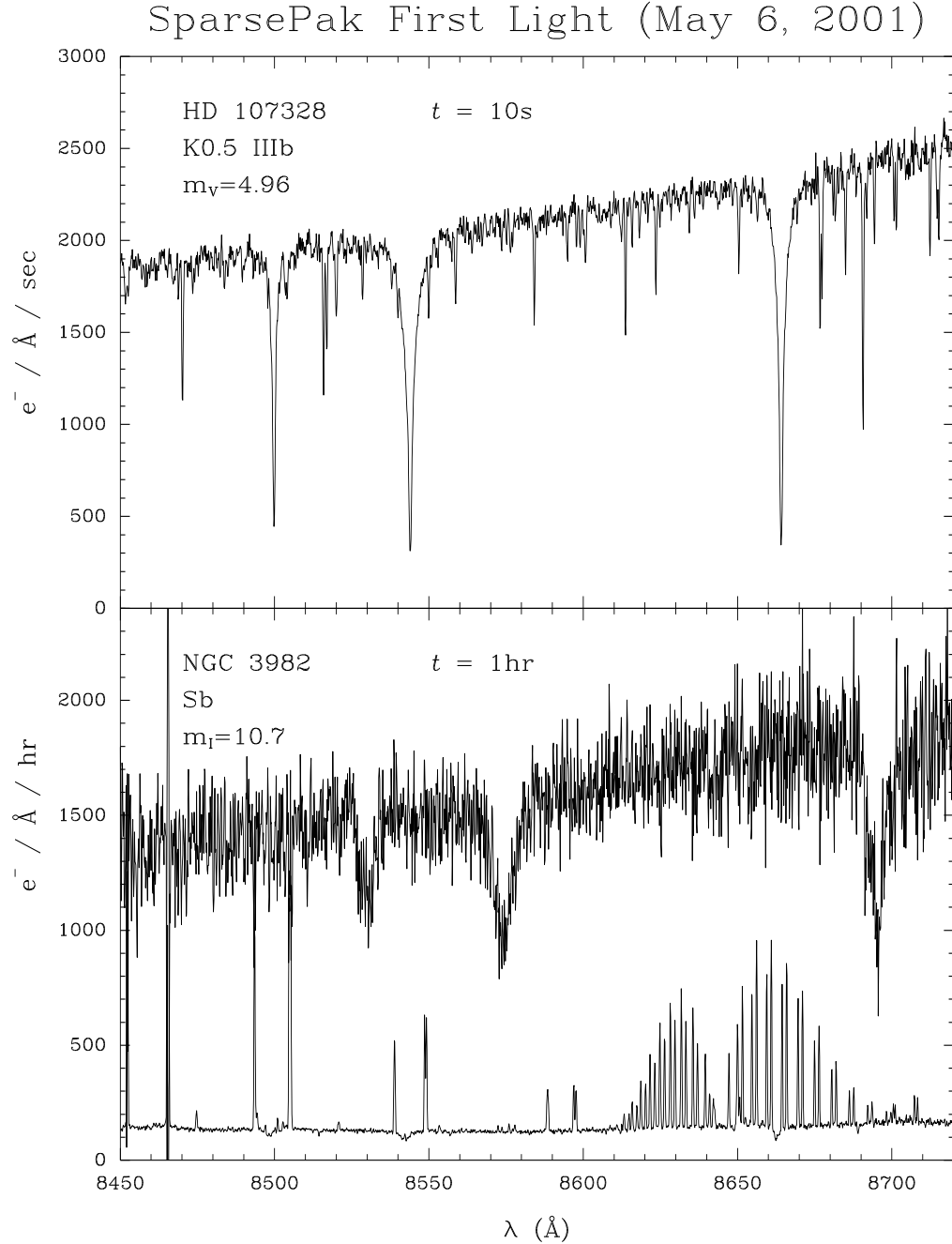


Fig. 6.5. Spectra containing the Ca II near-infrared triplet of a K0III star (top panel) and of a high surface-brightness disk galaxy (bottom panel) at a spectral resolution of  $\frac{\Delta\lambda}{\lambda} = 22,000$  with  $500\mu\text{m}$  fibers. Observations of the star were taken while drifting star across fibers in order to fill all fiber modes. The galaxy spectra in the bottom panel comes from a fiber centered about 8 arcsec from the center of the galaxy. The spectra at the bottom of the bottom panel is the mean sky spectra scaled by a factor of  $\frac{1}{10}$ , showing a well-resolved molecular band between 8610–8690 Å. These emission lines have been well-subtracted from the galaxy image. By coadding fibers, we were able to measure a velocity width from the Ca triplet at three galaxy scale lengths.

## Appendix

### Atlas

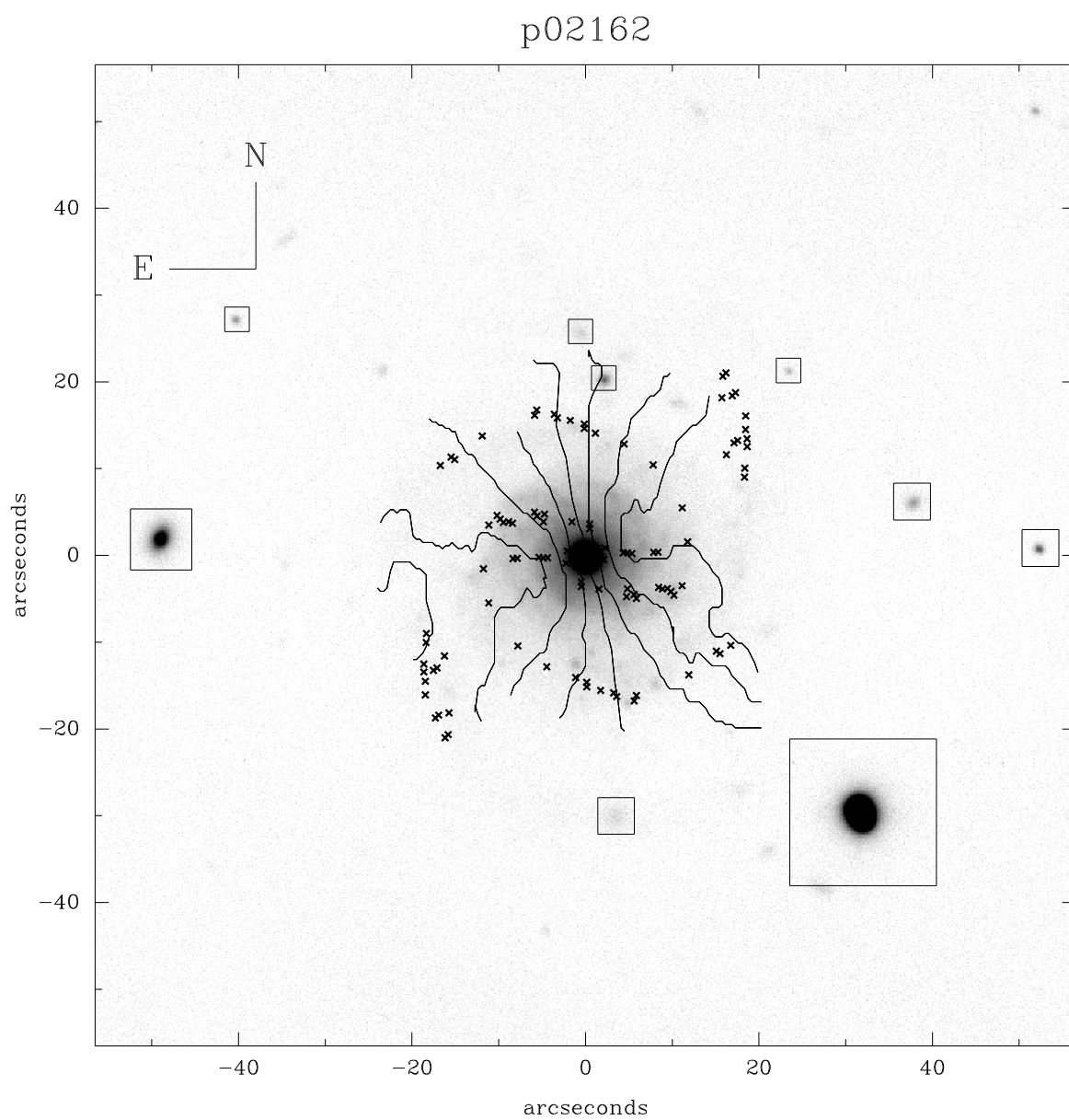
This atlas presents both kinematic and photometric data for the 39 sample galaxies. The sample selection process and photometric observations are described in §2.2 and §2.3. The kinematic observations are described in §3.2. Data for each galaxy is presented as a series of 4 figures:

- The first figure contains the optical image (typically *R*-band), velocity field (§3.4.1), and x's marking the the position angle at each radius as defined by isophote ellipse fitting (§2.4.4). In the process of fitting isophotes, stars were masked from the image. The masked stars are boxed; no points within the boxes were included in the IRAF *ellipse* routine fits.
- The second, multi-paneled figure charts the asymmetry indices and Fourier amplitudes and phases. The top panel contains the rotational asymmetry index (§2.4.5.1), while the central five panels contain Fourier decomposition amplitudes,  $A_m$ , and phases,  $\phi_m$ , for modes,  $1 < m < 3$  (§2.4.5.2). The bottom panel contains the quadrature sum,  $A_{1+3} \equiv (A_1^2 + A_3^2)^{1/2}$ . An annulus is defined between two radii corresponding to 1.5 and 2.5 disk scale lengths. Asymmetry measurements within this annulus are listed in Tables 2.10 (*R*-band) and 2.11 (*I*-band). Different line styles mark data from different runs or photometric bands. The data is identified by telescope (w=WIYN, k=KPNO 2.1m, mcd=McDonald 2.7m), date

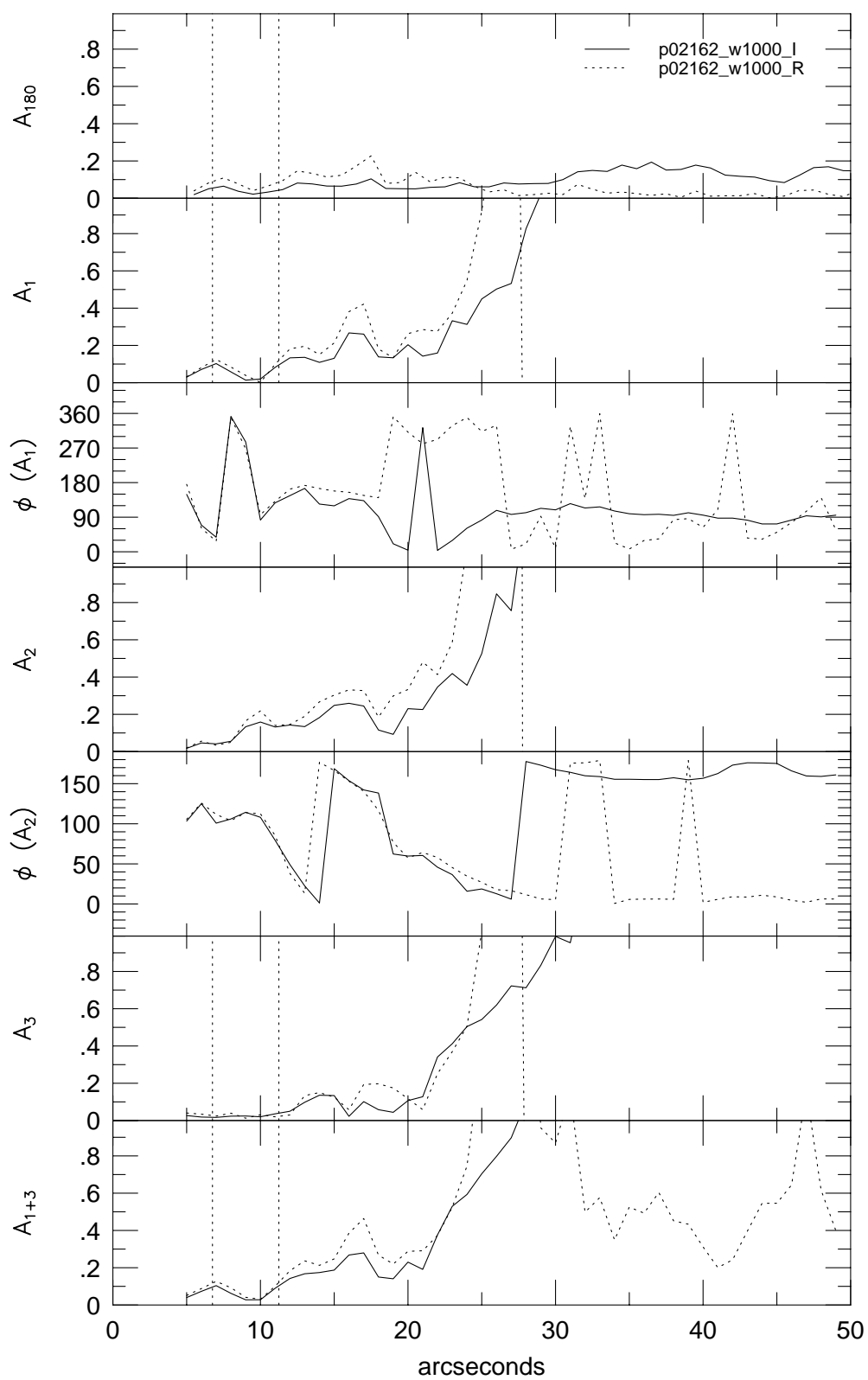
(month/year), and band ( $R$  or  $I$ ). Note that Fourier amplitudes diverge at outer radii (typically 3 scale lengths). This behavior, observed by Rix & Zaritsky (1995), has been attributed to low signal to noise ratios in the outer disk. However, even with bigger radial bins, this problem persists.

- The third, multi-paneled figure contains data gathered from the surface brightness profile (§2.4.2). The top panel contains the surface brightness profiles, calibrated using the zero-points in Table 2.5. Note that not all data is photometric (see Table 2.4), but still has been calibrated using these zero-points. All data in other panels of this figure are independent of these zero-points. The second panel contains the disk luminosity growth curve (monotonically increasing function) and  $\eta$  profile (non-monotonically decreasing function;  $\eta \equiv I(r)/\langle I(r) \rangle$ ) (§2.4.2). We measured concentration indices from the intersection of the growth curve and the dotted lines corresponding to 0.2 and 0.8 [ $C_{80:20} \equiv 5 \log(r[80\%]/r[20\%])$ ]. The half light radius,  $r_{1/2}$ , is the radius corresponding to the intersection of the dotted line at 0.5 and the growth curve. The Petrosian  $\eta$  radius,  $r_{\eta=0.2}$  is measured from the point the dotted line corresponding to 0.2 crosses the  $\eta$  function. The next panel contains the spiral index,  $\Sigma \equiv \frac{\sigma(R)}{(\sigma_S^2(R) + \sigma_B^2)^{1/2}}$  (§2.4.4.1)  $\Sigma$  should be unity if there is no apparent spiral structure at a given radius. The fourth and fifth panels contain radial profiles of position angles and axis ratios measured with the IRAF *ellipse* routine (§2.4.4.3). In each of the bottom three panels, the radius corresponding to 3 disk scale lengths is marked by a dotted line. Axis ratios and position angles were typically measured between 3 and 4 scale lengths.

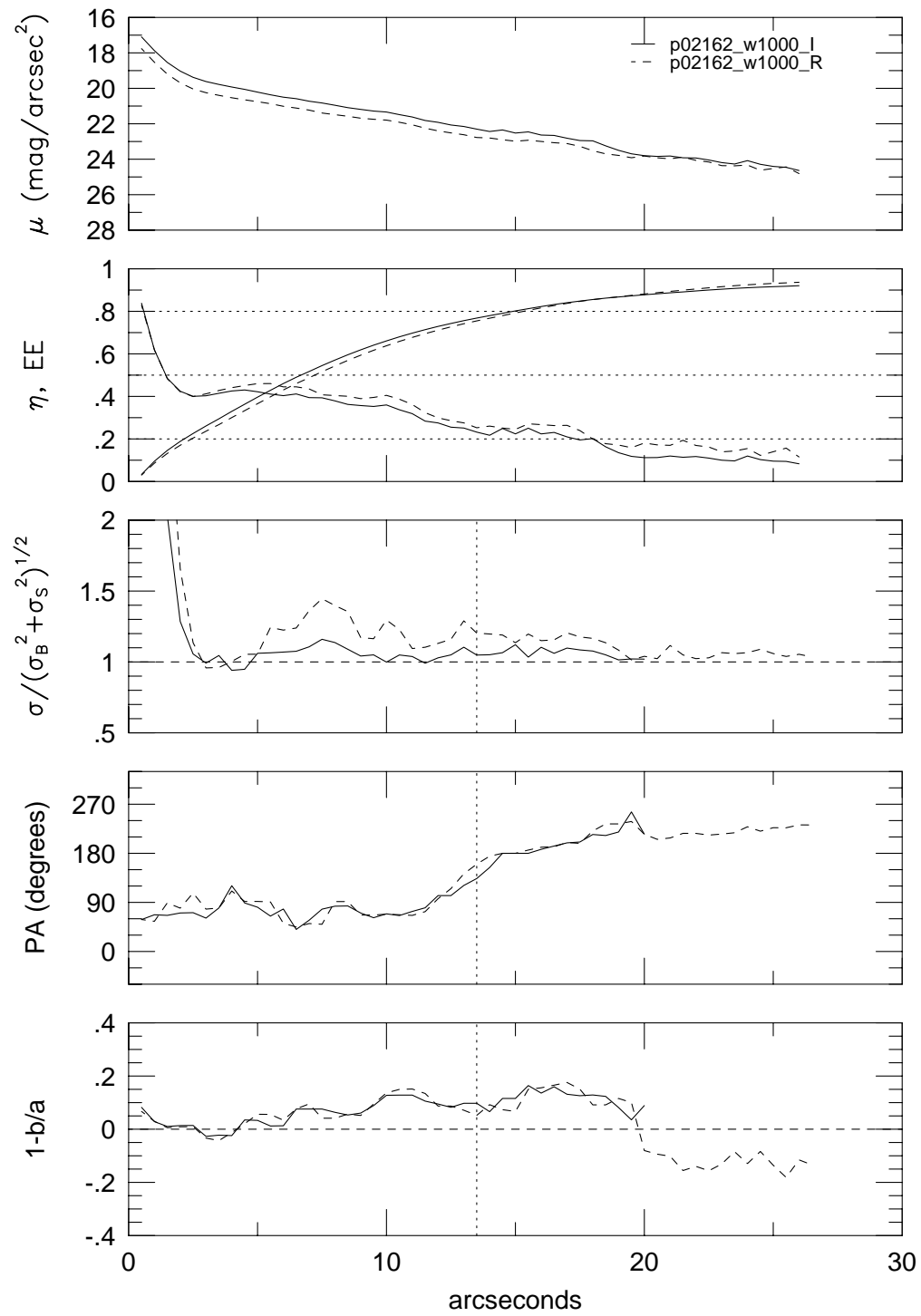
- The fourth and final panel contains the rotation curve (§3.4.2.1) and DensePak continuum measurements (§3.4.3.3). Rotation curves are produced as follows: After fitting velocity-field models to the data, as described in §3.4.3, each DensePak velocity centroid can be projected to the major axis radius,  $R$ , where  $R$  is measured in the galaxy plane. Positions  $|\theta| < 20^\circ$ , where  $\theta$  is the angle from the major axis in the galaxy plane, are marked with dark, open circles. Slightly lighter x's mark data  $20^\circ < |\theta| < 40^\circ$ . Finally, light filled triangles mark data  $40^\circ < |\theta| < 60^\circ$ . It is difficult to distinguish between data from different regimes in  $\theta$  — an indication of a good velocity-field fit. The solid lines mark the model hyperbolic-tangent model rotation curve (Equation 3.7). PGC 5345, PGC 23913, and PGC 70962 do not have rotation curves or continuum maps because model fits did not converge for these three galaxies. The bottom panel contains continuum magnitudes, calculated from  $-2.5 \log \text{Counts}_{\text{cont}}$ . (see §3.3.1), with arbitrary zero-point, as measured between  $6600\text{\AA} < \lambda < 6800\text{\AA}$ . While the quality of our continuum data varies a great deal due to the conditions in which they were taken (continuum measurements were more suspect during bright time), these plots demonstrate that for most galaxies the kinematic and photometric centers of the galaxies are aligned.



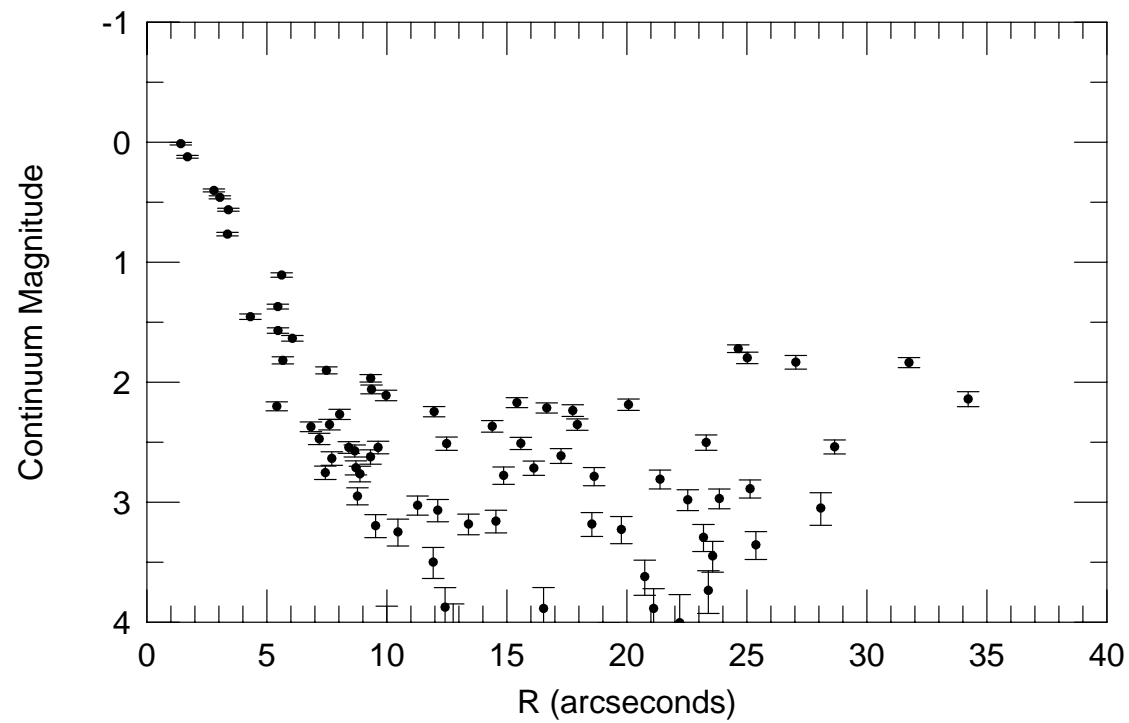
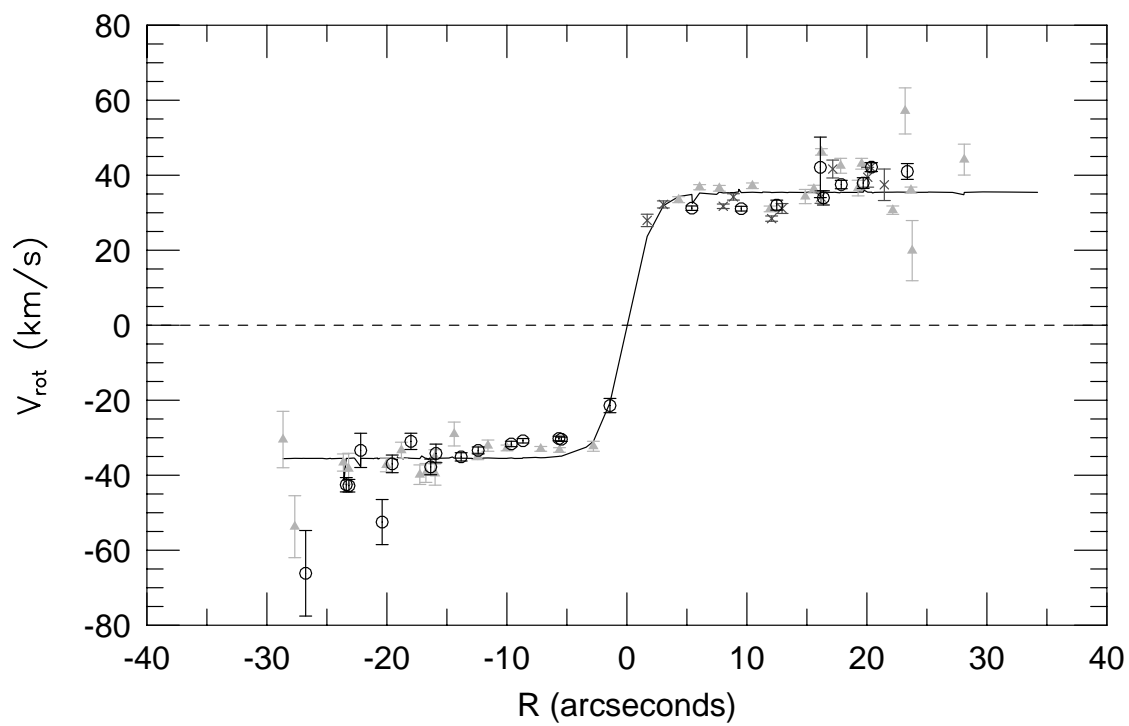
p02162



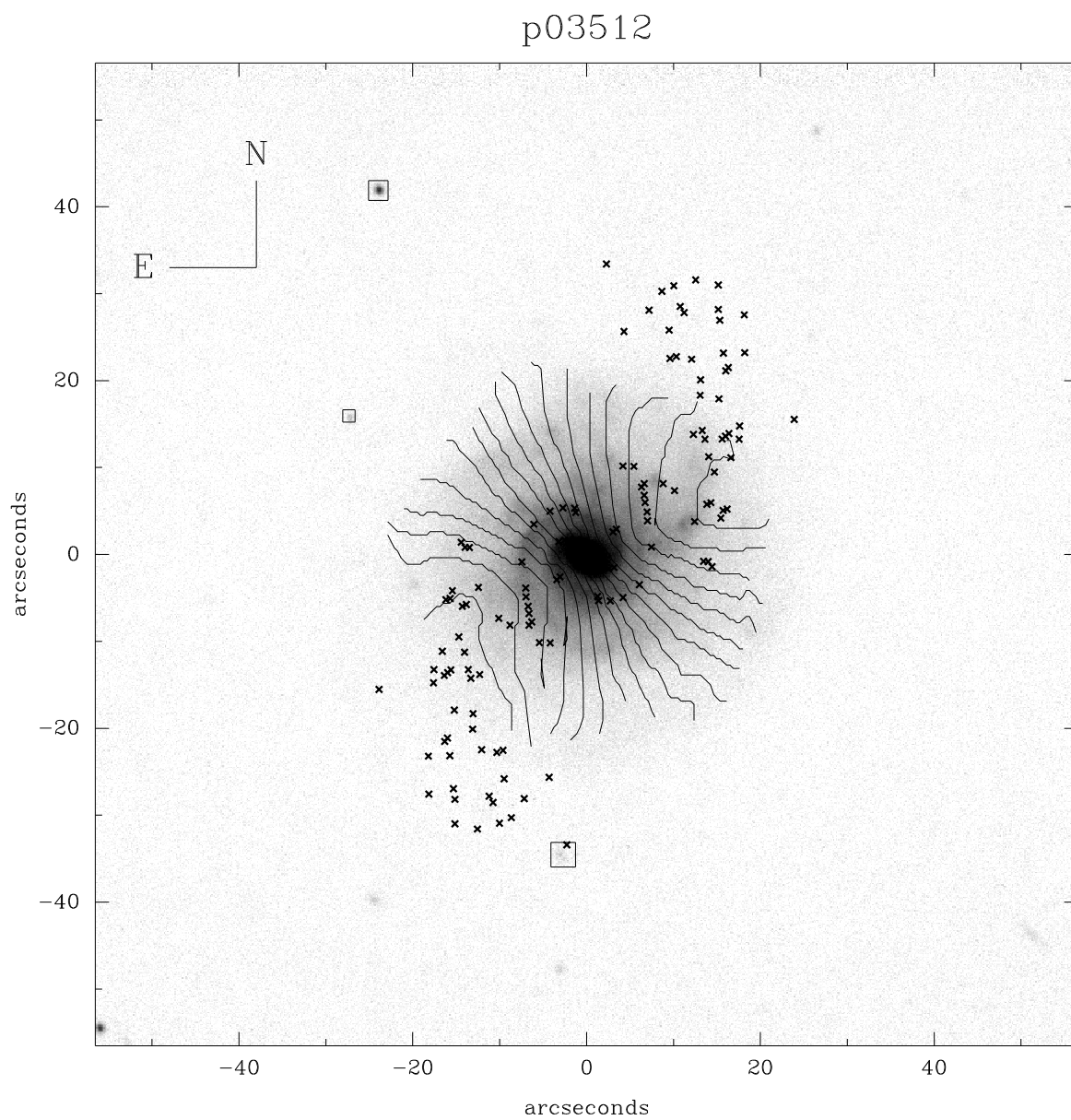
p02162



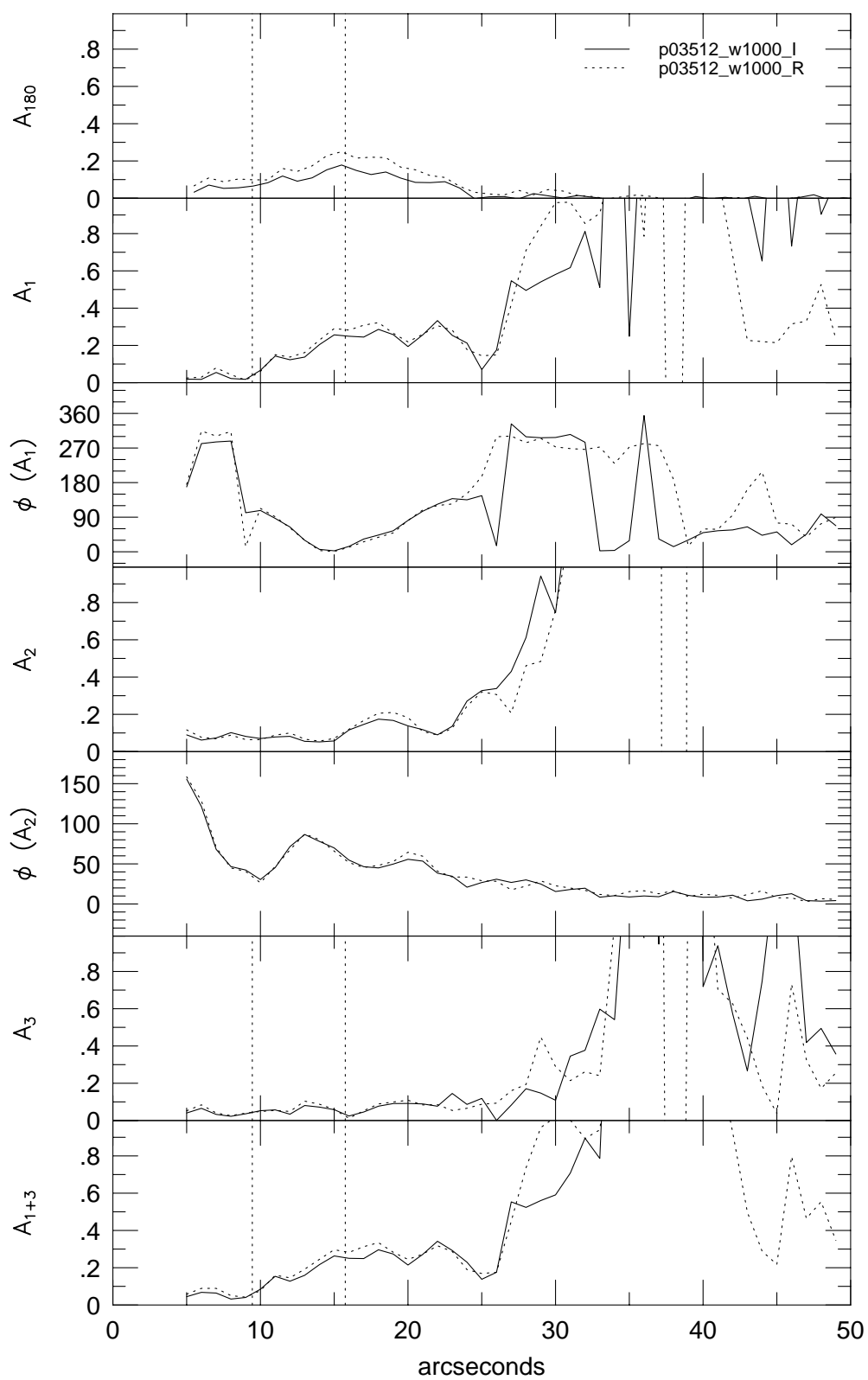
p02162

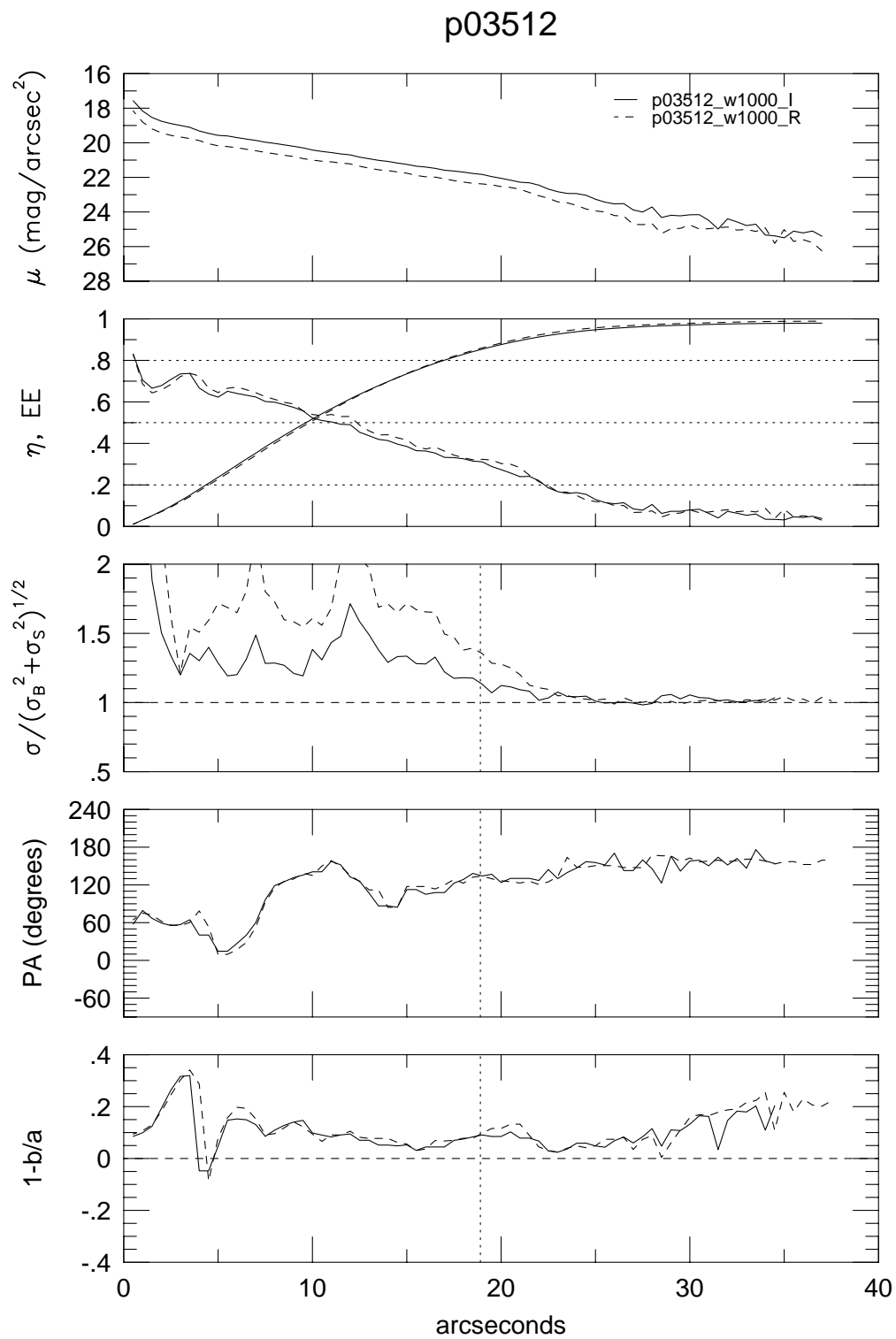




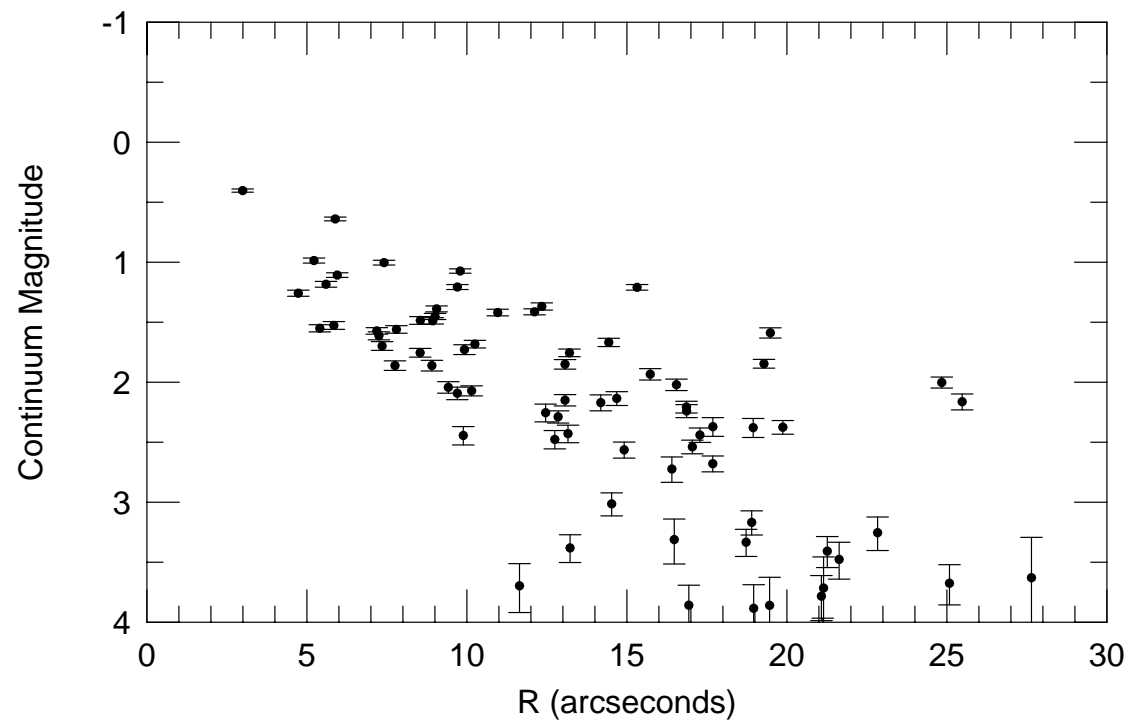
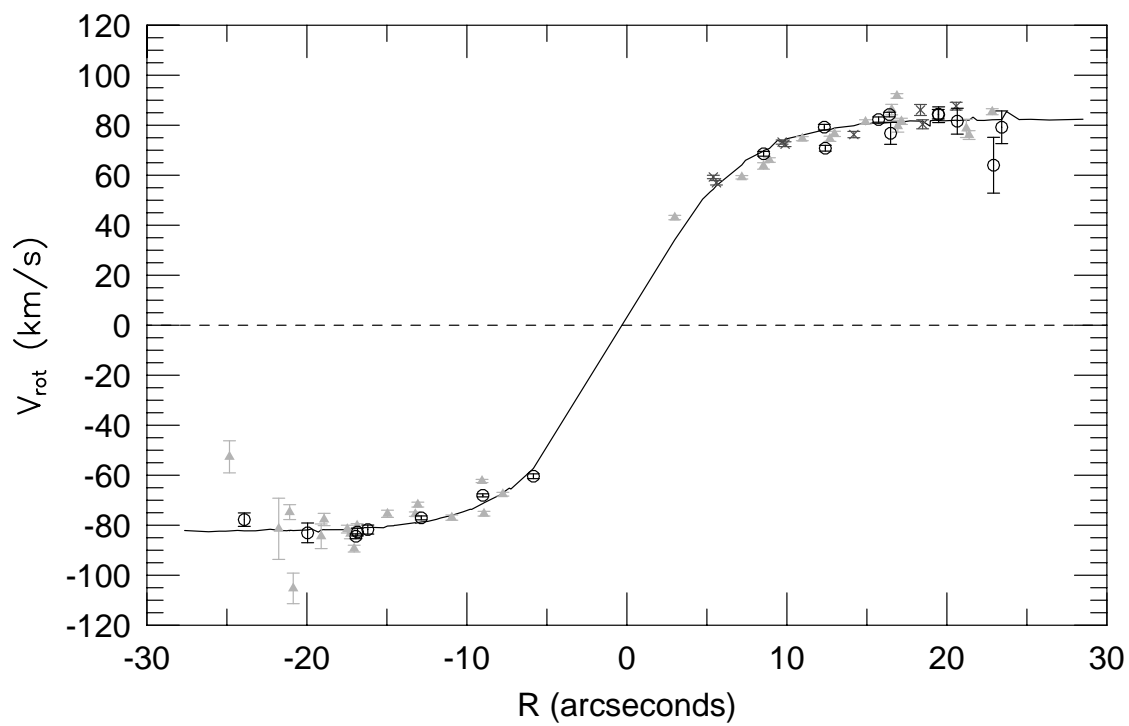


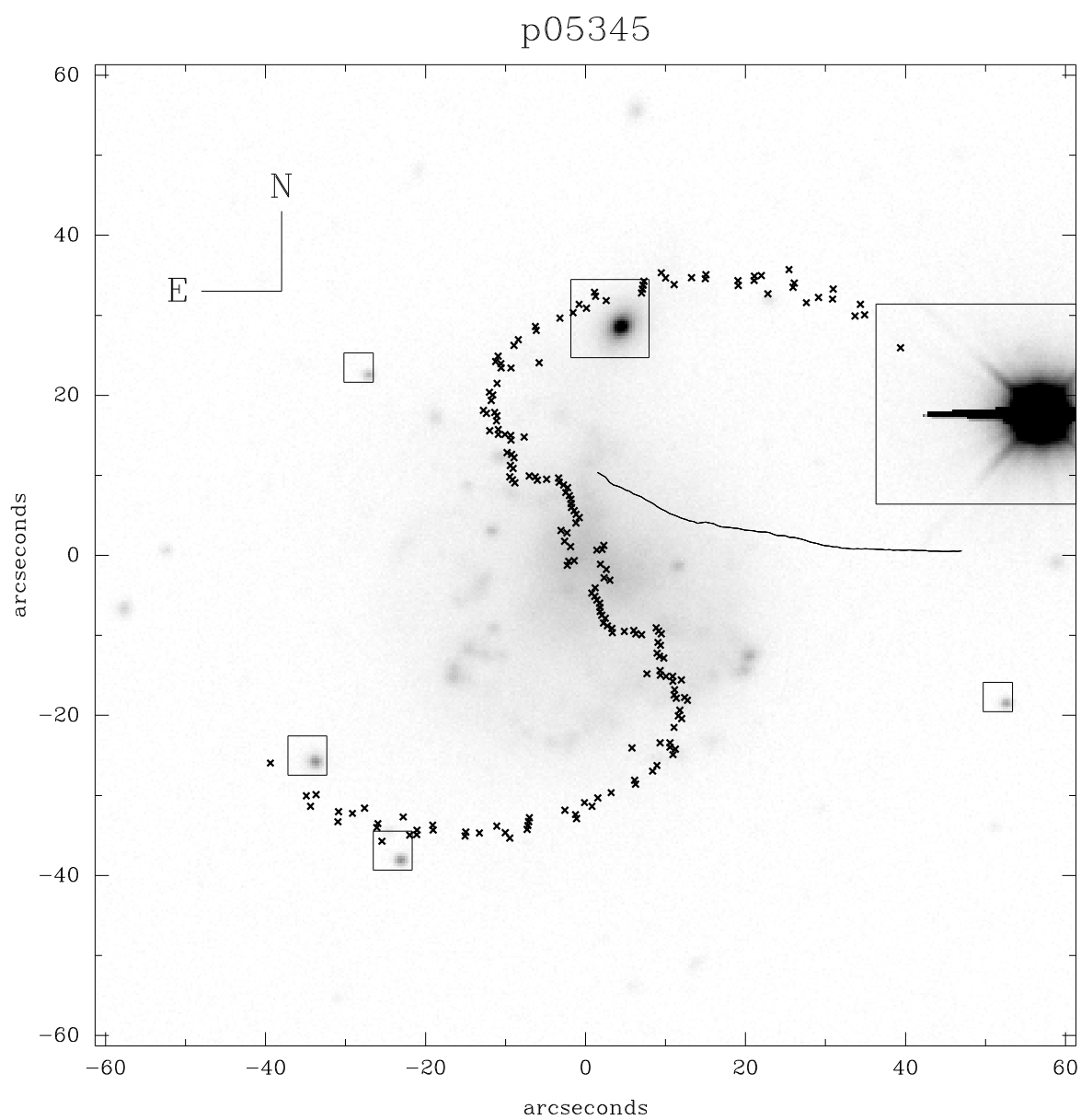
p03512



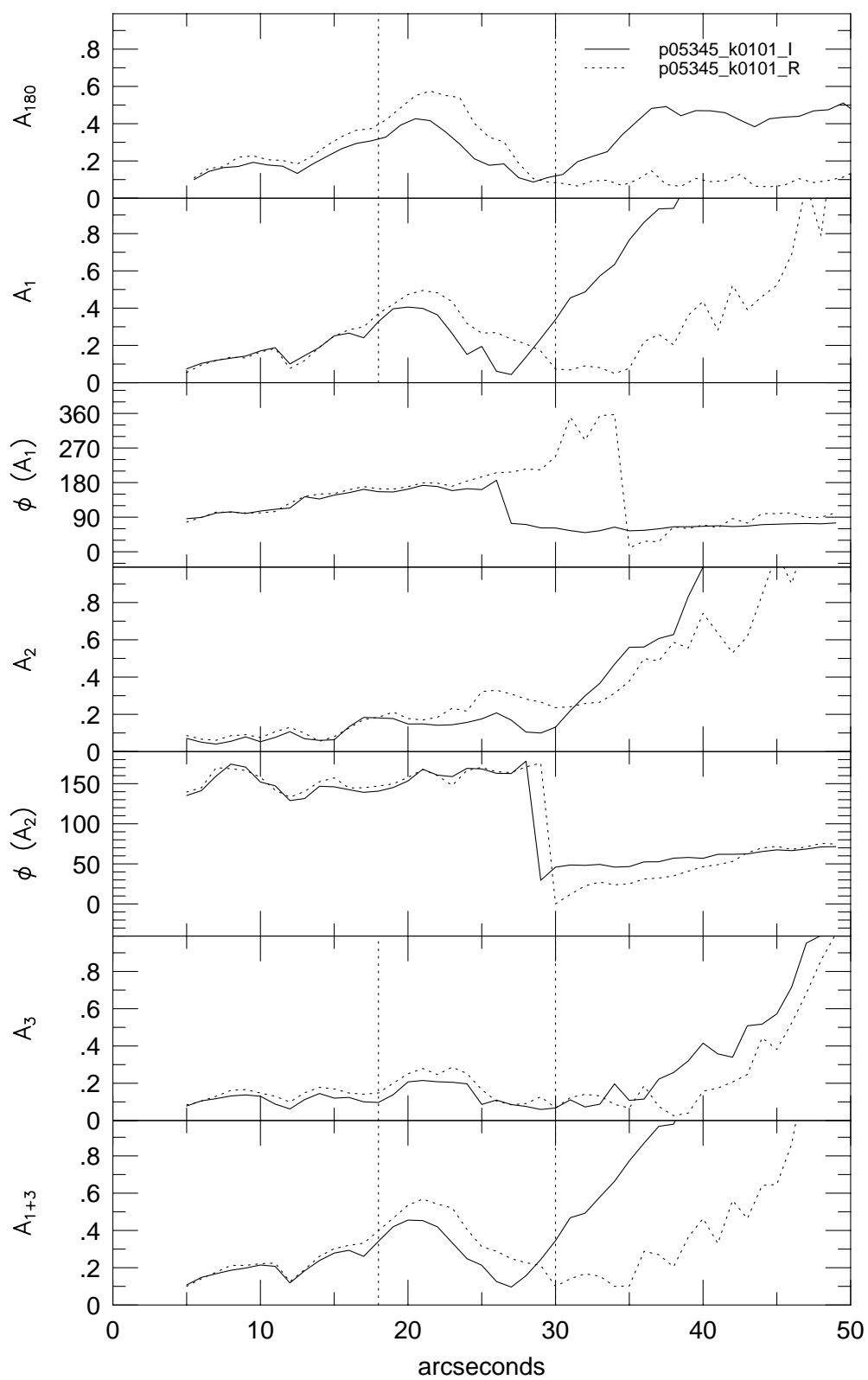


p03512

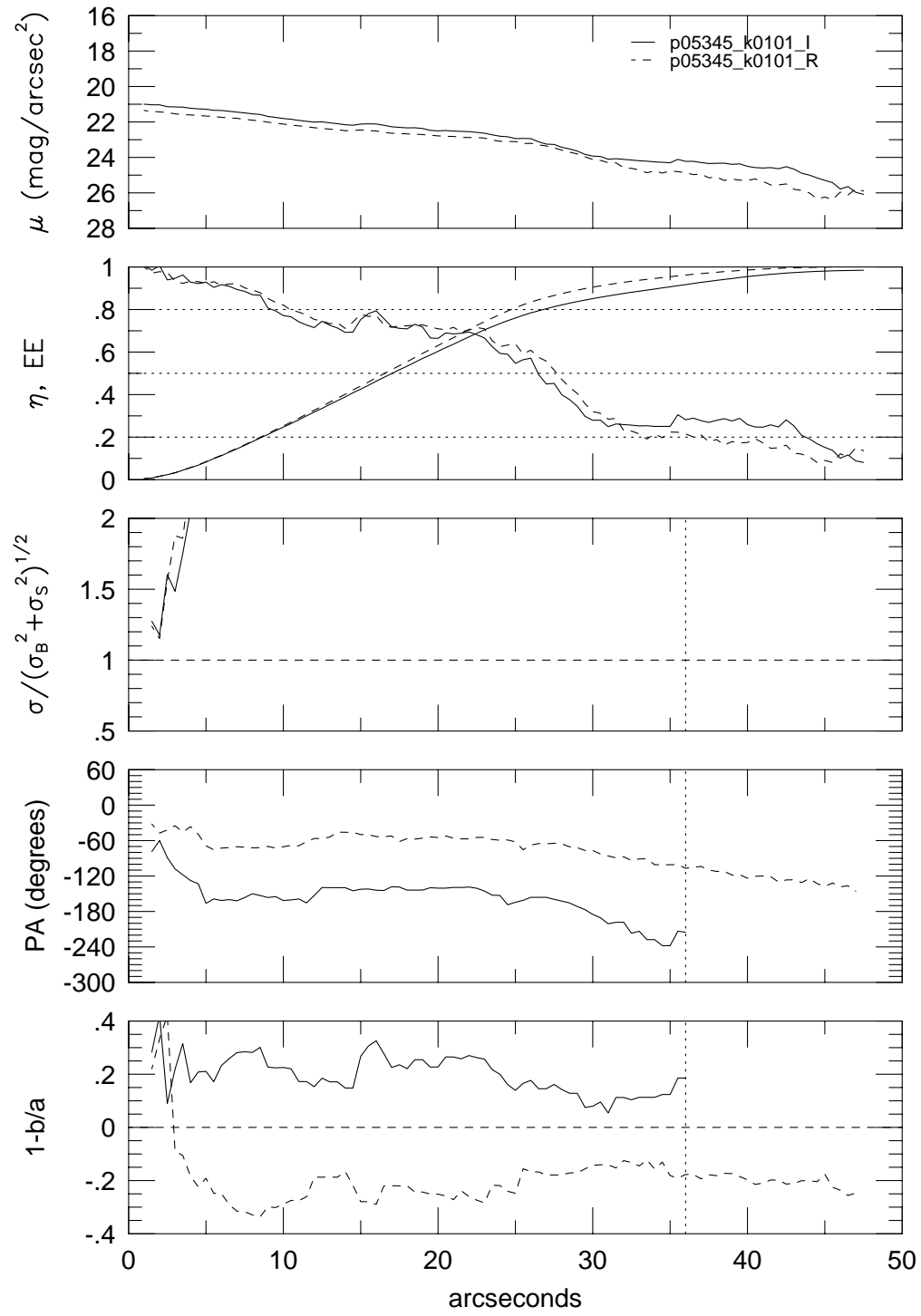




p05345

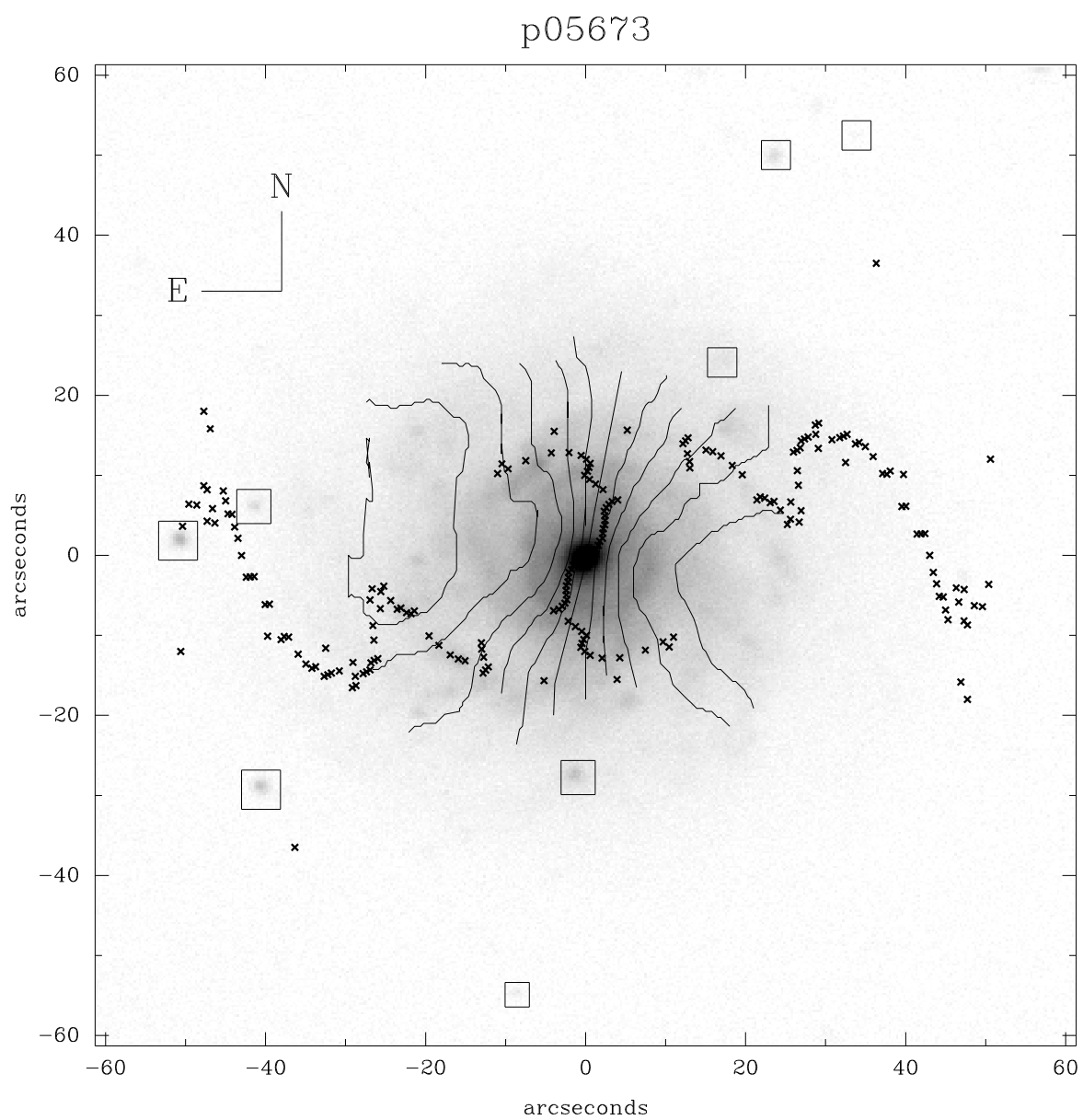


p05345

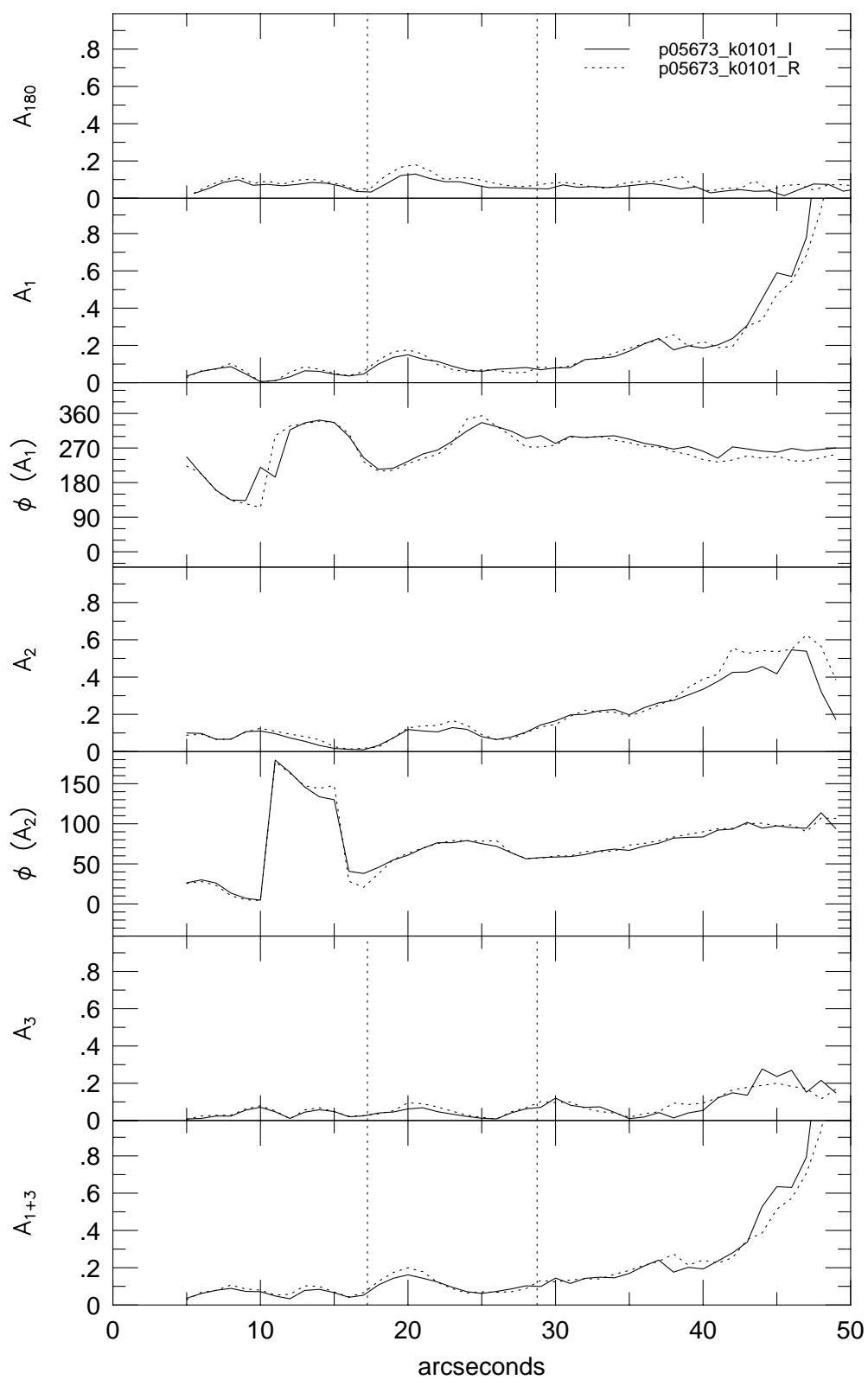




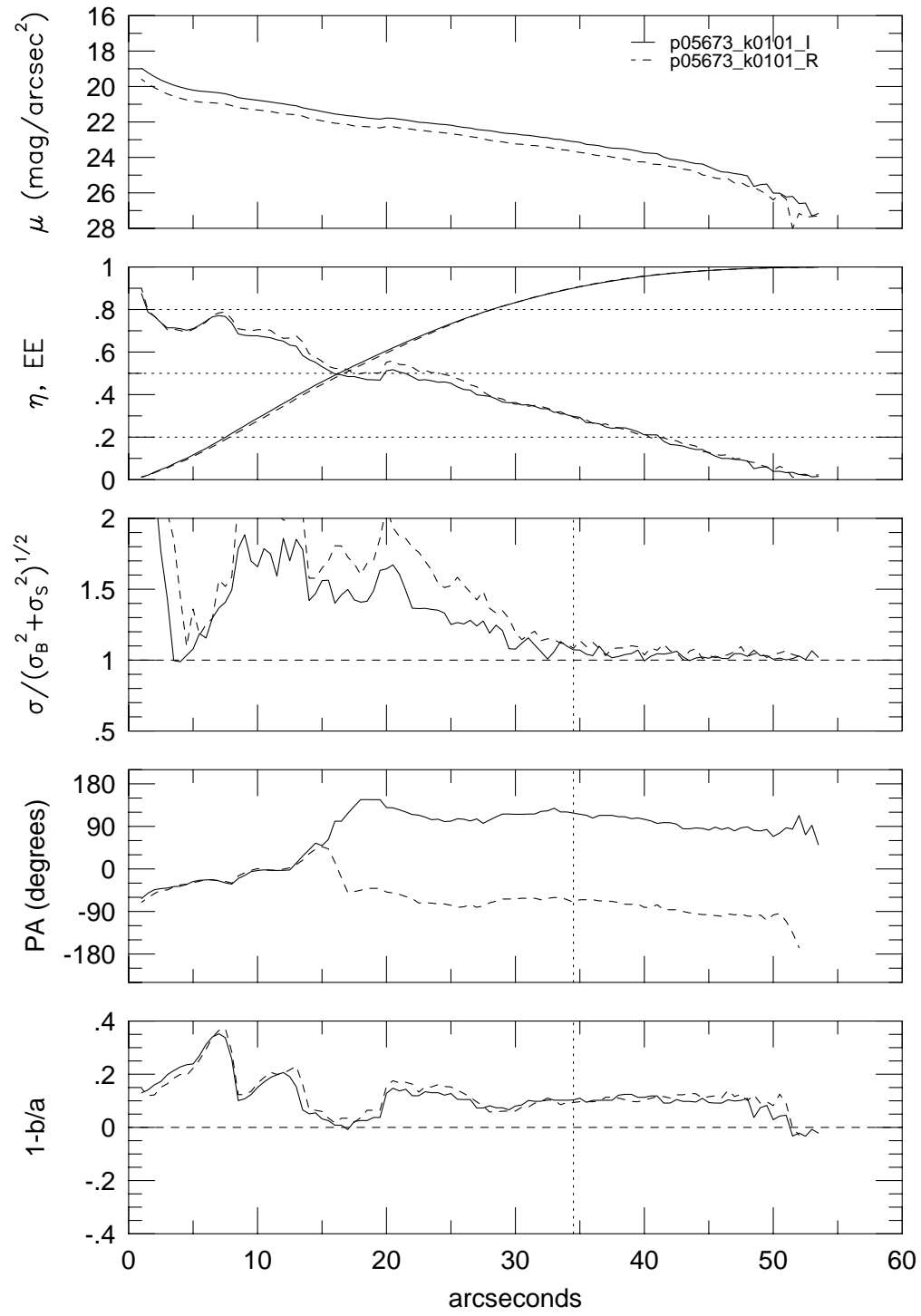




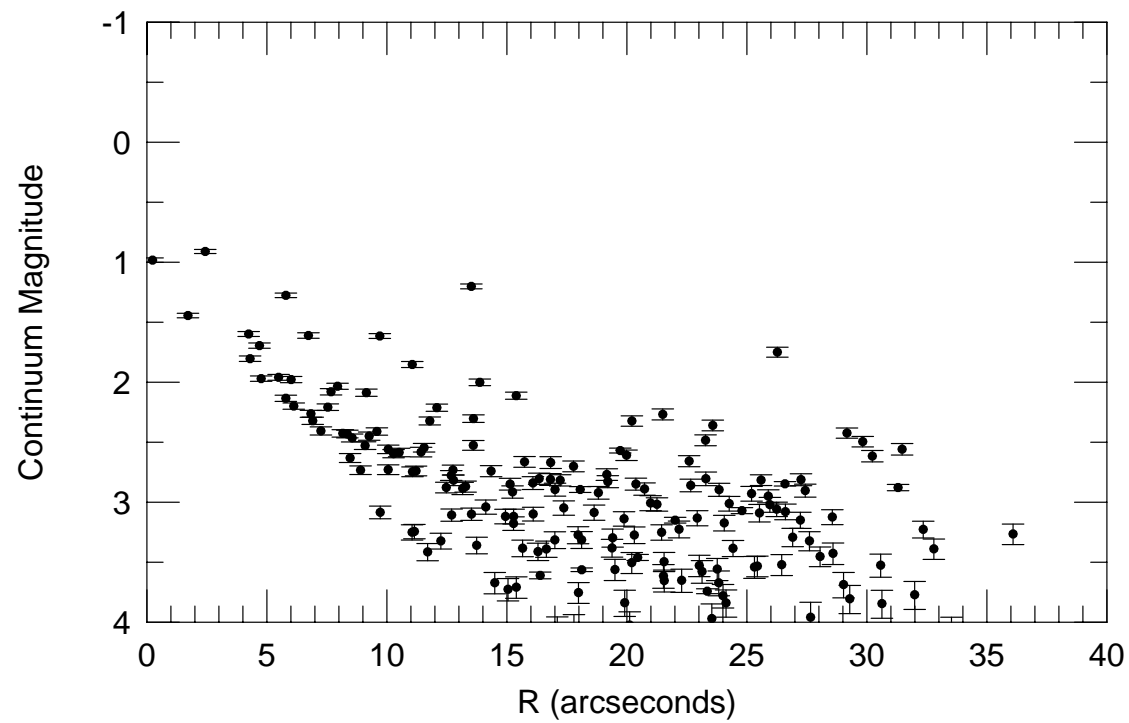
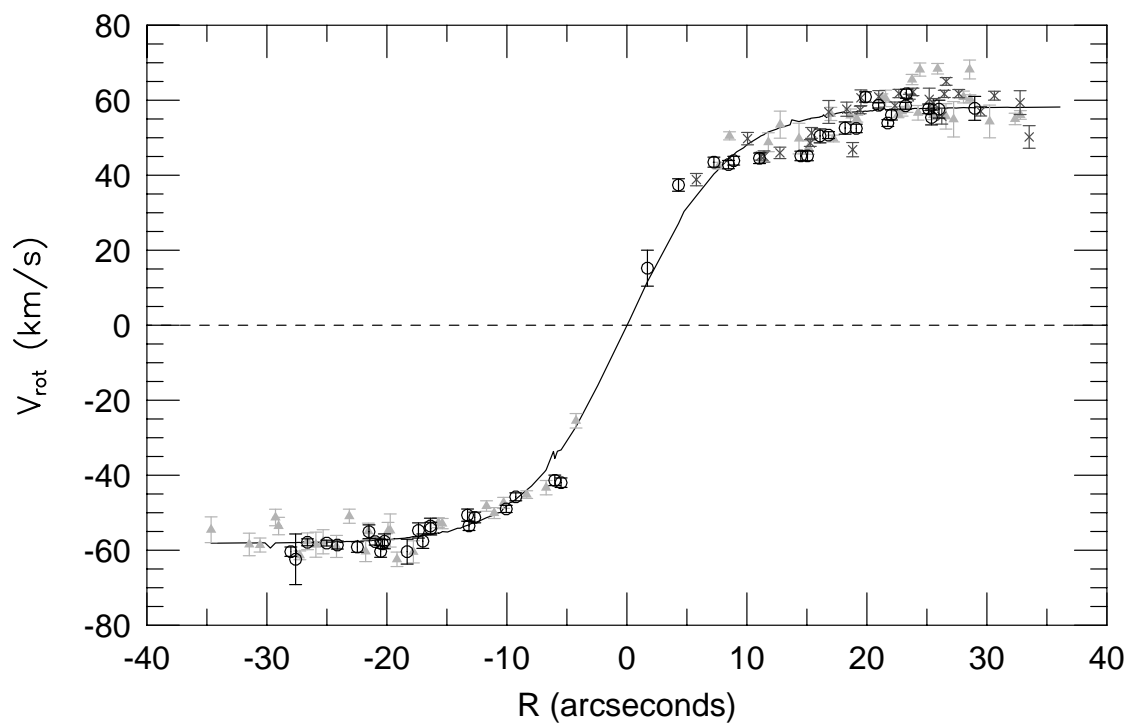
p05673

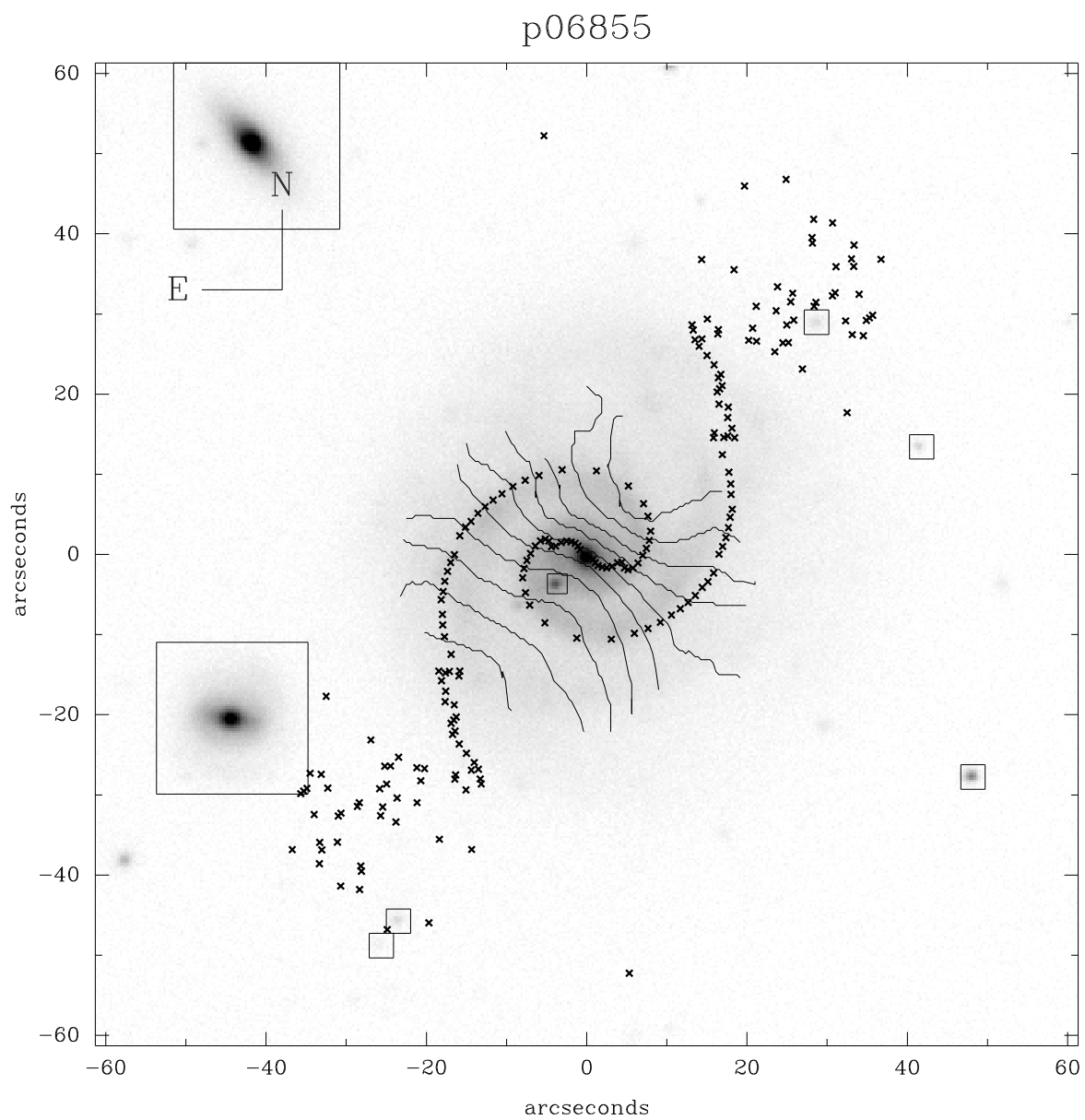


p05673

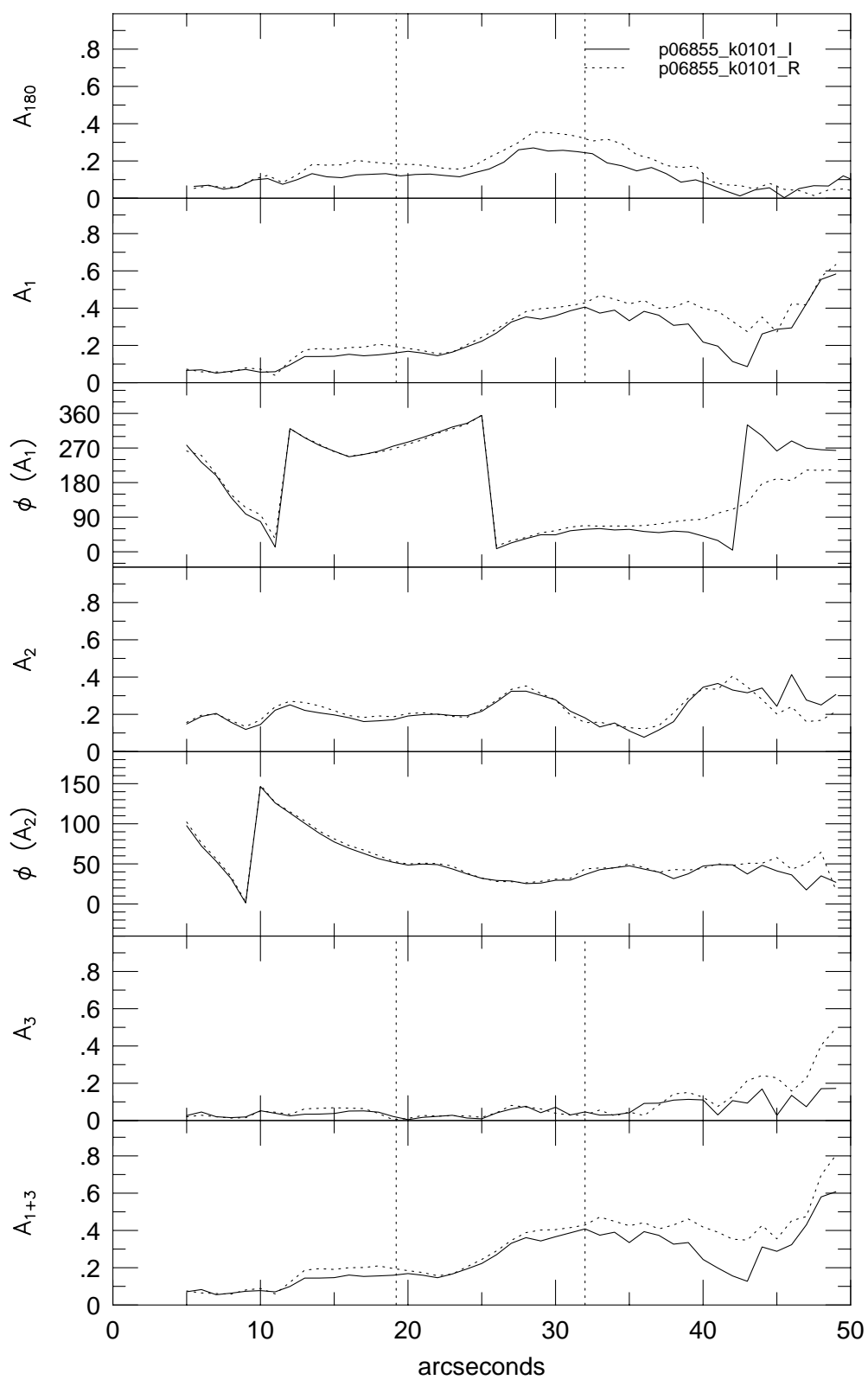


p05673

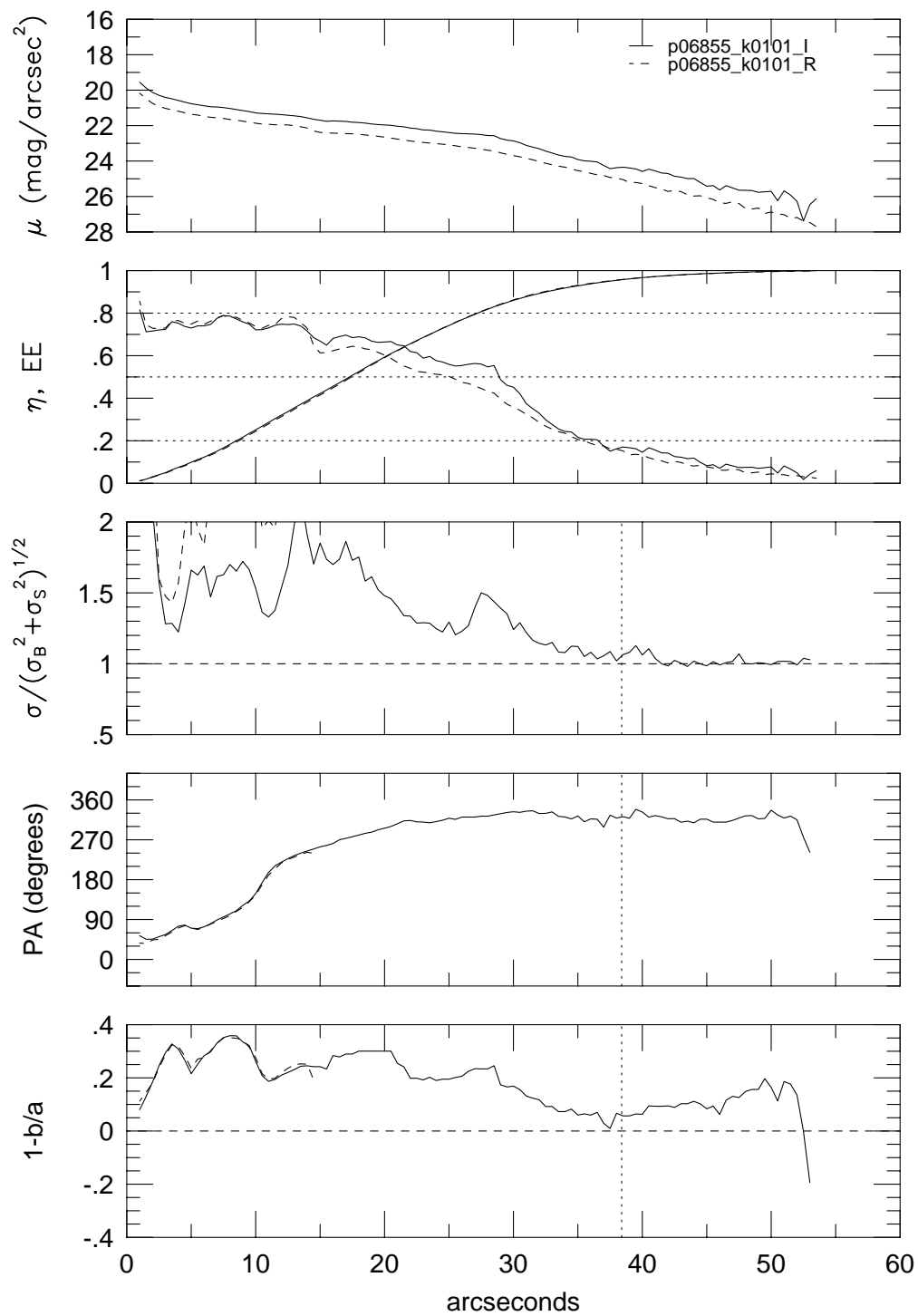




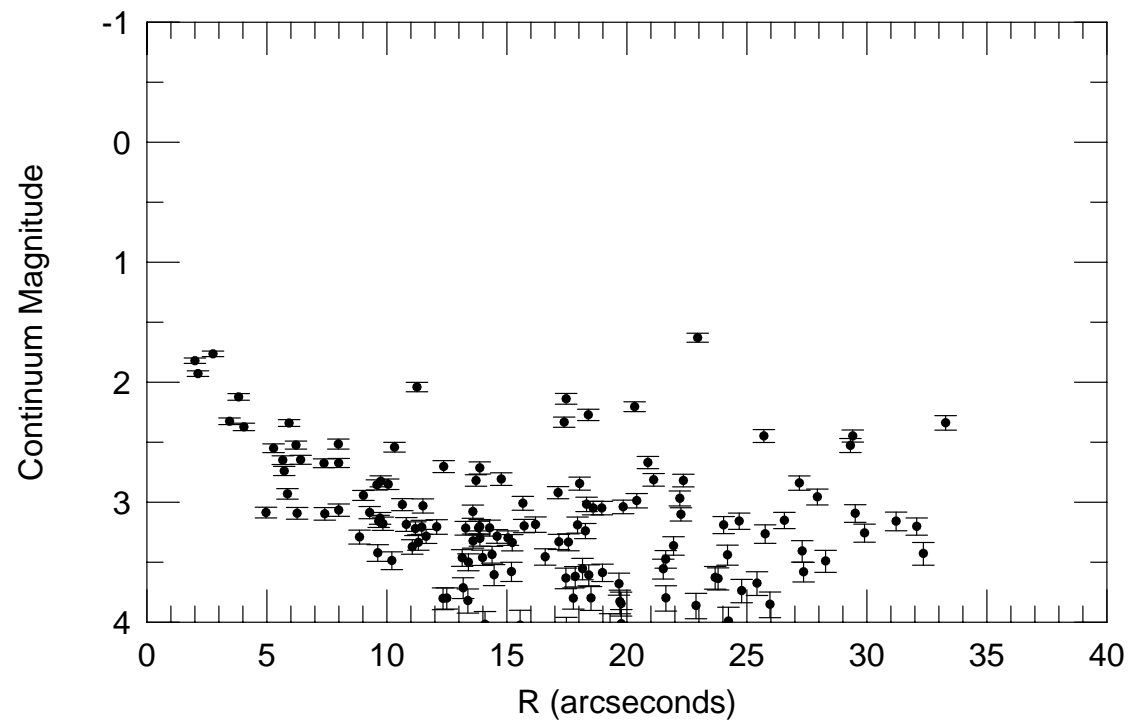
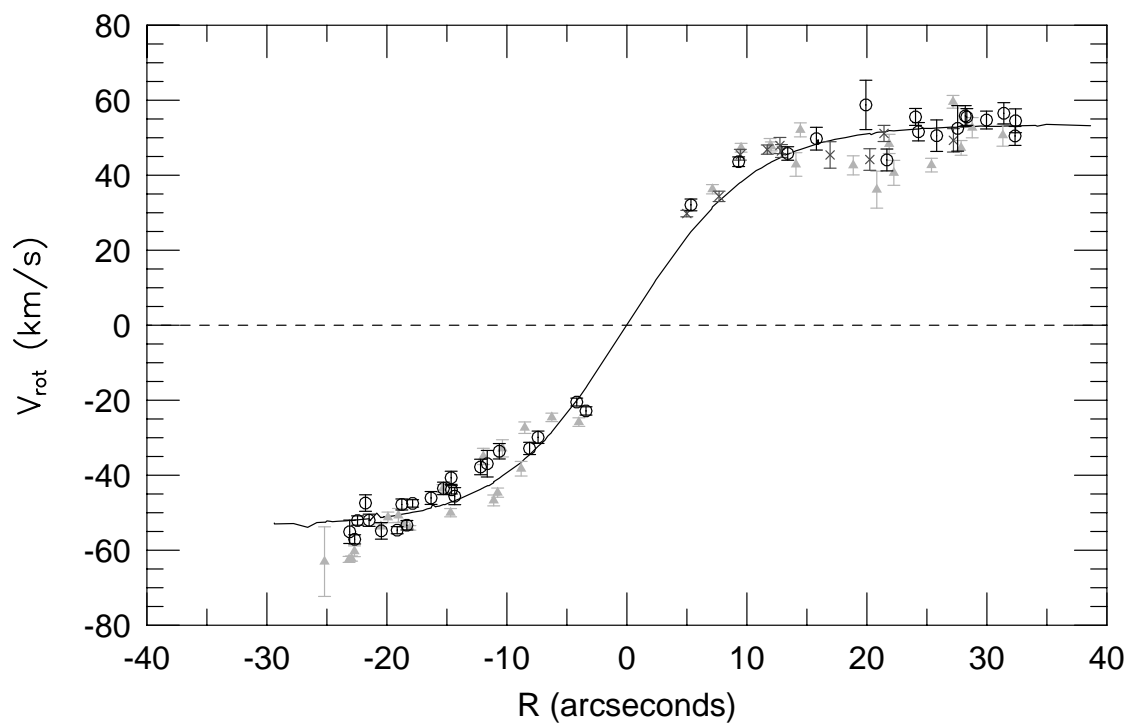
p06855



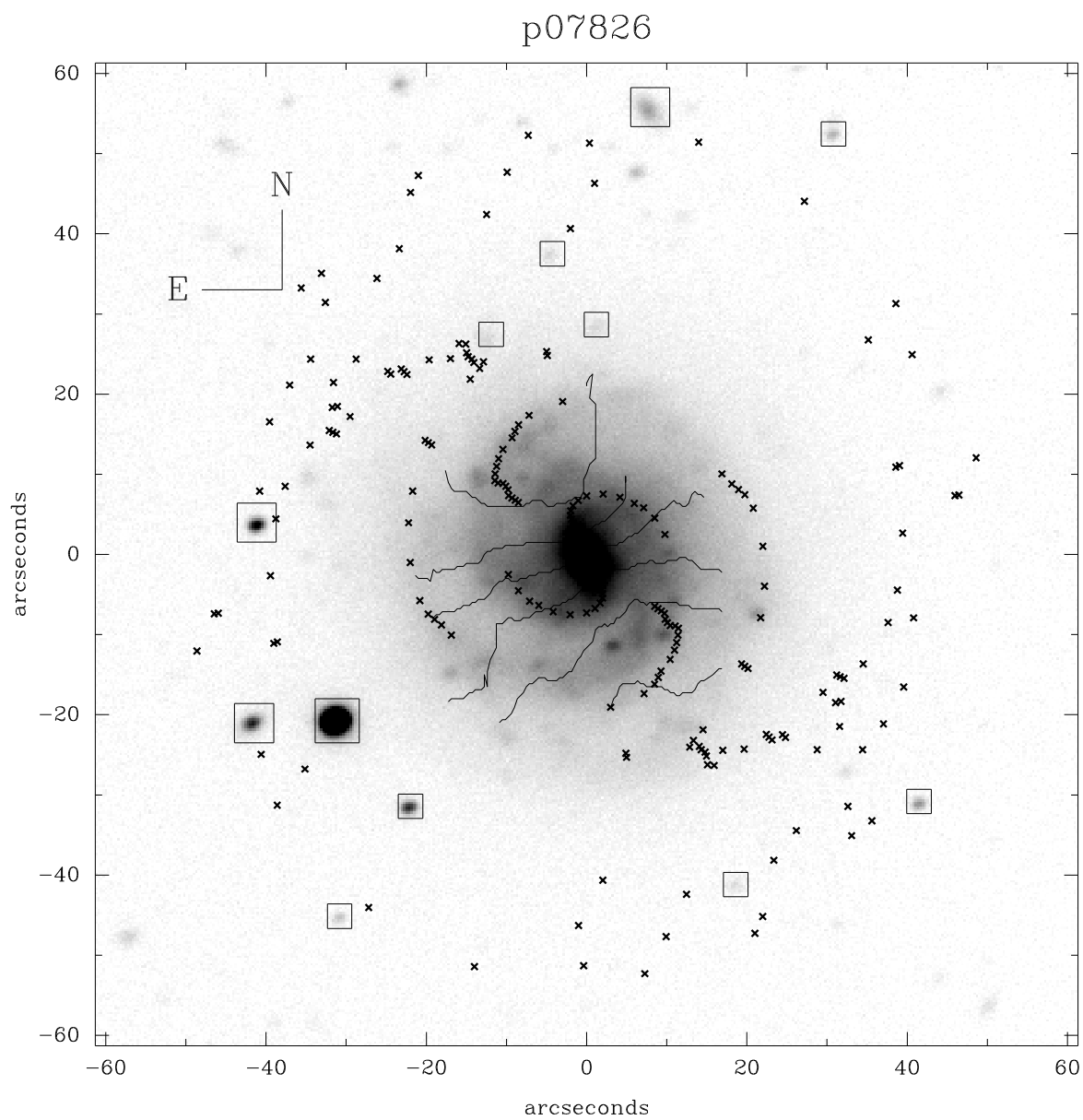
p06855



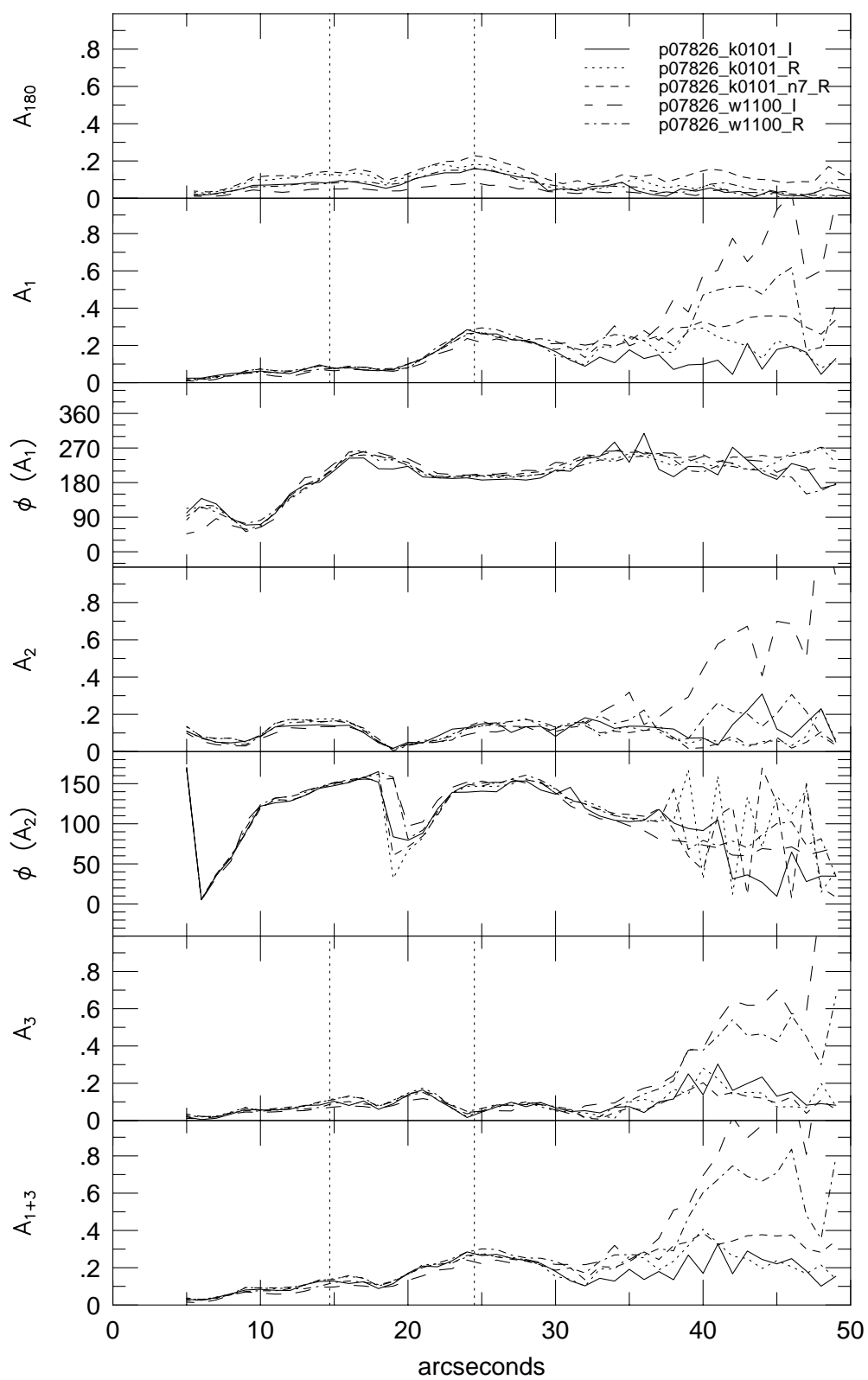
p06855



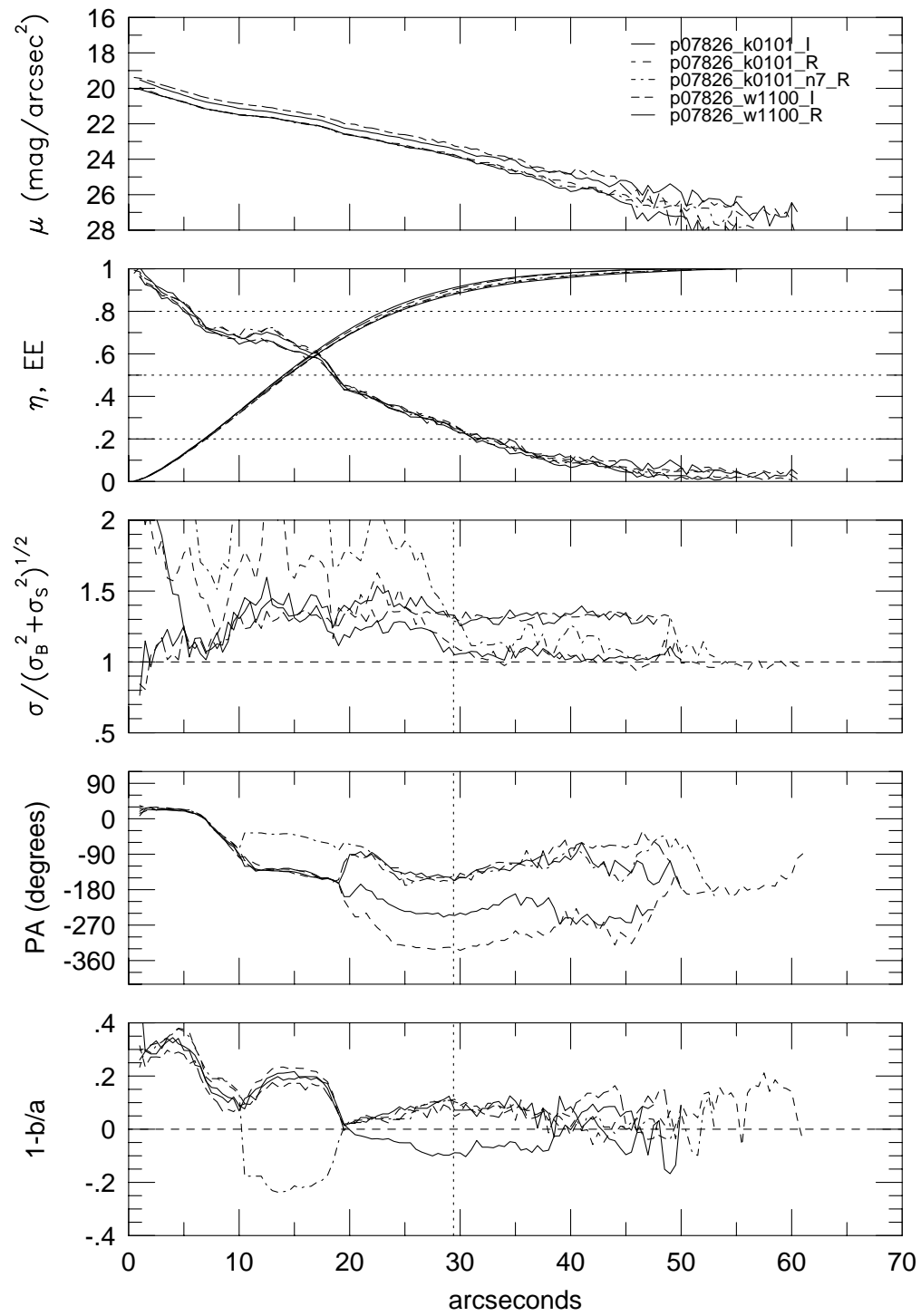




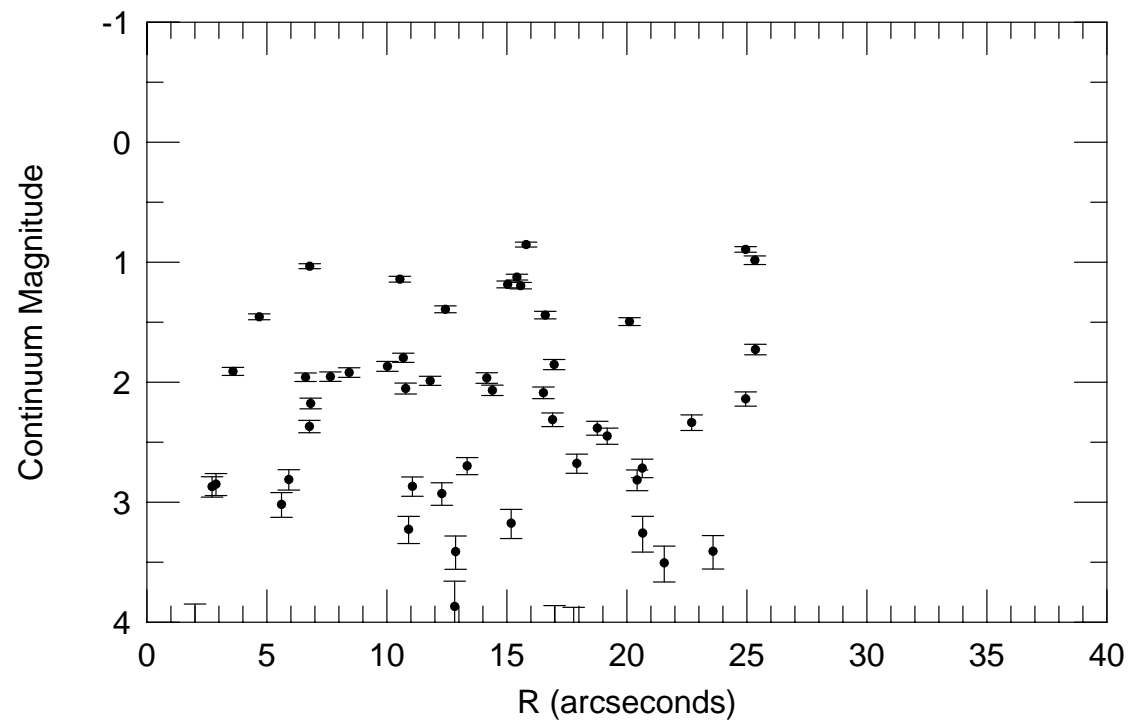
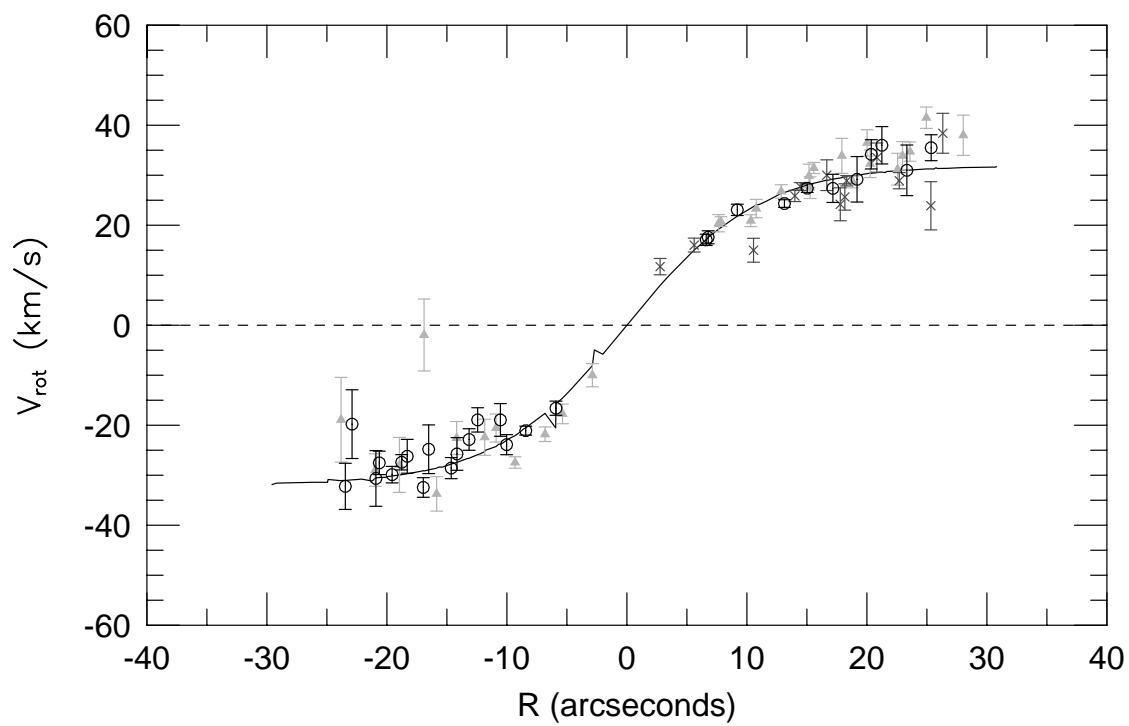
p07826

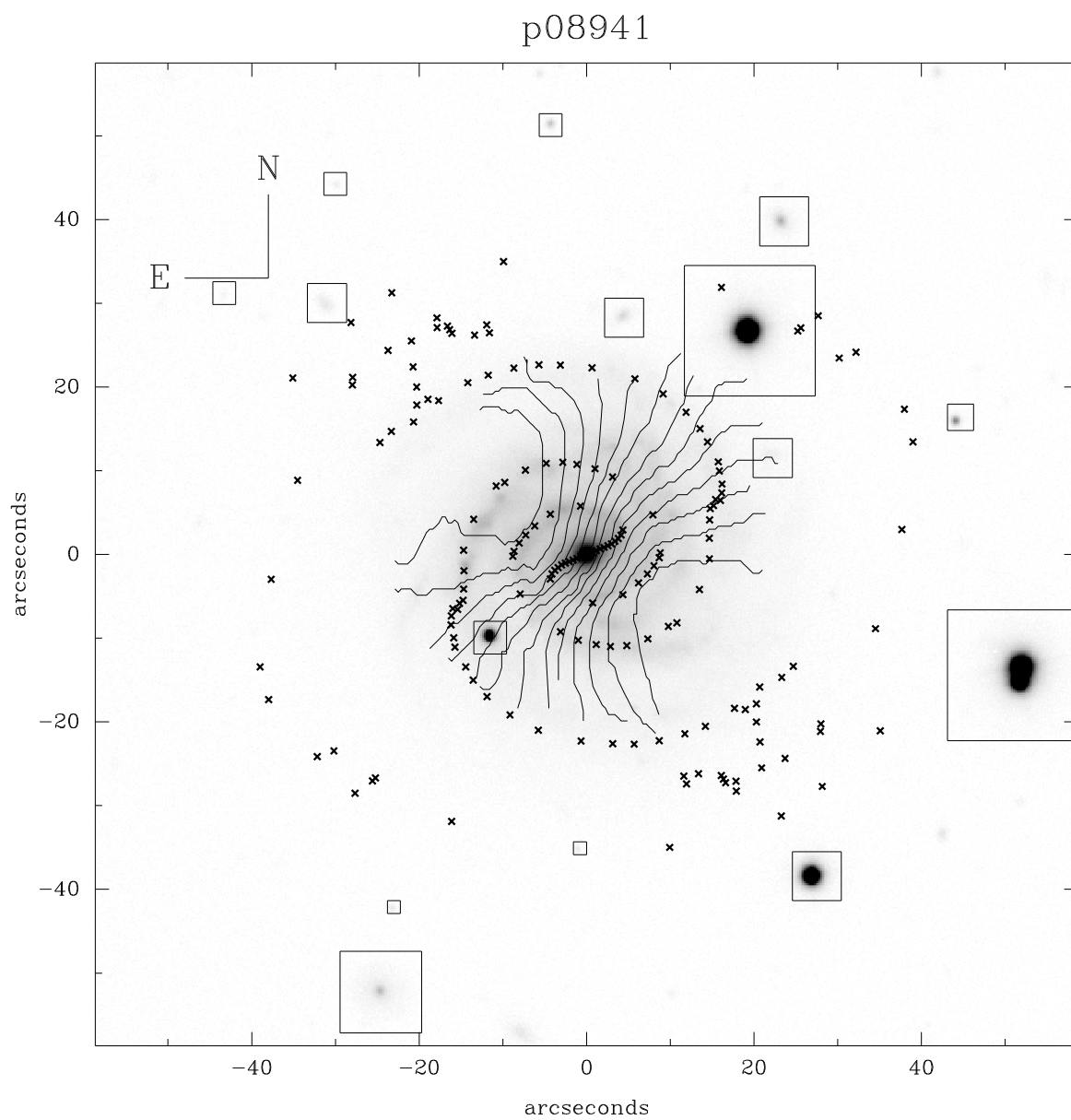


p07826

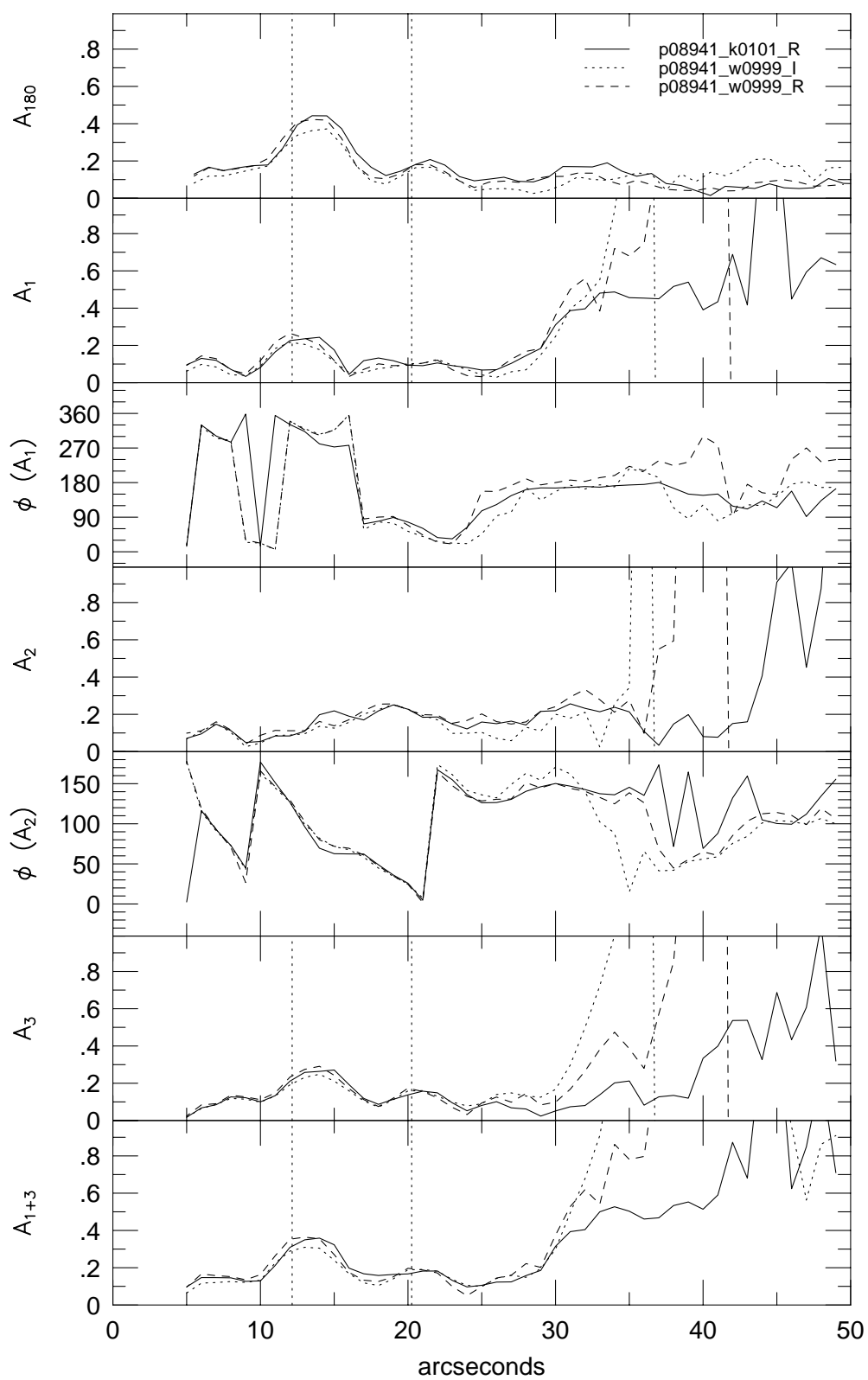


p07826

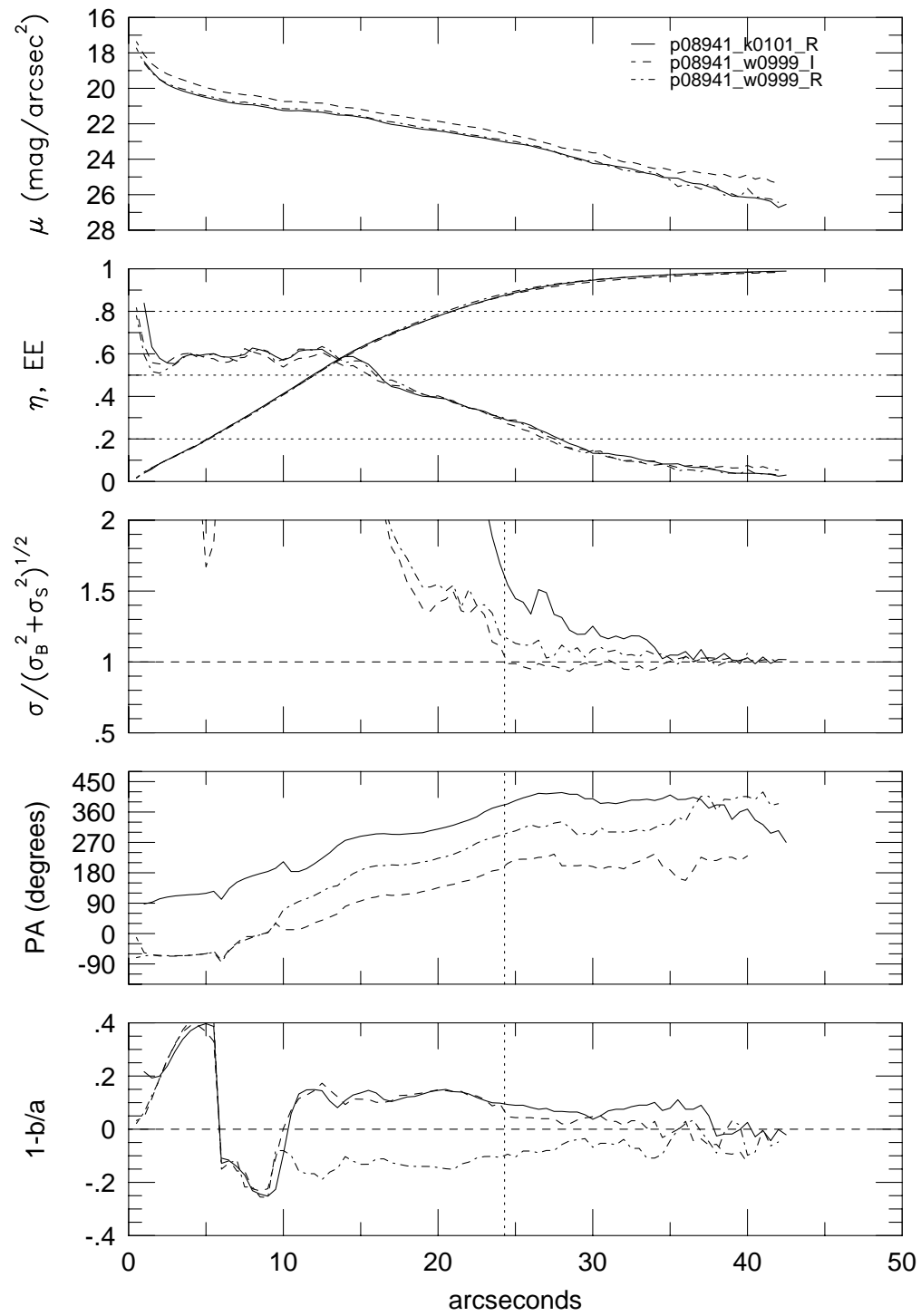




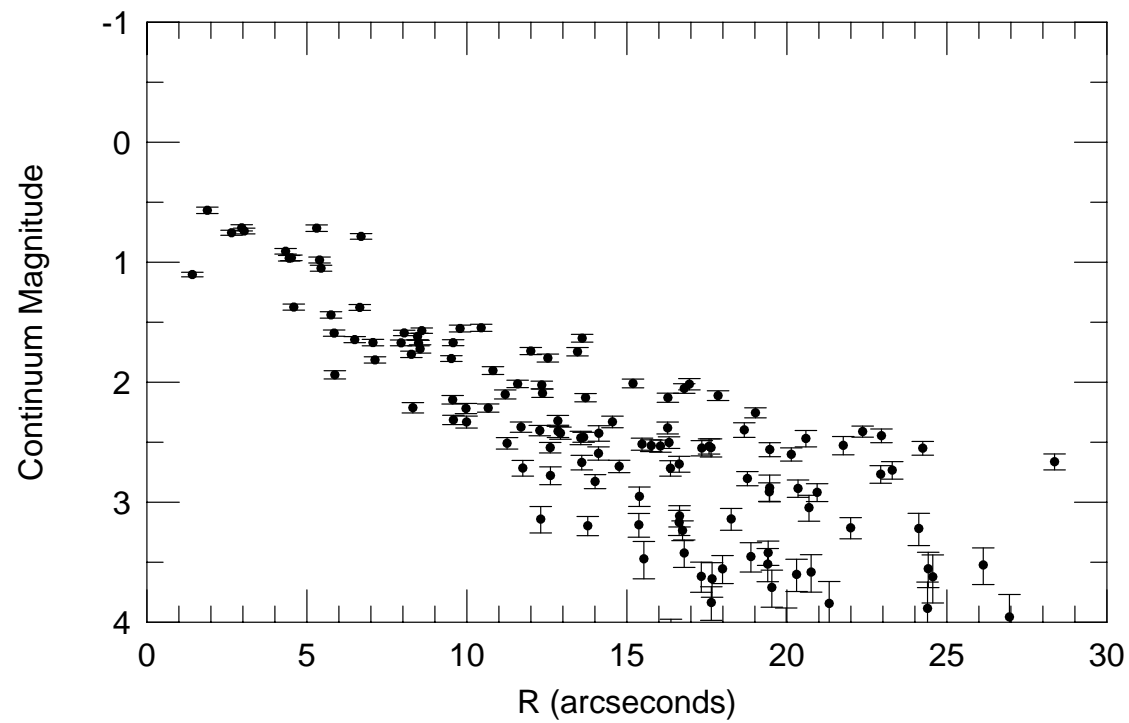
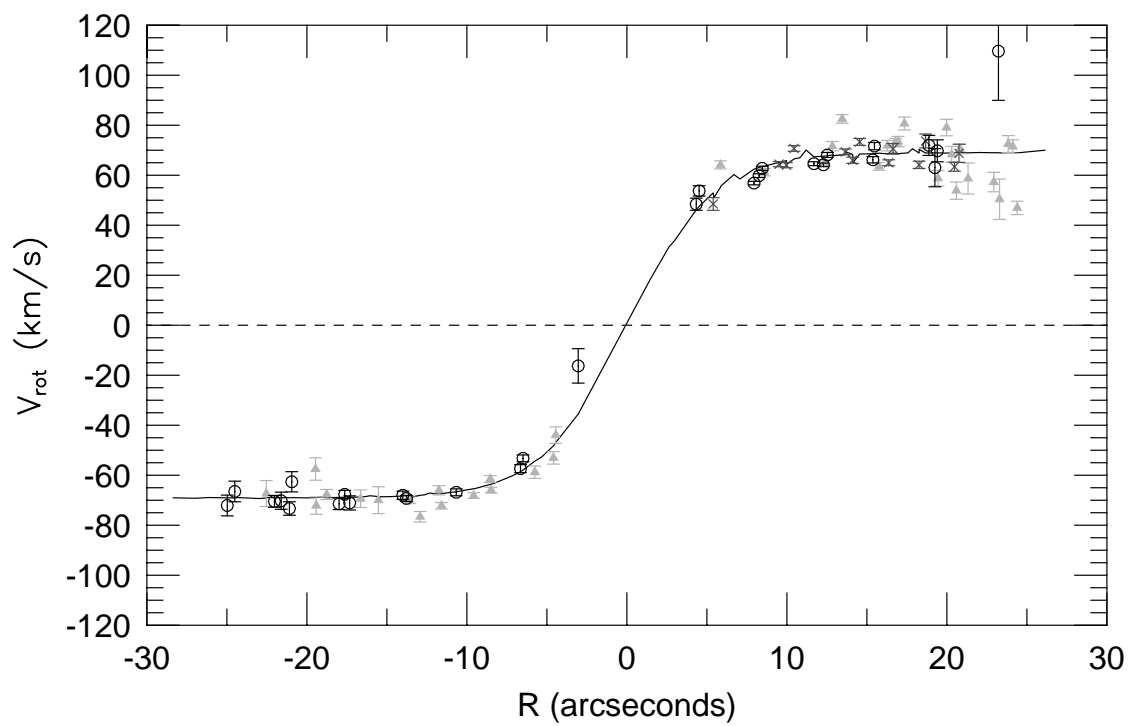
p08941



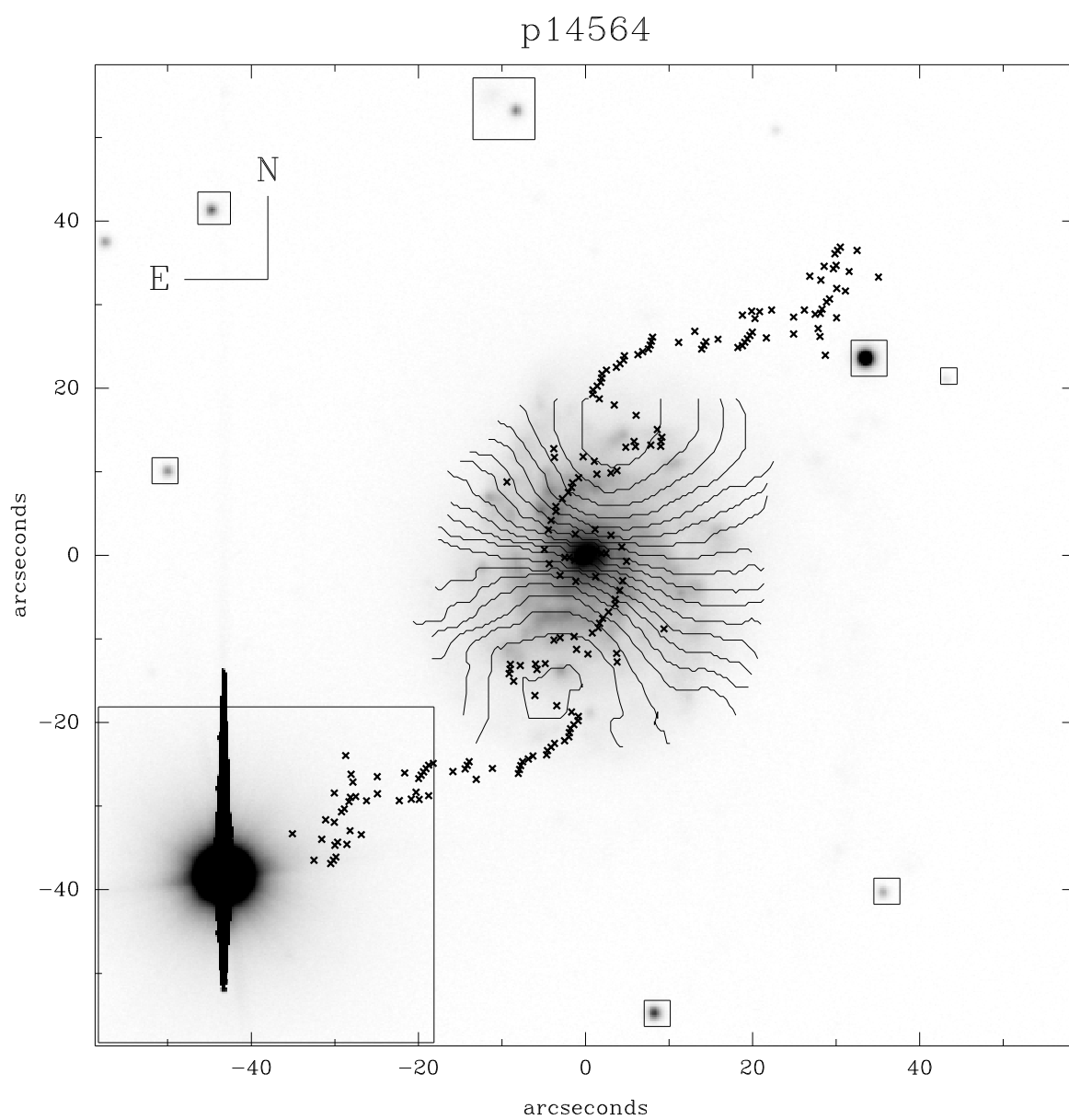
p08941



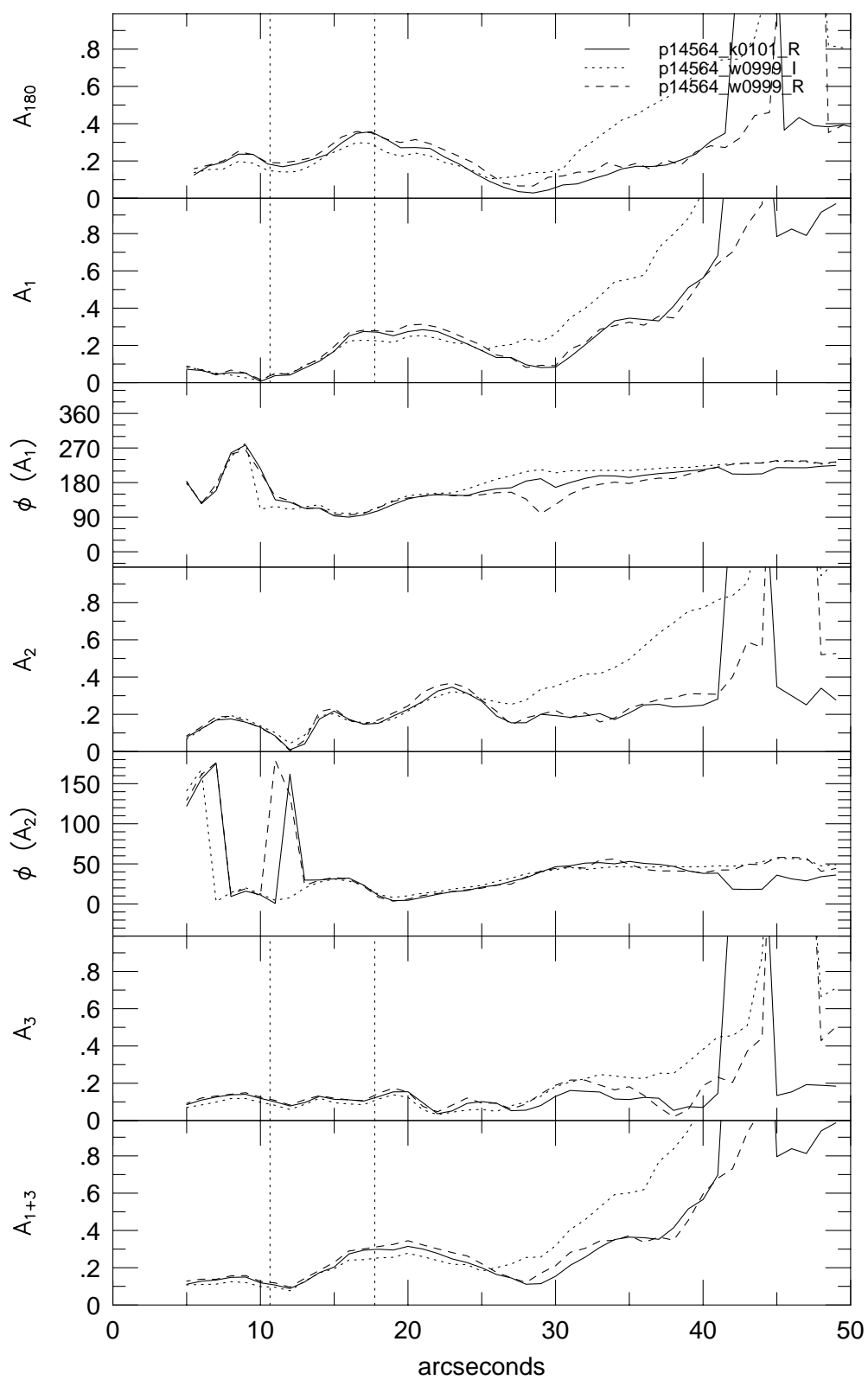
p08941



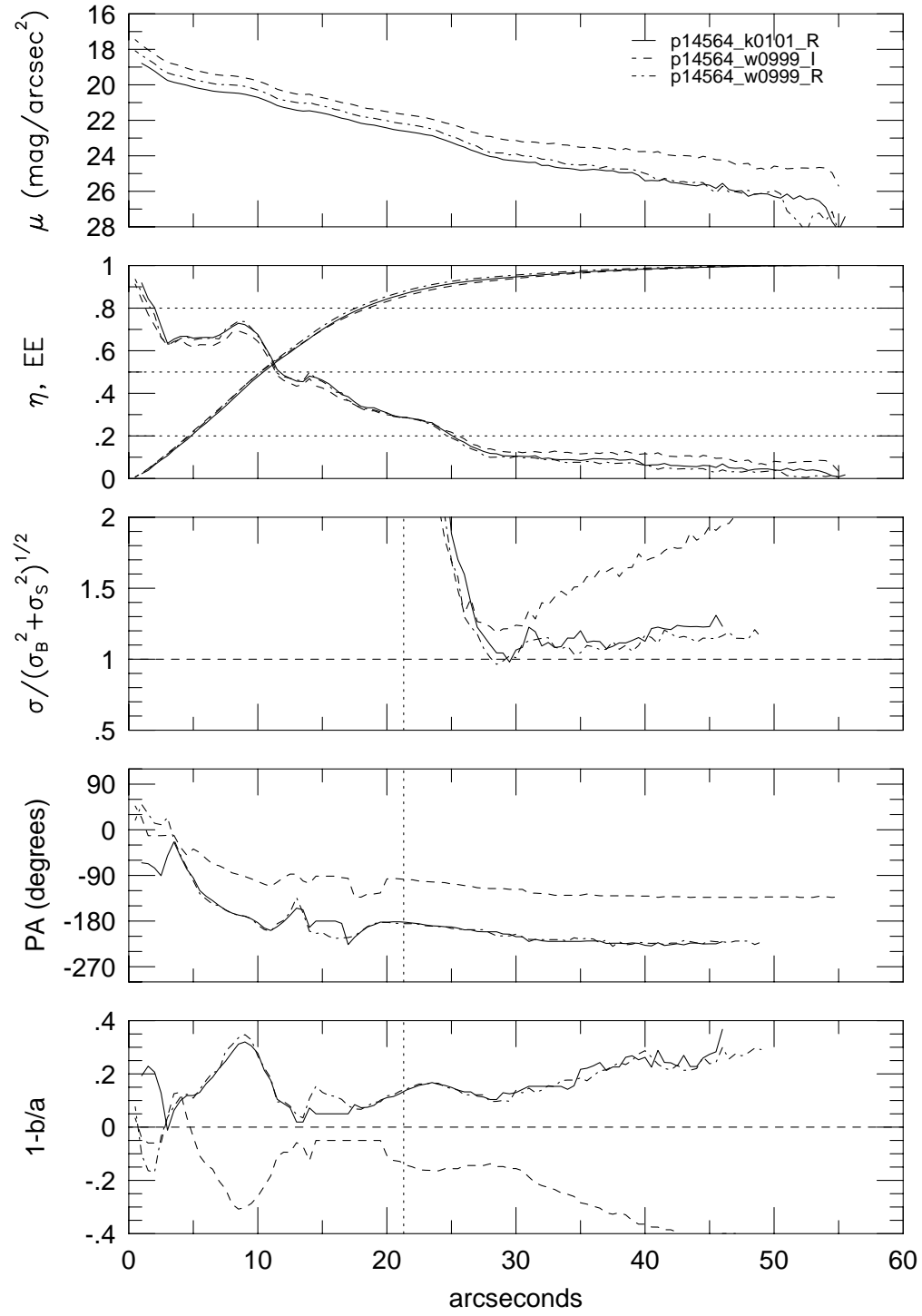




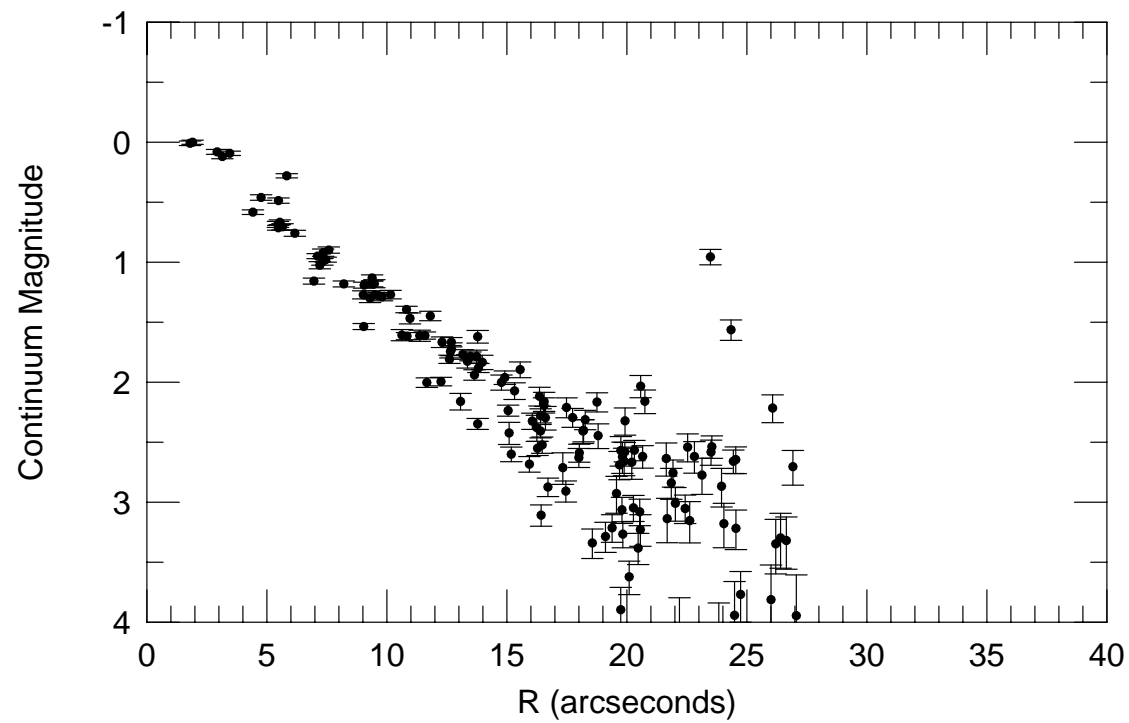
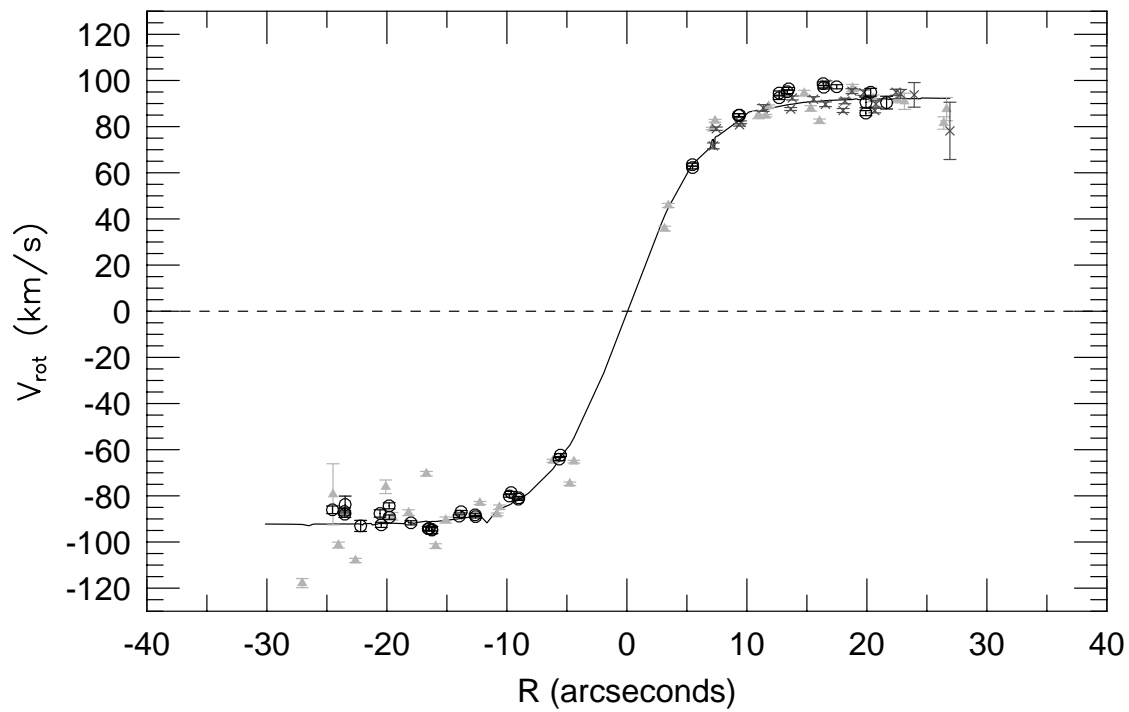
p14564

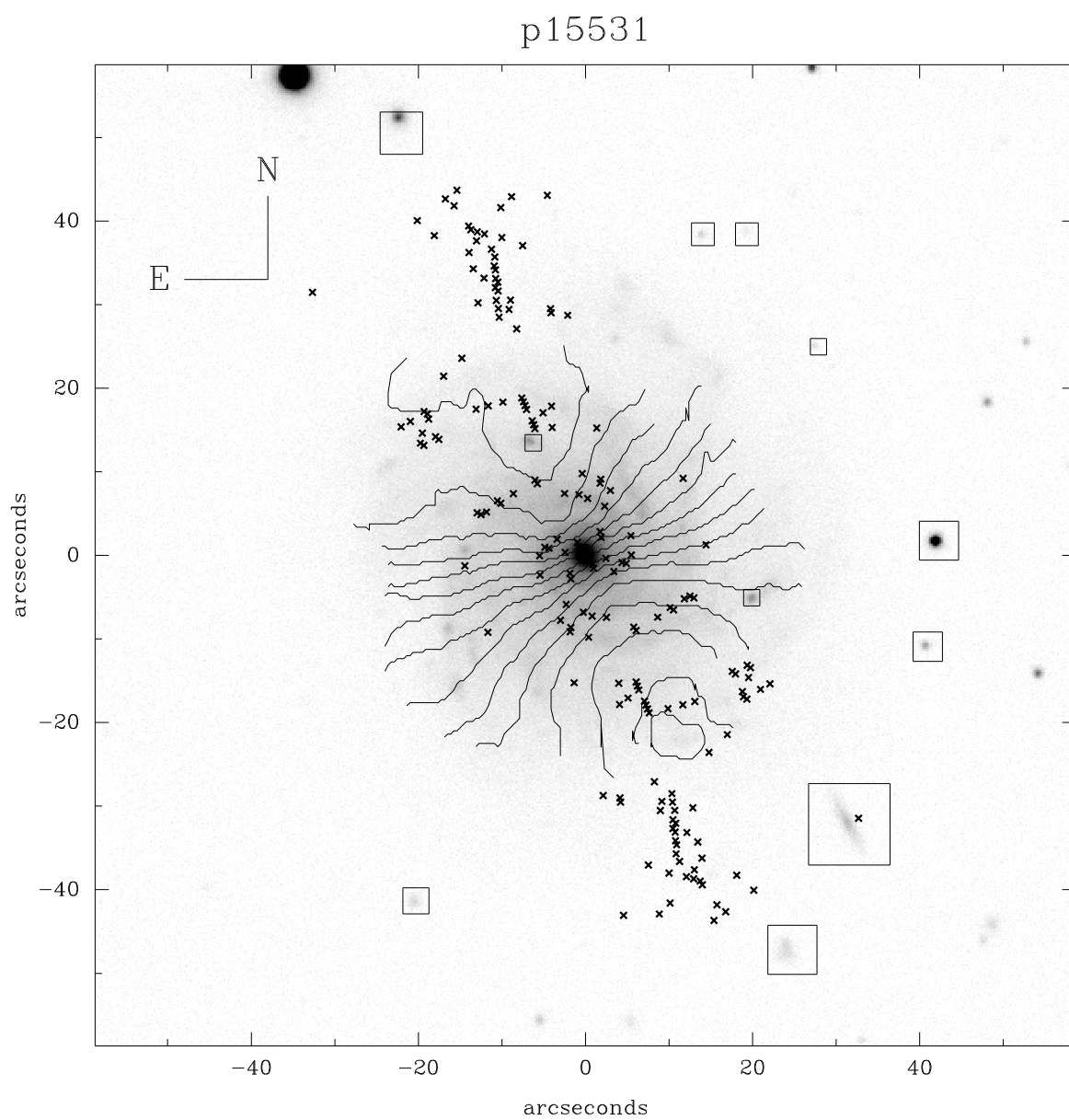


p14564

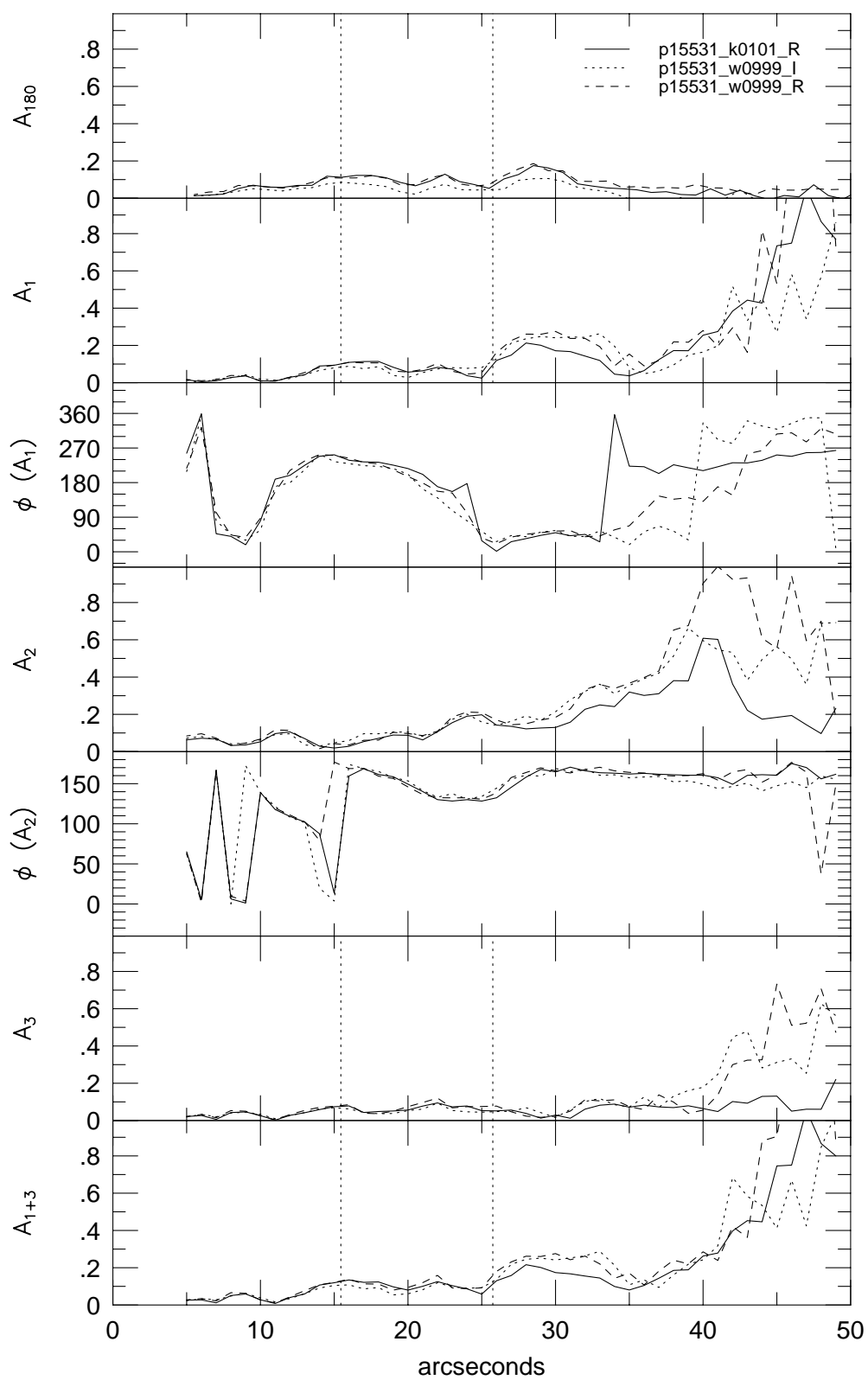


p14564

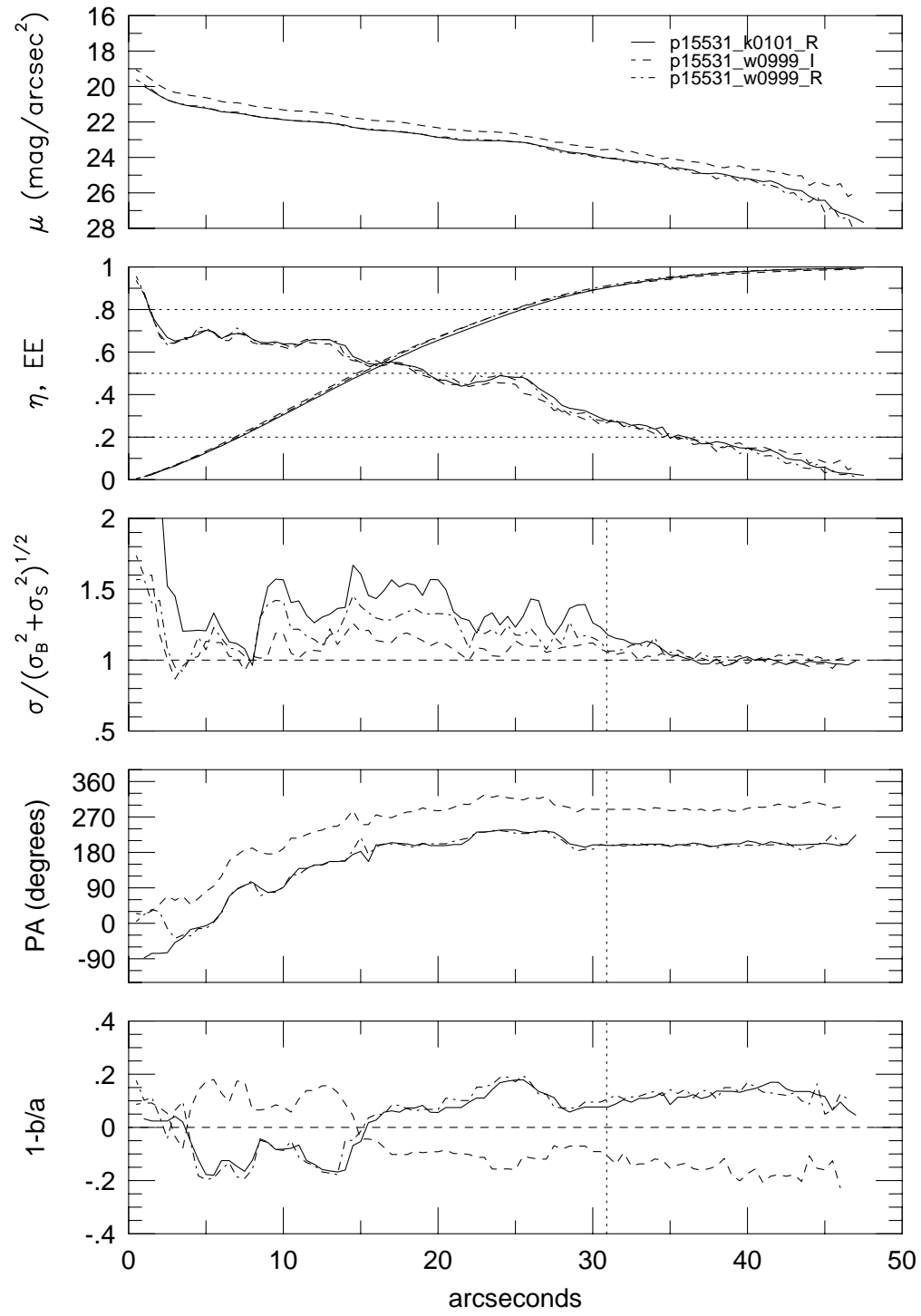




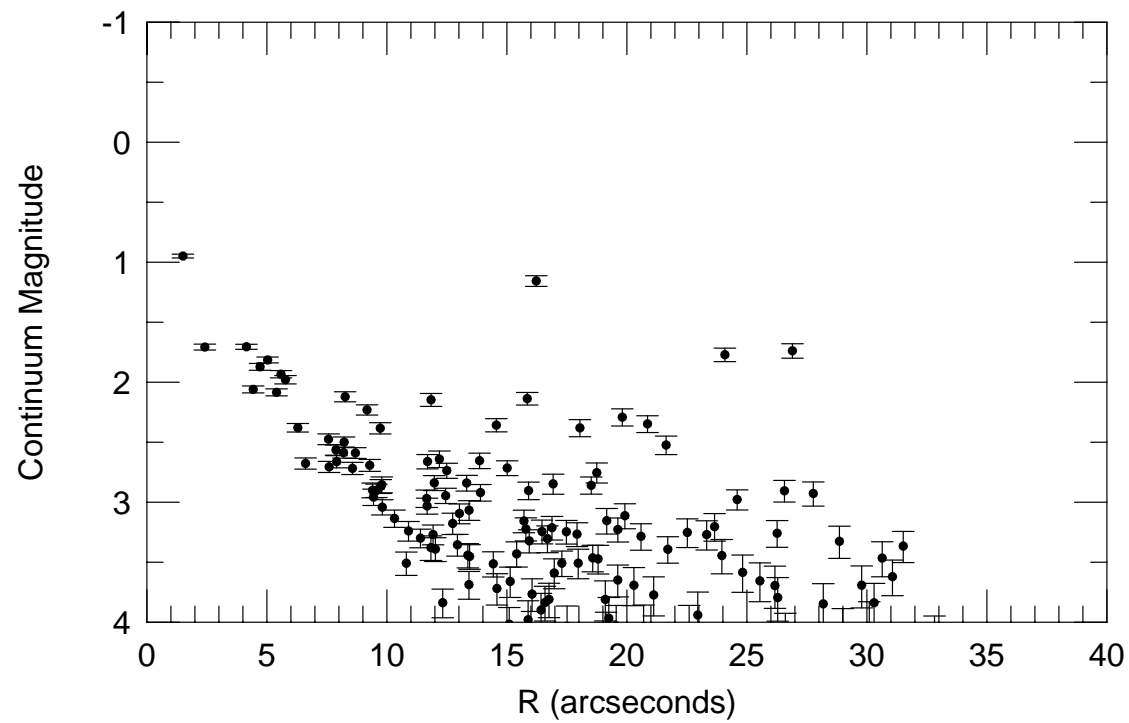
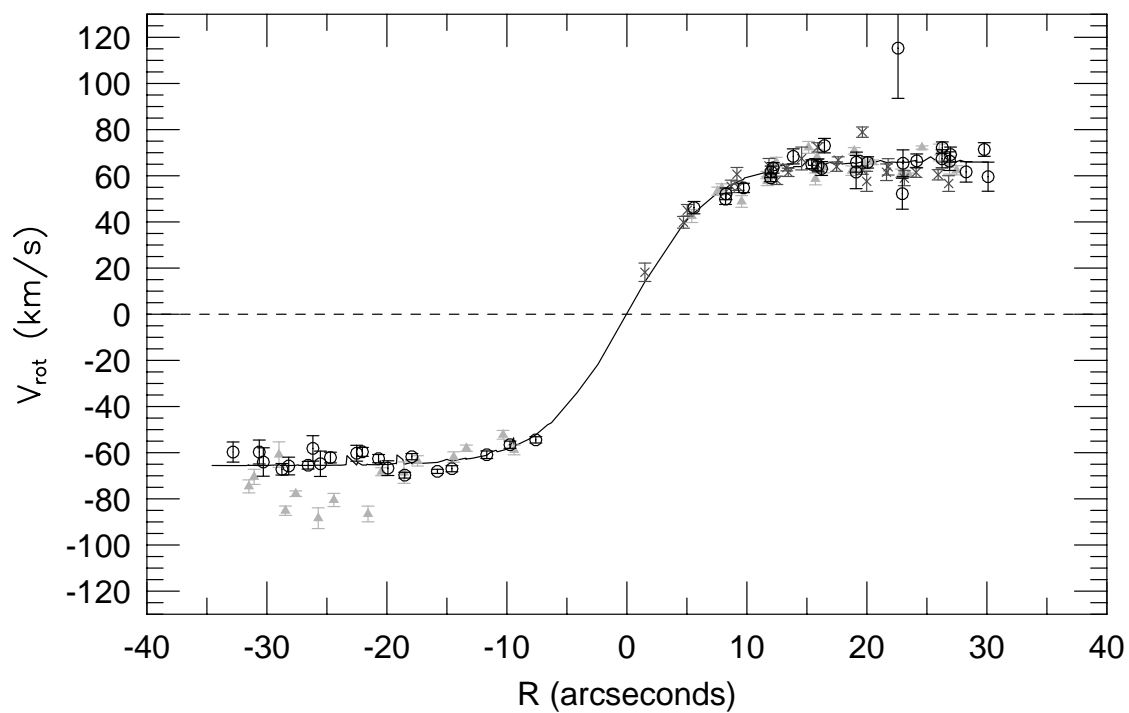
p15531



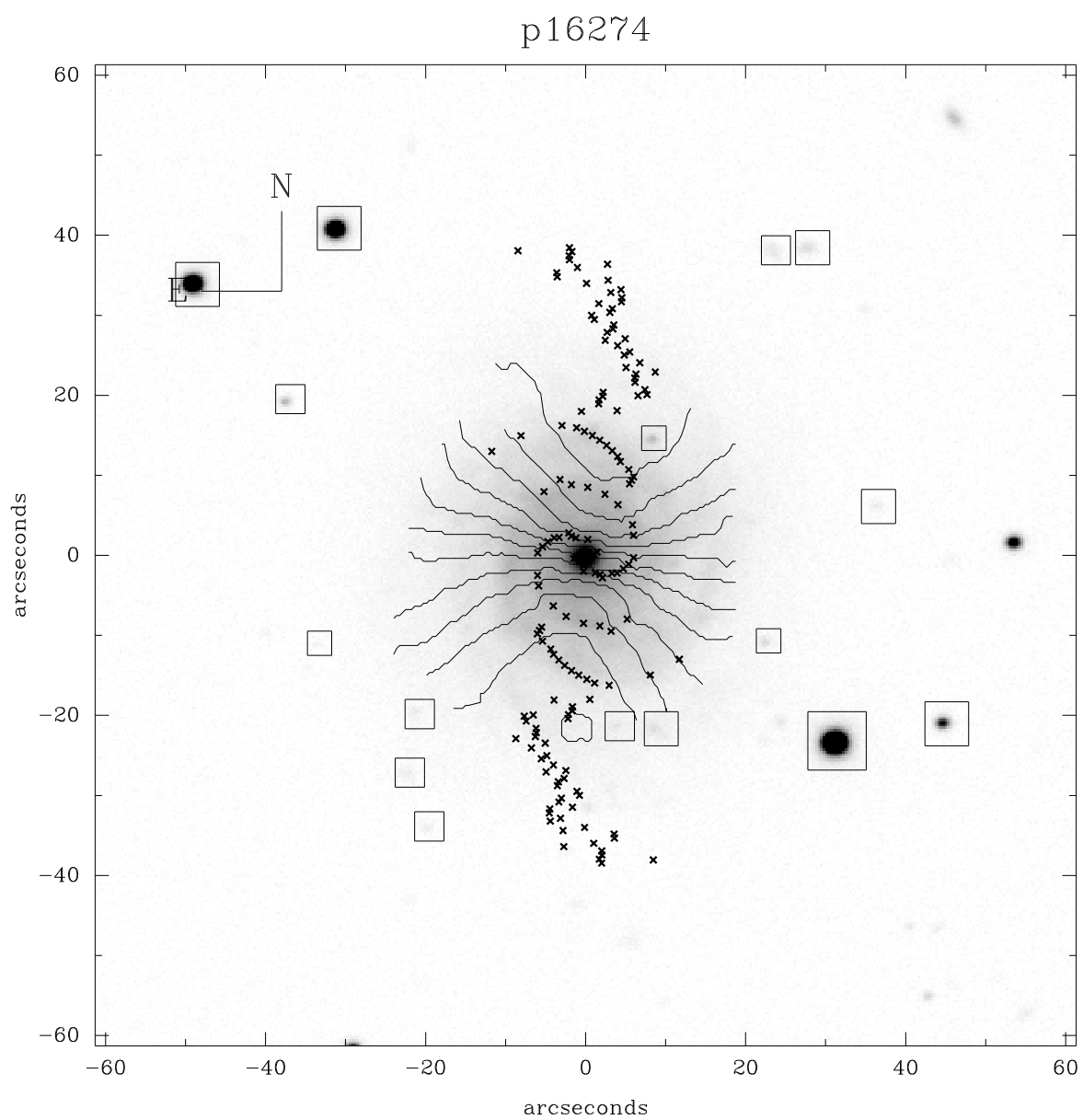
p15531



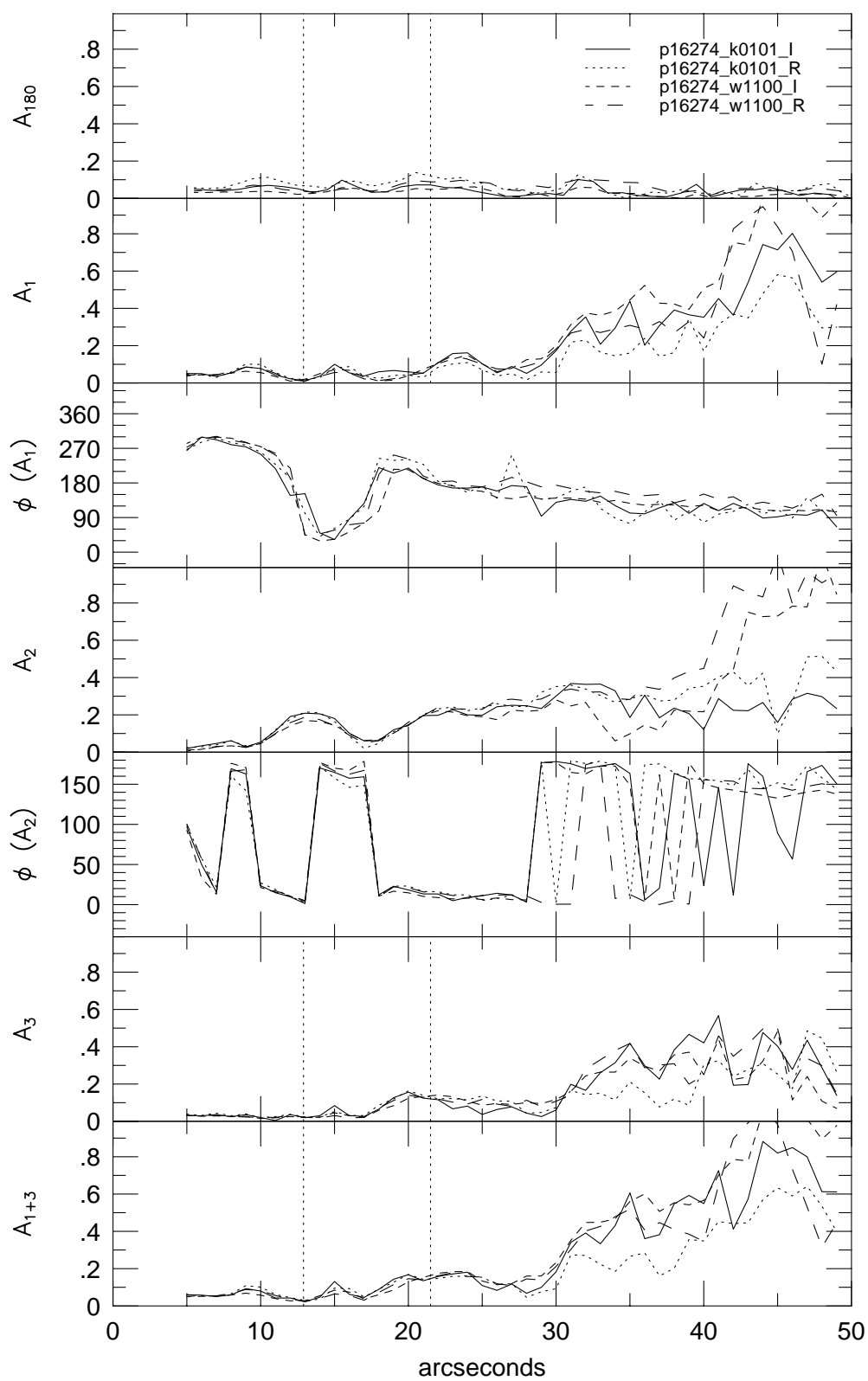
p15531



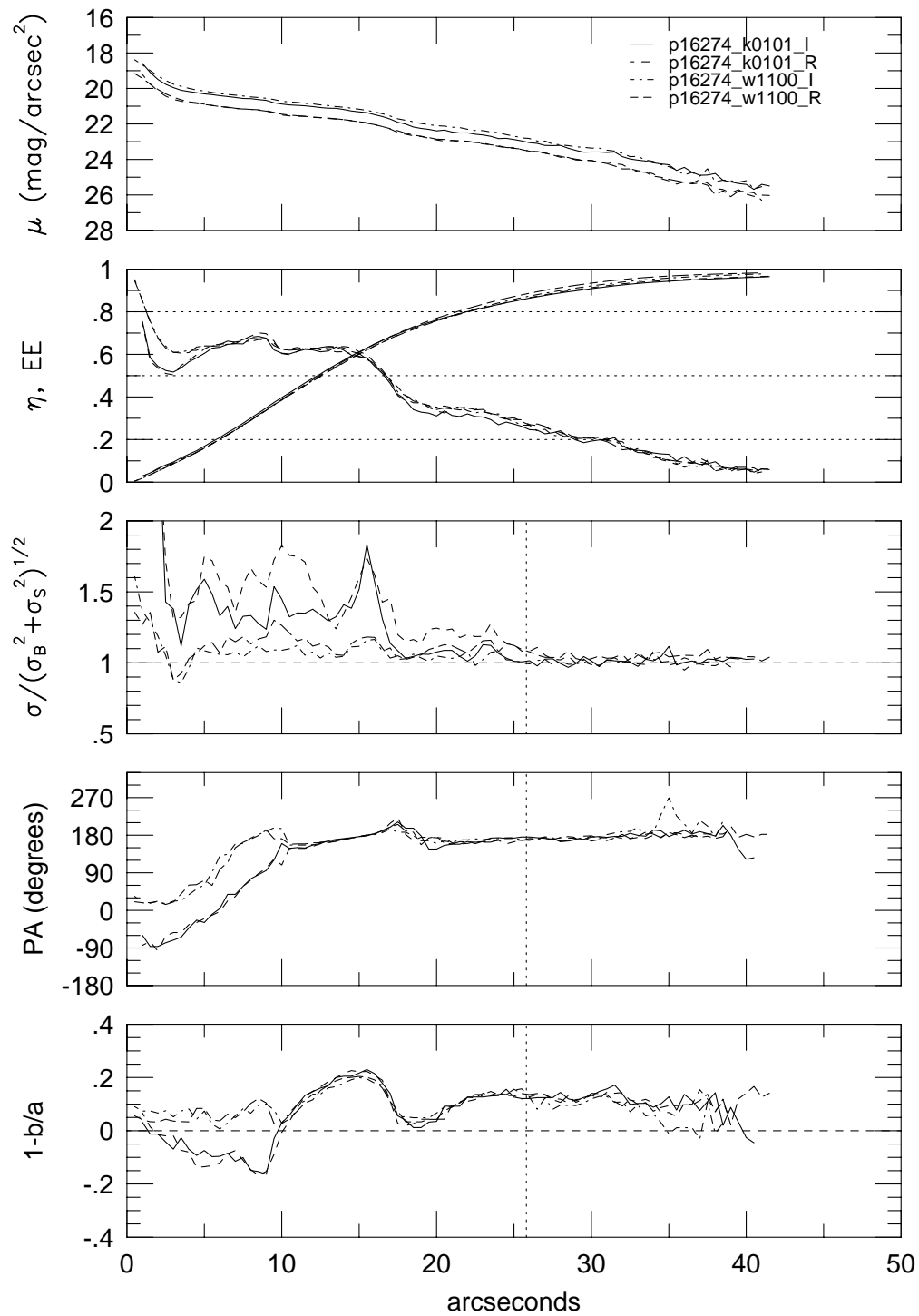




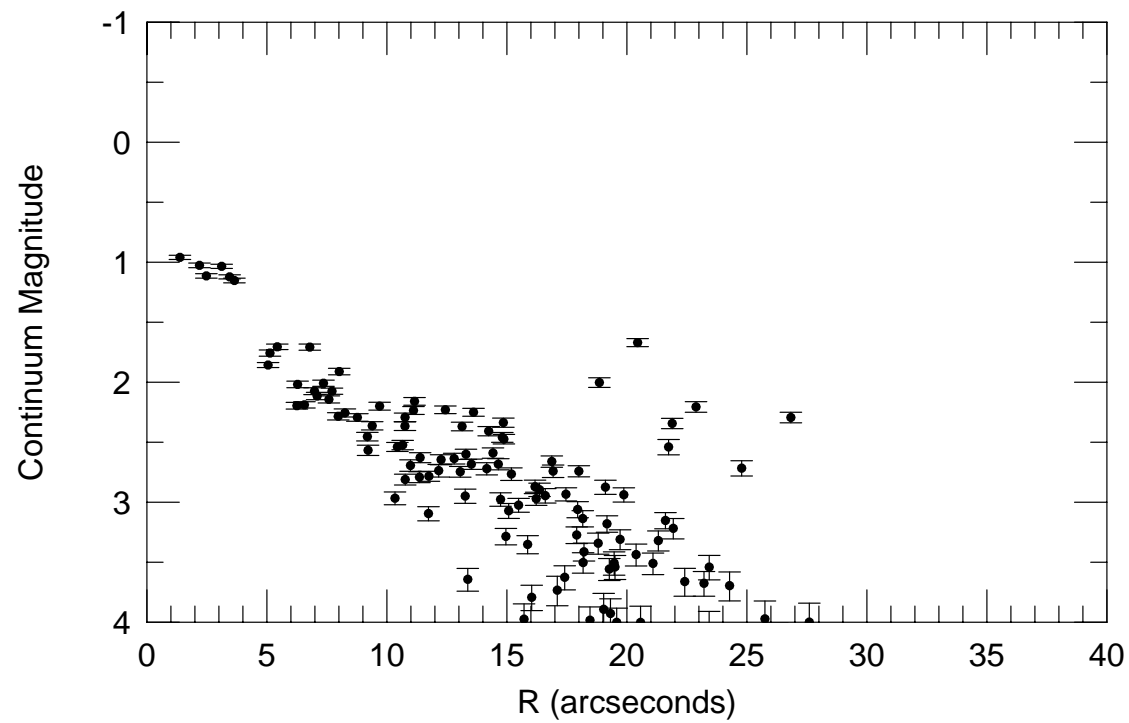
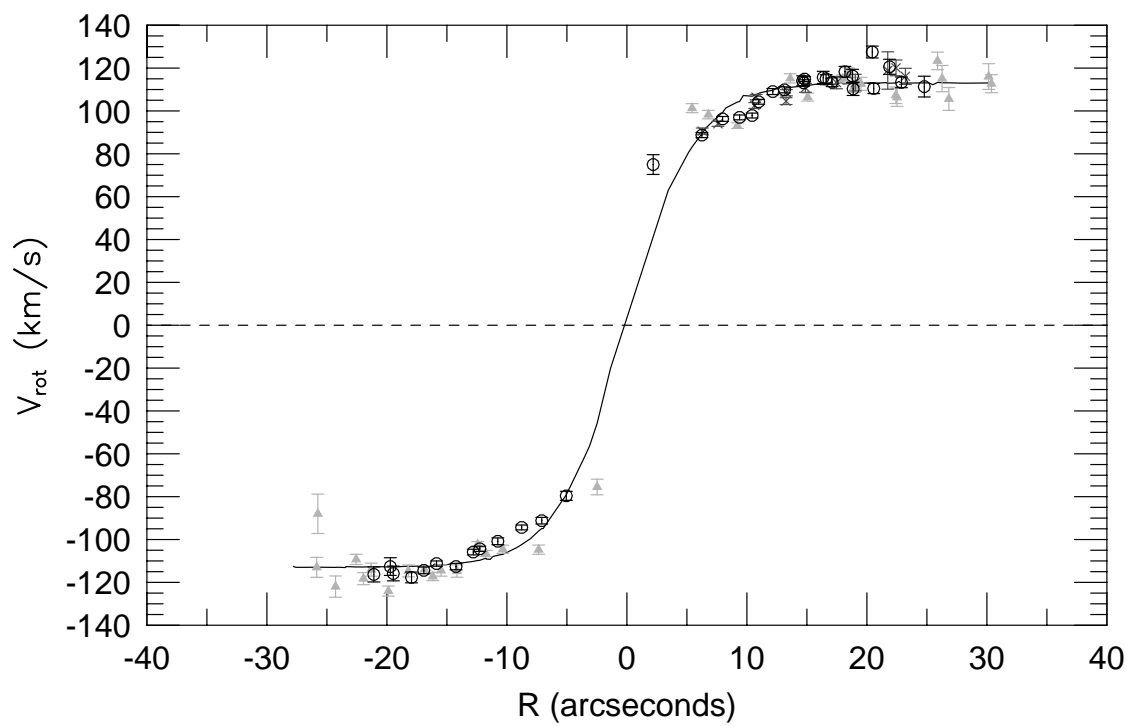
p16274

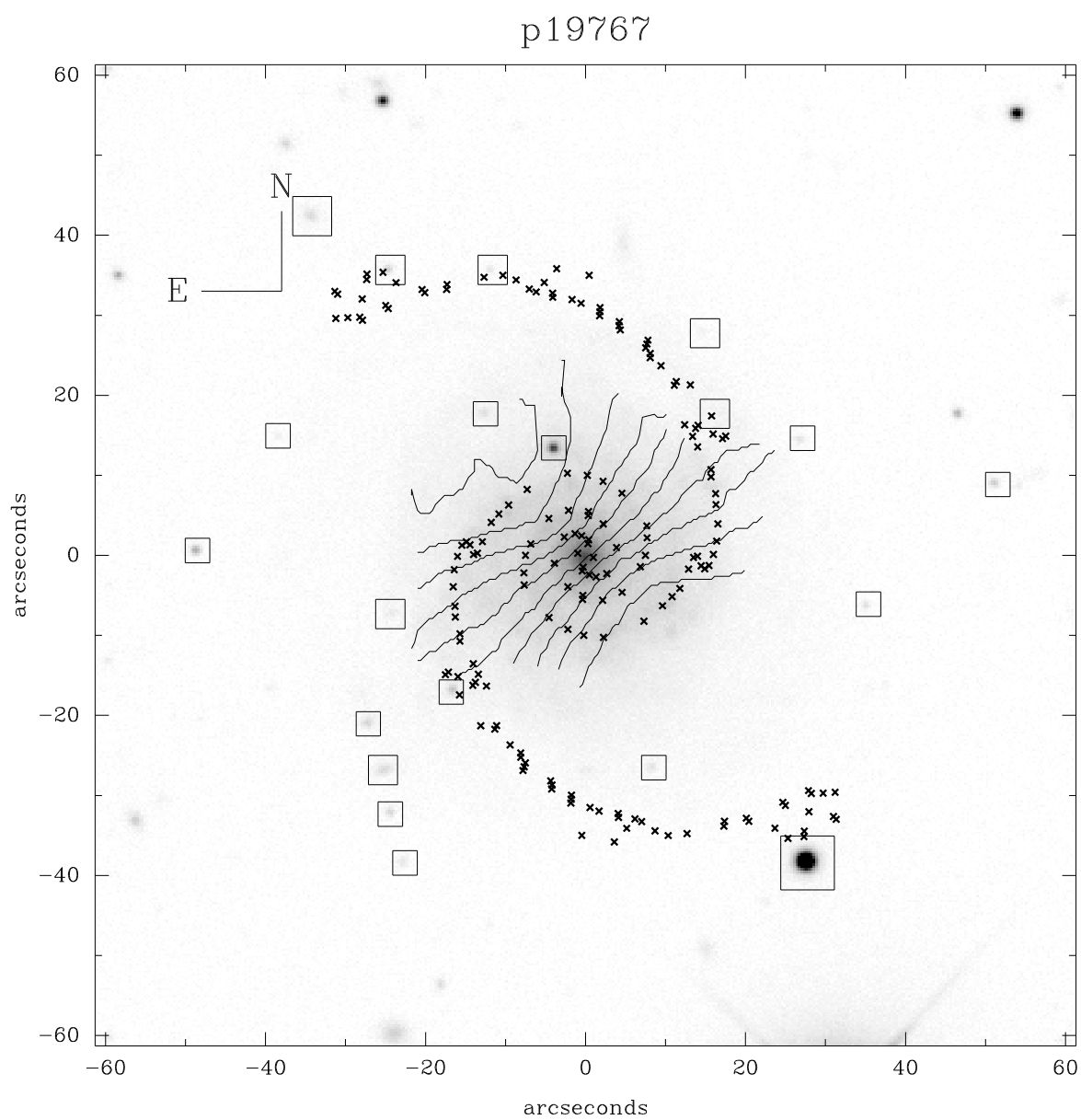


p16274

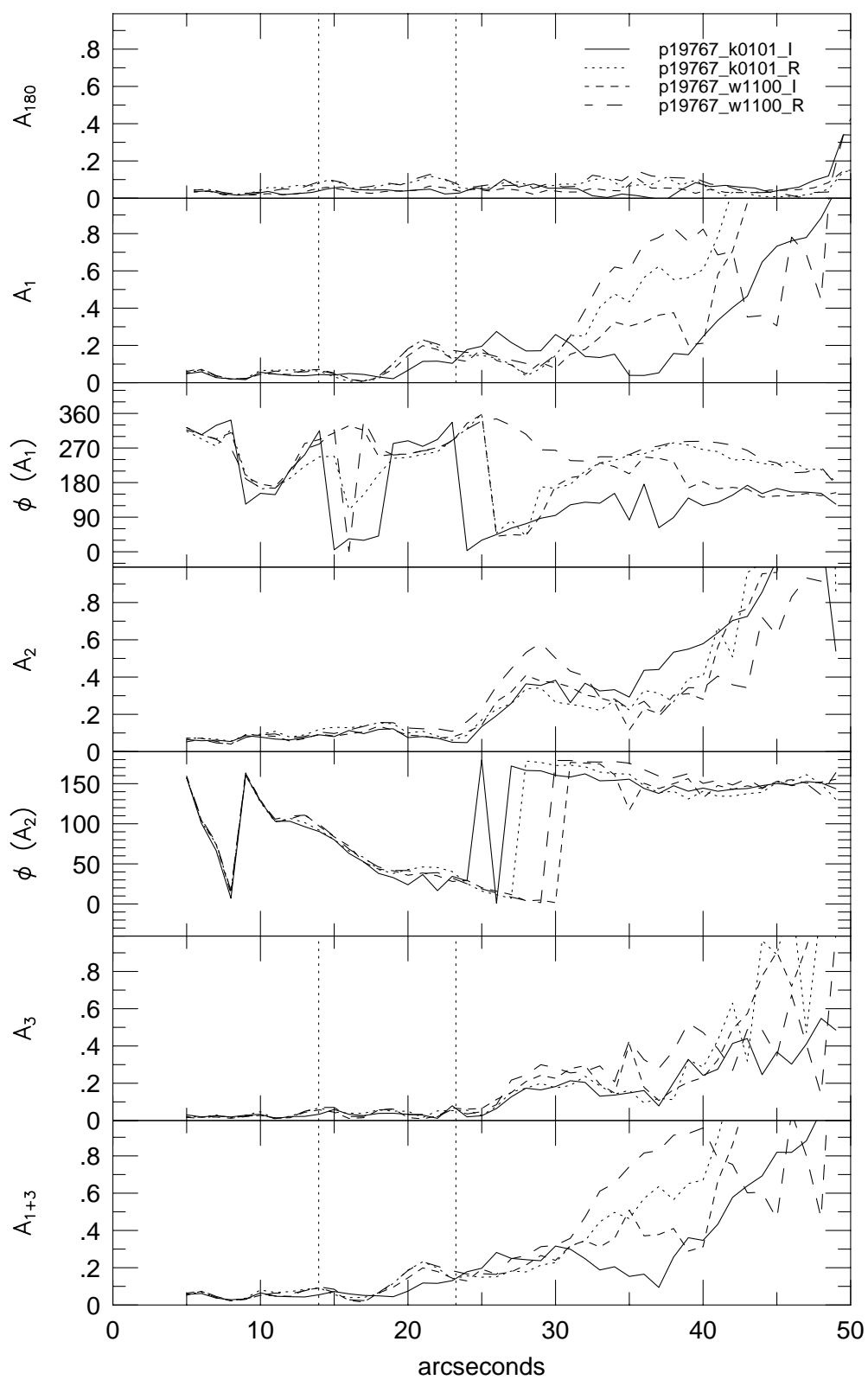


p16274

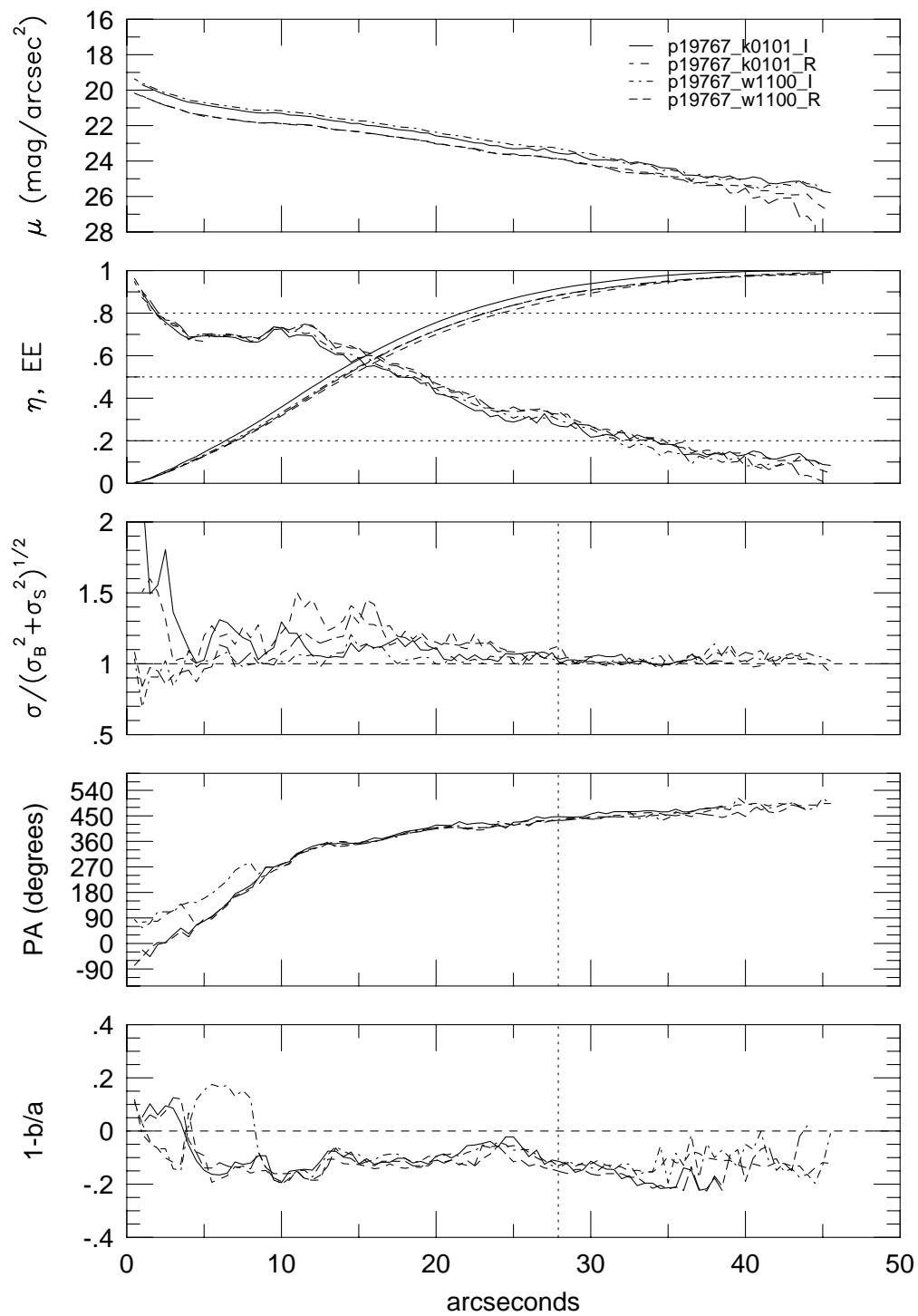




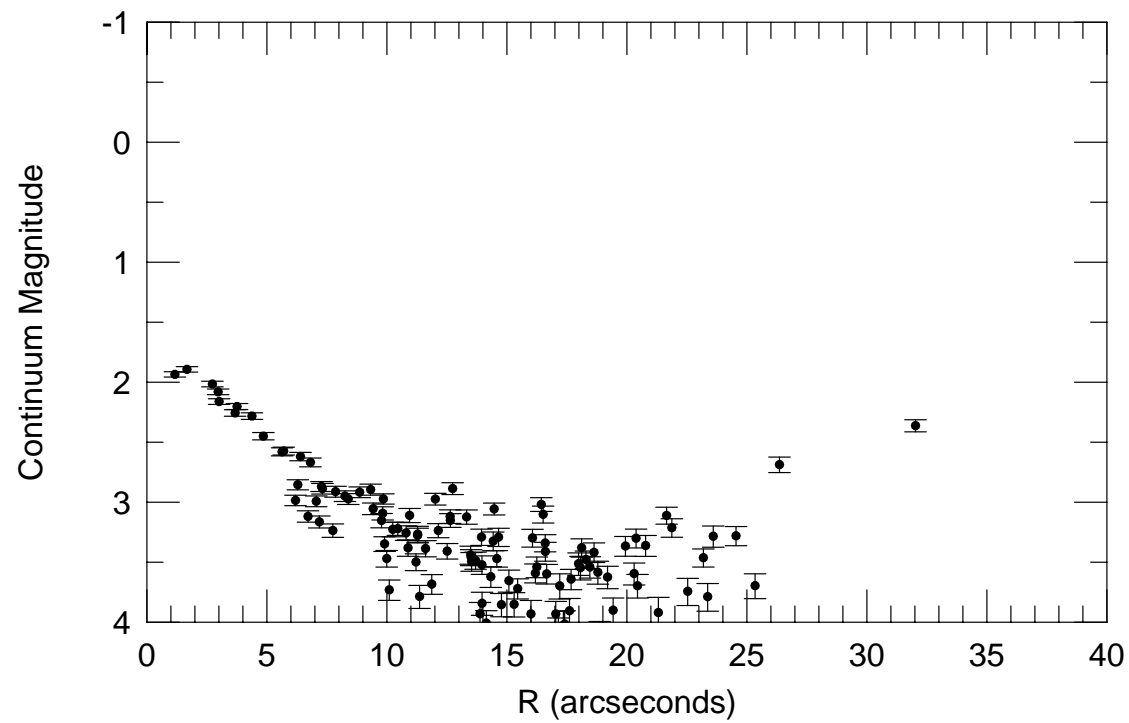
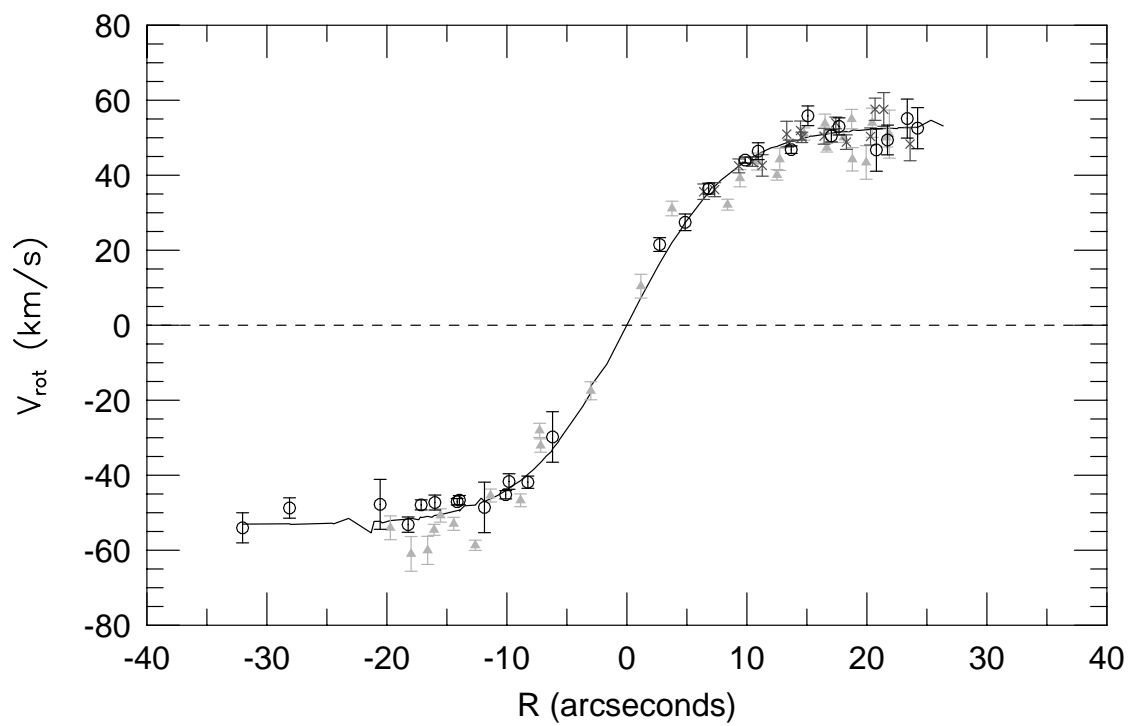
p19767



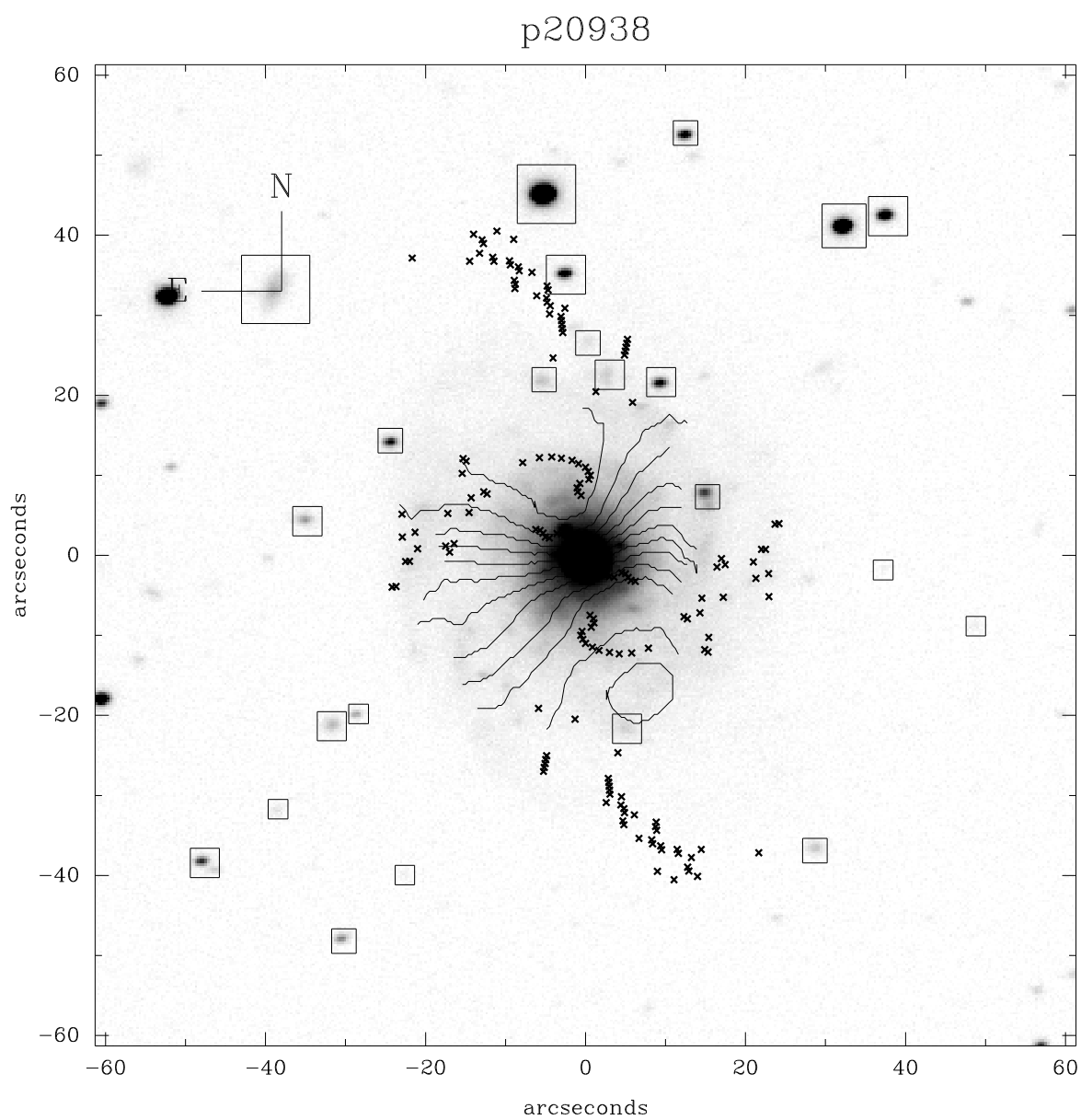
p19767



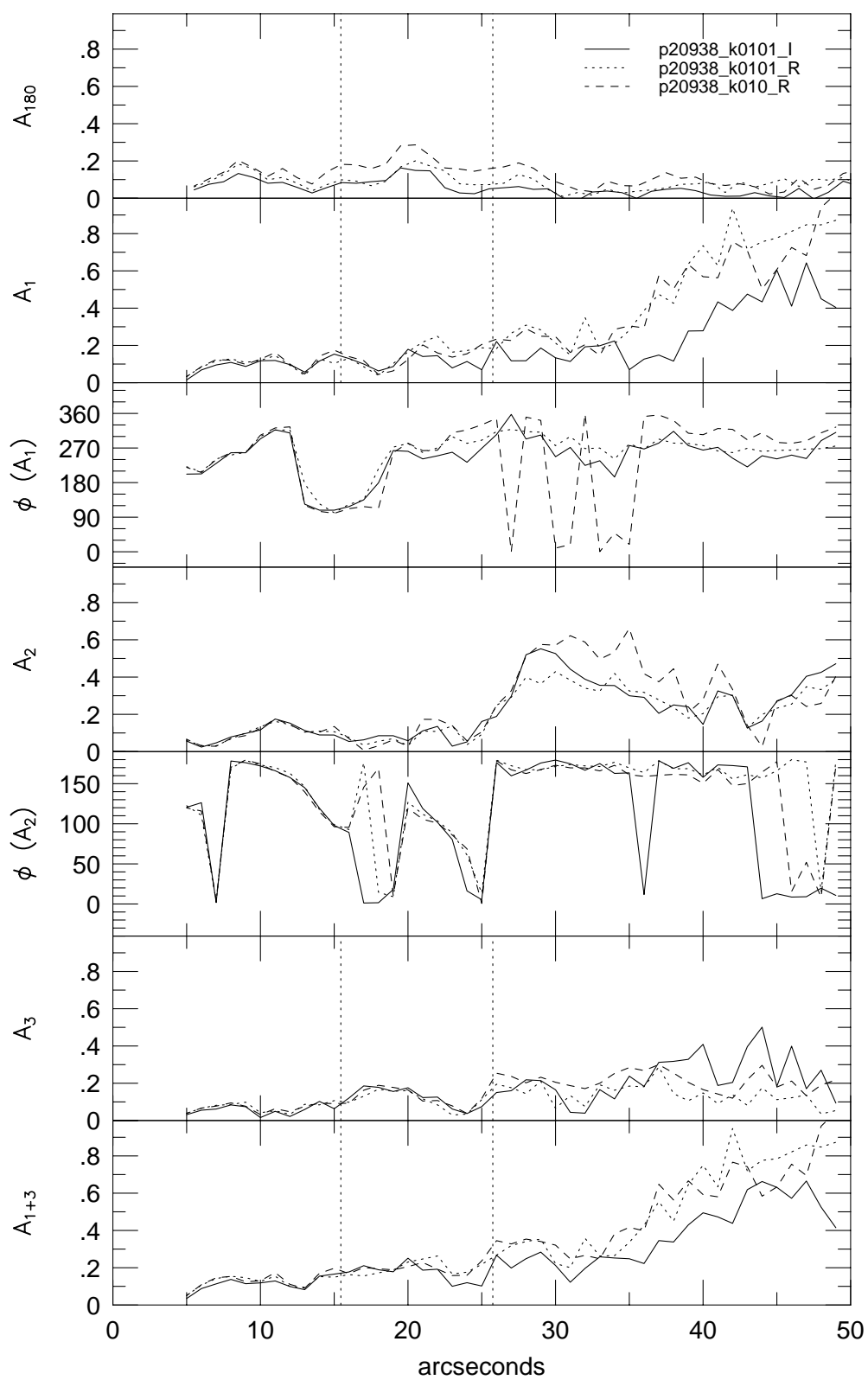
p19767



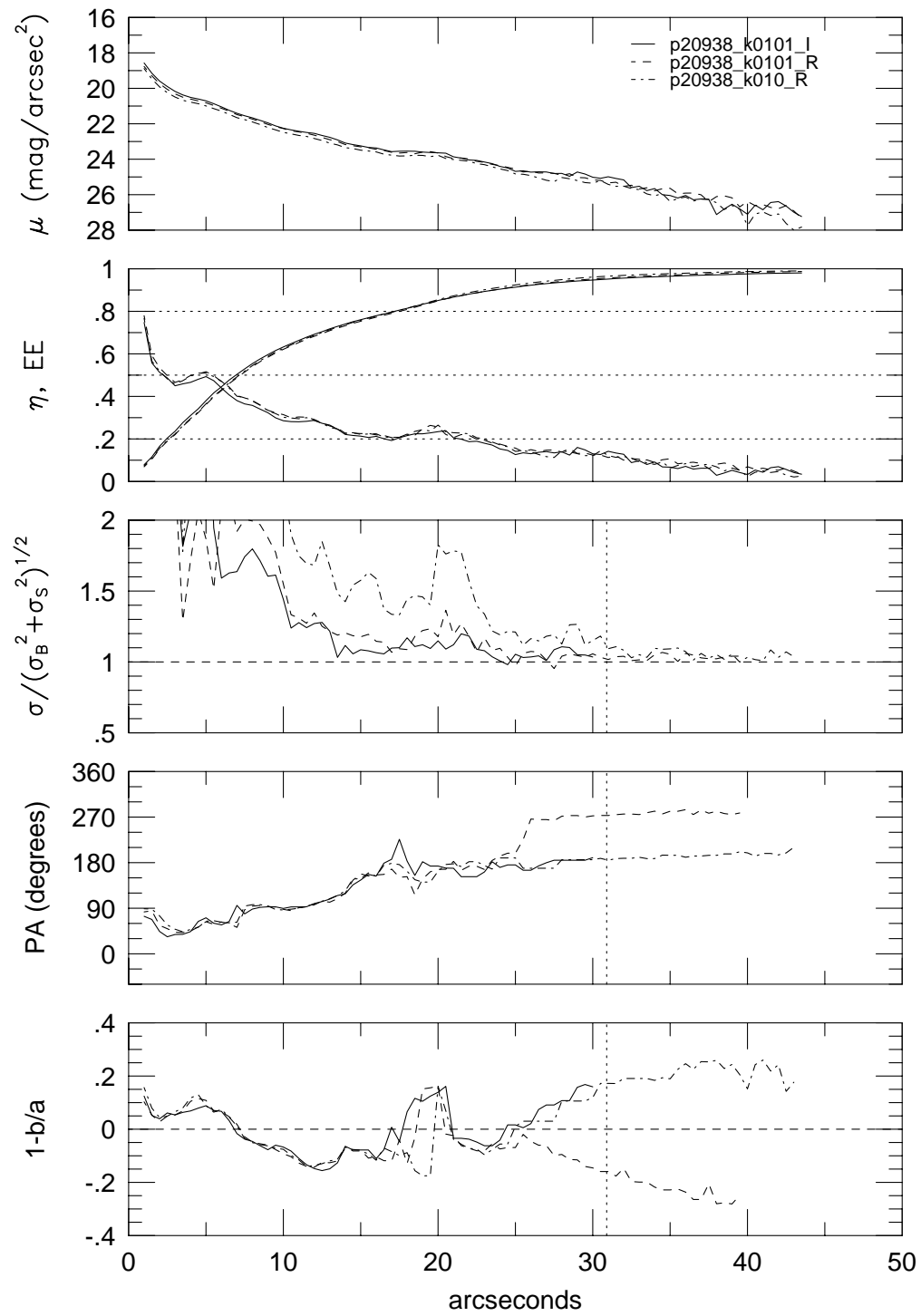




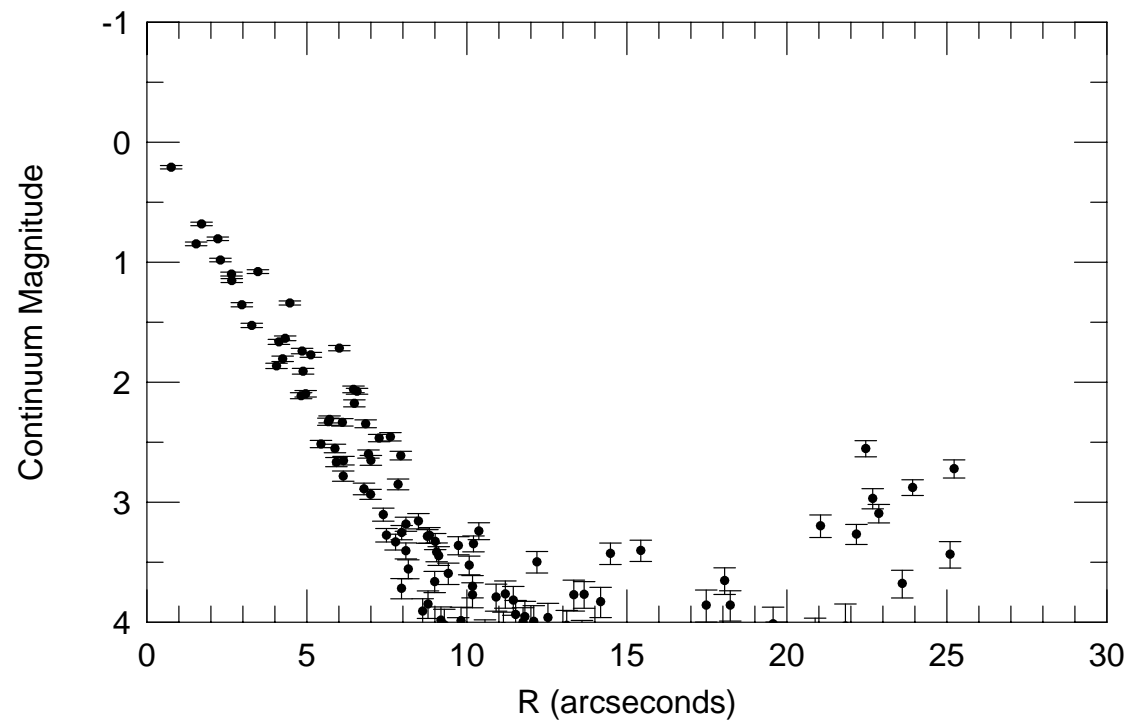
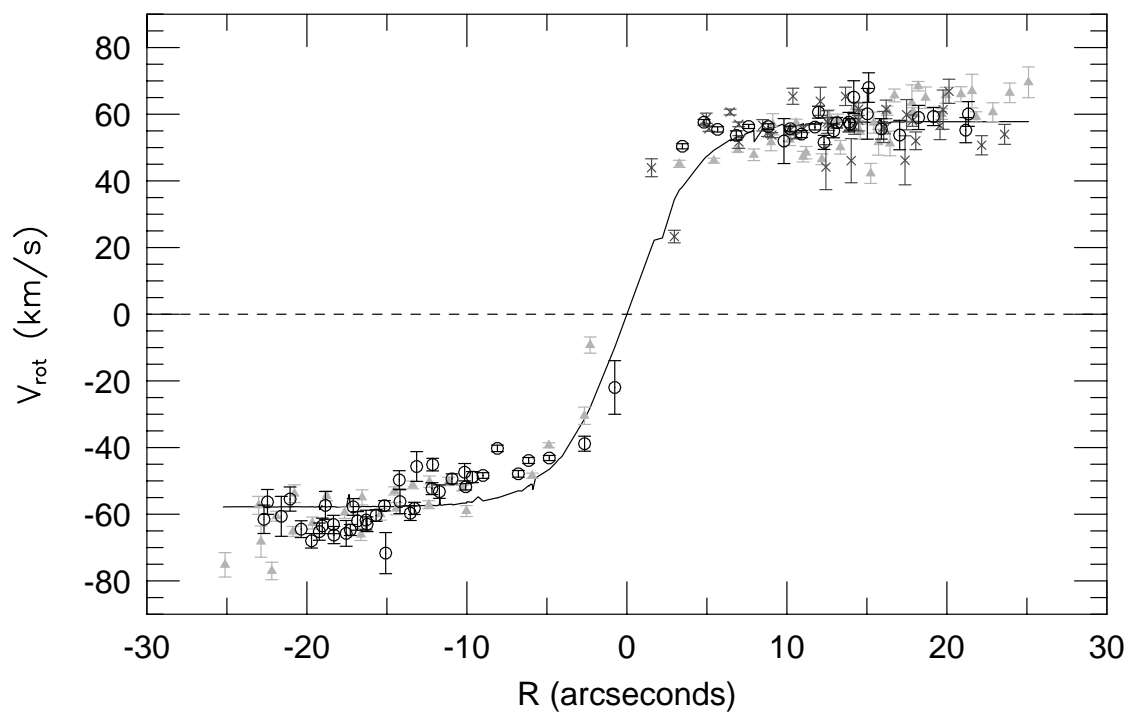
p20938

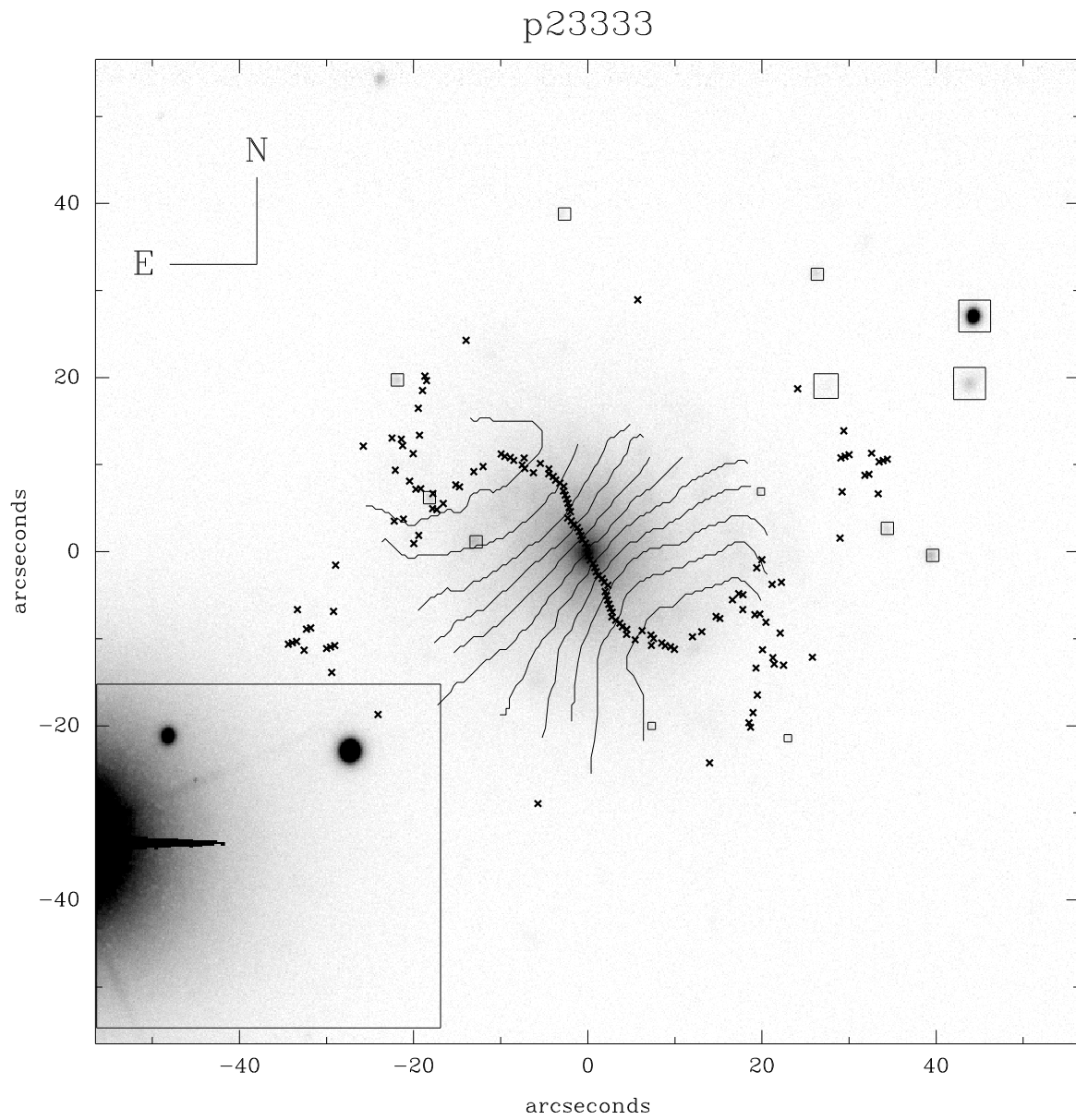


## p20938

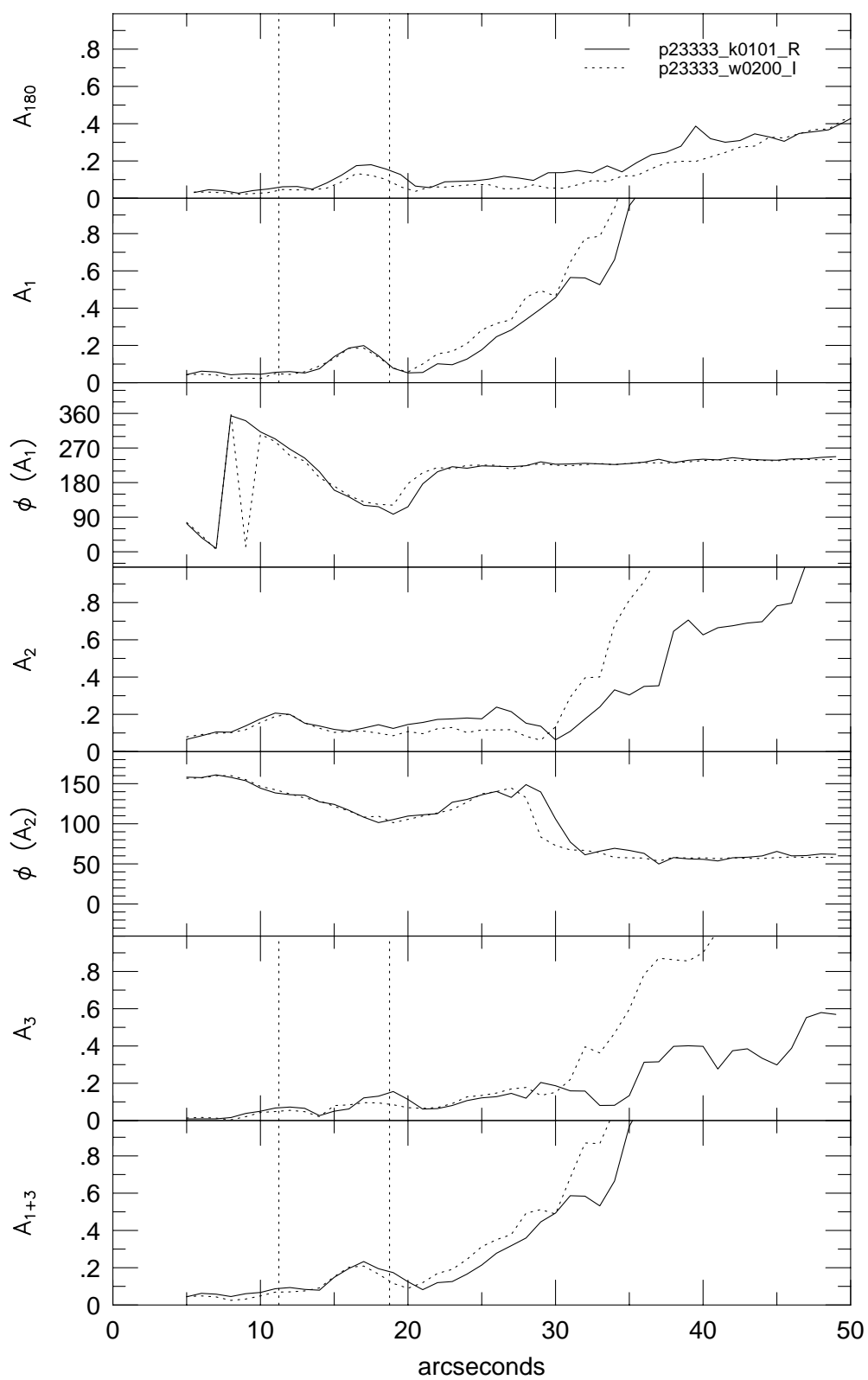


p20938

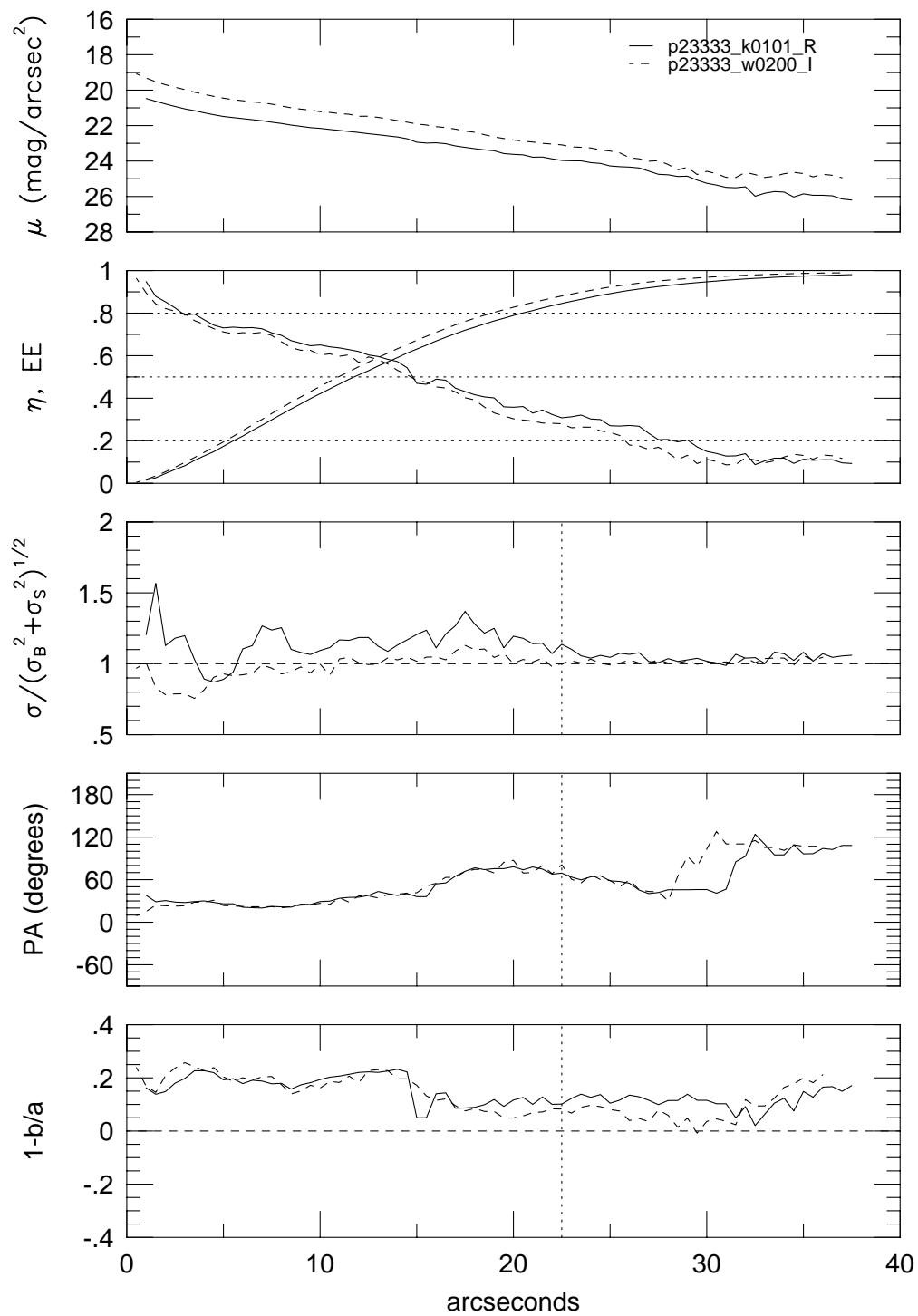




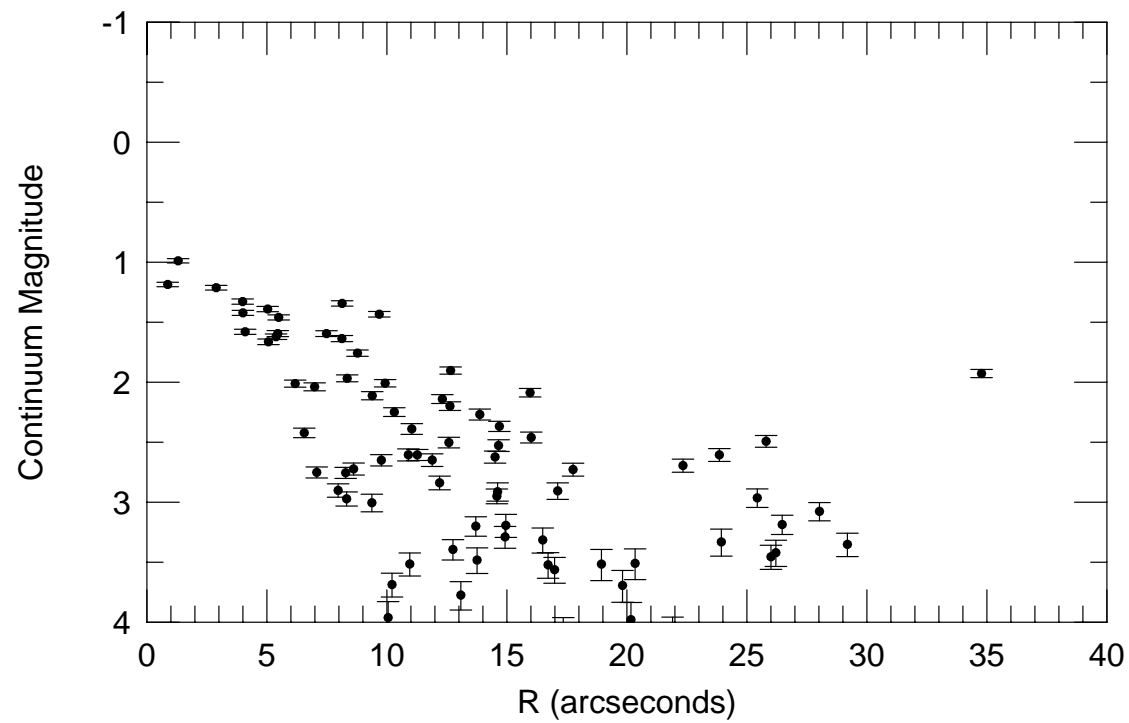
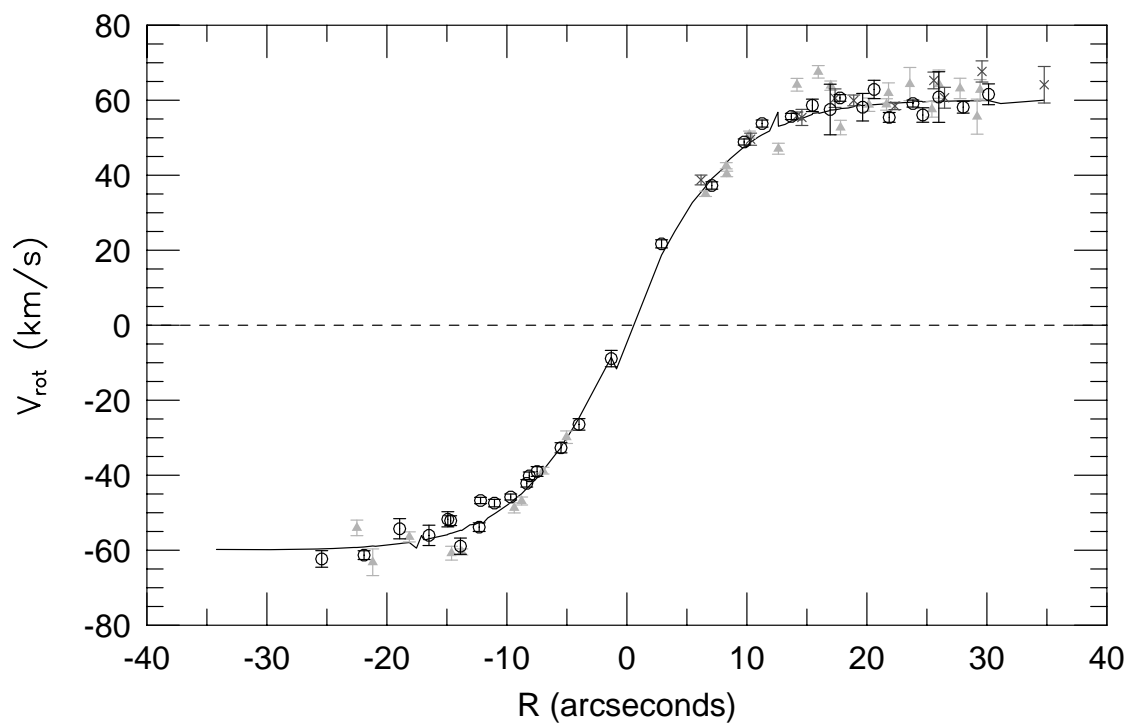
p23333



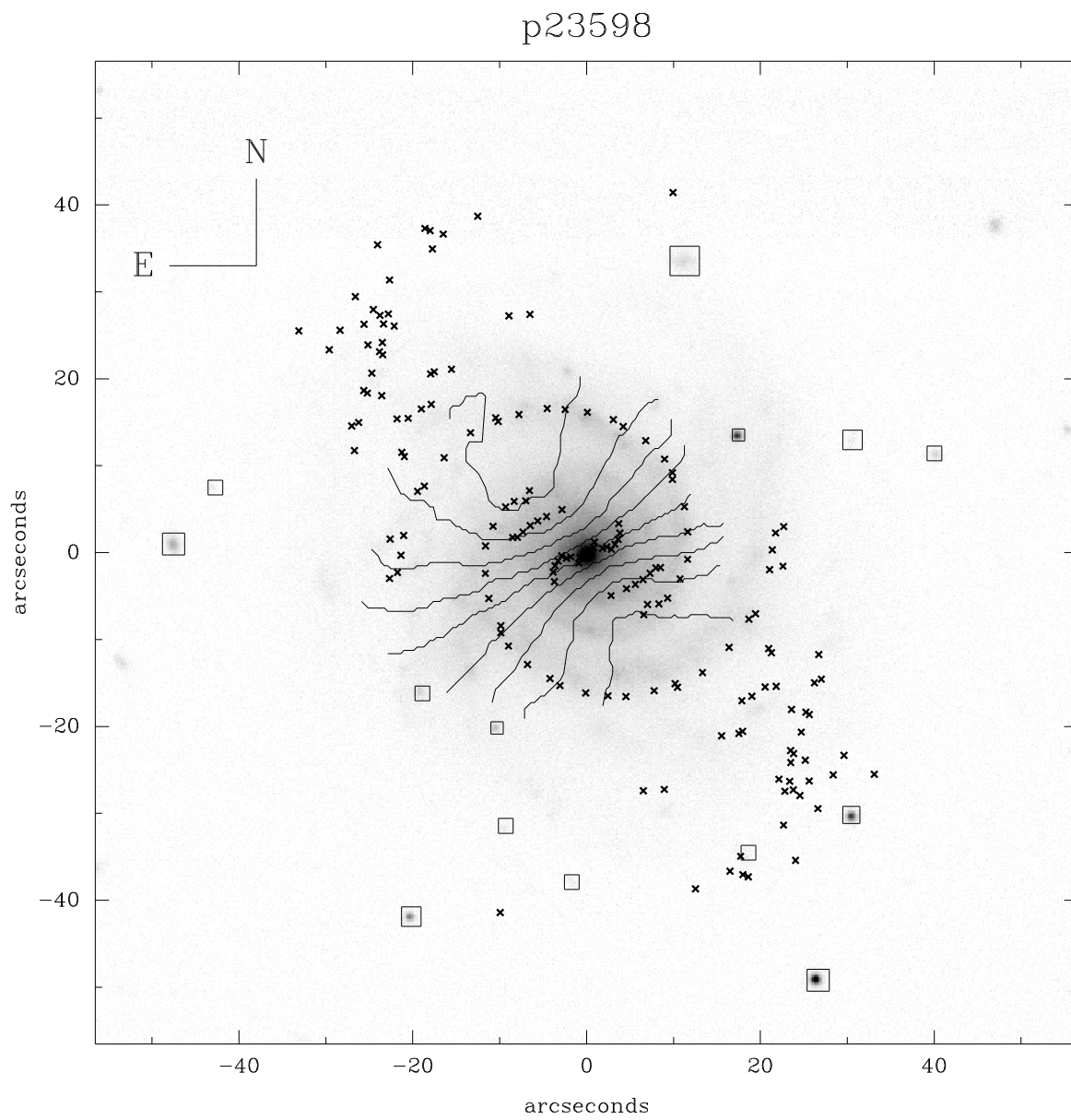
p23333



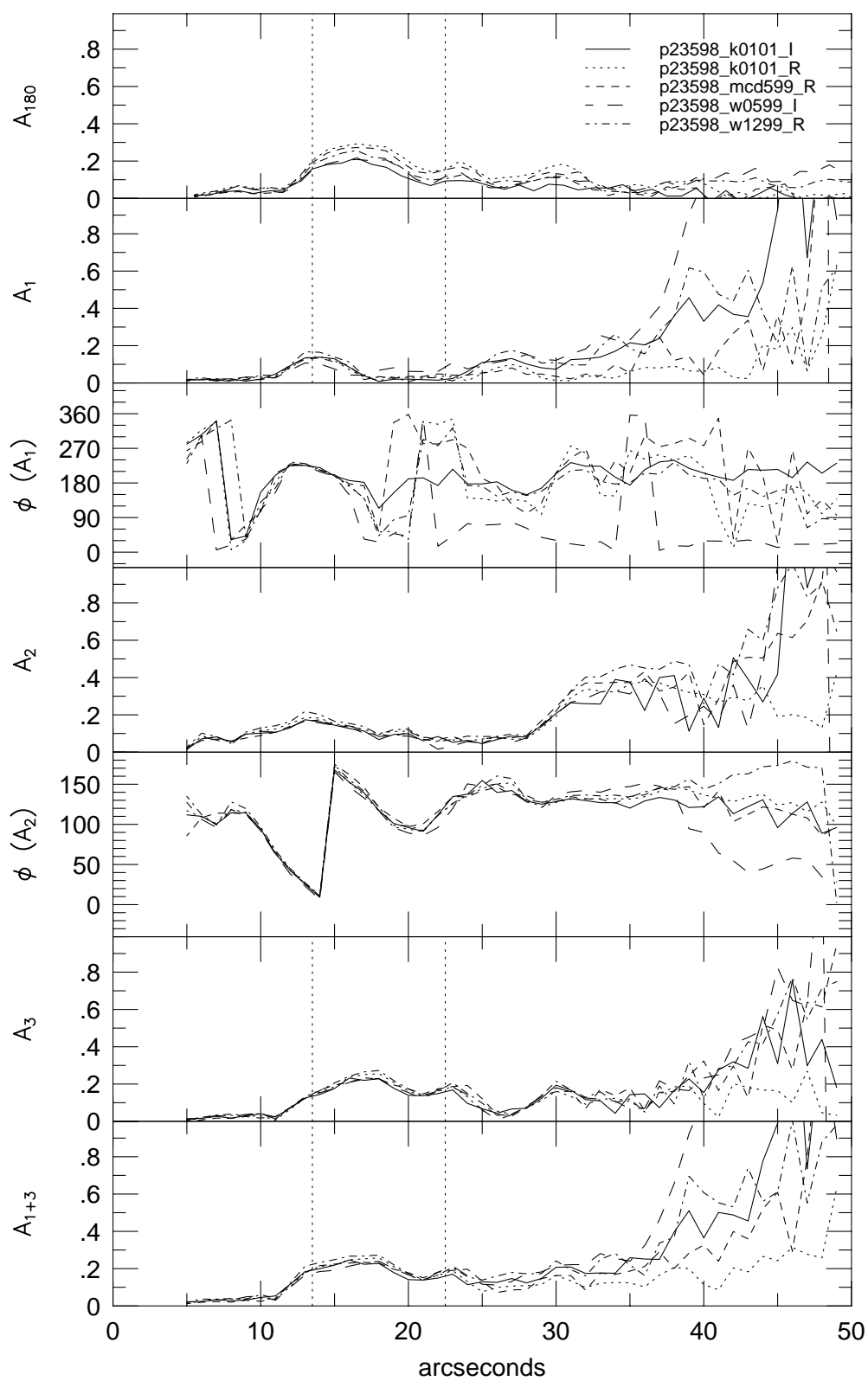
p23333



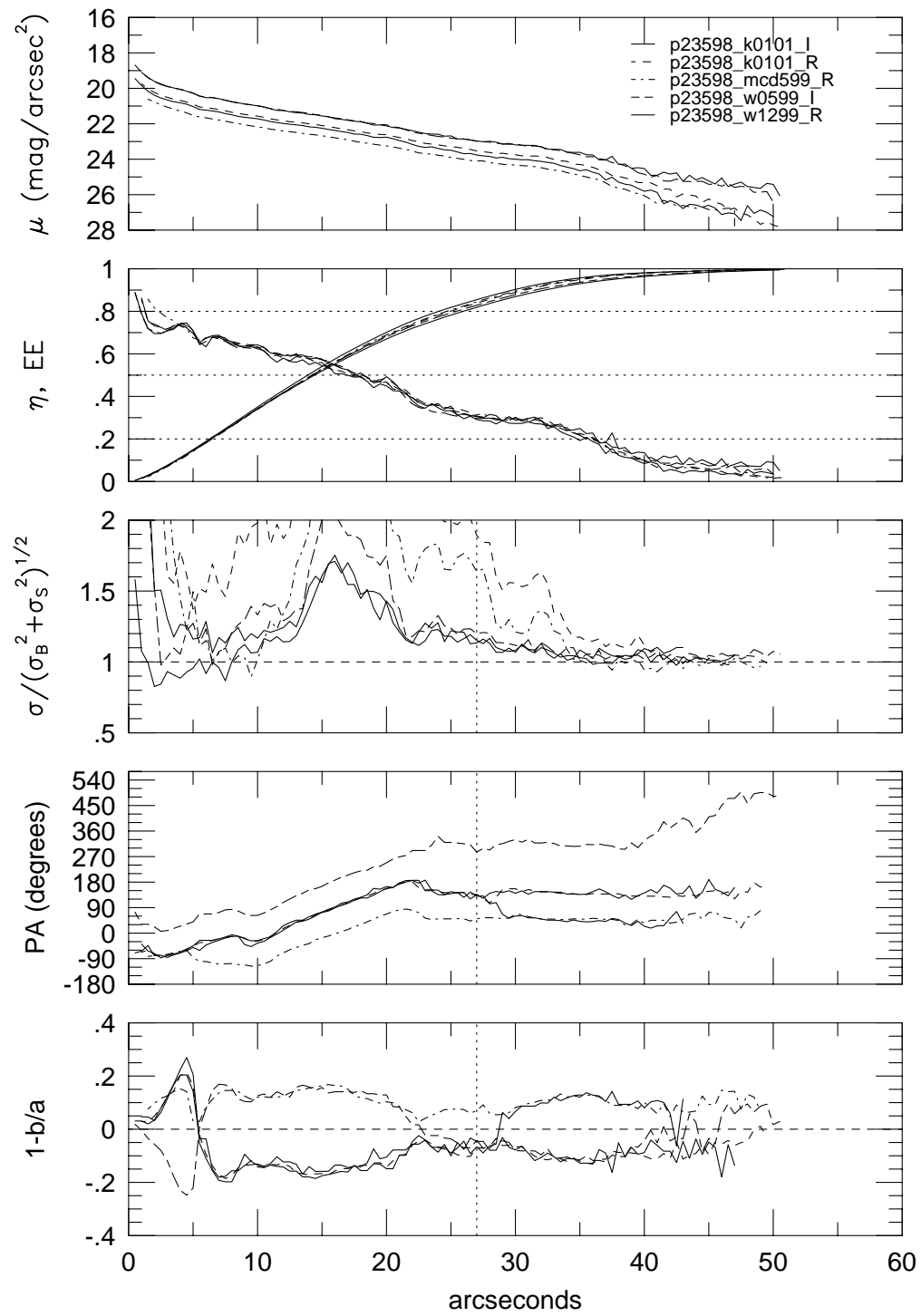




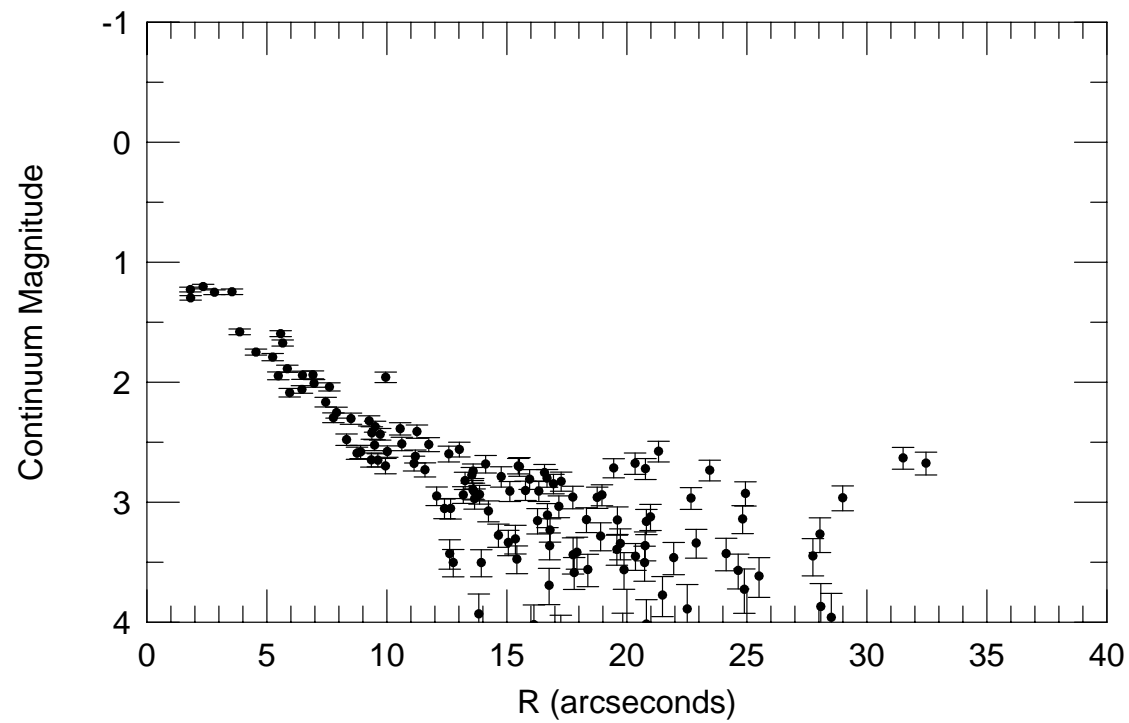
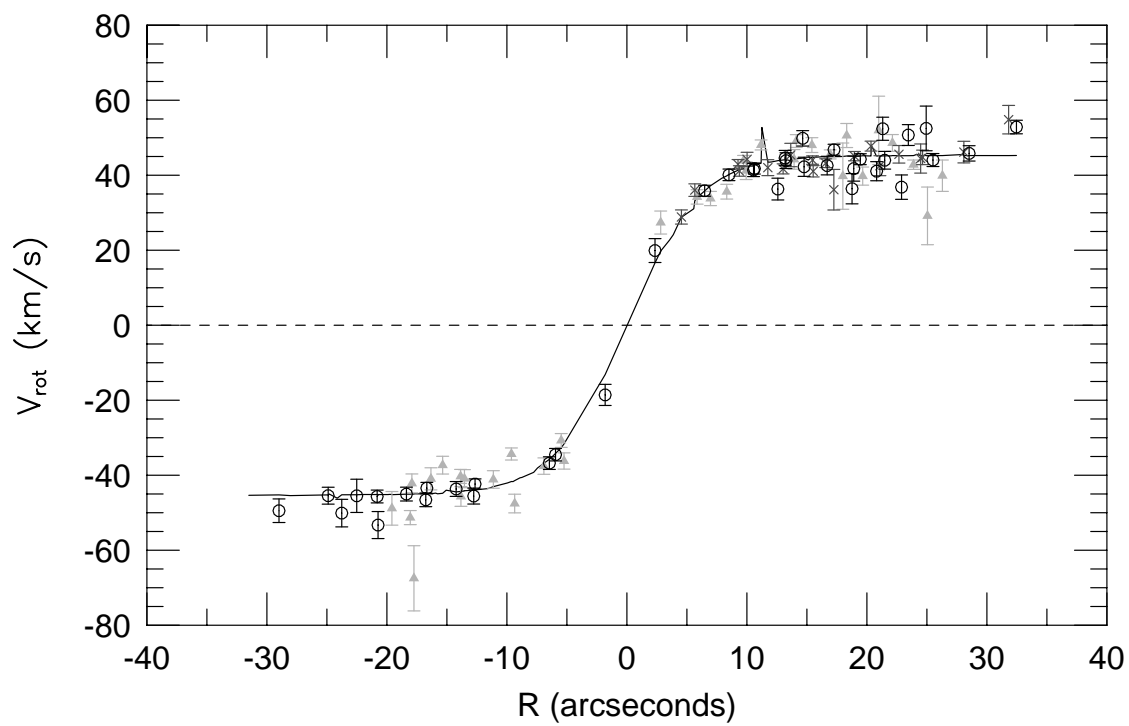
p23598

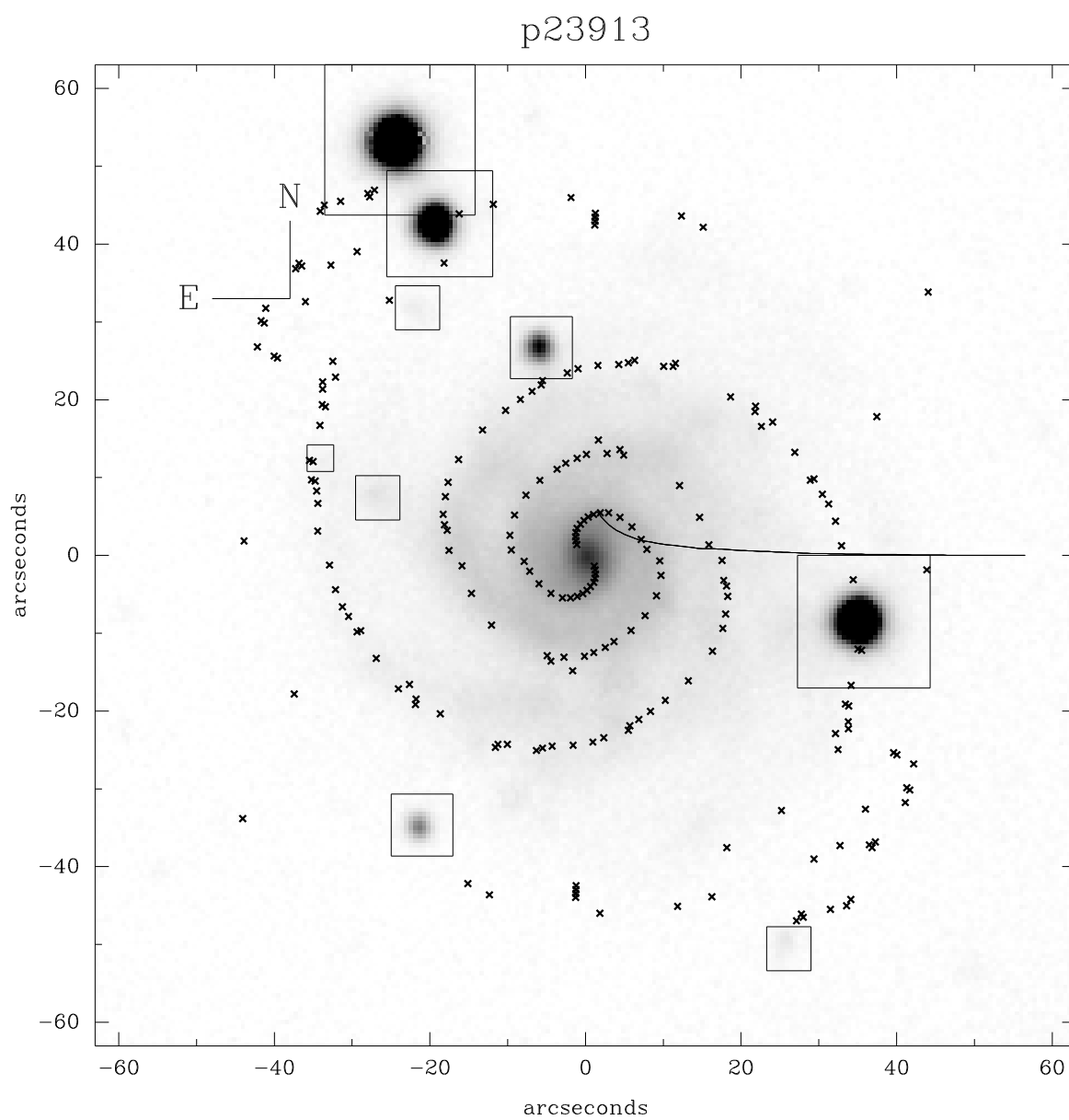


## p23598

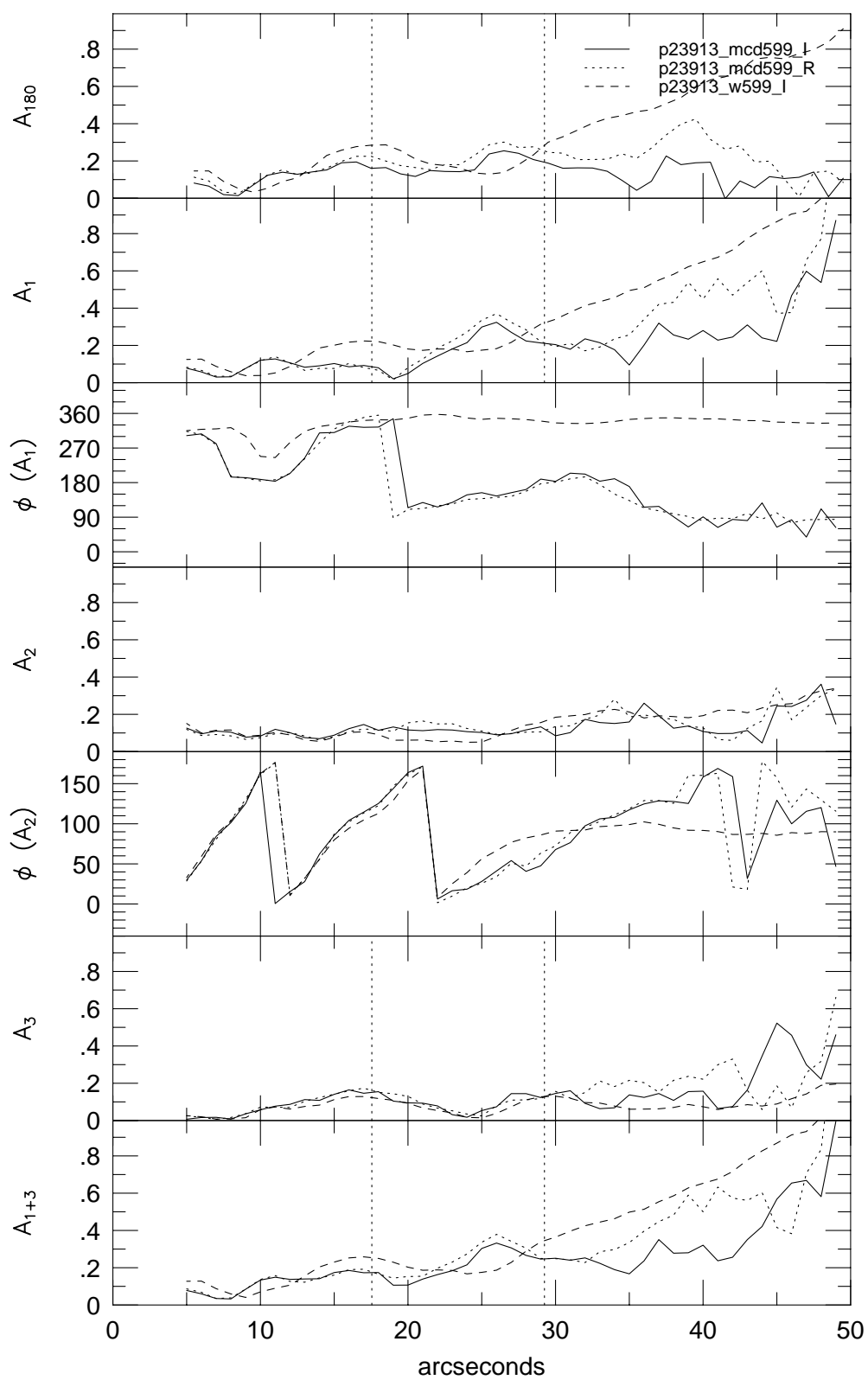


p23598

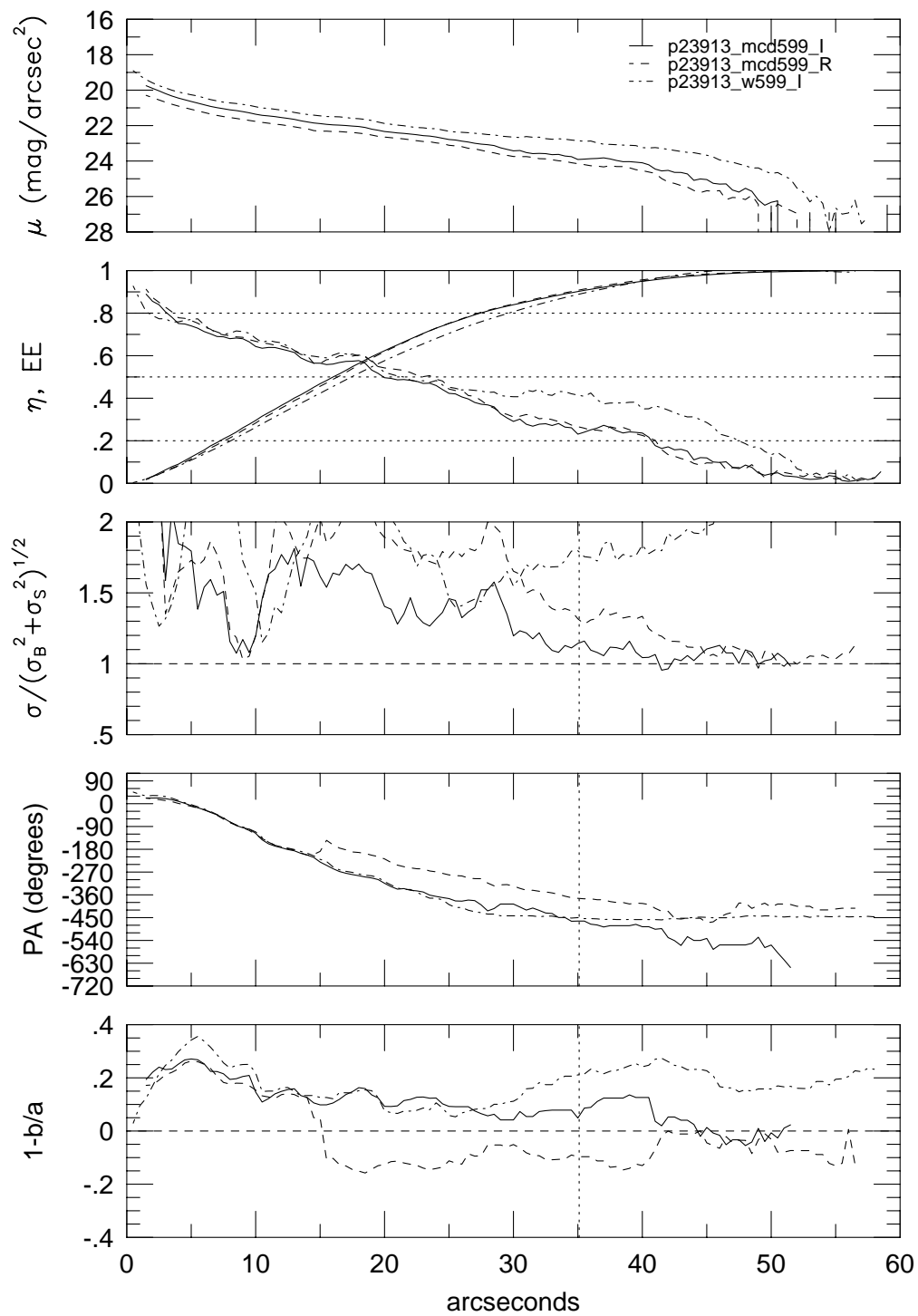




p23913

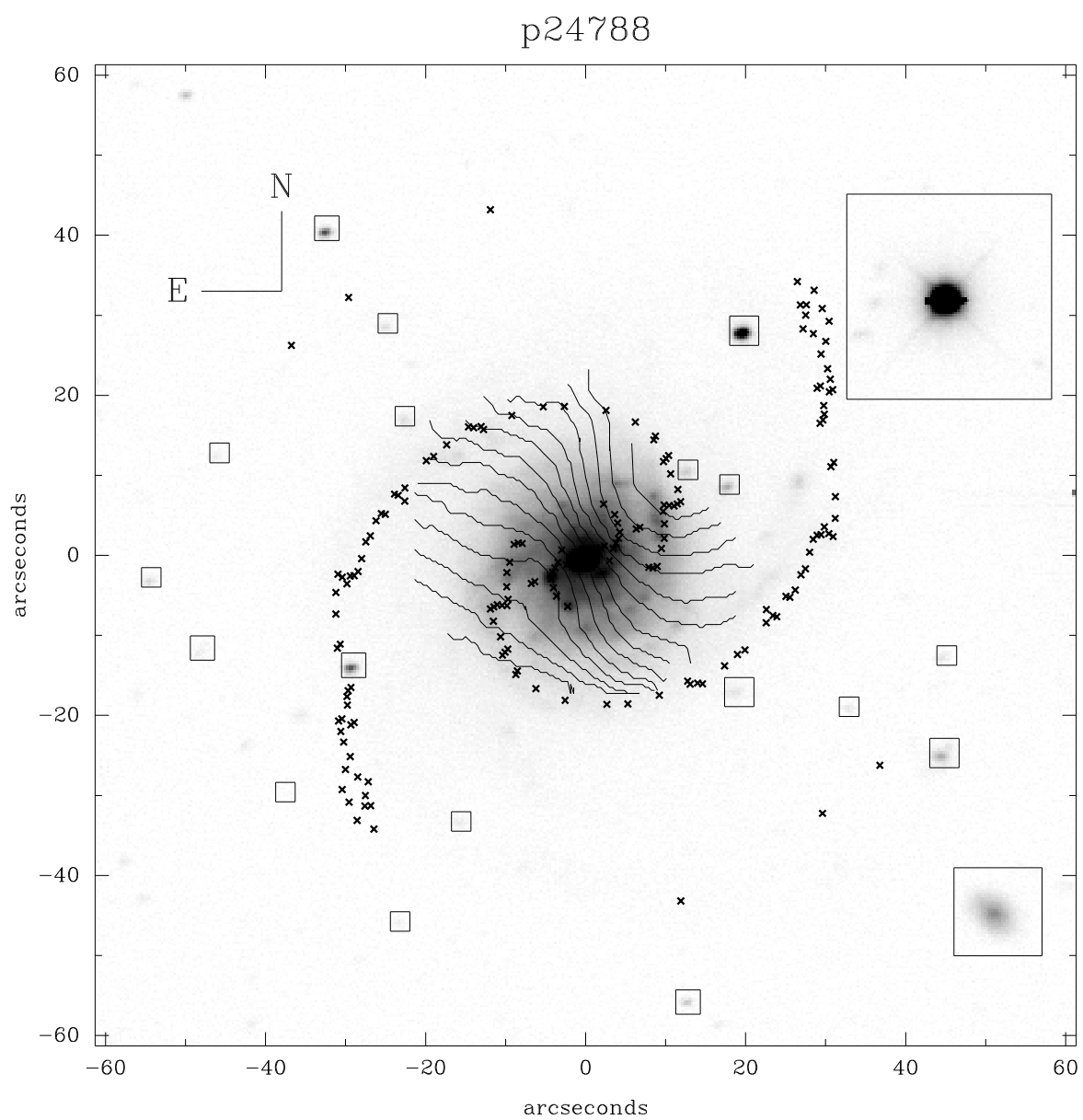


## p23913

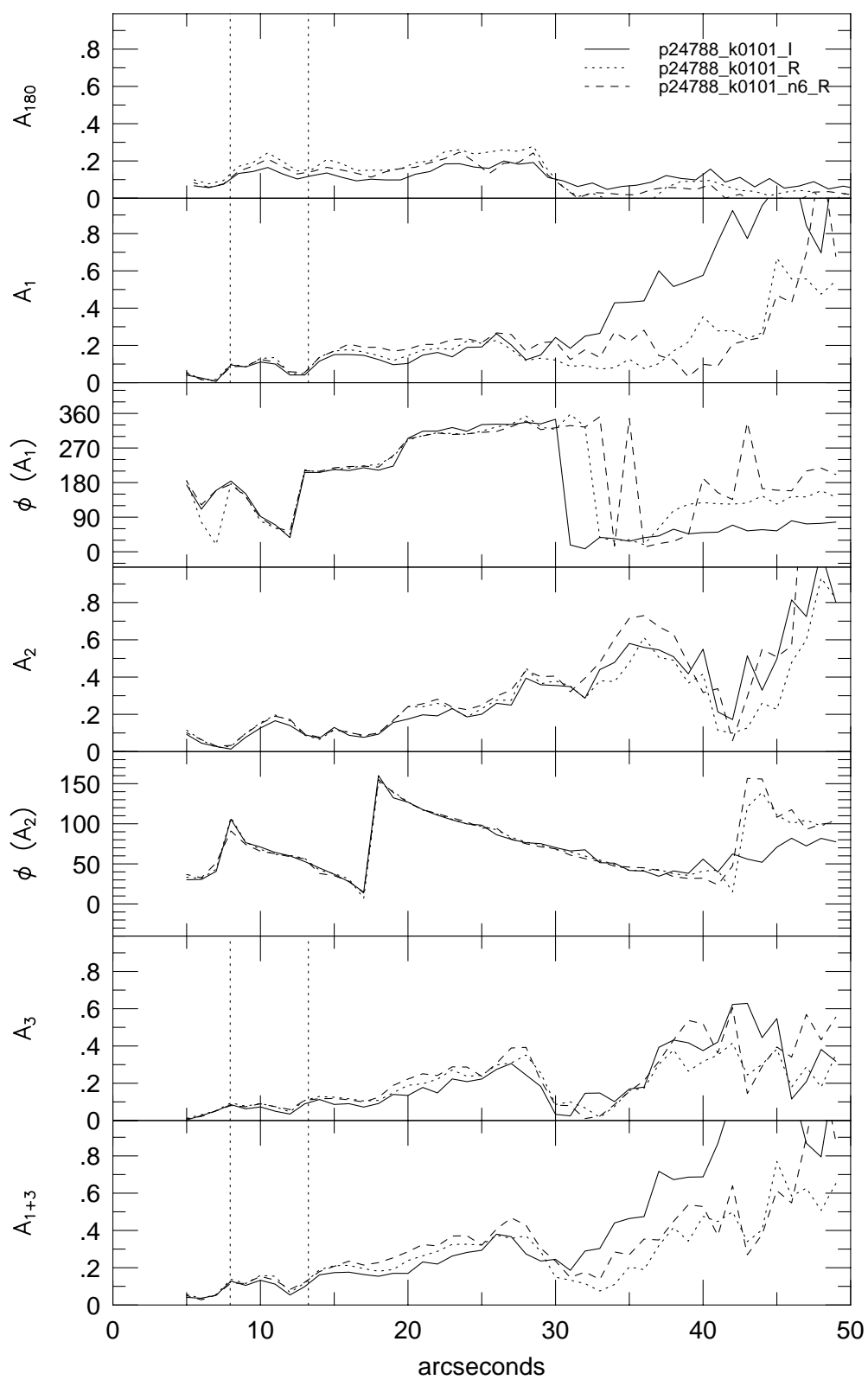




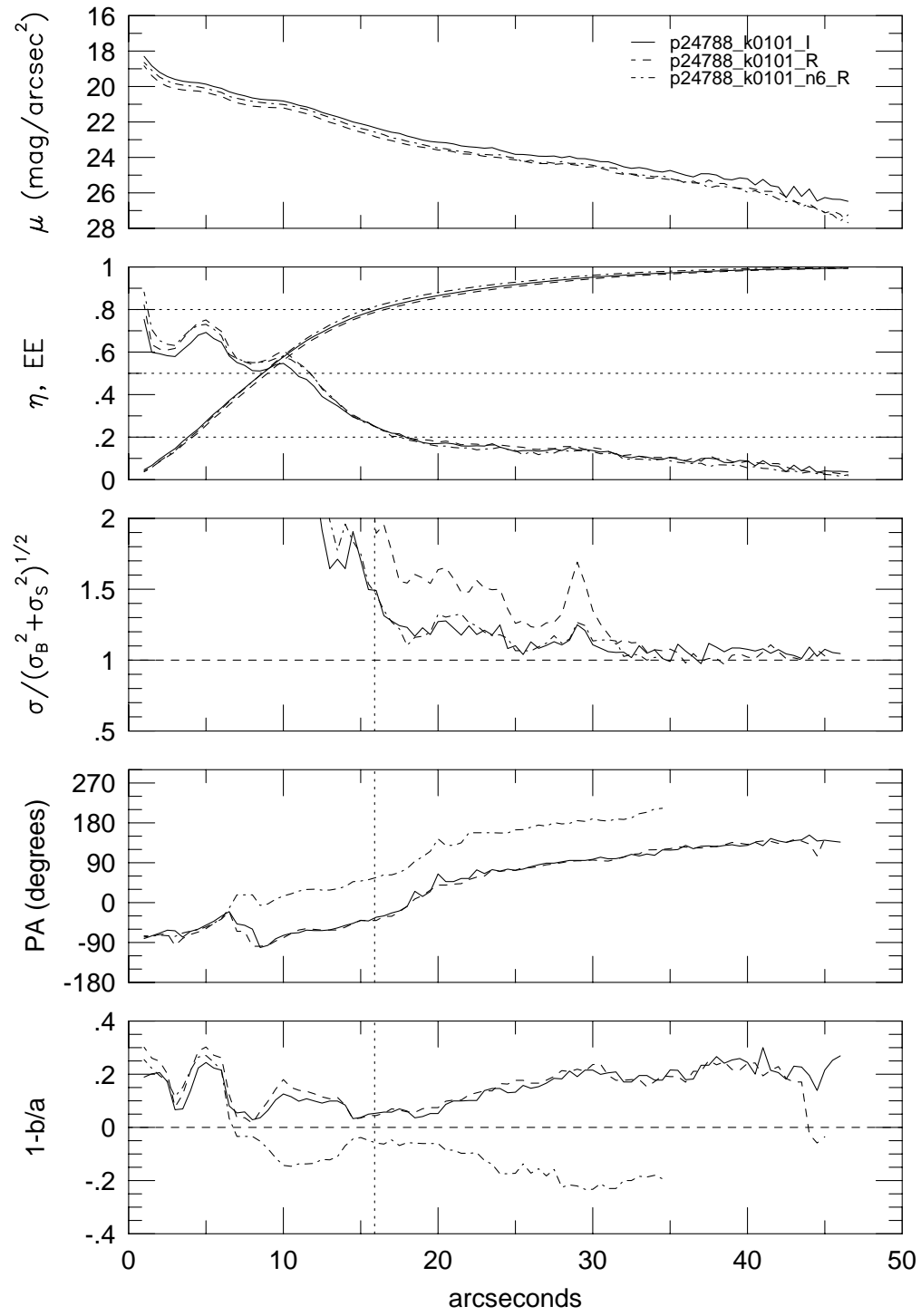




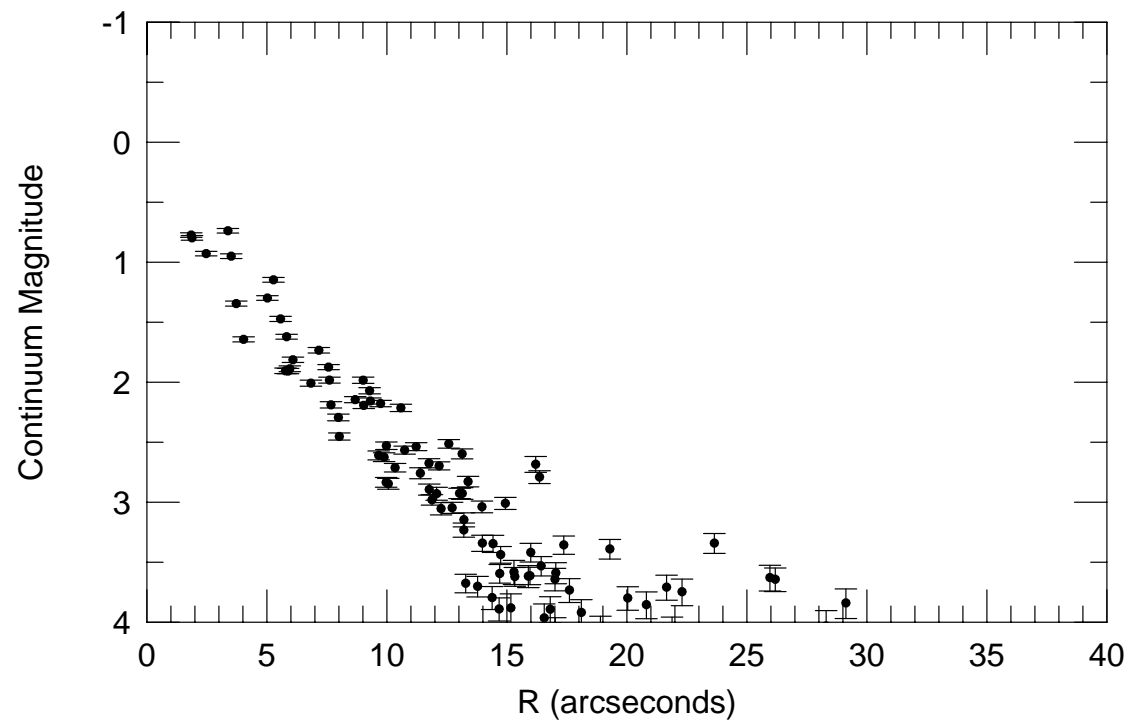
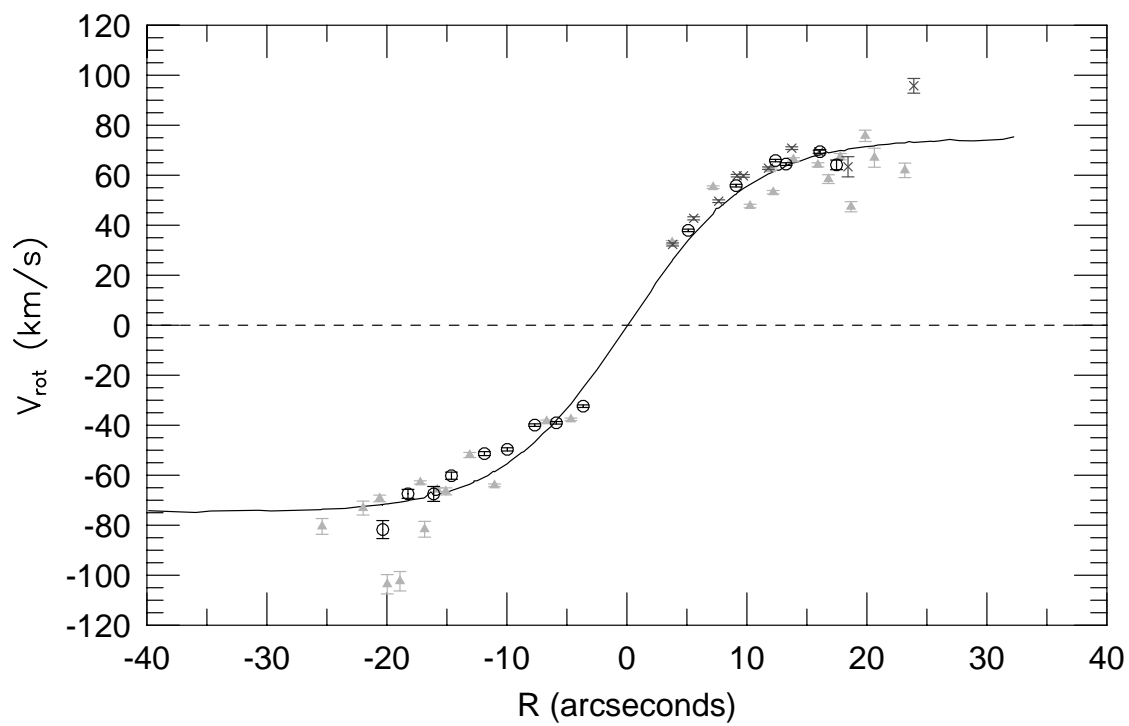
p24788

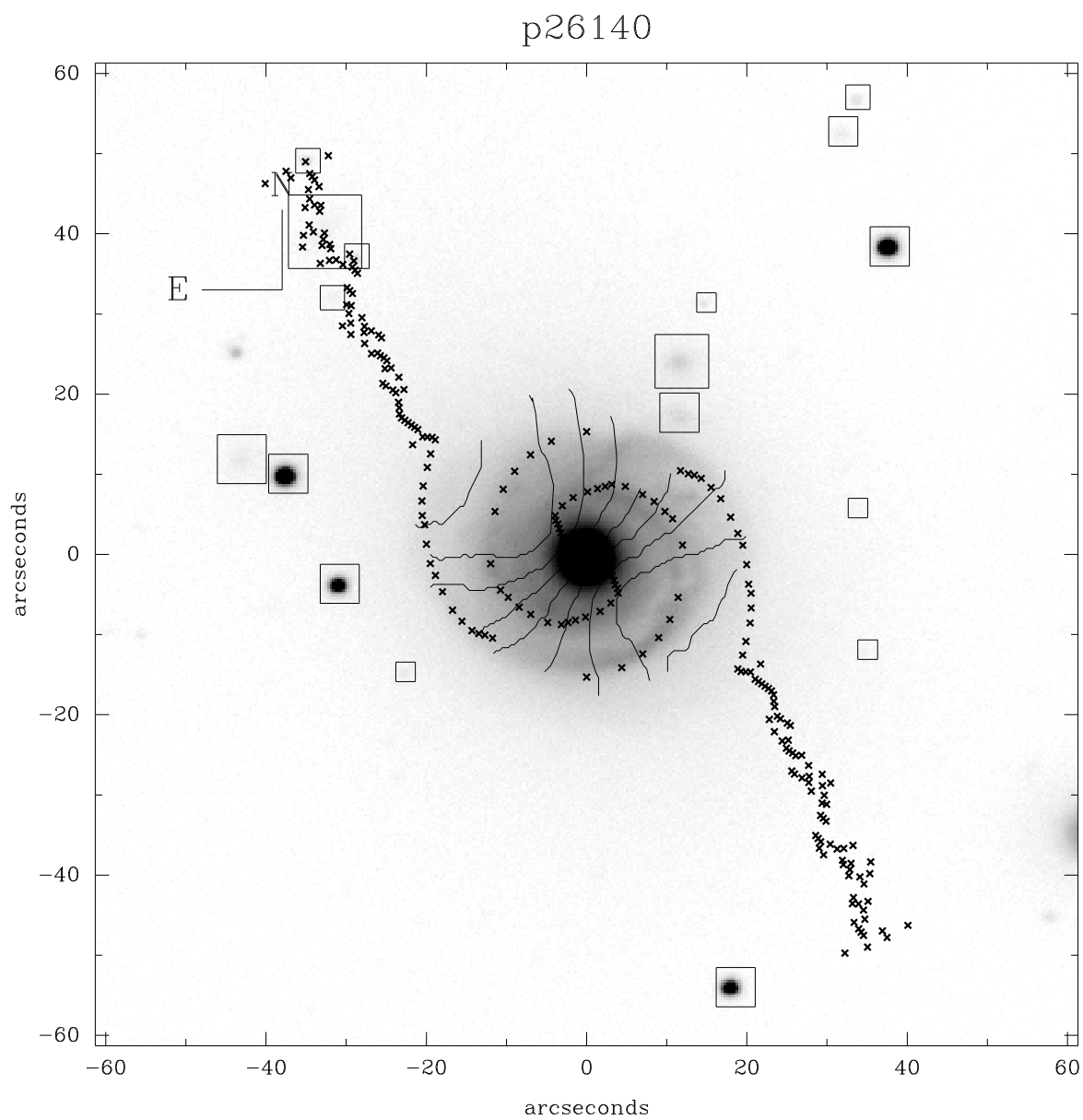


## p24788

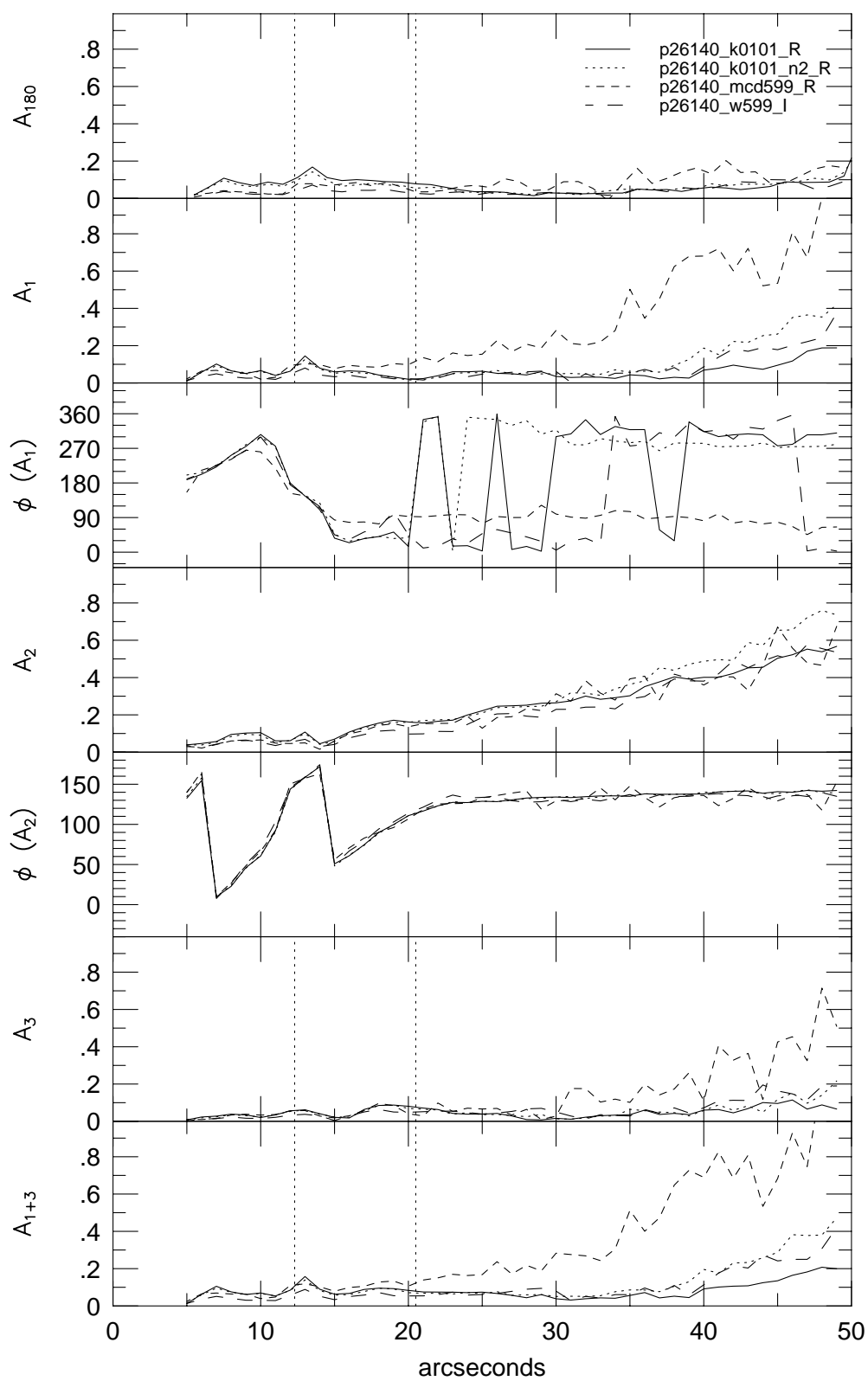


p24788

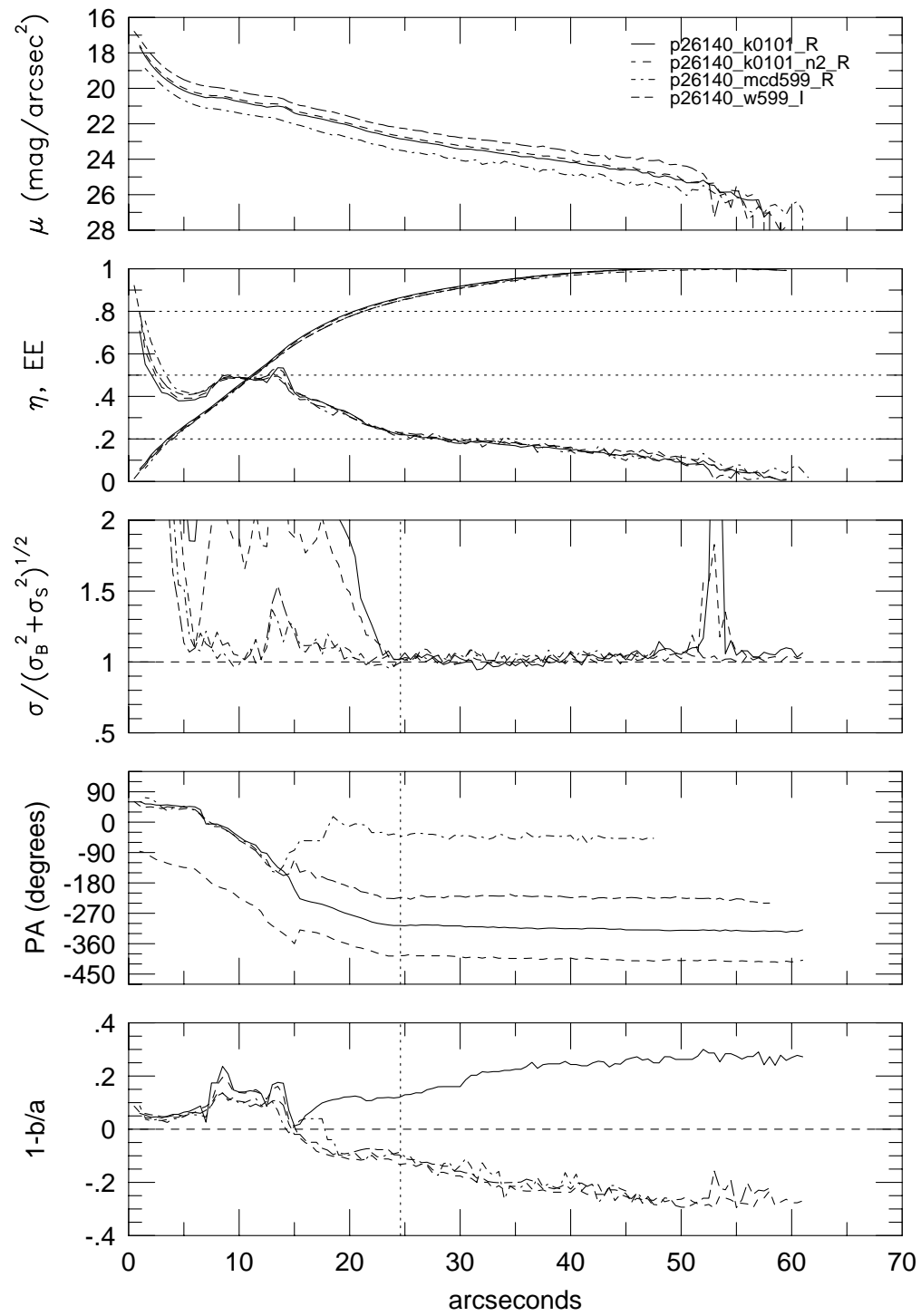




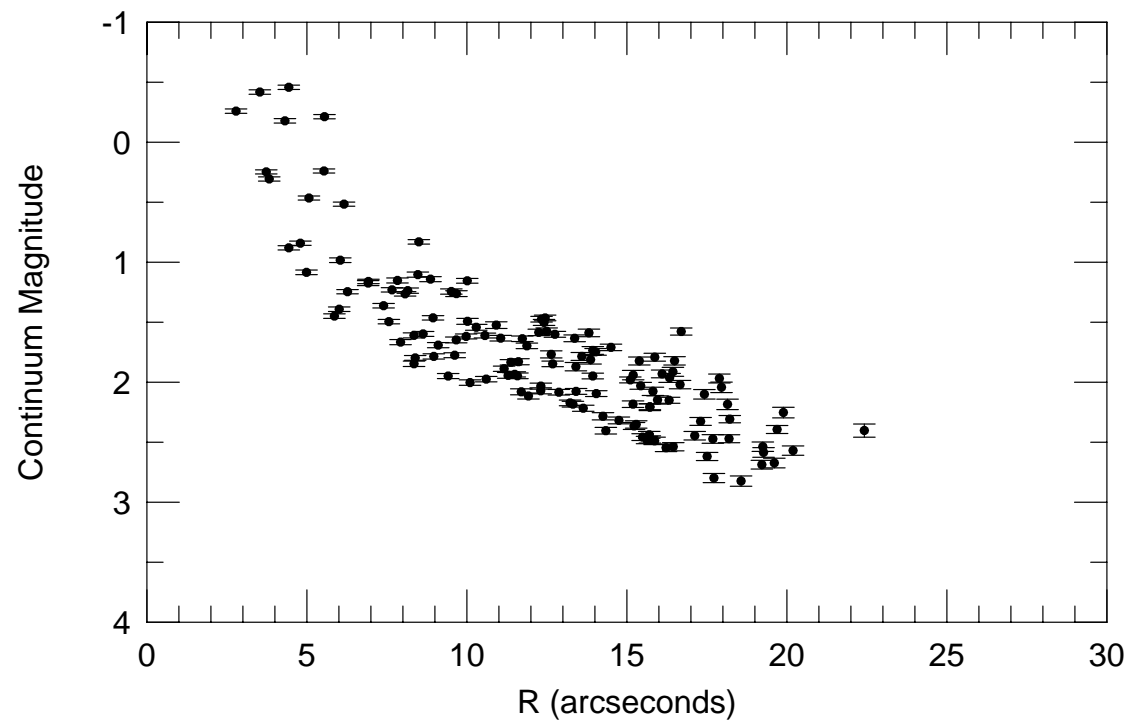
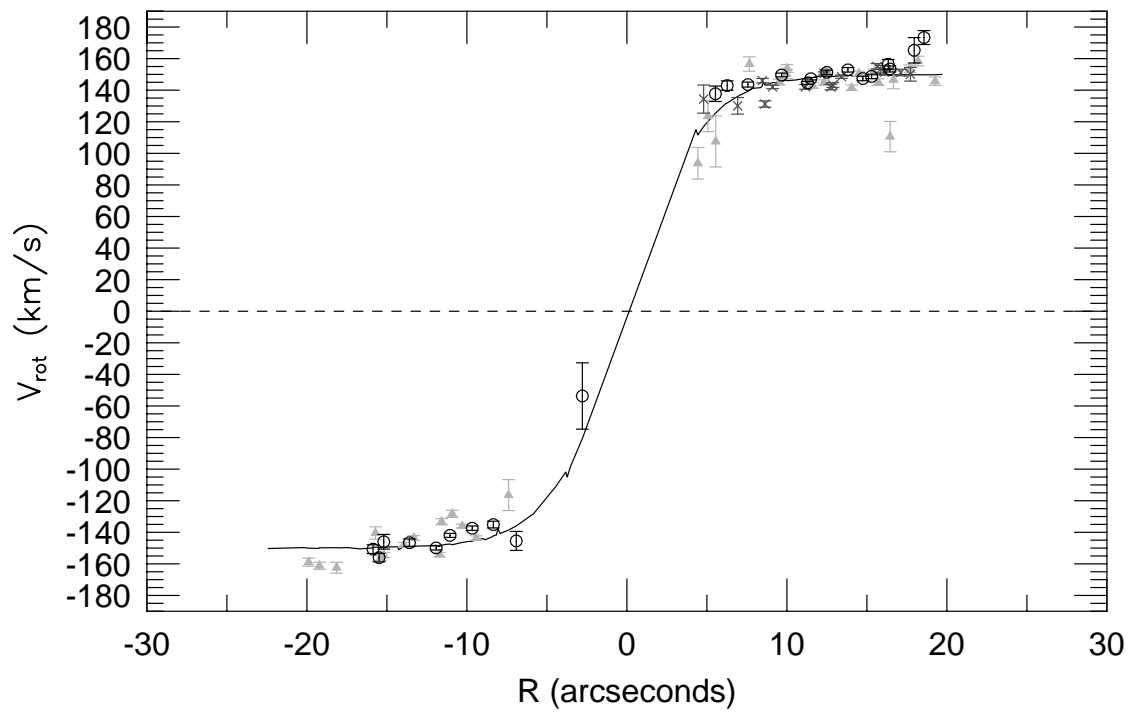
## p26140



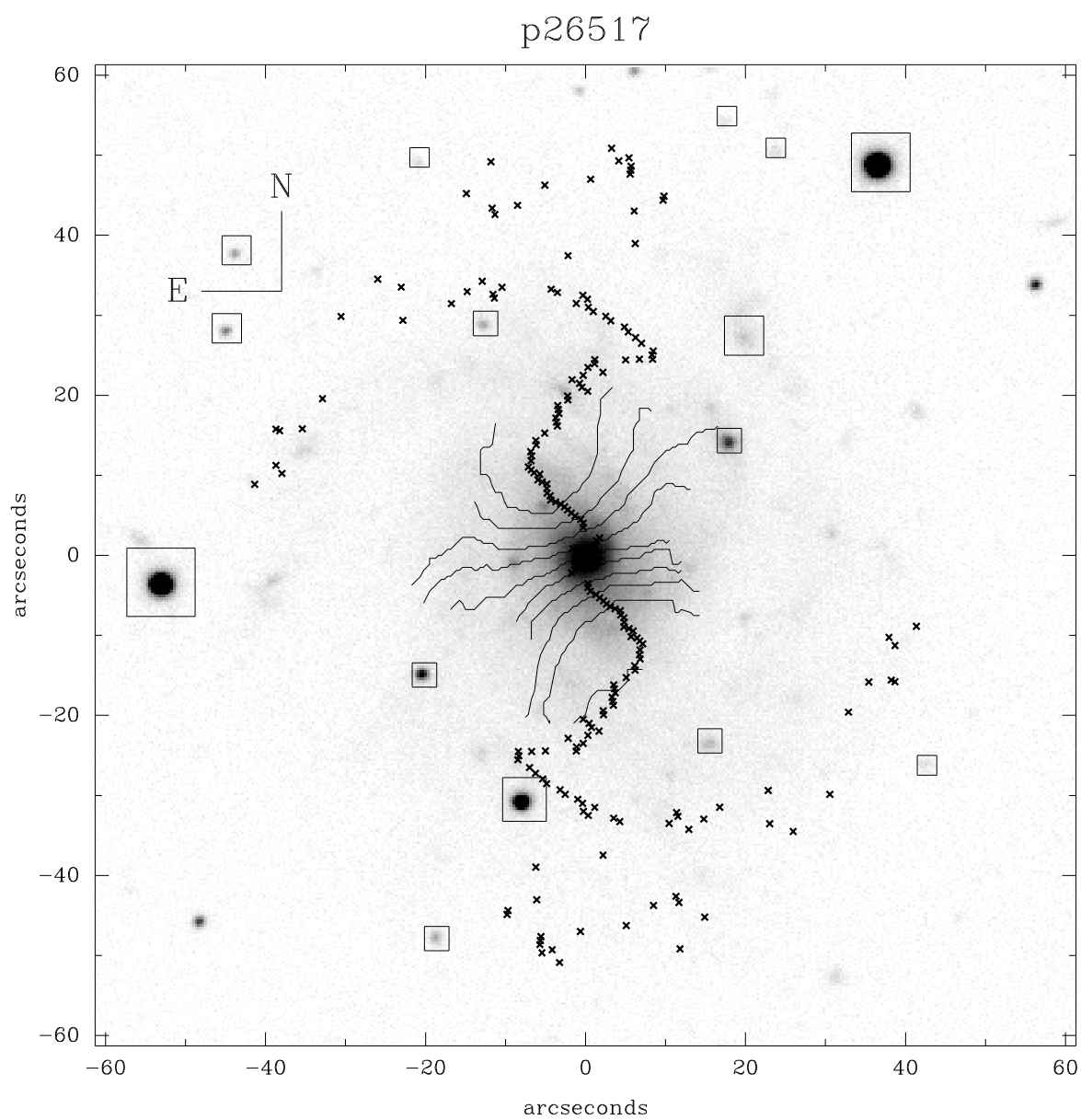
## p26140



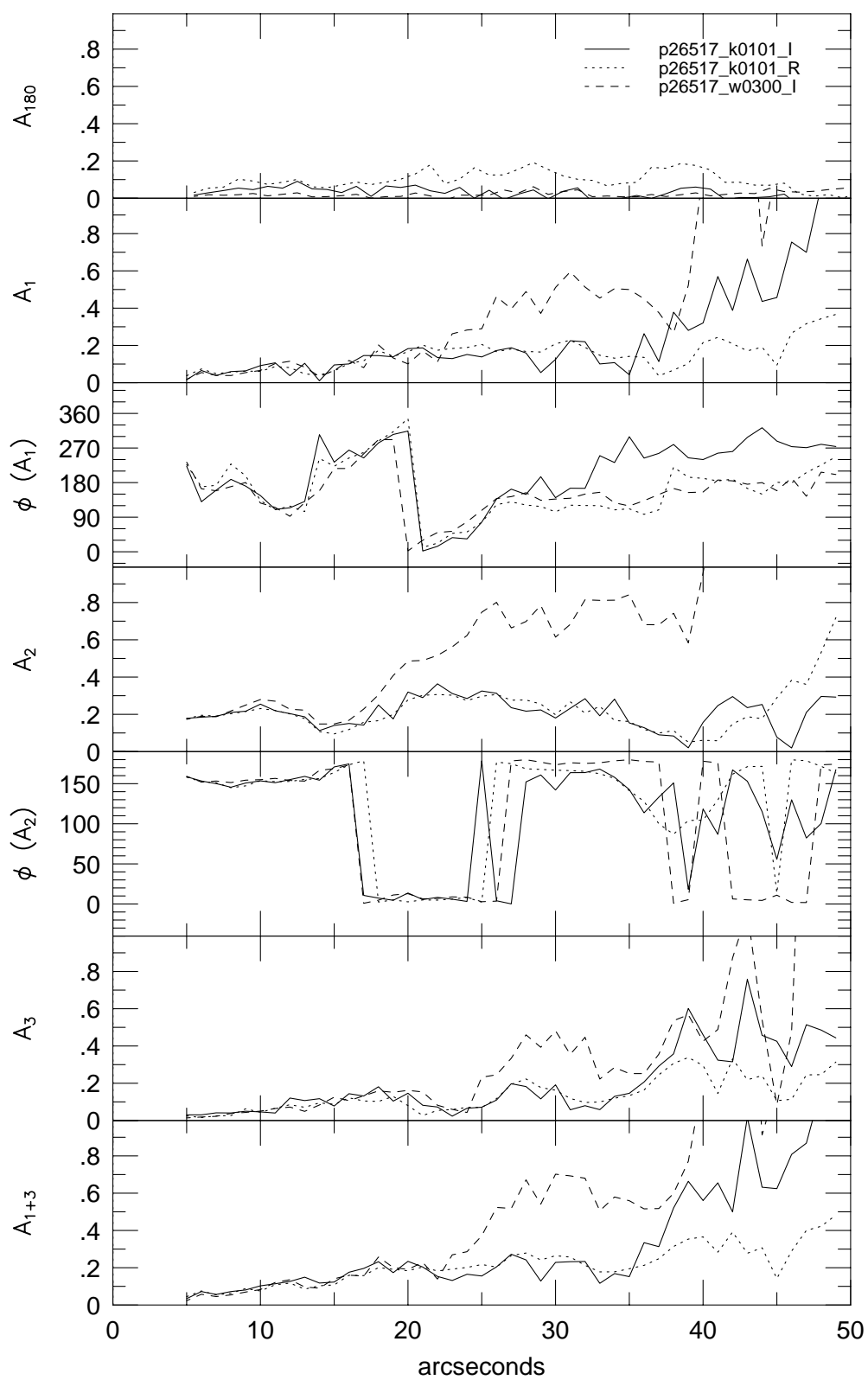
p26140



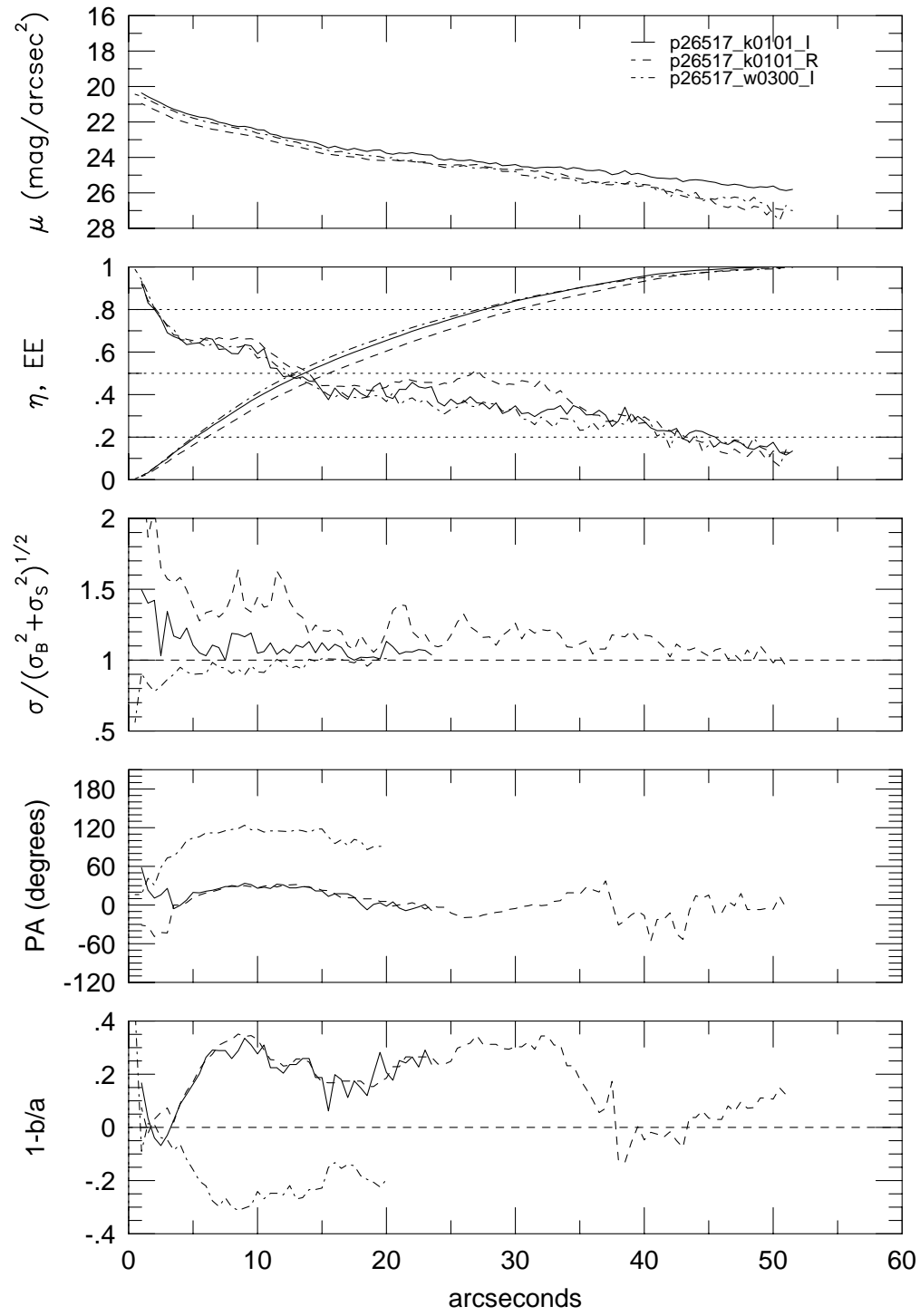




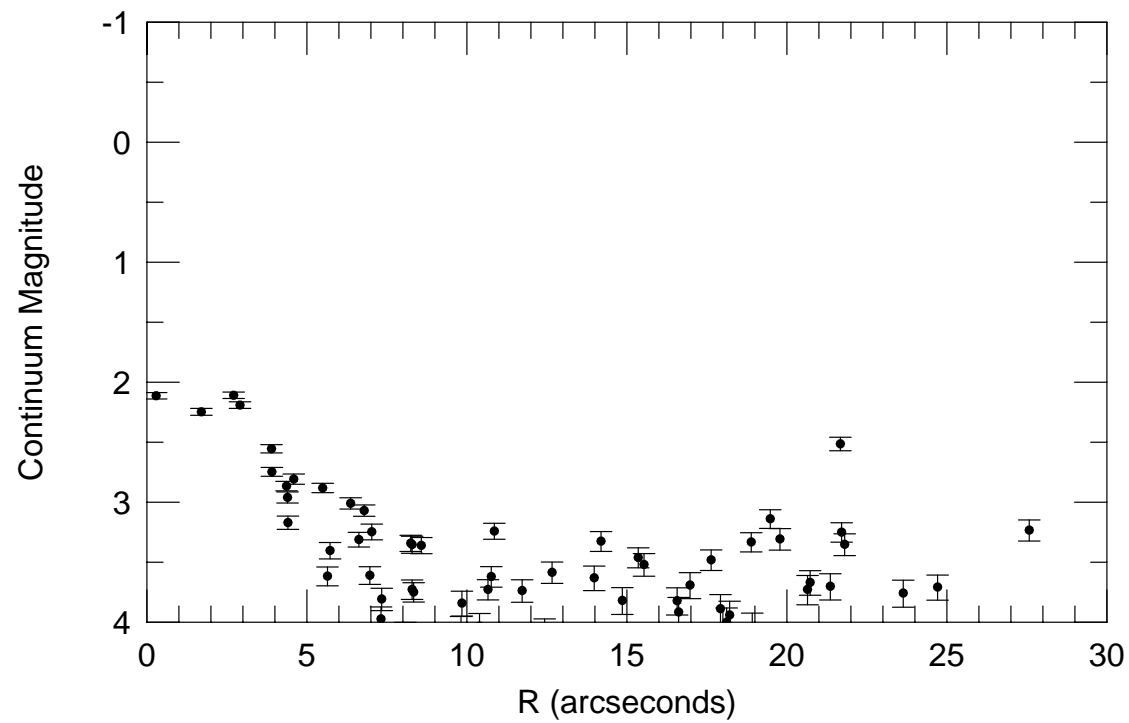
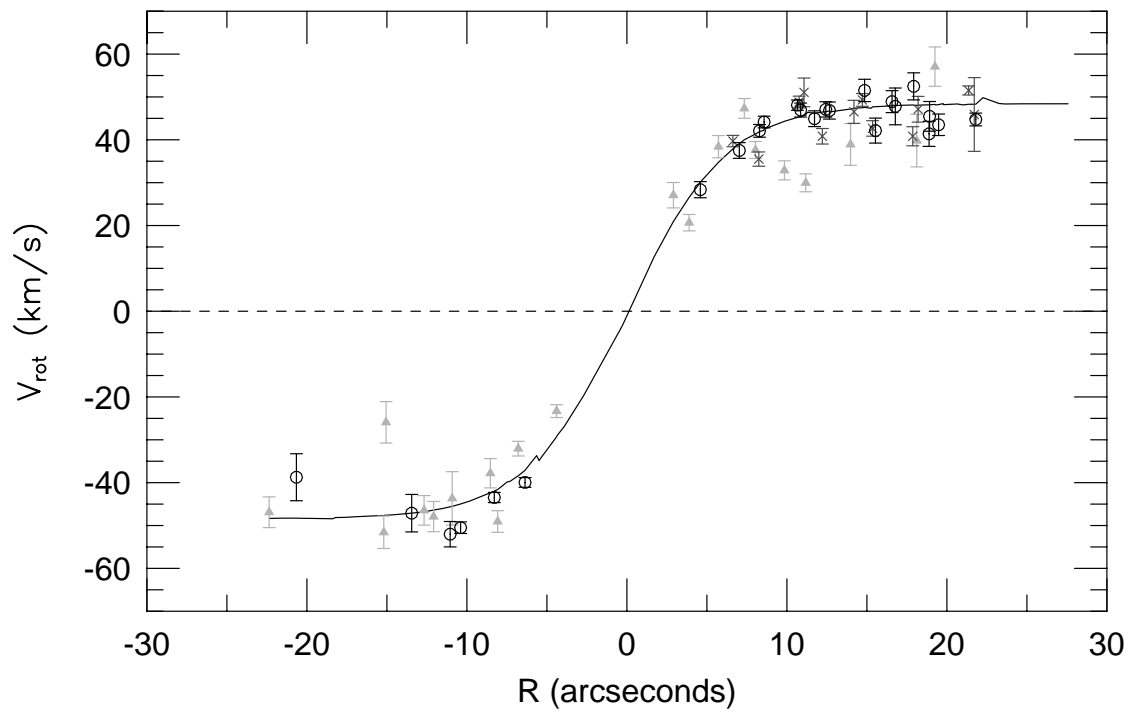
p26517

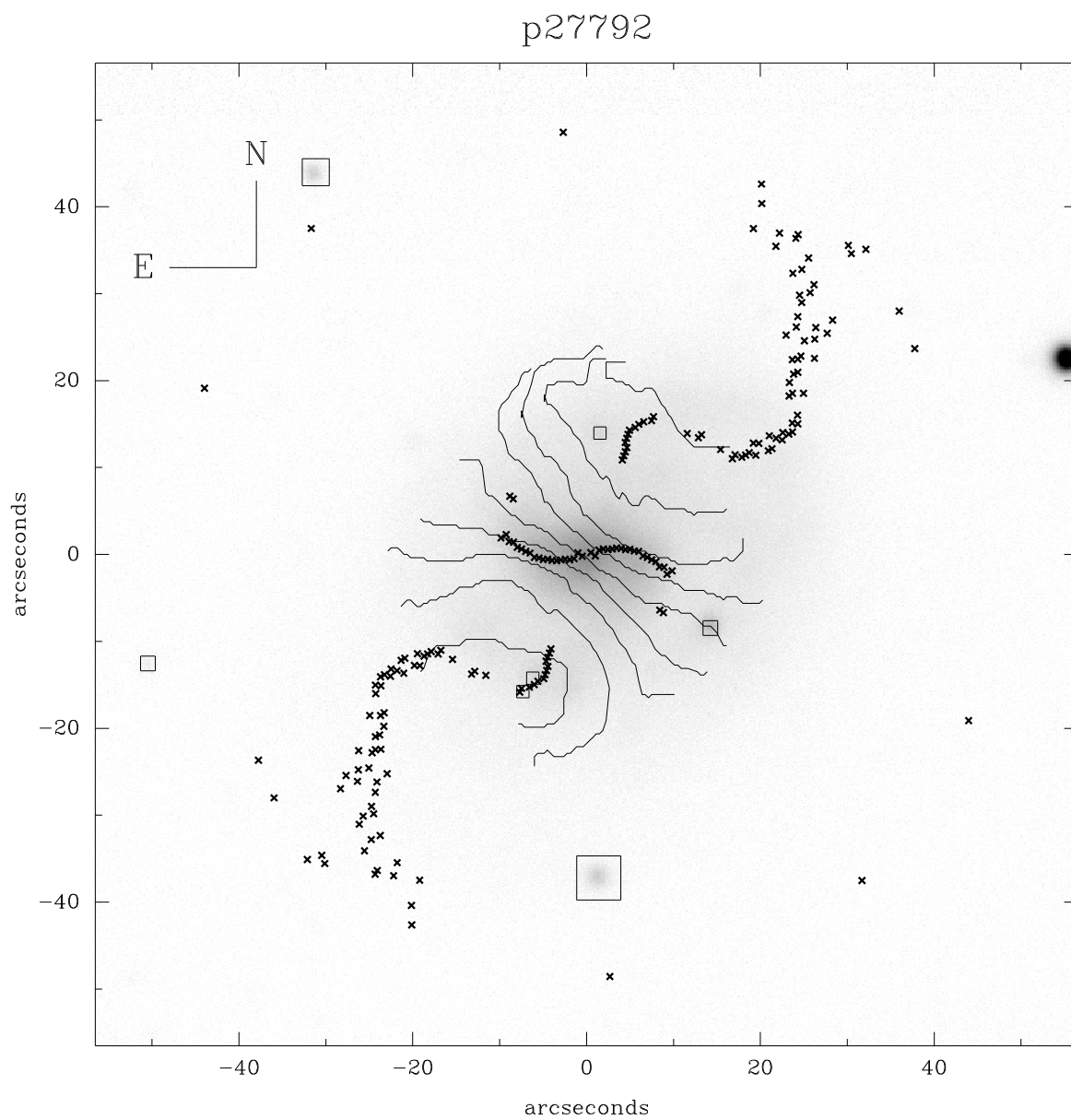


p26517

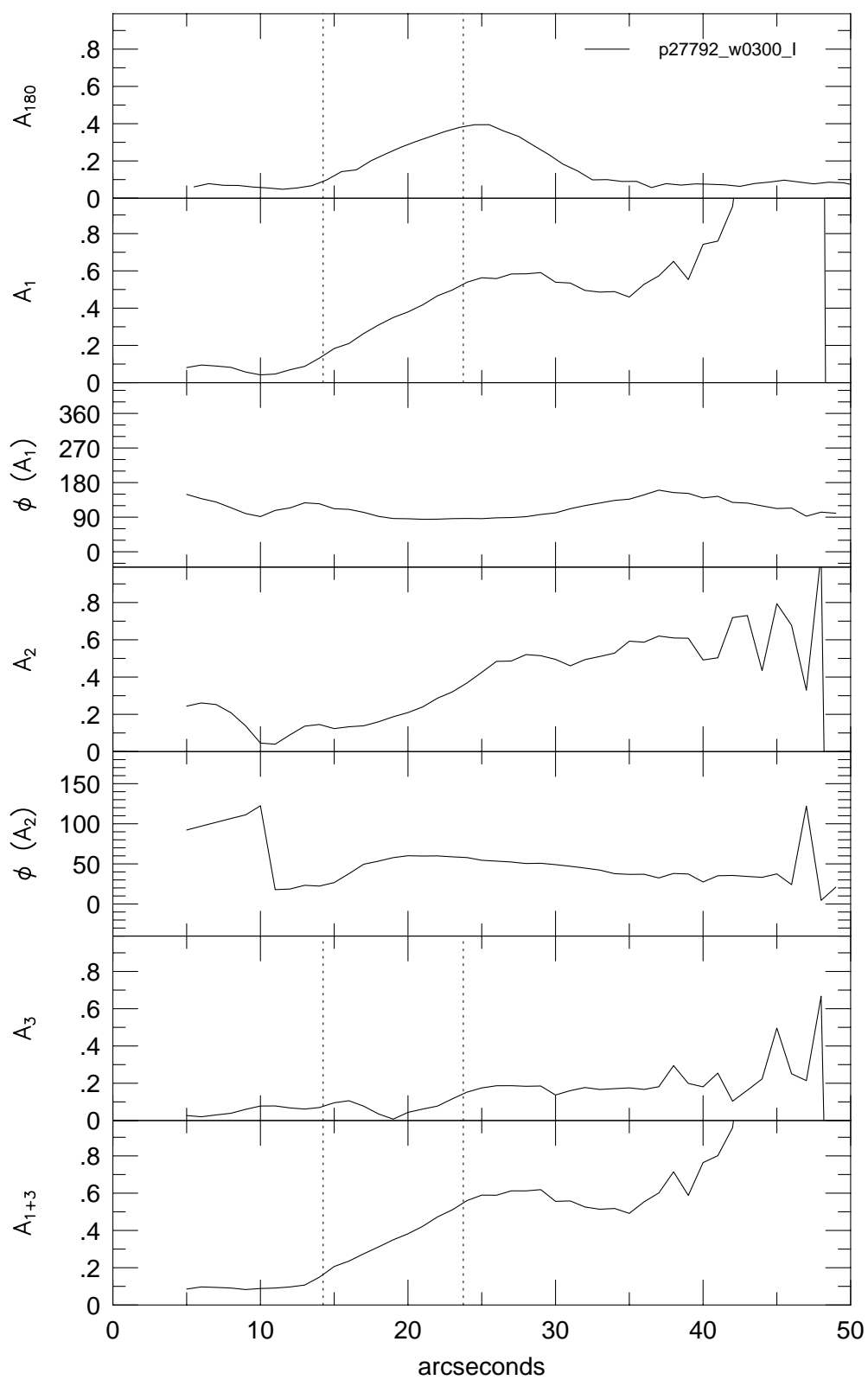


p26517

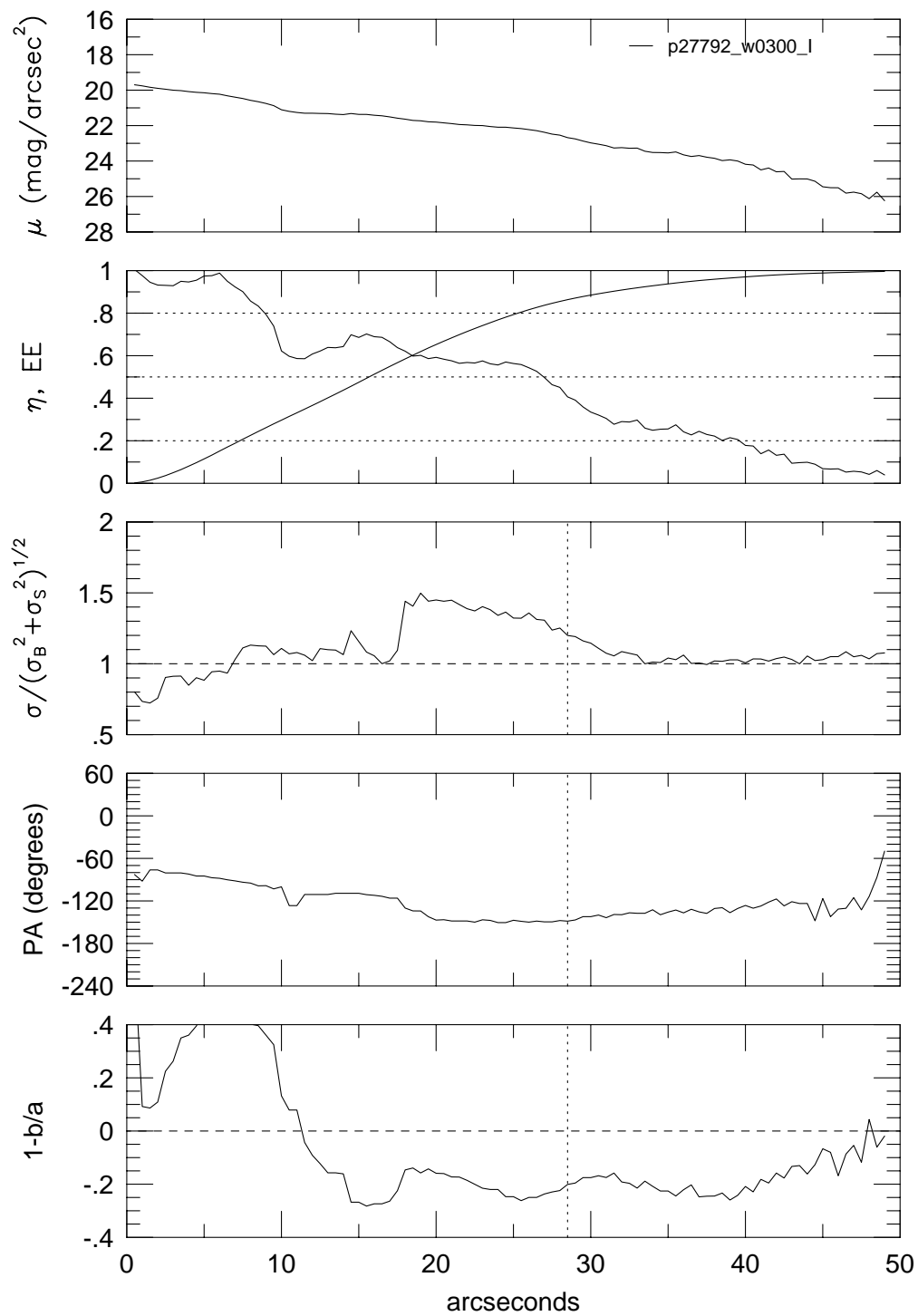




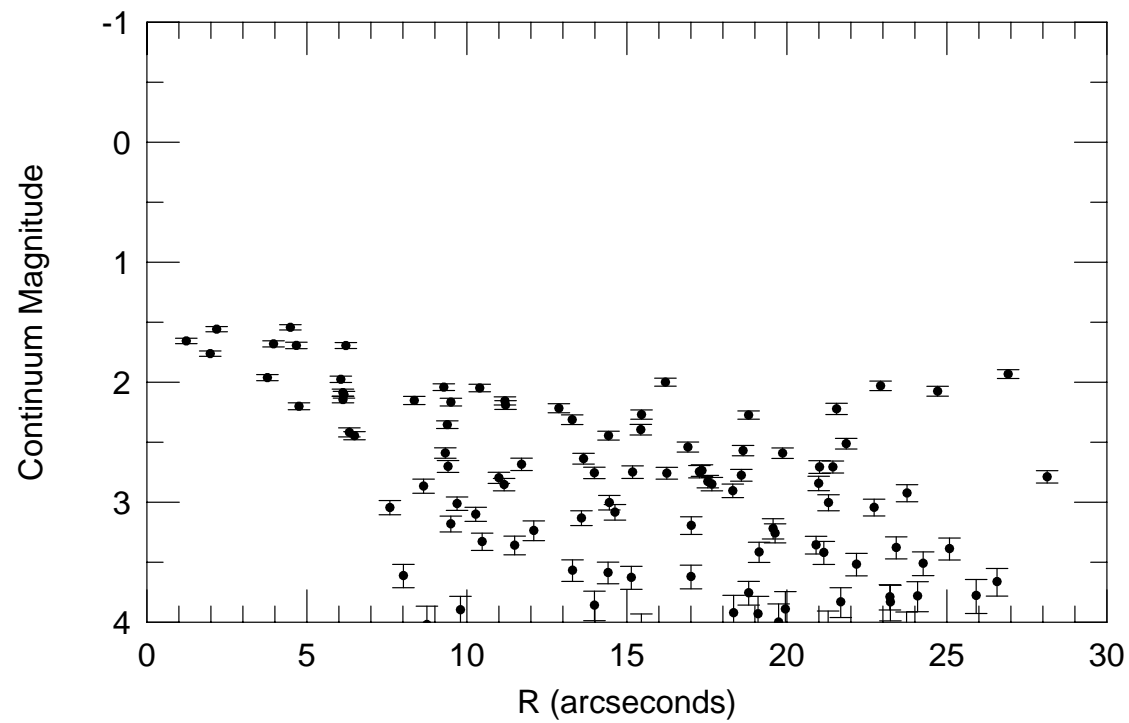
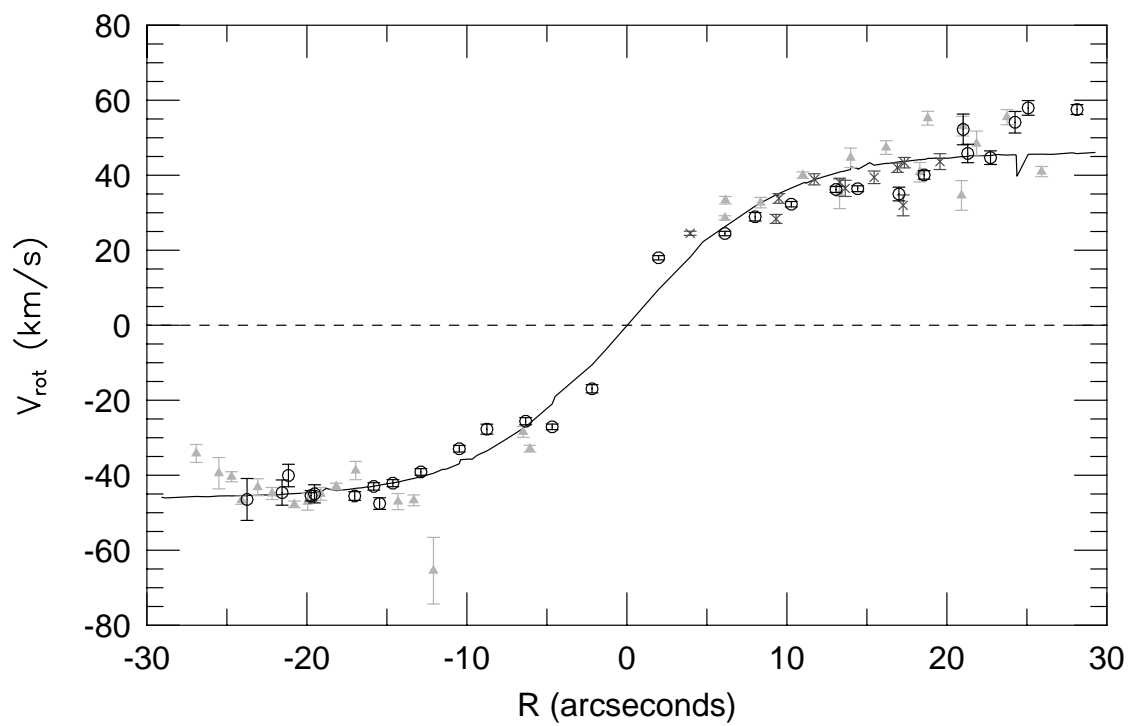
p27792



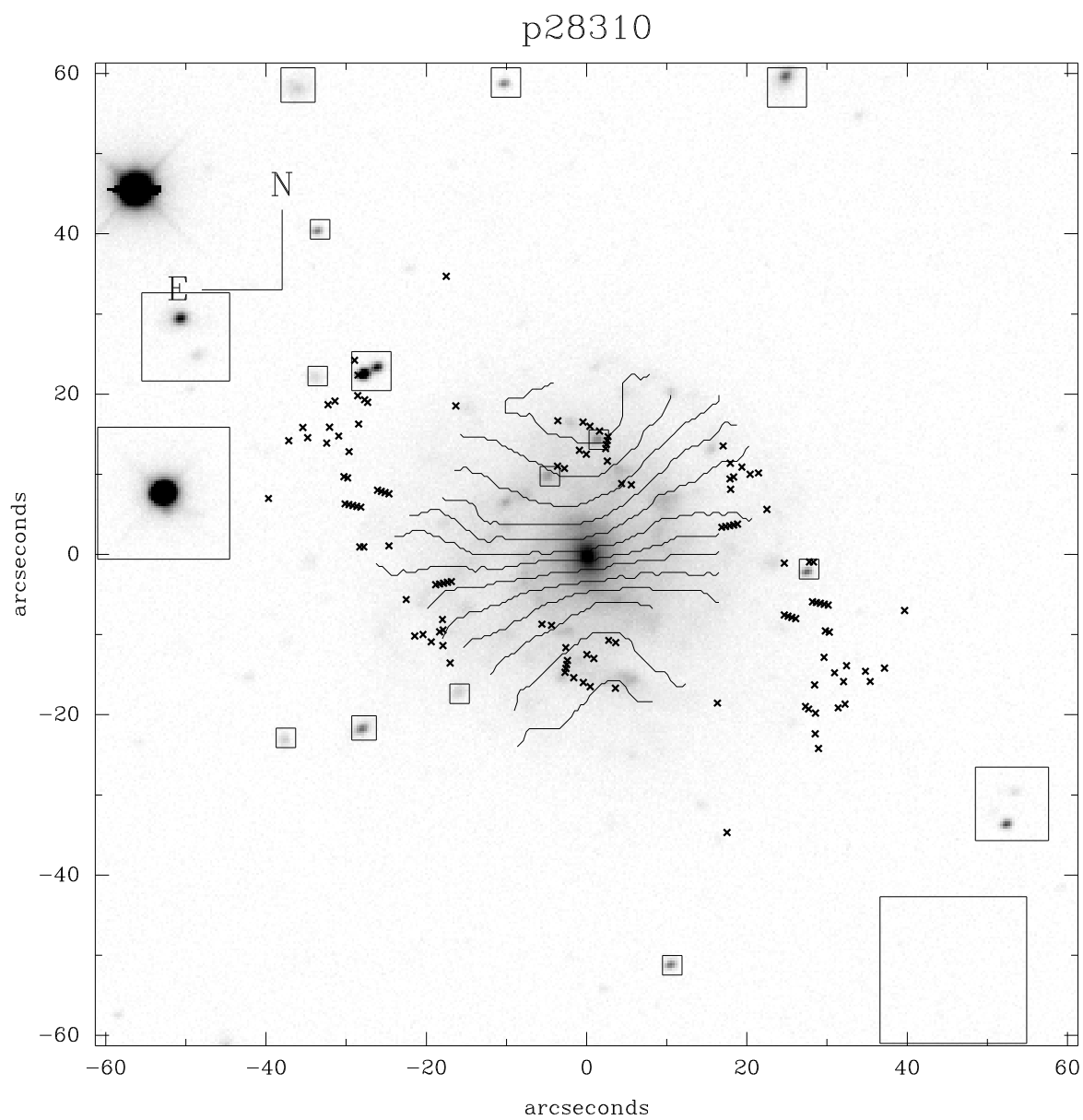
p27792



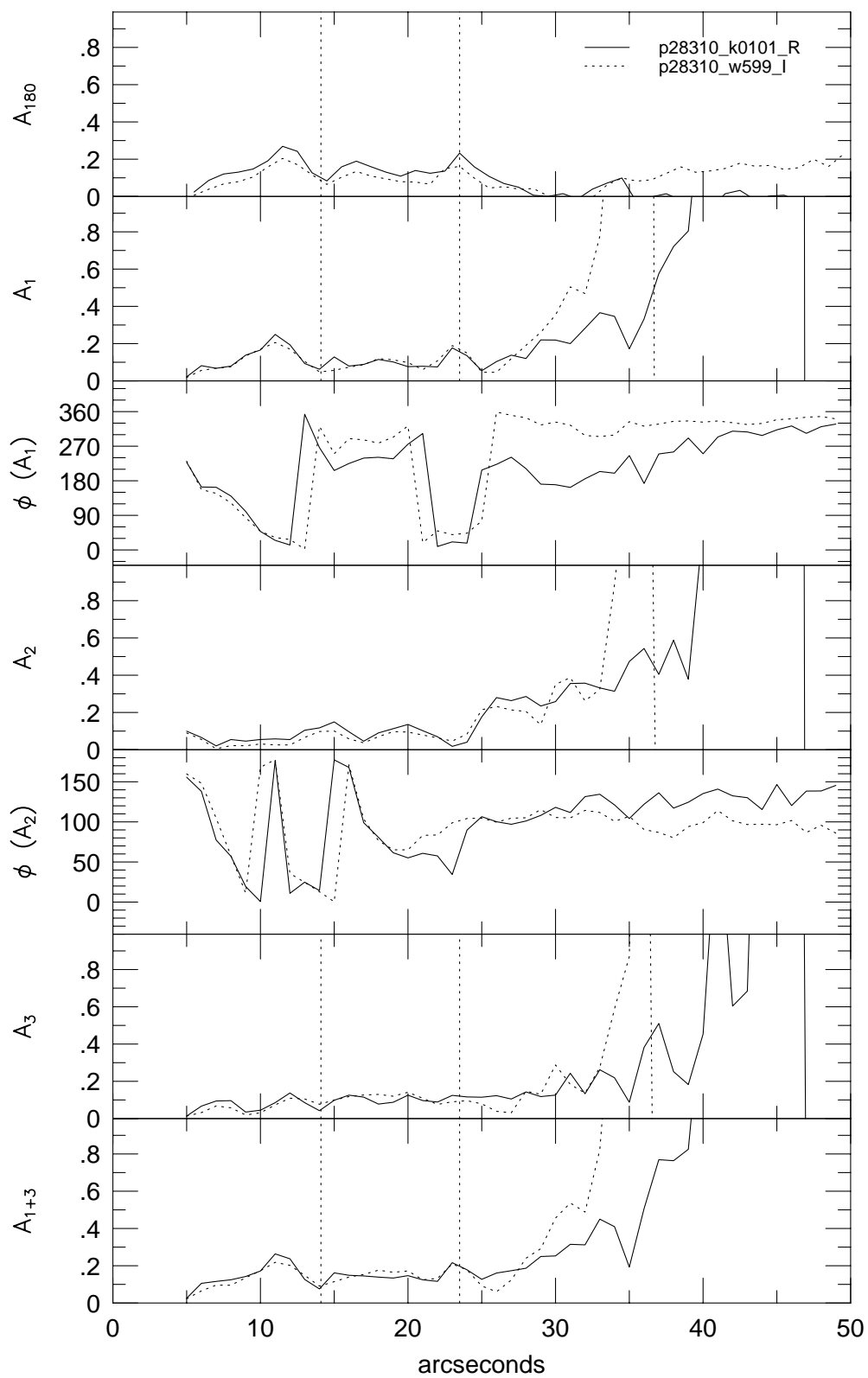
p27792



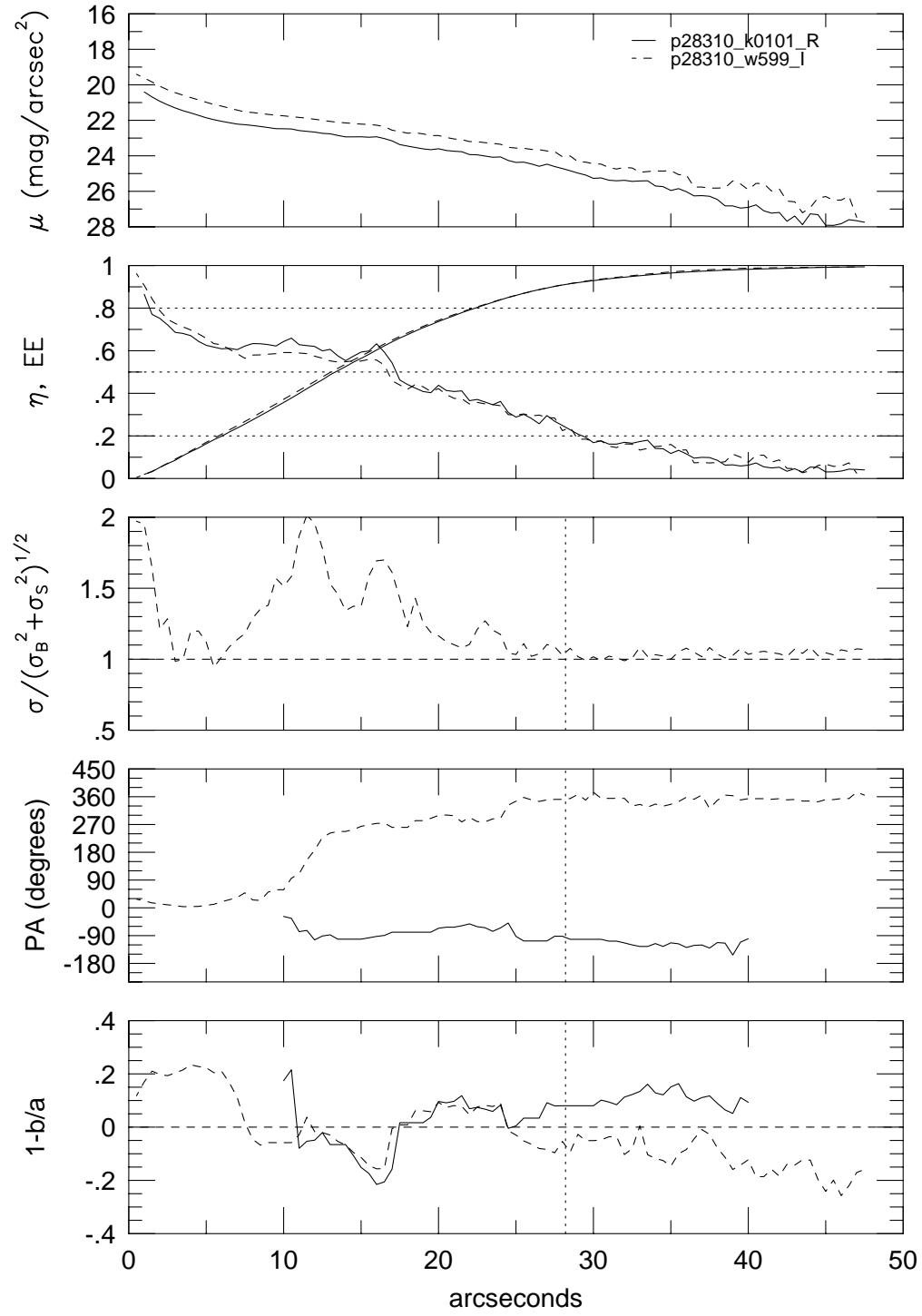




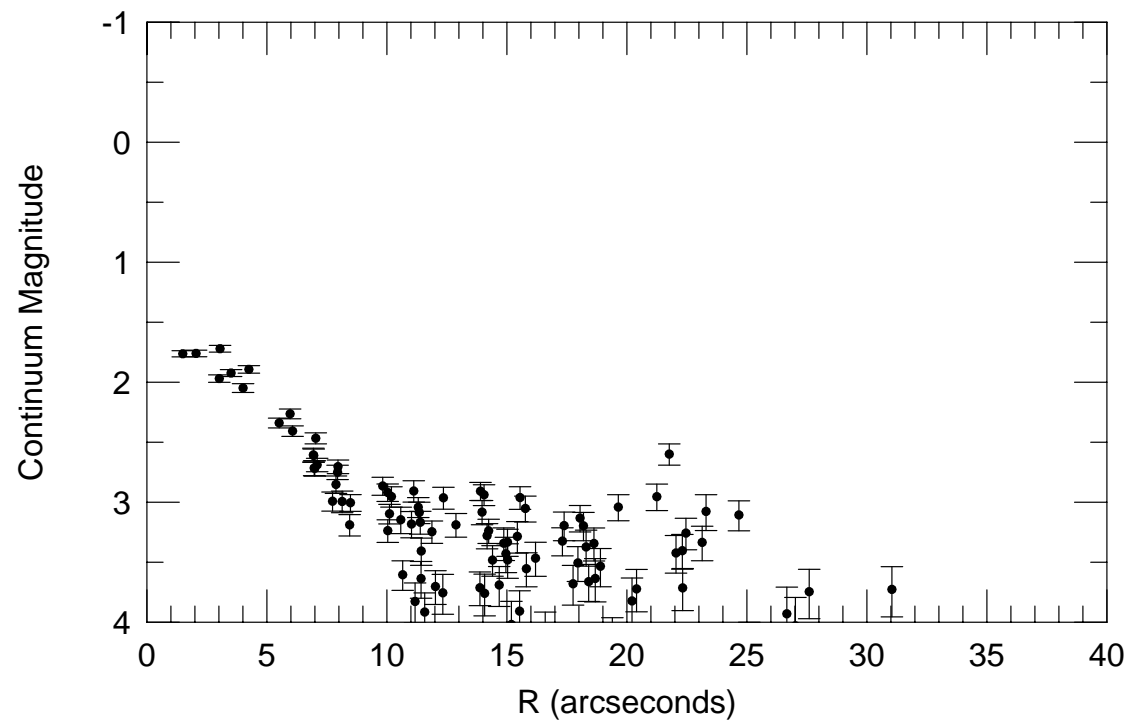
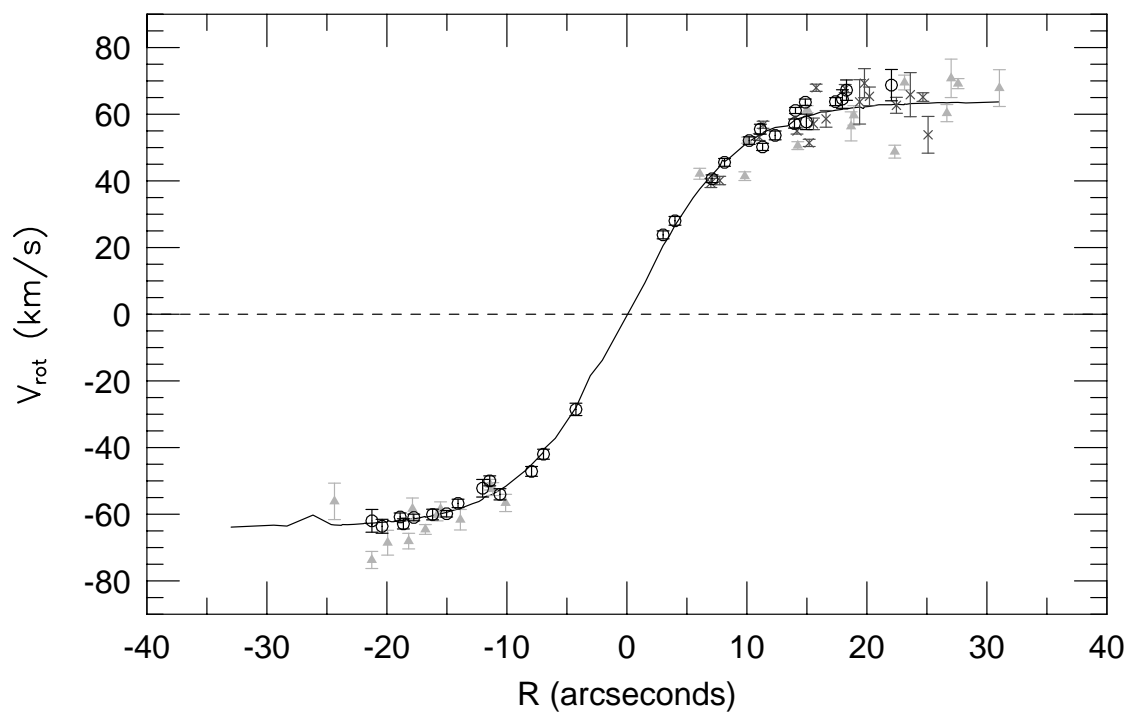
## p28310

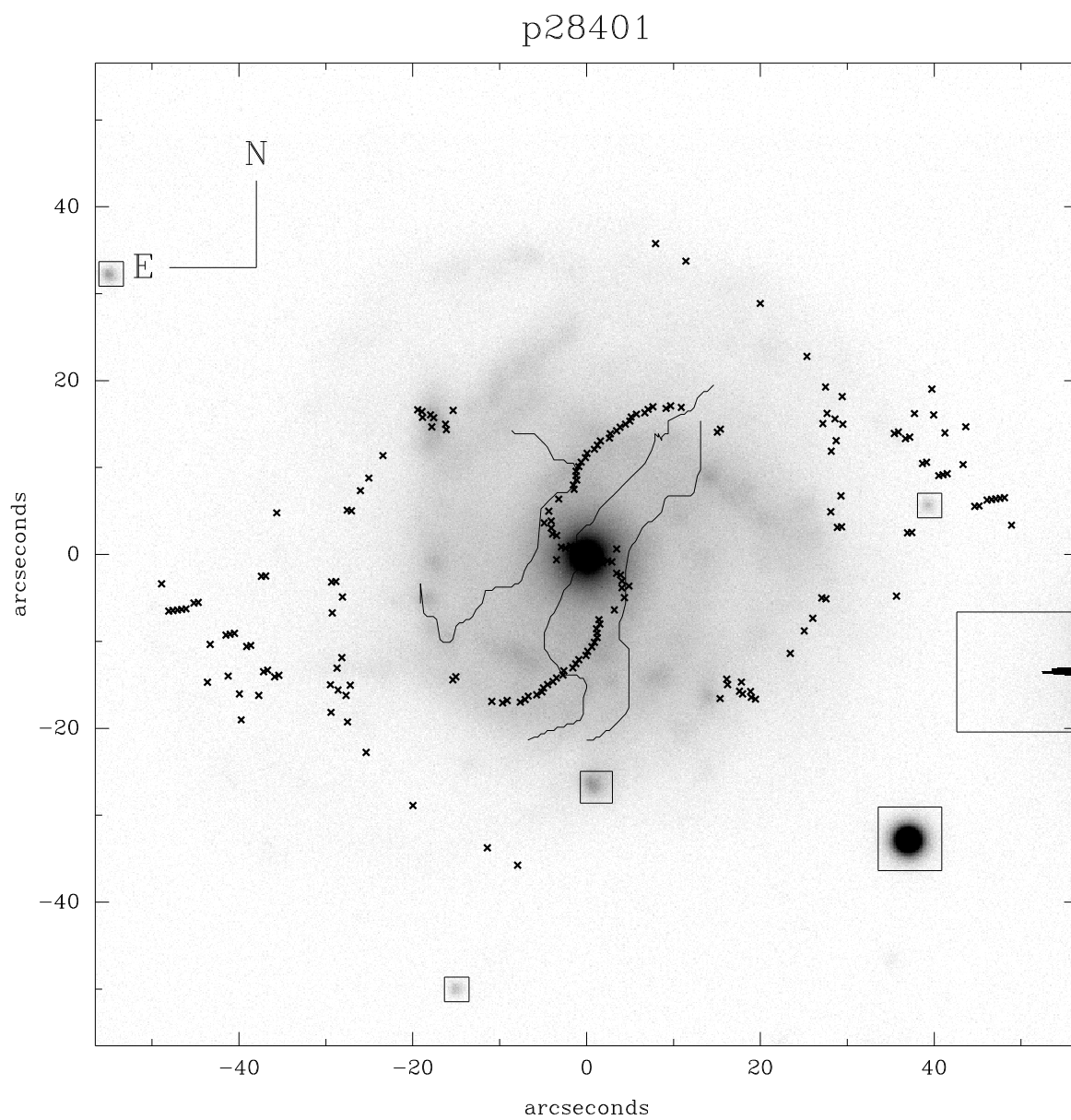


## p28310

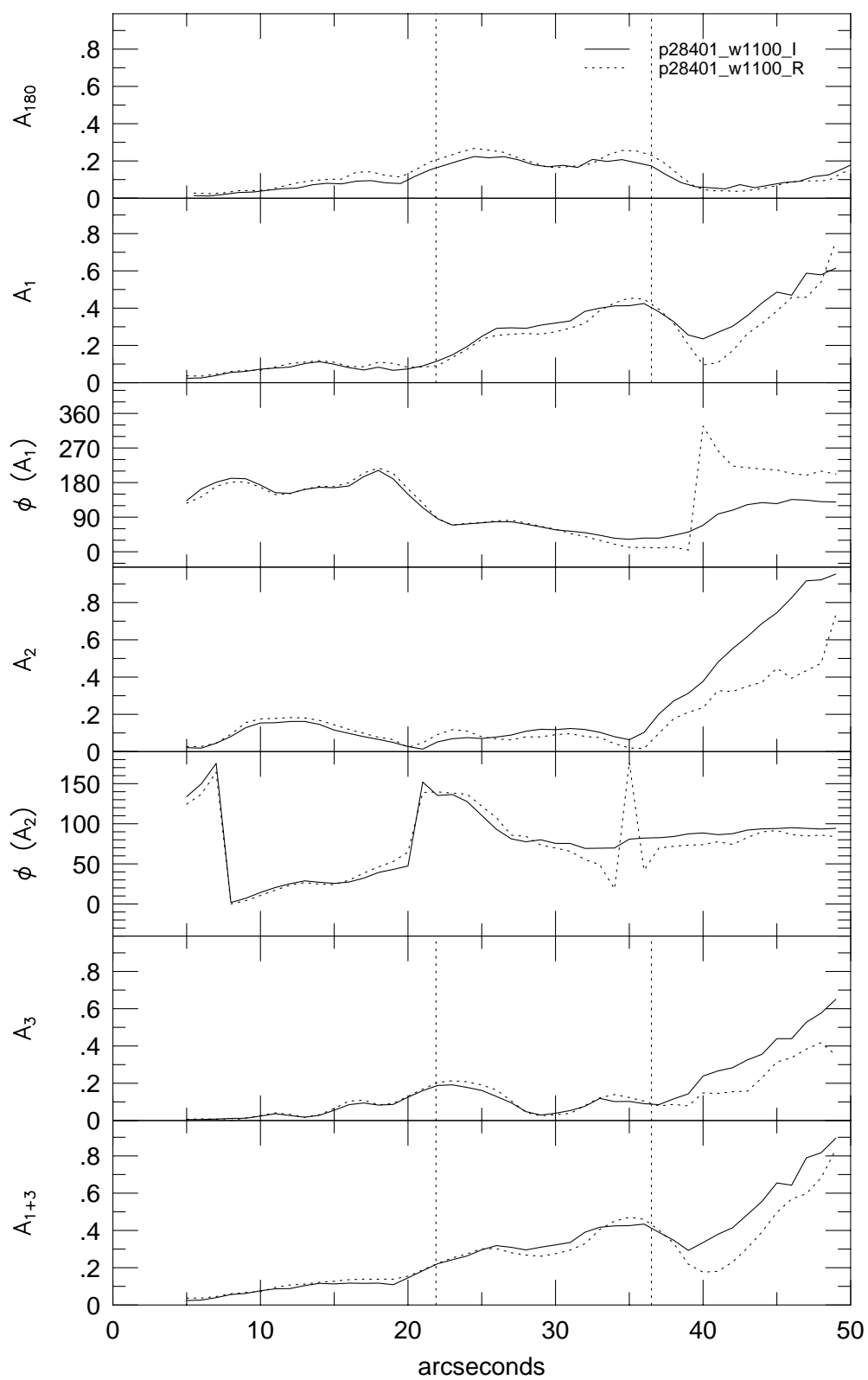


p28310

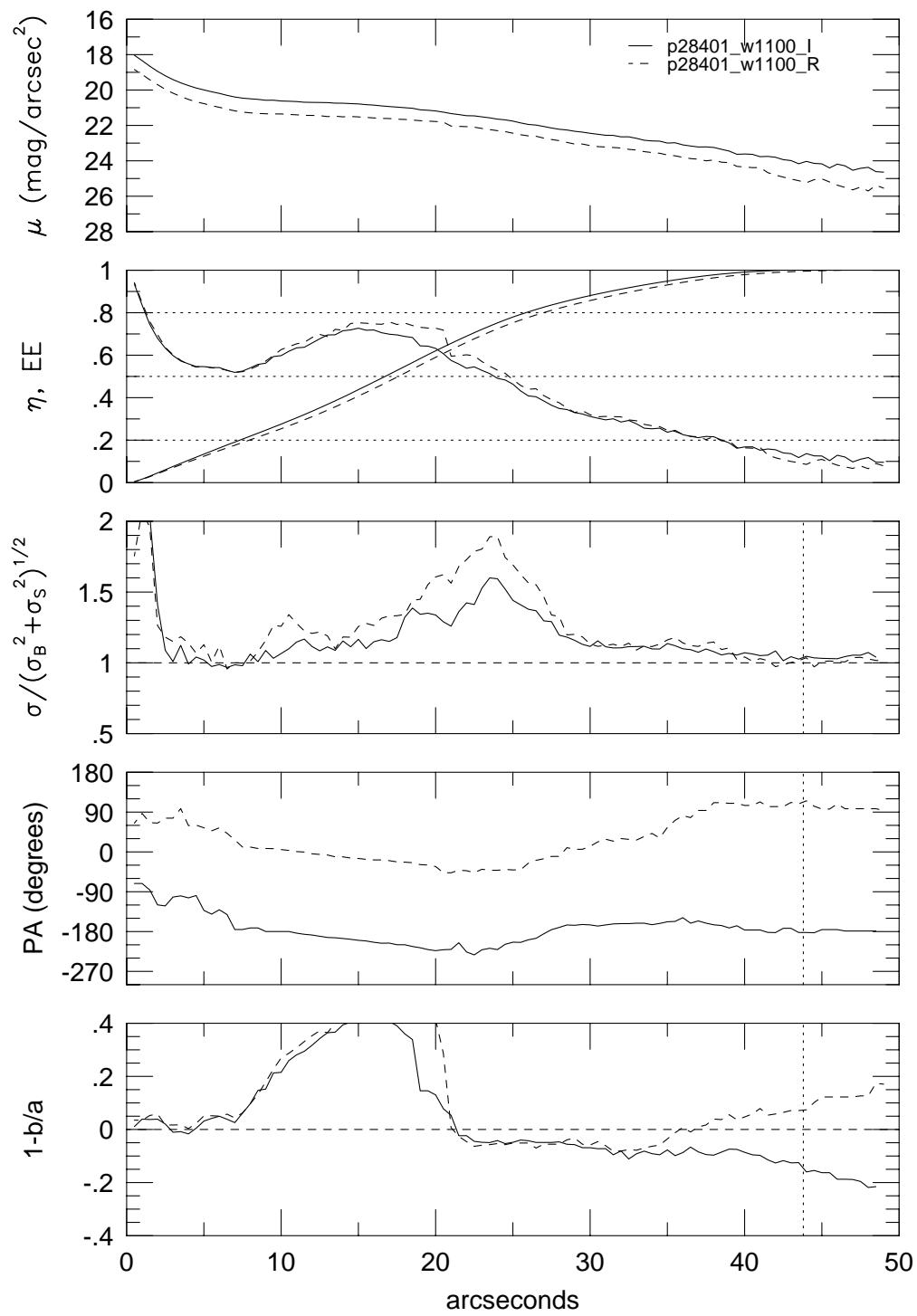




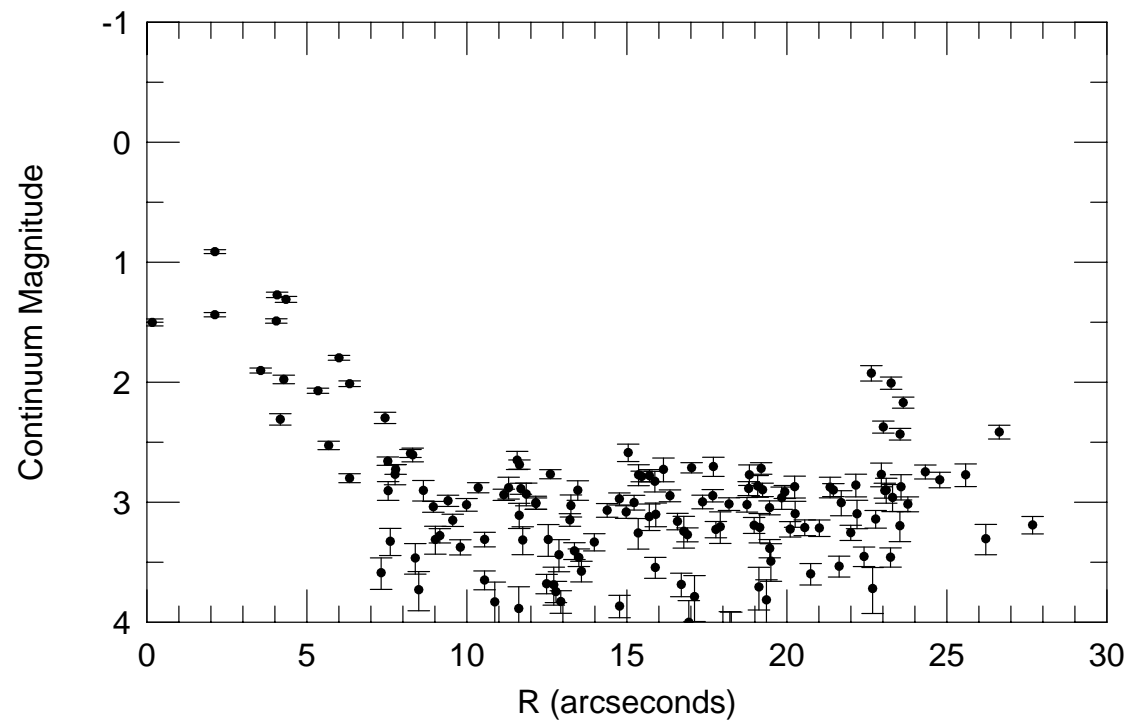
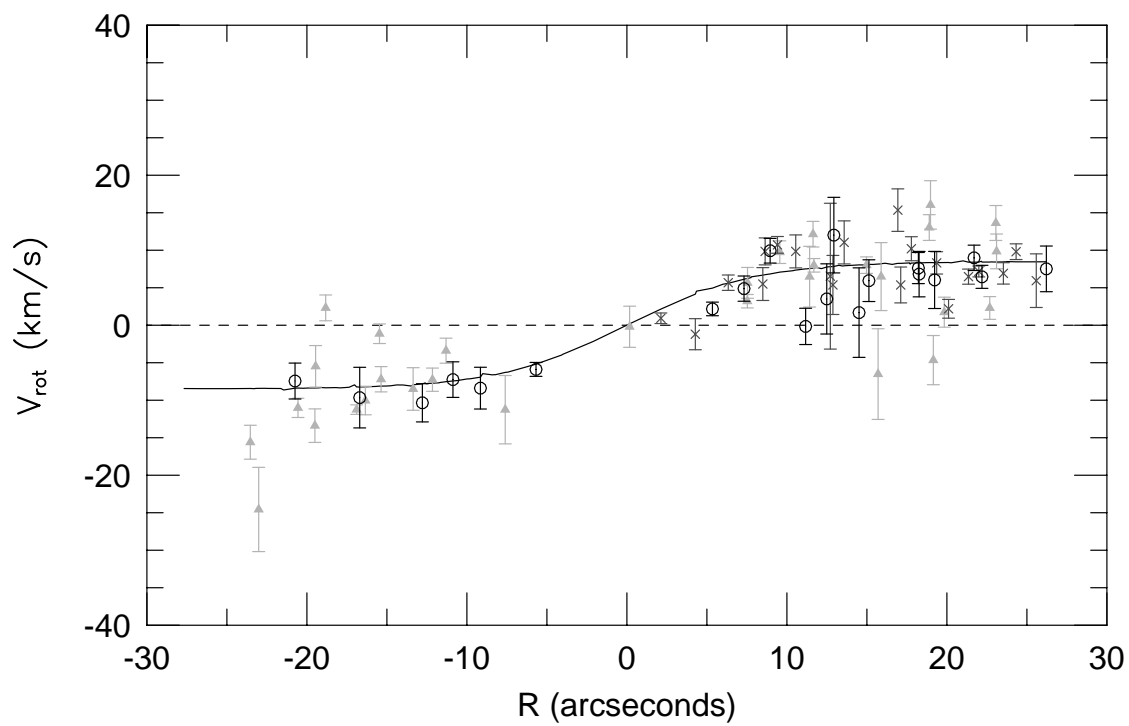
p28401



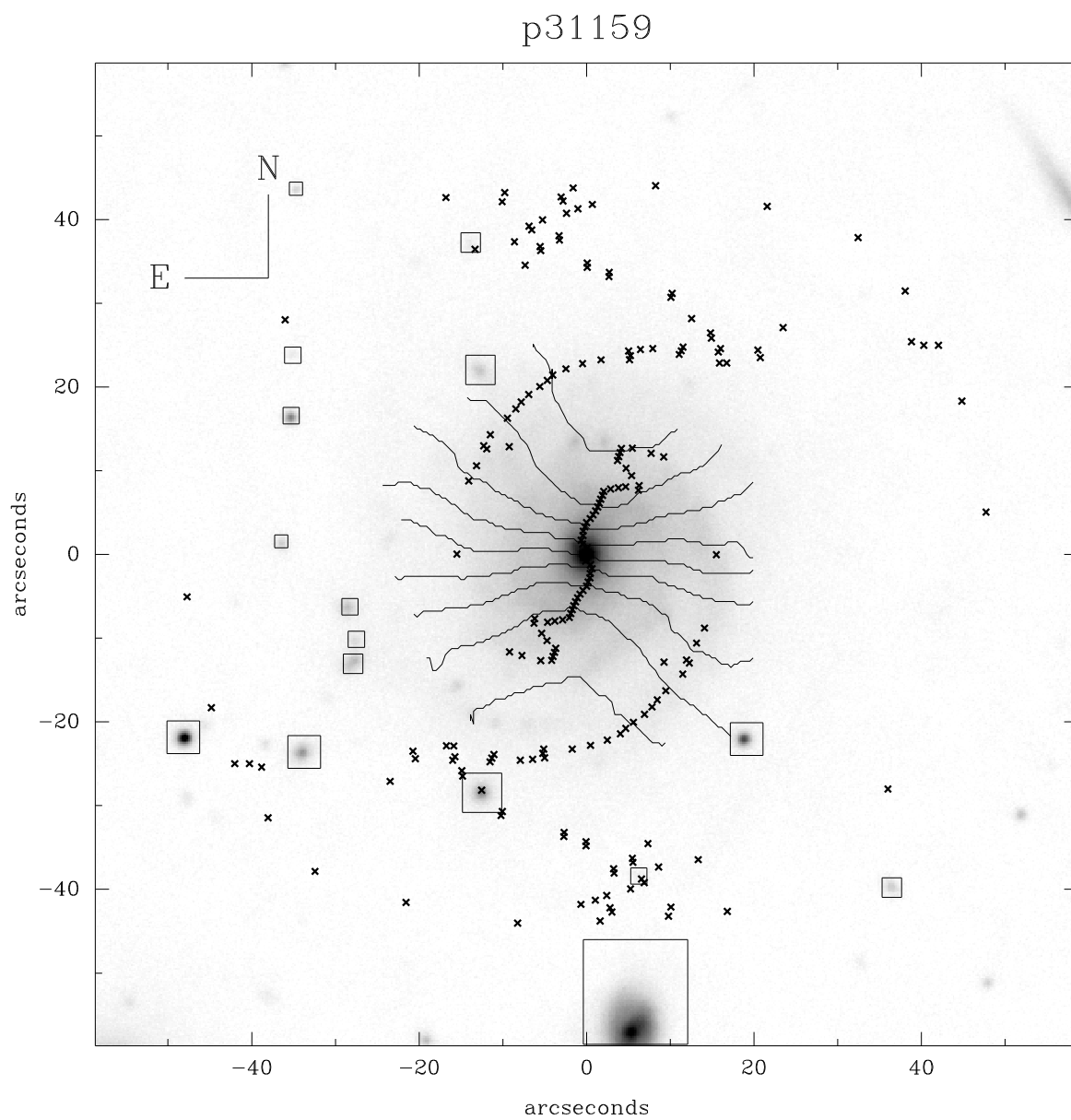
p28401



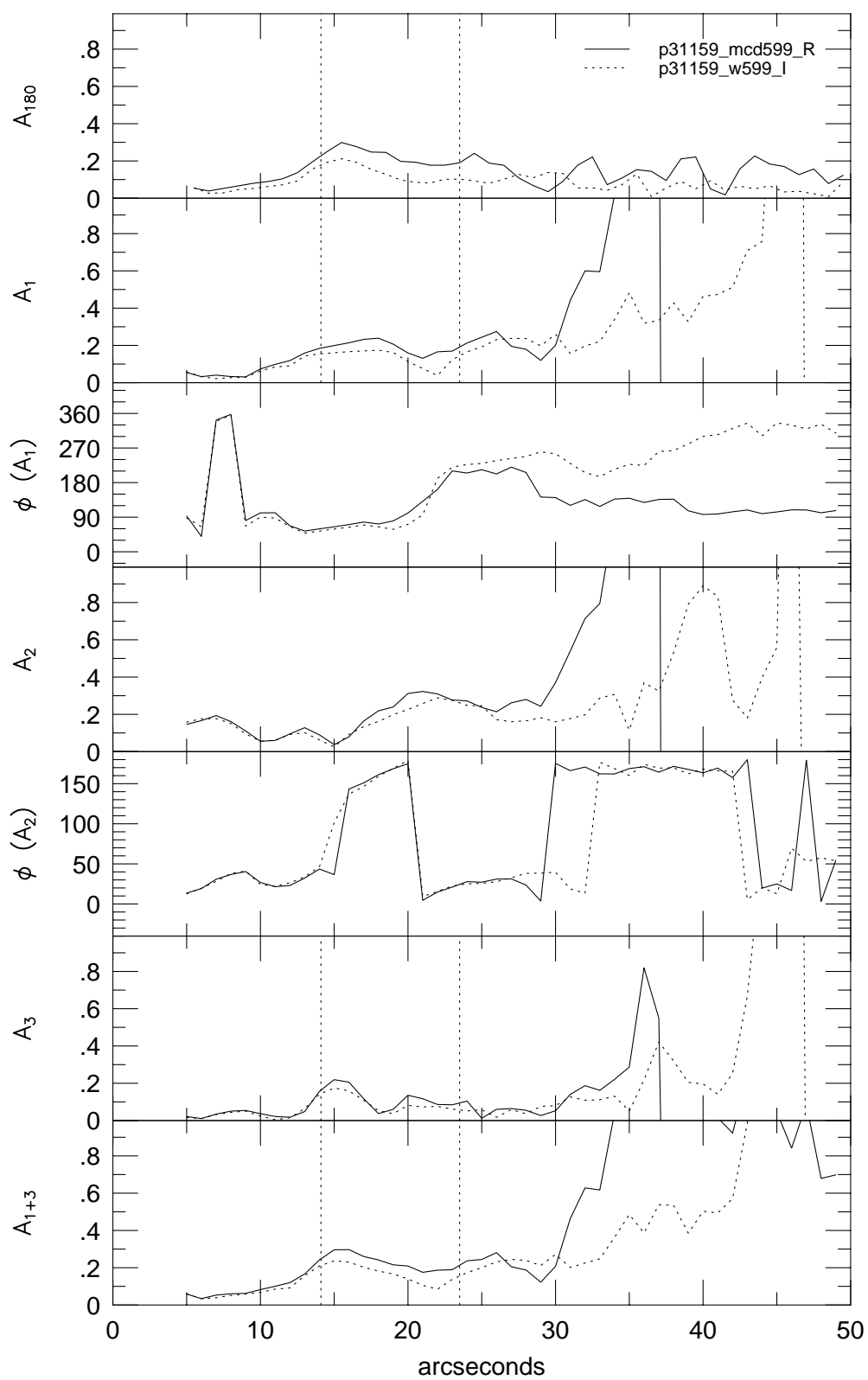
p28401



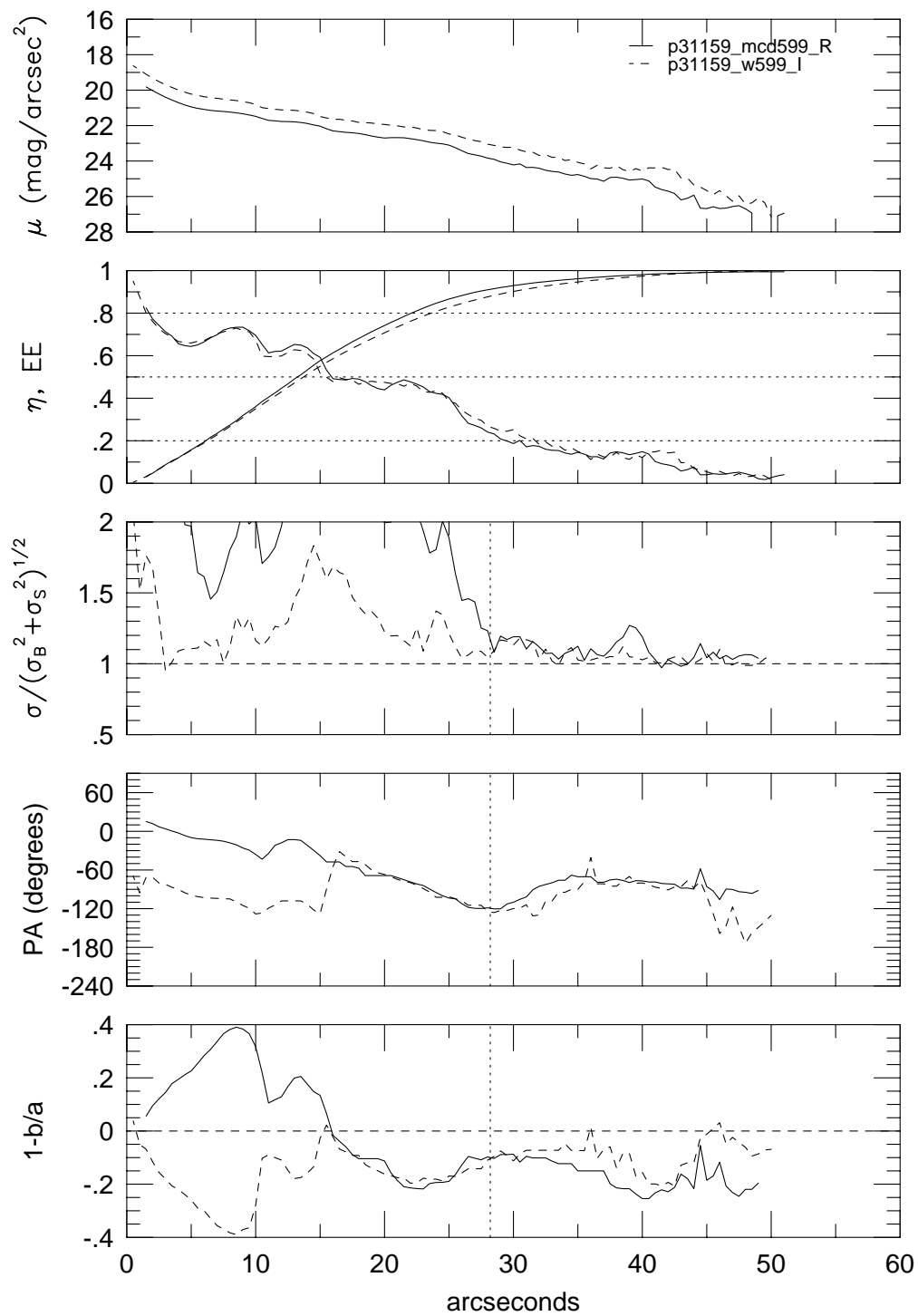




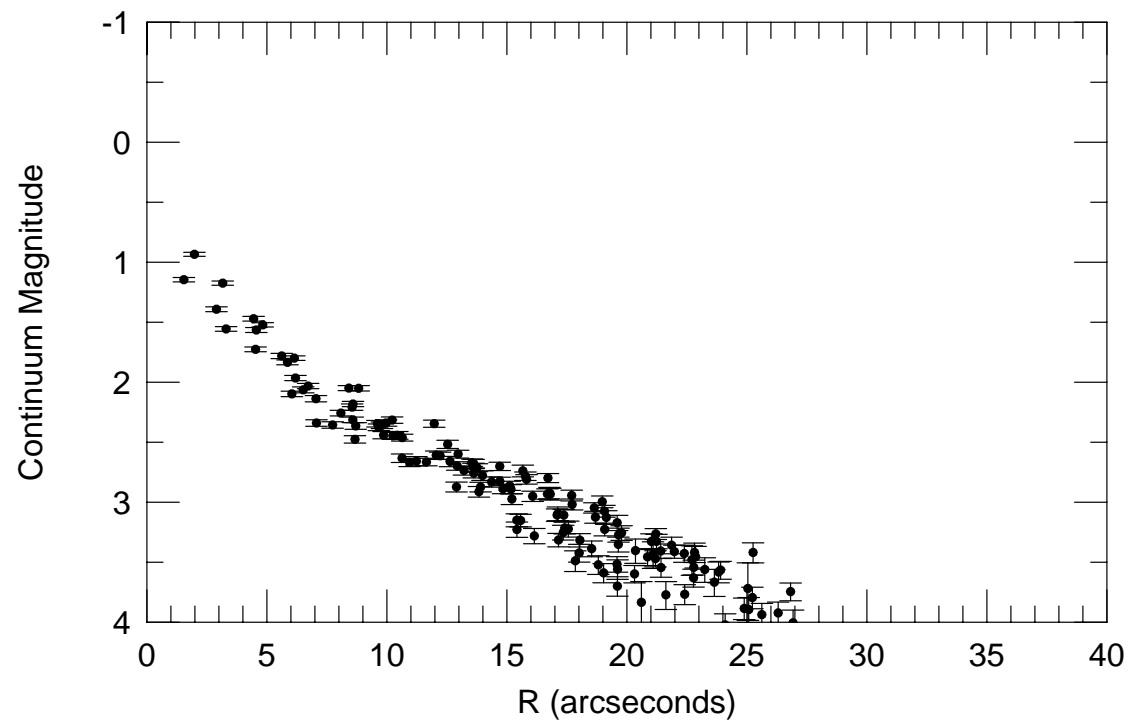
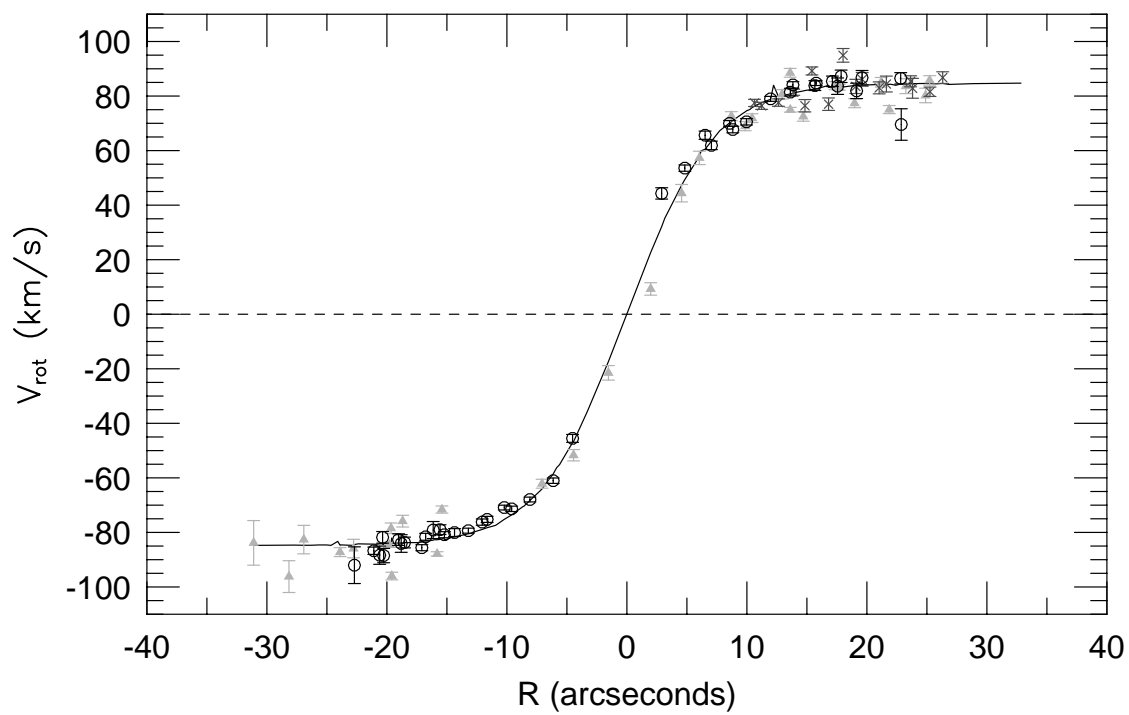
## p31159

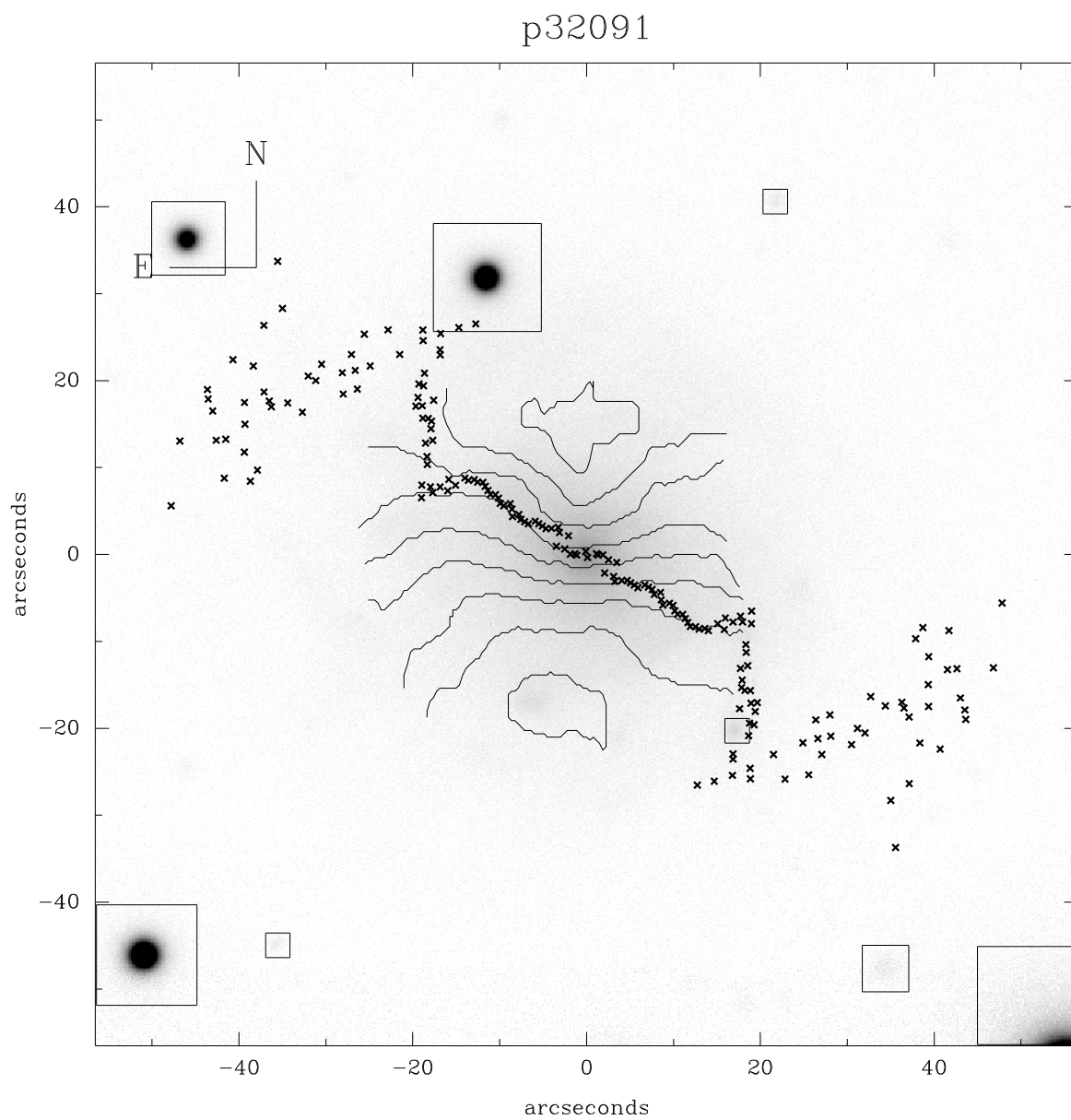


## p31159

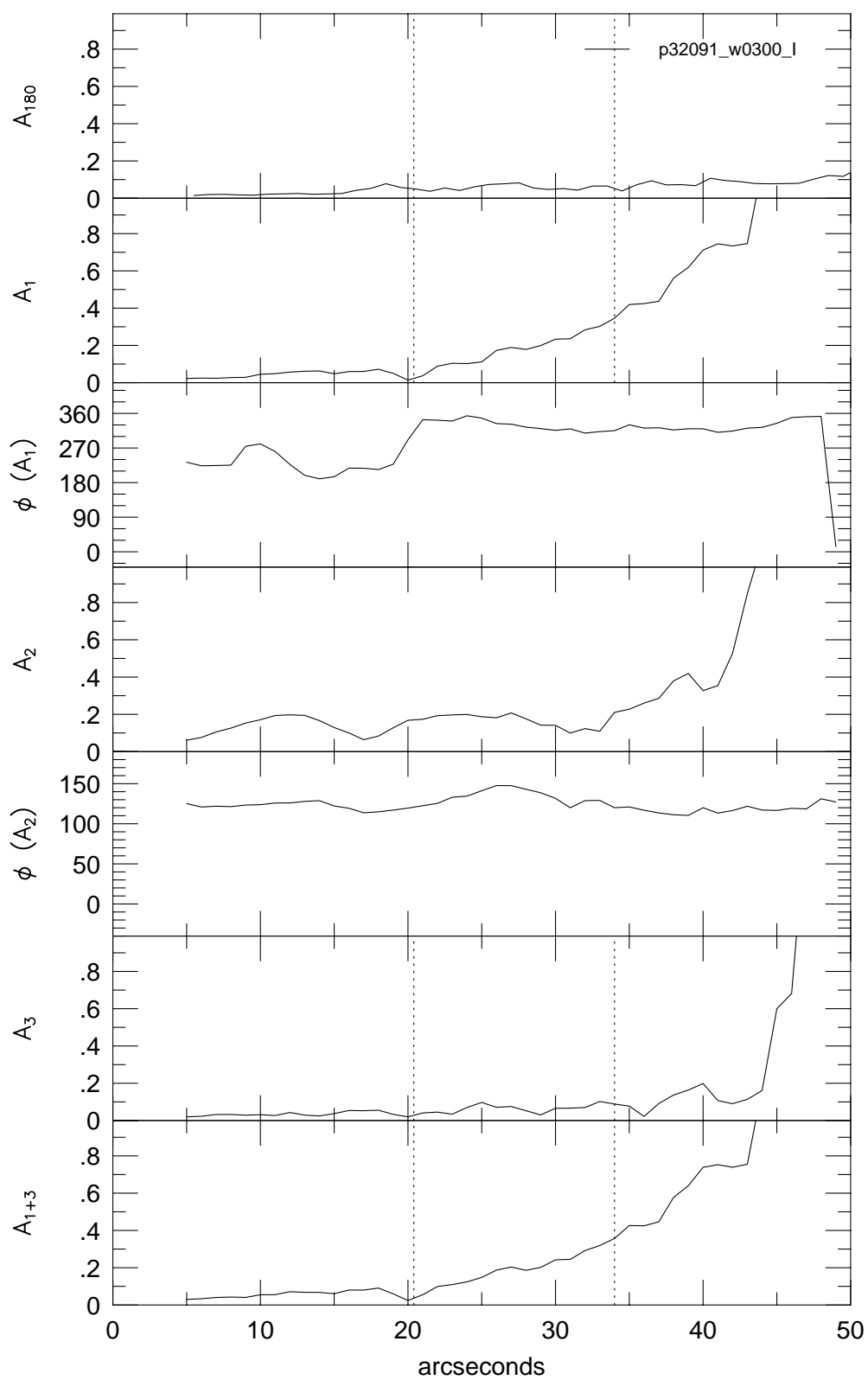


p31159

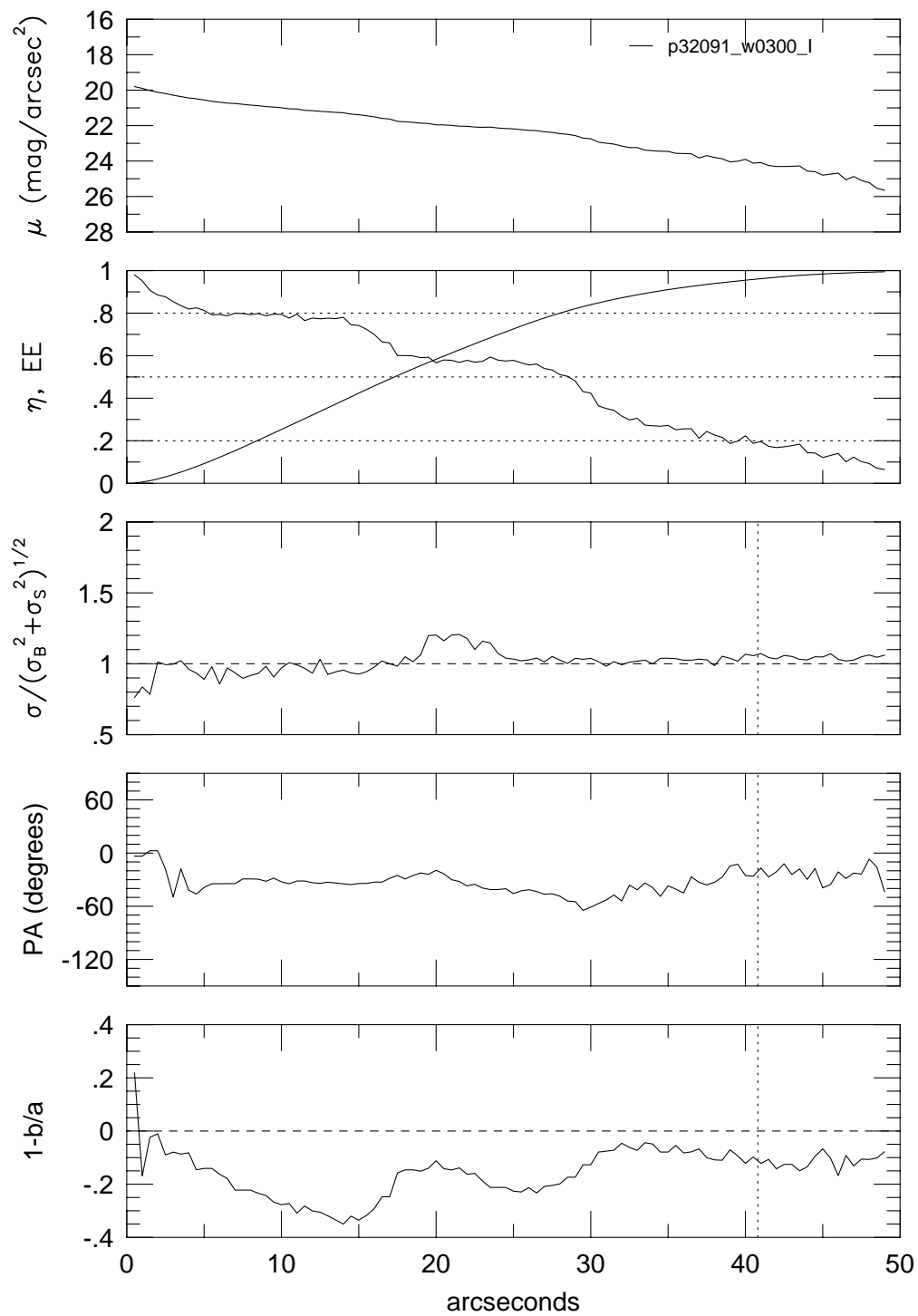




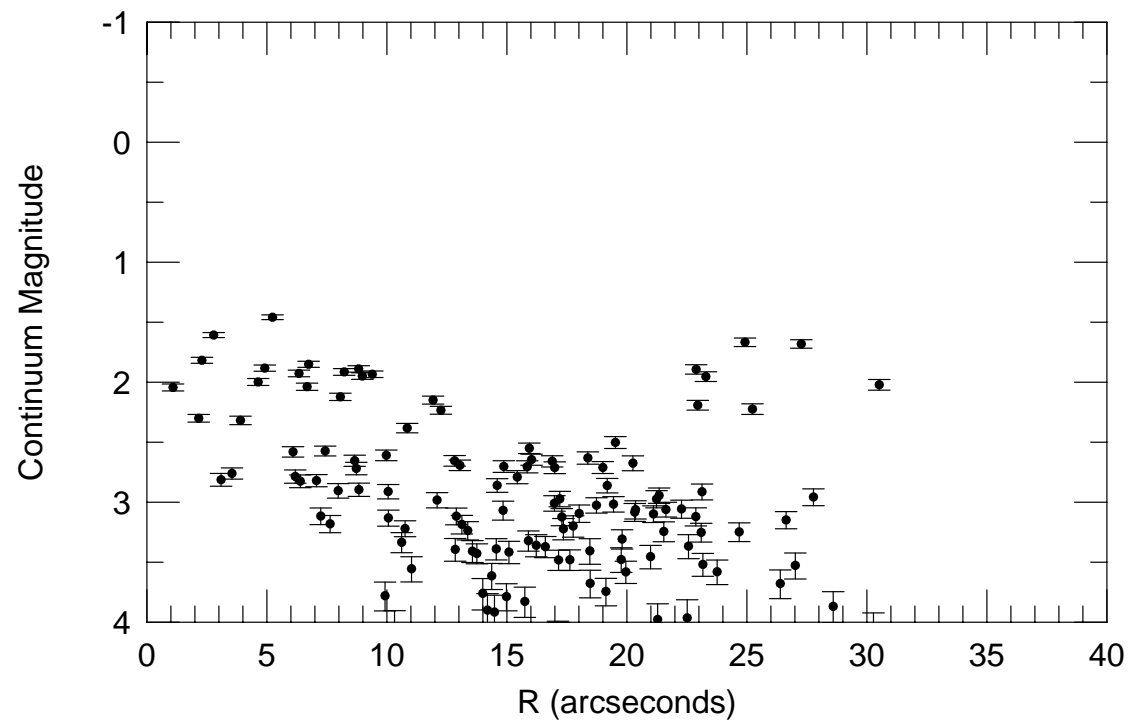
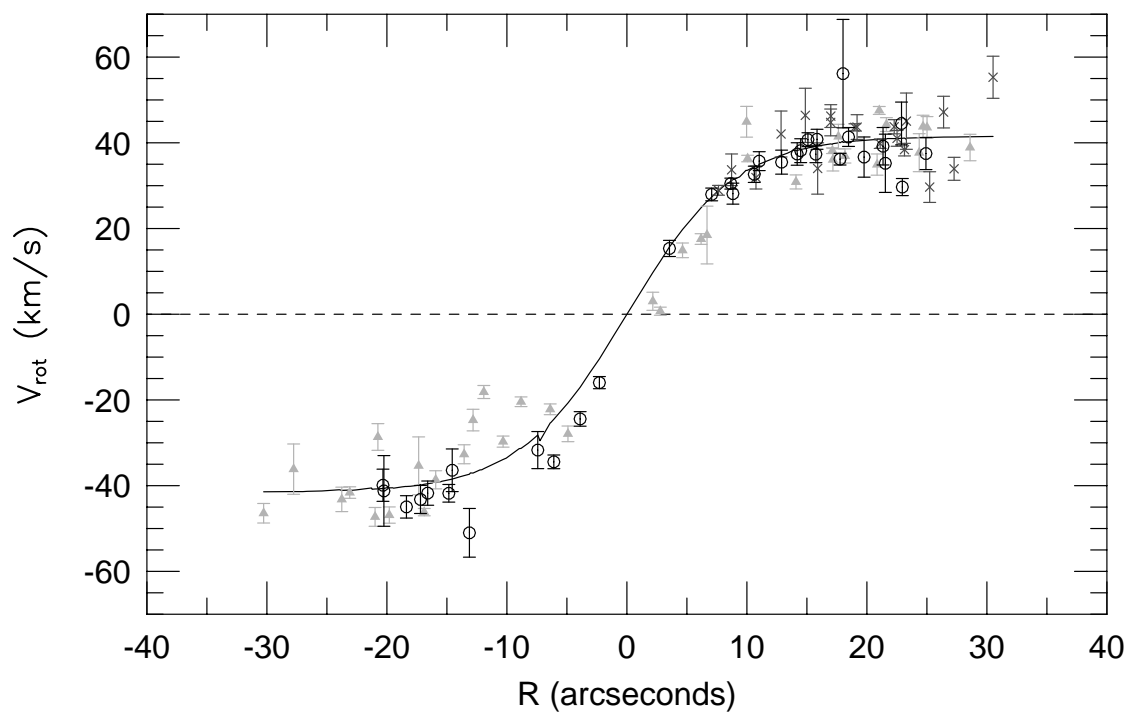
p32091



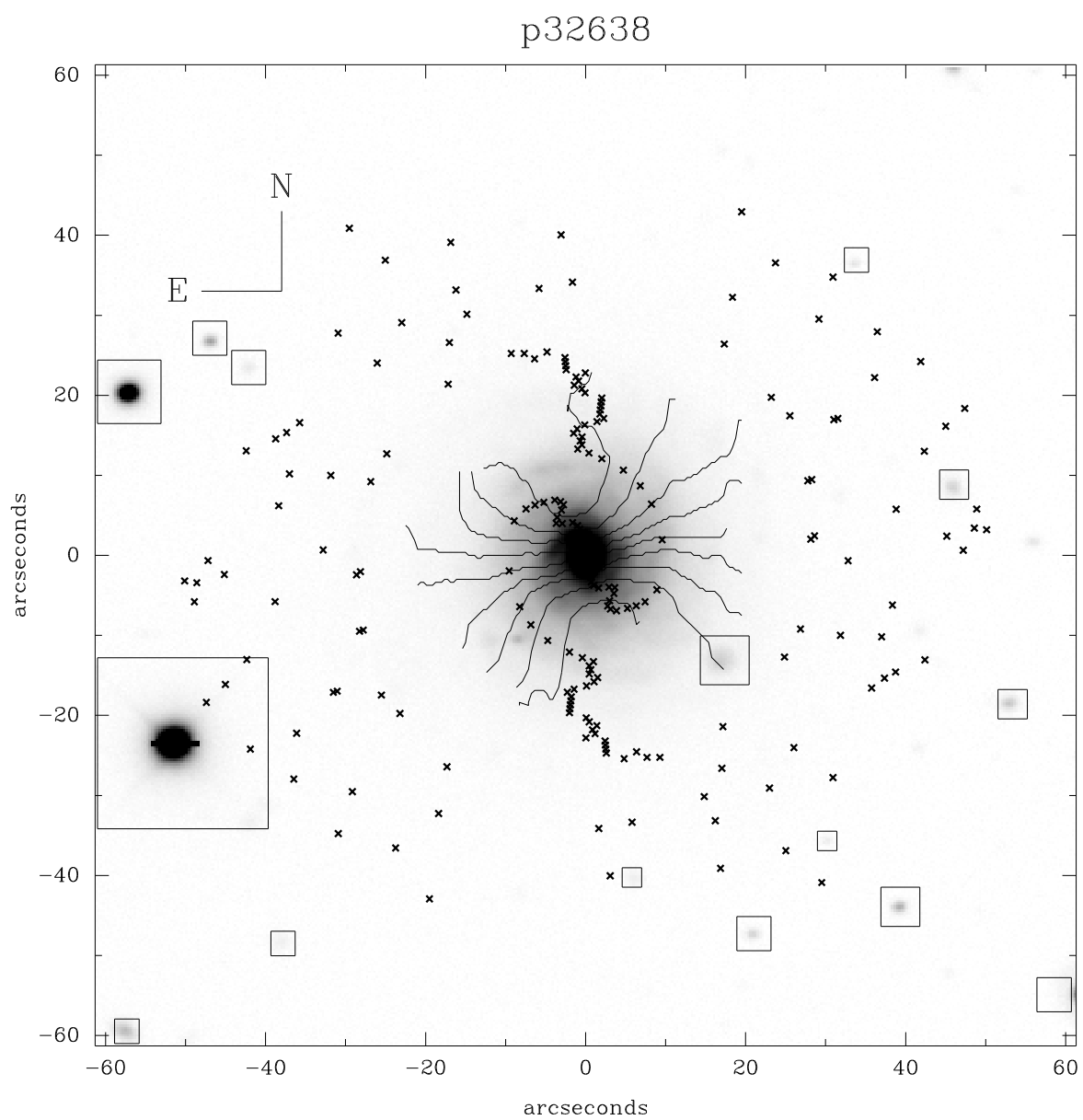
p32091



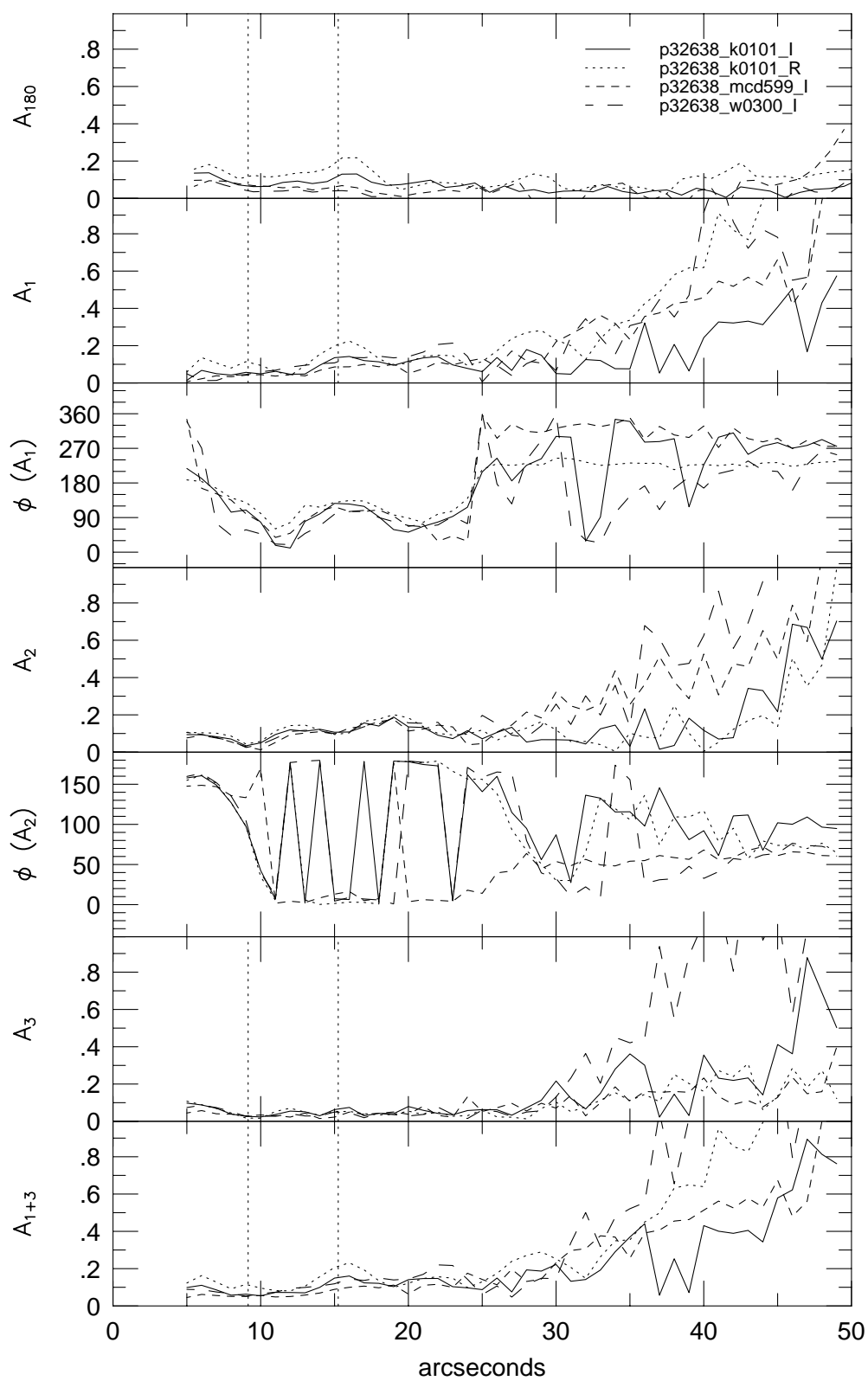
p32091



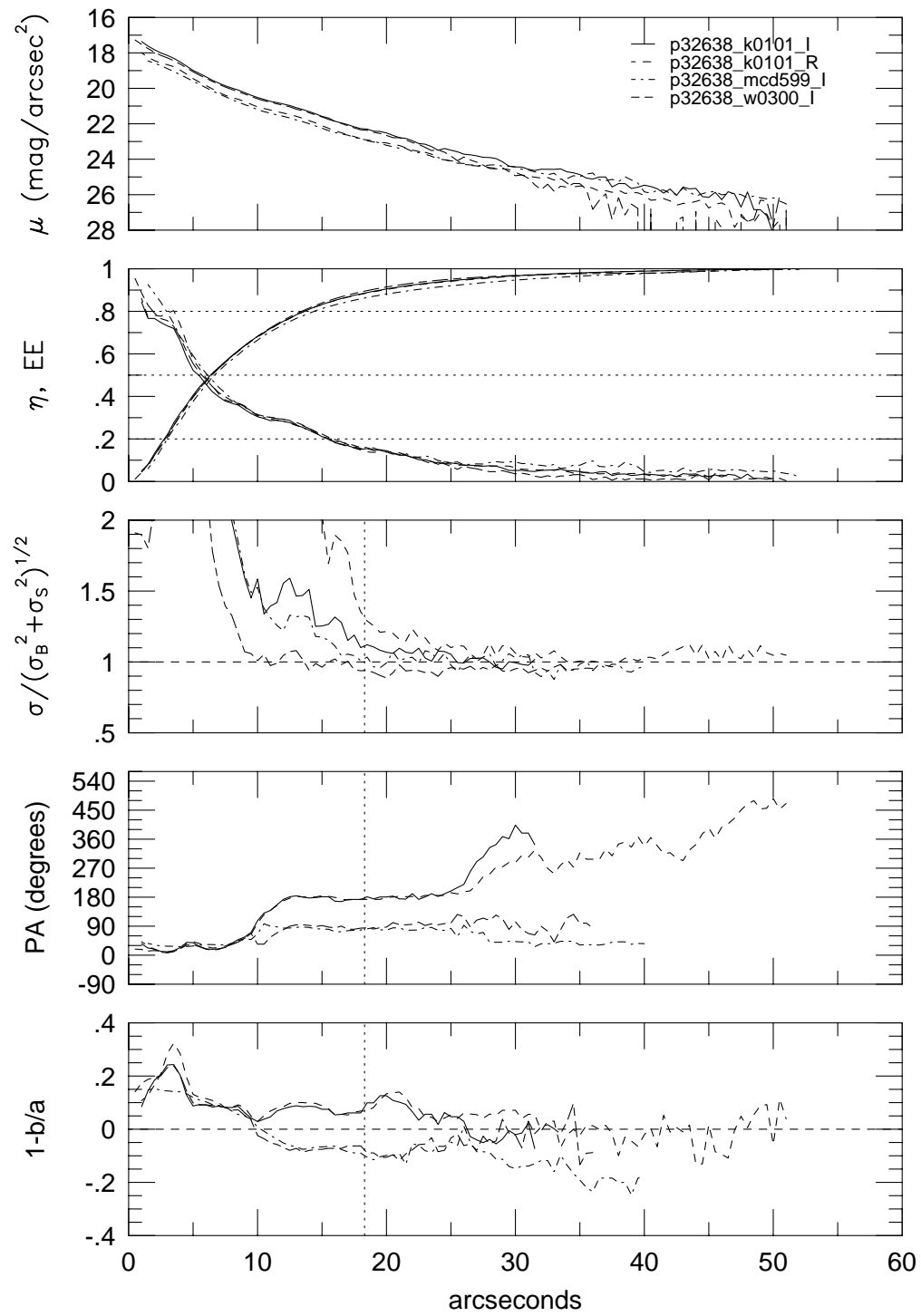




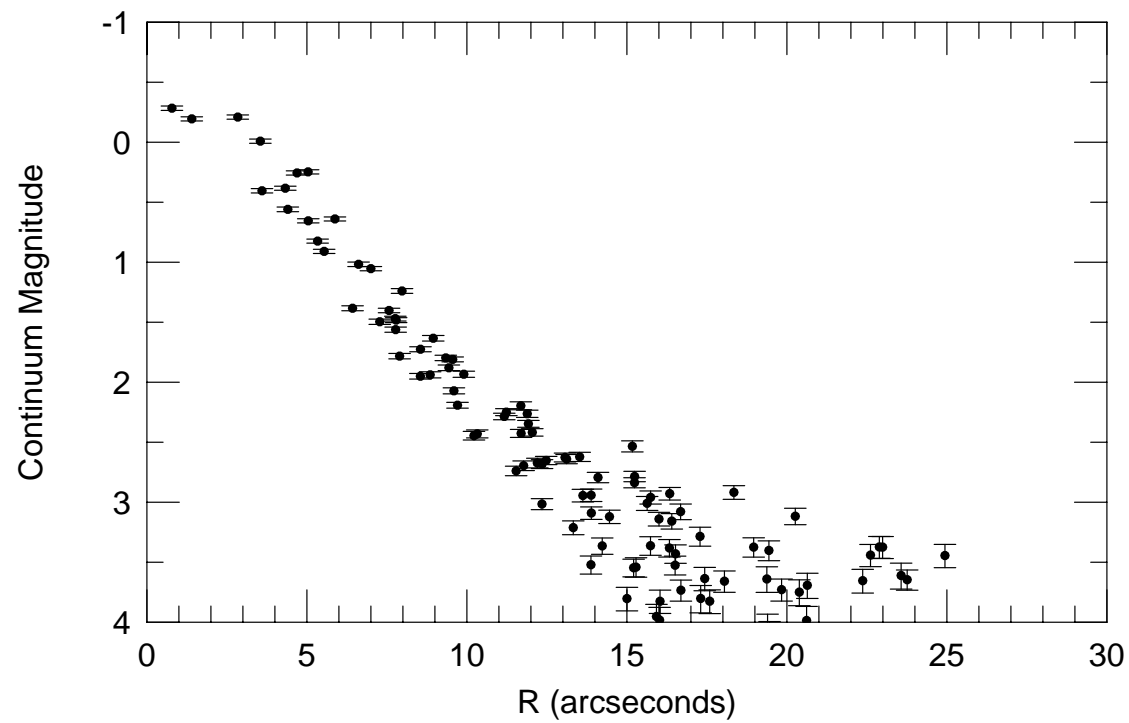
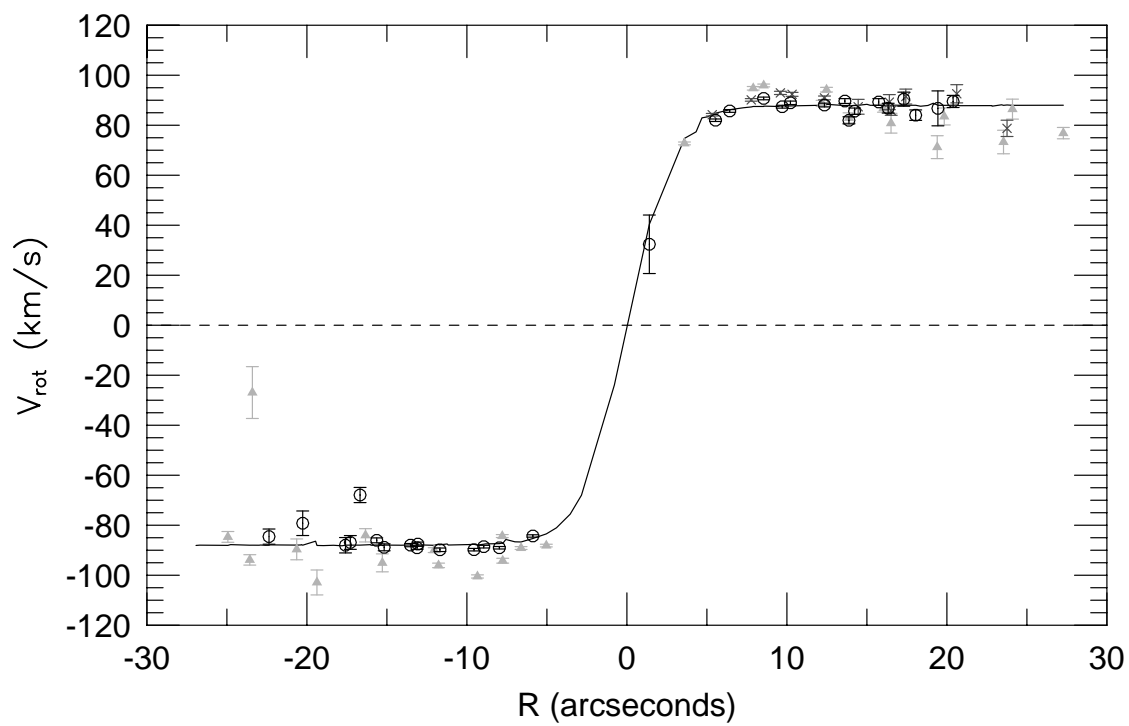
p32638

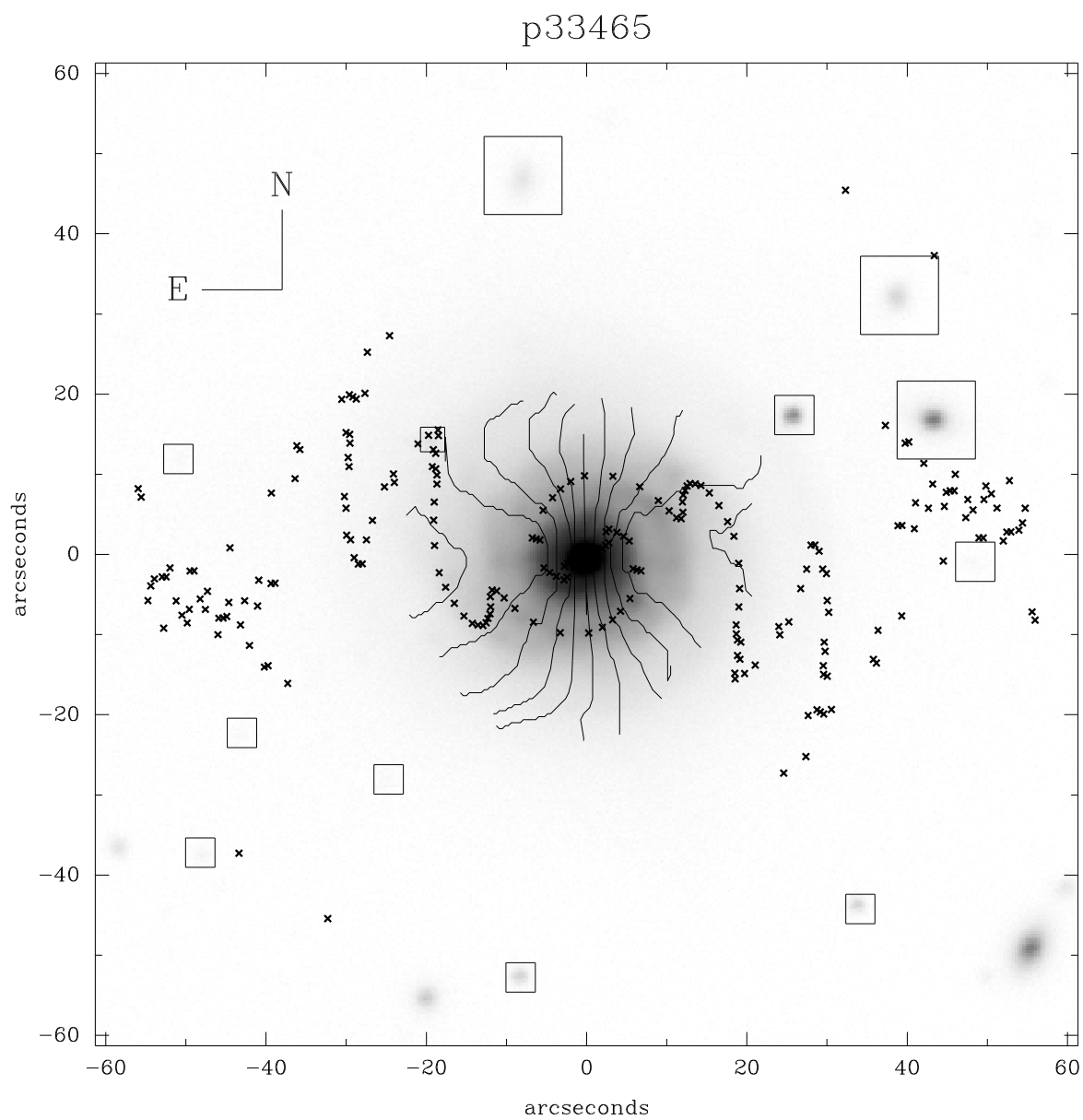


## p32638

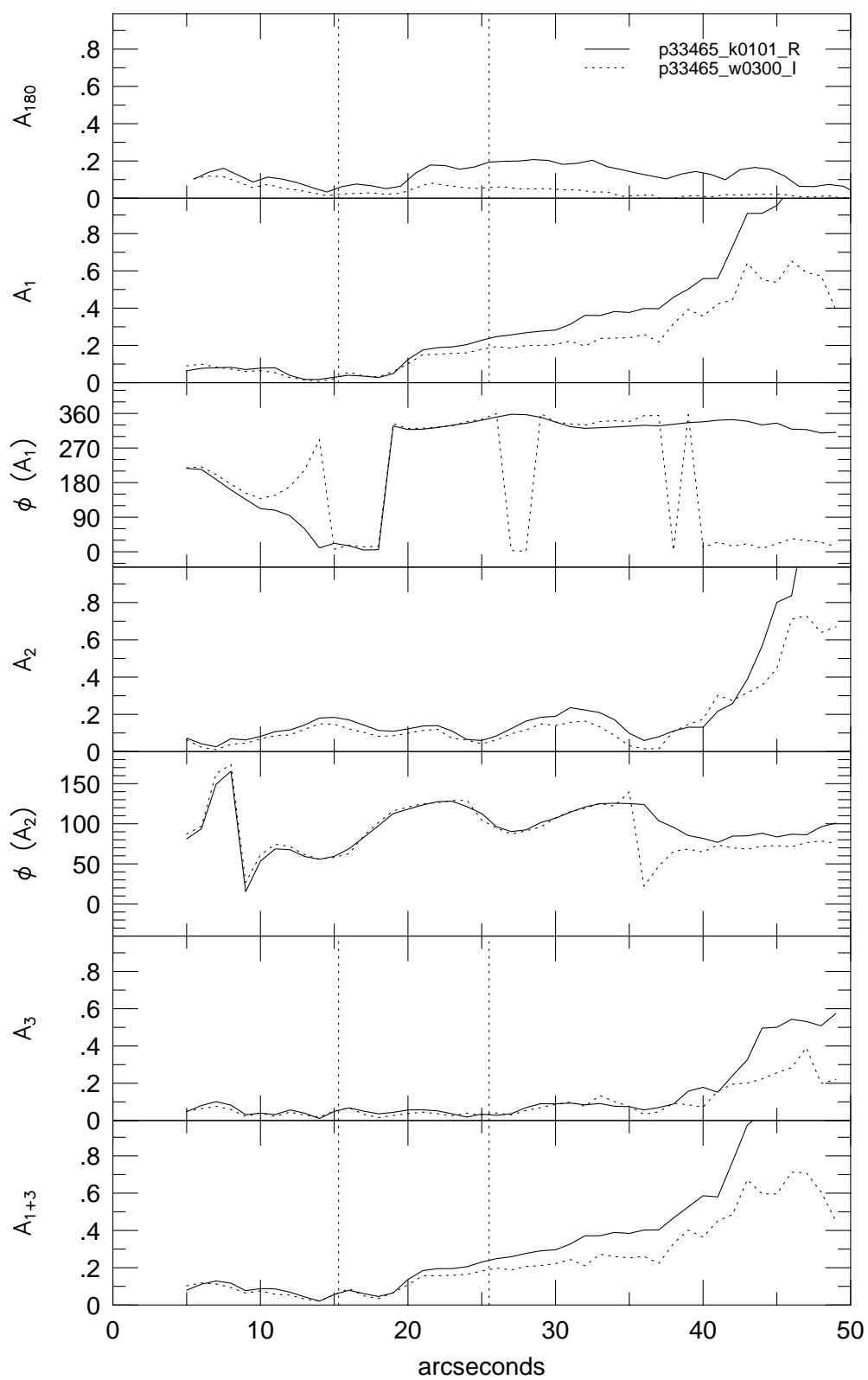


p32638

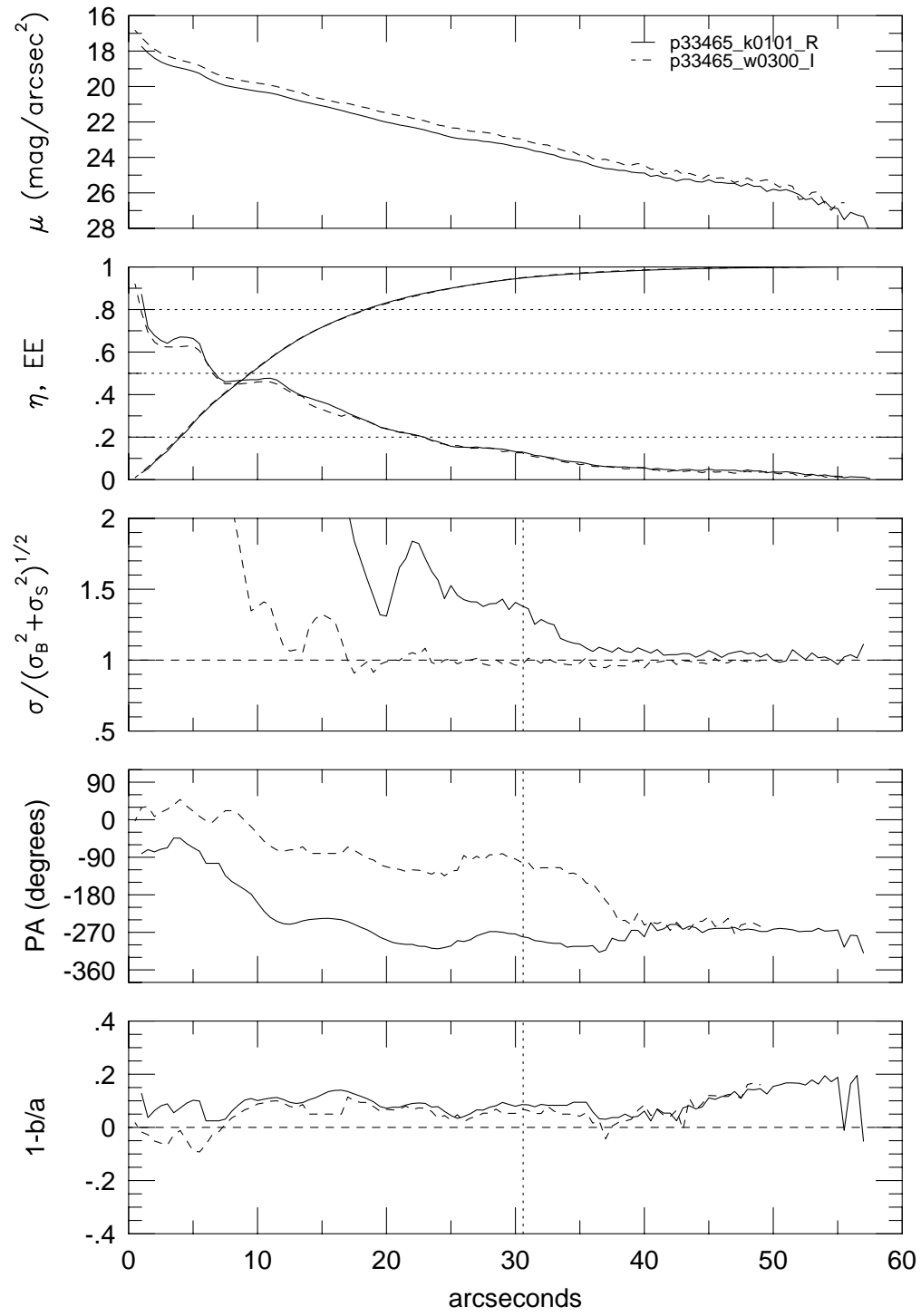




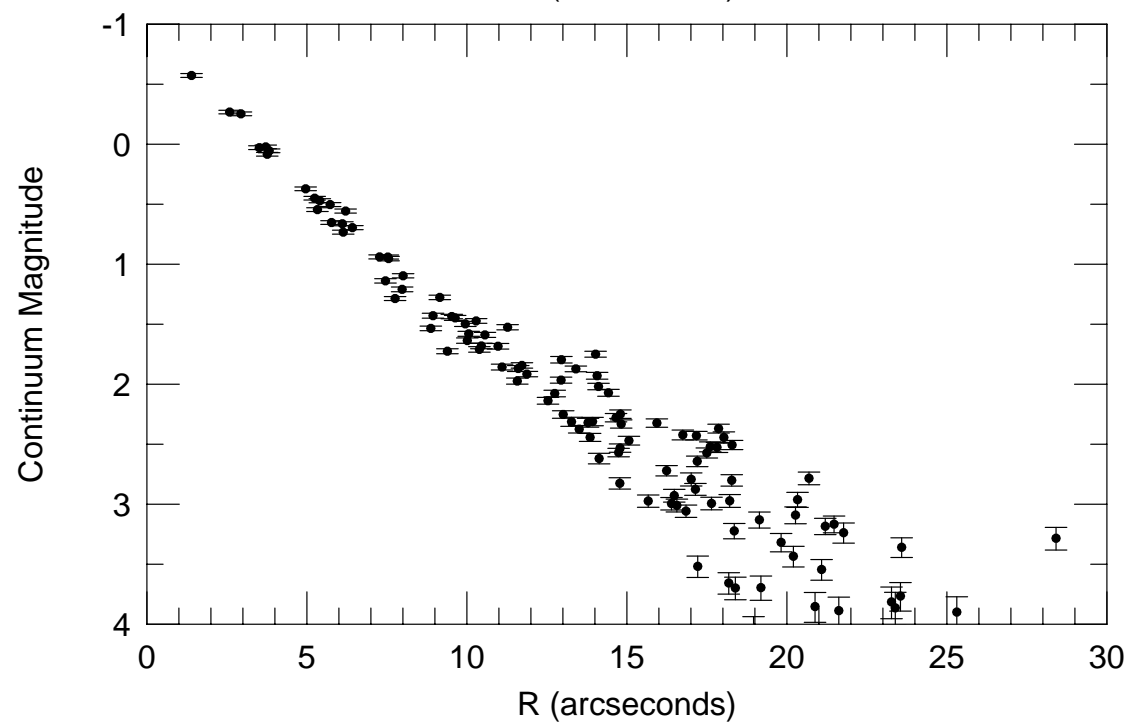
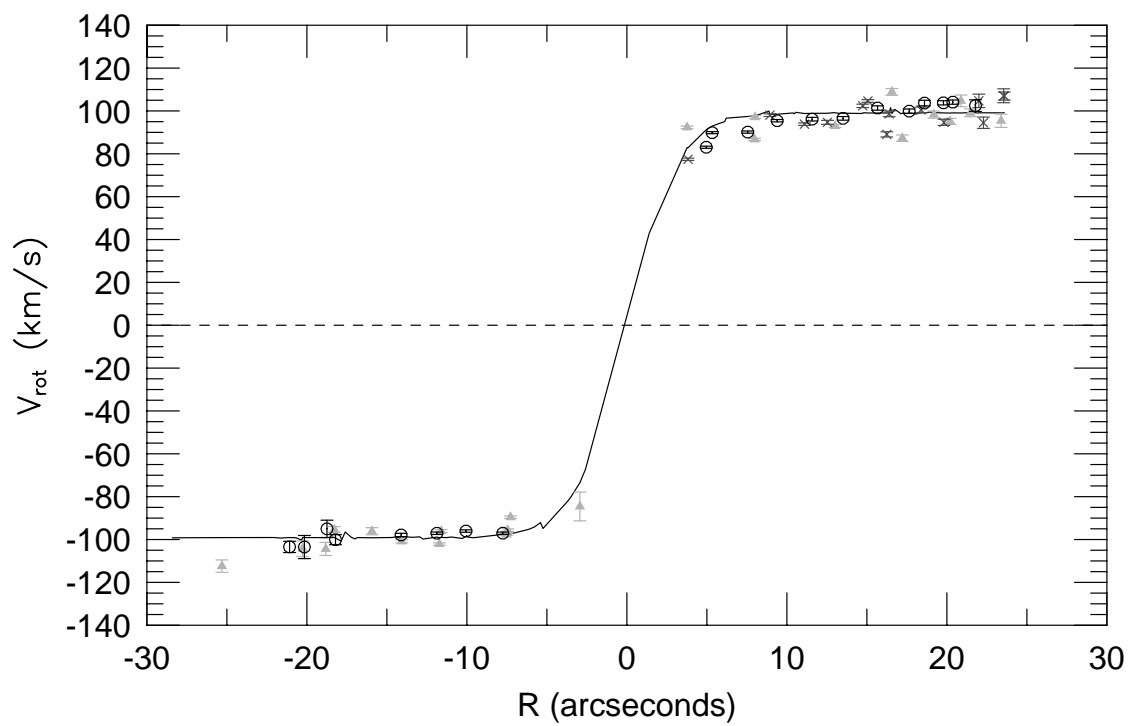
p33465



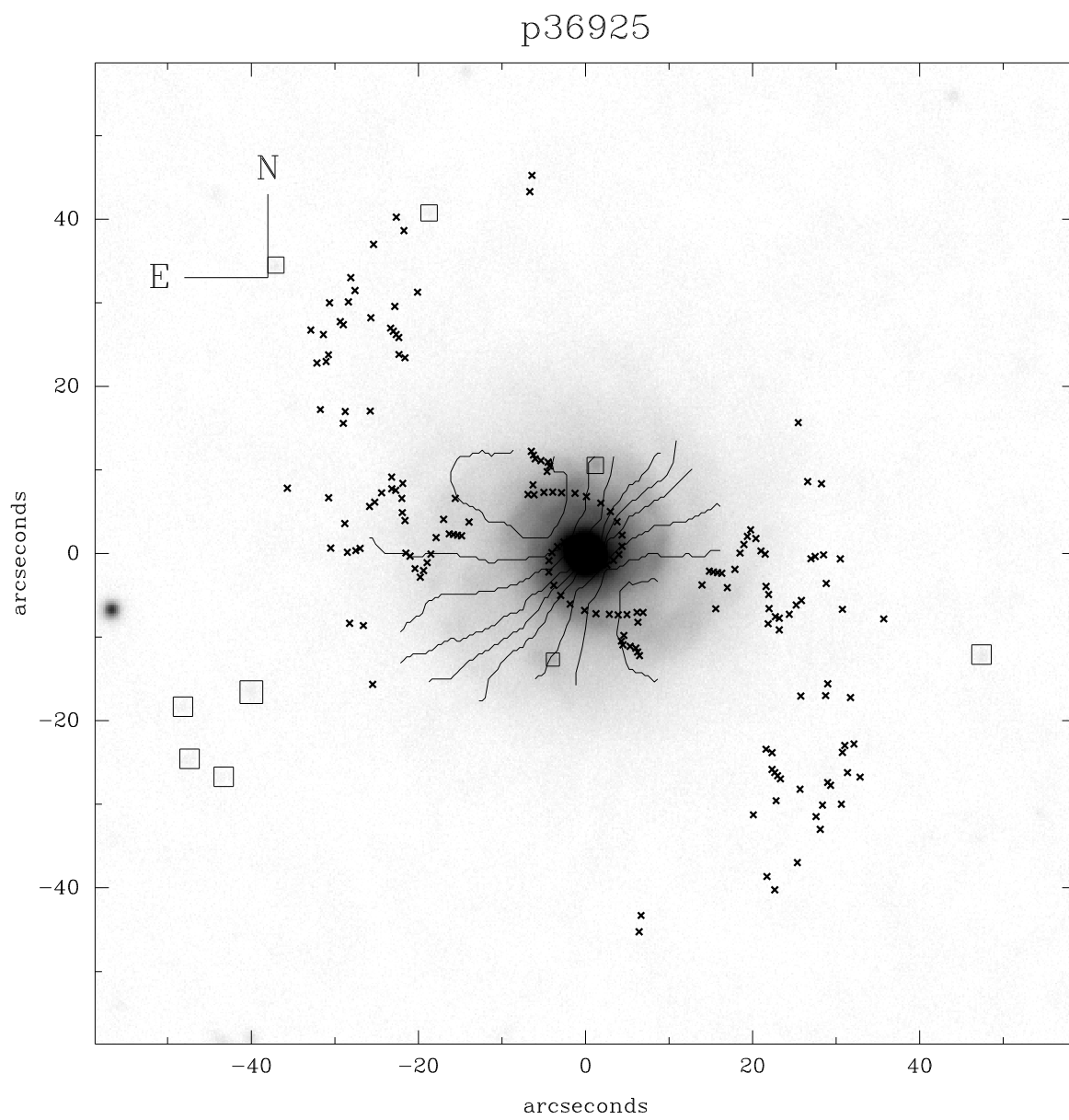
## p33465



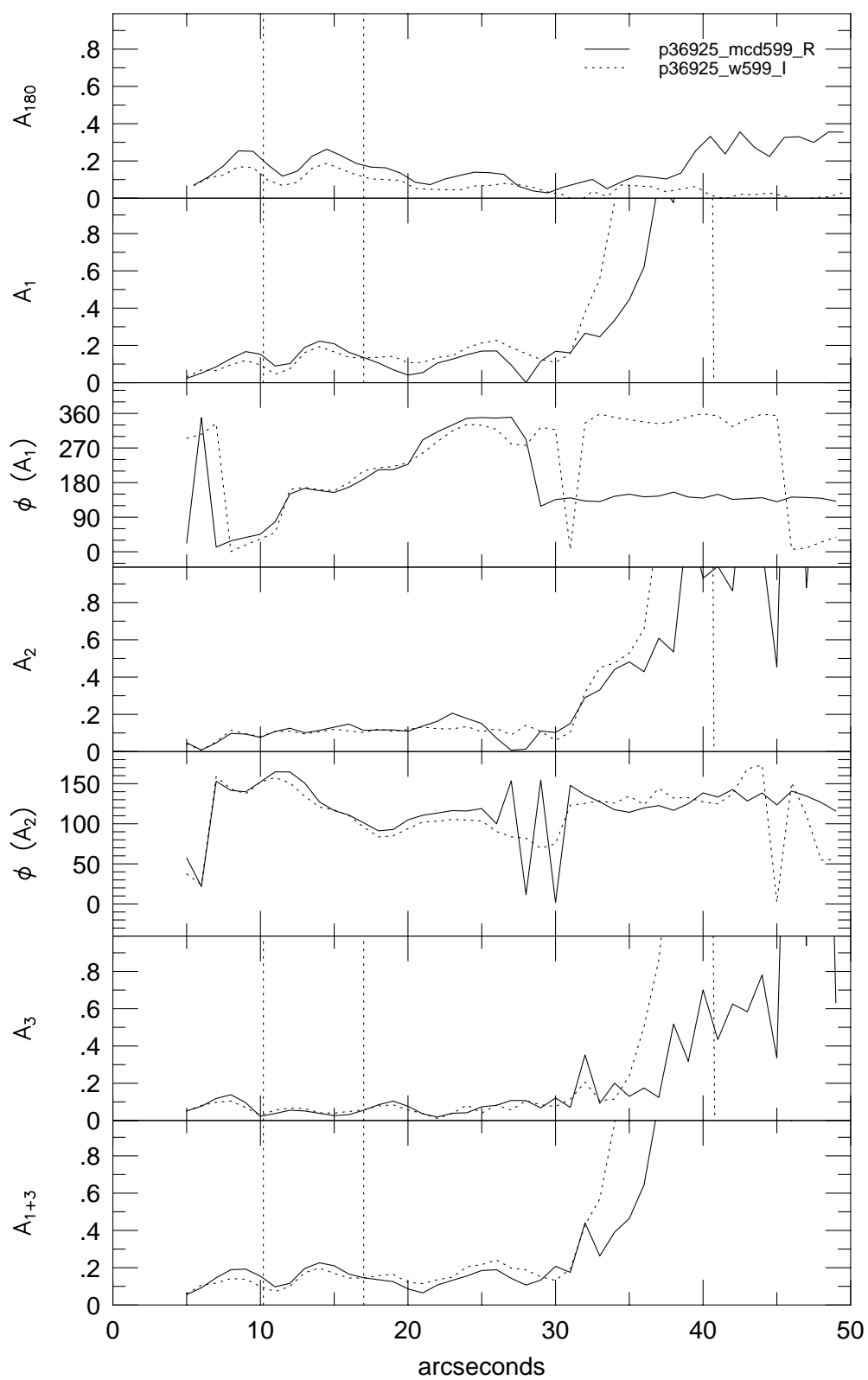
p33465



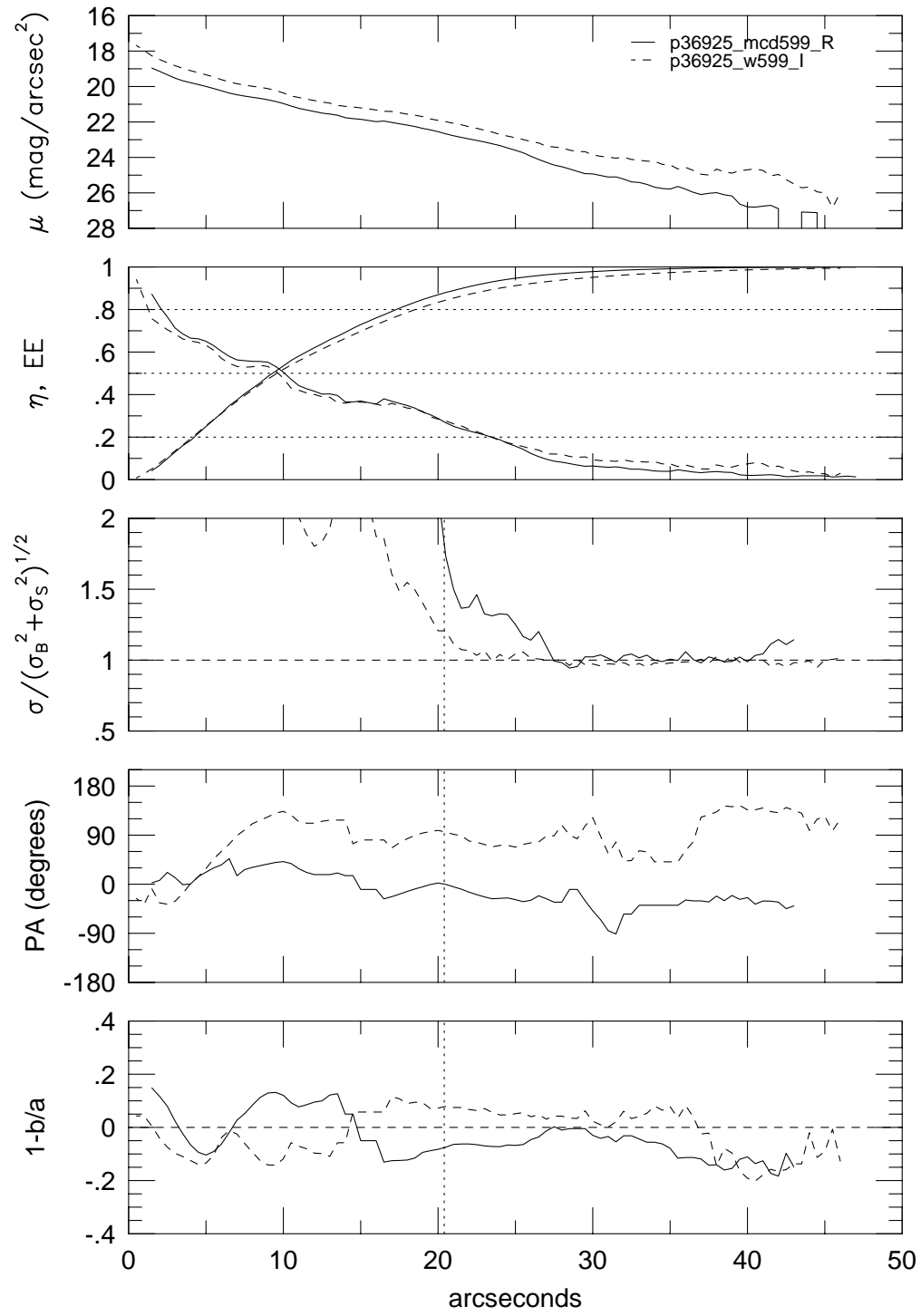




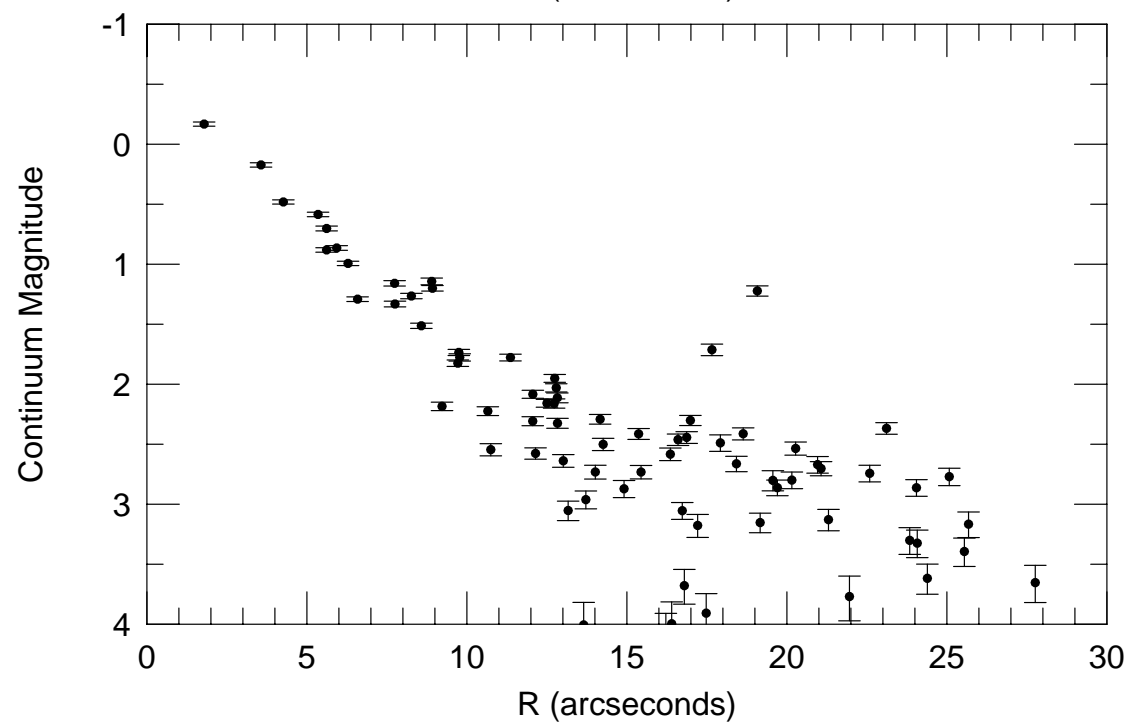
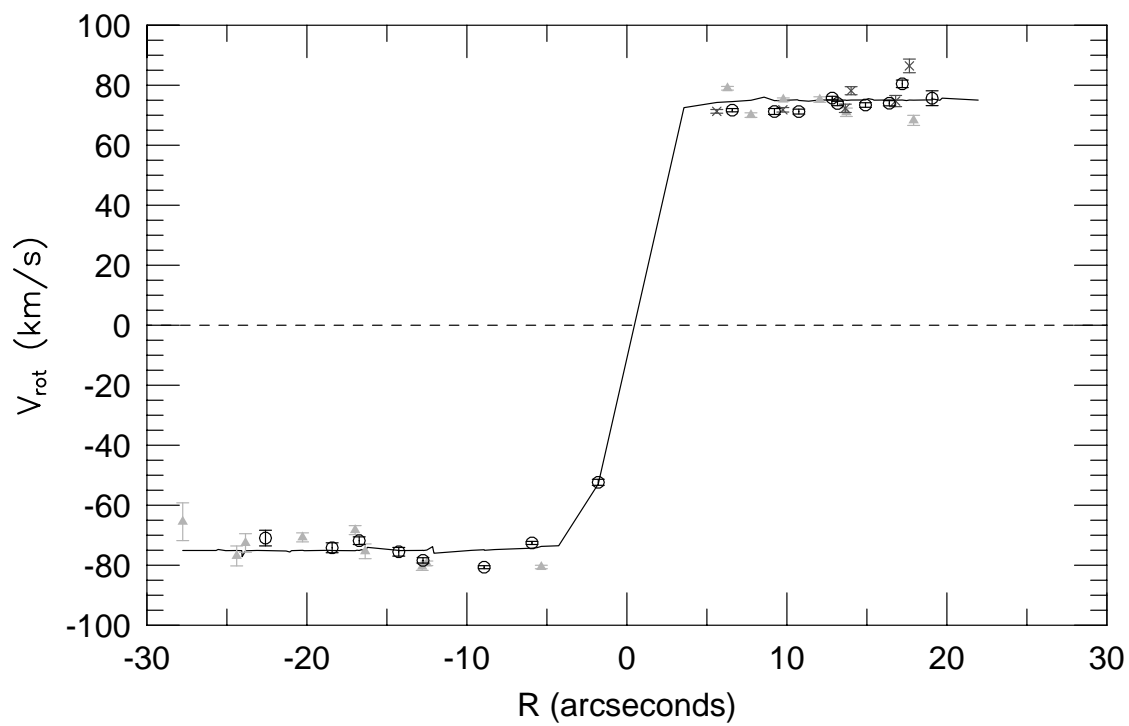
p36925

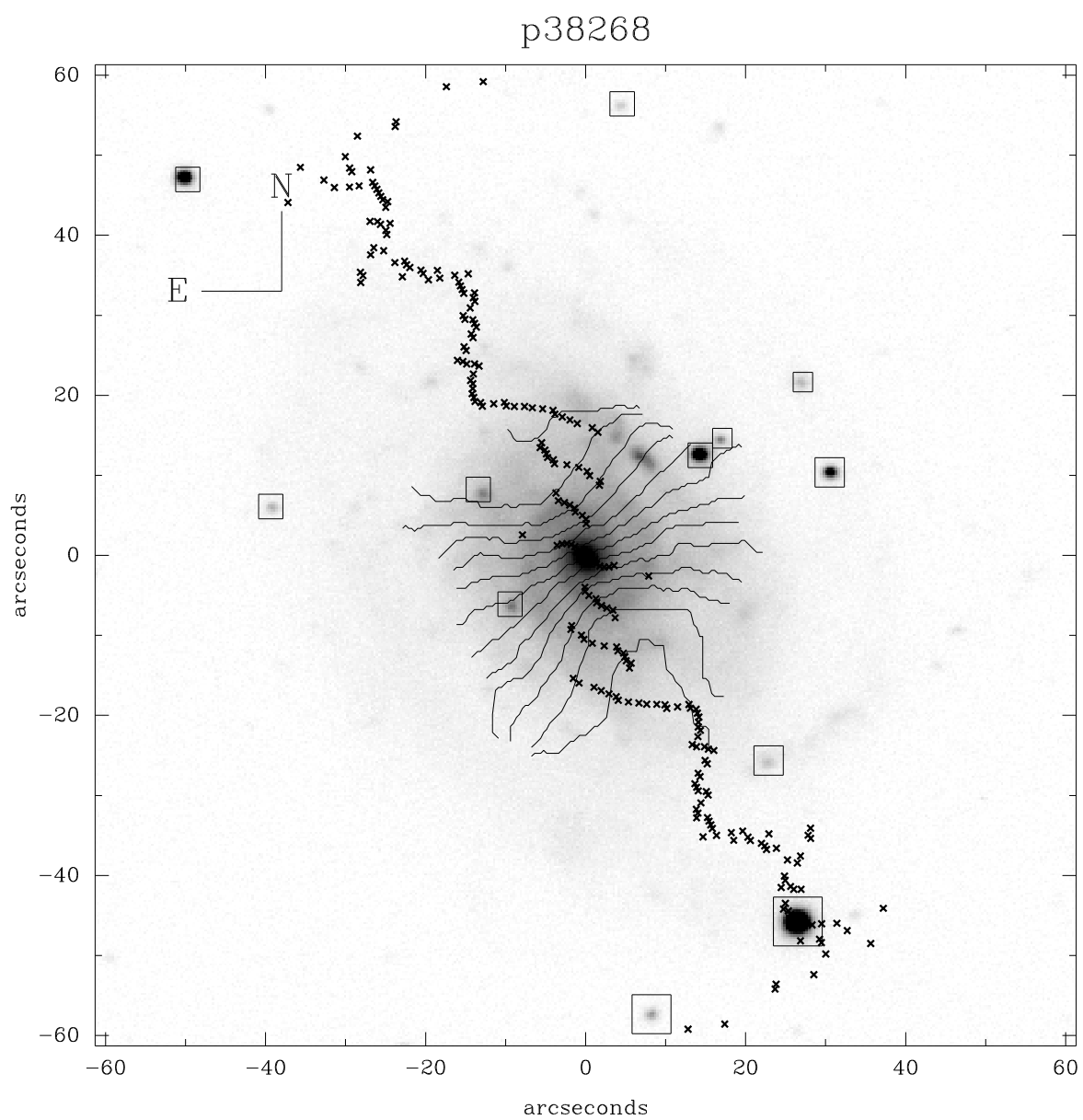


p36925

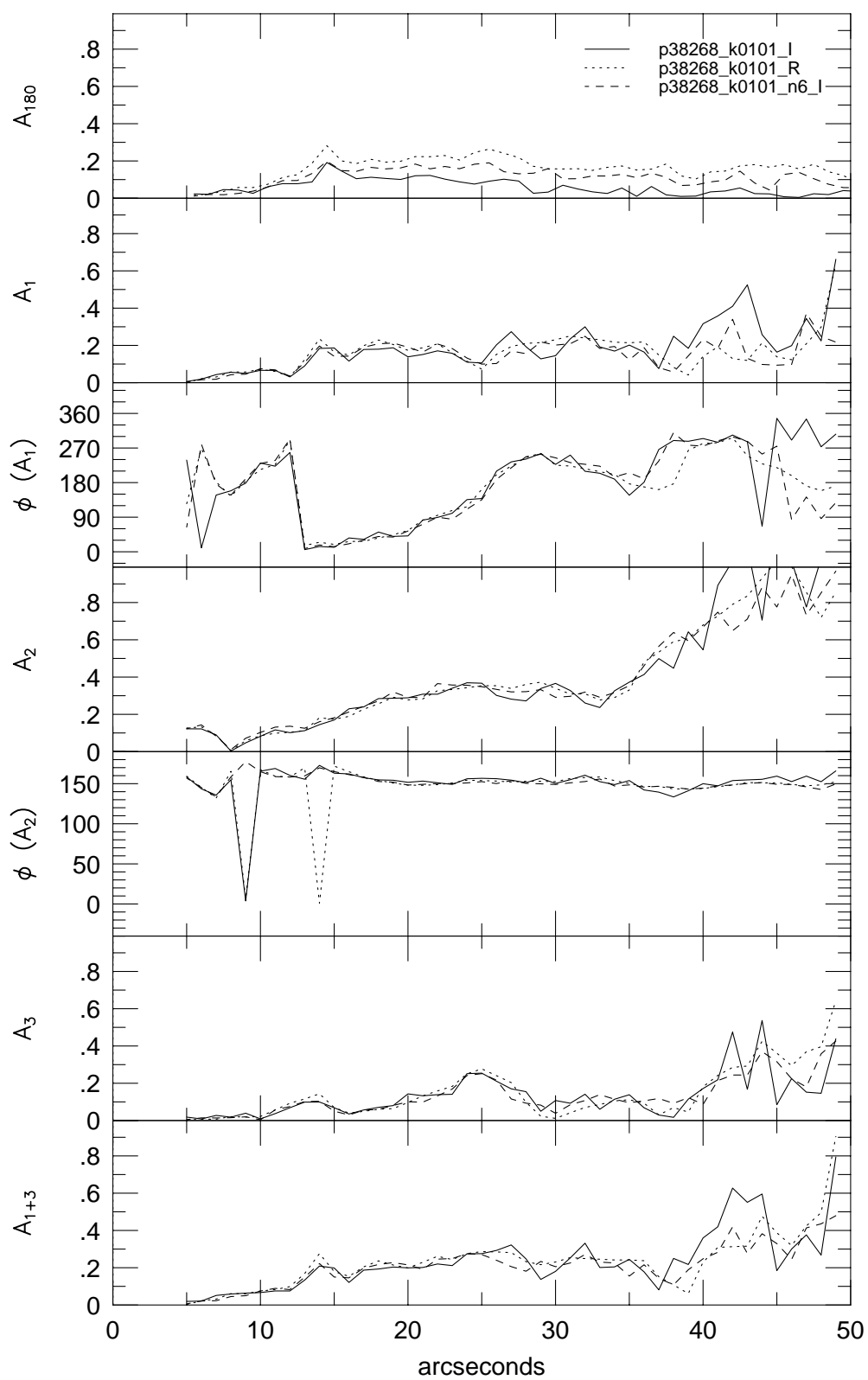


p36925

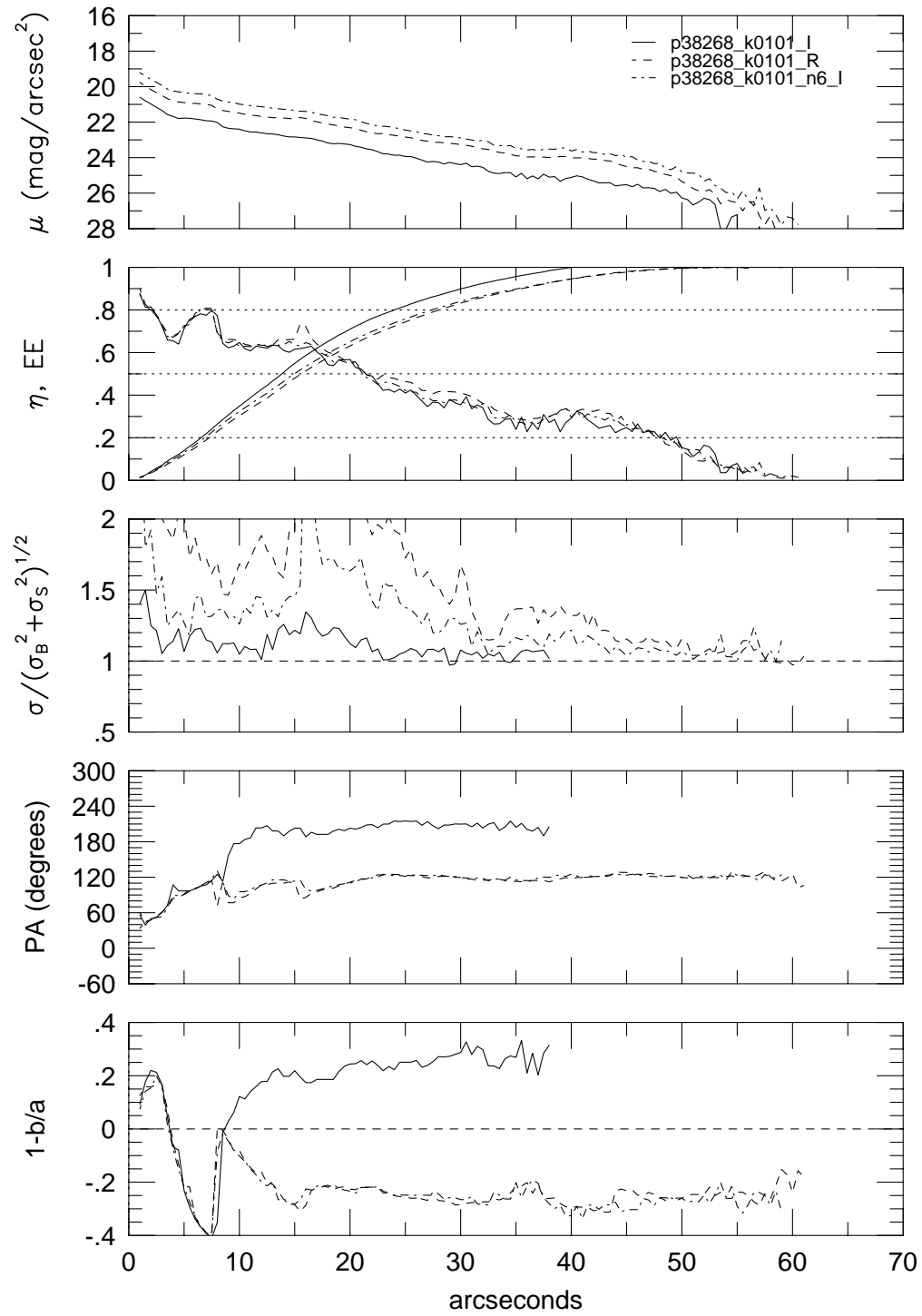




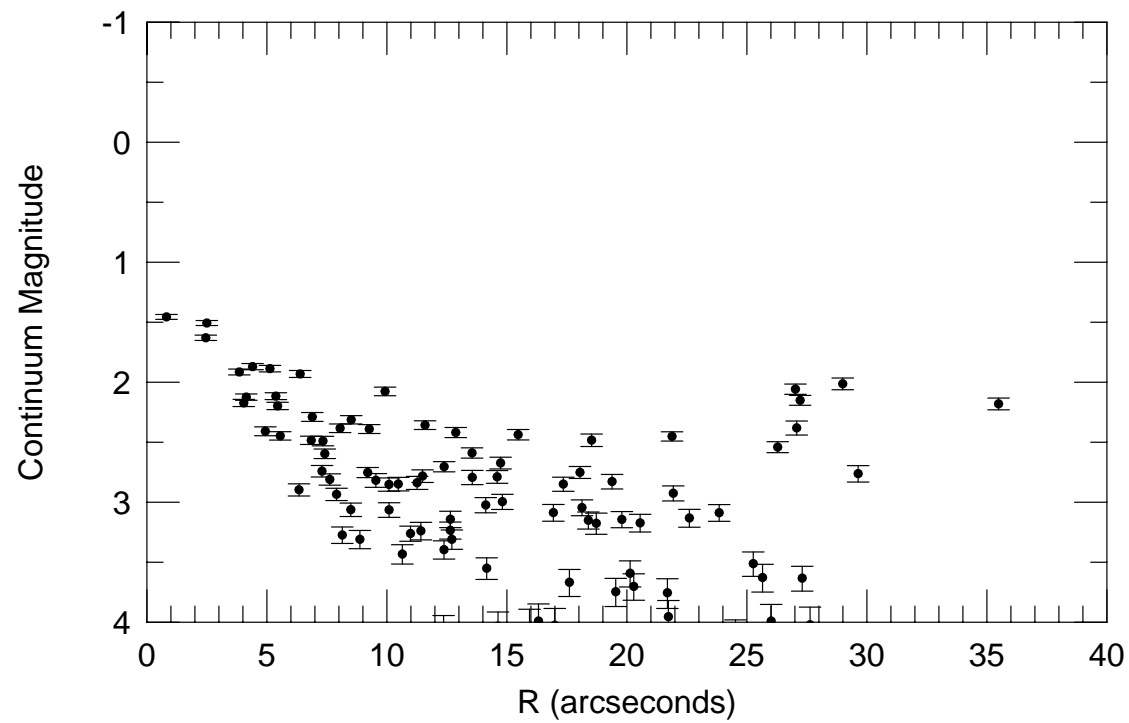
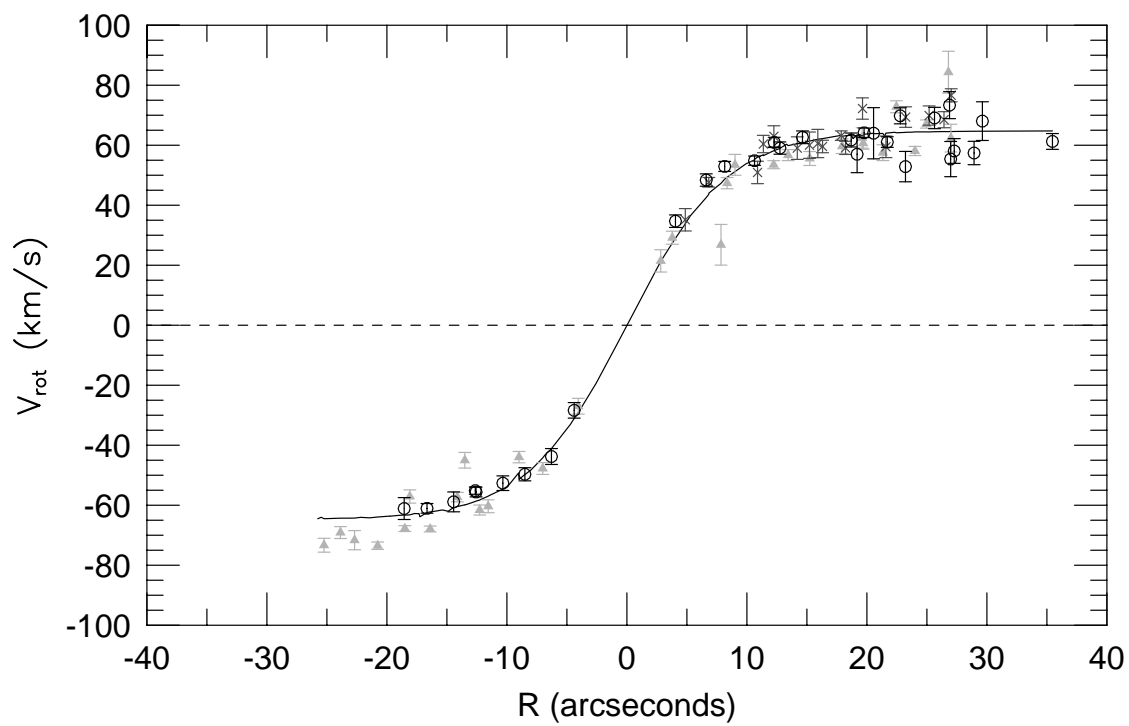
p38268



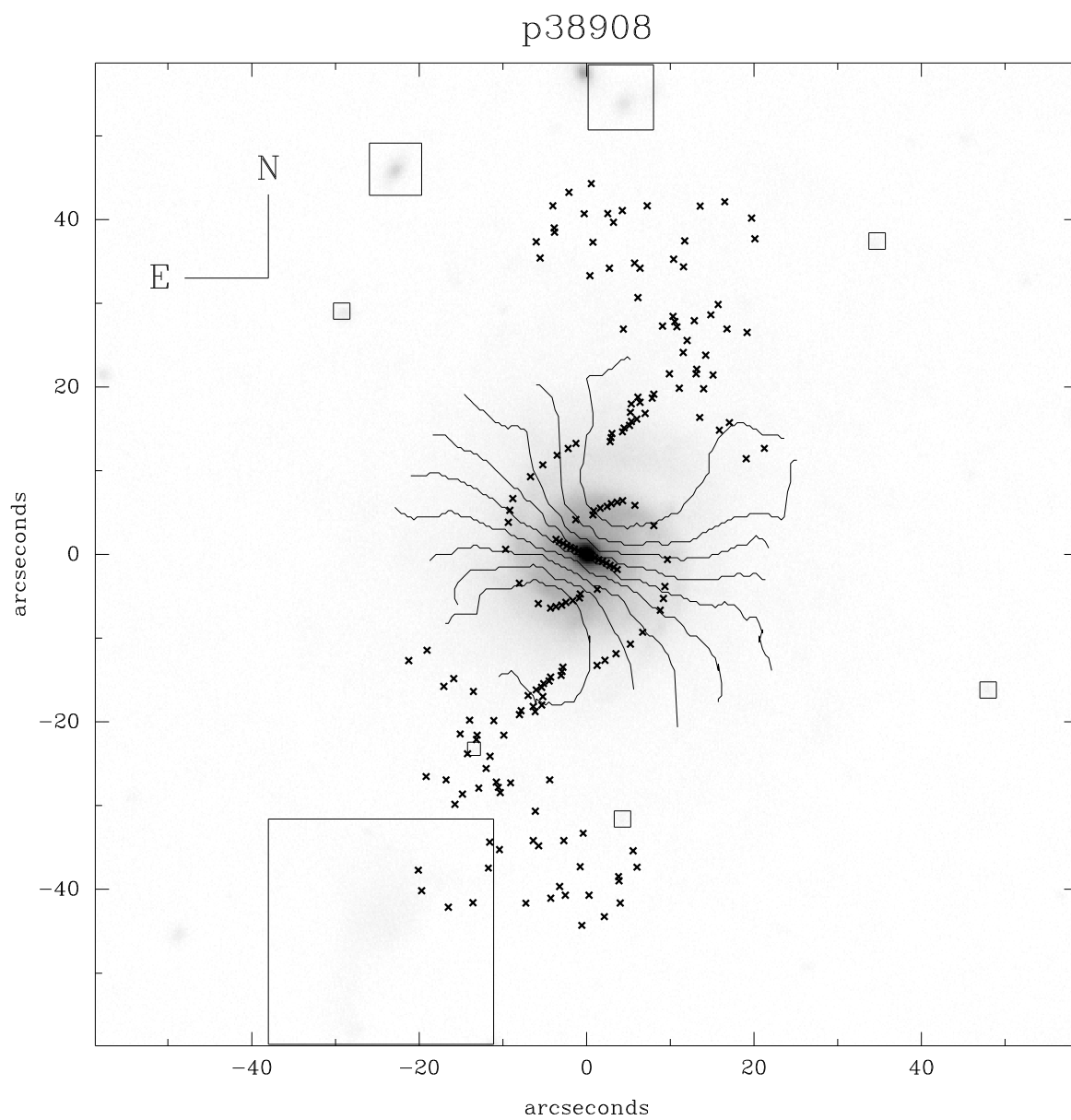
p38268



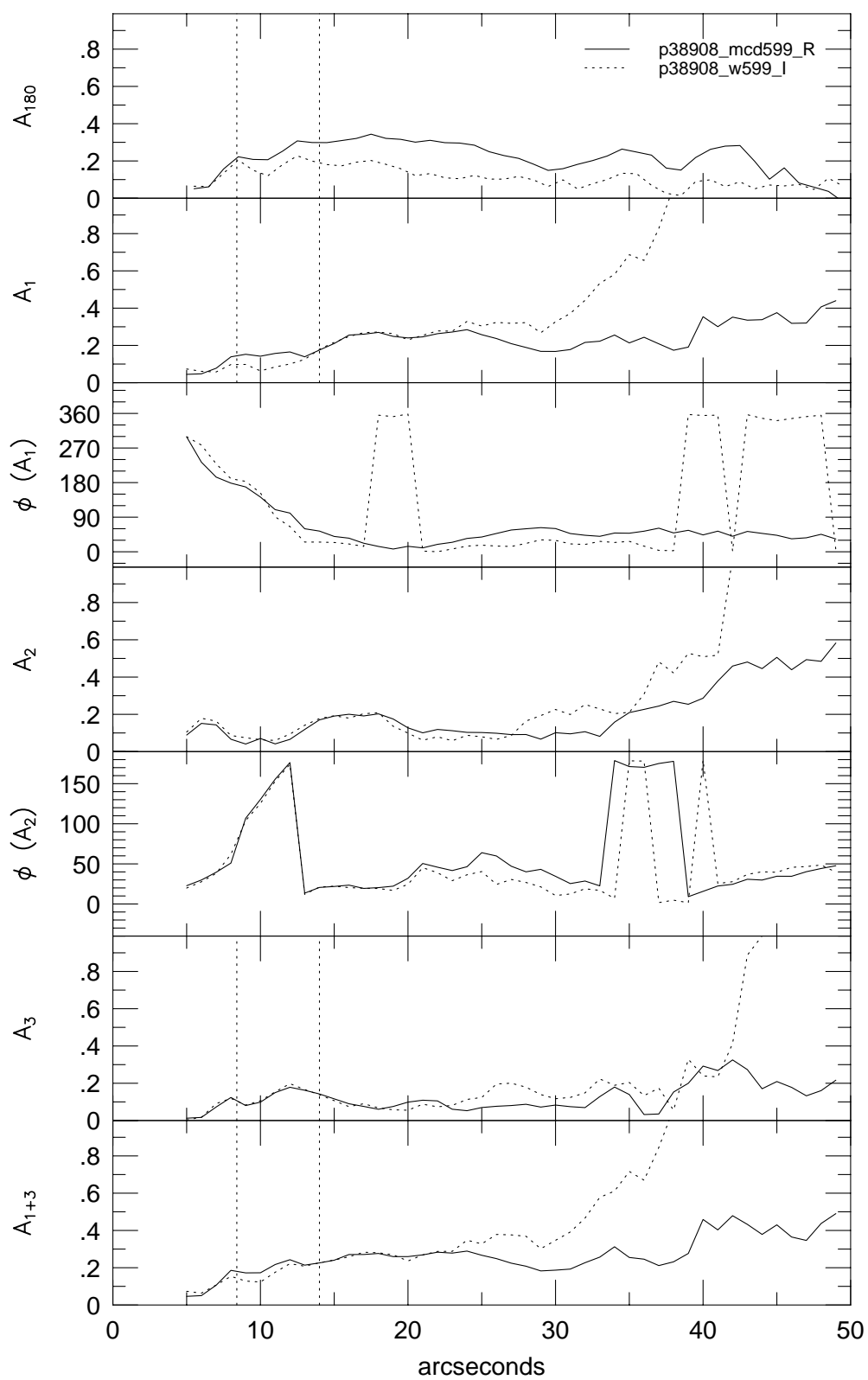
p38268



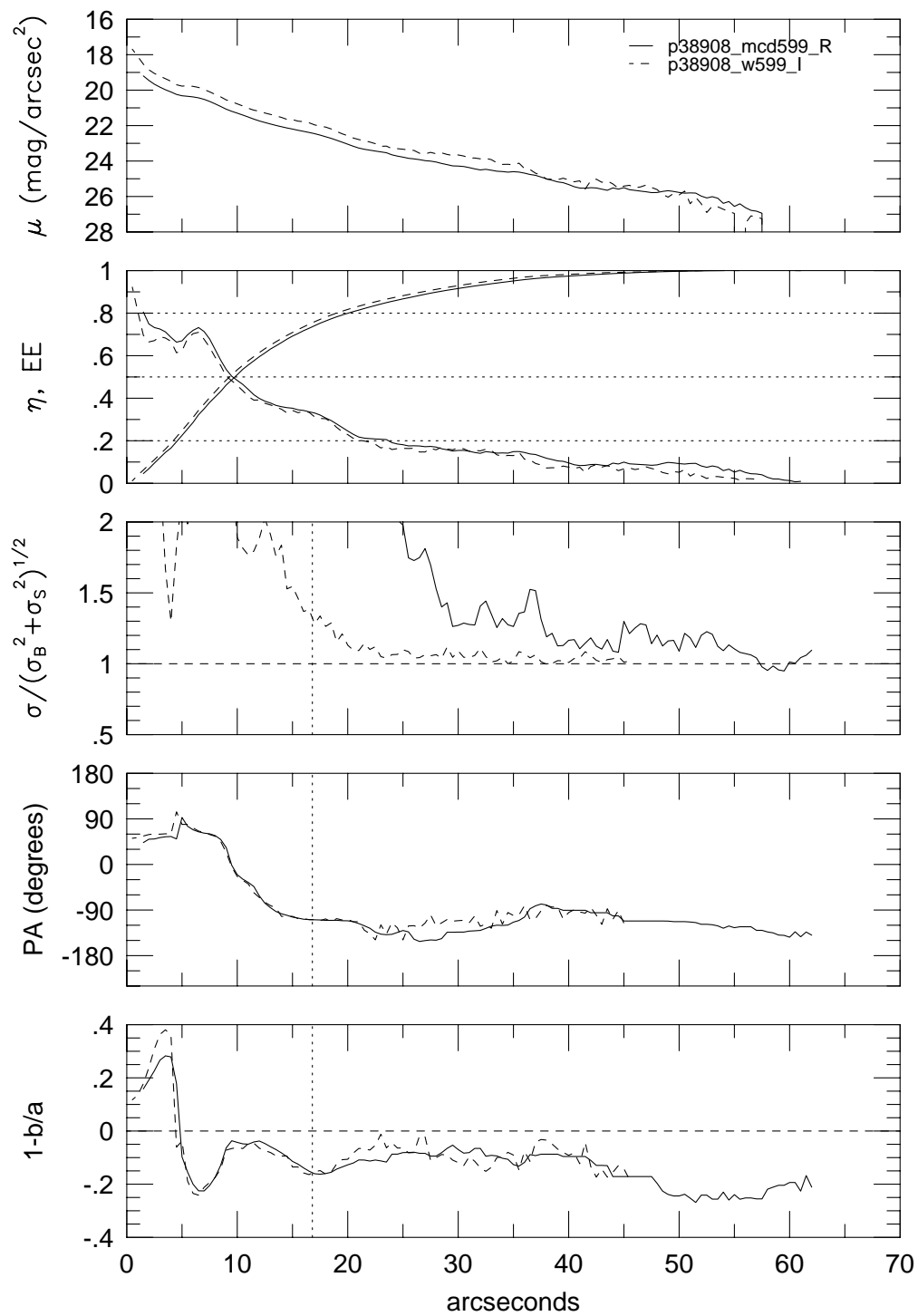




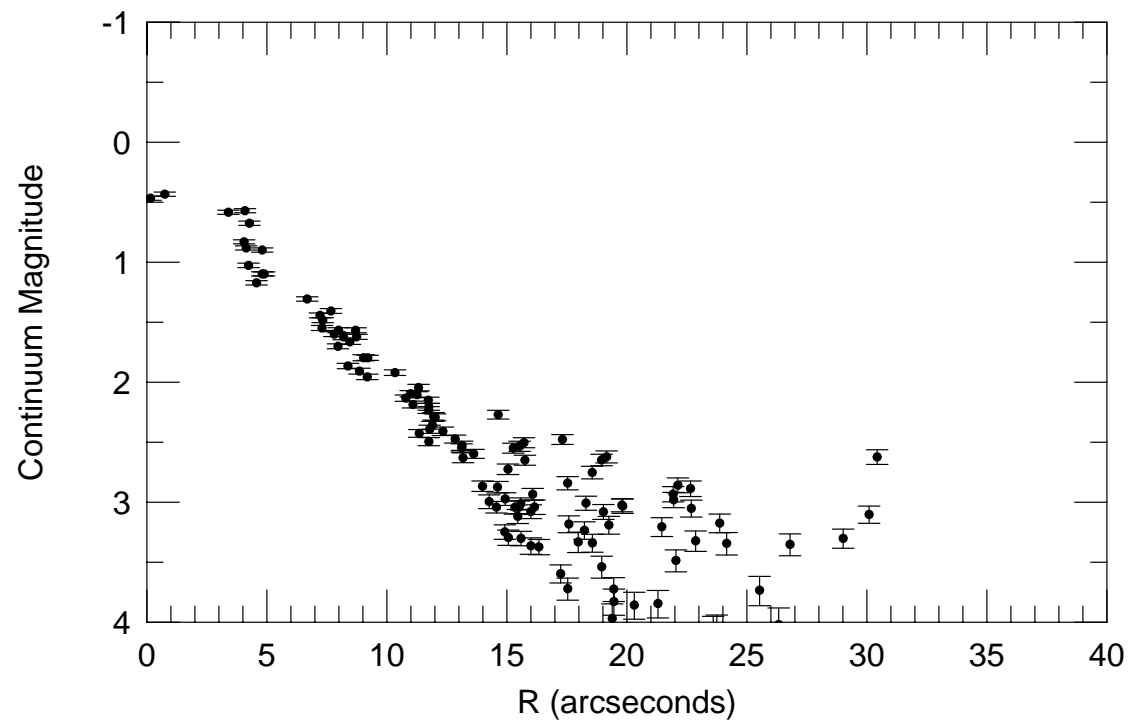
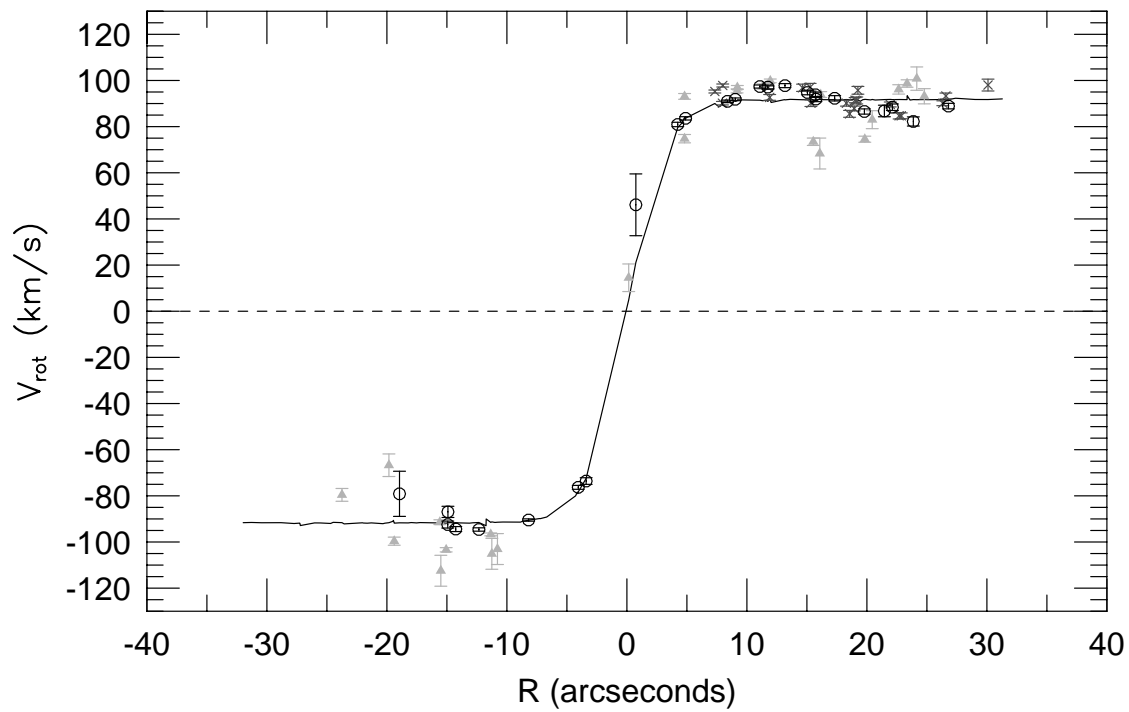
p38908

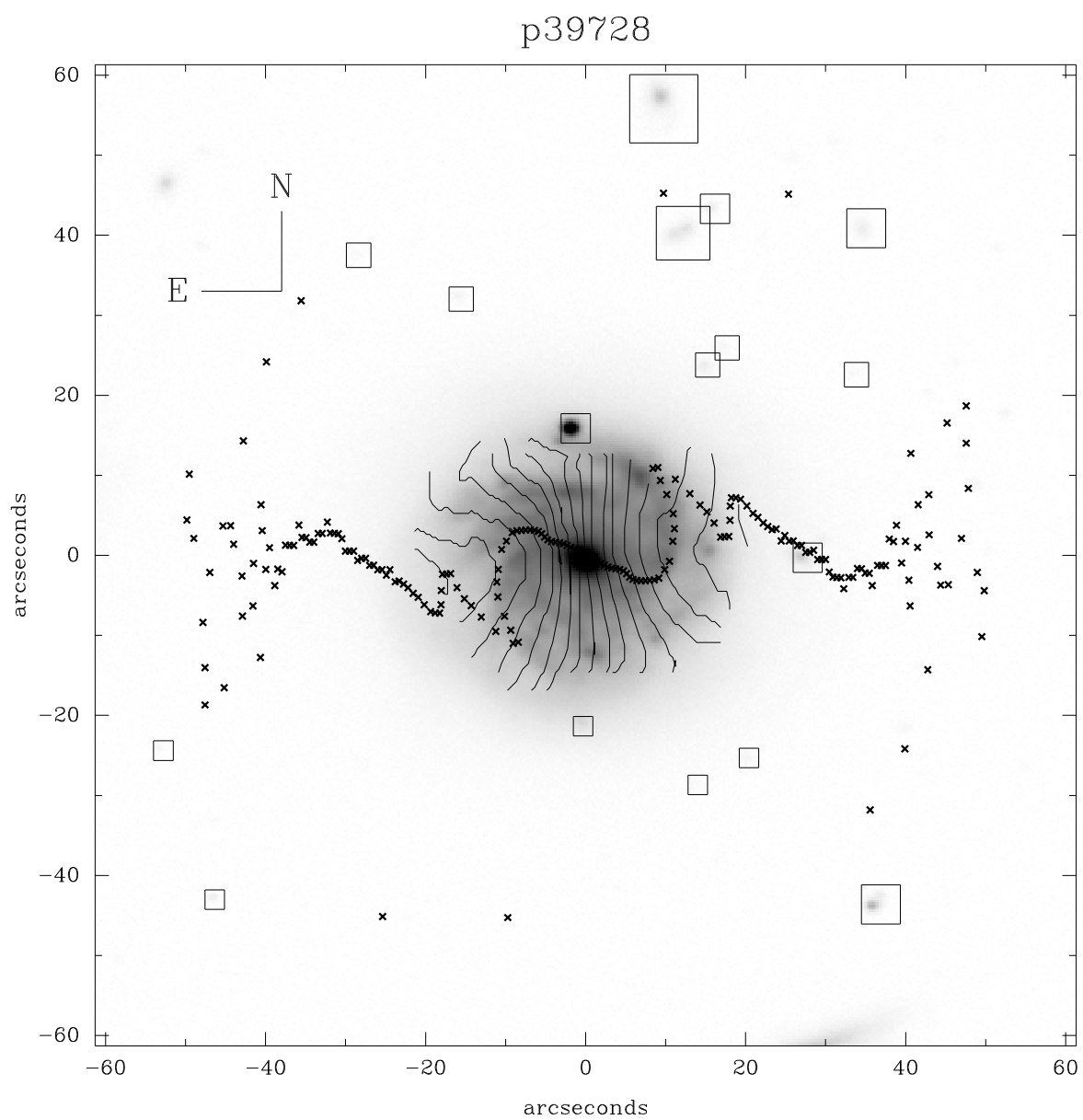


p38908

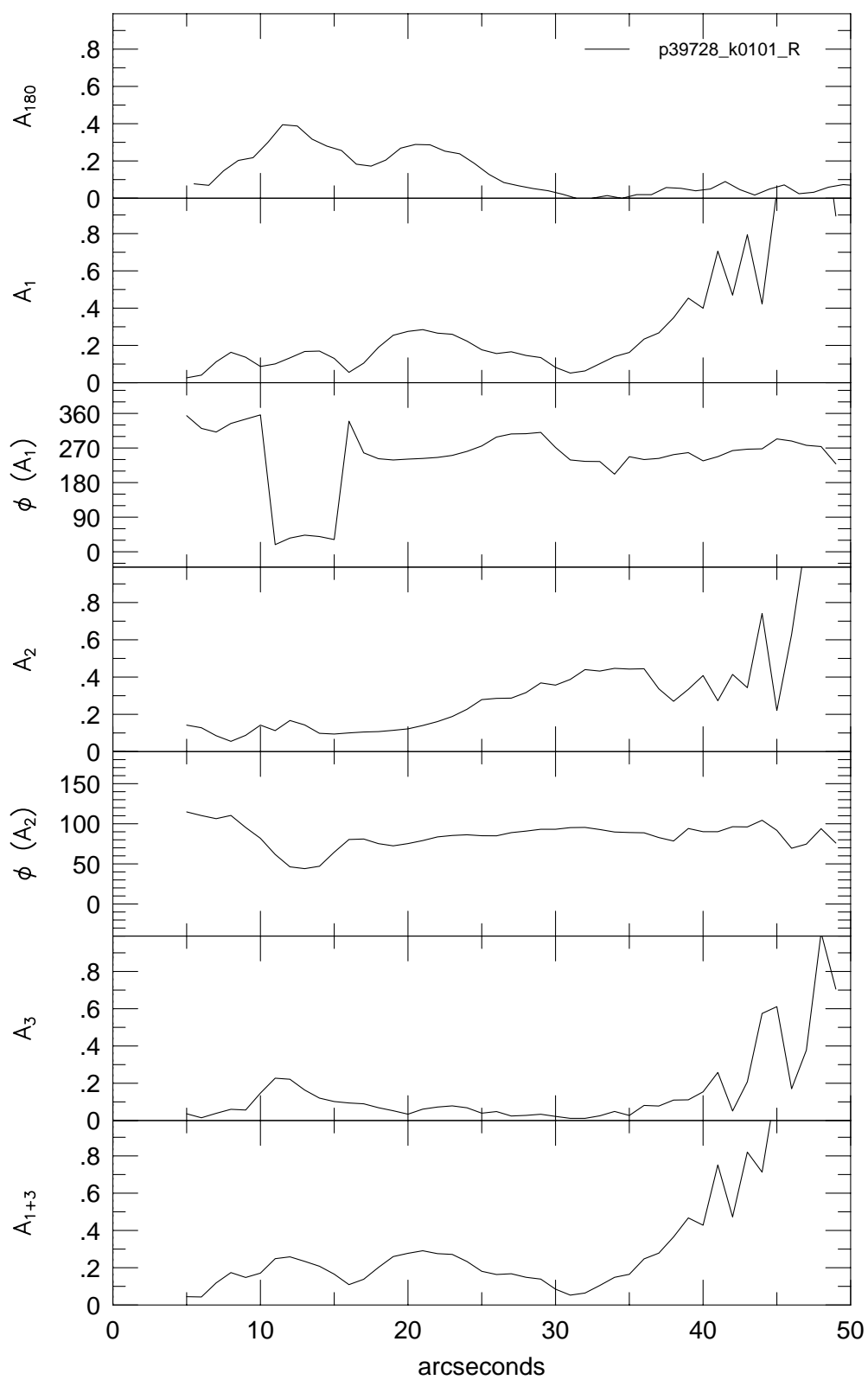


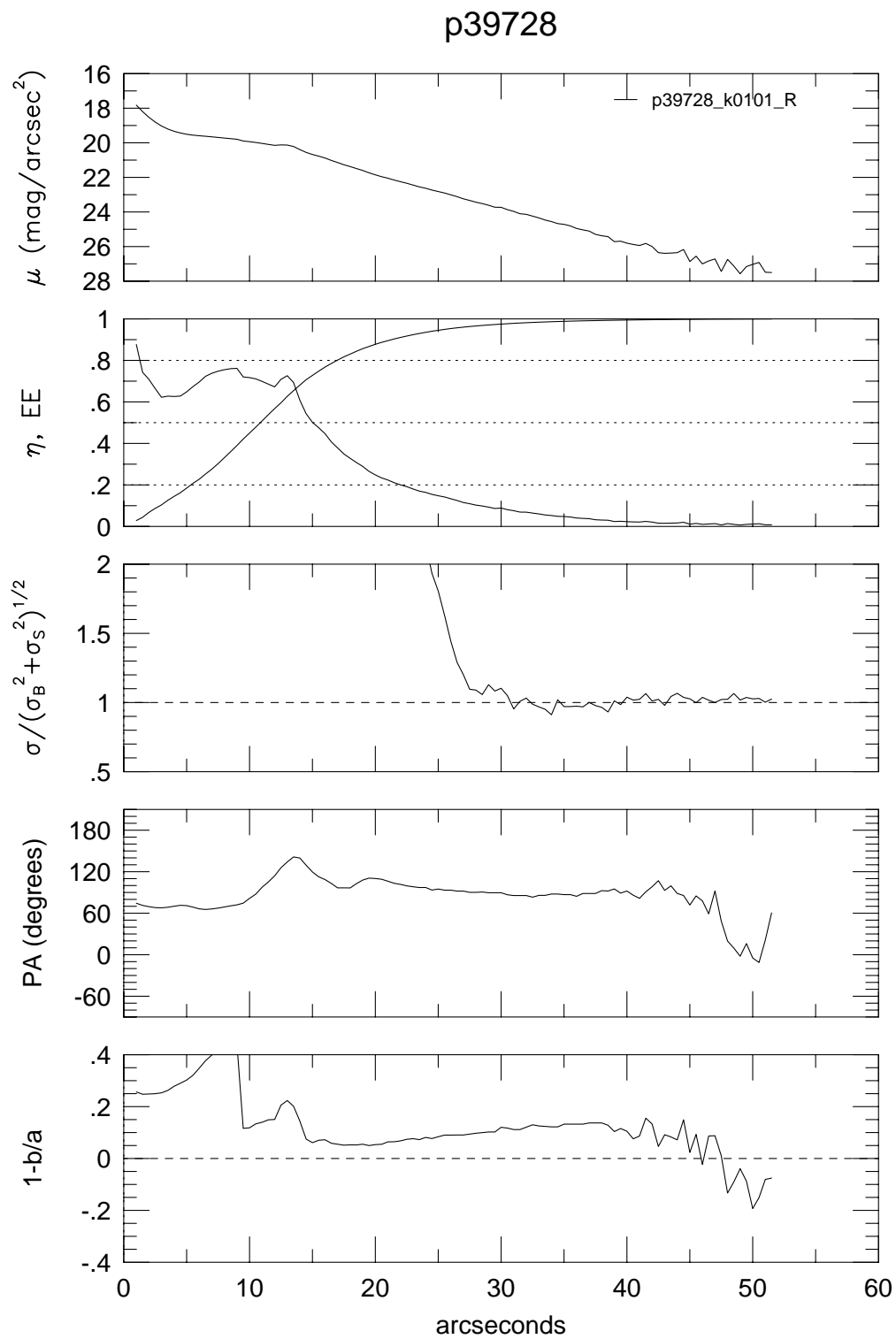
p38908



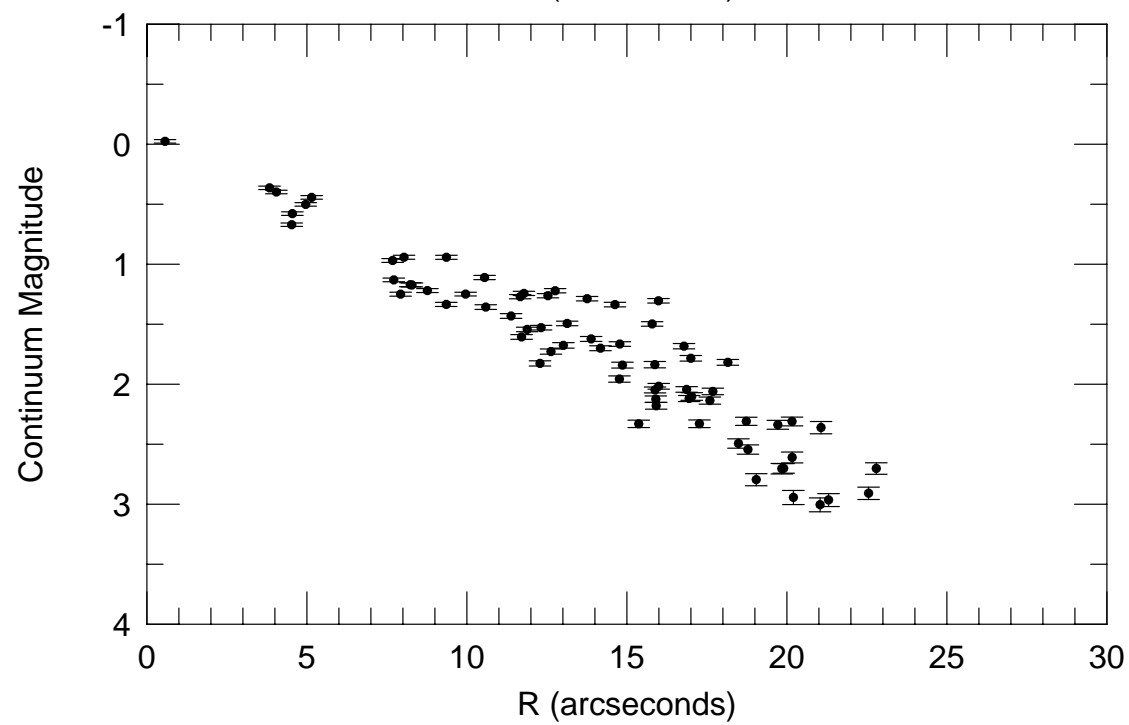
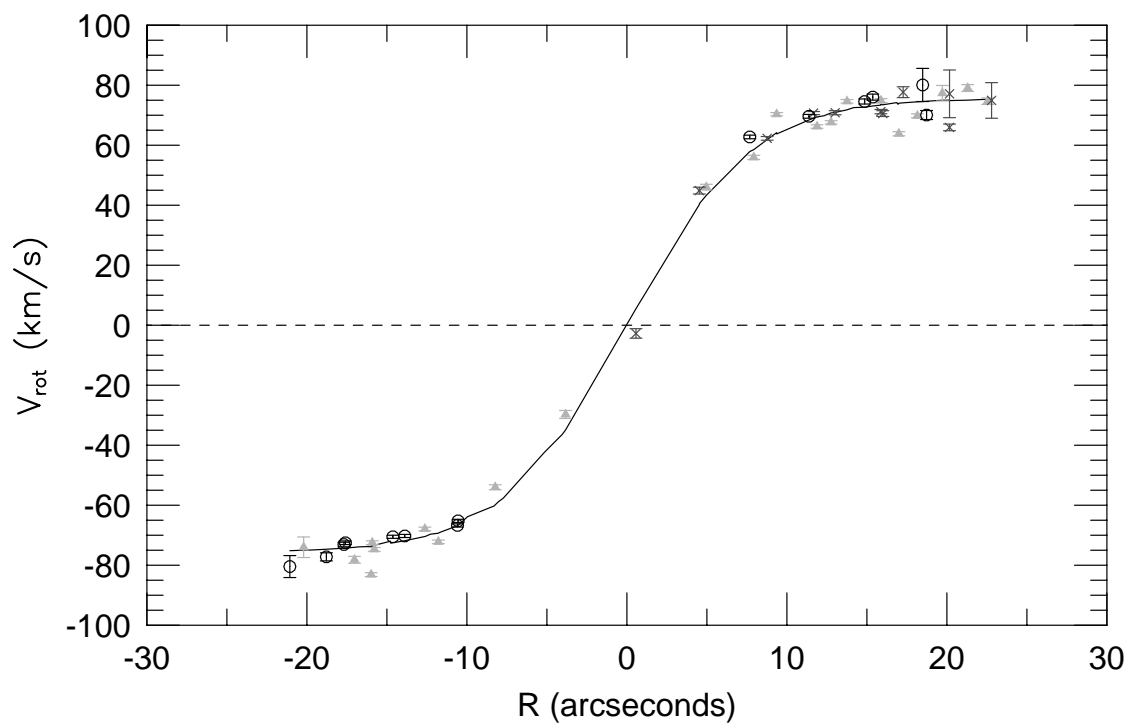


p39728

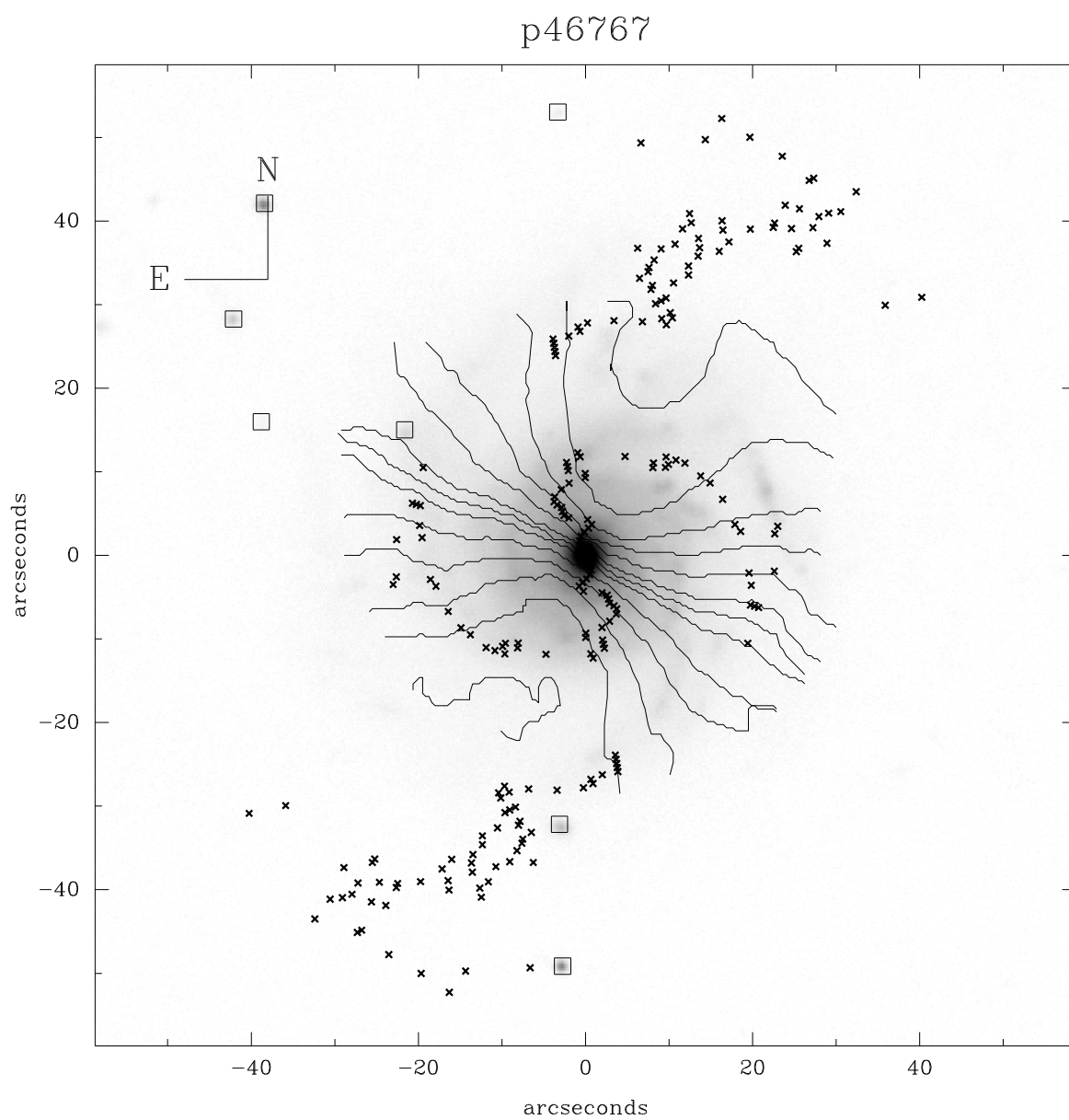




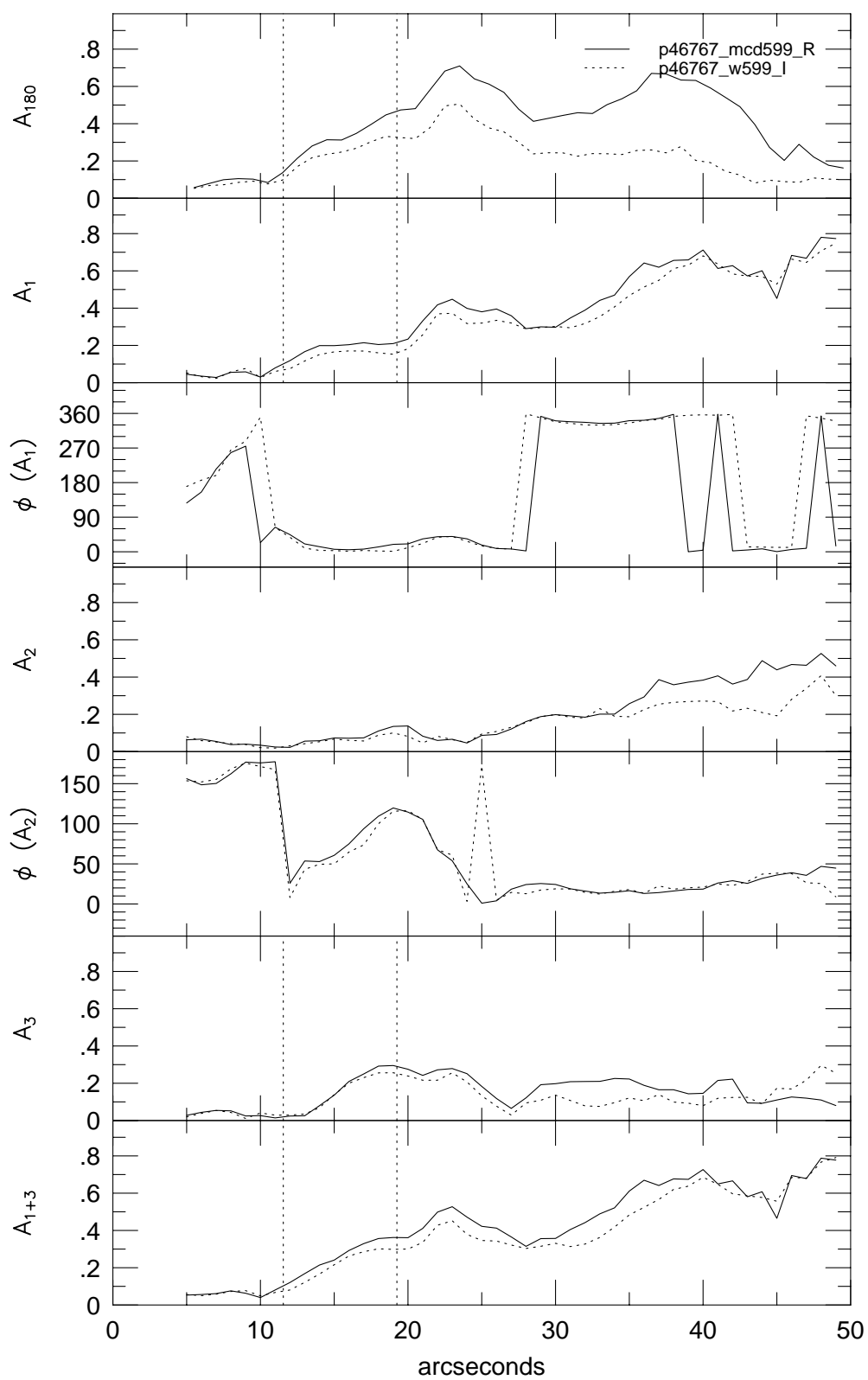
p39728



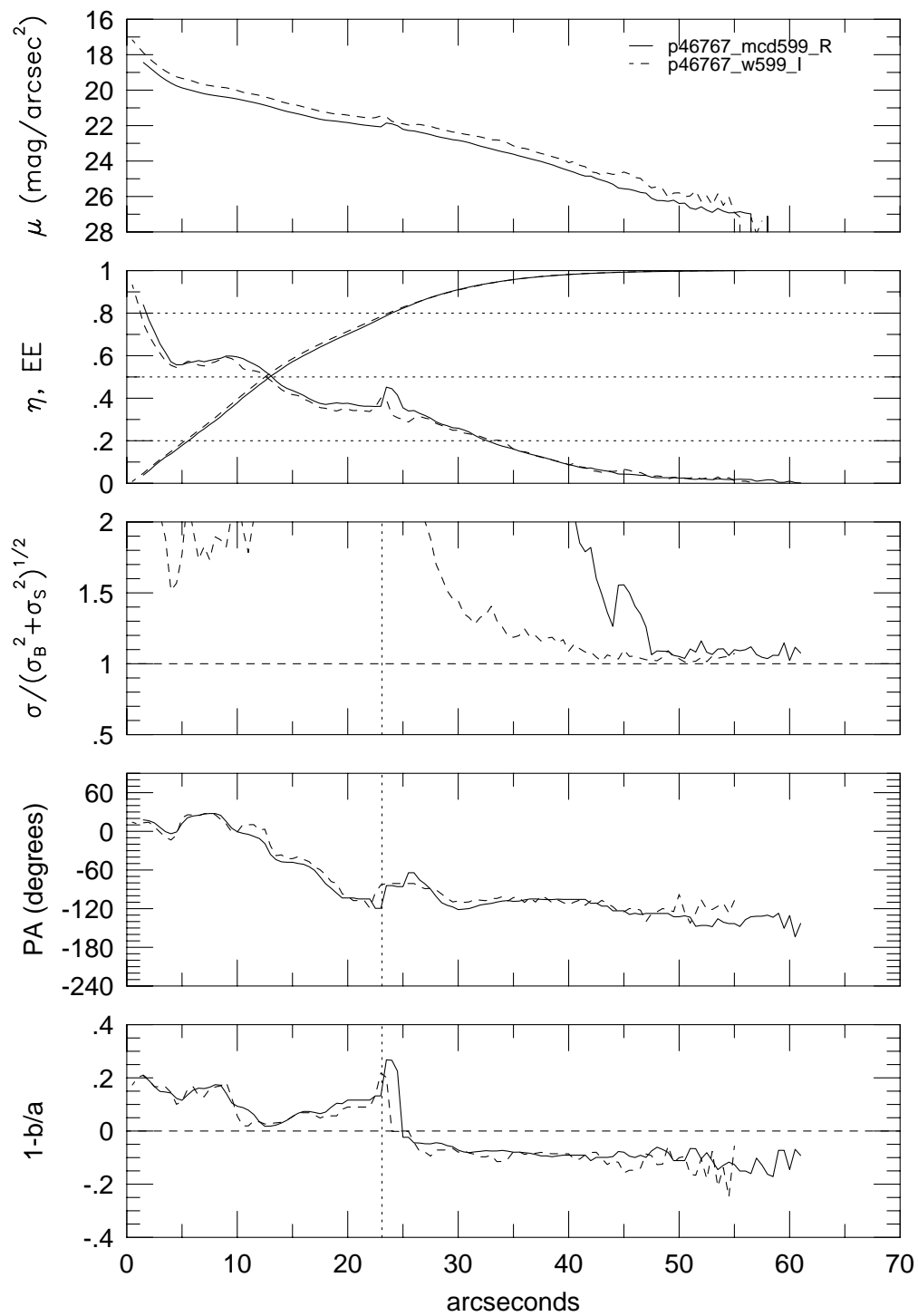




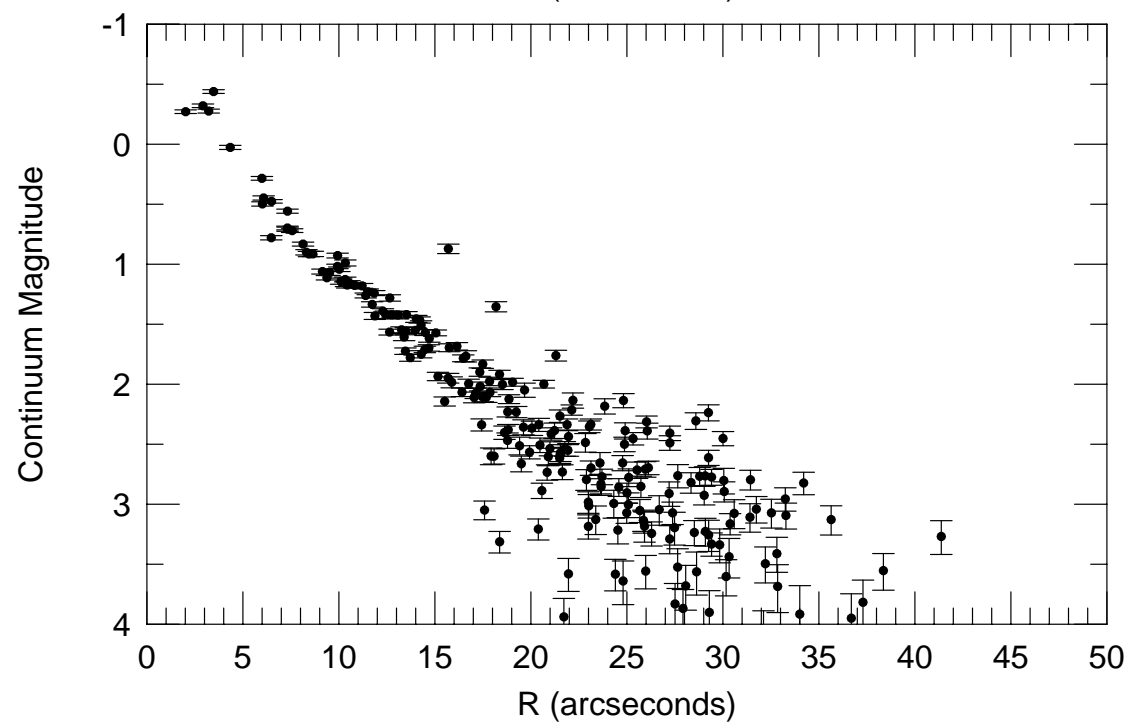
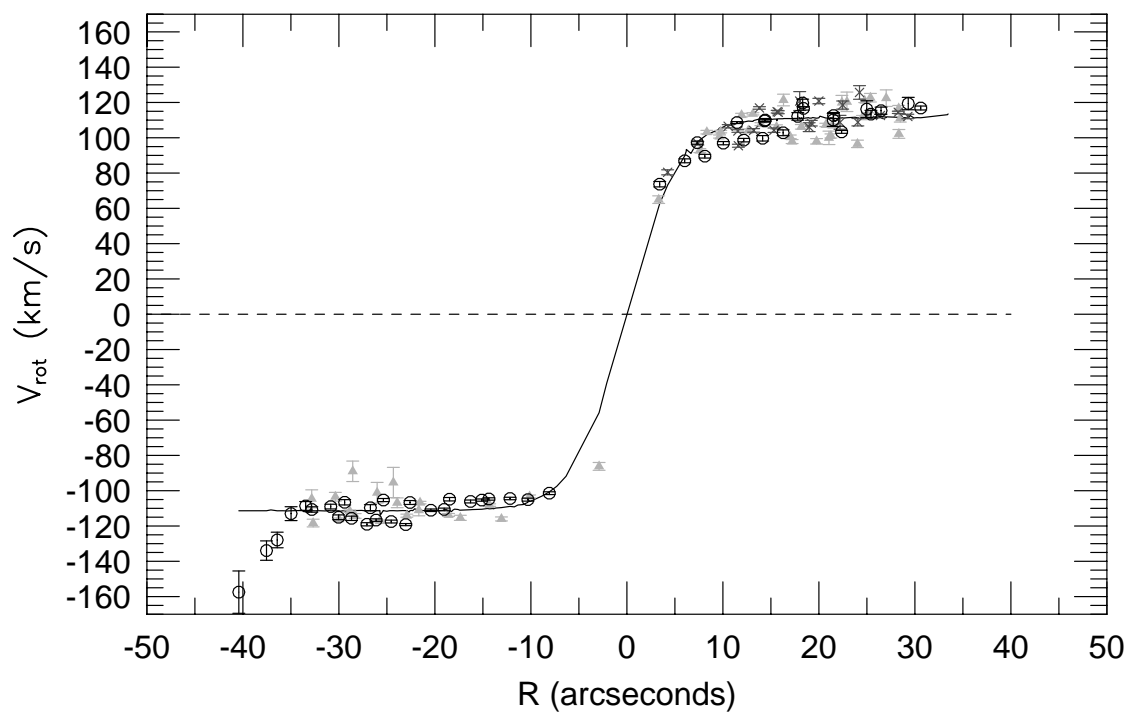
p46767

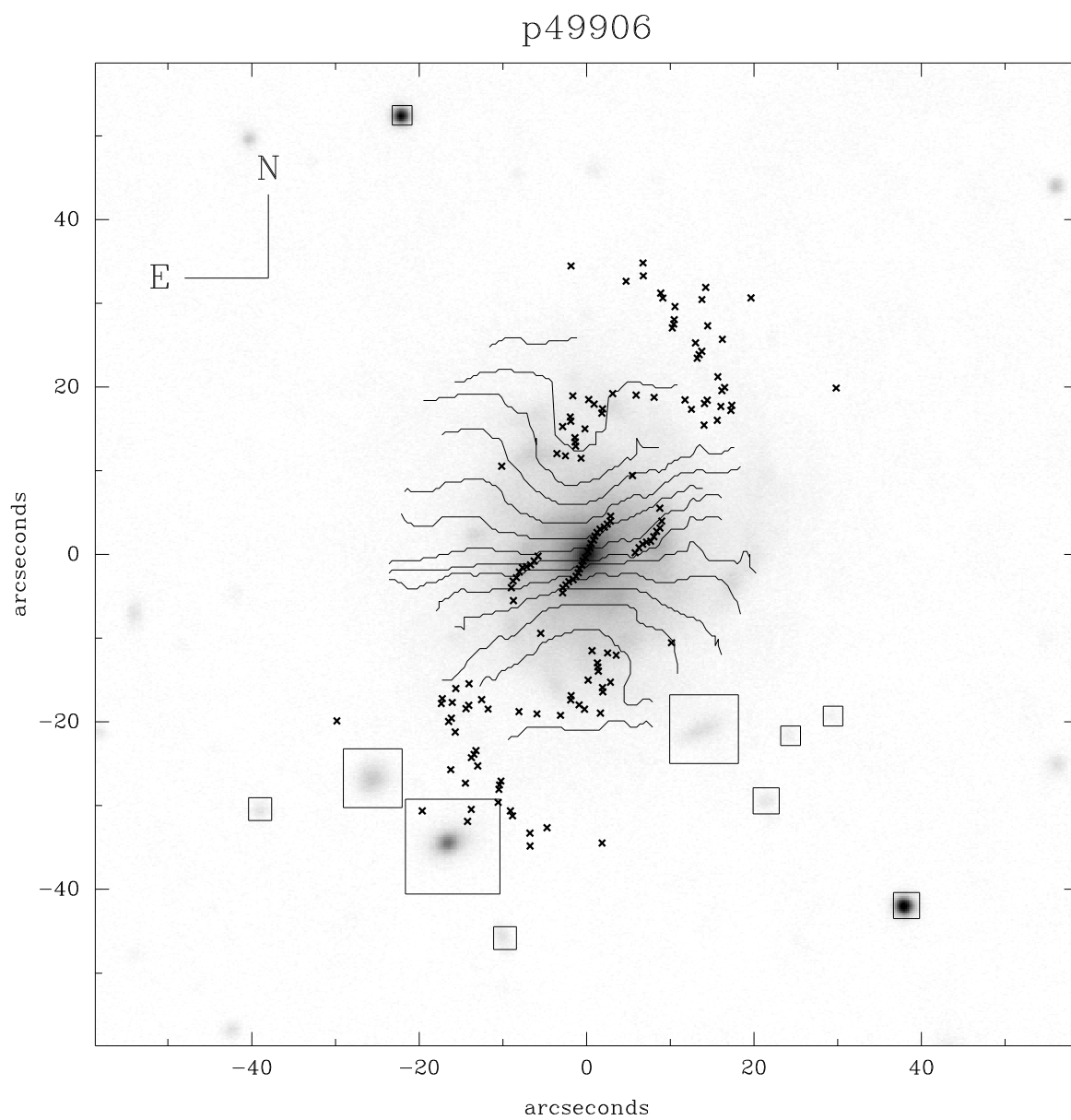


## p46767

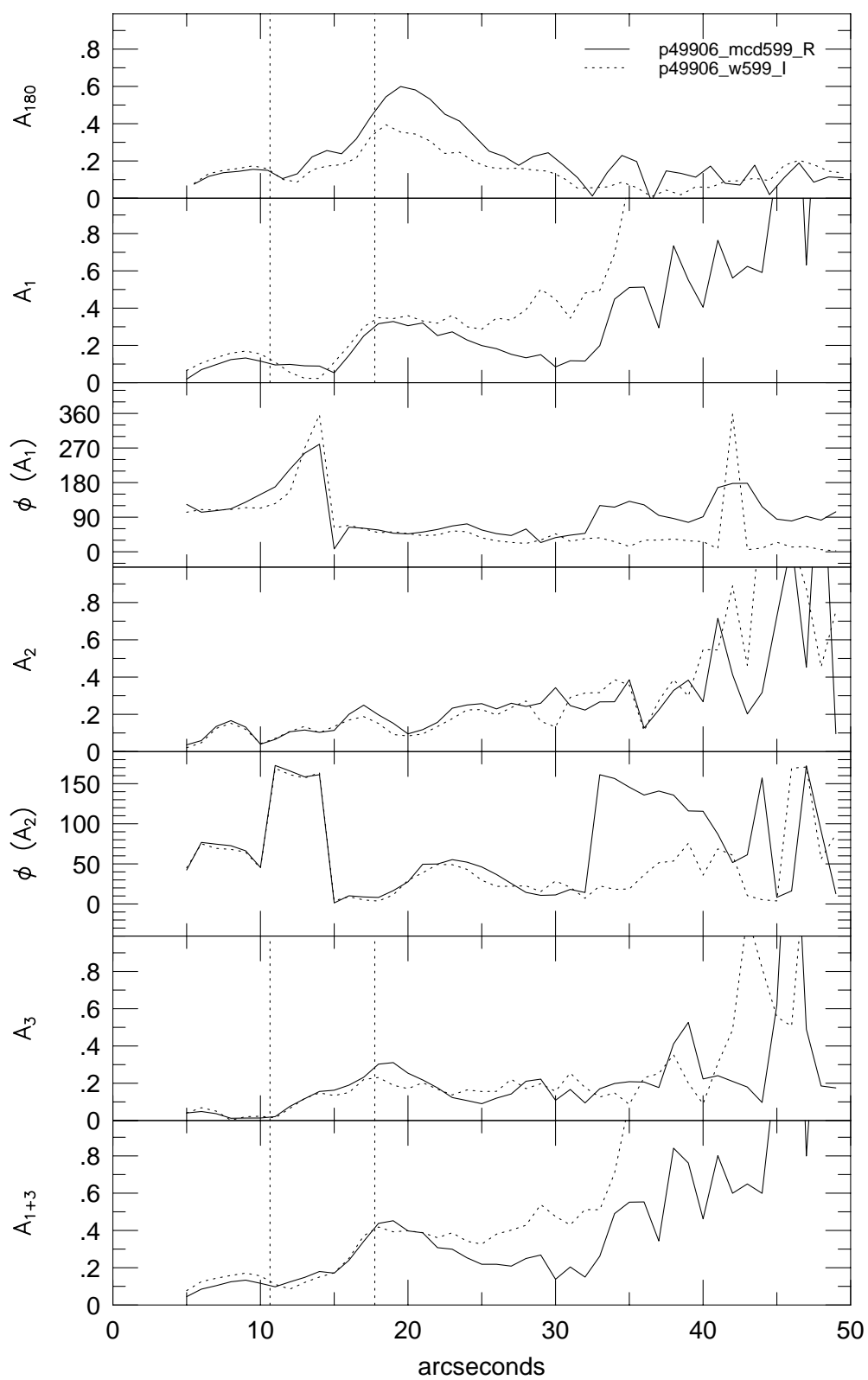


p46767

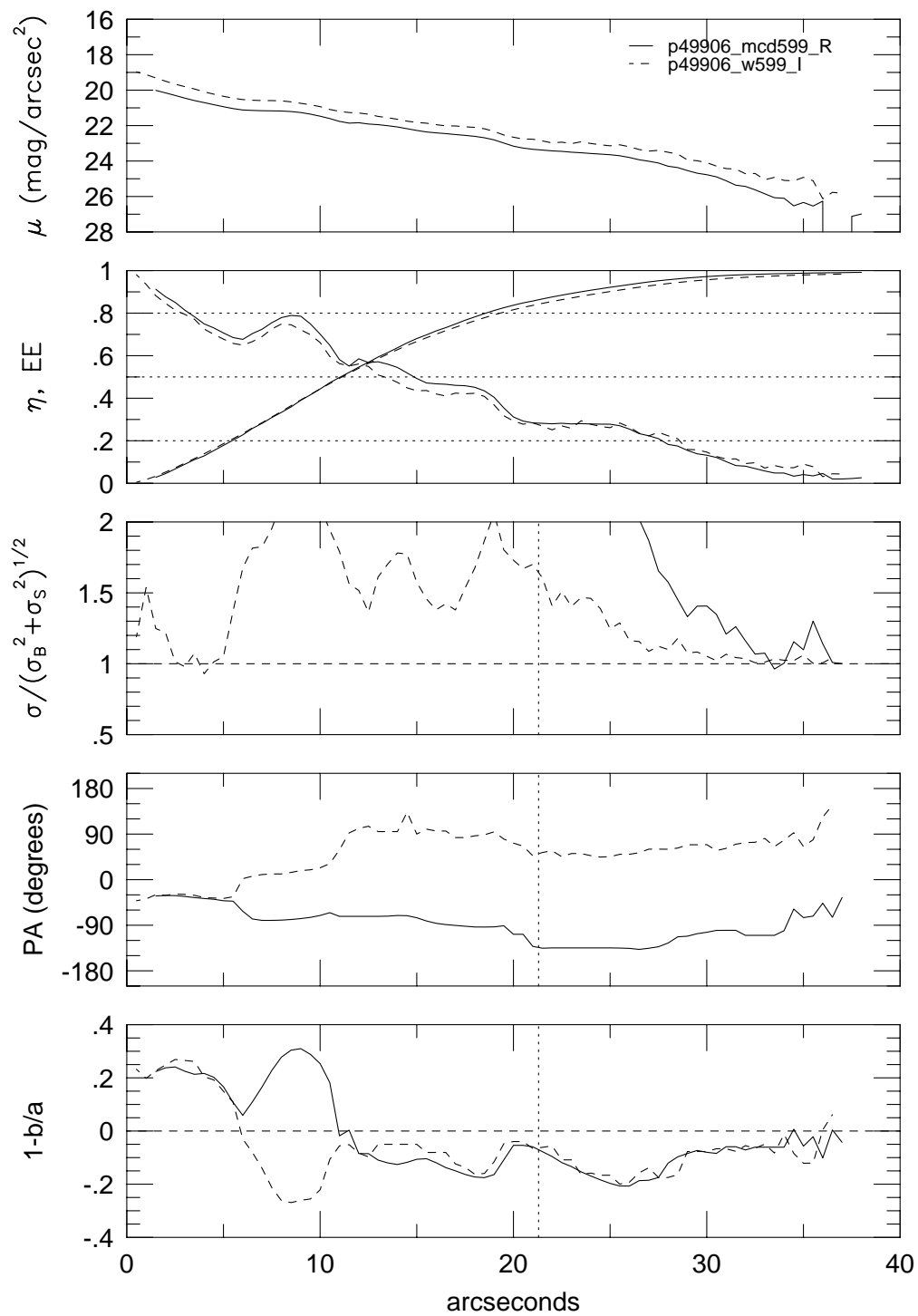




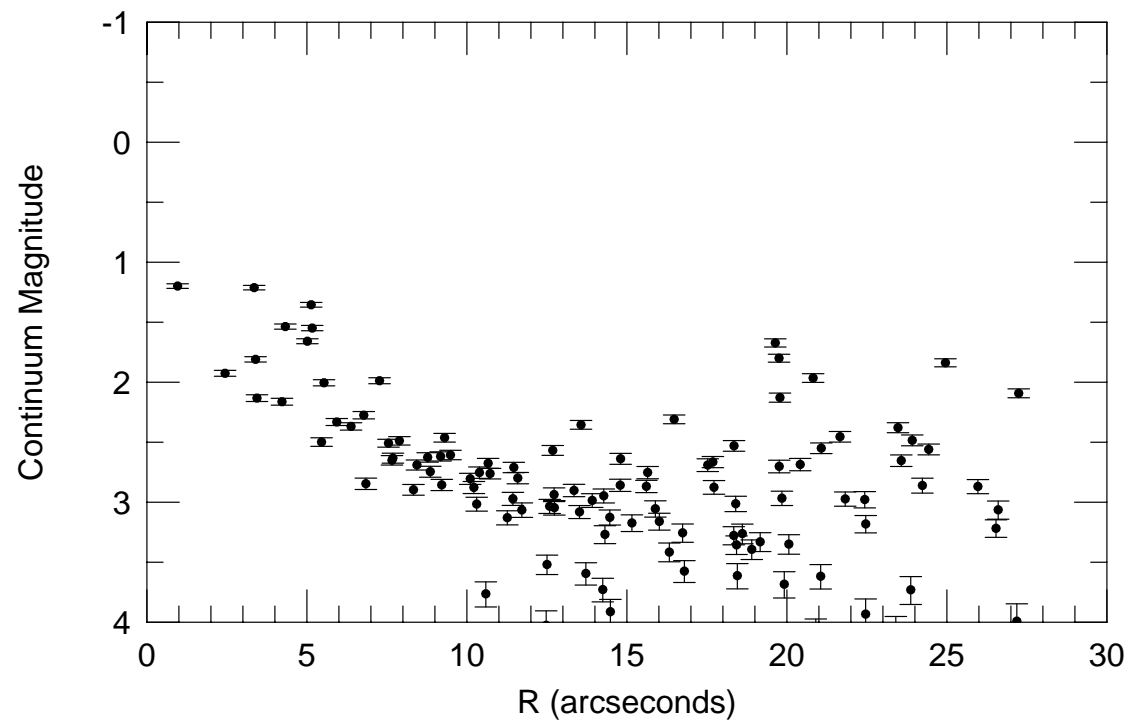
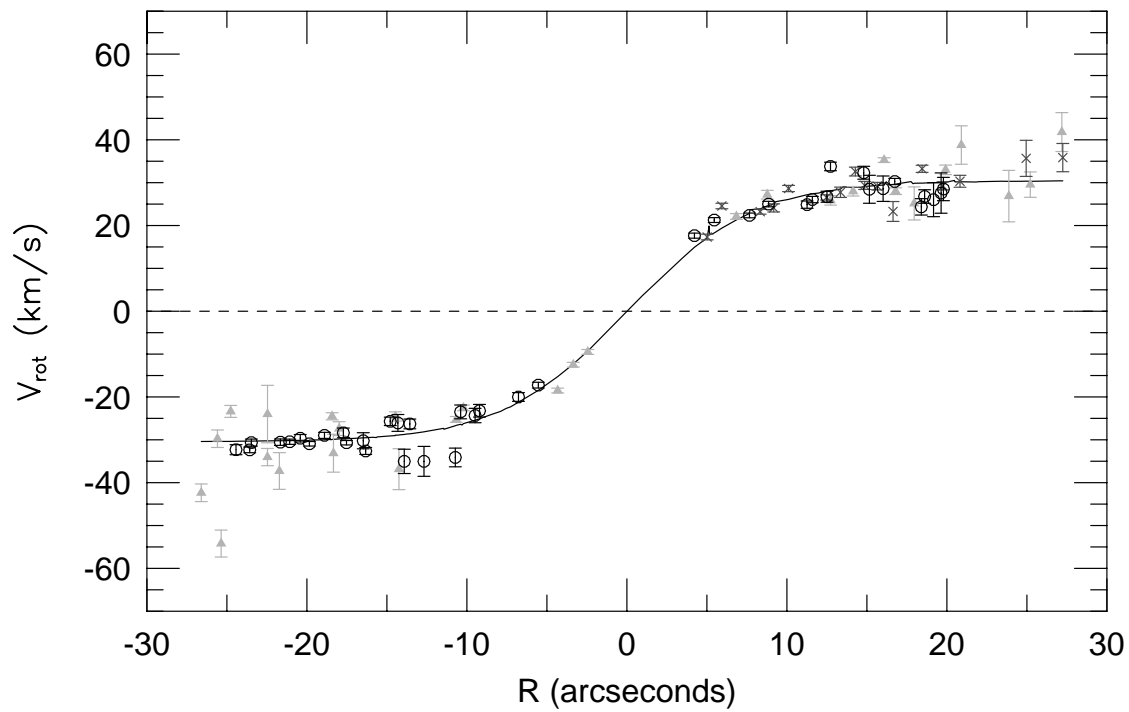
p49906



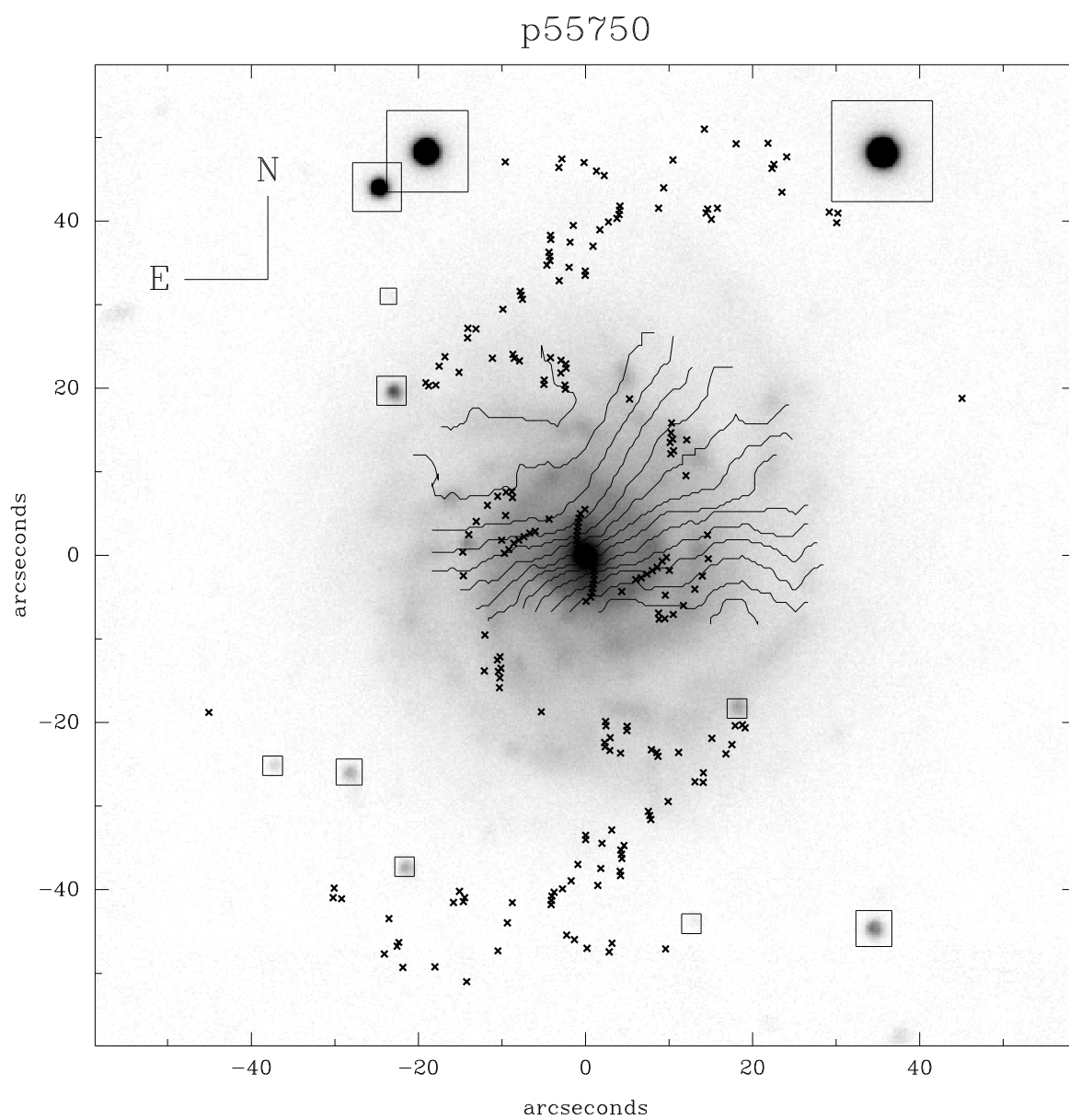
p49906



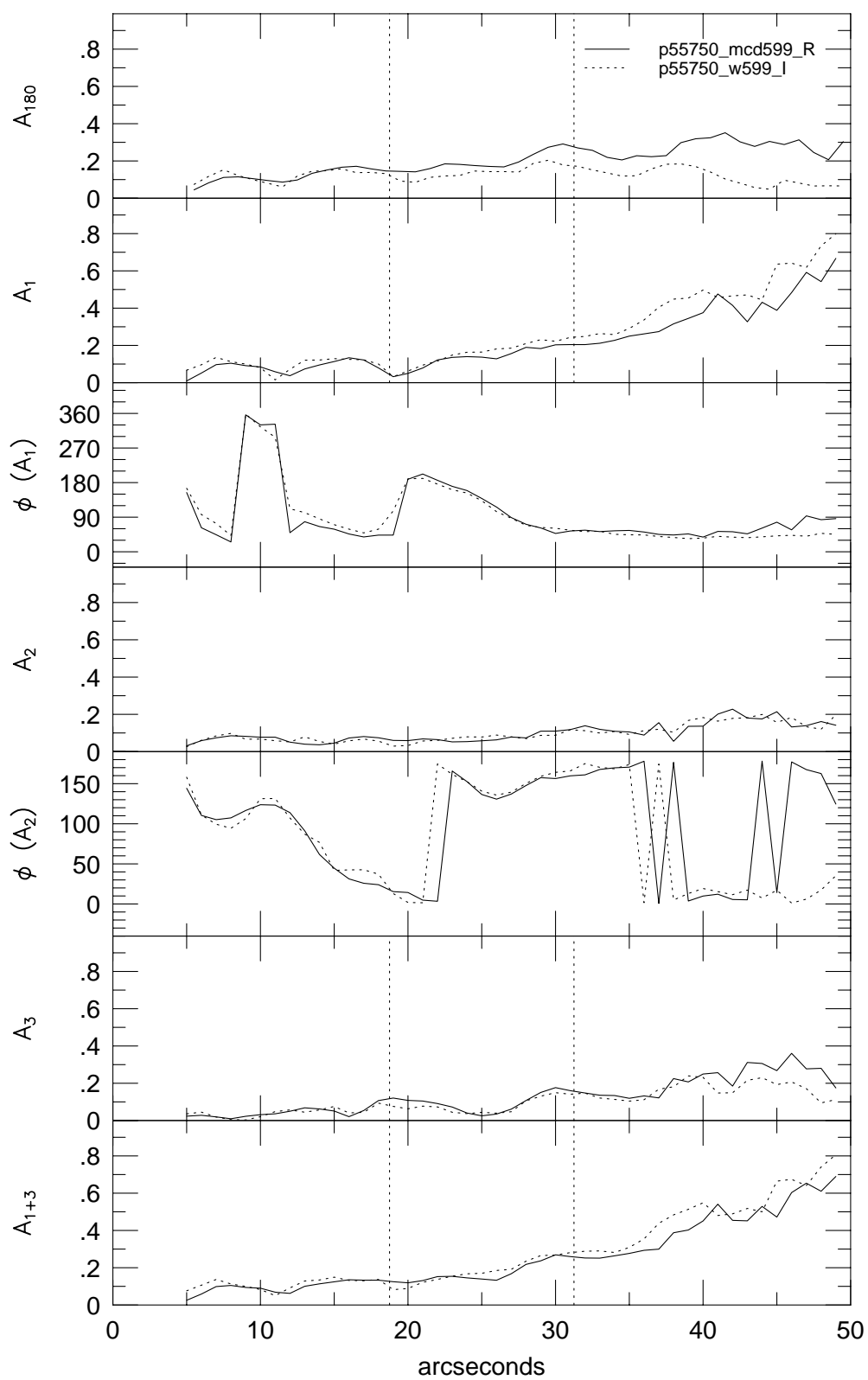
p49906



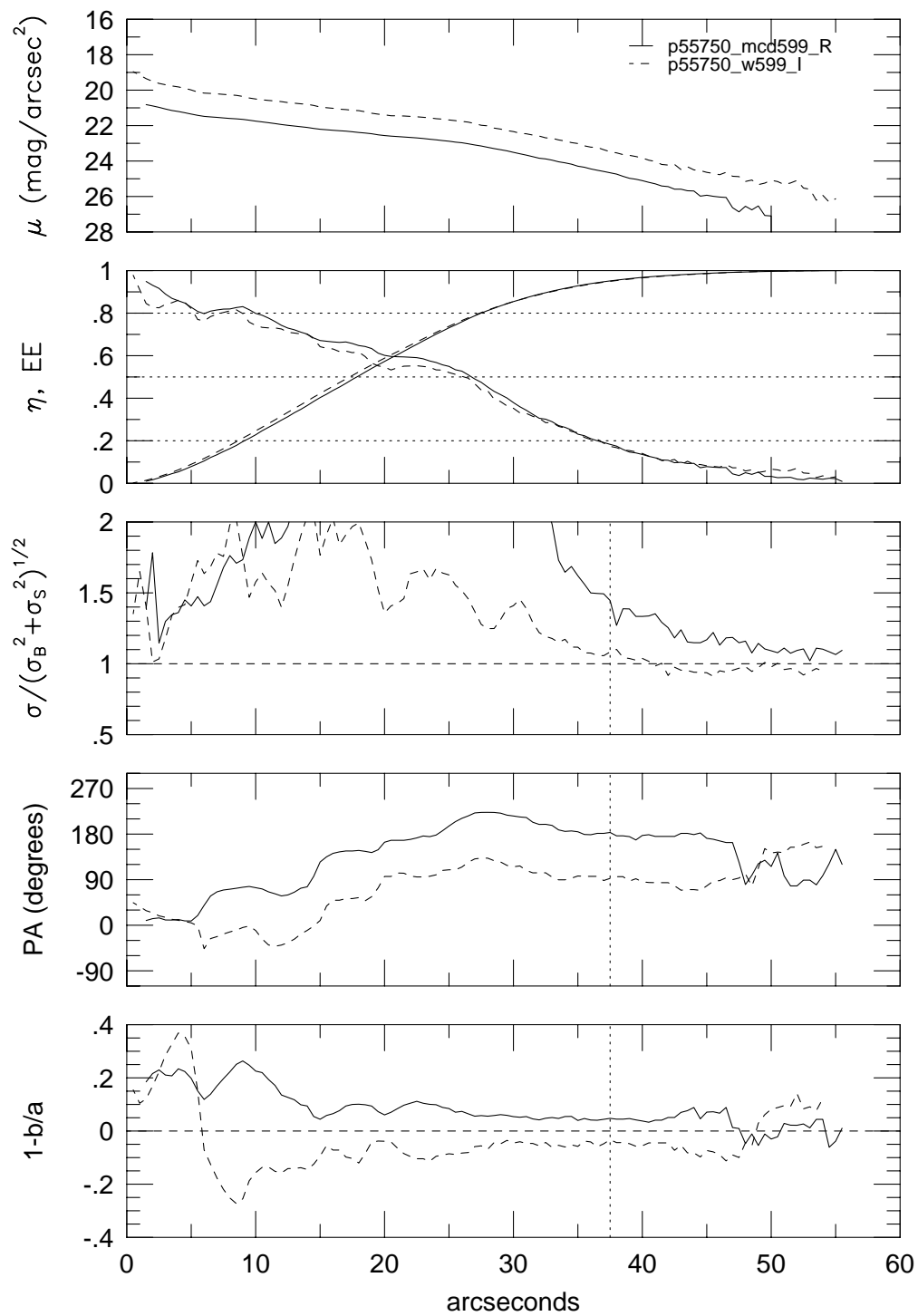




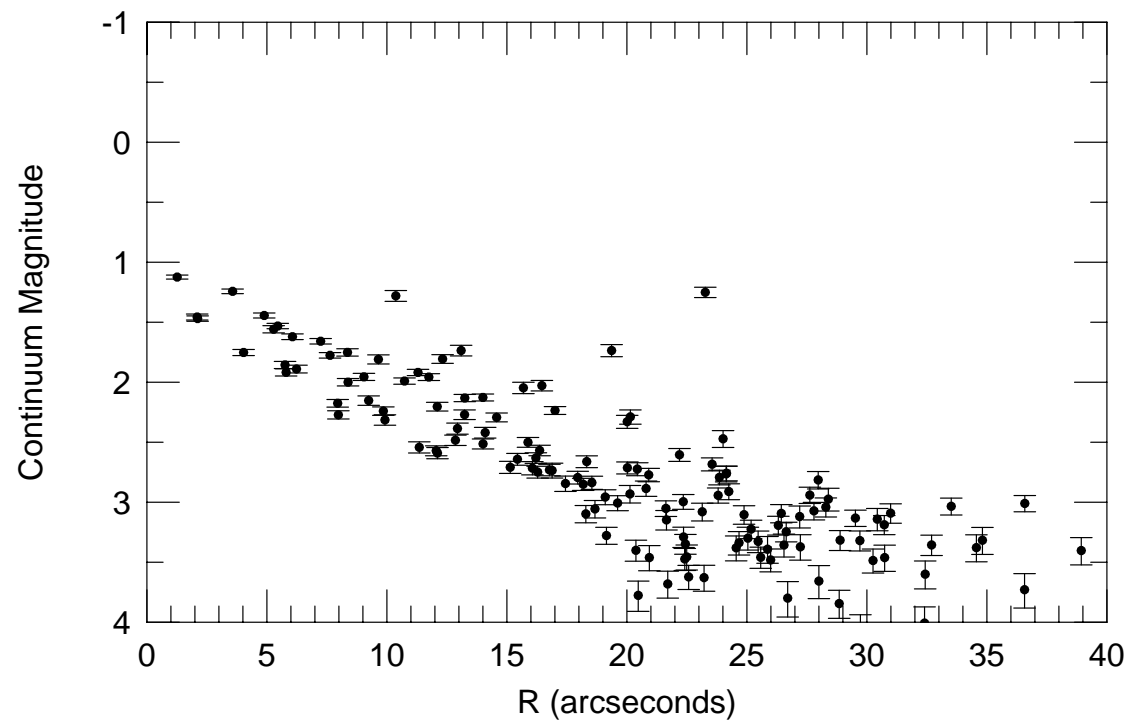
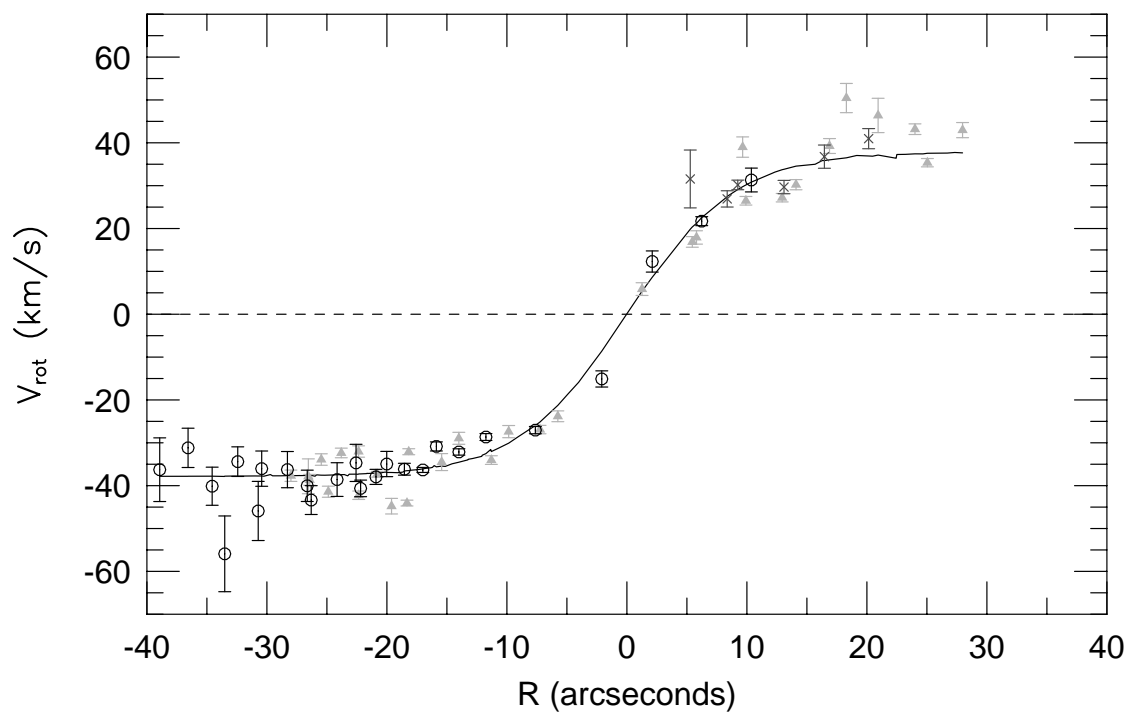
p55750

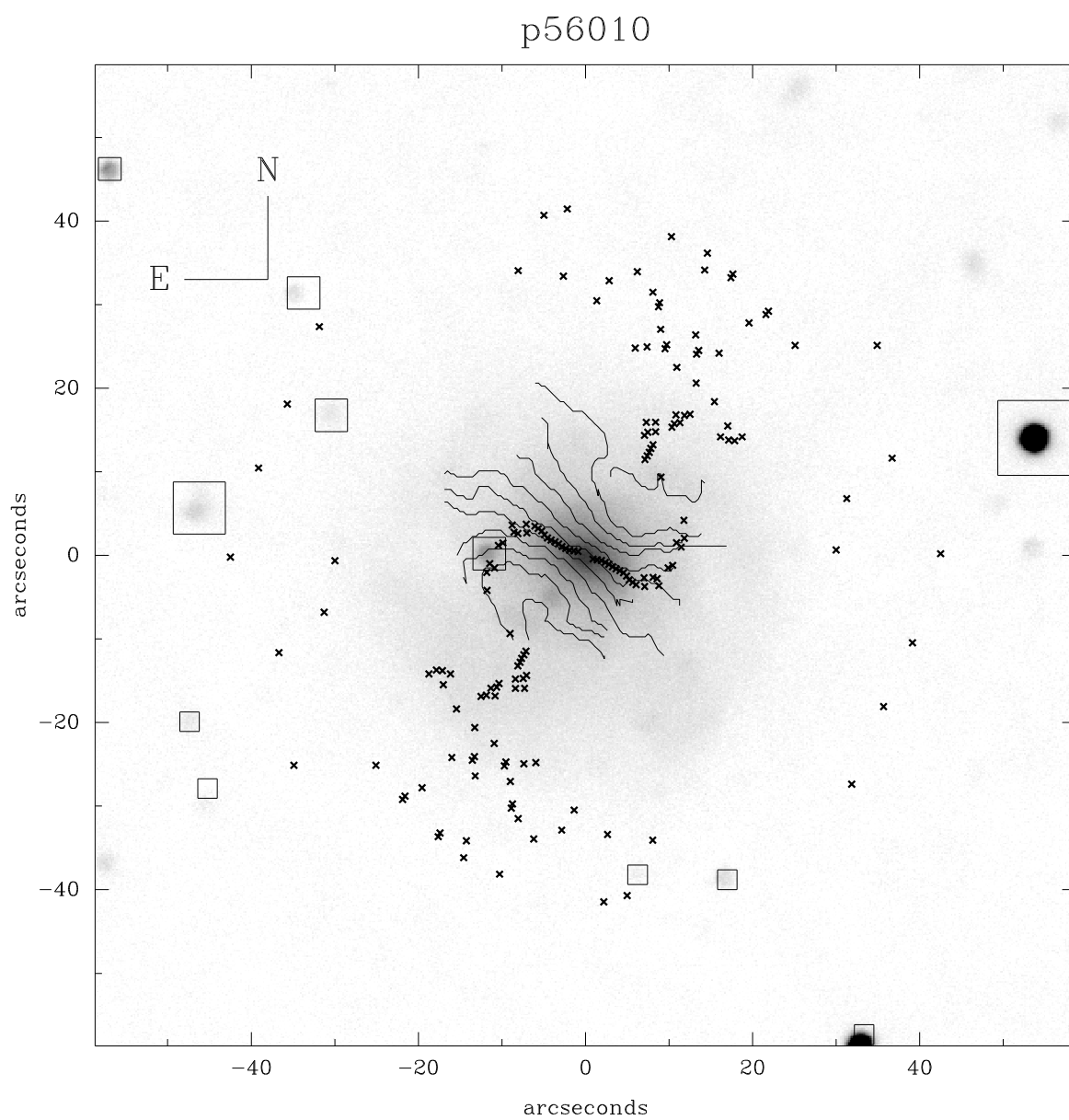


## p55750

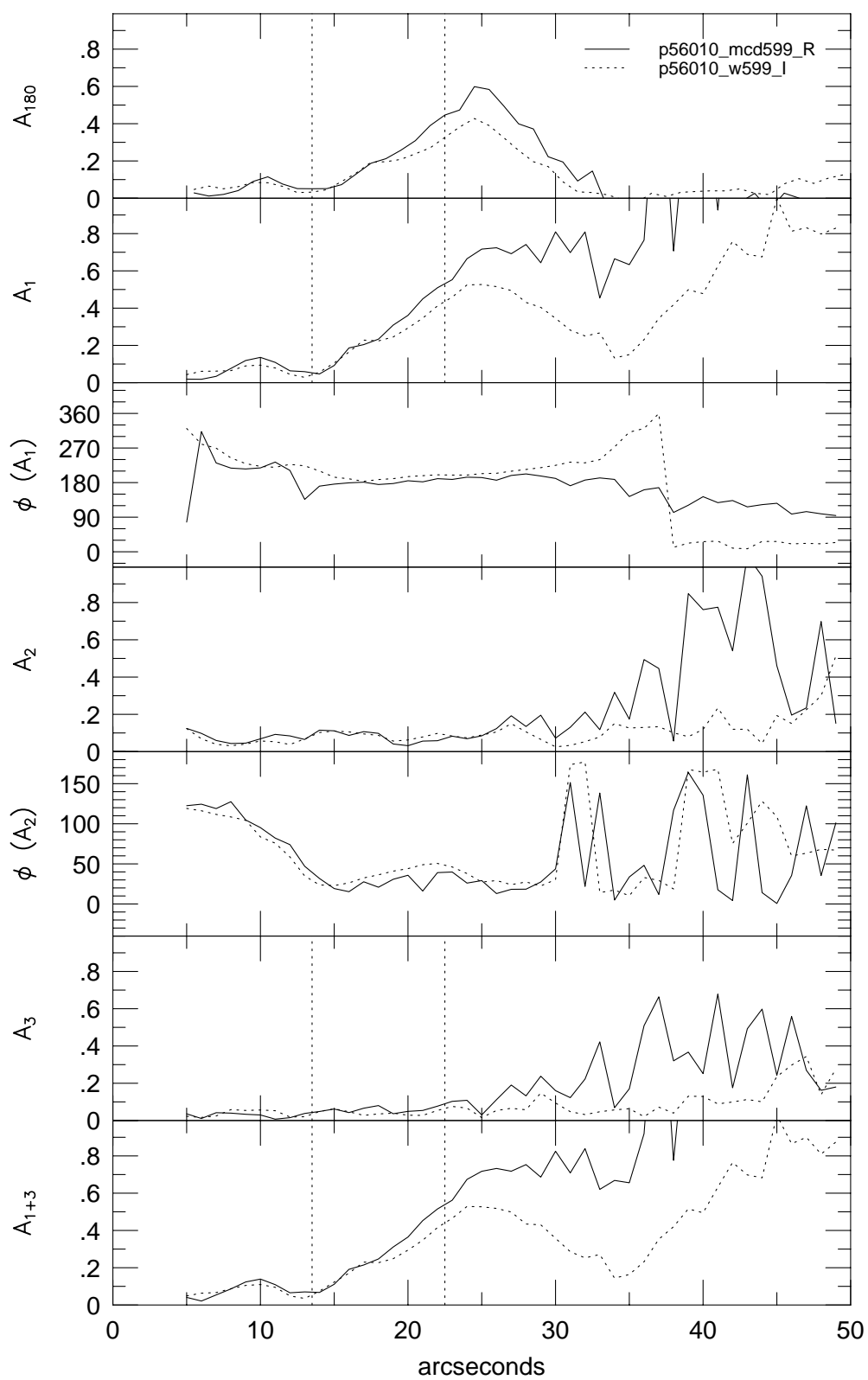


p55750

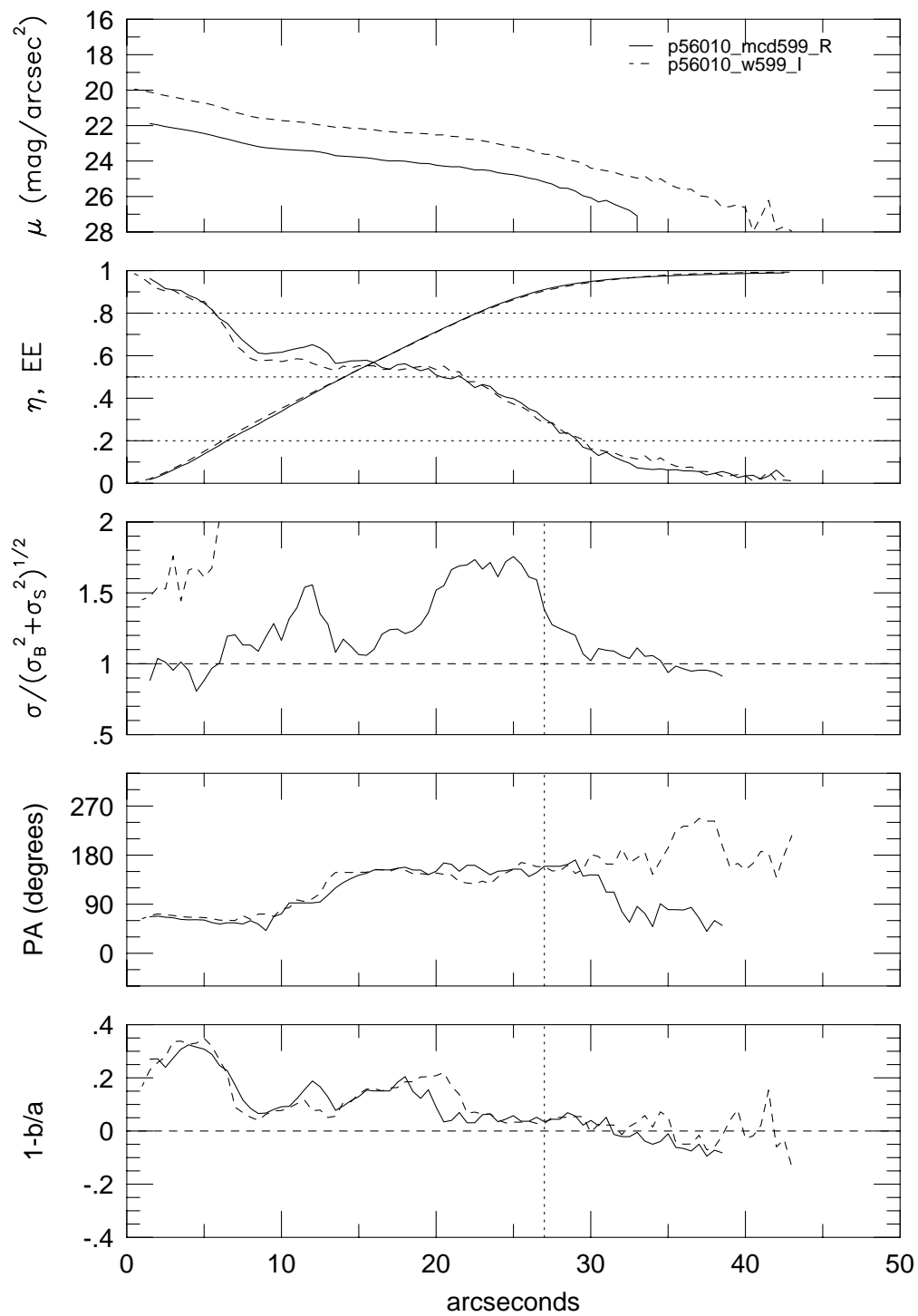




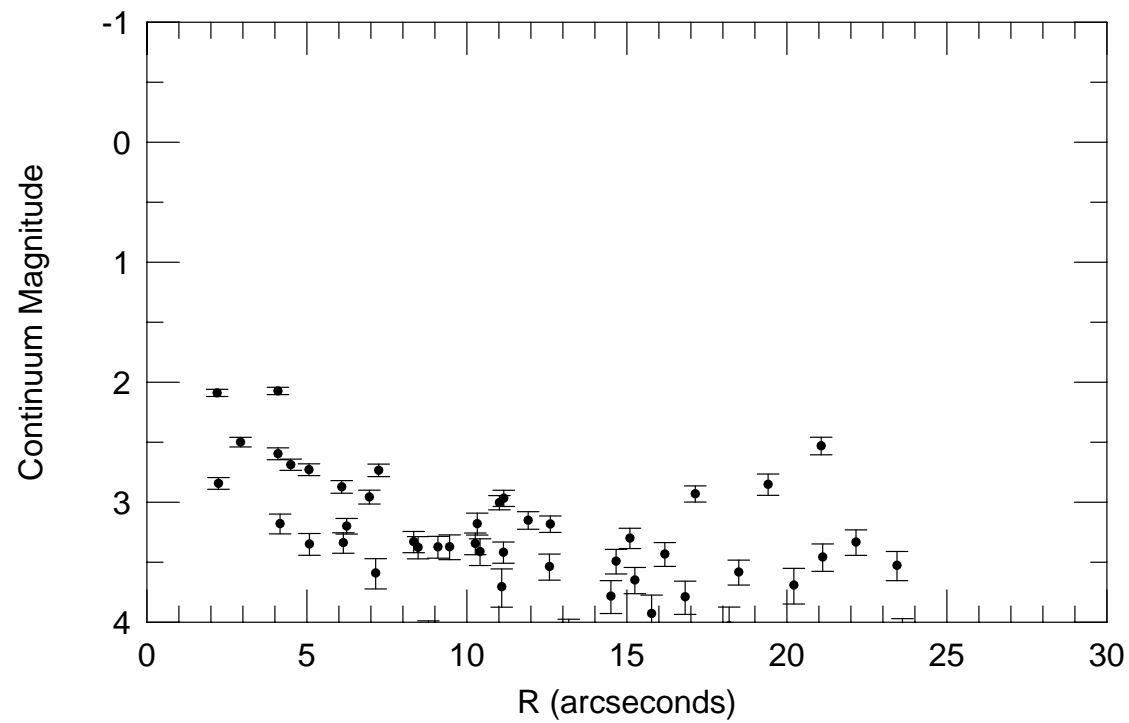
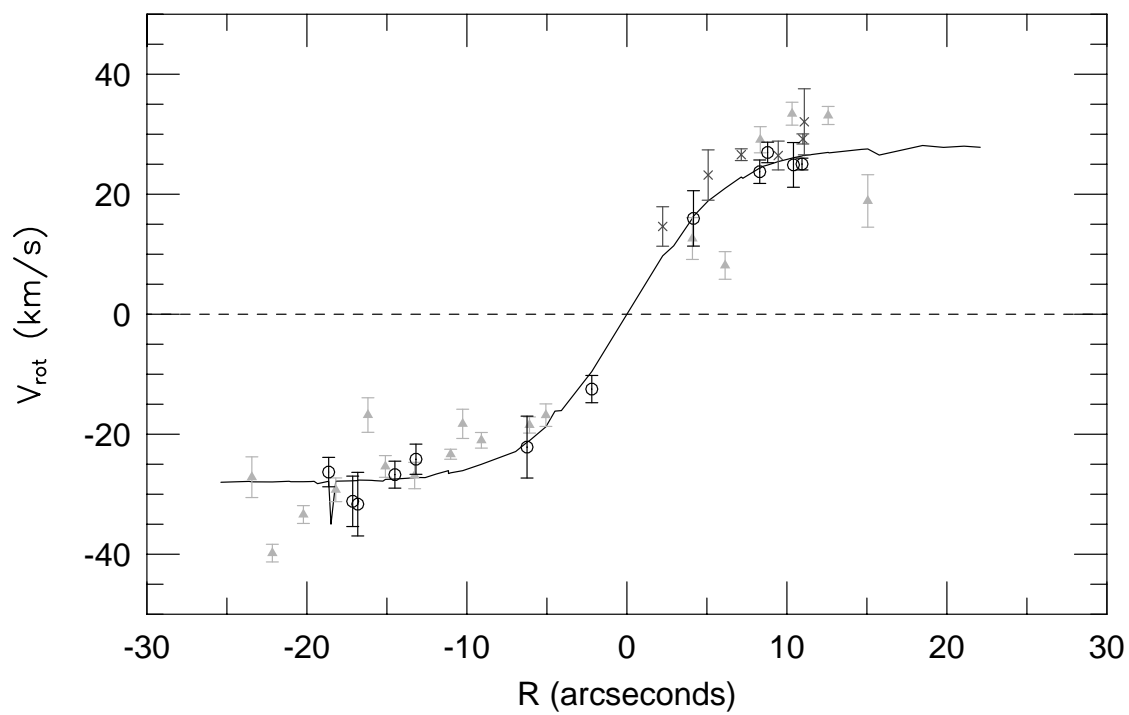
## p56010



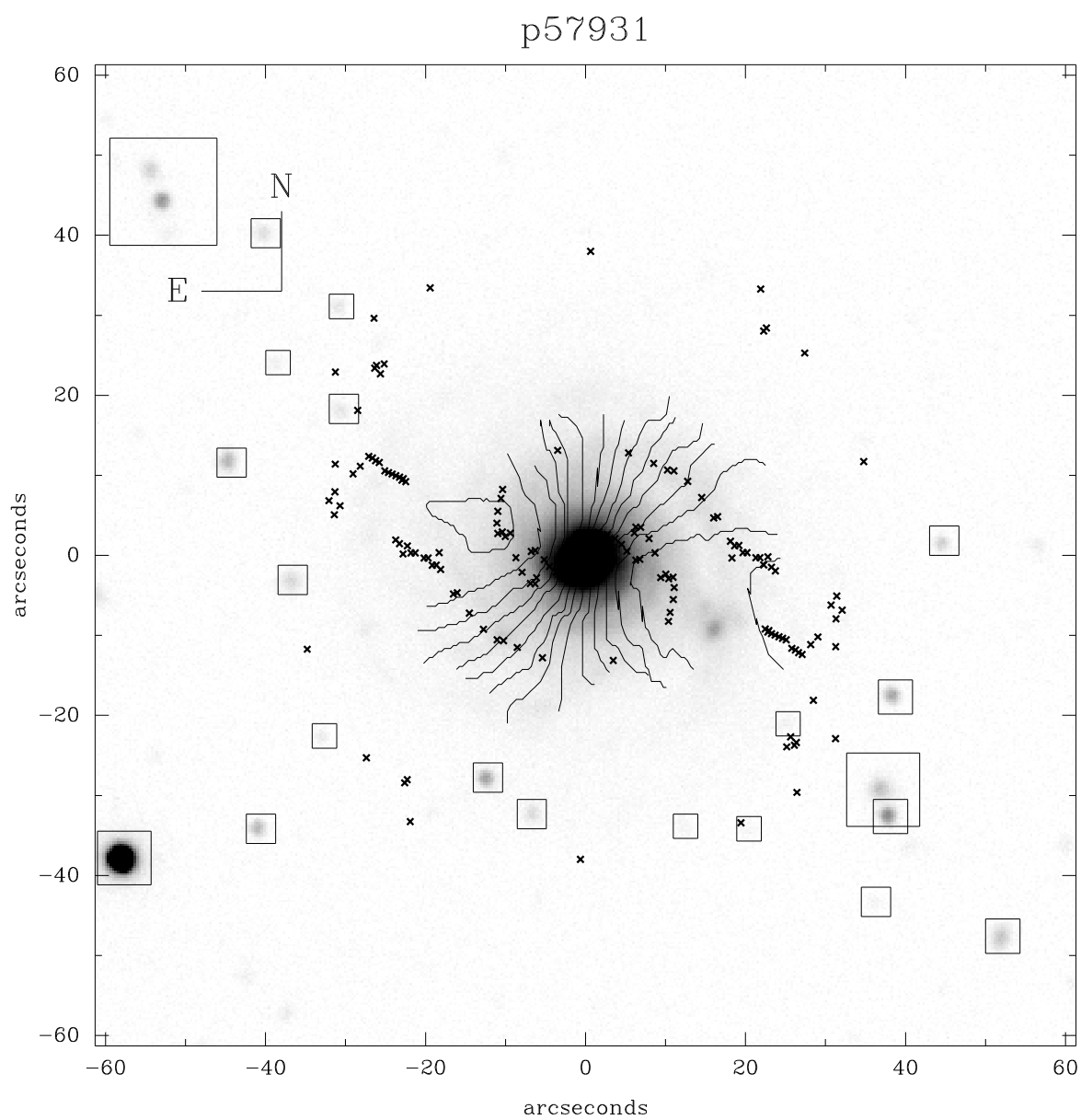
## p56010



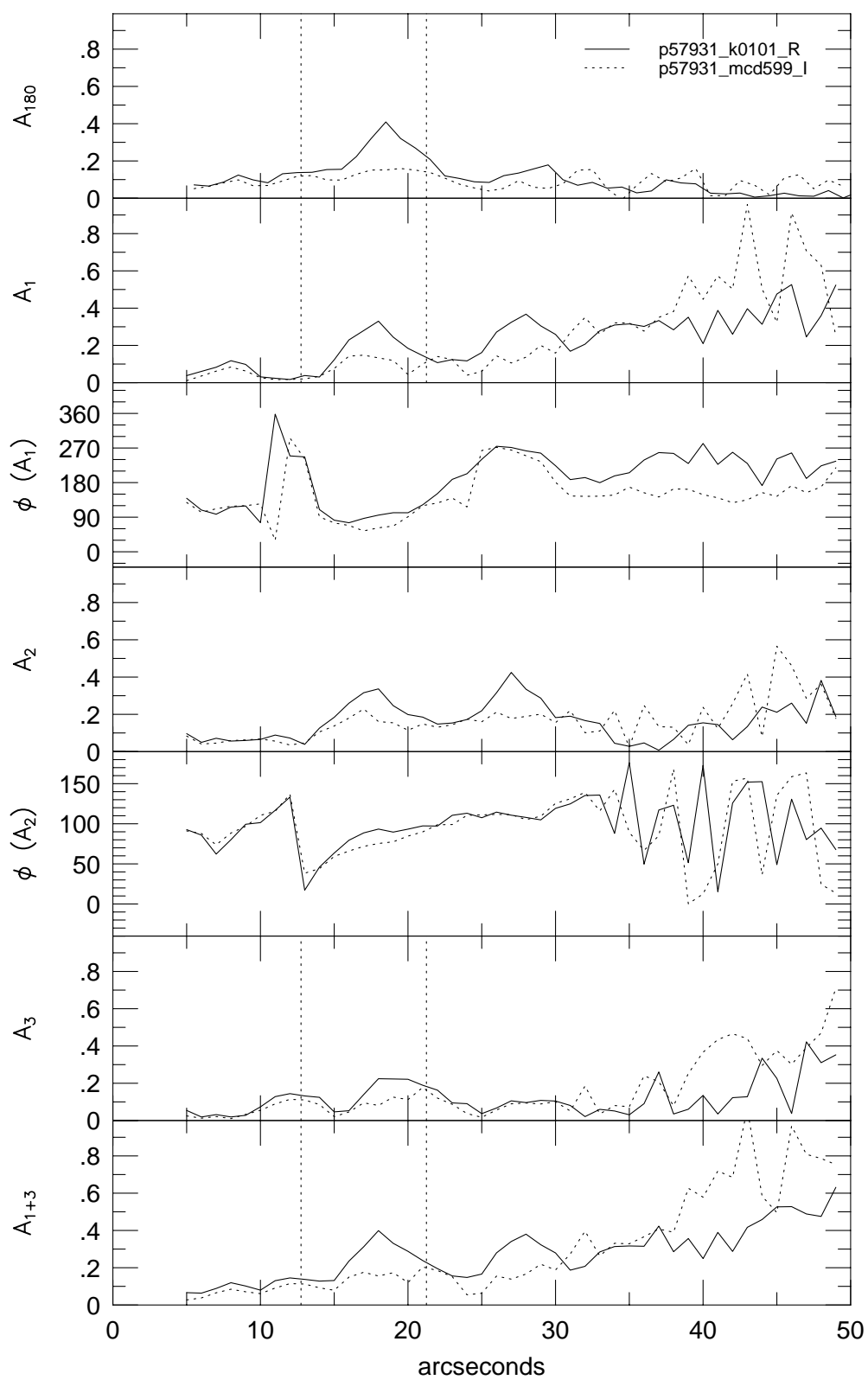
p56010



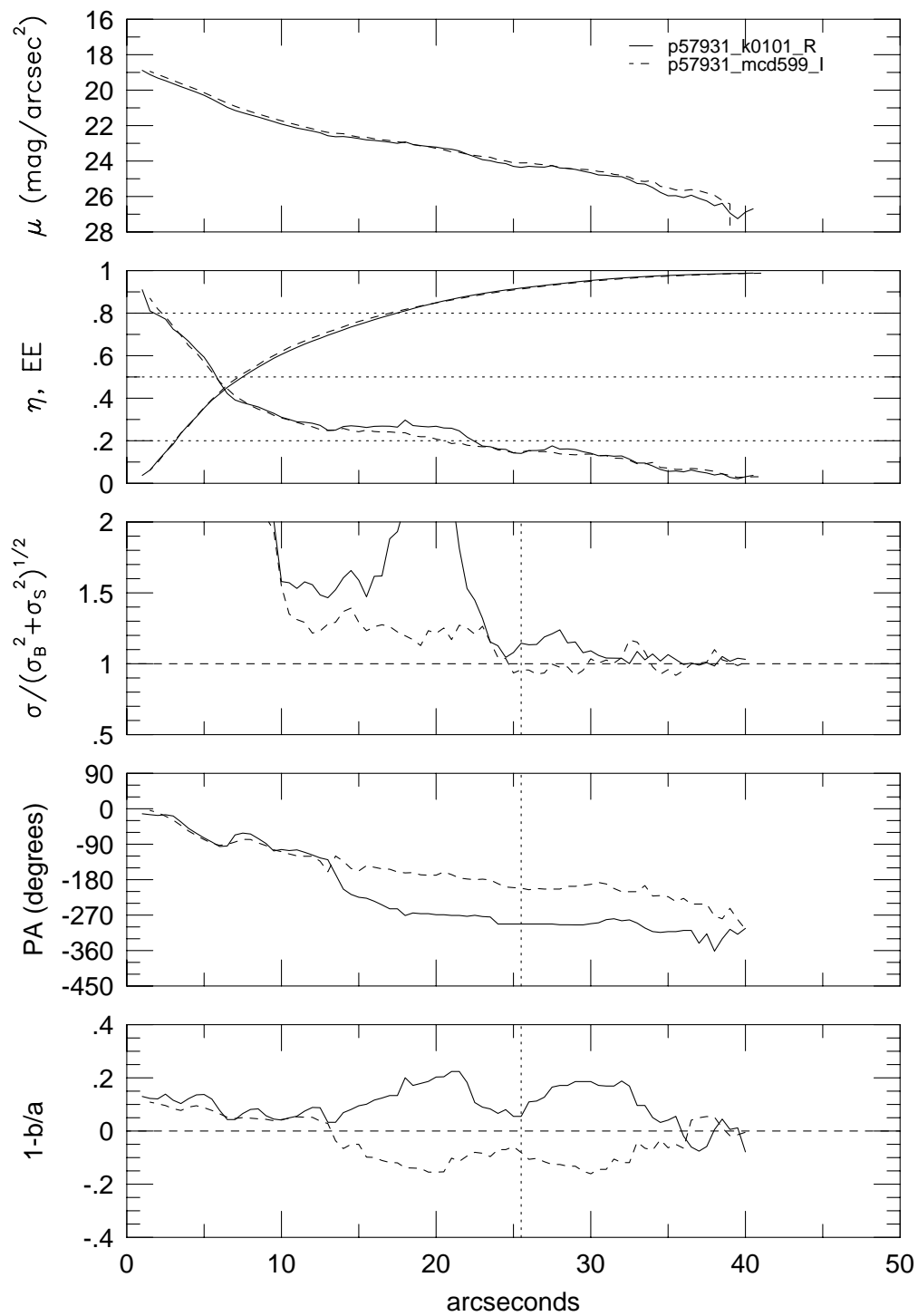




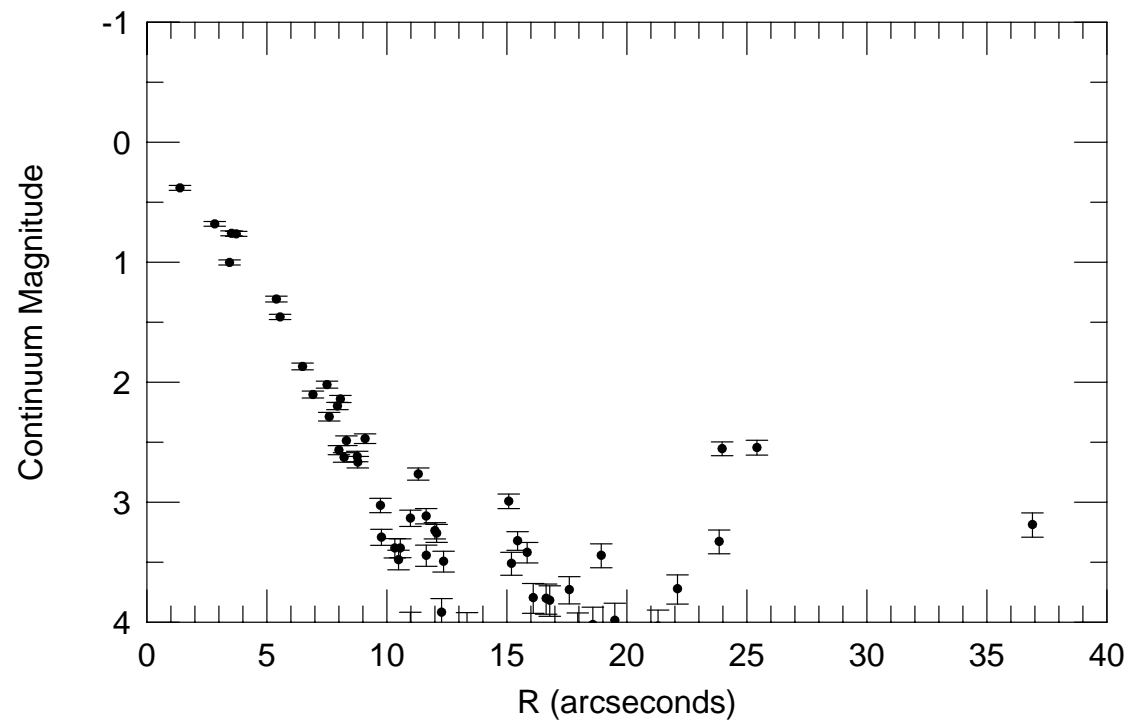
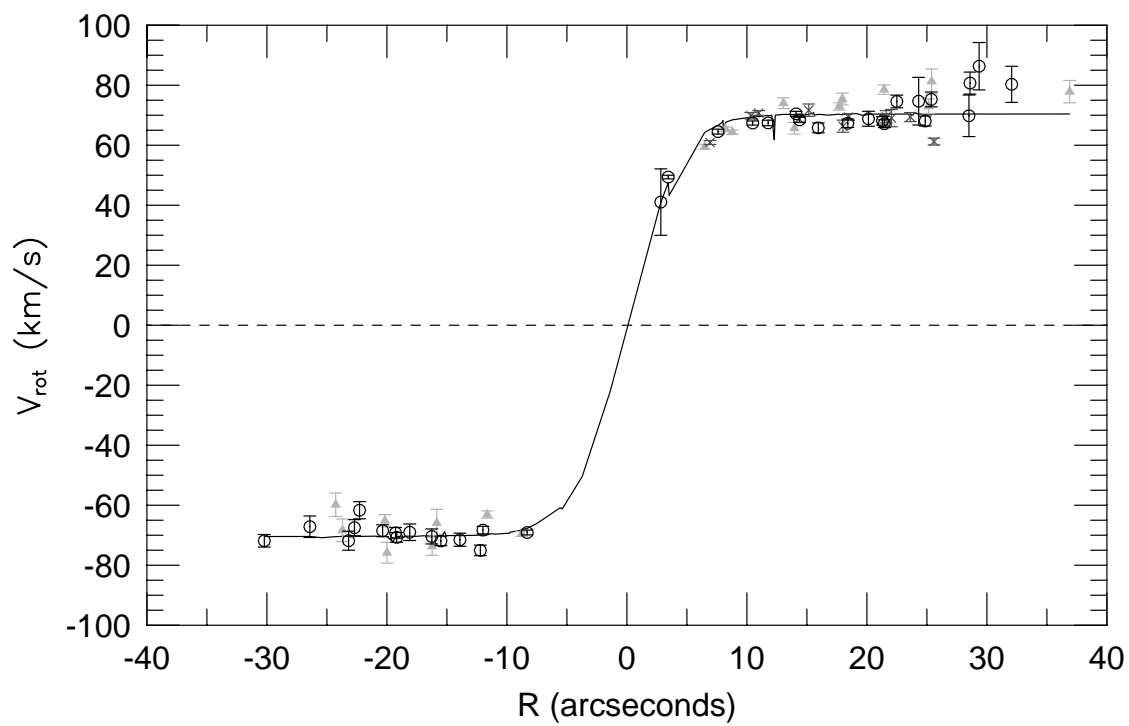
p57931

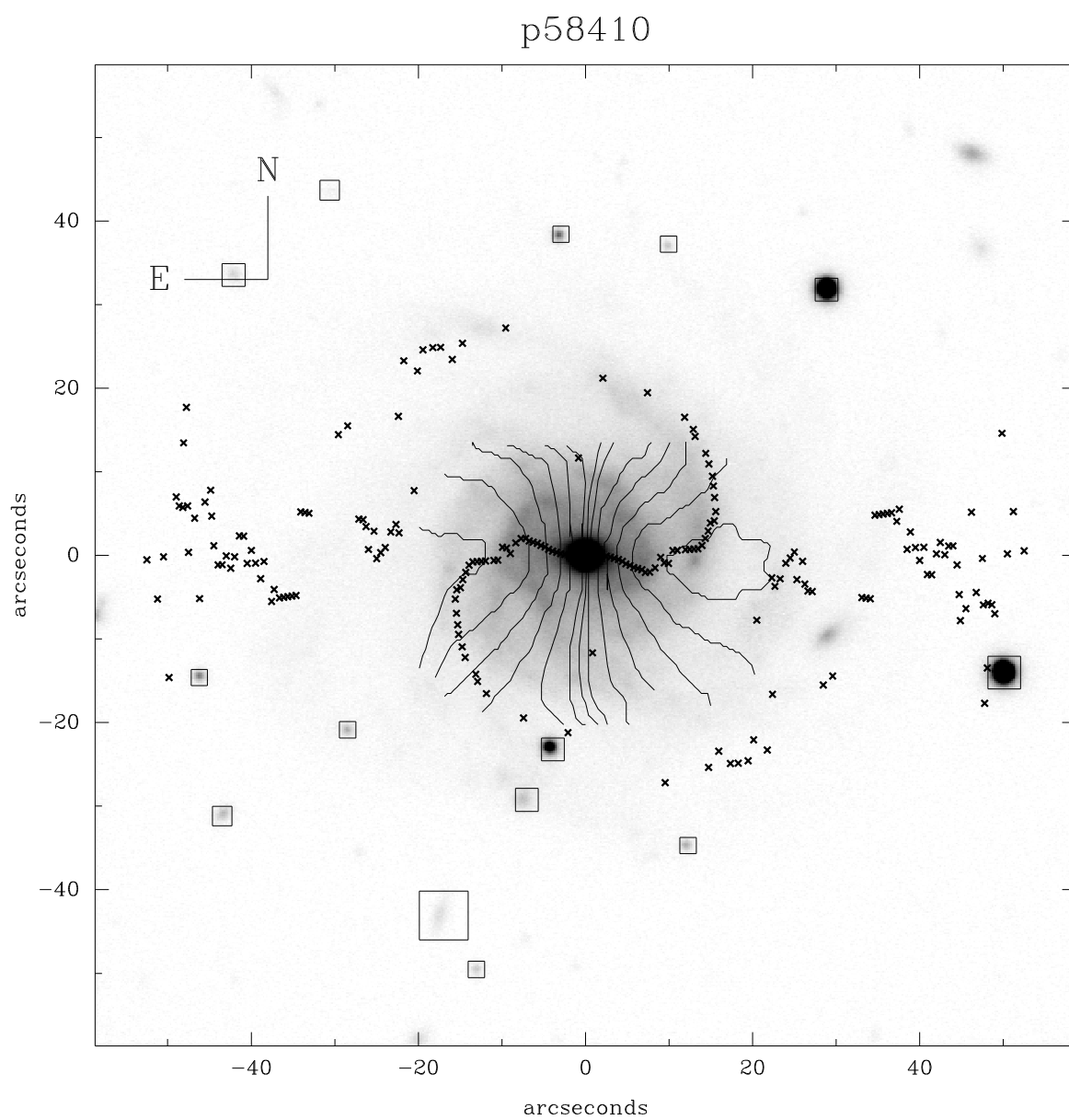


## p57931

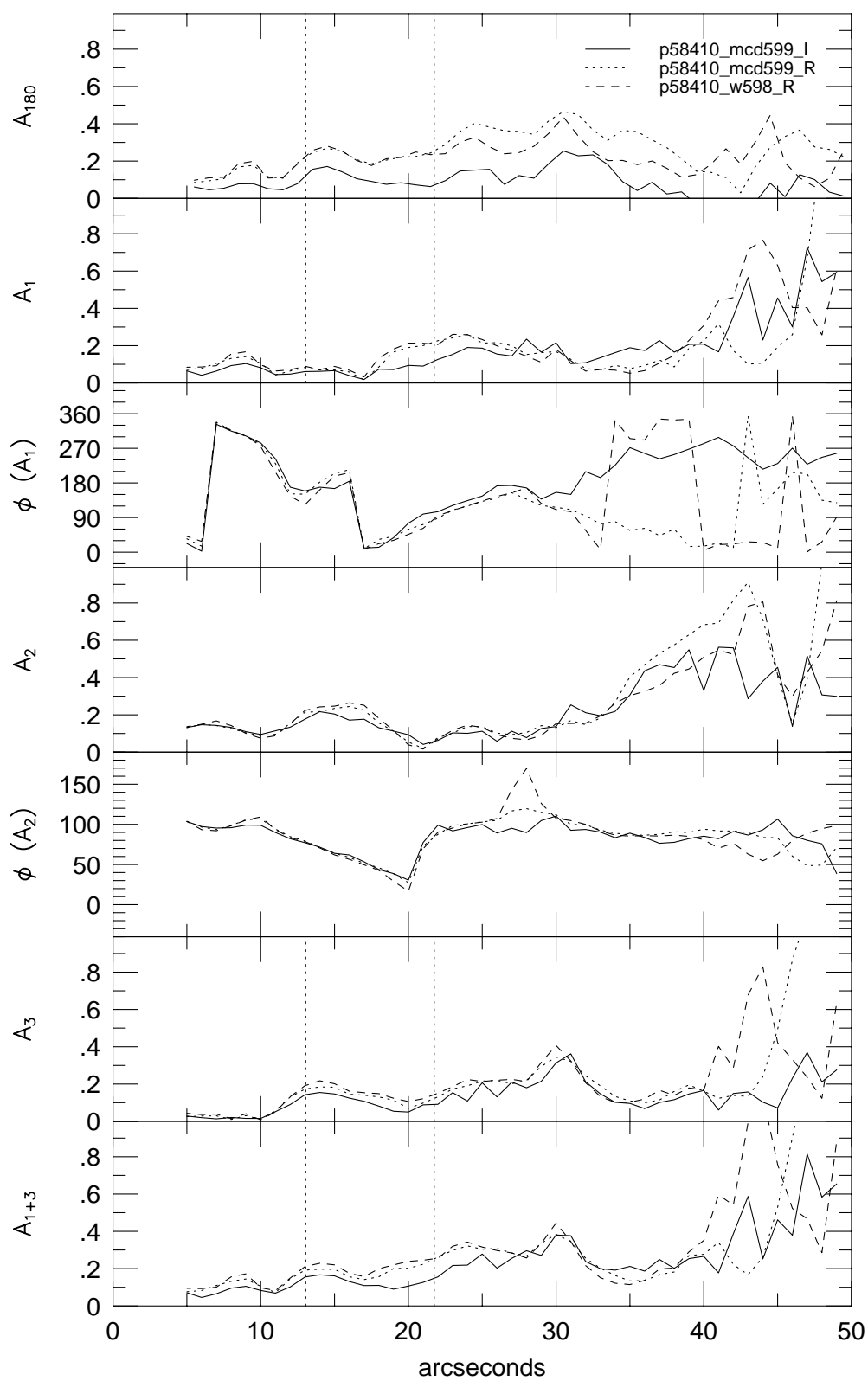


p57931

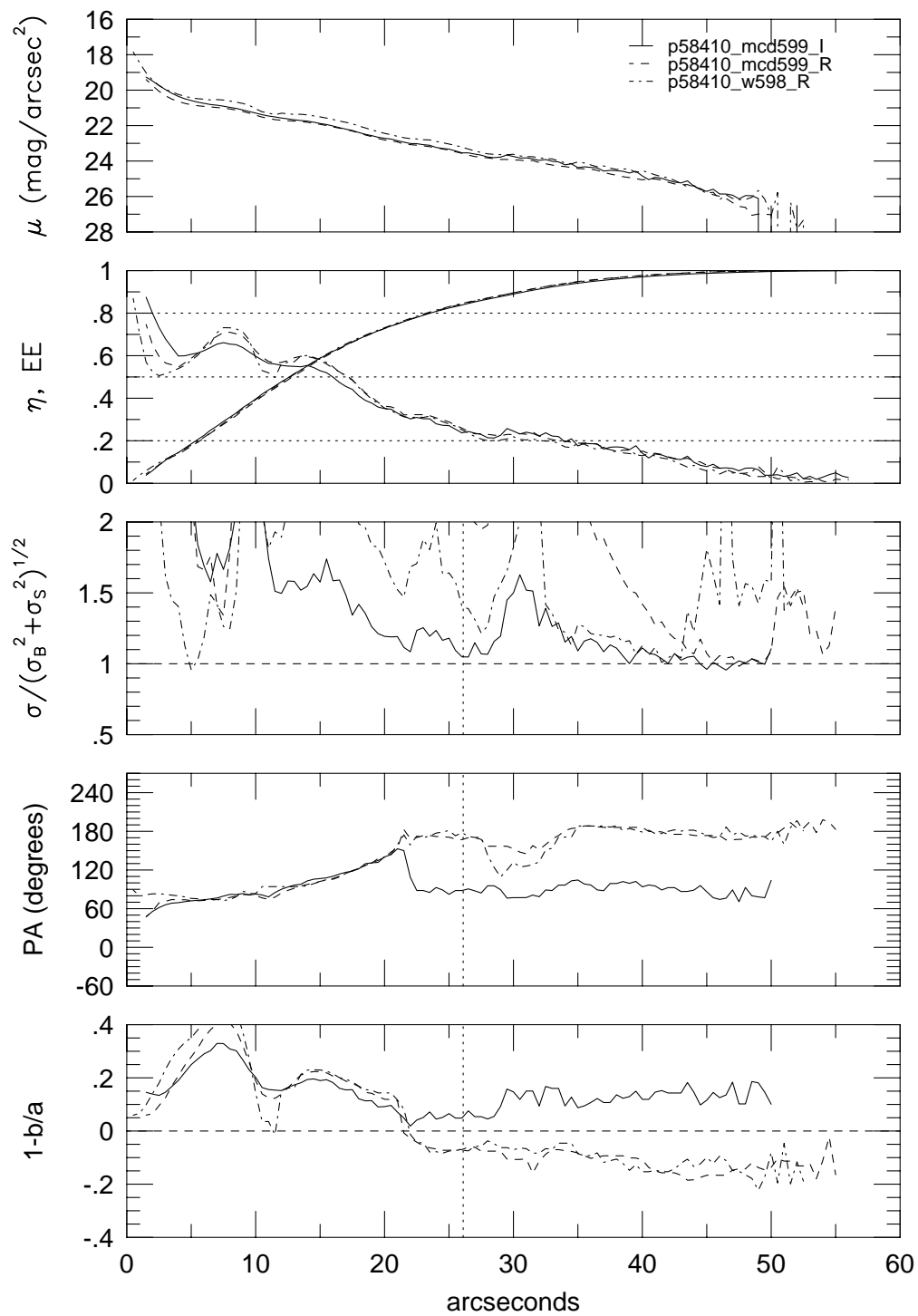




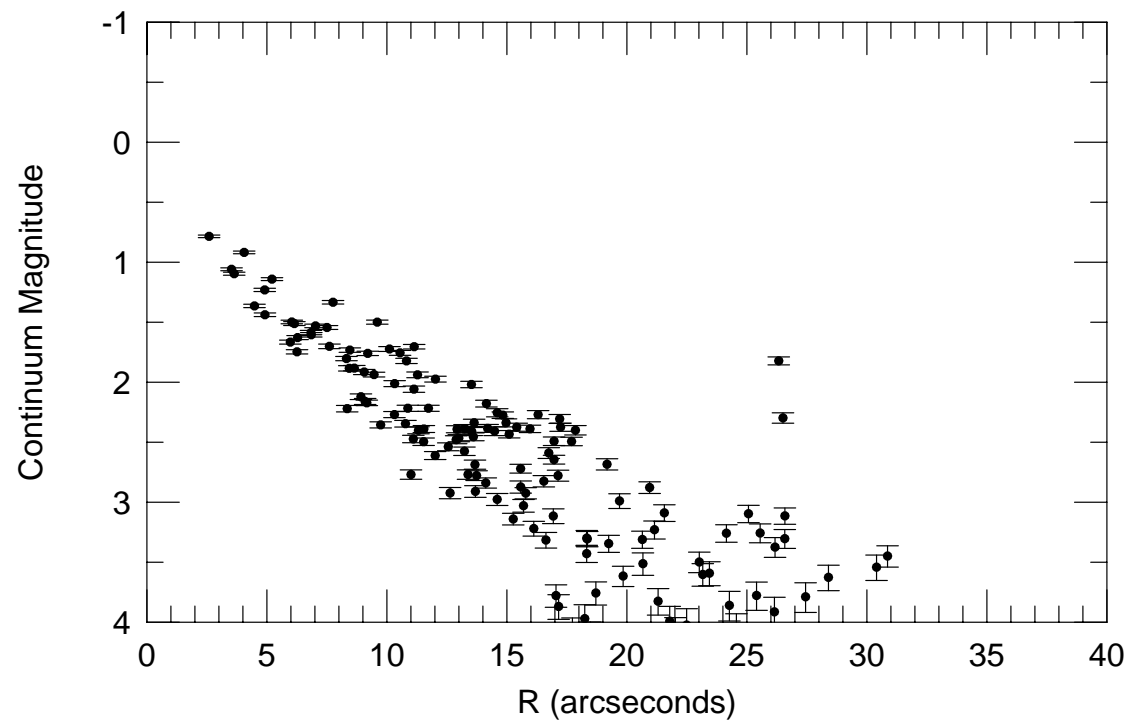
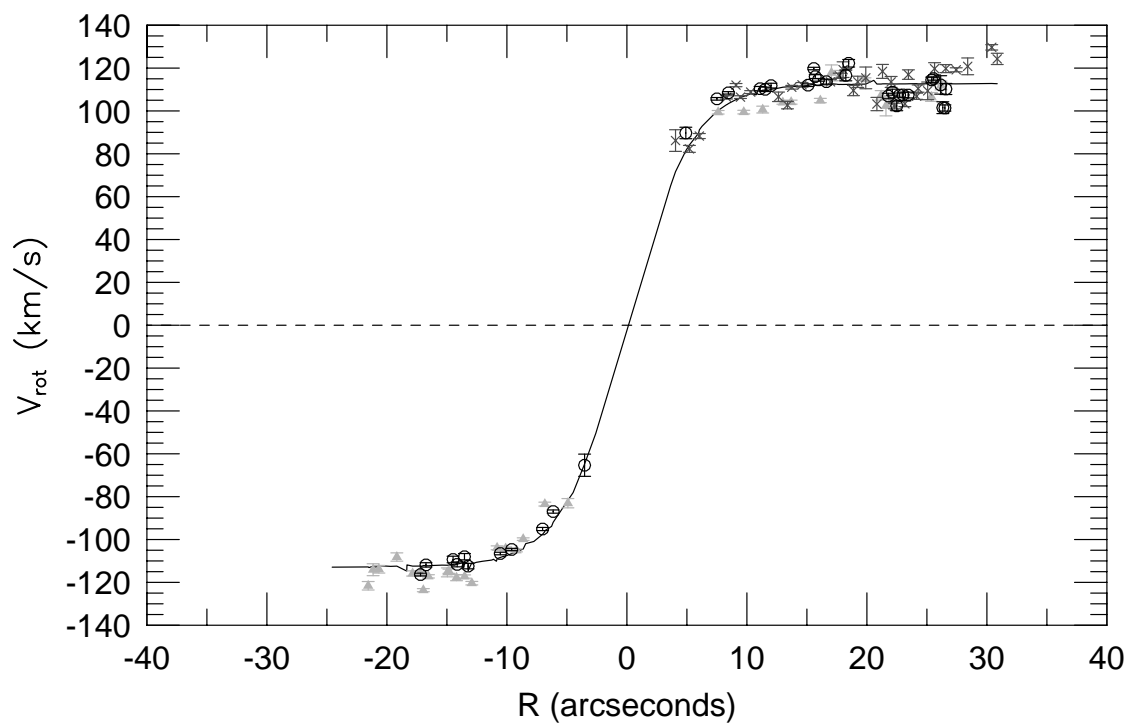
p58410



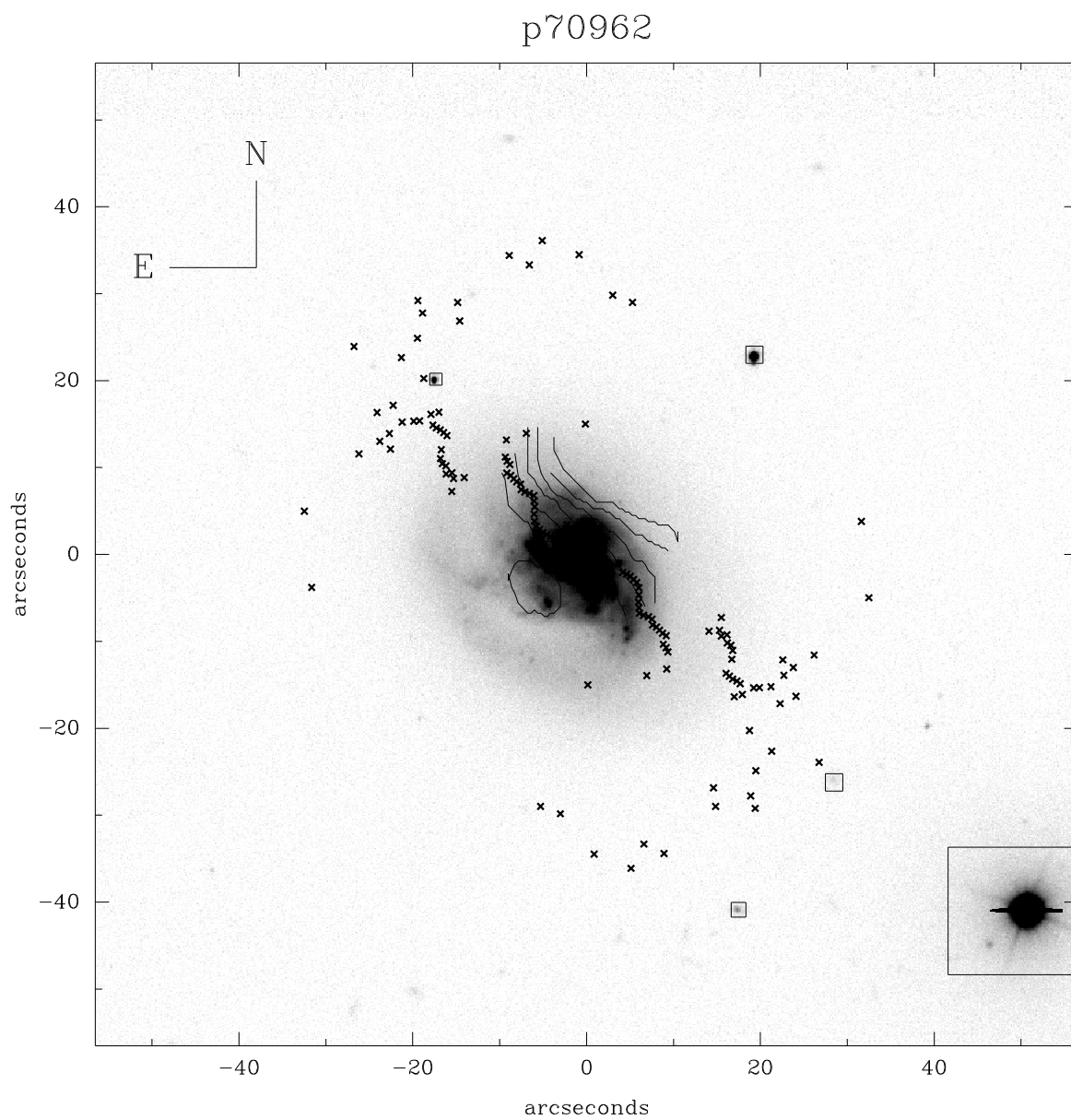
## p58410



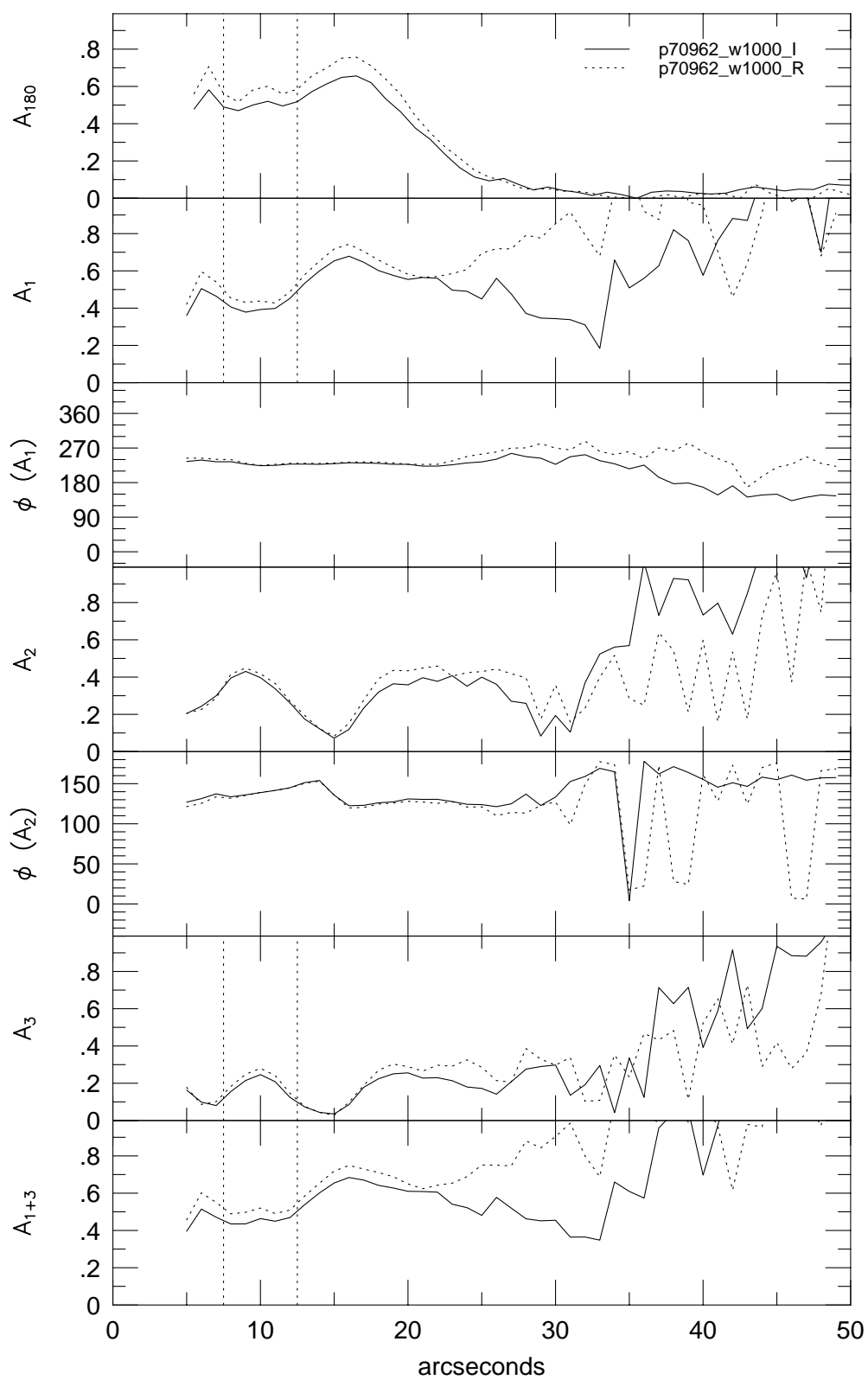
p58410



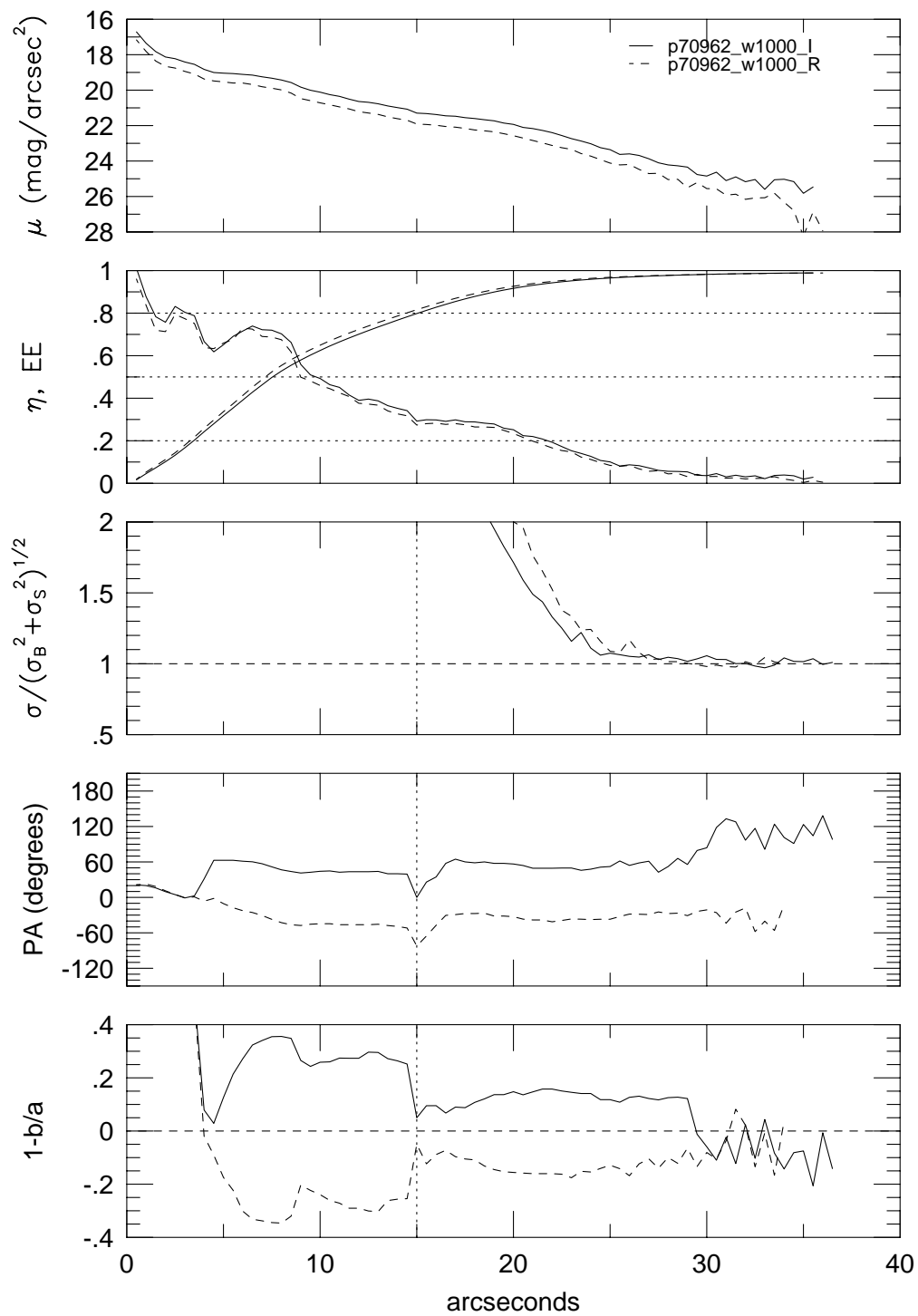




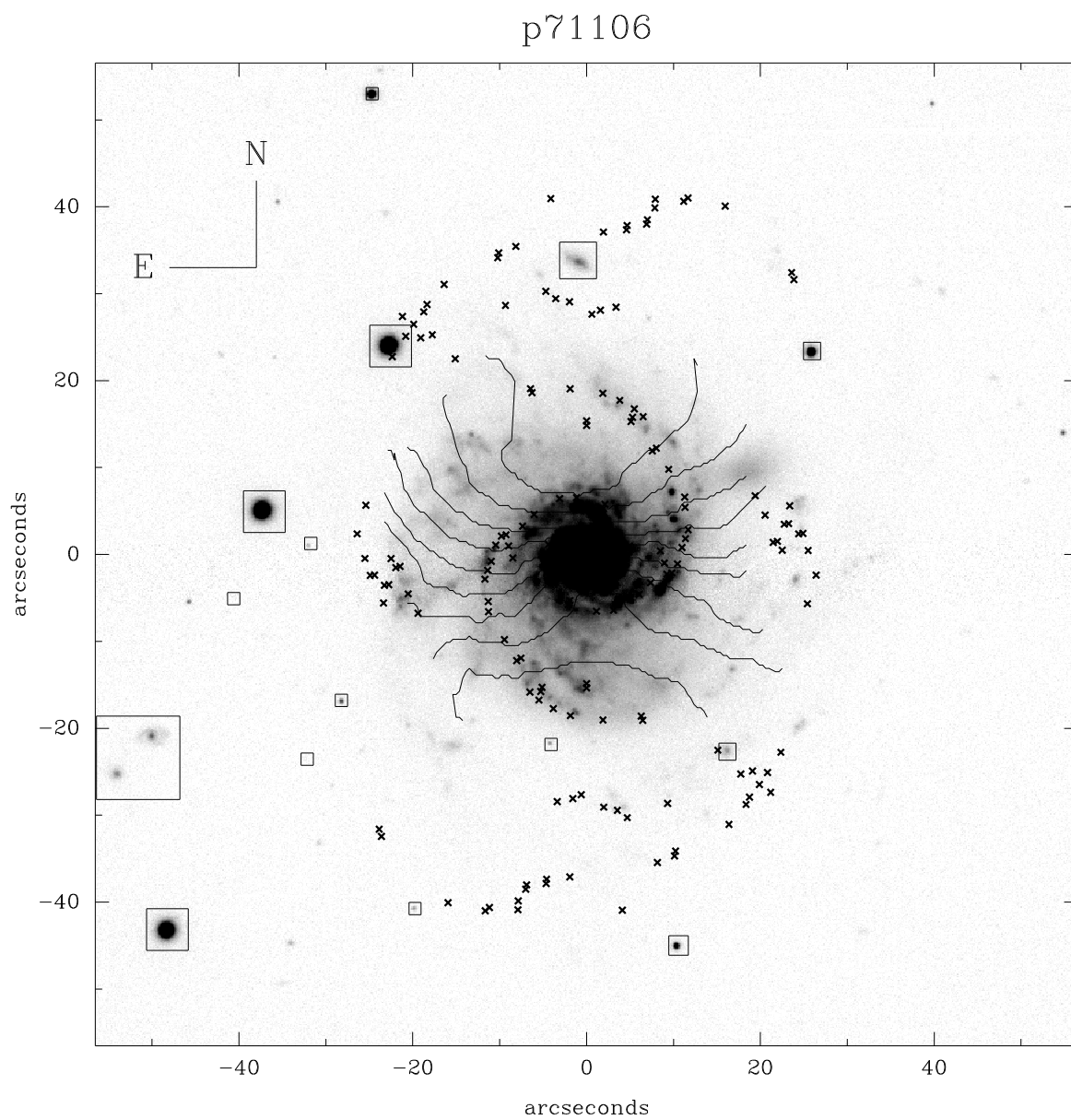
p70962



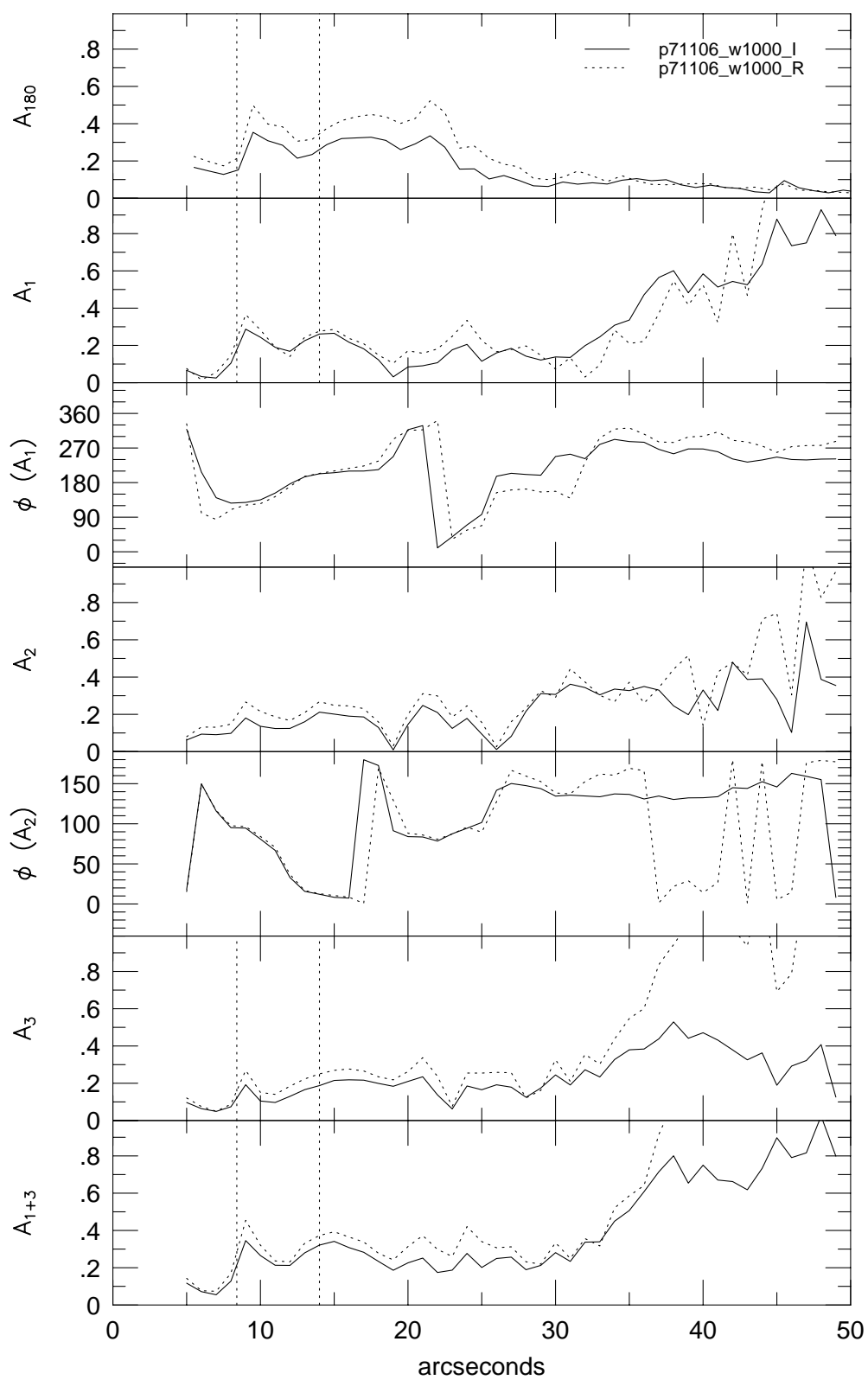
p70962



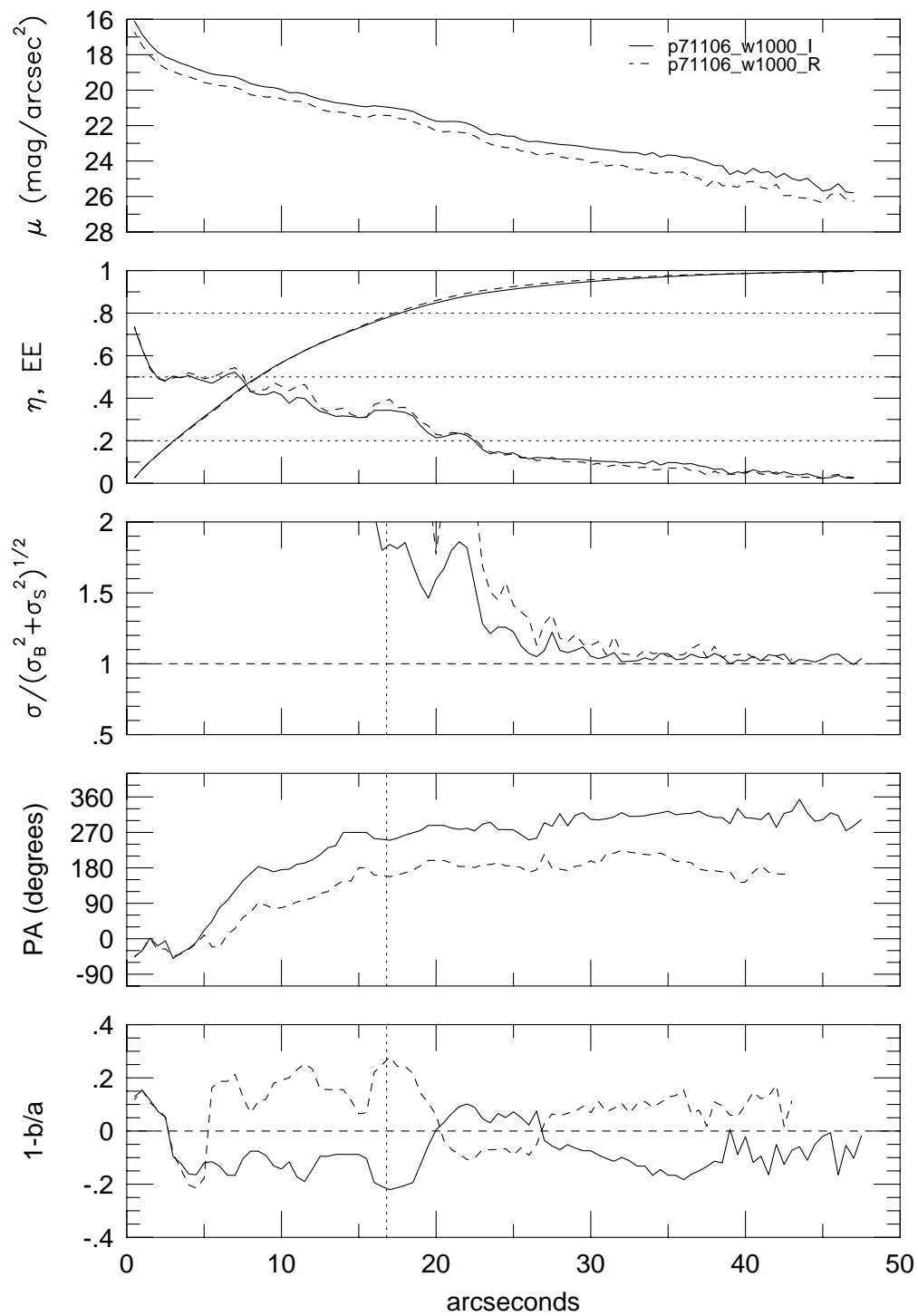




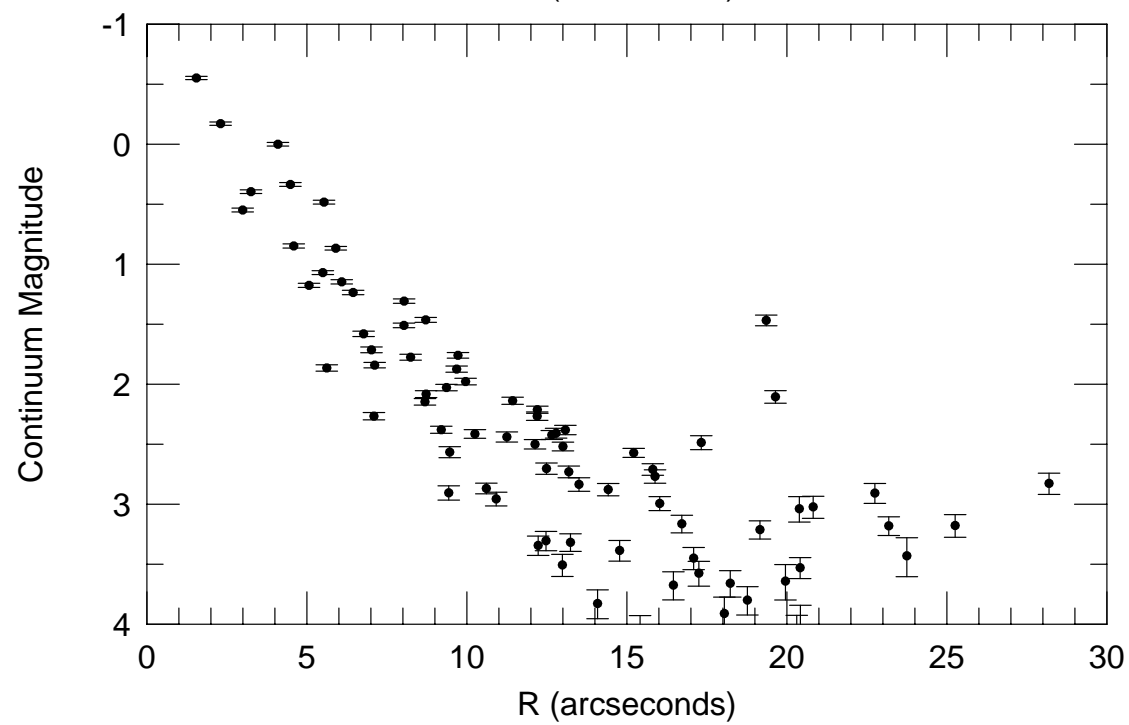
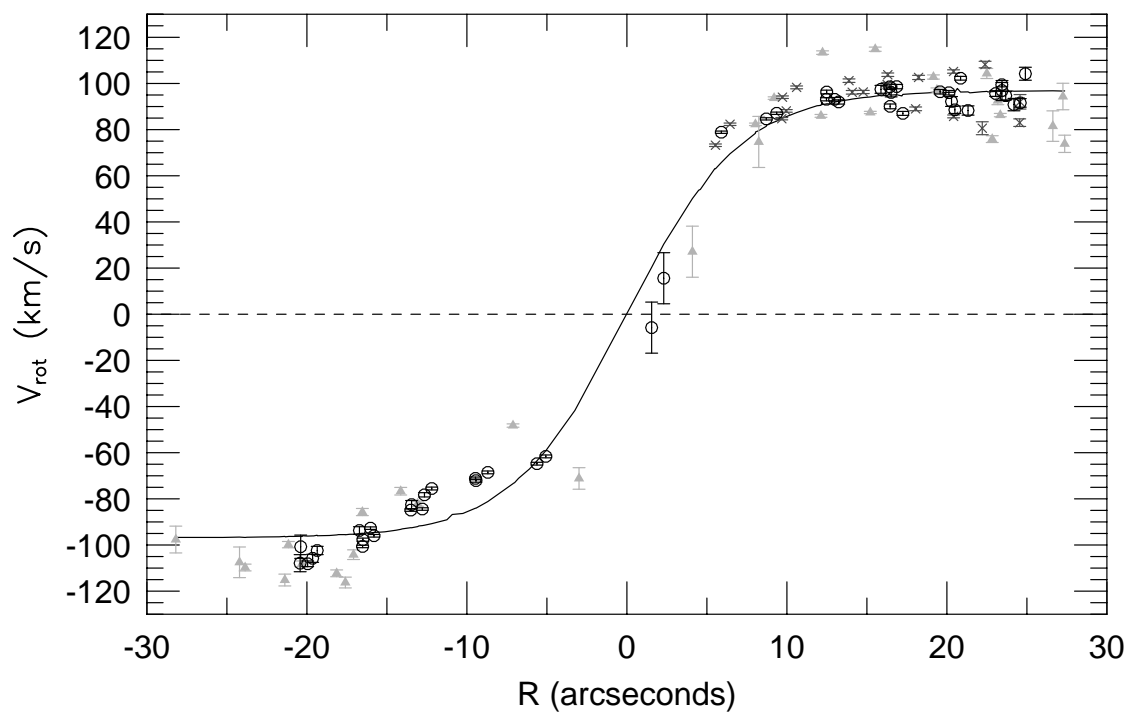
## p71106



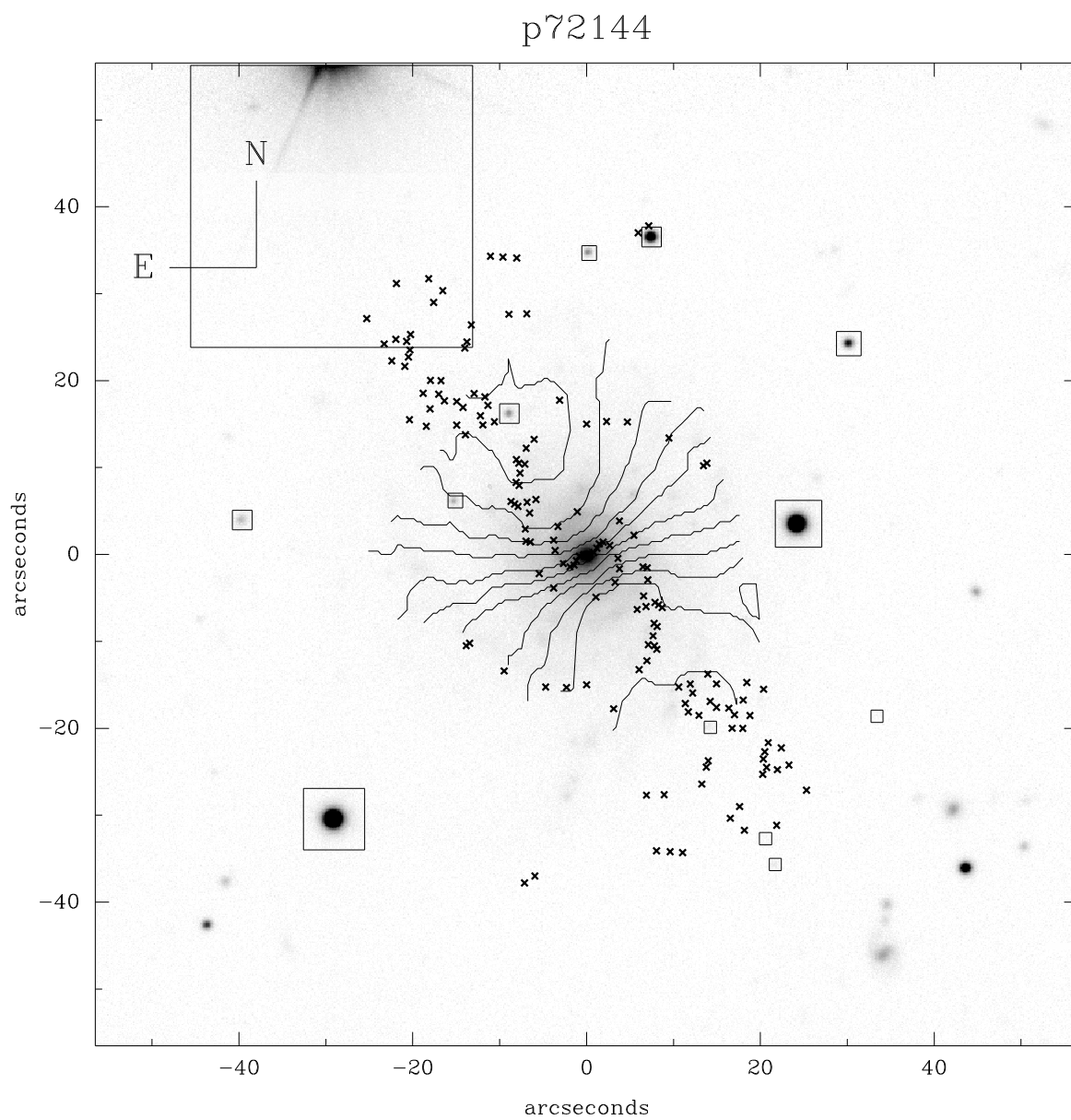
## p71106



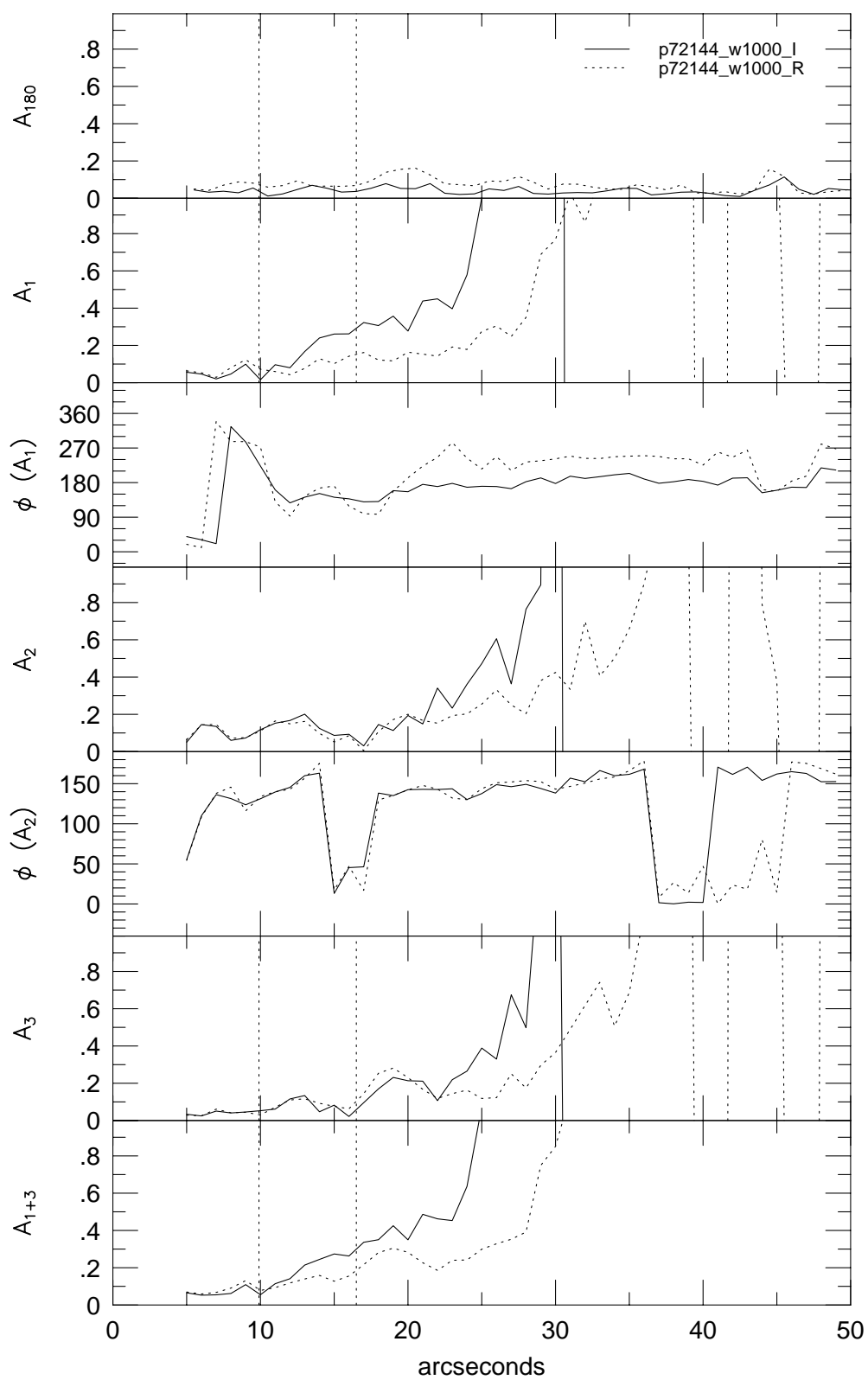
p71106



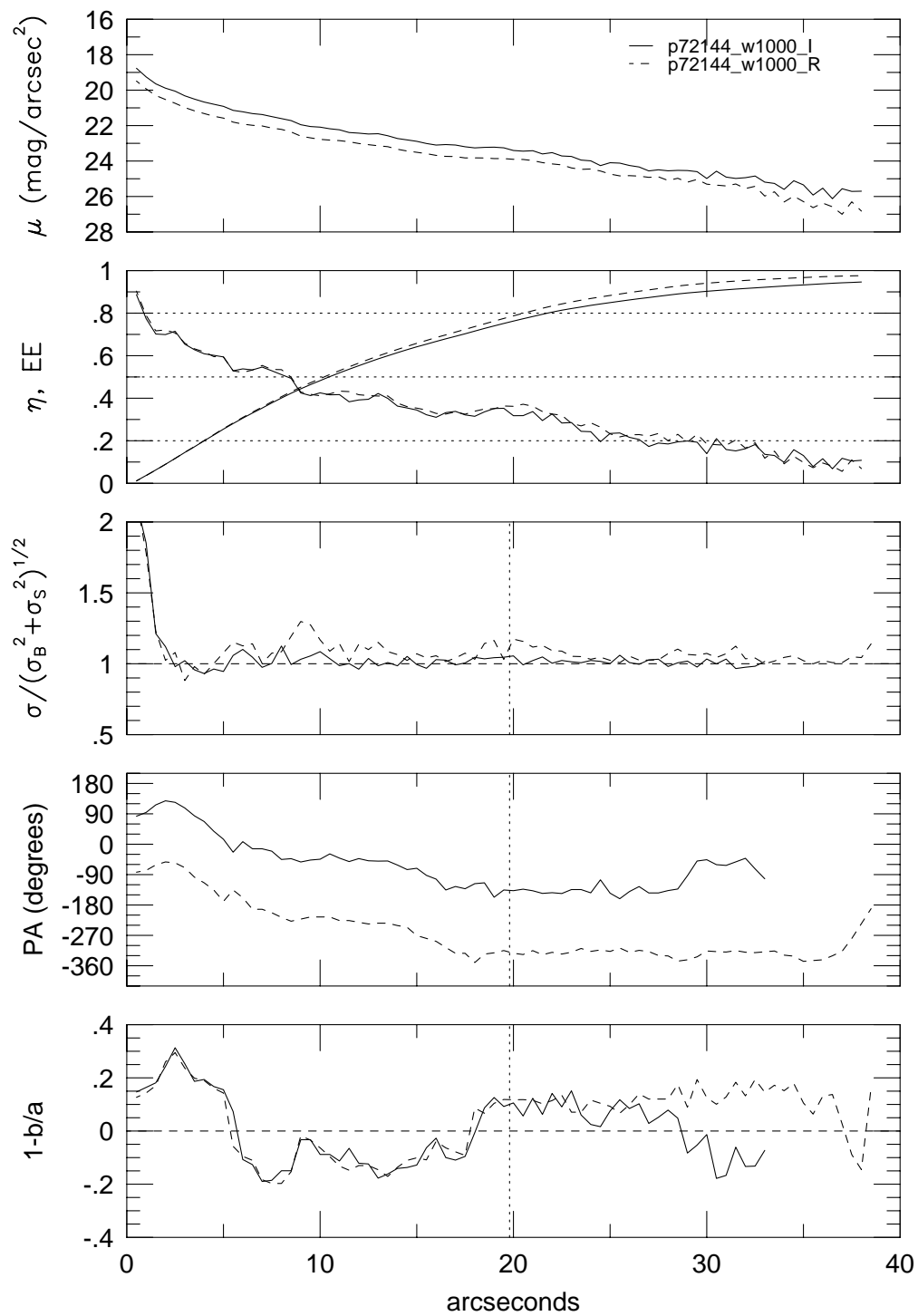




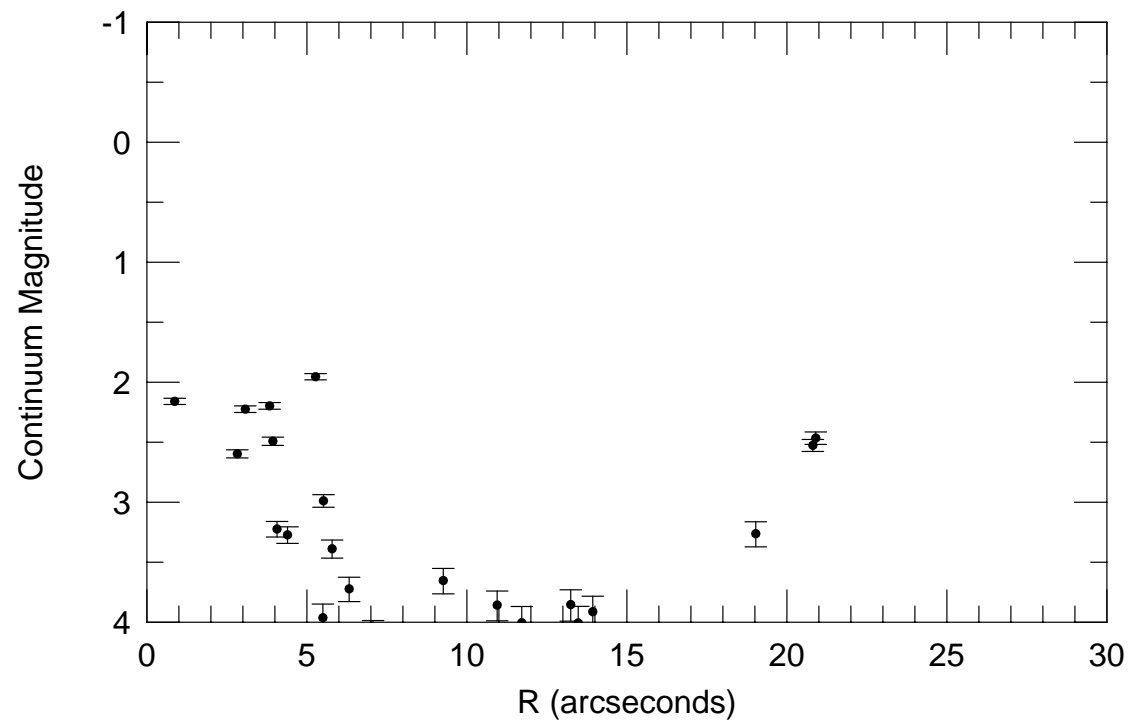
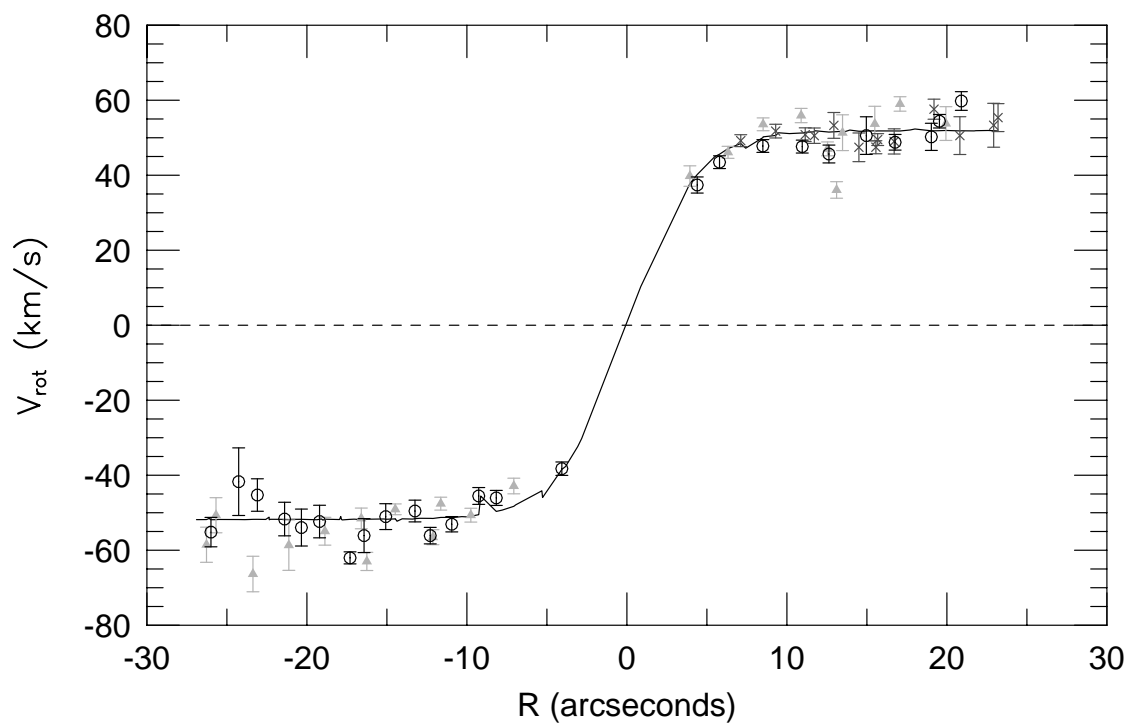
p72144

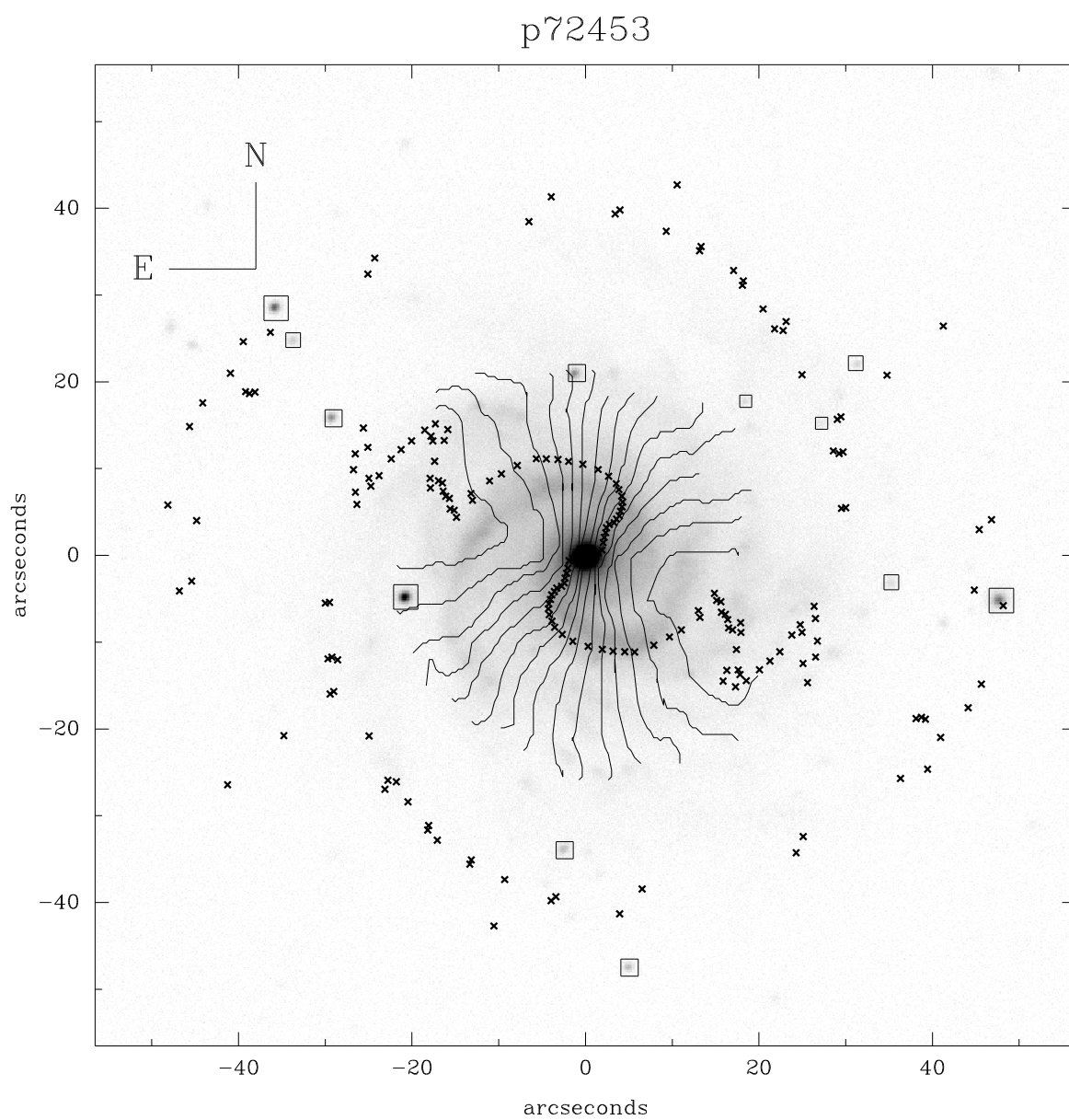


p72144

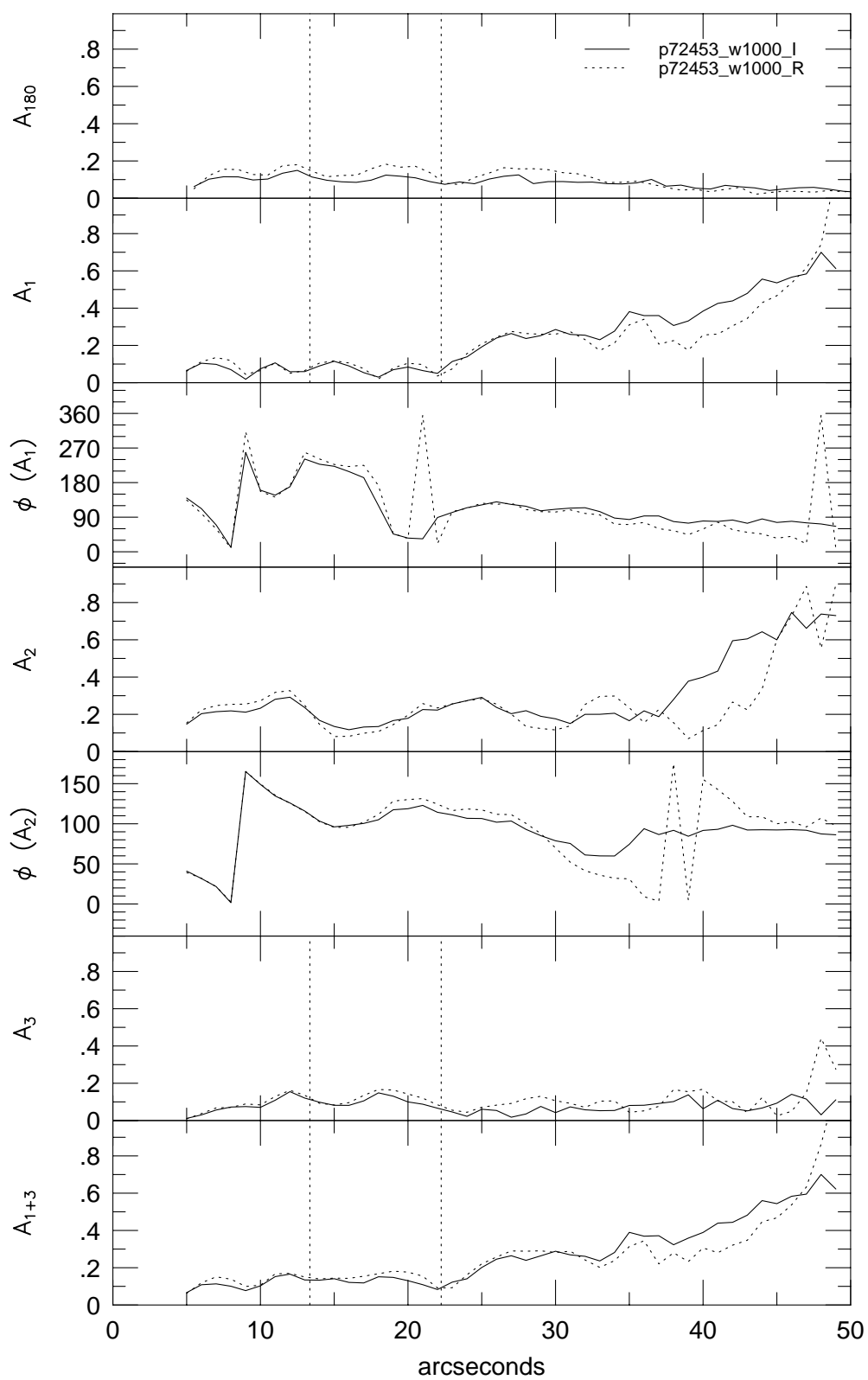


p72144

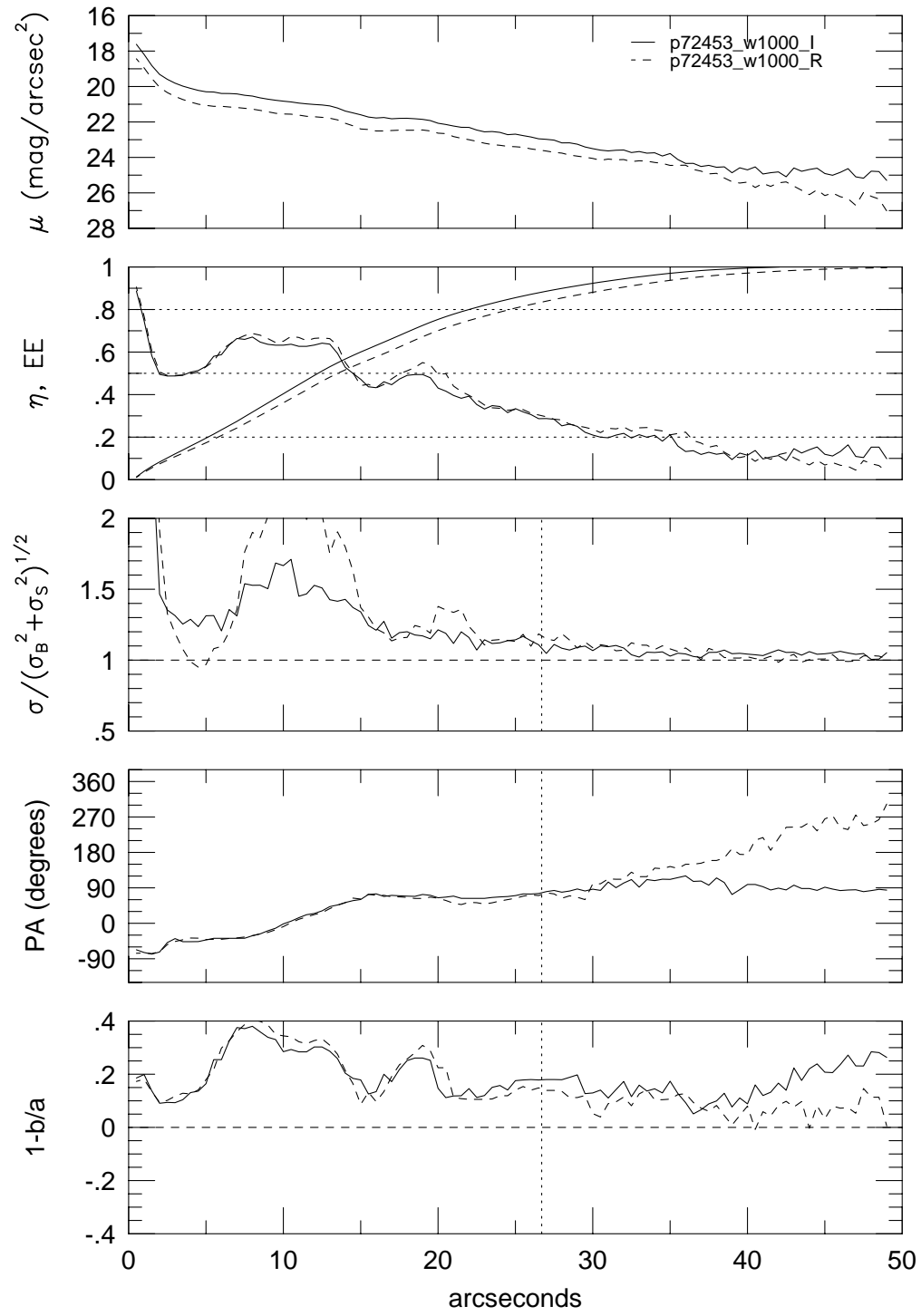




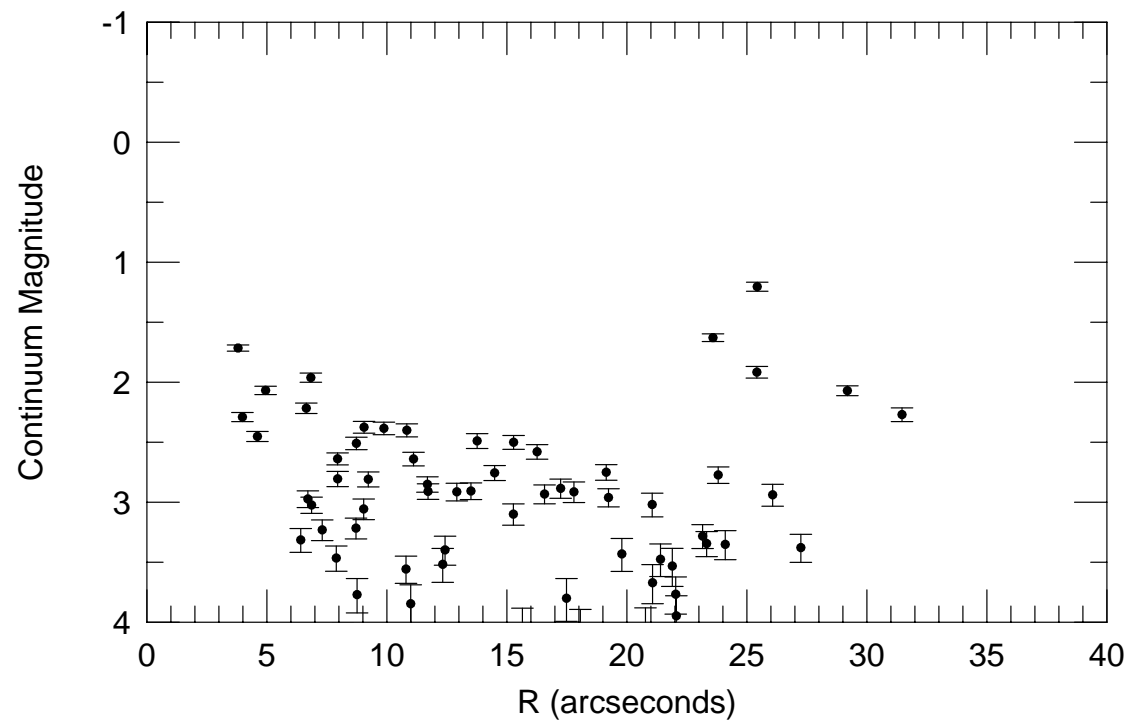
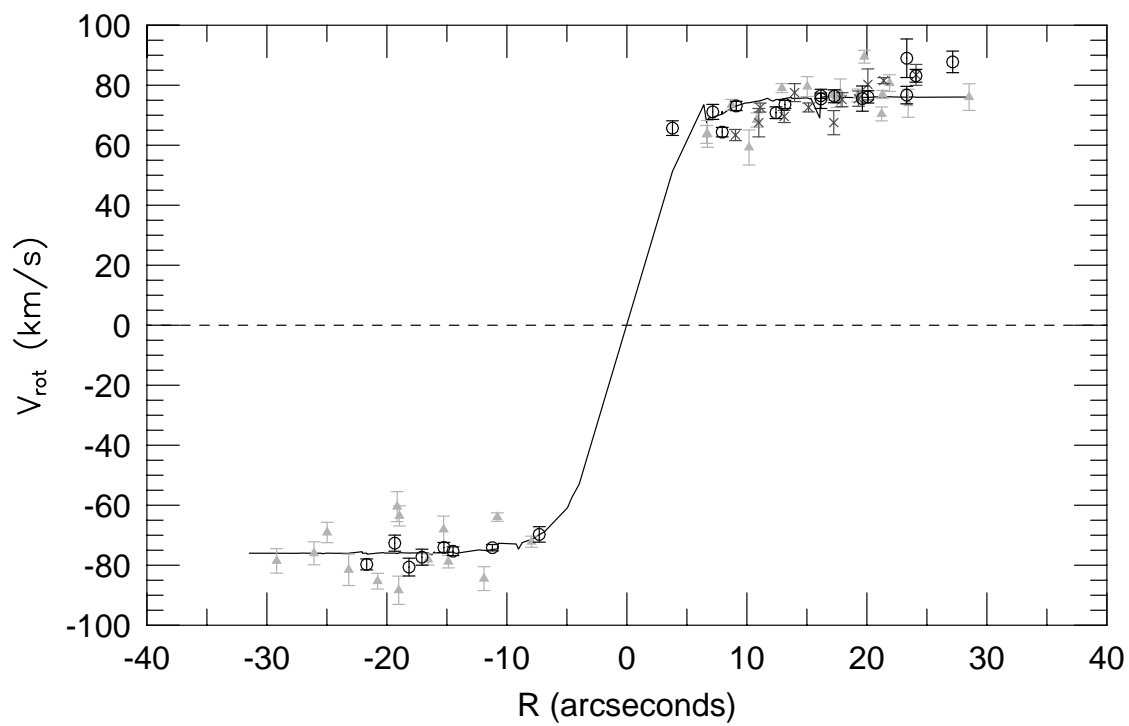
p72453



p72453



p72453





## Bibliography

- Aalto, S., Hüttemeister, S., Scoville, N.Z., Thaddeus, P. 1999, *Ap.J.*, 552, 165
- Abraham, R.G., Tanvir, N.R., Santiago, B.X., Ellis, R.S., Glazebrook, K. & van den Bergh, S. 1996, *M.N.R.A.S.*, 279, L47
- Abraham, R.G., van den Bergh, S., Glazebrook, K., Ellis, R.S., Santiago, B.X., Surma, P. & Griffiths, R.E. 1996, *Ap.J.S.*, 107, 1
- Adler, D.S. & Westpfahl, D.J. 1996, *A. J.*, 111, 735
- Alfaro, E.J. *et al.* 2001, *Ap.J.*, 550, 253
- Andersen, D.R., Bershad, M.A., Sparke, L.S., Gallagher, J.S. & Wilcots, E.M. 2001, *Ap.J.*, L., 551, 131
- Andredakis, Y.C. & Sanders, R.H. 1994, *M.N.R.A.S.*, 267, 283
- Baldwin, J. E., Lynden-Bell, D., & Sancisi, R. 1980, *MNRAS*, 193, 313
- Barden, S. C., Sawyer, D. G., & Honeycutt, R. K. 1998, *SPIE*, 3355, 892
- Battaner, E. & Florido, E. 2000, *astro-ph/0010475*
- Beauvais, C. & Bothun, G. 1999, *Ap.J.S.*, 125, 99
- Begeman, K. 1987, Ph.D. Thesis, Univeristy of Groningen
- Begeman, K. 1989, *A&A*, 223, 47

- Begeman, K., Broeils, A.H. & Sanders, R.H. 1991, M.N.R.A.S., 249, 523
- Bernstein, G.M. *et al.* 1994, A. J., 107, 1962
- Bershady, M.A., Jangren, A., Conselice, C.J. 2000, A. J., 119, 2645
- Bershady, M.A. & Andersen, D.R. 2001, ASP Conf. Ser. 230: Galaxy Disks and Disk Galaxies, p. 589
- Bershady, M.A., Andersen, D.R., Harker, J., Verheijen, M.A. 2001, *in preparation*
- Bicay & Giovanelli 1986, AJ, 91, 705
- Biermann *et al.* 1979, A&A, 75, 19
- Bieging & Biermann, 1983, AJ, 88, 161
- Binney, J. & De Vaucouleurs, G. 1981, MNRAS, 194, 679
- Binney, J. 1978, M.N.R.A.S., 183, 501
- Boroson, T. 1981, Ap.J.S., 46, 177
- Bosma, A. 1981a, A. J., 86, 1791
- Bosma, A. 1981b, A. J., 86, 1825
- Bothun *et al.* 1985, ApJS, 57, 423
- Briggs, F.H. 1990, Ap.J., 352, 15
- Broeils, A.H. 1992, Ph.D. Thesis, Univeristy of Groningen
- Cardelli, J.A., Clayton, G.C. & Mathis, J.S. 1989, Ap.J., 345, 245

- Christodoulou, D.M., Tohline, J.E., Steiman-Cameron, T.Y. 1993, Ap.J., 416, 74
- Comins, N.F., Lovelace, R.V.E., Zeltwanger, T., Shorey, P. 1997, Ap.J., L., 484, 33
- Conselice, C. J., Bershady, M. A., & Jangren, A. 2000, ApJ, 529, 886
- Courteau, S. 1992, P.A.S.P., 104, 976
- Courteau, S. 1996, Ap.J.S., 103, 363
- Courteau, S. 1997, A. J., 114, 2402
- Courteau, S. & Rix, H.W. 1999, Ap.J., 513, 561
- Cousins, A.W.J. 1978, MNASSA, 37, 8
- Dalcanton, J., Spergel, D.N. & Summers, F.J. 1997, Ap.J., 482, 659
- Dale, D.A. *et al.* 2001, A. J., 121, 1886
- Davies, R.L. *et al.* 2001, Ap.J., L., 548, L33
- de Blok, W.J.G., McGaugh, S.S., Bosma, A., Rubin, V.C. 2001, Ap.J., L., 552, 23
- de Jong, R.S. 1996a, A&A Supplement Series, 118, 557
- de Jong, R.S. 1996b, A&A, 313, 45
- de Vaucouleurs, G. 1953, M.N.R.A.S., 113, 134
- de Vaucouleurs, G. 1959, Handbuch der Physik, 53, 275
- de Vaucouleurs, G. *et al.* 1991, Third Reference Catalogue of Bright Galaxies (New York: Springer-Verlag).

- Driver, S.P., Fernandez-Soto, A., Couch, W. J., Odewahn, S. C., Windhorst, R.A.,  
Phillips, S., Lanzetta, K. & Yahil, A. 1998, Ap.J., L., 496, L93
- Driver, S.P., Windhorst, R.A., & Griffiths, R.E. 1995, Ap.J., 453, 48
- Dubinski, J., Carlberg, R.G. 1991, Ap.J., 378, 496
- Dubinski, J. 1994 Ap.J., 431, 617
- Fasano, G., Pisani, A., Vio, R., Girardi, M. 1993, Ap.J., 416, 546
- Fouqué, P., Durand, N., Bottinelli, L., Gouguenheim, L., Paturel, G. 1990, A&A Supplement Series, 86, 473
- Frankston, M., Schild, R. 1976, A. J., 81, 500
- Franx, M., Illingworth, G., Heckman, T. 1989, A. J., 98, 538
- Franx, M. & De Zeeuw, T. 1992, ApJ Letters, 392, L47
- Freeman, K.C. 1970, Ap.J., 160, 811
- Frei, A., Guhathakurta, P., Gunn, J.E. & Tyson, J.A. 1996, A. J., 111 ,174
- Freudling, Haynes, Giovanelli 1992, ApJS, 79, 157
- Fukugita, M., Shimasaku, K. & Ichikawa, T. 1995, P.A.S.P., 107, 945
- Garwood *et al.* 1987, AJ, 322, 88
- Gavazzi 1987, AJ, 320, 96
- Gerssen, J., Kuijken, K., Merrifield, M.R. 1997, M.N.R.A.S., 306, 926

- Gilmore, G.F., King, I.R. & van der Kruit, P.C. 1990, *The Milky Way as a Galaxy*, eds. R. Buser & I.R. King (University Science Books, CA), p 212
- Giovanelli, R., *et al.* 1986, *AJ*, 92, 250
- Giovanelli & Haynes, M.P. 1993, *AJ*, 105, 1271
- Giovanelli, R., *et al.* 1994, *A. J.*, 107, 2036
- Giovanelli, R., *et al.* 1995, *A. J.*, 110, 1059
- Giovanelli, R., *et al.* 1996, *Ap.J., L.*, 464, 99
- Giovanelli, R., *et al.* 1997, *Ap.J., L.*, 477, 1
- Grosbøl, P. J. 1985, *A&A Supplement Series*, 60, 261
- Haynes, M.P., & Giovanelli 1984, *AJ*, 89, 758
- Haynes, M.P., *et al.* 1988, *AJ*, 95, 607
- Haynes, M.P., & Giovanelli 1991, *ApJS*, 77, 331
- Haynes, M.P., *et al.* 1997, *AJ*, 113, 1197
- Haynes, M. P., van Zee, L., Hogg, D. E., Roberts, M. S., & Maddalena, R. J. 1998, *AJ*, 115, 62
- Hoekstra, H., van Albada, T.S. & Sancisi, R. 2001, *MNRAS*, 323, 453
- Huizinga, J. E. & van Albada, T. S. 1992, *MNRAS*, 254, 677
- Jedrzejewski, R.I. 1987, *M.N.R.A.S.*, 226, 747

- Jiménez-Vicente, J., Battaner, E., Rozas, M. Castañeda, H., Porcel, C 1999, A&A, 342, 417
- Jiménez-Vicente, J., Battaner, E. 2000, A&A, 358, 812
- Jog, C.J. 1997, ApJ, 488, 642
- Jog, C.J. 1999, ApJ, 522, 661
- Jog, C.J. 2000, ApJ, 542, 216
- Junqueira, S., & Combes, F. 1996, A&A, 312, 703
- Kennicutt, R.C., Edgar, B.K., Hodge, P.W. 1989, Ap.J., 337, 761
- Kent, S.M. 1985, Ap.J.S., 59, 115
- Kent, S.M. 1986, Ap.J.S., 91, 1301
- Kormendy, J. 1977, Ap.J., 217, 406
- Kormendy, J. & Bruzual, A.G. 1978, Ap.J., L., 223, 63
- Kornreich, D. A., Haynes, M. P., & Lovelace, R. V. E. 1998, AJ, 116, 2154
- Kornreich, D. A., Haynes, M. P., Lovelace, R. V. E., & van Zee, L. 2000, AJ, 120, 139
- Kornreich, D. A., Haynes, M. P., Jore, K.P., Lovelace, R. V. E. 2001, AJ, 121, 1358
- Krabbe, A., Colina, L., Thatte, N. & Kroker, H. 1997, Ap.J., 476, 98
- Kranz, T., Slyz, A., Rix, H.W. 2001, astro-ph/0107239
- Kuijken, K. & Tremaine, S. 1994, Ap.J., 421, 178

- Lambas, D. G., Maddox, S. J., & Loveday, J. 1992, MNRAS, 258, 404
- Landolt, A.U. 1983, A. J., 88, 853
- Levine, S.E. & Sparke, L.S. 1998, Ap.J., L., 496, 13
- Lewis *et al.* 1985 ApJS, 59, 161
- Lewis 1987, ApJS, 63, 515
- Lu *et al.* 1993, ApJS, 88, 383
- Magrelli, G., Bettoni, D. & Galletta, G. 1992, MNRAS, 256, 500
- Mathewson, D.S., Ford, V.L., & Buchhorn, M. 1992, Ap.J.S., 81, 413
- Matthews, L.D., van Driel, W., Monnier-Ragaigne, D. 2000, A&A, 365, 1
- Matthews, L.D., van Driel, W., Gallagher, J.S. 1998, A. J., 116, 1169
- McGaugh, S.S. & de Blok, W.J.G. 1998, Ap.J., 499, 66
- Mo, H.J., Mao, S., & White, S.D.M. 1998, MNRAS, 295, 319
- Möllenhoff, C. & Heidt, J. 2001, A&A, 368, 16
- Moriondo, G., Giovanardi, C., Hunk, L.K. 1998, A&AS, 130, 81
- Navarro, J.F., Frenk, C.S. & White, S.D. 1996, Ap.J., 462, 563
- Navarro, J.F., Frenk, C.S. & White, S.D. 1997, Ap.J., 490, 493
- Paturel, G., *et al.* 1997, A&A Supplement Series, 124, 109
- Palunas, P., Williams, T.B. 2000, A. J., 120, 2884

- Petrosian, V. 1976, Ap.J., L., 209, L1
- Pierce, M.J. & Tully, R.B. 1988, Ap.J., 330, 579
- Pierce, M.J. & Tully, R.B. 1992, Ap.J., 387, 47
- Press, W.H., Flannery, B.P., Teukolsky, S.A. & Vetterling, W.T. 1992, Numerical Recipes  
(Cambridge: Cambridge Univ. Press)
- Prieto, M., Aguerri, J.A.L., Varela, A.M., Muñoz-Tunñón, C. 2001, A&A, 367, 405
- Raychaudhury, S., *et al.* 1997, A. J., 113, 2046
- Richter & Huchtmeier 1991, A&AS, 87, 425
- Richter, O. G. & Sancisi, R. 1994, A&A Letters, 290, L9
- Rix, H. W. & Zaritsky, D. 1995, ApJ, 447, 82
- Rix, H.W., Guhathakurta, P., Colless, M. & Ing, K. 1997, M.N.R.A.S., 285, 779
- Roberts, W.W. 1969, Ap.J., 158, 123
- Rozas, M., Zurita, A., Beckman, J.E., Pérez, D. 2000 A&AS, 142, 259
- Rubin *et al.* 1976, AJ, 81, 687
- Rubin, V.C., Ford, W.K. & Thonnard, N. 1980, Ap.J., 238, 471
- Rubin, V.C., Waterman, A.H., & Kenney, J.D.P. 1999, A. J., 118, 236
- Rudnick, G. & Rix, H. W. 1998, AJ, 116, 1163
- Rudnick, G., Rix, H.W. & Kennicutt, R.C. 2000; Ap.J., 538, 569



- Sandage, A. & Perelmuter, J.-M. 1991, *Ap.J.*, 370, 455
- Schade, D., Lilly, S.J., Crampton, D., Hammer, F., Le Fevre, O. & Tresse, L. 1995, *Ap.J.*, L., 451, L1
- Schlegel, D.J., Finkbeiner, D.P., Davis, M. 1998, *Ap.J.*, 500, 525
- Schneider *et al.* 1992, *ApJS*, 81, 5
- Schoenmakers, R. H. M., Franx, M., & De Zeeuw, P. T. 1997, *MNRAS*, 292, 349
- Schoenmakers, R. H. M. 1999, Ph.D. Thesis from Rijkuniversiteit Groningen, Netherlands
- Schombert, J.M. & Bothun, G.D. 1987, *AJ*, 93, 60
- Schommer, R.A., Bothun, G.D., Williams, T.B. & Mould, J.R. 1993, *A. J.*, 105, 97
- Sicking, F.J. 1997, Ph.D. Thesis from Rijkuniversiteit Groningen, Netherlands
- Simien, F. & de Vaucouleurs 1986, *Ap.J.* 428, 511
- Statler, T.S. 1994, *Ap.J.*, 425, 500
- Steinmetz, M. & Navarro, J. 1999, *Ap.J.*, 513, 550
- Steinmetz, M. & Navarro, J. 2000, *Ap.J.*, 538, 477
- Strauss, M.A. & Willick, J.A. 1995, *PhR*, 261, 271
- Swaters, R.A., Schoenmakers, R.H.M., Sancisi, R., van Albada, T.S. 1999, *MNRAS*, 304, 330

- Theureau *et al.* 1998, A&AS, 125, 409
- Theureau *et al.* 1998, A&AS, 130, 333
- Tully, R. B. & Fisher, J. R. 1977, A&A, 54, 661
- Tully, R. B. & Fouqué, P. 1985, Ap.J.S., 58, 67
- Tully, R.B., *et al.* 1998, A. J., 115, 2264
- van den Bosch, F.C. 2000, Ap.J., 530, 177
- van den Bosch, F.C., Burkert, A., Swaters, R.A. 2001, MNRAS, 326, 1205
- van den Bosch, F.C., Swaters, R.A. 2001, MNRAS, 325, 1017
- van der Hulst, J. P. Terlouw, K. Begeman, W. Zwitter and P.R. Roelfsema, 1992, ASPCS, 25, 131
- van der Kruit, P.C. 1995, IAU Symp. 164: Stellar Populations, p. 205
- van Driel *et al.* 1995, ApJ, 444, 80
- Verheijen, M.A.W. & Sancisi, R. 2001, A&A, 370, 765
- Verheijen, M.A.W. 2001, astro-ph/0108225
- Visser, H.C.D. 1980, A& A, 88, 149
- Vogelaar, M.G.R. & Terlouw, J.P. 2001, *to appear in* Astronomical Data Analysis Software and Systems X, eds. F. A. Primini, F.R. Harnden, Jr., H. E. Payne, ASPCS 25
- Weinberg, M.D. 1995, Ap.J., L., 445, 31

Willick, J.A. 1990, Ap.J., L., 351, 5

Willick, J.A. 1999, Ap.J., 516, 177

Zaritsky, D. & Rix, H. W. 1997, ApJ, 477, 118

# Vita

## David Roger Andersen

Born May 25, 1972, Milwaukee, Wisconsin, USA

### Education

Ph.D., Astronomy & Astrophysics, 2001, The Pennsylvania State University

B.A., Physics, Mathematics, Astronomy, 1995, University of Wisconsin – Madison

### Awards, Scholarships and Grants

NASA Graduate Student Research Proposal (GSRP) Fellow, 1999-2001

Sigma Xi Grant in Aid of Research Fellow, 1999

NASA Pennsylvania Space Grant Consortium Fellow, 1997-1998

National Science Foundation Graduate Fellowship Honorable Mention, 1997

National Science Foundation Graduate Fellowship Honorable Mention, 1996

Eberly College of Science Graduate Fellowship, 1995-1996

Admitted to  $\Phi$ BK Honors Fraternity, 1995

National Merit Scholarship Recipient, 1990-1994

### Selected Publications

Andersen, D.R., Bershadsky, M.A., Sparke, L.S., Gallagher, J.S., Wilcots, E.M. “The Measurement of Disk Ellipticity in Nearby Spiral Galaxies,” 2001, *Ap.J.*, L., 551, L131

Andersen, D.R., Bershadsky, M.A., Sparke, L.S., Gallagher, J.S., Wilcots, E.M., van Driel, W., Monnier-Ragaine, D. “H $\alpha$  Velocity Fields of Normal Spiral Disks,” 2001, in *Galaxy Disks and Disk Galaxies*, eds. J. Funes & S. Corsini, ASPCS 230, 267

Bershadsky, M.A., Andersen, D.R. “The Assembly and Evolution of Spiral Disks,” 2001, in *Galaxy Disks and Disk Galaxies*, eds. J. Funes & S. Corsini, ASPCS 230, 598

Bershadsky, M.A., Andersen, D.R. “The Evolution of Spiral Disks,” 2000, in *Dynamics of Galaxies*, eds F. Combes, G.A. Mamon, & V. Charmandaris, ASPCS 197, 175

Andersen, D.R., Bershadsky, M.A., “Galaxy Kinematics with Integral Field Spectroscopy,” 1999, *Galaxy Dynamics*, eds. D. Merritt, M. Valluri, J. Sellwood, ASPCS 182, 215

Andersen, D.R., Bershadsky, M.A., Ramsey, L.W., “Spider: The Formated Field Unit for the Hobby Eberly Telescope,” 1998, *BAAS*, 193, 1005

Bershadsky, M.A., Andersen, D.R., Ramsey, L.W., Horner, S.D., “Galaxy Kinematics with Integral Field Spectroscopy and the Hobby-Eberly Telescope,” 1999, *Fiber Optics in Astronomy III*, eds. S. Arribas, E. Mediavilla, F. Watson, ASPCS, 152, 253

Harlow, J.J.B., Ramsey, L.W., Andersen, D.R., Fleig, J.D., Rhoads, B.T., Engel, L.G., “The Upgraded Fiber Optic Echelle Spectrograph,” 1996, *BAAS*, 189, 4207

Andersen, D.R., Ögelman, H. “Search for Thermal Afterglow from PSR0656+14,” 1997, *ApJ*, 475, 300